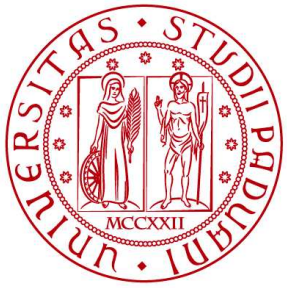

UNIVERSITÀ
DEGLI STUDI
DI PADOVA

Head office: Università degli Studi di Padova

Centro di Ateneo di Studi e Attività Spaziali "G. Colombo" - CISAS

---

Ph.D. COURSE IN: Scienze, Tecnologie e Misure Spaziali (STMS)

CURRICULUM: Scienze e Tecnologie per Applicazioni Satellitari e Aeronautiche (STASA)

CYCLE XXXVI

# AN IMPROVED PERIDYNAMIC FRAMEWORK FOR THE ACCURATE SOLUTION OF MULTI-PHYSICS PROBLEMS

**Coordinator:** *Ch.mo Prof. Francesco Picano*

**Supervisor:** *Ch.mo Prof. Ugo Galvanetto*

**Co-Supervisor:** *Ch.mo Prof. Mirco Zaccariotto*

**Ph.D. student:** *Francesco Scabbia*

To *Cori*,
*Maria Elena*,
and *Renato*

# Summary

Fracture phenomena can have severe consequences, such as human casualties and financial losses due to catastrophic failures in aerospace structures. High temperature gradients, hostile environmental actions, excessive mechanical loading, or extreme events are only a few of the possible causes of fracture. Experimental analysis of the fracture phenomenon in materials is costly as it requires the destruction of specimens or components under test. This is the reason why, in the last decades, many numerical tools have been developed to virtually simulate crack initiation and propagation.

Since cracks are, in mathematical terms, discontinuities in the displacement field, classical continuum mechanics is not suitable for modeling cracks due to the presence of spatial derivatives in the governing equations. Numerical methods, such as interface elements with cohesive zone modeling, extended finite element method, and phase field method, have been devised to equip the classical formulation with the capability of simulating fracture. However, each of these numerical methods exhibits some drawbacks. Peridynamics is a nonlocal continuum theory that reformulates the governing equations by replacing the spatial derivatives with integrals, so that cracks can be defined without mathematical inconsistencies. In peridynamic models, fracture is an intrinsic material response, and cracks can initiate, propagate, branch, or coalesce in the most energetically favorable paths, in agreement with experimental observations.

Peridynamics has some drawbacks that are typical of nonlocal models. The peridynamic surface effect is an undesired variation in the stiffness properties of the material in the region near the boundary of the body. This effect is due to the fact that the points close to the boundary have an incomplete integration domain. Furthermore, peridynamic boundary conditions should be imposed on a layer of finite thickness. However, since experiments provide only local measurements at the boundary of the domain, it is often desirable to impose local boundary conditions in a nonlocal model. Another shortcoming is that, since peridynamics is based on an integral operator, numerical integration plays a fundamental role in the discretization of these models. If the peridynamic integral operator is numerically evaluated in an inaccurate way, the numerical results may not converge to the analytical peridynamic solution. Finally, the computational cost of peridynamics models is higher than that of local models, because nodes interact at a larger distance.

The main objective of this work is to mitigate all the above-mentioned issues:

- The peridynamic surface effect has been analytically and numerically analyzed in ordinary state-based peridynamics, highlighting the characteristic hardening/softening behavior near the boundaries of a body (see Chapters 2 and 3).

- An algorithm for the numerical calculation of the peridynamic stress tensor and the force flux has been developed in 1D, 2D, and 3D models (see Chapters 2, 3 and 4).

- The Taylor-based extrapolation method with the nearest-node strategy has been developed to mitigate the peridynamic surface effect in bodies with a possibly complex geometry (see Chapters 2, 3 and 4). This method determines the displacements of the fictitious nodes introduced around the body as functions of the displacements of the nodes within the body.

- The surface node method has been devised to impose local boundary conditions in peridynamics models (see Chapter 4). The surface nodes are used to discretize the boundary of the body, and their motion is governed by the equation of the force flux.

- An efficient algorithm to accurately compute the quadrature weights in 2D and 3D peridynamic models has been developed (see Chapter 5). Using this algorithm, the numerical results show smaller errors and smoother convergence behavior.

- An improved coupling technique between peridynamics and Carrera unified formulation, a very efficient classical model based on the finite element method, has been devised to reduce the computational cost of the simulations (see Chapter 6).

All algorithms and numerical methods mentioned above were validated by many numerical examples.

Using this improved peridynamic framework, a specific fracture mechanism has been analyzed, namely the crack propagation due to oxidation of zirconium carbide and its subsequent volumetric expansion. Zirconium carbide is a very promising candidate for considerably improving the performance of nuclear reactors used in space missions or for green energy production. However, poor knowledge of the behavior of this material under oxidation hinders its use in nuclear applications. The volumetric expansion of zirconium oxide is in fact the cause of fragmentation and repeated delamination, a phenomenon that increases the oxidation rate.

This complex multi-physics problem has been solved by means of a peridynamic model, and the main results are the following:

- A new stability criterion of an explicit time integration method for the peridynamic diffusion equation has been derived with the eigenvalue technique (see Chapter 7). Unlike previous stability criteria, the new criterion takes into account the influence of the boundary conditions (applied with the surface node method) on numerical stability.

- Various convergence analyses have been conducted to study the impact of a discontinuity at the boundary in the initial conditions of a peridynamic diffusion problem, which describes the sudden exposure to oxygen of a zirconium carbide sample (see Chapter 7). If the very early times of the simulation are neglected, the convergence rate is the same as that of a peridynamic diffusion problem without discontinuities in the initial conditions.

- In a peridynamic diffusion model with a phase change (from carbide to oxide), the interface is autonomously moving depending only on the material properties, whereas a special condition at the interface, such as the Stefan condition, is required in classical models. The accuracy of the autonomous motion of the interface has been verified with a numerical example (see Chapter 7).
- The importance of two layers across the oxidation front, i.e., the intermediate layer and the transition layer, in the reaction mechanisms of zirconium carbide oxidation has been highlighted by the careful observation of experimental measurements (see Chapter 8).
- A peridynamic model of zirconium carbide oxidation has been developed and through a calibration process the diffusivity of zirconium oxide in the intermediate layer and the oxidation rate in the transition layer have been quantified (see Chapter 8).
- The novel peridynamic model of zirconium carbide oxidation is also able to predict the growth of the oxide and determine the shape and dimensions of the remaining unoxidized carbide (see Chapter 8).

The same modeling approach can also be used, after the appropriate recalibration of material properties, to simulate phenomena similar to zirconium carbide oxidation, such as oxidation of transition metal carbides of group IV and lithiation in solid-state batteries.

# Sommario

I fenomeni di frattura nei materiali possono causare delle gravi conseguenze, come morti umane e perdite finanziarie dovute a fallimenti catastrofici nelle strutture aerospaziali. Alcuni esempi delle possibili cause che provocano cricche sono gli alti gradienti di temperatura, i carichi meccanici eccessivi o gli eventi estremi. Tuttavia, l'analisi sperimentale di questi fenomeni di frattura è costosa visto che richiede la distruzione dei provini o dei componenti testati. Per questo motivo, molti metodi numerici sono stati sviluppati negli ultimi decenni per simulare in modo virtuale la propagazione delle cricche.

La meccanica classica del continuo non è adatta a modellare le cricche, ovvero discontinuità nel campo degli spostamenti, perché nelle equazioni che governano la deformazione del corpo sono presenti delle derivate rispetto alle coordinate spaziali. Per fornire alla formulazione classica la capacità di simulare fenomeni di frattura, sono stati sviluppati alcuni metodi numerici, come per esempio gli elementi di interfaccia modellati con una legge coesiva (*cohesive zone modeling*), il metodo generalizzato degli elementi finiti (*extended finite element method*) e il metodo del campo di fase (*phase field method*), ma ognuno di questi metodi manifesta degli svantaggi. Invece, la peridinamica è una teoria non locale del continuo che riformula le equazioni del moto sostituendo le derivate rispetto alle coordinate spaziali con degli integrali in modo tale che le cricche possano essere definite metamaticamente senza incongruenze. Infatti, la frattura nei modelli peridinamici è data da una risposta intrinseca del materiale, e le cricche possono avere origine, propagarsi, dividersi o unirsi nei percorsi più favorevoli a livello energetico. Per questa ragione, i risultati delle simulazioni peridinamiche riproducono in maniera eccellente le osservazioni sperimentali.

Tuttavia, la peridinamica ha degli svantaggi che sono tipici dei modelli non locali. Il primo è l'effetto peridinamico di superficie, una variazione indesiderata delle proprietà di rigidezza del materiale nella regione vicina al contorno del corpo. Questo effetto è dovuto al fatto che i punti del corpo vicino al contorno hanno un dominio di integrazione incompleto. Inoltre, le condizioni al contorno in peridinamica dovrebbero essere imposte su uno strato di materiale con uno spessore finito, contrariamente a quanto solitamente avviene negli esperimenti in cui si misurano le quantità di interesse solo sul contorno del dominio. Quindi, spesso c'è bisogno di imporre condizioni al contorno locali in un modello non locale. Un altro inconveniente è che l'integrazione numerica ha un ruolo fondamentale nella discretizzazione dei modelli peridinamici, dato che questa teoria è basata su un operatore integrale. Infatti, se l'operatore peridinamico è valutato in una maniera inaccurata, i risultati numerici potrebbero non convergere alla soluzione analitica peridinamica. Infine, il costo computazionale dei modelli peridinamici è più elevato rispetto a quello dei modelli locali

perché i nodi interagiscono ad una distanza maggiore.

L'obiettivo principale di questo lavoro è di mitigare tutti i problemi appena menzionati:

- L'effetto peridinamico di superficie è stato analizzato in modo analitico e numerico per la peridinamica ordinaria basata sugli stati (*ordinary state-based peridynamics*), evidenziando il comportamento caratteristico di aumento/riduzione della rigidezza vicino al contorno di un corpo (vedi Capitoli 2 e 3).

- È stato sviluppato un algoritmo per la valutazione numerica del tensore peridinamico delle tensioni e del flusso di forza per modelli 1D, 2D e 3D (vedi Capitoli 2, 3 e 4).

- Per mitigare l'effetto peridinamico di superficie in corpi con qualsiasi geometria (anche complessa), è stato sviluppato il metodo dell'estrapolazione basato sulla serie di Taylor con la strategia di usare i nodi più vicini (vedi Capitoli 2, 3 e 4). Questo metodo determina gli spostamenti dei nodi fittizi aggiunti intorno al corpo come funzioni degli spostamenti dei nodi interni al corpo.

- Il metodo dei nodi di superficie è stato ideato per imporre condizioni al contorno locali in modelli peridinamici (vedi Capitolo 4). I nodi di superficie sono usati per discretizzare il contorno del corpo e il loro moto è governato dall'equazione del flusso di forza.

- È stato sviluppato un algoritmo efficiente per il calcolo accurato dei pesi di quadratura per modelli peridinamici 2D e 3D (vedi Capitolo 5). Usando questo algoritmo, i risultati numerici mostrano errori minori e un miglior comportamento a convergenza.

- Per ridurre il tempo computazionale delle simulazioni, è stata sviluppata una tecnica migliorata di accoppiamento tra la peridinamica e la formulazione unificata di Carrera (*Carrera unified formulation*), un modello classico molto efficiente basato sul metodo degli elementi finiti (vedi Capitolo 6).

Tutti i metodi e gli algoritmi menzionati sono stati validati con molti esempi numerici.

Usando questi nuovi strumenti numerici nel contesto della peridinamica, è stata analizzata la propagazione di cricche causata dall'ossidazione del carburo di zirconio e dalla sua conseguente espansione volumetrica. Il carburo di zirconio è un materiale molto promettente, candidato per migliorare considerevolmente le prestazioni dei reattori nucleari usati per missioni spaziali o per la produzione di energia pulita. Tuttavia, la limitata conoscenza del comportamento di questo materiale durante l'ossidazione ne ostacola l'uso in applicazioni nucleari. Infatti l'espansione volumetrica dell'ossido di zirconio ne provoca la frammentazione, che a sua volta aumenta la velocità di ossidazione.

Questo complesso problema multifisico è stato risolto attraverso un modello peridinamico, e i principali risultati sono i seguenti:

- È stato derivato un nuovo criterio per la stabilità di un metodo esplicito per l'integrazione temporale dell'equazione peridinamica di diffusione grazie ad una tecnica basata sugli autovalori (vedi Capitolo 7). A differenza dei metodi usati in precedenza, il nuovo

criterio tiene conto dell'influenza delle condizioni al contorno (applicate con il metodo dei nodi di superficie) sulla stabilità numerica.

- Sono state condotte diverse analisi di convergenza per studiare l'impatto di una discontinuità, posizionata sul contorno, nelle condizioni iniziali di un problema peridinamico di diffusione che descrive un'esposizione improvvisa all'ossigeno di un provino di carburo di zirconio (vedi Capitolo 7). Se si trascurano i momenti iniziali della simulazione, la velocità di convergenza è la stessa di quella di un problema peridinamico di diffusione senza discontinuità nelle condizioni iniziali.

- In un modello peridinamico di diffusione con cambio di fase (da carburo ad ossido), l'interfaccia può muoversi autonomamente a seconda solamente delle proprietà dei materiali, mentre nei modelli classici c'è la necessità di avere una condizione particolare all'interfaccia, come la condizione di Stefan. Attraverso un esempio numerico è stata verificata l'accuratezza con cui il moto autonomo dell'interfaccia viene riprodotto dal modello peridinamico (vedi Capitolo 7).

- Grazie all'osservazione delle misurazione sperimentali, è stata evidenziata l'importanza dello strato intermedio e dello strato di transizione nel meccanismo di reazione dell'ossidazione del carburo di zirconio (vedi Capitolo 8).

- Attraverso lo sviluppo di un modello peridinamico per l'ossidazione del carburo di zirconio, la diffusività dell'ossido di zirconio nello strato intermedio e la velocità di ossidazione nello strato di transizione sono state calibrate per riprodurre i dati sperimentali (vedi Capitolo 8).

- Il nuovo modello peridinamico per l'ossidazione del carburo di zirconio è anche in grado di predire la crescita volumetrica dell'ossido e di determinare la forma e le dimensioni del carburo rimasto non ossidato (vedi Capitolo 8).

Lo stesso approccio di modellazione può essere usato anche, dopo un'appropriata ricalibrazione delle proprietà dei materiali, per simulare fenomeni simili all'ossidazione del carburo di zirconio, come l'ossidazione dei carburi di metalli di transizione del gruppo IV e la litiazione in batterie allo stato solido.

# Acknowledgements

In the first place, I wish to express my utmost gratitude to my supervisor, Professor Ugo Galvanetto, and my co-supervisor, Professor Mirco Zaccariotto, for their unwavering support throughout my Ph.D. journey, for their mentorship that has contributed to my growth as a researcher, and for their unceasing availability for our regular meetings and discussions, consistently accompanied by joyful faces and radiant smiles.

I am sincerely thankful to Professor Florin Bobaru for giving me the opportunity to stay at the University of Nebraska-Lincoln for 6 months and work in close contact with him. In that period I have learned a lot not only from his extensive knowledge and expertise but also from his tireless passion for research and his great kindness. A special thanks goes to Professor Adam Larios for the insightful discussions during the "peridynamic group" meetings.

I am deeply grateful to my colleague Marco Enea and his Ph.D. supervisors, Professor Alfonso Pagani and Professor Erasmo Carrera, for giving me the opportunity to collaborate with the MUL2 research group at Politecnico di Torino. I have been welcomed to Torino as a long-time member of the team, and their willingness to share the knowledge contributed significantly to my Ph.D. work.

All the results that I was able to obtain in these years would not have been achieved without the support of my better half, Cori, and my parents, Maria Elena and Renato. The presence of Cori at home has a calming and relaxing effect on my life, allowing me to carry out my work without side thoughts. I really appreciated her careful attention to my work-related talks about technical and non-technical topics, those moments were very helpful to protect my mind from overthinking and stress. I would like to express my heartfelt thanks to my parents for having taught me the desire of continuously improving myself, for always motivating me to do my best, and for supporting me in any possible way.

I am deeply thankful to my entire family, especially to my little brother Federico and my grandparents. Federico has always been my first fan, and his supportive and cheerful attitude encouraged me to give everything to achieve my goals. My grandparents have believed in me since the very beginning and have been an endless source of confidence and self-esteem, being extremely proud of me even before I achieved anything at all. A special thanks goes to my second family (Cori's family) for the carefree Sundays spent talking together and playing with my nephews.

Finally but not less importantly, I would like to thank my long-time friends, my basketball teammates and coaches, and my colleagues at the university, in Lincoln, and met at the conferences. All the conversations and laughter that we shared have played a fundamental role in my life.

# List of publications

## Papers

1. F. Scabbia, M. Zaccariotto, U. Galvanetto. "A novel and effective way to impose boundary conditions and to mitigate the surface effect in state-based Peridynamics". *International Journal for Numerical Methods in Engineering*, 2021, DOI: 10.1002/nme.6773.

2. F. Scabbia, M. Zaccariotto, U. Galvanetto. "A new method based on Taylor expansion and nearest-node strategy to impose Dirichlet and Neumann boundary conditions in ordinary state-based Peridynamics". *Computational Mechanics*, 2022, DOI: 10.1007/s00466-022-02153-2.

3. F. Scabbia, M. Zaccariotto, U. Galvanetto. "A new surface node method to accurately model the mechanical behavior of the boundary in 3D state-based peridynamics". *Journal of Peridynamics and Nonlocal Modeling*, 2023, DOI: 10.1007/s42102-022-00094-1.

4. F. Scabbia, M. Zaccariotto, U. Galvanetto. "Accurate computation of partial volumes in 3D peridynamics". *Engineering with Computers*, 2023, DOI: 10.1007/s00366-022-01725-3.

5. F. Scabbia, M. Enea. "An improved coupling of 3D state-based peridynamics with high-order 1D finite elements to reduce spurious effects at interfaces". *International Journal for Numerical Methods in Engineering*, 2023, DOI: 10.1002/nme.7297.

6. F. Scabbia, C. Gasparrini, M. Zaccariotto, U. Galvanetto, A. Larios, F. Bobaru. "Moving interfaces in peridynamic diffusion models and the influence of discontinuous initial conditions: Numerical stability and convergence". Accepted to *Computers and Mathematics with Applications*, 2023.

7. F. Scabbia, C. Gasparrini, M. Zaccariotto, U. Galvanetto, F. Bobaru. "A peridynamic model for oxidation and damage in zirconium carbide ceramics". Submitted to *Journal of Nuclear Materials*, 2023.

## Proceedings

1. F. Scabbia, M. Zaccariotto, U. Galvanetto. "An effective method for imposing peridynamic boundary conditions and mitigating the surface effect". *AIDAA XXVI International Congress*, August 31 and September 1-3, 2021, Pisa, Italy.

2. M. Enea, F. Scabbia, A. Pagani, M. Zaccariotto, E. Carrera, U. Galvanetto. "One-dimensional high order finite elements embedding 3D state-based peridynamic subdomains". *AIDAA XXVI International Congress*, August 31 and September 1-3, 2021, Pisa, Italy.

3. U. Galvanetto, F. Scabbia, M. Zaccariotto. "Accurate numerical integration in 3D meshless peridynamic models". *$8^{th}$ International Conference on Structural Engineering, Mechanics and Computation (SEMC)*, September 5-7, 2022, Cape Town, South Africa.

4. F. Scabbia, M. Zaccariotto, U. Galvanetto. "Exact computation of the cube-sphere intersection volume to improve peridynamic numerical integration". *$10^{th}$ International Conference on Design, Modelling and Experiments of Advanced Structures and Systems (DeMEASS2020)*, May 1-4, 2022, Scopello, Italy.

5. M. Enea, F. Scabbia, A. Pagani, M. Zaccariotto, E. Carrera, U. Galvanetto. "Analysis of beam structures by combined 3D peridynamics and refined 1D finite elements". *$10^{th}$ International Conference on Design, Modelling and Experiments of Advanced Structures and Systems (DeMEASS2020)*, May 1-4, 2022, Scopello, Italy.

6. F. Scabbia, M. Zaccariotto, U. Galvanetto, F. Bobaru. "Peridynamic simulation of elastic wave propagation by applying the boundary conditions with the surface node method". *III Aerospace PhD-Days*, April 16-19, 2023, Bertinoro, Italy.

7. F. Scabbia, M. Zaccariotto, U. Galvanetto. "Surface node method for the peridynamic simulation of elastodynamic problems with Neumann boundary conditions". *AIDAA XXVII International Congress*, September 4-7, 2023, Padova, Italy.

## Abstracts

1. U. Galvanetto, T. Ni, F. Pesavento, M. Zaccariotto, F. Scabbia, B.A. Schrefler. "Hybrid FEM and peridynamic simulation of hydraulic fracture propagation in saturated porous media". *Workshop on Experimental and Computational Fracture Mechanics (WFM)*, February 26-28, 2020, Baton Rouge, Louisiana, USA.

2. F. Scabbia, M. Zaccariotto, U. Galvanetto. "A note on the surface effect in OSB-PD models". *$3^{rd}$ annual meeting of the SIAM Texas-Louisiana Section*, October 16-18, 2020, College Station, Texas, USA.

3. U. Galvanetto, F. Scabbia, M. Zaccariotto. "How to reduce the surface effect and to apply the boundary conditions in 1D peridynamic models". *$16^{th}$ U.S. National Congress on Computational Mechanics*, July 25-29, 2021, virtual event.

4. F. Scabbia, M. Zaccariotto, U. Galvanetto. "An innovative method to manage non-local boundaries in ordinary state-based Peridynamics". *XVI International Conference on Computational Plasticity, Fundamentals and Applications (COMPLAS2021)*, September 7-9, 2021, Barcelona, Spain.

5. F. Scabbia, M. Zaccariotto, U. Galvanetto. "An innovative method to correct the boundary issues in Peridynamics". *$11^{th}$ European Solid Mechanics Conference (ESMC2022)*, July 4-8, 2022, Galway, Ireland.

6. F. Scabbia, M. Zaccariotto, U. Galvanetto. "On the imposition of non-local boundary conditions in Peridynamics to avoid undesired stiffness fluctuations". *$9^{th}$ GACM Colloquium on Computational Mechanics for Young Scientists from Academia and Industry (GACM2022)*, September 21-23, 2022, Essen, Germany.

7. F. Scabbia, M. Zaccariotto, U. Galvanetto. "How to improve the numerical integration in peridynamic models". *$10^{th}$ International Congress of Croatian Society of Mechanics (ICCSM2022)*, September 28-30, 2022, Pula, Croatia.

8. U. Galvanetto, F. Scabbia, M. Zaccariotto. "A method to reduce the surface effect and to impose in a local way the BC in Peridynamics models". *Society of Engineering Science Annual Technical Meeting (SES2022)*, October 16-19, 2022, College Station, Texas, USA.

9. U. Galvanetto, F. Scabbia, M. Zaccariotto. "On the surface effect and the imposition of the BC in Peridynamics". *Conference on Computational Science and Engineering (CSE2023)*, February 27-28 and March 1-3, 2023, Amsterdam, Holland.

10. M. Zaccariotto, F. Scabbia, U. Galvanetto. "A unified strategy to mitigate the surface effect and to impose in a local way the boundary conditions in Peridynamics models". *$7^{th}$ International Conference on Computational Modeling of Fracture and Failure of Materials and Structures (CFRAC2023)*, June 21-23, 2023, Prague, Czech Republic.

11. U. Galvanetto, T. Ni, F. Scabbia, A. Pirzadeh, M. Zaccariotto. "New trends in applied computational peridynamics". *NanoInnovation Conference and Exhibition 2023*, September 18-22, 2023, Rome, Italy.

# Contents

# Chapter 1

# Introduction

## 1.1 Motivation

Fracture phenomena can have severe consequences, such as human casualties and financial losses. For example, large structures in civil engineering may collapse due to a variety of concurrent causes, such as fatigue, corrosion, lack of maintenance, and design deficiencies. Unfortunately, there are many tragic examples of structural failure throughout history. The Tacoma Narrows Bridge collapsed in 1940 after four months from its completion due to excessive oscillations caused by dynamic wind loading [1]. In 1967, the collapse of the Silver Bridge due to the cleavage failure of an eyebar resulted in the deaths of 46 people [2]. More recently, in August 2018, a section of the Morandi Bridge in Italy broke down, killing 43 people [3].

In aerospace engineering, the integrity of aircrafts must be assessed in scheduled inspections to ensure passenger safety. However, no information about the status of the aircraft is available in-between the inspections, which can result in an unexpected catastrophic failure. In this regard, several flight accidents occurred due to structural failures, such as Aloha Airlines Flight 243 in 1988 [4], American Airlines Flight 587 in 2001 [5], and Southwest Airlines Flight 1380 in 2018 [6]. Furthermore, each aircraft has to be grounded for several hours/days during inspections, with a consequent significant financial loss.

In certain specific applications, fracture can even be caused intentionally to obtain beneficial results. For example, hydraulic fracturing, also called "fracking", consists of drilling a well and injecting a high-pressure fluid to promote fracture in the underground rocks [7, 8]. This controlled fracture process allows one to increase the flow of natural gas or oil from the reservoirs. To improve the durability of large concrete structures, artificial punchouts can be intentionally introduced in order to control crack propagation and accommodate thermal expansion and contraction and drying shrinkage, such as in concrete pavements [9, 10]. Another example in which fracture is induced by strategically placing explosives is the controlled demolition of buildings [11]. Furthermore, fracture plays a fundamental role in many industry processes, such as in cutting and machining [12].

In this thesis, a specific fracture mechanism will be analyzed, namely the crack propagation due to volumetric expansion. For example, in the oxidation of zirconium carbide, the change of phase leads to a considerable volume dilatation that generates stresses and

fractures in the material. Zirconium oxide is indeed subjected to fragmentation and repeated delamination, a phenomenon that increases the oxidation rate [13, 14]. When this phenomenon is better understood and appropriate countermeasures for safety are taken, the zirconium carbide will allow considerably improved performance of nuclear reactors used in space missions or for green energy production. A similar mechanism is responsible for the relatively low number of life cycles of solid-state batteries: lithium intercalation induces an extreme volume expansion that may end in the fracture of the battery electrodes [15, 16].

As the above-mentioned examples may suggest, fracture phenomena can be very hard to fully understand because of many factors that can be their cause, such as high temperature gradients, hostile environmental actions, excessive mechanical loading, or extreme events. Experimental analysis of the fracture phenomenon in materials is costly as it requires the destruction of specimens or components under test. Furthermore, fracture experiments are often affected by poor repeatability. Some analytical solutions to fracture problems are available, but they are limited to particular geometries and loadings of the samples. Therefore, the preferred way to analyze fracture phenomena is by using numerical methods to model crack initiation and propagation. If possible, the numerical results of the virtual simulation should be validated by a few specific experiments, decreasing the number of broken samples and, therefore, the overall cost.

The numerical methods most commonly used to simulate fracture are briefly reviewed in the following section.

### 1.1.1 Numerical modeling of fracture: from classical mechanics to peridynamics

Classical Continuum Mechanics (CCM) relies on partial differential equations to model the structural behavior of a body. The most popular method to solve complex structural problems is to adopt a weak formulation of the equilibrium equations discretized with the Finite Element Method (FEM) [17, 18]. However, all methods based on CCM use spatial derivatives of the displacement field in their formulation of the governing equations of motion. These spatial derivatives are difficult to defined where discontinuities, such as cracks, appear in the displacement field. For this underlying reason, classical continuum mechanics is not suitable for modeling fracture and some ad-hoc strategies must be adopted to handle discontinuities in those methods. Hereinafter, the most used extensions of CCM to model fracture are presented:

- *Element deletion* (or *erosion*) [19–21]: the stiffness of elements with sufficiently large strains is considerbly reduced, so that those elements no longer contribute to the stiffness of the body. In other words, elements subjected to strains larger than a critical predefined value are "deleted" as if a crack passed through those elements. However, their mass and inertia are retained in the model. Although element erosion is the simplest method to simulate fracture in FEM models, the crack path is affected by extreme mesh sensitivity [22].

- *Interface elements with cohesive zone modeling* [23–25]: interface elements governed

by a traction-separation law are introduced at the boundaries of finite elements. These interface elements can be thought of as a (deformable and, eventually, breakable) "glue" in-between the finite elements. However, since cracks are forced to propagate along finite element boundaries, this method exhibits a strong mesh dependency [26, 27]. This is the reason why interface elements are often used when the crack path is known a-priori.

- *Extended Finite Element Method* (XFEM) [28–31]: this method uses additional discontinuous enrichment functions in the finite elements along the crack surfaces and near the crack tip to model such singularities in the displacement field. XFEM allows the crack to pass through the elements by tracking its path with a level set function, preventing in this way the high mesh sensivity for the crack path typical of the element deletion method and the use of interface elements. Nevertheless, the implementation of XFEM can lead to arbitrarily ill-conditioned stiffness matrices [32–35] and a deterioration of the convergence rate due to the loss of the partition of unity property in the so-called *blending elements*, i.e., the elements adjacent to enriched elements [36–38]. More importantly, cracks of length approaching the element size cannot be accurately represented [39], such as in the case of crack nucleation. In addition to that, multiple crack coalescing or branching (splitting of the crack into two separate cracks) require special treatments in the XFEM formulation [40–45], and no reliable crack branching criteria are available. Furthermore, the material fracture energy has to be modified to properly reproduce the crack propagation speed obtained in the experimental observations [22].

- *Phase field method* [46–52]: to avoid the problem of tracking the path of the crack, fracture is modeled as a diffuse crack by means of a damage variable, called the "phase field", that has a gradual transition from intact material to fractured regions. This unknown damage variable is introduced as an extra degree of freedom for each node and is determined by solving partial differential equations based on the variational principle that crack propagation should follow the path of least energy. The introduction of a regularization parameter, i.e., a length scale, in the fracture model allows to avoid the lack of convergence under grid refinement of other classical methods [48]. The phase field method is characterized by high computational costs, since, in the vicinity of cracks, the mesh size should be less than half of the regularization parameter [53, 54]. Crack nucleation, branching, and coalescing are modeled with some success by this method, even though branching phenomena are obtained when they are not observed in the experiments, such as in the Kalthoff-Winkler test in [55]. Moreover, the angle of crack propagation does not accurately match that observed in the experiments, such as in the Kalthoff-Winkler test [56] and in a branching test [57]. The most likely reason for these inconsistencies is that, in phase field models, damage keeps growing in time perpendicularly to the crack direction, even where stresses have already been released because of the crack propagation itself. The "thickening" of the cracks can be seen, for example, in the numerical results of [57–59].

An extensive review of these and other possible methods that can be used to model fracture

can be found in [60].

To overcome the limitations of classical continuum mechanics, the peridynamic theory was devised in 2000 by Silling [61]. Peridynamics (PD) is a nonlocal continuum theory that reformulates the governing equations by replacing the spatial derivatives with integrals over a finite-radius spherical region [61–64]. Peridynamic models consider long-range interactions, called "bonds", between material points. Bonds are allowed to break when their deformation exceeds a predefined limit based on the material fracture energy [65]. With this simple fracture criterion, any complex crack pattern, such as crack initiation, coalescence, branching, and kinking, can be modeled with ease. For example, crack branching, including crack propagation speed, has been successfully reproduced in [66–68]. The angle of crack propagation observed experimentally in the Kalthoff-Winkler test has been obtained with the PD numerical model in [69]. The improved ability of the PD models to reproduce realistic crack paths is shown compared to those of the interface elements with cohesive zone modeling and XFEM in [70] and compared to that of the phase field method in [57].

Peridynamics has been successfully applied to a wide range of fracture problems under quasi-static [71–73] and dynamic [66–68, 74] conditions. PD numerical results of impact problems exhibit complex fragmentation patterns similar to those observed in the experiments [75–83]. Fatigue phenomena can be modeled with peridynamics as well [84–86]. It is worth noting that both brittle [87–90] and ductile [91–94] fractures have been simulated in the peridynamic framework.

Anisotropic materials have also been modeled with peridynamics [95–99]. Furthermore, a stochastic homogenization technique has been developed to model fracture in heterogeneous media [100–103]. Notable results have been obtained for specific materials, such as concrete [104–108], composites [109–115], geomaterials [116–119], and biomaterials [120–123].

Peridynamics has been used to reformulate partial differential equations governing various phenomena, including transient heat conduction (or diffusion) [124–126], viscous fluid flow [127], corrosion [128–131], and fluid flow in a porous medium [132, 133]. In these peridynamic reformulations, discontinuities can be included without any mathematical inconsistency. Peridynamics has demonstrated its capabilities in handling multi-physics problems involving fracture, such as thermo-mechanical [134, 135], mechano-chemical [136–138], electro-mechanical [139–143], and poro-elastic [144] problems.

A broad review of possible applications of peridynamic theory is given in [145], which also highlights the exponential growth in time of citations of the first article about peridynamics, testifying the increasing interest of the academic community in this field.

### 1.1.2 Scope of the work

The nonlocal nature of the peridynamic theory allows one to model with ease crack initiation and propagation. However, peridynamics suffers from some drawbacks that are typical of nonlocal models:

- the so-called *PD surface effect*, an undesired stiffness variation near the boundary of the body;

- the problems of imposing local boundary conditions in a nonlocal model;
- the need for an accurate numerical integration of the peridynamic equations;
- the high computational cost due to the large number of interactions between material points.

These issues are explained in detail in Section 1.2.5.

This work aims to mitigate all these issues. The Surface Node Method (SNM) has been devised to reduce (and, under some conditions, completely eliminate) the PD surface effect and to accurately impose local boundary conditions in peridynamic models (see Section 1.3.1). A novel algorithm to compute PD quadrature coefficients and improve the accuracy of numerical results has been developed (see Section 1.3.2). The coupling of peridynamics with an advanced FEM formulation, namely the Carrera Unified Formulation (CUF), has been realized, so that regions in which cracks are not likely to propagate can be modeled with CUF, resulting in an enhanced computational efficiency (see Section 1.3.3).

This improved peridynamic framework has been then used to model the complex multiphysics phenomenon of the oxidation of zirconium carbide (ZrC), a very promising candidate for being used as a coating in the next-generation of nuclear reactors. The zirconium oxide undergoes a large volumetric expansion compared to ZrC, which results in the propagation of cracks and repeated delaminations of the oxide from the bulk of the material. Therefore, cracks become preferential paths for the oxygen to diffuse within the ZrC, increasing in this way the oxidation rate. Since cracks play a fundamental role in ZrC oxidation, a reliable numerical tool, such as peridynamics, is required to faithfully reproduce the experimental observations of this phenomenon (see Section 1.3.4).

The structure of the thesis is as follows. Section 1.2 presents an overview of the peridynamic theory, its numerical discretization, and the description of the main drawbacks. Section 1.3 describes the original contributions to the peridynamic framework. Chapters 2, 3, and 4 are the three papers that explain the surface node method, a new method to mitigate the surface effect and impose boundary conditions in peridynamic models. Chapter 5 is the paper that describes the algorithm for the accurate numerical integration of peridynamic equations. Chapter 6 is the paper that presents the coupling between peridynamics and the FEM-based Carrera unified formulation. Chapters 7 and 8 are the papers that, respectively, delve into the numerical aspects and the phenomenological modeling of ZrC oxidation within the improved peridynamic framework. Chapter 9 concludes the work with the final remarks and proposes precise future research activities.

## 1.2 Overview of the peridynamic theory

On the one hand, the equation of motion in classical continuum mechanics for a point $\mathbf{x}$ at time $t \geq 0$ is given as

$$\rho(\mathbf{x})\,\ddot{\mathbf{u}}(\mathbf{x},t) = \nabla \cdot \boldsymbol{\sigma}(\mathbf{x},t) + \mathbf{b}(\mathbf{x},t) \tag{1.1}$$

where $\rho$ is the density of the material, $\ddot{\mathbf{u}}$ is the acceleration field, $\nabla \cdot \boldsymbol{\sigma}$ is the divergence of the Cauchy stress tensor, and $\mathbf{b}$ is the external force density. The constitutive law relates the Cauchy stress tensor $\boldsymbol{\sigma}$ to the strain tensor $\boldsymbol{\varepsilon}$, that contains the derivatives of the displacement field. Hence, Equation 1.1 is a partial differential equation that, together with appropriate boundary conditions, governs the mechanical behavior of continuous materials.

On the other hand, the equation of motion at a point $\mathbf{x}$ at time $t \geq 0$ in a body $\mathcal{B}$ modeled with peridynamics is given by [61, 62]

$$\rho(\mathbf{x})\, \ddot{\mathbf{u}}(\mathbf{x}, t) = \int_{\mathcal{H}_\mathbf{x}} \mathbf{f}(\mathbf{x}, \mathbf{x}', t)\, \mathrm{d}V_{\mathbf{x}'} + \mathbf{b}(\mathbf{x}, t)\,, \tag{1.2}$$

where $\mathbf{f}$ is the force state (force per unit volume squared), $\mathcal{H}_\mathbf{x}$ is the finite-size integration region around point $\mathbf{x}$, and $V_{\mathbf{x}'}$ is the volume of a point $\mathbf{x}'$ within $\mathcal{H}_\mathbf{x}$. It is worth noting that the force state $\mathbf{f}$ depends on the displacement field but not on its derivatives.

Comparing Equations 1.1 and 1.2, it is evident that the divergence of the stress tensor in classical continuum mechanics was replaced by the integral over a region of finite size. In other words, the classical formulation involving the derivatives of the displacement field was replaced by an integral formulation that depends solely on the displacement field. This fact is of paramount importance because the peridynamic formulation of the equation of motion (Equation 1.2) is valid regardless the presence of discontinuities in the displacement field. Peridynamics is therefore suitable to model crack initiation and propagion without any mathematical inconsistencies, which is not true for methods based on classical continuum mechanics.

The peridynamic theory (from the Greek word *peri*, which means "nearby") was devised by Silling in 2000. The first version of peridynamics, called *bond-based* peridynamics, relies on pairwise interaction forces between material points [61]. However, bond-based models have the limitation that Poisson ratio has a fixed value (1/4 in 3D and 2D plane strain models, 1/3 in 2D plane stress models [146]). To overcome this issue, the second version of peridynamics, called *state-based* peridynamics, was developed [62]. The interaction forces in state-based peridynamics depend on the collective deformation of the bonds within the neighborhood. The details of the two versions of the peridynamic theory are explained in the following sections.

Figure 1.1 shows a body modeled with peridynamics that is subjected to a displacement field $\mathbf{u}$. The interaction between $\mathbf{x}$ and $\mathbf{x}'$ is named *bond* and is identified by the relative position vector between the two points in the reference (or initial) configuration:

$$\boldsymbol{\xi} = \mathbf{x}' - \mathbf{x}\,. \tag{1.3}$$

The integration region $\mathcal{H}_\mathbf{x}$ in Equation 1.2, called the *neighborhood*, is chosen to be a segment, a circle, and a sphere in 1D, 2D, and 3D models, respectively. The neighborhood is the set of all points that interact with the *source point* $\mathbf{x}$ and is defined as

$$\mathcal{H}_\mathbf{x} = \left\{ \mathbf{x}' \in \mathcal{B}(t=0) : \|\mathbf{x}' - \mathbf{x}\| \leq \delta \right\}, \tag{1.4}$$

where $\delta > 0$, named *horizon size*, is the radius that represents the largest distance at which two points can interact. The points within the neighborhood are often called *family points*.

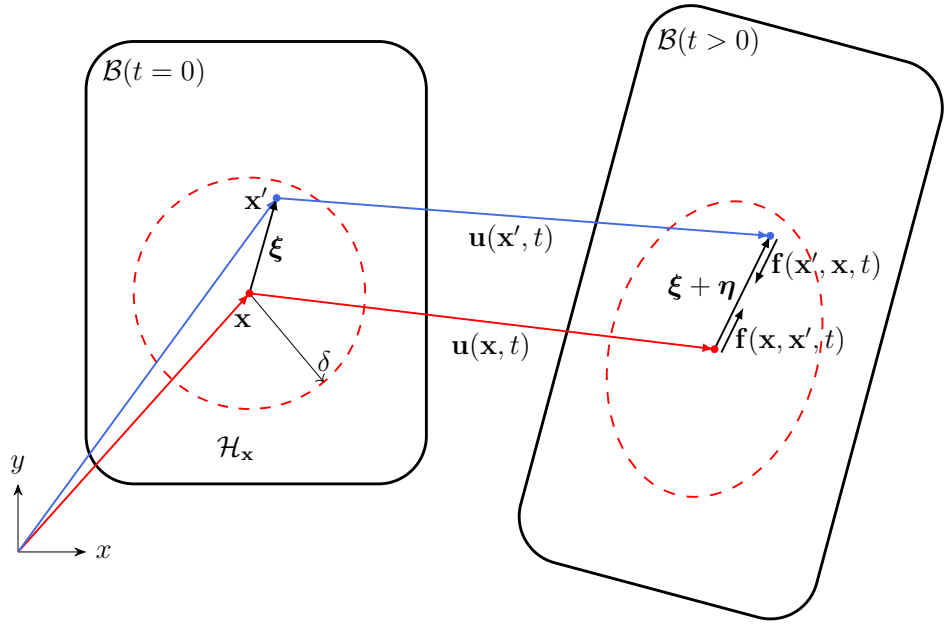


Figure 1.1: *Body modeled with peridynamics in the reference configuration* $\mathcal{B}(t=0)$ *and deformed configuration* $\mathcal{B}(t>0)$.

In the deformed configuration of the body (see Figure 1.1), the points $\mathbf{x}$ and $\mathbf{x}'$ are, in general, displaced differently. The relative displacement vector of the bond $\boldsymbol{\xi}$ is denoted by

$$\boldsymbol{\eta} = \mathbf{u}(\mathbf{x}',t) - \mathbf{u}(\mathbf{x},t)\,. \tag{1.5}$$

Note that $\boldsymbol{\xi}+\boldsymbol{\eta}$ represents the bond in the deformed configuration, as shown in Figure 1.2. When the body is deformed, internal forces, called force states, arise in the bonds to restore the overall equilibrium with the inertial and external forces, as dictated in Equation 1.2.

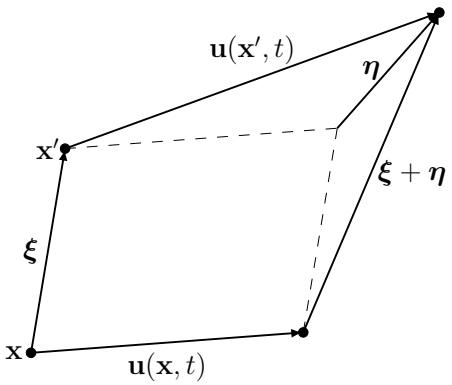


Figure 1.2: *Representation of the bond* $\boldsymbol{\xi}$ *and its deformed state* $\boldsymbol{\xi}+\boldsymbol{\eta}$.

For simplicity's sake, we consider from now on the peridynamic equilibrium equation

under quasi-static conditions:

$$-\int_{\mathcal{H}_{\mathbf{x}}} \mathbf{f}(\mathbf{x},\mathbf{x}')\,\mathrm{d}V_{\mathbf{x}'} = \mathbf{b}(\mathbf{x})\,. \tag{1.6}$$

The dependence on time can be reintegrated with straightforward considerations. It is worth noting that the difference between bond-based and state-based peridynamics lies in the different formulations of the force states of the bonds.

### 1.2.1 Bond-based peridynamics

The bond-based peridynamic theory was presented by Silling in 2000 [61]. Bond-based peridynamics is a special case of state-based peridynamics when the value of the Poisson ratio is 1/4 in 3D and 2D plane strain models or 1/3 in 2D plane stress models [147]. This reveals the intrinsic limitation of the bond-based formulation: the Poisson ratio cannot be arbitrarily chosen in the model but it is limited to the previously mentioned values. However, bond-based peridynamics is much simpler and computationally efficient than state-based peridynamics. Therefore, the use of bond-based peridynamics is recommended when the Poisson ratio has little or no influence on the final results.

#### Pairwise force

In bond-based peridynamics, the force state $\mathbf{f}$ is formulated as a pairwise force between the points of the bond [61]. A first restriction on the pairwise force is given by Newton's third law:

$$\mathbf{f}(\mathbf{x},\mathbf{x}') = -\mathbf{f}(\mathbf{x}',\mathbf{x})\,. \tag{1.7}$$

In words, the interaction force that point $\mathbf{x}$ exerts on $\mathbf{x}'$ has the same magnitude and opposite direction of the force that $\mathbf{x}'$ exerts on $\mathbf{x}$. Furthermore, the conservation of angular momentum yields

$$(\boldsymbol{\xi}+\boldsymbol{\eta}) \times \mathbf{f}(\mathbf{x},\mathbf{x}') = \mathbf{0}\,. \tag{1.8}$$

Hence, the second restriction is that the pairwise force is aligned with the deformed bond at any time. The unit vector in the direction of the deformed bond is defined as

$$\mathbf{m} = \frac{\boldsymbol{\xi}+\boldsymbol{\eta}}{\|\boldsymbol{\xi}+\boldsymbol{\eta}\|}\,. \tag{1.9}$$

In bond-based peridynamics, a material is defined as microelastic if it satisfies the following condition [61]:

$$\oint_{\Gamma} \mathbf{f}(\mathbf{x},\mathbf{x}')\,\mathrm{d}\mathbf{x}' = \mathbf{0}\,, \tag{1.10}$$

where $\Gamma$ is any closed curve and $\mathrm{d}\mathbf{x}'$ represents the differential vector path length along $\Gamma$. Similarly to the definition of elasticity in classical continuum mechanics, the condition in Equation 1.10 means that no net work, due to the interaction with a fixed point $\mathbf{x}$, is done on any material point $\mathbf{x}'$ moving along any closed path.

Since in this work we consider only homogeneous isotropic materials, the pairwise force can be also expressed as a function of the relative position and relative displacement vectors: $\mathbf{f}(\boldsymbol{\xi}, \boldsymbol{\eta})$. As a consequence of the microelasticity condition in Equation 1.10, there exists a differentiable scalar-valued function $w$, named *micropotential*, such that

$$\mathbf{f}(\boldsymbol{\xi}, \boldsymbol{\eta}) = \frac{\partial w(\boldsymbol{\xi}, \boldsymbol{\eta})}{\partial \boldsymbol{\eta}} \,. \tag{1.11}$$

In bond-based peridynamics, the linearized pairwise force for a microelastic material subjected to a displacement field such that $\|\boldsymbol{\eta}\| \ll \|\boldsymbol{\xi}\|$ is given, omitting errors of order $\mathcal{O}(\|\boldsymbol{\eta}\|^2)$, as [61]

$$\mathbf{f}(\boldsymbol{\xi}, \boldsymbol{\eta}) = \frac{\partial \mathbf{f}(\boldsymbol{\xi}, \mathbf{0})}{\partial \boldsymbol{\eta}} \, \boldsymbol{\eta} = \mathbf{C}(\boldsymbol{\xi}) \, \boldsymbol{\eta} \,, \tag{1.12}$$

where *micromodulus function* $\mathbf{C}(\boldsymbol{\xi})$ is a second-order tensor. From the condition on the pairwise force in Equation 1.7, the micromodulus function complies with the following restriction:

$$\mathbf{C}(\boldsymbol{\xi}) = \mathbf{C}(-\boldsymbol{\xi}) \,. \tag{1.13}$$

Furthermore, the micromodulus function is symmetric in a linear microelastic material:

$$\mathbf{C}(\boldsymbol{\xi}) = \mathbf{C}^{\top}(\boldsymbol{\xi}) \,. \tag{1.14}$$

The *prototype microelastic brittle* material model [65] is a simple and effective constitutive model to naturally incorporate fracture in the formulation. Bonds can be thought of as linear springs that can break if they exceed their maximum strain. The *bond stretch*, equivalent to the strain of the bond, is defined as [65]

$$s(\boldsymbol{\xi}, \boldsymbol{\eta}) = \frac{\|\boldsymbol{\xi} + \boldsymbol{\eta}\| - \|\boldsymbol{\xi}\|}{\|\boldsymbol{\xi}\|} \,. \tag{1.15}$$

Note that the definition of bond stretch is different from the definition of strain given in classical continuum mechanics in the fact that it does *not* involve spatial derivatives of the displacement field. In a prototype microelastic brittle material, the pairwise force depends on the bond stretch such that [65]

$$\mathbf{f}(\boldsymbol{\xi}, \boldsymbol{\eta}) = c(\boldsymbol{\xi}) \, \mu(\boldsymbol{\xi}, \boldsymbol{\eta}) \, s(\boldsymbol{\xi}, \boldsymbol{\eta}) \, \mathbf{m} \,, \tag{1.16}$$

where $c$ is the *micromodulus*, that is the stiffness of the bond, $\mathbf{m}$ is the unit vector in the direction of the deformed bond, and $\mu$ is a history-dependent scalar-valued function to introduce the concept of broken bonds:

$$\mu(\boldsymbol{\xi}, \boldsymbol{\eta}) = \begin{cases} 1 & \text{if } s(\boldsymbol{\xi}, \boldsymbol{\eta}) < s_0 \text{ for any previous or current } \boldsymbol{\eta} \,, \\ 0 & \text{otherwise,} \end{cases} \tag{1.17}$$

where $s_0$ is the critical bond stretch. This means that, as soon as the stretch in a bond exceeds the critical stretch, that bond is considered irreversibly broken and the pairwise

force between the interacting points is no longer present. The magnitude of the pairwise force in a prototype microelastic brittle material as a function of the bond stretch is shown in Figure 1.3.

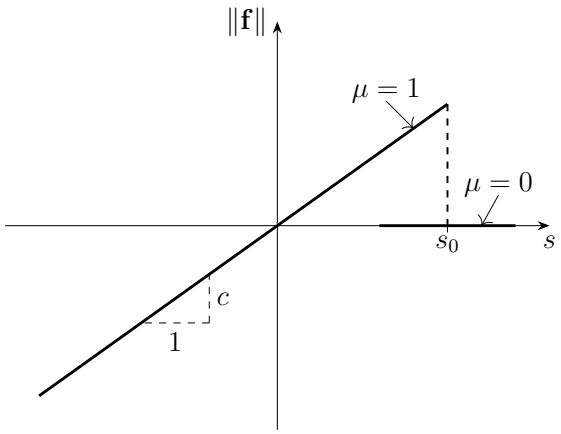


Figure 1.3: *Magnitude of the pairwise force as a function of the bond stretch in a prototype microelastic brittle material* [65].

Under the assumption of a displacement field such that $\|\boldsymbol{\eta}\| \ll \|\boldsymbol{\xi}\|$, the bond stretch and the bond direction vector can be simplified respectively as $s = (\boldsymbol{\eta} \cdot \mathbf{m})/\|\boldsymbol{\xi}\|$ and $\mathbf{m} = \boldsymbol{\xi}/\|\boldsymbol{\xi}\|$. Therefore, the pairwise force can be expressed as

$$\mathbf{f}(\boldsymbol{\xi}, \boldsymbol{\eta}) = c(\boldsymbol{\xi})\, \mu(\boldsymbol{\xi}, \boldsymbol{\eta})\, \frac{\boldsymbol{\eta} \cdot \mathbf{m}}{\|\boldsymbol{\xi}\|}\, \mathbf{m} = \frac{c(\boldsymbol{\xi})}{\|\boldsymbol{\xi}\|}\, \mu(\boldsymbol{\xi}, \boldsymbol{\eta})\, (\mathbf{m} \otimes \mathbf{m})\, \boldsymbol{\eta} = \mu(\boldsymbol{\xi}, \boldsymbol{\eta})\, \mathbf{C}(\boldsymbol{\xi})\, \boldsymbol{\eta}\,, \tag{1.18}$$

where "$\otimes$" stands for the dyadic product between two vectors. For simplicity's sake, the micromodulus is often chosen as a constant: $c(\boldsymbol{\xi}) = c$.

### Calibration of micromodulus

The micromodulus in bond-based peridynamic models is often calibrated in such a way as to obtain, under homogeneous isotropic deformation, the same strain energy density as in classical continuum mechanics. The strain energy density at a point $\mathbf{x}$ of a homogeneous isotropic linear elastic solid under homogeneous isotropic deformation $\varepsilon$, for a Poisson ratio equal to 1/4 in 3D and 2D plane strain models and 1/3 in 2D plane stress models (due to the limitations of bond-based peridynamics [146]), is given as

$$W_{cl}(\mathbf{x}) = \begin{cases} 3E\,\varepsilon^2 & \text{in 3D,} \\ \dfrac{8E}{5}\,\varepsilon^2 & \text{in 2D plane strain,} \\ \dfrac{3E}{2}\,\varepsilon^2 & \text{in 2D plane stress,} \\ \dfrac{E}{2}\,\varepsilon^2 & \text{in 1D,} \end{cases} \tag{1.19}$$

where $E$ is the Young modulus of the material.

The peridynamic strain energy density at a material point $\mathbf{x}$ can be computed from the micropotential as [61]

$$W(\mathbf{x}) = \frac{1}{2}\int_{\mathcal{H}_\mathbf{x}} w(\boldsymbol{\xi},\boldsymbol{\eta})\,\mathrm{d}V_{\mathbf{x}'}\,, \tag{1.20}$$

where the factor $1/2$ appears because the energy density of a bond is shared equally between the two interacting points. For a body under homogeneous isotropic deformation $\varepsilon$, the bond stretch $s$ is a constant for any bond and $\boldsymbol{\eta} = \varepsilon\boldsymbol{\xi} = \varepsilon\|\boldsymbol{\xi}\|\mathbf{m}$. Therefore, by combining Equations 1.11 and 1.18 for an unbroken bond ($\mu = 1$), the micropotential can be computed as

$$w(\boldsymbol{\xi},\boldsymbol{\eta}) = \int \mathbf{f}(\boldsymbol{\xi},\boldsymbol{\eta})\cdot\mathrm{d}\boldsymbol{\eta} = \int \left[\frac{c}{\xi}\,(\mathbf{m}\otimes\mathbf{m})\,\varepsilon\xi\mathbf{m}\right]\cdot\xi\mathbf{m}\,\mathrm{d}\varepsilon = \frac{c\,\varepsilon^2\,\xi}{2}\,, \tag{1.21}$$

where $\xi = \|\boldsymbol{\xi}\|$ and $\eta = \|\boldsymbol{\eta}\|$. Hence, by using spherical and polar coordinates, respectively, in 3D and 2D, the peridynamic strain energy density is given as

$$W(\mathbf{x}) = \begin{cases} \dfrac{1}{2}\displaystyle\int_0^\delta \frac{c\,\varepsilon^2\,\xi}{2}\,4\pi\xi^2\,\mathrm{d}\xi = \frac{\pi\,c\,\varepsilon^2\,\delta^4}{4} & \text{in 3D,} \\[2ex] \dfrac{1}{2}\displaystyle\int_0^\delta \frac{c\,\varepsilon^2\,\xi}{2}\,2\pi t\xi\,\mathrm{d}\xi = \frac{\pi\,t\,c\,\varepsilon^2\,\delta^3}{6} & \text{in 2D,} \\[2ex] \dfrac{1}{2}\displaystyle\int_0^\delta \frac{c\,\varepsilon^2\,\xi}{2}\,2A\,\mathrm{d}\xi = \frac{A\,c\,\varepsilon^2\,\delta^2}{4} & \text{in 1D,} \end{cases} \tag{1.22}$$

where $t$ is the thickness of the plate and $A$ is the cross-sectional area of the bar. Note that the peridynamic strain energy density is computed in a point with a complete neighborhood, i.e., assuming that the body is infinite.

Thus, equating the strain energy densities of bond-based peridynamics and classical continuum mechanics (Equations 1.19 and 1.22), the micromodulus is obtained as [65, 148, 149]

$$c = \begin{cases} \dfrac{12E}{\pi\,\delta^4} & \text{in 3D,} \\[2ex] \dfrac{48E}{5\pi\,t\,\delta^3} & \text{in 2D plane strain,} \\[2ex] \dfrac{9E}{\pi\,t\,\delta^3} & \text{in 2D plane stress,} \\[2ex] \dfrac{2E}{A\,\delta^2} & \text{in 1D.} \end{cases} \tag{1.23}$$

This results are valid for a constant micromodulus, i.e., $c(\boldsymbol{\xi}) = c$. However, other types of functions can be chosen, such as the "triangular" function, which have different convergence behaviors when the horizon size tends to 0, i.e., when the peridynamic solution converges to that of classical continuum mechanics [149–151].

### Failure criterion

The peridynamic theory allows one to introduce the concept of damage and failure in a relatively straightforward way. As shown in Equation 1.16, bonds irreversibly break when

they reach their maximum stretch. Broken bonds can no longer "carry" pairwise forces and, therefore, it is as if they are deleted from the model. This method is capable of handling crack nucleation, propagation, branching, and kinking without any ad hoc criterion. A possible explanation on why peridynamics can predict crack branching with ease is the fact that bonds in arbitrary directions can break, allowing cracks to have the necessary freedom to follow the most energetically favorable path [68].

The critical bond stretch $s_0$ can be determined by considering an infinite homogeneous isotropic body with a planar fracture surface that completely separates two parts of it. Apart from the fracture process, any dissipative phenomena near the crack tip are neglected. The critical energy release rate $G_0$ is a measurable macroscopic quantity that represents the energy dissipated per unit of fracture surface area during crack growth. The critical bond stretch can be related to the critical energy release rate by computing the energy required for the crack to grow in the body modeled by peridynamics, i.e., the integral of the energy within the broken bonds. In a prototype microelastic brittle material under isotropic homogeneous deformation, the micropotential of a bond at its breaking point is given as [65]

$$w_0(\boldsymbol{\xi}) = \int_0^{s_0} \mathbf{f}(\boldsymbol{\xi}, \boldsymbol{\eta}) \cdot \mathrm{d}\boldsymbol{\eta} = \int_0^{s_0} c\, s\, \xi \, \mathrm{d}s = \frac{c\, s_0^2\, \xi}{2}\,. \tag{1.24}$$

$w_0$ can be interpreted as the work done to break a single bond. The critical energy release rate is equal to the work per unit area required to break bonds connecting points on opposite sides of the fracture surface [65, 66, 152]:

$$G_0 = \begin{cases} \displaystyle\int_0^{\delta}\int_0^{2\pi}\int_z^{\delta}\int_0^{\cos^{-1}(z/\xi)} \frac{c\, s_0^2\, \xi}{2}\, \xi^2 \sin\phi \, \mathrm{d}\phi \, \mathrm{d}\xi \, \mathrm{d}\theta \, \mathrm{d}z = \frac{\pi\, c\, s_0^2\, \delta^5}{10} & \text{in 3D,} \\ \displaystyle 2t \int_0^{\delta}\int_z^{\delta}\int_0^{\cos^{-1}(z/\xi)} \frac{c\, s_0^2\, \xi}{2}\, \xi \, \mathrm{d}\phi \, \mathrm{d}\xi \, \mathrm{d}z = \frac{\pi\, t\, c\, s_0^2\, \delta^4}{4} & \text{in 2D,} \\ \displaystyle A \int_0^{\delta}\int_z^{\delta} \frac{c\, s_0^2\, \xi}{2} \, \mathrm{d}\xi \, \mathrm{d}z = \frac{A\, c\, s_0^2\, \delta^3}{6} & \text{in 1D.} \end{cases} \tag{1.25}$$

The integration limits are shown in Figure 1.4. Therefore, the critical bond stretch can be obtained as

$$s_0 = \begin{cases} \displaystyle\sqrt{\frac{10G_0}{\pi\, c\, \delta^5}} = \sqrt{\frac{5G_0}{6E\delta}} & \text{in 3D,} \\ \displaystyle\sqrt{\frac{4G_0}{\pi\, t\, c\, \delta^4}} = \sqrt{\frac{5G_0}{12E\delta}} & \text{in 2D plane strain,} \\ \displaystyle\sqrt{\frac{4G_0}{\pi\, t\, c\, \delta^4}} = \sqrt{\frac{4G_0}{9E\delta}} & \text{in 2D plane stress,} \\ \displaystyle\sqrt{\frac{6G_0}{A\, c\, \delta^3}} = \sqrt{\frac{3G_0}{E\delta}} & \text{in 1D.} \end{cases} \tag{1.26}$$

These values of critical bond stretch are used in Equation 1.17 to determine the history-dependent variable $\mu$ whose effect is to remove the contribution to stiffness of broken bonds.

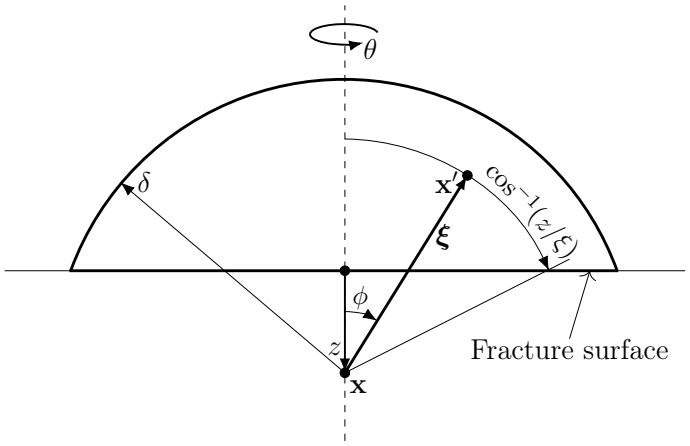


Figure 1.4: *Representation of the integration limits to compute the energy release rate in peridynamic models* [65].

Finally, the damage index at a point $\mathbf{x}$ is defined as [65]

$$\varphi(\mathbf{x}) = 1 - \frac{\int_{\mathcal{H}_\mathbf{x}} \mu(\boldsymbol{\xi}, \boldsymbol{\eta})\, \mathrm{d}V_{\mathbf{x}'}}{\int_{\mathcal{H}_\mathbf{x}} \mathrm{d}V_{\mathbf{x}'}}\,. \tag{1.27}$$

In words, the damage index is the ratio between the number of broken bonds and the total number of bonds initially connected to point $\mathbf{x}$. By its definition, the damage index has values between 0 and 1, where $\varphi = 0$ indicates the situation in which the source point still has all interactions with its family points and $\varphi = 1$ means that the source point is completely disconnected from other points. If a straight crack passes close to a point, that point has a damage index close to $\varphi = 0.5$ because almost half of its interactions were lost. Note that the damage index does not appear in the constitutive modeling of the pairwise force. In fact, material failure is fully characterized by the critical bond stretch criterion, whereas the damage index is used only to visualize the crack path in the post-processing of the results.

### 1.2.2 State-based peridynamics

Bond-based peridynamics assumes that points interact through a pairwise force indipendent of the deformation conditions of other points. This formulation has several limitations in material modeling, among which there are the restriction on the choice of the Poisson ratio (for instance, $\nu = 1/4$ in 3D models) and the difficulty in modelling the ductile behavior in metals. Experiments indeed showed that the plastic response in metals is induced by shear deformation, whereas, by allowing bonds to have permanent deformation, only the plastic behavior due to volumetric strains can be modeled in bond-based peridynamics. The restriction on the Poisson ratio can be addressed by introducing rotational degrees of freedom in the model [96, 97, 104].

State-based peridynamics was introduced in [62] as a generalization of the bond-based version to address all the aforementioned limitations. This is possible since the force that arises within the bonds, i.e., the force state $\mathbf{f}$, is a function of the collective deformation of

the whole neighborhood. In contrast to bond-based peridynamics, the force that a point $\mathbf{x}$ exerts on another point $\mathbf{x}'$ can be different from the force that $\mathbf{x}'$ exerts on $\mathbf{x}$, as shown in Figure 1.5. Moreover, the new version of the peridynamic theory can be subdivided into *ordinary* and *non-ordinary* state-based peridynamics in which, respectively, the force state is aligned and unaligned to the current bond direction (see Figure 1.5).

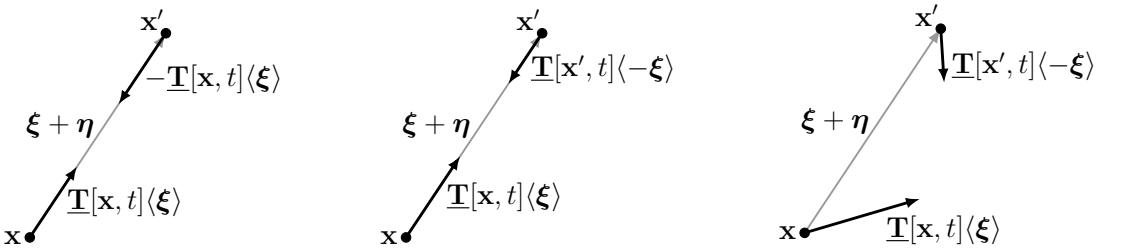


(a) *Bond-based PD.* (b) *Ordinary state-based PD.* (c) *Non-ordinary state-based PD.*

Figure 1.5: *Comparison of the force density vector states* $\underline{\mathbf{T}}$ *for different versions of the peridynamic theory* [62]. *The relation between the force state and the force density vector states is defined in Equation 1.34.*

Non-ordinary state-based peridynamics allows one to incorporate constitutive models directly from classical continuum mechanics, i.e., without the calibration of peridynamic properties to the classical ones [62]. These types of models are often called *peridynamic correspondence models*. However, the computational efficiency of non-ordinary state-based models is lower than that of ordinary state-based models. Furthermore, due to the unalignment of the force state with the direction of the bond, materials modeled with non-ordinary state-based peridynamics suffer from instability issues, such as zero-energy modes. Hence, these models require additional stabilization techniques to obtain reasonable numerical results [153–155].

More details on non-ordinary state-based peridynamics can be found in [62, 156]. In this work, only ordinary state-based peridynamics is reviewed, beginning with the concept of state.

### Definition of peridynamic states

Peridynamic states can be subdivided into scalar and vector states that, respectively, map a quantity into a scalar value or a vector. The quantity to which the states are applied is denoted in angle brackets $\langle\cdot\rangle$, whereas the variables on which the states depend are denoted in square brackets $[\cdot]$. Peridynamic states are often applied to the bond vector $\boldsymbol{\xi}$ and depend on the positions of a point, e.g., $\mathbf{x}$, and the time $t$. Scalar states are denoted by underlined non-bold lowercase letters, e.g., $\underline{a}[\mathbf{x}, t]\langle\boldsymbol{\xi}\rangle$, whereas vector states are denoted by underlined bold uppercase letters, e.g., $\underline{\mathbf{A}}[\mathbf{x}, t]\langle\boldsymbol{\xi}\rangle$. The main mathematical properties of the peridynamic states are defined in [62].

The concept of vector state might seem similar to that of second-order tensor since they both map vectors into vectors, but a state in general can be non-linear and discontinuous. Therefore, one may argue that a symmetric second-order tensor is a special case of vector

state. Figure 1.6 schematically shows the different mappings of a second-order tensor and a vector state.

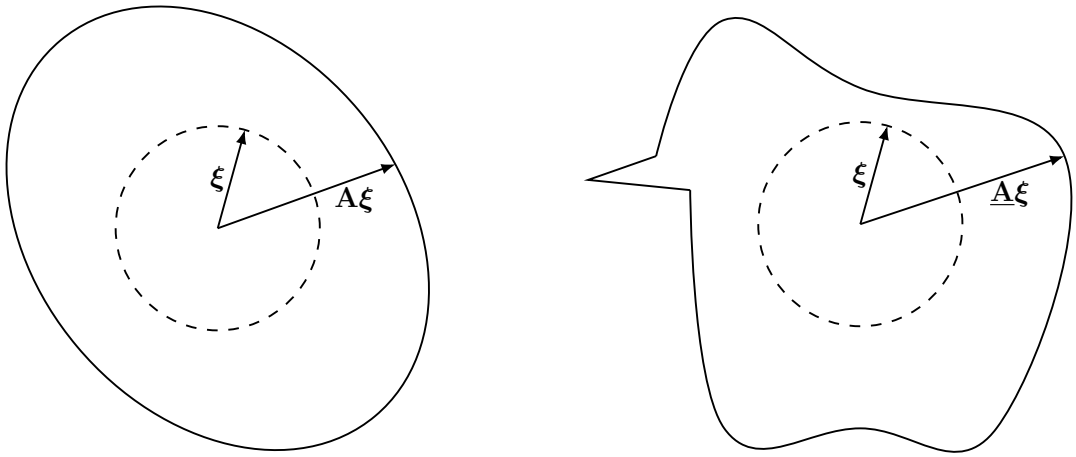


(a) *Symmetric second-order tensor* $\mathbf{A}$. (b) *Vector state* $\underline{\mathbf{A}}$.

Figure 1.6: *A symmetric second order tensor* $\mathbf{A}$ *maps a sphere into an ellipsoid, whereas a vector state maps it into a more complex and possibly discontinuous shape* [62].

An important concept is differentiability of a function of a state, e.g., $\Psi(\underline{\mathbf{A}})$. Suppose that there exists a state-valued function denoted $\nabla\Psi$ such that for any state $\underline{\mathbf{A}}$ and any increment $d\underline{\mathbf{A}}$

$$\Psi(\underline{\mathbf{A}} + d\underline{\mathbf{A}}) = \Psi(\underline{\mathbf{A}}) + \int_{\mathcal{H}_{\mathbf{x}}} \nabla\Psi(\underline{\mathbf{A}})\, d\underline{\mathbf{A}}\, \mathrm{d}V_{\mathbf{x}'} + \mathcal{O}(\|d\underline{\mathbf{A}}\|^2)\,, \tag{1.28}$$

then $\Psi$ is said to be *differentiable* and $\nabla\Psi$ is the Fréchet derivative $\Psi$ [62]. When $\Psi$ is a scalar-valued function of a vector state, $\nabla\Psi$, if it exists, is a vector state. Fréchet derivatives have many of the familiar properties of common derivatives [62].

Some commonly used states to compute the force state are defined hereinafter. Consider a bond $\boldsymbol{\xi} = \mathbf{x}' - \mathbf{x}$ connecting two points $\mathbf{x}$ and $\mathbf{x}'$. The relative displacement vector of the bond $\boldsymbol{\xi}$ in the deformed configuration is denoted by $\boldsymbol{\eta} = \mathbf{u}(\mathbf{x}', t) - \mathbf{u}(\mathbf{x}, t)$. According to these notations, the *reference position vector state* and the *deformation vector state* are respectively defined as

$$\underline{\mathbf{X}}\langle\boldsymbol{\xi}\rangle = \boldsymbol{\xi}\,, \tag{1.29}$$

$$\underline{\mathbf{Y}}\langle\boldsymbol{\xi}\rangle = \boldsymbol{\xi} + \boldsymbol{\eta}\,, \tag{1.30}$$

where $\boldsymbol{\xi}+\boldsymbol{\eta}$ is the relative position of the points in the deformed configuration (see Figure 1.2). The norms of reference vector state and deformation vector state, respectively, represent the bond length in initial and deformed configuration. These quantities are named the *reference position scalar state* and *deformation scalar state*:

$$\underline{x}\langle\boldsymbol{\xi}\rangle = \|\boldsymbol{\xi}\|\,, \tag{1.31}$$

$$\underline{y}\langle\boldsymbol{\xi}\rangle = \|\boldsymbol{\xi} + \boldsymbol{\eta}\|\,. \tag{1.32}$$

In order to describe the axial elongation of the bond, the *extension scalar state* is defined as

$$\underline{e}\langle\boldsymbol{\xi}\rangle = \|\boldsymbol{\xi}+\boldsymbol{\eta}\| - \|\boldsymbol{\xi}\|\,. \tag{1.33}$$

Furthermore, a scalar state $\underline{\omega}$, named *influence function*, can be arbitrarily chosen to "weight" quantities integrated over the neighborhood. The influence function is prescribed to be spherical, i.e., dependent on the bond length but not its direction. In order to obtain numerical stability, it is recommended to choose a constant or monotonically descending influence function with increasing distance from the source point [149]. Different shapes of $\underline{\omega}$ do not substantially change the solution, but they may confer different numerical properties for the peridynamic solution converging to that obtained with classical continuum mechanics [150, 151]. Some examples of commonly used influence functions are $\underline{\omega} = 1$ [157], $\underline{\omega} = 1/\|\boldsymbol{\xi}\|^n$ where $n$ is a positive integer number [158], and $\underline{\omega} = \exp(-\|\boldsymbol{\xi}\|^2/\delta^2)$ [159].

The force state used to evaluate the internal forces in the equation of motion (Equation 1.2) is defined in state-based peridynamics as [62]

$$\mathbf{f}(\mathbf{x},\mathbf{x}',t) = \underline{\mathbf{T}}[\mathbf{x},t]\langle\boldsymbol{\xi}\rangle - \underline{\mathbf{T}}[\mathbf{x}',t]\langle-\boldsymbol{\xi}\rangle\,, \tag{1.34}$$

where $\underline{\mathbf{T}}$ is called *force density vector state*. In ordinary state-based peridynamics, the force density vector state is aligned with the corresponding bond for any deformation [62], as shown in Figure 1.5b. Therefore, the force density vector state in this case can be rewritten as

$$\underline{\mathbf{T}}[\mathbf{x},t]\langle\boldsymbol{\xi}\rangle = \underline{t}[\mathbf{x},t]\langle\boldsymbol{\xi}\rangle\,\frac{\boldsymbol{\xi}+\boldsymbol{\eta}}{\|\boldsymbol{\xi}+\boldsymbol{\eta}\|} = \underline{t}[\mathbf{x},t]\langle\boldsymbol{\xi}\rangle\,\underline{\mathbf{M}}\langle\boldsymbol{\xi}\rangle\,, \tag{1.35}$$

where $\underline{t}$ is called *force density scalar state* and $\underline{\mathbf{M}}$ is the *deformed direction vector state*, which is the unit vector state in the direction of the deformed bond.

Ordinary state-based peridynamics is a generalization of the bond-based version of the theory. Bond-based peridynamics restricts the force density vector state that the material point $\mathbf{x}$ exerts on another point $\mathbf{x}'$ to be equal to the one that $\mathbf{x}'$ exerts $\mathbf{x}$, i.e., $\underline{\mathbf{T}}[\mathbf{x}',t]\langle-\boldsymbol{\xi}\rangle = -\underline{\mathbf{T}}[\mathbf{x},t]\langle\boldsymbol{\xi}\rangle$ as shown in Figure 1.5a. Thus, the force density vector state is related to the pairwise force $\mathbf{f}(\boldsymbol{\xi},\boldsymbol{\eta})$ in bond-based peridynamics as follows [62]:

$$\underline{\mathbf{T}}[\mathbf{x},t]\langle\boldsymbol{\xi}\rangle = \frac{1}{2}\,\mathbf{f}(\boldsymbol{\xi},\boldsymbol{\eta})\,. \tag{1.36}$$

This restriction is removed in ordinary state-based peridynamics, in which $\underline{\mathbf{T}}[\mathbf{x},t]\langle\boldsymbol{\xi}\rangle$ and $\underline{\mathbf{T}}[\mathbf{x}',t]\langle-\boldsymbol{\xi}\rangle$ can have different magnitudes, as shown in Figure 1.5b. However, from the definition of the force density vector state in ordinary state-based peridynamics it follows that Newton's third law, i.e., $\mathbf{f}(\mathbf{x},\mathbf{x}',t) = -\mathbf{f}(\mathbf{x}',\mathbf{x},t)$, and the conservation of angular momentum, i.e., $\underline{\mathbf{Y}}\langle\boldsymbol{\xi}\rangle \times \mathbf{f}(\mathbf{x},\mathbf{x}',t) = \mathbf{0}$, still hold (see Figure 1.7).

### Calibration of peridynamic mechanical properties

In order to calibrate the force density scalar state, the strain energy density computed with classical continuum mechanics and ordinary state-based peridynamics is equalized when

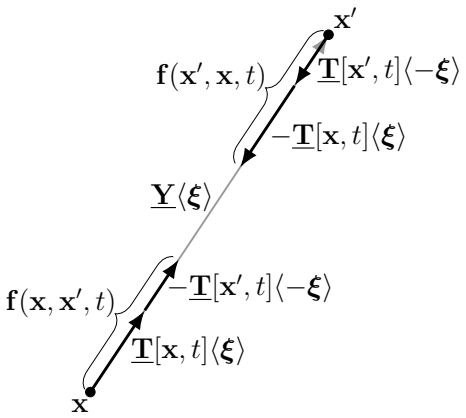


Figure 1.7: *Schematic representation of the force states* $\mathbf{f}$ *acting on points* $\mathbf{x}$ *and* $\mathbf{x'}$ *of a generic bond in ordinary state-based peridynamic.*

the body is under the same homogeneous deformation conditions in both approaches [62, 160]. This calibration procedure is similar to the calibration of the micromodulus in bond-based peridynamics. For simplicity's sake, quasi-static conditions are considered hereinafter.

In classical continuum mechanics, homogeneous deformation for sufficiently small displacements is described by the strain tensor $\boldsymbol{\varepsilon}(\mathbf{x})$ in a generic point $\mathbf{x}$. The strain tensor can be subdivided into the volumetric strain tensor $\boldsymbol{\varepsilon}^v(\mathbf{x})$ and the deviatoric strain tensor $\boldsymbol{\varepsilon}^d(\mathbf{x})$, such that $\boldsymbol{\varepsilon} = \boldsymbol{\varepsilon}^v + \boldsymbol{\varepsilon}^d$. On the one hand, the volumetric strain tensor that describes the change of volume due to deformation, is defined as [161]

$$\boldsymbol{\varepsilon}^v = \frac{1}{3}\theta_{cl}\mathbf{1}\,, \tag{1.37}$$

where $\mathbf{1}$ is the identity matrix and $\theta_{cl}$, called *dilatation*, is the trace of the strain energy tensor:

$$\theta_{cl} = \sum_{i=1}^{3} \varepsilon_{ii}\,, \tag{1.38}$$

where $\varepsilon_{ii}$ are the diagonal components of the strain tensor. Note that the subscript $cl$ indicates that the dilatation is computed in the framework of classical continuum mechanics. On the other hand, the deviatoric strain tensor that describes the change of shape caused by deformation, is defined as

$$\boldsymbol{\varepsilon}^d = \boldsymbol{\varepsilon} - \frac{1}{3}\theta_{cl}\mathbf{1}\,. \tag{1.39}$$

Thus, the strain energy density in classical continuum mechanics for a homogeneous

isotropic linear elastic solid is given using Einstein notation as

$$W_{cl}(\mathbf{x}) = \begin{cases} \dfrac{K}{2}\theta_{cl}^2 + G\varepsilon_{ij}^d\varepsilon_{ij}^d & \text{in 3D,} \\ \left[\dfrac{K}{2} + \dfrac{G}{9}\right]\theta_{cl}^2 + G\varepsilon_{ij}^d\varepsilon_{ij}^d & \text{in 2D plane strain,} \\ \left[\dfrac{K}{2} + \left(\dfrac{\nu+1}{3(2\nu-1)}\right)^2 G\right]\theta_{cl}^2 + G\varepsilon_{ij}^d\varepsilon_{ij}^d & \text{in 2D plane stress,} \\ \left[\dfrac{K}{2} + 2\left(\dfrac{\nu+1}{3(2\nu-1)}\right)^2 G\right]\theta_{cl}^2 + G\left(\varepsilon_{11}^d\right)^2 & \text{in 1D,} \end{cases} \tag{1.40}$$

where $K$ is the bulk modulus, $G$ is the shear modulus, and $\varepsilon_{ij}^d$ are the components of the deviatoric strain tensor. Note that $i, j = 1, 2, 3$ in 3D and $i, j = 1, 2$ in 2D. The bulk and shear moduli can be calculated in terms of the Young modulus and Poisson ratio as $K = E/(3(1-2\nu))$ and $G = E/(2(1+\nu))$, respectively.

Two quantities similar to the dilatation and the deviatoric strain in classical continuum mechanics should be formulated in the peridynamic framework in order to define the peridynamic strain energy density. Therefore, in state-based peridynamics, the dilation at a point $\mathbf{x}$ is defined as [62]

$$\theta(\mathbf{x}) = \frac{c_\theta}{m}\int_{\mathcal{H}_\mathbf{x}} \underline{\omega}\,\underline{x}\,\underline{e}\,\mathrm{d}V_{\mathbf{x}'}\,, \tag{1.41}$$

where $c_\theta$ is the dilatation coefficient and $m$ the weighted volume. The weighted volume, used to normalize the dilatation for different values of the horizon size $\delta$ and the influence function $\underline{\omega}$, is defined as

$$m(\mathbf{x}) = \int_{\mathcal{H}_\mathbf{x}} \underline{\omega}\,\underline{x}^2\,\mathrm{d}V_{\mathbf{x}'}\,. \tag{1.42}$$

The value of the dilatation coefficient is determined by equalizing the dilatations in an infinite body, under the homogeneous isotropic deformation $\varepsilon$, modeled with classical continuum mechanics and peridynamics. The infinite body assumption derives from the need to have a completely full neighborhood for each point in the peridynamic model. On the one hand, recalling Equation 1.38, the dilatation computed with classical continuum mechanics is given as

$$\theta_{cl} = \begin{cases} 3\,\varepsilon & \text{in 3D,} \\ 2\,\varepsilon & \text{in 2D plane strain,} \\ \dfrac{2(1-2\nu)}{1-\nu}\,\varepsilon & \text{in 2D plane stress,} \\ (1-2\nu)\,\varepsilon & \text{in 1D.} \end{cases} \tag{1.43}$$

On the other hand, in the peridynamic model, the homogeneous isotropic deformation can be expressed as $\underline{\mathbf{Y}} = (1+\varepsilon)\underline{\mathbf{X}}$. This yields an extension scalar state equal to $\underline{e} = \underline{y} - \underline{x} = \varepsilon\underline{x}$

and a peridynamic dilatation equal to

$$\theta(\mathbf{x}) = \frac{c_\theta}{m} \int_{\mathcal{H}_\mathbf{x}} \underline{\omega}\, \underline{x}^2\, \varepsilon \, \mathrm{d}V_{\mathbf{x}'} = c_\theta\, \varepsilon \,. \tag{1.44}$$

Hence, by equalizing the dilatations obtained with the two approaches ($\theta = \theta_{cl}$), the dilatation coefficient is given as

$$c_\theta = \begin{cases} 3 & \text{in 3D,} \\ 2 & \text{in 2D plane strain,} \\ \dfrac{2(1-2\nu)}{1-\nu} & \text{in 2D plane stress,} \\ 1-2\nu & \text{in 1D.} \end{cases} \tag{1.45}$$

The *deviatoric extension scalar state* of a bond is defined in a way similar to the deviatoric strain tensor in classical continuum mechanics (see Equation 1.39) [62]:

$$\underline{e}^d = \underline{e} - \frac{\theta \underline{x}}{3} \,. \tag{1.46}$$

At this point, suppose that the peridynamic strain energy density at a point $\mathbf{x}$ of a linear elastic material is given as [62]

$$W(\mathbf{x}) = \frac{k}{2}\theta^2 + \frac{\alpha}{2m} \int_{\mathcal{H}_\mathbf{x}} \underline{\omega} \left(\underline{e}^d\right)^2 \mathrm{d}V_{\mathbf{x}'} \,, \tag{1.47}$$

where $k$ and $\alpha$ are the peridynamic constants which must be determined by comparison with the classical strain energy density.

To do so, an infinite body under homogeneous deformation is considered. Note that these assumptions entail that $\theta = \theta_{cl}$ and that the deviatoric strain tensor $\boldsymbol{\varepsilon}^d$ is constant in the whole body. Using Einstein notation, the deviatoric extension scalar state $\underline{e}^d$ in this case can be determined as though the bond vector $\boldsymbol{\xi}$ would have been elongated by the effect of the deviatoric strain tensor [62, 160]:

$$\underline{e}^d = \boldsymbol{\xi} \cdot \boldsymbol{\varepsilon}^d \frac{\boldsymbol{\xi}}{\|\boldsymbol{\xi}\|} = \frac{1}{\|\boldsymbol{\xi}\|}\, \xi_i\, \varepsilon^d_{ij}\, \xi_j \tag{1.48}$$

where $\varepsilon^d_{ij}$ are the components of the deviatoric strain tensor, and $\xi_i$ or $\xi_j$ are the components of the bond vector $\boldsymbol{\xi}$. Note that the indices of the components vary from 1 to $N$, where $N$ is the number of dimensions of the model. Using this relation, the deviatoric strain energy density in the peridynamic framework can be rewritten as

$$\begin{aligned} W^d(\mathbf{x}) &= \frac{\alpha}{2m} \int_{\mathcal{H}_\mathbf{x}} \underline{\omega} \left(\underline{e}^d\right)^2 \mathrm{d}V_{\mathbf{x}'} \\ &= \frac{\alpha}{2m} \int_{\mathcal{H}_\mathbf{x}} \frac{\underline{\omega}}{\|\boldsymbol{\xi}\|^2} \left(\xi_i\, \varepsilon^d_{ij}\, \xi_j\right) \left(\xi_p\, \varepsilon^d_{pq}\, \xi_q\right) \mathrm{d}V_{\mathbf{x}'} \end{aligned}$$

$$= \frac{\alpha}{2m}\,\varepsilon_{ij}^{d}\varepsilon_{pq}^{d}\int_{\mathcal{H}_{\mathbf{x}}}\frac{\underline{\omega}}{\|\boldsymbol{\xi}\|^{2}}\,\xi_i\xi_j\xi_p\xi_q\,\mathrm{d}V_{\mathbf{x}'}\,. \tag{1.49}$$

Note that, due to the symmetry of the integration domain, the integral of terms with at least one odd power of any component of the direction of the bond is zero.

The integration of the peridynamic deviatoric strain energy density is carried out here only for the 1D case:

$$W^{d}(\mathbf{x}) = \frac{\alpha}{2m}\left(\varepsilon_{11}^{d}\right)^{2}\int_{\mathcal{H}_{\mathbf{x}}}\frac{\underline{\omega}}{\xi_1^{2}}\,\xi_1^{4}\,\mathrm{d}V_{\mathbf{x}'} = \frac{\alpha}{2m}\left(\varepsilon_{11}^{d}\right)^{2}\int_{\mathcal{H}_{\mathbf{x}}}\underline{\omega}\xi_1^{2}\,\mathrm{d}V_{\mathbf{x}'} = \frac{\alpha}{2}\left(\varepsilon_{11}^{d}\right)^{2}. \tag{1.50}$$

In the 2D and 3D cases, polar and spherical coordinates are, respectively, employed for the integration (for more details, see [62, 160]). Therefore, the strain energy density in an infinite body modeled with ordinary state-based peridynamics under homogeneous deformation is given as

$$W(\mathbf{x}) = \begin{cases} \dfrac{k}{2}\theta^{2} + \dfrac{\alpha}{15}\,\varepsilon_{ij}^{d}\varepsilon_{ij}^{d} & \text{in 3D,} \\ \left(\dfrac{k}{2} + \dfrac{\alpha}{144}\right)\theta^{2} + \dfrac{\alpha}{8}\,\varepsilon_{ij}^{d}\varepsilon_{ij}^{d} & \text{in 2D plane strain,} \\ \left(\dfrac{k}{2} + \dfrac{\alpha\,(1+\nu)^{2}}{144\,(1-2\nu)^{2}}\right)\theta^{2} + \dfrac{\alpha}{8}\,\varepsilon_{ij}^{d}\varepsilon_{ij}^{d} & \text{in 2D plane stress,} \\ \dfrac{k}{2}\theta^{2} + \dfrac{\alpha}{2}\left(\varepsilon_{11}^{d}\right)^{2} & \text{in 1D,} \end{cases} \tag{1.51}$$

where $i, j = 1, 2, 3$ in 3D and $i, j = 1, 2$ in 2D.

Hence, the peridynamic constants $k$ and $\alpha$ can be simply derived by comparing Equations 1.40 and 1.51:

$$\alpha = \begin{cases} 15G & \text{in 3D,} \\ 8G & \text{in 2D,} \\ 2G & \text{in 1D.} \end{cases} \tag{1.52}$$

$$k = \begin{cases} K & \text{in 3D,} \\ K + \dfrac{1}{9}G & \text{in 2D plane strain,} \\ K + \dfrac{(\nu+1)^{2}}{9(2\nu-1)^{2}}G & \text{in 2D plane stress,} \\ K + \dfrac{2(\nu+1)^{2}}{9(2\nu-1)^{2}}G & \text{in 1D.} \end{cases} \tag{1.53}$$

As a final remark, it is worth noting that the two theories of peridynamics and classical continuum mechanics have the same solution only if the horizon size $\delta$ goes to 0 [162] or in the case of a homogeneous deformation, i.e., a linear displacement field. In numerical models, it is impossible to have a peridynamic model with $\delta = 0$. Thus, when the condition of homogeneous deformation is not satisfied, peridynamics and classical continuum mechanics have different solutions, as highlighted in [163, 164]. This is why spurious effects are present at the interfaces of the coupling between peridynamics and methods based on

classical continuum mechanics, such as FEM [165].

**Force density scalar state**

To determine the magnitude of the force states in ordinary state-based peridynamics, the force density scalar state $\underline{t}$ is defined as the Fréchet derivative of the peridynamic strain energy density with respect to the extension scalar state [62]:

$$\underline{t} = \nabla W(\underline{e})\,. \tag{1.54}$$

The definition of Fréchet derivative (see Equation 1.28) applied to $W$ as a function of the extension scalar state $\underline{e}$ is given as

$$W(\underline{e} + d\underline{e}) = W(\underline{e}) + \int_{\mathcal{H}_{\mathbf{x}}} \nabla W(\underline{e})\, d\underline{e}\, \mathrm{d}V_{\mathbf{x}'} + \mathcal{O}(\|d\underline{e}\|^2)\,, \tag{1.55}$$

where $d\underline{e}$ is an increment of the extension scalar state. From the definition of dilatation (Equation 1.41), it follows that

$$\theta(\underline{e}+d\underline{e}) = \frac{c_\theta}{m}\int_{\mathcal{H}_{\mathbf{x}}} \underline{\omega}\,\underline{x}\,(\underline{e}+d\underline{e})\,\mathrm{d}V_{\mathbf{x}'} = \frac{c_\theta}{m}\int_{\mathcal{H}_{\mathbf{x}}} \underline{\omega}\,\underline{x}\,\underline{e}\,\mathrm{d}V_{\mathbf{x}'} + \frac{c_\theta}{m}\int_{\mathcal{H}_{\mathbf{x}}} \underline{\omega}\,\underline{x}\,d\underline{e}\,\mathrm{d}V_{\mathbf{x}'} = \theta + d\theta\,, \tag{1.56}$$

where $d\theta$ is the increment of dilatation. Similarly, the definition of the deviatoric extension scalar state (Equation 1.46) yields

$$\underline{e}^d(\underline{e} + d\underline{e}) = (\underline{e} + d\underline{e}) - \frac{(\theta + d\theta)\underline{x}}{3} = \left(\underline{e} - \frac{\theta\,\underline{x}}{3}\right) + \left(d\underline{e} - \frac{d\theta\,\underline{x}}{3}\right) = \underline{e}^d + d\underline{e}^d\,, \tag{1.57}$$

where $d\underline{e}^d$ is the increment of the deviatoric extension scalar state.

Therefore, the strain energy density $W(\underline{e} + d\underline{e})$ due to the increment $d\underline{e}$ is computed (dropping the second order terms of the increments) as

$$\begin{aligned}
W(\underline{e} + d\underline{e}) &= \frac{k}{2}\,(\theta + d\theta)^2 + \frac{\alpha}{2m}\int_{\mathcal{H}_{\mathbf{x}}} \underline{\omega}\,\left(\underline{e}^d + d\underline{e}^d\right)^2 \mathrm{d}V_{\mathbf{x}'} \\
&= \frac{k}{2}\left(\theta^2 + 2\,\theta\,d\theta\right) + \frac{\alpha}{2m}\int_{\mathcal{H}_{\mathbf{x}}} \underline{\omega}\left[\left(\underline{e}^d\right)^2 + 2\,\underline{e}^d\,d\underline{e}^d\right]\mathrm{d}V_{\mathbf{x}'} \\
&= W(\underline{e}) + k\,\theta\,d\theta + \frac{\alpha}{m}\int_{\mathcal{H}_{\mathbf{x}}} \underline{\omega}\,\underline{e}^d\,d\underline{e}^d\,\mathrm{d}V_{\mathbf{x}'} \\
&= W(\underline{e}) + \frac{k\,\theta\,c_\theta}{m}\int_{\mathcal{H}_{\mathbf{x}}} \underline{\omega}\,\underline{x}\,d\underline{e}\,\mathrm{d}V_{\mathbf{x}'} + \frac{\alpha}{m}\int_{\mathcal{H}_{\mathbf{x}}} \underline{\omega}\,\underline{e}^d\left(d\underline{e} - \frac{\underline{x}\,c_\theta}{3m}\int_{\mathcal{H}_{\mathbf{x}}} \underline{\omega}\,\underline{x}\,d\underline{e}\,\mathrm{d}V_{\mathbf{x}'}\right)\mathrm{d}V_{\mathbf{x}'} \\
&= W(\underline{e}) + \int_{\mathcal{H}_{\mathbf{x}}}\left[\frac{k\,\theta\,c_\theta}{m}\,\underline{\omega}\,\underline{x} + \frac{\alpha}{m}\,\underline{\omega}\,\underline{e}^d - \frac{c_\theta\,\alpha}{3m^2}\left(\int_{\mathcal{H}_{\mathbf{x}}} \underline{\omega}\,\underline{x}\,\underline{e}^d\,\mathrm{d}V_{\mathbf{x}'}\right)\underline{\omega}\,\underline{x}\right] d\underline{e}\,\mathrm{d}V_{\mathbf{x}'}\,.
\end{aligned} \tag{1.58}$$

When this formula is compared with Equation 1.55, the force density scalar state for a linear

peridynamic material is given as:

$$\underline{t} = \frac{c_\theta}{m}\left[k\theta - \frac{\alpha}{3m}\int_{\mathcal{H}_\mathbf{x}} \underline{\omega}\,\underline{x}\,\underline{e}^d\,\mathrm{d}V_{\mathbf{x}'}\right]\underline{\omega}\,\underline{x} + \frac{\alpha}{m}\,\underline{\omega}\,\underline{e}^d\,. \tag{1.59}$$

Finally, the force density scalar state can be simplified as

$$\begin{aligned}\underline{t} &= \frac{c_\theta}{m}\left[k\theta - \frac{\alpha}{3m}\int_{\mathcal{H}_\mathbf{x}} \underline{\omega}\,\underline{x}\left(\underline{e} - \frac{\theta\underline{x}}{3}\right)\mathrm{d}V_{\mathbf{x}'}\right]\underline{\omega}\,\underline{x} + \frac{\alpha}{m}\,\underline{\omega}\left(\underline{e} - \frac{\theta\underline{x}}{3}\right)\\ &= \frac{c_\theta}{m}\left[k\theta - \frac{\alpha\theta}{3c_\theta} + \frac{\alpha\theta}{9}\right]\underline{\omega}\,\underline{x} + \frac{\alpha}{m}\,\underline{\omega}\,\underline{e} - \frac{\alpha}{3m}\,\underline{\omega}\,\underline{x}\,\theta\\ &= \left(c_\theta k + \frac{c_\theta - 6}{9}\,\alpha\right)\frac{\underline{\omega}\,\underline{x}}{m}\,\theta + \alpha\,\frac{\underline{\omega}}{m}\,\underline{e}\,,\end{aligned} \tag{1.60}$$

where the values of the constants $c_\theta$, $k$, and $\alpha$ are given in Equations 1.45, 1.53, and 1.52, respectively. For conciseness of notation, the coefficient $k_\theta$ is defined as

$$k_\theta = c_\theta k + \frac{c_\theta - 6}{9}\,\alpha\,, \tag{1.61}$$

Therefore, the force state in ordinary state-based peridynamics is given as [62]

$$\begin{aligned}\mathbf{f}(\mathbf{x},\mathbf{x}',t) &= \underline{t}[\mathbf{x},t]\langle\boldsymbol{\xi}\rangle\,\underline{\mathbf{M}}\langle\boldsymbol{\xi}\rangle - \underline{t}[\mathbf{x}',t]\langle-\boldsymbol{\xi}\rangle\,\underline{\mathbf{M}}\langle-\boldsymbol{\xi}\rangle\\ &= \underline{\omega}\langle\boldsymbol{\xi}\rangle\left[k_\theta\,\underline{x}\langle\boldsymbol{\xi}\rangle\left(\frac{\theta(\mathbf{x})}{m(\mathbf{x})} + \frac{\theta(\mathbf{x}')}{m(\mathbf{x}')}\right) + \alpha\left(\frac{1}{m(\mathbf{x})} + \frac{1}{m(\mathbf{x}')}\right)\underline{e}\langle\boldsymbol{\xi}\rangle\right]\underline{\mathbf{M}}\langle\boldsymbol{\xi}\rangle,\end{aligned} \tag{1.62}$$

where the following equalities have been used: $\underline{e}\langle\boldsymbol{\xi}\rangle = \underline{e}\langle-\boldsymbol{\xi}\rangle$, $\underline{\omega}\langle\boldsymbol{\xi}\rangle = \underline{\omega}\langle-\boldsymbol{\xi}\rangle$, $\underline{x}\langle\boldsymbol{\xi}\rangle = \underline{x}\langle-\boldsymbol{\xi}\rangle$, and $\underline{\mathbf{M}}\langle\boldsymbol{\xi}\rangle = -\underline{\mathbf{M}}\langle-\boldsymbol{\xi}\rangle$. In state-based peridynamics, a point $\mathbf{x}$ interacts with all the points within its neighborhood $\mathcal{H}_\mathbf{x}$. Note that the interaction force, i.e., the force state in Equation 1.62, depends also on the dilatation $\theta(\mathbf{x}')$ of the neighboring point $\mathbf{x}'$. This means that a point interacts directly with all points up to a distance equal to $\delta$ and indirectly with all points up to a distance equal to $2\delta$.

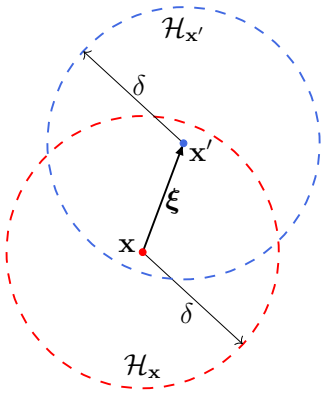


Figure 1.8: *In state-based peridynamics, a point* $\mathbf{x}$ *interacts directly with any point* $\mathbf{x}'$ *within the neighborhood* $\mathcal{H}_\mathbf{x}$ *and indirectly with all the points within the neighborhood* $\mathcal{H}_{\mathbf{x}'}$.

**Linearized peridynamic model**

The linearization of the state-based version of peridynamics is presented in [166] and is hereinafter briefly summarized. To perform the linearization, the notion of *double state* must be introduced. As suggested by the name, double states operate on two bonds. Therefore, for example, the notation $\underline{\mathbb{D}}[\mathbf{x}]\langle\boldsymbol{\xi},\boldsymbol{\zeta}\rangle$ means that the double state $\underline{\mathbb{D}}$ depends on the position $\mathbf{x}$ and is applied to the bonds $\boldsymbol{\xi}=\mathbf{x}'-\mathbf{x}$ and $\boldsymbol{\zeta}=\mathbf{x}''-\mathbf{x}$. The value of a double state is a second-order tensor and its components are denoted as $\underline{D}_{ij}\langle\boldsymbol{\xi},\boldsymbol{\zeta}\rangle$. The *adjoint* of $\underline{\mathbb{D}}$, denoted by $\underline{\mathbb{D}}^\dagger$, is defined as

$$\underline{D}^\dagger_{ij}\langle\boldsymbol{\xi},\boldsymbol{\zeta}\rangle=\underline{D}_{ji}\langle\boldsymbol{\zeta},\boldsymbol{\xi}\rangle\qquad\forall\,\boldsymbol{\xi},\boldsymbol{\zeta}\in\mathcal{H}_{\mathbf{x}}\,. \tag{1.63}$$

Note that the order of both the indices and the bonds is changed when taking the adjoint. $\underline{\mathbb{D}}$ is *self-adjoint* if $\underline{\mathbb{D}}=\underline{\mathbb{D}}^\dagger$.

Let $\mathbf{u}$ be a displacement field applied to a body $\mathcal{B}$ modeled with state-based peridynamics with an horizon size $\delta$. The *displacement vector state* associated with $\mathbf{u}$ is defined as [166]

$$\underline{\mathbf{U}}[\mathbf{x},t]\langle\boldsymbol{\xi}\rangle=\mathbf{u}(\mathbf{x}',t)-\mathbf{u}(\mathbf{x},t)=\boldsymbol{\eta}\,. \tag{1.64}$$

A displacement field $\mathbf{u}$ on $\mathcal{B}$ is *small* if $\|\boldsymbol{\eta}\|\ll\delta$ for any time $t$. This definition is analogous to $\|\nabla\mathbf{u}\|\ll 1$ in classical continuum mechanics, but it allows for discontinuities in the displacement field $\mathbf{u}$. If the displacement field $\mathbf{u}$ is small, the force density vector state can be linearized as follows:

$$\underline{\mathbf{T}}[\mathbf{x},t]\langle\boldsymbol{\xi}\rangle=\int_{\mathcal{H}_{\mathbf{x}}}\underline{\mathbb{K}}[\mathbf{x}]\langle\boldsymbol{\xi},\boldsymbol{\zeta}\rangle\,\underline{\mathbf{U}}[\mathbf{x},t]\langle\boldsymbol{\zeta}\rangle\,\mathrm{d}V_{\mathbf{x}''}\,, \tag{1.65}$$

where $\underline{\mathbb{K}}$ is a double state called the *modulus state* and defined as the Fréchet derivative of the force density vector state:

$$\underline{\mathbb{K}}=\nabla\underline{\mathbf{T}}(\underline{\mathbf{U}})\,. \tag{1.66}$$

If the material is elastic, the linearized force density vector state given in Equation 1.65 can be obtained as $\underline{\mathbf{T}}=\nabla W$, where $W$ is the linearized strain energy density for small displacements:

$$\begin{aligned}W(\underline{\mathbf{U}})&=\frac{1}{2}\int_{\mathcal{H}_{\mathbf{x}}}\underline{\mathbf{U}}[\mathbf{x},t]\langle\boldsymbol{\xi}\rangle\cdot\underline{\mathbf{T}}[\mathbf{x},t]\langle\boldsymbol{\xi}\rangle\,\mathrm{d}V_{\mathbf{x}'}\\&=\frac{1}{2}\int_{\mathcal{H}_{\mathbf{x}}}\underline{\mathbf{U}}[\mathbf{x},t]\langle\boldsymbol{\xi}\rangle\cdot\left(\int_{\mathcal{H}_{\mathbf{x}}}\underline{\mathbb{K}}[\mathbf{x}]\langle\boldsymbol{\xi},\boldsymbol{\zeta}\rangle\,\underline{\mathbf{U}}[\mathbf{x},t]\langle\boldsymbol{\zeta}\rangle\,\mathrm{d}V_{\mathbf{x}''}\right)\mathrm{d}V_{\mathbf{x}'}\\&=\frac{1}{2}\int_{\mathcal{H}_{\mathbf{x}}}\underline{U}_i[\mathbf{x},t]\langle\boldsymbol{\xi}\rangle\cdot\left(\int_{\mathcal{H}_{\mathbf{x}}}\underline{K}_{ij}[\mathbf{x}]\langle\boldsymbol{\xi},\boldsymbol{\zeta}\rangle\,\underline{U}_j[\mathbf{x},t]\langle\boldsymbol{\zeta}\rangle\,\mathrm{d}V_{\mathbf{x}''}\right)\mathrm{d}V_{\mathbf{x}'}\,,\end{aligned} \tag{1.67}$$

where "$\cdot$" stands for scalar product operation between vectors. In the last line of Equation 1.67, Einstein notation was used. This yields

$$\underline{\mathbb{K}}=\nabla\nabla W(\underline{\mathbf{U}})\,. \tag{1.68}$$

Due to the property of self-adjointness of second Fréchet derivatives (see [166] for details),

the modulus state is self-adjoint:

$$\underline{\mathbb{K}} = \underline{\mathbb{K}}^{\dagger} \,. \tag{1.69}$$

This condition is analogous to the major symmetry of the fourth-order elasticity tensor $\mathbf{C}$ in classical continuum mechanics for elastic materials, i.e., $C_{ijkl} = C_{klij}$. Furthermore, the balance of angular momentum for a linearized force density vector state can be expressed as

$$\int_{\mathcal{H}_{\mathbf{x}}} \underline{\mathbf{Y}}[\mathbf{x},t]\langle\boldsymbol{\xi}\rangle \times \left( \int_{\mathcal{H}_{\mathbf{x}}} \underline{\mathbb{K}}[\mathbf{x}]\langle\boldsymbol{\xi},\boldsymbol{\zeta}\rangle \, \underline{\mathbf{U}}[\mathbf{x},t]\langle\boldsymbol{\zeta}\rangle \, \mathrm{d}V_{\mathbf{x}''} \right) \mathrm{d}V_{\mathbf{x}'} = \mathbf{0} \,. \tag{1.70}$$

This condition is analogous to the minor simmetry of the fourth-order elasticity tensor $\mathbf{C}$ in classical continuum mechanics, i.e., $C_{ijkl} = C_{jikl}$, which ensures the symmetry of the stress tensor.

The force density vector state is obtained by combing Equations 1.35 and 1.60 as

$$\underline{\mathbf{T}}\langle\boldsymbol{\xi}\rangle = \left[ k_\theta \, \frac{\underline{\omega}(\|\boldsymbol{\xi}\|) \, \|\boldsymbol{\xi}\|}{m} \, \theta + \alpha \, \frac{\underline{\omega}(\|\boldsymbol{\xi}\|)}{m} \, \underline{e}\langle\boldsymbol{\xi}\rangle \right] \underline{\mathbf{M}}\langle\boldsymbol{\xi}\rangle \,, \tag{1.71}$$

where $\underline{\mathbf{M}}\langle\boldsymbol{\xi}\rangle = \boldsymbol{\xi}/\|\boldsymbol{\xi}\|$ is the unit vector of the bond direction when small displacements are assumed. Under this assumption, the extension scalar state can be rewritten as

$$\underline{e}\langle\boldsymbol{\xi}\rangle = \boldsymbol{\eta} \cdot \underline{\mathbf{M}}\langle\boldsymbol{\xi}\rangle = \underline{\mathbf{U}}\langle\boldsymbol{\xi}\rangle \cdot \underline{\mathbf{M}}\langle\boldsymbol{\xi}\rangle \,. \tag{1.72}$$

Thus, the peridynamic dilatation for small displacements becomes

$$\theta(\mathbf{x}) = \frac{c_\theta}{m} \int_{\mathcal{H}_{\mathbf{x}}} \underline{\omega} \, \underline{x} \, \underline{\mathbf{U}}\langle\boldsymbol{\xi}\rangle \cdot \underline{\mathbf{M}}\langle\boldsymbol{\xi}\rangle \, \mathrm{d}V_{\mathbf{x}'} = \frac{c_\theta}{m} \int_{\mathcal{H}_{\mathbf{x}}} \underline{\omega}(\|\boldsymbol{\xi}\|) \, \boldsymbol{\xi} \cdot \underline{\mathbf{U}}\langle\boldsymbol{\xi}\rangle \, \mathrm{d}V_{\mathbf{x}'} \,. \tag{1.73}$$

Consider an increment $d\underline{\mathbf{U}}$ of the displacement vector state, resulting in an increment $d\underline{e}$ of the extension scalar state and $d\theta$ of the dilatation. For later use, the Dirac delta function is defined as

$$\boldsymbol{\Delta}(\boldsymbol{\zeta} - \boldsymbol{\xi}) = \begin{cases} 1 & \text{if } \ \boldsymbol{\zeta} - \boldsymbol{\xi} = \mathbf{0} \,, \\ 0 & \text{otherwise.} \end{cases} \tag{1.74}$$

The force density vector state due to the increment $d\underline{\mathbf{U}}$ is given as

$$\begin{aligned}
\underline{\mathbf{T}}(\underline{\mathbf{U}} + d\underline{\mathbf{U}}) &= \left[ k_\theta \, \frac{\underline{\omega}(\|\boldsymbol{\xi}\|) \, \|\boldsymbol{\xi}\|}{m} \, (\theta + d\theta) + \alpha \, \frac{\underline{\omega}(\|\boldsymbol{\xi}\|)}{m} \, (\underline{e} + d\underline{e}) \right] \underline{\mathbf{M}}\langle\boldsymbol{\xi}\rangle \\
&= \underline{\mathbf{T}}(\underline{\mathbf{U}}) + \left[ k_\theta \, \frac{\underline{\omega}(\|\boldsymbol{\xi}\|) \, \|\boldsymbol{\xi}\|}{m} \, d\theta + \alpha \, \frac{\underline{\omega}(\|\boldsymbol{\xi}\|)}{m} \, (d\underline{\mathbf{U}}\langle\boldsymbol{\xi}\rangle \cdot \underline{\mathbf{M}}\langle\boldsymbol{\xi}\rangle) \right] \underline{\mathbf{M}}\langle\boldsymbol{\xi}\rangle \\
&= \underline{\mathbf{T}}(\underline{\mathbf{U}}) + k_\theta \, \frac{\underline{\omega}(\|\boldsymbol{\xi}\|) \, \boldsymbol{\xi}}{m} \, d\theta + \alpha \, \frac{\underline{\omega}(\|\boldsymbol{\xi}\|)}{m} \, (\underline{\mathbf{M}}\langle\boldsymbol{\xi}\rangle \otimes \underline{\mathbf{M}}\langle\boldsymbol{\xi}\rangle) \, d\underline{\mathbf{U}}\langle\boldsymbol{\xi}\rangle \\
&= \underline{\mathbf{T}}(\underline{\mathbf{U}}) + k_\theta \, \frac{\underline{\omega}(\|\boldsymbol{\xi}\|) \, \boldsymbol{\xi}}{m} \, \frac{c_\theta}{m} \int_{\mathcal{H}_{\mathbf{x}}} \underline{\omega}(\|\boldsymbol{\zeta}\|) \, \boldsymbol{\zeta} \cdot d\underline{\mathbf{U}}\langle\boldsymbol{\zeta}\rangle \, \mathrm{d}V_{\mathbf{x}''} \\
&\qquad + \alpha \, \frac{\underline{\omega}(\|\boldsymbol{\xi}\|)}{m} \, (\underline{\mathbf{M}}\langle\boldsymbol{\xi}\rangle \otimes \underline{\mathbf{M}}\langle\boldsymbol{\xi}\rangle) \int_{\mathcal{H}_{\mathbf{x}}} \boldsymbol{\Delta}(\boldsymbol{\zeta} - \boldsymbol{\xi}) \, d\underline{\mathbf{U}}\langle\boldsymbol{\zeta}\rangle \, \mathrm{d}V_{\mathbf{x}''}
\end{aligned}$$

$$
\begin{aligned}
&= \underline{\mathbf{T}}(\underline{\mathbf{U}}) + \int_{\mathcal{H}_{\mathbf{x}}} \underline{\omega}(\|\boldsymbol{\xi}\|) \left[ \frac{c_\theta \, k_\theta}{m^2} \, \underline{\omega}(\|\boldsymbol{\zeta}\|) \, (\boldsymbol{\xi} \otimes \boldsymbol{\zeta}) \right. \\
&\qquad \left. + \frac{\alpha}{m} \, (\underline{\mathbf{M}}\langle \boldsymbol{\xi} \rangle \otimes \underline{\mathbf{M}}\langle \boldsymbol{\xi} \rangle) \, \boldsymbol{\Delta}(\boldsymbol{\zeta} - \boldsymbol{\xi}) \right] d\underline{\mathbf{U}}\langle \boldsymbol{\zeta} \rangle \, \mathrm{d}V_{\mathbf{x}''} \\
&= \underline{\mathbf{T}}(\underline{\mathbf{U}}) + \int_{\mathcal{H}_{\mathbf{x}}} \underline{\omega}(\|\boldsymbol{\xi}\|) \left[ \frac{c_\theta \, k_\theta}{m^2} \, \underline{\omega}(\|\boldsymbol{\zeta}\|) + \frac{\alpha}{m} \, \frac{\boldsymbol{\Delta}(\boldsymbol{\zeta} - \boldsymbol{\xi})}{\|\boldsymbol{\xi}\| \, \|\boldsymbol{\zeta}\|} \right] (\boldsymbol{\xi} \otimes \boldsymbol{\zeta}) \, d\underline{\mathbf{U}}\langle \boldsymbol{\zeta} \rangle \, \mathrm{d}V_{\mathbf{x}''} \, ,
\end{aligned}
\tag{1.75}
$$

where "$\otimes$" stands for the dyadic product between two vectors. Note that the Dirac delta function is introduced because the last term on the right-hand side of Equation 1.75 is non-null only when $\boldsymbol{\xi} = \boldsymbol{\zeta}$. In fact, this term is analogous to the pairwise force in bond-based peridynamics (see Equation 1.18), in which each bond responds indipendently from the other bonds in the neighborhood. Hence, from the definition of the Fréchet derivative (see Equation 1.28), the modulus state is given as [166]

$$
\underline{\mathbb{K}}\langle \boldsymbol{\xi}, \boldsymbol{\zeta} \rangle = \underline{\omega}(\|\boldsymbol{\xi}\|) \left[ \frac{c_\theta \, k_\theta}{m^2} \, \underline{\omega}(\|\boldsymbol{\zeta}\|) + \frac{\alpha}{m} \, \frac{\boldsymbol{\Delta}(\boldsymbol{\zeta} - \boldsymbol{\xi})}{\|\boldsymbol{\xi}\| \, \|\boldsymbol{\zeta}\|} \right] (\boldsymbol{\xi} \otimes \boldsymbol{\zeta}) \, . \tag{1.76}
$$

The peridynamic equation of motion expressed in terms of displacement can be derived by using the linearized constitutive models with no additional approximations [166]:

$$
\begin{aligned}
\rho(\mathbf{x}) \, \ddot{\mathbf{u}}(\mathbf{x}, t) &= \int_{\mathcal{H}_{\mathbf{x}}} \left( \underline{\mathbf{T}}[\mathbf{x}, t]\langle \boldsymbol{\xi} \rangle - \underline{\mathbf{T}}[\mathbf{x}', t]\langle -\boldsymbol{\xi} \rangle \right) \mathrm{d}V_{\mathbf{x}'} + \mathbf{b}(\mathbf{x}, t) \\
&= \int_{\mathcal{H}_{\mathbf{x}}} \left( \int_{\mathcal{H}_{\mathbf{x}}} \underline{\mathbb{K}}[\mathbf{x}]\langle \boldsymbol{\xi}, \boldsymbol{\zeta} \rangle \, \underline{\mathbf{U}}[\mathbf{x}, t]\langle \boldsymbol{\zeta} \rangle \, \mathrm{d}V_{\mathbf{x}''} \right. \\
&\qquad \left. - \int_{\mathcal{H}_{\mathbf{x}'}} \underline{\mathbb{K}}[\mathbf{x}']\langle -\boldsymbol{\xi}, \boldsymbol{\gamma} \rangle \, \underline{\mathbf{U}}[\mathbf{x}', t]\langle \boldsymbol{\gamma} \rangle \, \mathrm{d}V_{\mathbf{x}'''} \right) \mathrm{d}V_{\mathbf{x}'} + \mathbf{b}(\mathbf{x}, t) \, ,
\end{aligned}
\tag{1.77}
$$

where $\rho$ is the material density, $\ddot{\mathbf{u}}$ is the acceleration field, and $\mathbf{b}$ is the external force density. The notation of the bonds involved in this computation, i.e., $\boldsymbol{\xi} = \mathbf{x}' - \mathbf{x}$, $\boldsymbol{\zeta} = \mathbf{x}'' - \mathbf{x}$, and $\boldsymbol{\gamma} = \mathbf{x}''' - \mathbf{x}'$, are shown in Figure 1.9. Recalling the definition of displacement vector state, i.e., $\underline{\mathbf{U}}[\mathbf{x}, t]\langle \boldsymbol{\zeta} \rangle = \mathbf{u}(\mathbf{x}'', t) - \mathbf{u}(\mathbf{x}, t)$ and $\underline{\mathbf{U}}[\mathbf{x}', t]\langle \boldsymbol{\gamma} \rangle = \mathbf{u}(\mathbf{x}''', t) - \mathbf{u}(\mathbf{x}', t)$, the equation of motion is rearranged as

$$
\begin{aligned}
\rho(\mathbf{x}) \, \ddot{\mathbf{u}}(\mathbf{x}, t) = &\int_{\mathcal{H}_{\mathbf{x}}} \int_{\mathcal{H}_{\mathbf{x}}} \underline{\mathbb{K}}[\mathbf{x}]\langle \boldsymbol{\xi}, \boldsymbol{\zeta} \rangle \, \mathbf{u}(\mathbf{x}'', t) \, \mathrm{d}V_{\mathbf{x}''} \, \mathrm{d}V_{\mathbf{x}'} \\
&- \left( \int_{\mathcal{H}_{\mathbf{x}}} \int_{\mathcal{H}_{\mathbf{x}}} \underline{\mathbb{K}}[\mathbf{x}]\langle \boldsymbol{\xi}, \boldsymbol{\zeta} \rangle \, \mathrm{d}V_{\mathbf{x}''} \, \mathrm{d}V_{\mathbf{x}'} \right) \mathbf{u}(\mathbf{x}, t) \\
&- \int_{\mathcal{H}_{\mathbf{x}}} \int_{\mathcal{H}_{\mathbf{x}'}} \underline{\mathbb{K}}[\mathbf{x}']\langle -\boldsymbol{\xi}, \boldsymbol{\gamma} \rangle \, \mathbf{u}(\mathbf{x}''', t) \, \mathrm{d}V_{\mathbf{x}'''} \, \mathrm{d}V_{\mathbf{x}'} \\
&+ \int_{\mathcal{H}_{\mathbf{x}}} \left( \int_{\mathcal{H}_{\mathbf{x}'}} \underline{\mathbb{K}}[\mathbf{x}']\langle -\boldsymbol{\xi}, \boldsymbol{\gamma} \rangle \, \mathrm{d}V_{\mathbf{x}'''} \right) \mathbf{u}(\mathbf{x}', t) \, \mathrm{d}V_{\mathbf{x}'} + \mathbf{b}(\mathbf{x}, t) \, .
\end{aligned}
\tag{1.78}
$$

Note that, as stated previously, in state-based peridynamics, a point interacts with all points up to a distance of $2\delta$, in contrast to a maximum distance of interaction equal to $\delta$ in

bond-based peridynamics. This is the reason why state-based peridynamic models are less computationally efficient than bond-based ones.

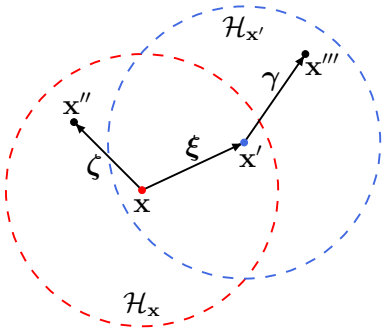


Figure 1.9: *Notation for the bonds used to compute the force state in linearized state-based peridynamics. Points* $\mathbf{x}'$ *and* $\mathbf{x}''$ *lie within the neighborhood* $\mathcal{H}_{\mathbf{x}}$ *of point* $\mathbf{x}$ *and point* $\mathbf{x}'''$ *lies within the neighborhood* $\mathcal{H}_{\mathbf{x}'}$ *of point* $\mathbf{x}'$.

### Failure criterion

Damage in bond-based peridynamics is evaluated with the bond stretch criterion [65]: whenever a bond elongation exceeds a prescribed limit, the bond is broken and its contribution to stiffness vanishes. This failure criterion is based only on the bond elongation, thus it neglects the deviatoric deformation energy stored in the bond and is suitable for loading cases close to mode I and II failures [167]. However, it has been shown that this simple failure criterion can be used in ordinary state-based peridynamics as well [168]. Other failure criteria, such as those based on critical bond energy [169], strain invariants [71] and stress tensor [170], can be found in the literature.

In ordinary state-based peridynamics, the bond stretch is defined as [171]

$$\underline{s}\langle\boldsymbol{\xi}\rangle = \frac{\underline{e}\langle\boldsymbol{\xi}\rangle}{\underline{x}\langle\boldsymbol{\xi}\rangle}\,. \tag{1.79}$$

As in bond-based peridynamics, $\underline{s}$ assumes the meaning of strain of the bond. Even if it has not been justified from a mathematical standpoint, the same critical bond stretch $s_0$ as that obtained in bond-based peridynamics (see Equation 1.26) is often used to determine whether a bond is broken. Following an approach similar to that adopted in bond-based peridynamics, the values of critical bond stretch for mode I in ordinary state-based peridynamics were computed in [63, Chapter 6]. In order to assess the bond status (broken or unbroken), a history-dependent scalar state (to be multiplied to the force state in the equation of motion) is introduced:

$$\underline{\mu}\langle\boldsymbol{\xi}\rangle = \begin{cases} 1 & \text{if } \underline{s}\langle\boldsymbol{\xi}\rangle < s_0 \text{ for any previous or current } \underline{e}\langle\boldsymbol{\xi}\rangle\,, \\ 0 & \text{otherwise} \end{cases} \tag{1.80}$$

Once the bond is broken, its stiffness irreversibly vanishes.

The damage index of a peridynamic point $\mathbf{x}$ is evaluated as

$$\varphi(\mathbf{x}) = 1 - \frac{\int_{\mathcal{H}_\mathbf{x}} \underline{\omega}\, \underline{\mu}\, \mathrm{d}V_{\mathbf{x}'}}{\int_{\mathcal{H}_\mathbf{x}} \underline{\omega}\, \mathrm{d}V_{\mathbf{x}'}} \,. \tag{1.81}$$

The damage index ranges between 0 and 1 when the point $\mathbf{x}$ has repectively all intact or all broken bonds. A damage index close to $\varphi = 0.5$ indicates that there is a straight crack passing nearby the point. It is worth noting that the damage index is not involved in the breakage of bonds, but it is only used to visualize crack propagation in the post-processing stage.

### 1.2.3 Peridynamic stress tensor and force flux

Stress is a fundamental concept in classical continuum mechanics. Analogously, the notion of peridynamic stress is of paramount importance in modeling a body with the peridynamic theory. Hereinafter, the definition of the peridynamic stress tensor and the force flux introduced in [172] are reviewed.

#### Peridynamic stress tensor

The peridynamic stress tensor is defined at a point $\mathbf{x}$ with a complete neighborhood as [172]

$$\boldsymbol{\nu}(\mathbf{x}) = \frac{1}{2} \int_\Omega \int_0^\delta \int_s^\delta \mathbf{f}(\mathbf{x}', \mathbf{x}'') \otimes \mathbf{m}\, r^2 \, \mathrm{d}r \, \mathrm{d}s \, \mathrm{d}\Omega_\mathbf{m} \,, \tag{1.82}$$

where $\mathbf{x}' = \mathbf{x} - s\mathbf{m}$ is a point lying on the opposite direction of the bond direction $\mathbf{m}$ at a distance $s$ from $\mathbf{x}$, $\mathbf{x}'' = \mathbf{x} + (r - s)\mathbf{m}$ is a point lying on the bond direction $\mathbf{m}$ at a distance $r$ form $\mathbf{x}'$, $\Omega$ is a sphere with a unit radius centered in $\mathbf{x}$, and $\mathrm{d}\Omega_\mathbf{m}$ is the differential solid angle on $\Omega$ in any bond direction $\mathbf{m}$. For conciseness of notation, the dependence on time of $\boldsymbol{\nu}(\mathbf{x}, t)$ was dropped. Note that the points $\mathbf{x}'$ and $\mathbf{x}''$ are connected by a bond passing through point $\mathbf{x}$, as shown in Figure 1.10. Moreover, $s = \|\mathbf{x}' - \mathbf{x}\|$ is the distance between points $\mathbf{x}$ and $\mathbf{x}'$, whereas $r = \|\mathbf{x}'' - \mathbf{x}'\|$ is the length of the bond between $\mathbf{x}'$ and $\mathbf{x}''$.

The definition of the integration domains allows to take into account all the bonds passing through point $\mathbf{x}$. The position of point $\mathbf{x}' = \mathbf{x} - s\mathbf{m}$ is integrated over the dashed line depicted in Figure 1.10. Since the maximum interaction distance is the horizon size $\delta$, the above mentioned dashed line extends in the opposite direction of the bond direction $\mathbf{m}$ from 0 to $\delta$, limits that correspond to the limits of the integration domain of the second integral on the right-hand side of Equation 1.82. Since the computation of the peridynamic stress tensor involves only the bonds intersecting $\mathbf{x}$, point $\mathbf{x}'' = \mathbf{x} + (r - s)\mathbf{m}$ must be on the opposite side of $\mathbf{x}'$ with respect to $\mathbf{x}$. This means that the bond length $r$ must be greater than $s$ (and again smaller than $\delta$ due to the limit of the interaction distance). Therefore, the integration domain of the innermost integral of Equation 1.82 is the dashdotted line along the bond direction $\mathbf{m}$ extending form $s$ to $\delta$, as shown in Figure 1.10. The bond direction $\mathbf{m}$ is integrated over all possible directions, i.e., over the unit sphere $\Omega$ centered in $\mathbf{x}$ (see outermost integral in Equation 1.82). However, the same force state of each bond is integrated twice

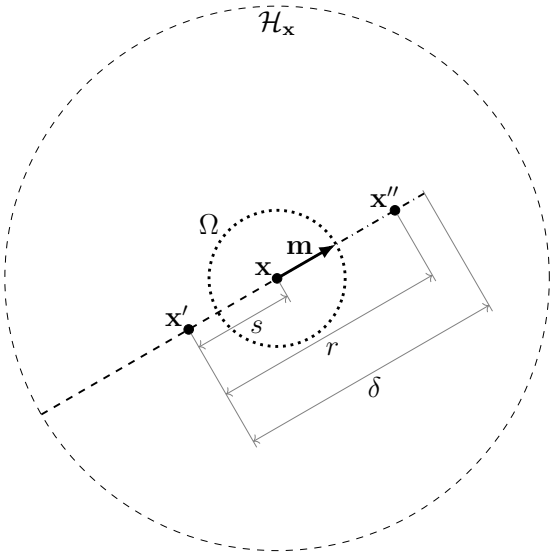


Figure 1.10: *Integration domains of the variables involved in the computation of the peridynamic stress tensor at point* $\mathbf{x}$*: the bond direction* $\mathbf{m}$ *is integrated over the unit sphere* $\Omega$ *(dotted line), the distance* $s$ *of point* $\mathbf{x}'$ *from* $\mathbf{x}$ *(in the opposite direction of* $\mathbf{m}$*) is integrated between* $0$ *and* $\delta$ *(dashed line), and the bond length* $r$ *is integrated between* $s$ *and* $\delta$ *(dashdotted line).*

because any bond passing through $\mathbf{x}$ (between $\mathbf{x}'$ and $\mathbf{x}''$) has a corresponding bond in the opposite direction (between $\mathbf{x}''$ and $\mathbf{x}'$). This is the reason why the factor $1/2$ appears at the beginning of Equation 1.82.

It is worth noting that the integral over the unit sphere $\Omega$ does not depend on the variables $s$ and $r$ and, analogously, the integrals related to the distances between points, i.e., $s$ and $r$, do not depend on the bond direction $\mathbf{m}$. Conversely, the integrals related to $s$ and $r$ are interdependent. This is due to the fact that the points $\mathbf{x}'$ and $\mathbf{x}''$ have to lie on opposite sides with respect to $\mathbf{x}$ in order to pass through it. Considering the order of the integrals given in the definition of the peridynamic stress tensor (Equation 1.82), the "starting point" $\mathbf{x}'$ of the bond is fixed when the bond length is integrated. In other words, for any distance $s$ of $\mathbf{x}'$ from $\mathbf{x}$, all the possible bond lengths $r$ are taken into account in the integration by "stretching" the bond itself. This concept is illustrated in Figure 1.11a.

It is possible to interchange the order of the integrals related to $s$ and $r$. This implies that the bond length $r$ is considered fixed when the distance $s$ of $\mathbf{x}'$ from $\mathbf{x}$ is integrated. In other words, for any bond length $r$, all the possible bonds passing through point $\mathbf{x}$ are taken into account in the integration by "sliding" the bond so that it has different starting points $\mathbf{x}'$. In this case, the distance $s$ of the starting point $\mathbf{x}'$ from point $\mathbf{x}$ must be smaller than the bond length $r$ in order that points $\mathbf{x}'$ and $\mathbf{x}''$ lie on opposite sides with respect to point $\mathbf{x}$, as shown in Figure 1.11b. Hence, the peridynamic stress tensor at a point $\mathbf{x}$ with a complete neighborhood can be rewritten as

$$\begin{aligned}\boldsymbol{\nu}(\mathbf{x}) &= \frac{1}{2}\int_{\Omega}\int_{0}^{\delta}\int_{0}^{r}\mathbf{f}(\mathbf{x}',\mathbf{x}'')\otimes\mathbf{m}\,r^2\,\mathrm{d}s\,\mathrm{d}r\,\mathrm{d}\Omega_{\mathbf{m}}\\ &= \frac{1}{2}\int_{\mathcal{H}_{\mathbf{x}}}\int_{0}^{r}\mathbf{f}(\mathbf{x}',\mathbf{x}'')\otimes\mathbf{m}\,\mathrm{d}s\,\mathrm{d}V_{\mathbf{x}''}\,,\end{aligned} \tag{1.83}$$

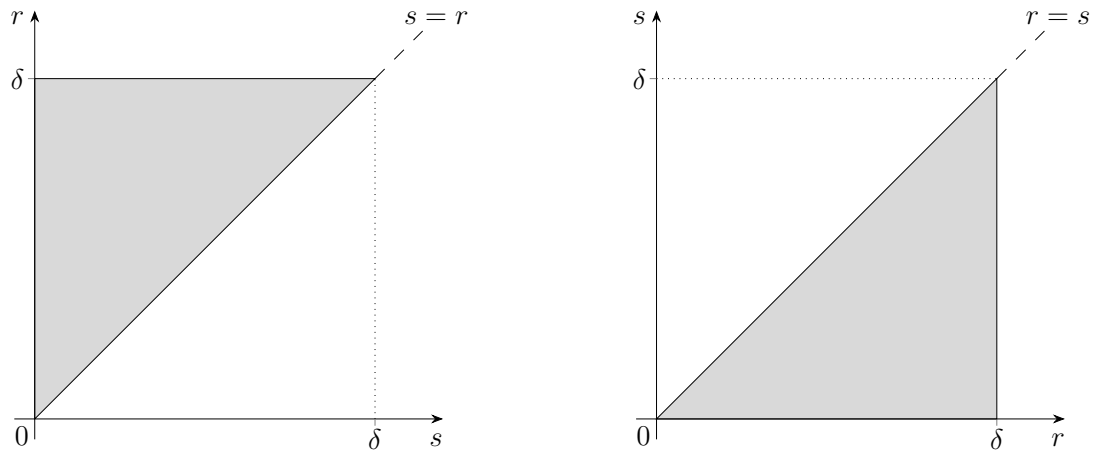


(a) *For any value of $s$ between 0 and $\delta$, $r$ lies between $s$ and $\delta$ (see the integration limits in Equation 1.82).*

(b) *For any value of $r$ between 0 and $\delta$, $s$ lies between 0 and $r$ (see the integration limits in Equation 1.83).*

Figure 1.11: *Integration domain for the computation of the peridynamic stress tensor for a fixed bond direction.*

where $\mathrm{d}V_{\mathbf{x}''} = r^2\,\mathrm{d}r\,\mathrm{d}\Omega_{\mathbf{m}}$.

The computation of the peridynamic stress tensor can be simplified when assuming homogeneous deformation. Under this assumption, bonds with the same length $r$ and direction $\mathbf{m}$ have the same force state in any position of the body, i.e., $\mathbf{f}$ does not depend on $s$. Therefore, Equation 1.83 yields

$$\begin{aligned}\boldsymbol{\nu}(\mathbf{x}) &= \frac{1}{2}\int_{\mathcal{H}_{\mathbf{x}}}\left(\int_0^r \mathrm{d}s\right)\mathbf{f}(\mathbf{x},\mathbf{x}'')\otimes\mathbf{m}\,\mathrm{d}V_{\mathbf{x}''}\\ &= \frac{1}{2}\int_{\mathcal{H}_{\mathbf{x}}} r\,\mathbf{f}(\mathbf{x},\mathbf{x}'')\otimes\mathbf{m}\,\mathrm{d}V_{\mathbf{x}''}\,.\end{aligned} \tag{1.84}$$

Note that the force state for $s = 0$, namely $\mathbf{f}(\mathbf{x},\mathbf{x}'')$, was conveniently chosen in this formula. It is worth recalling that the peridynamic stress tensor is equal to that of classical continuum mechanics under the assumption of homogeneous deformation [165].

In state-based peridynamics, the force state is expressed from Equation 1.34 in terms of the force density vector state as $\mathbf{f}(\mathbf{x}',\mathbf{x}'') = \underline{\mathbf{T}}[\mathbf{x}']\langle\boldsymbol{\zeta}\rangle - \underline{\mathbf{T}}[\mathbf{x}'']\langle-\boldsymbol{\zeta}\rangle$, where $\boldsymbol{\zeta} = \mathbf{x}'' - \mathbf{x}'$. Since the same force state is summed twice within the integral (once for $\boldsymbol{\zeta}$ and another one for $-\boldsymbol{\zeta}$), both $\underline{\mathbf{T}}[\mathbf{x}']\langle\boldsymbol{\zeta}\rangle$ and $\underline{\mathbf{T}}[\mathbf{x}'']\langle-\boldsymbol{\zeta}\rangle$ appear twice in the sum of force density vector states. If each force state is considered applied twice to the corresponding bond, one can rewrite the peridynamic stress tensor from Equation 1.82 as [162]

$$\boldsymbol{\nu}(\mathbf{x}) = \int_\Omega\int_0^\delta\int_s^\delta \underline{\mathbf{T}}[\mathbf{x}']\langle\boldsymbol{\zeta}\rangle\otimes\mathbf{m}\,r^2\,\mathrm{d}r\,\mathrm{d}s\,\mathrm{d}\Omega_{\mathbf{m}}\,, \tag{1.85}$$

where the factor $1/2$ was simplified for the reason explained above. Interchanging the order

of the integrals, Equation 1.85 yields

$$\begin{aligned}\boldsymbol{\nu}(\mathbf{x}) &= \int_{\Omega}\int_{0}^{\delta}\int_{0}^{r} \underline{\mathbf{T}}[\mathbf{x}']\langle\boldsymbol{\zeta}\rangle \otimes \mathbf{m}\, r^2 \,\mathrm{d}s\,\mathrm{d}r\,\mathrm{d}\Omega_{\mathbf{m}} \\ &= \int_{\mathcal{H}_{\mathbf{x}}}\int_{0}^{r} \underline{\mathbf{T}}[\mathbf{x}']\langle\boldsymbol{\zeta}\rangle \otimes \mathbf{m}\,\mathrm{d}s\,\mathrm{d}V_{\mathbf{x}''}\,, \end{aligned} \tag{1.86}$$

where $\mathrm{d}V_{\mathbf{x}''} = r^2\,\mathrm{d}r\,\mathrm{d}\Omega_{\mathbf{m}}$. Under the assumption of homogeneous deformation, the peridynamic stress tensor can be rewritten as

$$\boldsymbol{\nu}(\mathbf{x}) = \int_{\mathcal{H}_{\mathbf{x}}} \underline{\mathbf{T}}[\mathbf{x}]\langle\boldsymbol{\xi}\rangle \otimes \boldsymbol{\xi}\,\mathrm{d}V_{\mathbf{x}'}\,, \tag{1.87}$$

where $\boldsymbol{\xi} = \mathbf{x}' - \mathbf{x}$.

### Peridynamic force flux

The peridynamic force flux corresponds to the concept of stress in classical continuum mechanics. It is indeed obtained in the classical way: $\boldsymbol{\tau}(\mathbf{x},\mathbf{n}) = \boldsymbol{\nu}(\mathbf{x})\,\mathbf{n}$, where $\mathbf{n}$ is a unit vector in the direction in which the force flux is intended to be computed. Thus, the force flux $\boldsymbol{\tau}(\mathbf{x},\mathbf{n})$ at point $\mathbf{x}$ in the direction of the unit vector $\mathbf{n}$ (see Figure 1.12) is derived from Equation 1.82 as [172]

$$\boldsymbol{\tau}(\mathbf{x},\mathbf{n}) = \frac{1}{2}\int_{\Omega}\int_{0}^{\delta}\int_{s}^{\delta} \mathbf{f}(\mathbf{x}',\mathbf{x}'')\,(\mathbf{m}\cdot\mathbf{n})\,r^2\,\mathrm{d}r\,\mathrm{d}s\,\mathrm{d}\Omega_{\mathbf{m}}\,, \tag{1.88}$$

where $\mathbf{x}' = \mathbf{x} - s\mathbf{m}$ and $\mathbf{x}'' = \mathbf{x} + (r-s)\mathbf{m}$. As in the definition of the peridynamic stress tensor, a factor $1/2$ is required, since the integration domain takes into account the magnitude of the force state of each bond twice (for both direction $\mathbf{m}$ and $-\mathbf{m}$). In state-based peridynamics, this factor can be simplified if the force density vector state is used in the formula of the force flux:

$$\boldsymbol{\tau}(\mathbf{x},\mathbf{n}) = \int_{\Omega}\int_{0}^{\delta}\int_{s}^{\delta} \underline{\mathbf{T}}[\mathbf{x}']\langle\boldsymbol{\zeta}\rangle\,(\mathbf{m}\cdot\mathbf{n})\,r^2\,\mathrm{d}r\,\mathrm{d}s\,\mathrm{d}\Omega_{\mathbf{m}}\,, \tag{1.89}$$

where $\boldsymbol{\zeta} = \mathbf{x}'' - \mathbf{x}'$.

Similarly to what is presented for the peridynamic stress tensor, the order of the integrals related to $s$ and $r$ can be interchanged, yielding

$$\begin{aligned}\boldsymbol{\tau}(\mathbf{x},\mathbf{n}) &= \frac{1}{2}\int_{\Omega}\int_{0}^{\delta}\int_{0}^{r} \mathbf{f}(\mathbf{x}',\mathbf{x}'')\,(\mathbf{m}\cdot\mathbf{n})\,r^2\,\mathrm{d}s\,\mathrm{d}r\,\mathrm{d}\Omega_{\mathbf{m}} \\ &= \frac{1}{2}\int_{\mathcal{H}_{\mathbf{x}}}\int_{0}^{r} \mathbf{f}(\mathbf{x}',\mathbf{x}'')\,(\mathbf{m}\cdot\mathbf{n})\,\mathrm{d}s\,\mathrm{d}V_{\mathbf{x}''}\,, \end{aligned} \tag{1.90}$$

where $\mathrm{d}V_{\mathbf{x}''} = r^2\,\mathrm{d}r\,\mathrm{d}\Omega_{\mathbf{m}}$. Under the assumption of homogeneous deformation, the peridy-

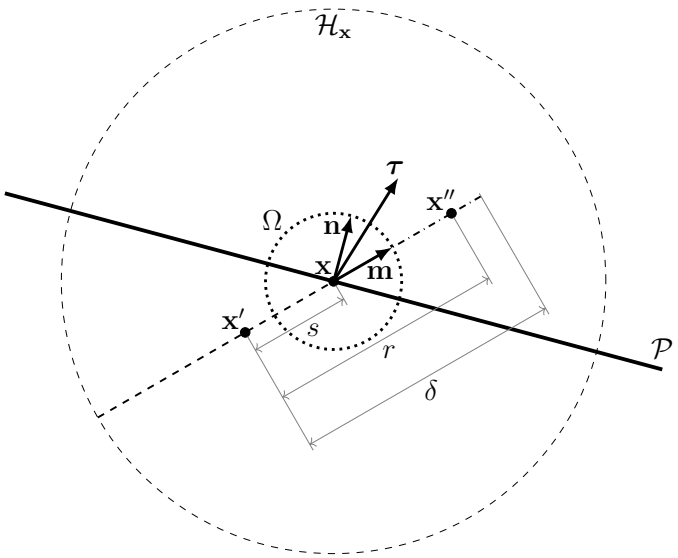


Figure 1.12: *Integration domains of the variables involved in the computation of the peridynamic force flux* $\boldsymbol{\tau}$ *at point* $\mathbf{x}$ *in direction* $\mathbf{n}$*: the bond direction* $\mathbf{m}$ *is integrated over the unit sphere* $\Omega$ *(dotted line), the distance* $s$ *of point* $\mathbf{x}'$ *from* $\mathbf{x}$ *(in the opposite direction of* $\mathbf{m}$*) is integrated between* $0$ *and* $\delta$ *(dashed line), and the bond length* $r$ *is integrated between* $s$ *and* $\delta$ *(dashdotted line). Points* $\mathbf{x}'$ *and* $\mathbf{x}''$ *lie in the different half-spaces generated by the plane* $\mathcal{P}$ *passing through point* $\mathbf{x}$ *with normal* $\mathbf{n}$*.*

namic force flux can be simplified as

$$\begin{aligned}\boldsymbol{\tau}(\mathbf{x},\mathbf{n}) &= \frac{1}{2}\int_{\mathcal{H}_\mathbf{x}} \left(\int_0^r \mathrm{d}s\right) \mathbf{f}(\mathbf{x},\mathbf{x}'')\,(\mathbf{m}\cdot\mathbf{n})\,\mathrm{d}V_{\mathbf{x}''} \\ &= \frac{1}{2}\int_{\mathcal{H}_\mathbf{x}} r\,\mathbf{f}(\mathbf{x},\mathbf{x}'')\,(\mathbf{m}\cdot\mathbf{n})\,\mathrm{d}V_{\mathbf{x}''}\,, \end{aligned} \tag{1.91}$$

where the force state for $s = 0$, namely $\mathbf{f}(\mathbf{x},\mathbf{x}'')$, was conveniently chosen since $\mathbf{f}$ does not depend on $s$ when assuming a homogeneous deformation. It is worth recalling that the peridynamic force flux is equal to the stress in classical continuum mechanics under this assumption [165].

As a mechanical interpretation, the force flux is the resultant of the forces per unit area of all bonds intersecting $\mathcal{P}$ in $\mathbf{x}$ [172]. In order to understand this, consider a plane $\mathcal{P}$ with normal $\mathbf{n}$ passing through point $\mathbf{x}$, as shown in Figure 1.13. Points $\mathbf{x}'$ and $\mathbf{x}''$ respectively lie in the different half-spaces generated by plane $\mathcal{P}$. The differential volumes of those points are $\mathrm{d}V_{\mathbf{x}'} = r^2\,\mathrm{d}s\,\mathrm{d}\Omega_\mathbf{m}$ and $\mathrm{d}V_{\mathbf{x}''} = r^2\,\mathrm{d}r\,\mathrm{d}\Omega_\mathbf{m}$. The differential area of point $\mathbf{x}'$, which is perpendicular to the bond direction $\mathbf{m}$, is the portion of a sphere centered in $\mathbf{x}''$ with a radius $r$ that subtends the differential solid angle $\mathrm{d}\Omega_\mathbf{m}$, namely $\mathrm{d}A_{\mathbf{x}'} = r^2\,\mathrm{d}\Omega_\mathbf{m}$. Similarly, the differential area $\mathrm{d}A_{\mathbf{x}''}$ on a sphere centered in $\mathbf{x}'$ with a radius $r$ is equal to $\mathrm{d}A_{\mathbf{x}'}$. As shown in Figure 1.13, the differential area of point $\mathbf{x}$ with normal $\mathbf{n}$ is the projection in direction $\mathbf{m}$ of $\mathrm{d}A_{\mathbf{x}'} = \mathrm{d}A_{\mathbf{x}''}$ on plane $\mathcal{P}$:

$$\mathrm{d}A_\mathbf{x} = \frac{r^2\,\mathrm{d}\Omega_\mathbf{m}}{\mathbf{m}\cdot\mathbf{n}}\,. \tag{1.92}$$

The total force that point $\mathbf{x}''$ exerts on $\mathbf{x}'$ is given as $\mathbf{f}(\mathbf{x}', \mathbf{x}'')\,\mathrm{d}V_{\mathbf{x}'}\,\mathrm{d}V_{\mathbf{x}''}$. Therefore, the bond force per unit area on plane $\mathcal{P}$ is given by

$$\frac{\mathbf{f}(\mathbf{x}', \mathbf{x}'')\,\mathrm{d}V_{\mathbf{x}'}\,\mathrm{d}V_{\mathbf{x}''}}{\mathrm{d}A_{\mathbf{x}}} = \mathbf{f}(\mathbf{x}', \mathbf{x}'')\,(\mathbf{m}\cdot\mathbf{n})\; r^2\,\mathrm{d}r\,\mathrm{d}s\,\mathrm{d}\Omega_{\mathbf{m}}\,, \tag{1.93}$$

which is the integrand for the computation of the peridynamic force flux (see Equation 1.88). Hence, the force flux is the sum of the forces, per unit area, of all bonds passing through the point $\mathbf{x}$.

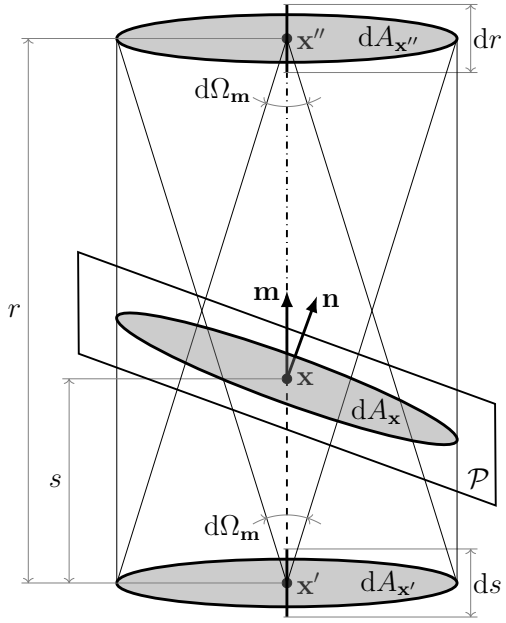


Figure 1.13: *Variables involved in the computation of the force flux* $\boldsymbol{\tau}(\mathbf{x}, \mathbf{n})$*: the differential volumes of points* $\mathbf{x}'$ *and* $\mathbf{x}''$ *are respectively* $\mathrm{d}V_{\mathbf{x}'} = \mathrm{d}s\,\mathrm{d}A_{\mathbf{x}'}$ *and* $\mathrm{d}V_{\mathbf{x}''} = \mathrm{d}r\,\mathrm{d}A_{\mathbf{x}''}$*, where* $\mathrm{d}A_{\mathbf{x}'} = \mathrm{d}A_{\mathbf{x}''} = r^2\,\mathrm{d}\Omega_{\mathbf{m}}$*, and the differential area* $\mathrm{d}A_{\mathbf{x}} = r^2\,\mathrm{d}\Omega_{\mathbf{m}}/(\mathbf{m}\cdot\mathbf{n})$ *is the projection of* $\mathrm{d}A_{\mathbf{x}'}$ *and* $\mathrm{d}A_{\mathbf{x}''}$ *on the plane* $\mathcal{P}$ [172].

### Convergence of the peridynamic stress tensor to the classical one

It was shown in [162] that, if the deformation of a body is sufficiently smooth, the peridynamic theory converges to the classical theory in the limit $\delta \to 0$. The main findings of that work are reported in the following. Note that the mechanical properties of the material should remain unchanged when the horizon size is reduced to zero. Therefore, the strain energy density of the peridynamic elastic material should be defined in such a way that it is the same under homogeneous deformation for any value of $\delta$.

For later use, the *shrikage parameter* is defined as

$$\varrho = \frac{\delta}{\delta_0}\,, \tag{1.94}$$

where $\delta_0$ is called the *reference horizon size*, the value of which remains fixed throughout the following discussion. It is worth noting that the shrinkage of the horizon size $\delta$ to zero

is obtained for $\varrho \to 0$. The *enlarged deformation vector state* is defined as [162]

$$\underline{\mathbf{E}}\langle \boldsymbol{\xi} \rangle = \varrho^{-1}\, \underline{\mathbf{Y}}\langle \varrho \boldsymbol{\xi} \rangle \,. \tag{1.95}$$

The enlarged deformation vector state can be interpreted as a "magnification" of the deformation vector state in the region near the source point, as shown in Figure 1.14.

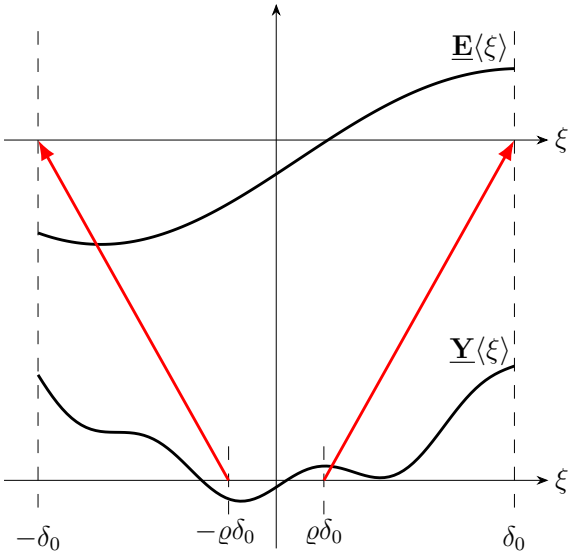


Figure 1.14: *Enlarged deformation vector state* $\underline{\mathbf{E}}$ *that maps the part of the deformation state* $\underline{\mathbf{Y}}$ *within the horizon size* $\delta = \varrho\delta_0$ *to the original horizon* $\delta_0$ [162].

In a peridynamic elastic material, let the strain energy density be a function of the enlarged deformation vector state:

$$W = W(\underline{\mathbf{Y}}) = W(\underline{\mathbf{E}}) \,. \tag{1.96}$$

If the deformation happens to be homogeneous (i.e., the classical deformation gradient tensor $\mathbf{F}(\mathbf{x}) = \nabla \mathbf{y}$ is homogeneous, where "$\nabla$" is the gradient operator and $\mathbf{y}$ is the position of point $\mathbf{x}$ in the deformed configuration), the enlarged deformation vector state is equal to the deformation vector state for any value of $\varrho$:

$$\underline{\mathbf{E}}\langle \boldsymbol{\xi} \rangle = \varrho^{-1}\, \underline{\mathbf{Y}}\langle \varrho \boldsymbol{\xi} \rangle = \varrho^{-1}\, \mathbf{F}(\mathbf{x})\, \varrho \boldsymbol{\xi} = \mathbf{F}(\mathbf{x})\, \boldsymbol{\xi} = \underline{\mathbf{Y}}\langle \boldsymbol{\xi} \rangle \,. \tag{1.97}$$

Therefore, the strain energy density of the peridynamic elastic material under homogeneous deformation is constant for any value of $\delta$.

Since the force density vector state is the Fréchet derivative of the strain energy density, an increment of the strain energy density due to an increment $d\underline{\mathbf{Y}}$ in the deformation vector state (and, consequently, an increment $d\underline{\mathbf{E}}$ in the enlarged deformation vector state) is given as [162]

$$\mathrm{d}W = \int_{\mathcal{H}_{\mathbf{x}}(\delta)} \underline{\mathbf{T}}(\underline{\mathbf{Y}})\langle \boldsymbol{\xi} \rangle \cdot d\underline{\mathbf{Y}}\langle \boldsymbol{\xi} \rangle \, \mathrm{d}V_{\mathbf{x}'} = \int_{\mathcal{H}_{\mathbf{x}}(\delta_0)} \underline{\mathbf{T}}(\underline{\mathbf{E}})\langle \boldsymbol{\xi}_0 \rangle \cdot d\underline{\mathbf{E}}\langle \boldsymbol{\xi}_0 \rangle \, \mathrm{d}V_{\mathbf{x}'_0} \,, \tag{1.98}$$

where $\boldsymbol{\xi}_0 = \boldsymbol{\xi}/\varrho$ is the "magnified" bond of $\boldsymbol{\xi} = \mathbf{x}' - \mathbf{x}$, $\mathcal{H}_{\mathbf{x}}(\delta)$ and $\mathcal{H}_{\mathbf{x}}(\delta_0)$ are the neighborhoods of point $\mathbf{x}$ with radiuses equal to the horizon size $\delta$ and the reference horizon size $\delta_0$, respectively. Note that in Equation 1.98 point $\mathbf{x}'$ lies within $\mathcal{H}_{\mathbf{x}}(\delta)$ and point $\mathbf{x}'_0 = \mathbf{x} + \boldsymbol{\xi}_0$ within $\mathcal{H}_{\mathbf{x}}(\delta_0)$. Changing the integration variable from $\boldsymbol{\xi}$ to $\varrho\boldsymbol{\xi}_0$ in the integral of the left-hand side, one obtains

$$\int_{\mathcal{H}_{\mathbf{x}}(\delta_0)} \underline{\mathbf{T}}(\underline{\mathbf{Y}})\langle\varrho\boldsymbol{\xi}_0\rangle \cdot d\underline{\mathbf{Y}}\langle\varrho\boldsymbol{\xi}_0\rangle\, \varrho^3 \,\mathrm{d}V_{\mathbf{x}'_0} = \int_{\mathcal{H}_{\mathbf{x}}(\delta_0)} \underline{\mathbf{T}}(\underline{\mathbf{E}})\langle\boldsymbol{\xi}_0\rangle \cdot \varrho^{-1} d\underline{\mathbf{Y}}\langle\varrho\boldsymbol{\xi}_0\rangle \,\mathrm{d}V_{\mathbf{x}'_0}\,. \tag{1.99}$$

Since this holds for any $d\underline{\mathbf{Y}}$, it follows that

$$\underline{\mathbf{T}}(\underline{\mathbf{Y}})\langle\varrho\boldsymbol{\xi}\rangle = \varrho^{-4}\, \underline{\mathbf{T}}(\underline{\mathbf{E}})\langle\boldsymbol{\xi}\rangle\,. \tag{1.100}$$

Let $\mathbf{y}$, representing the position of any point in the body in the deformed configuration, be a twice continuously differentiable function of $\mathbf{x}$. This is not a necessary condition for the peridynamic theory, but it is necessary for the comparison of peridynamics with classical continuum mechanics due to the limitations of the latter theory. Under this assumption, an increment $d\underline{\mathbf{Y}}$ in the deformation vector state in the vicinity of some point $\mathbf{x}$ is given by expanding with a Taylor series as

$$\begin{aligned} d\underline{\mathbf{Y}}\langle\varrho\boldsymbol{\xi}\rangle &= \underline{\mathbf{Y}}[\mathbf{x} + d\mathbf{x}]\langle\varrho\boldsymbol{\xi}\rangle - \underline{\mathbf{Y}}[\mathbf{x}]\langle\varrho\boldsymbol{\xi}\rangle \\ &= \mathbf{y}(\mathbf{x} + d\mathbf{x} + \varrho\boldsymbol{\xi}) - \mathbf{y}(\mathbf{x} + d\mathbf{x}) - \mathbf{y}(\mathbf{x} + \varrho\boldsymbol{\xi}) + \mathbf{y}(\mathbf{x}) \\ &= \mathbf{y}(\mathbf{x}) + \mathbf{F}(\mathbf{x})\,(d\mathbf{x} + \varrho\boldsymbol{\xi}) - \mathbf{y}(\mathbf{x}) - \mathbf{F}(\mathbf{x})\, d\mathbf{x} - \mathbf{y}(\mathbf{x}) - \mathbf{F}(\mathbf{x})\, \varrho\boldsymbol{\xi} + \mathbf{y}(\mathbf{x}) + \mathcal{O}(\varrho^2) \\ &= \mathcal{O}(\varrho^2)\,, \end{aligned} \tag{1.101}$$

where $d\mathbf{x} = \mathcal{O}(\varrho)$, and $\mathbf{F} = \partial\mathbf{y}/\partial\mathbf{y} = \nabla\mathbf{y}$ is the deformation gradient tensor.

Consider now the behavior of the peridynamic stress tensor in the limit $\delta \to 0$. Denote by $\boldsymbol{\zeta} = \mathbf{x}'' - \mathbf{x}'$ any bond passing through $\mathbf{x}$, with $\mathbf{x}' = \mathbf{x} - s\mathbf{m}$, and $\mathbf{x}'' = \mathbf{x} + (r - s)\mathbf{m}$ (see Figure 1.10). As $\delta \to 0$, both $r = \|\boldsymbol{\zeta}\|$ and $s = \|\mathbf{x}' - \mathbf{x}\|$ tend to zero. Let the bond $\boldsymbol{\zeta}_0$ be the "magnification" of $\boldsymbol{\zeta}$ (see Figure 1.14) such that $\boldsymbol{\zeta} = \varrho\boldsymbol{\zeta}_0$. Corrispondingly, the following relations hold: $r = \varrho r_0$ and $s = \varrho s_0$. Substituting Equation 1.100 into Equation 1.86, one obtains the peridynamic stress tensor in the limit $\delta \to 0$ (or $\varrho \to 0$) [162]:

$$\begin{aligned} \boldsymbol{\nu}_0(\mathbf{x}) &= \int_\Omega \int_0^\delta \int_0^r \underline{\mathbf{T}}(\underline{\mathbf{Y}}[\mathbf{x} - s\mathbf{m}])\langle\boldsymbol{\zeta}\rangle \otimes \mathbf{m}\, r^2 \,\mathrm{d}s\,\mathrm{d}r\,\mathrm{d}\Omega_{\mathbf{m}} \\ &= \int_\Omega \int_0^{\varrho\delta_0} \int_0^{\varrho r_0} \varrho^{-4} \underline{\mathbf{T}}(\underline{\mathbf{E}}[\mathbf{x} - s\mathbf{m}])\langle\boldsymbol{\zeta}\rangle \otimes \mathbf{m}\, r^2 \,\mathrm{d}s\,\mathrm{d}r\,\mathrm{d}\Omega_{\mathbf{m}} \\ &= \int_\Omega \int_0^{\delta_0} \int_0^{r_0} \varrho^{-4} \underline{\mathbf{T}}(\underline{\mathbf{E}}[\mathbf{x} - \varrho s_0\mathbf{m}])\langle\boldsymbol{\zeta}_0\rangle \otimes \mathbf{m}\, (\varrho r_0)^2\, \varrho\,\mathrm{d}s_0\, \varrho\,\mathrm{d}r_0\,\mathrm{d}\Omega_{\mathbf{m}} \\ &= \int_{\mathcal{H}_{\mathbf{x}}(\delta_0)} \int_0^{r_0} \underline{\mathbf{T}}(\underline{\mathbf{E}}[\mathbf{x} - \varrho s_0\mathbf{m}])\langle\boldsymbol{\zeta}_0\rangle \otimes \mathbf{m}\,\mathrm{d}s_0\,\mathrm{d}V_{\mathbf{x}''_0}\,, \end{aligned} \tag{1.102}$$

where the change of integration variables $r \leftrightarrow \varrho r_0$ and $s \leftrightarrow \varrho s_0$ was used, and $\mathrm{d}V_{\mathbf{x}''_0} = r_0^2\,\mathrm{d}r_0\,\mathrm{d}\Omega_{\mathbf{m}}$.

Considering Equation 1.101 with $d\mathbf{x} = -\varrho s_0\mathbf{m}$, the enlarged deformation vector state is

given as

$$\begin{aligned}\underline{\mathbf{E}}[\mathbf{x}-\varrho s_0\mathbf{m}]\langle\boldsymbol{\zeta}_0\rangle &= \varrho^{-1}\,\underline{\mathbf{Y}}[\mathbf{x}-\varrho s_0\mathbf{m}]\langle\varrho\boldsymbol{\zeta}_0\rangle\\ &= \varrho^{-1}\left(\underline{\mathbf{Y}}[\mathbf{x}]\langle\varrho\boldsymbol{\zeta}_0\rangle + d\underline{\mathbf{Y}}[\mathbf{x}]\langle\varrho\boldsymbol{\zeta}_0\rangle\right)\\ &= \varrho^{-1}\left(\mathbf{F}(\mathbf{x})\,\varrho\boldsymbol{\zeta}_0 + \mathcal{O}(\varrho^2)\right)\\ &= \mathbf{F}(\mathbf{x})\,\boldsymbol{\zeta}_0 + \mathcal{O}(\varrho)\,. \end{aligned} \tag{1.103}$$

To compare the constitutive modeling of peridynamics with that of classical continuum mechanics, it is assumed that $\underline{\mathbf{T}}$ is a continuously differentiable function of $\underline{\mathbf{Y}}$ so that

$$\begin{aligned}\underline{\mathbf{T}}(\underline{\mathbf{Y}})\langle\boldsymbol{\zeta}\rangle &= \underline{\mathbf{T}}(\underline{\mathbf{E}})\langle\boldsymbol{\zeta}_0\rangle\\ &= \underline{\mathbf{T}}(\mathbf{F}(\mathbf{x})\,\boldsymbol{\zeta}_0 + \mathcal{O}(\varrho))\langle\boldsymbol{\zeta}_0\rangle\\ &= \underline{\mathbf{T}}(\mathbf{F}(\mathbf{x})\,\boldsymbol{\zeta}_0)\langle\boldsymbol{\zeta}_0\rangle + \mathcal{O}(\varrho)\,. \end{aligned} \tag{1.104}$$

Since the force density vector state in the limit $\varrho\to 0$ is evaluated for a homogeneous deformation of the body (see Equation 1.87), the peridynamic stress tensor for a horizon size that goes to zero is given as

$$\boldsymbol{\nu}_0(\mathbf{x}) = \int_{\mathcal{H}_{\mathbf{x}}(\delta_0)} \underline{\mathbf{T}}(\mathbf{F}(\mathbf{x})\,\boldsymbol{\xi}_0)\langle\boldsymbol{\xi}_0\rangle \otimes \boldsymbol{\xi}_0\,\mathrm{d}V_{\mathbf{x}'_0}\,. \tag{1.105}$$

This peridynamic stress tensor is equal to the Piola-Kirchhoff stress tensor defined in classical continuum mechanics due to the fact that the stiffness coefficients of the force density vector state were determined by assuming a homogeneous deformation (see Equations 1.52 and 1.53). For simplicity of notation, the subscript 0 associated with the bonds will be dropped hereinafter.

If the assumption of small deformation is added to the discussion, the linearized force density vector state in the limit $\delta\to 0$ can be derived from Equation 1.65 as [166]

$$\begin{aligned}\underline{\mathbf{T}}(\mathbf{F}(\mathbf{x})\,\boldsymbol{\xi})\langle\boldsymbol{\xi}\rangle &= \int_{\mathcal{H}_{\mathbf{x}}(\delta_0)} \underline{\mathbb{K}}[\mathbf{x}]\langle\boldsymbol{\xi},\boldsymbol{\zeta}\rangle\,\underline{\mathbf{U}}[\mathbf{x},t]\langle\boldsymbol{\zeta}\rangle\,\mathrm{d}V_{\mathbf{x}''}\\ &= \int_{\mathcal{H}_{\mathbf{x}}(\delta_0)} \underline{\mathbb{K}}[\mathbf{x}]\langle\boldsymbol{\xi},\boldsymbol{\zeta}\rangle\,(\mathbf{H}\boldsymbol{\zeta})\,\mathrm{d}V_{\mathbf{x}''}\,, \end{aligned} \tag{1.106}$$

where $\boldsymbol{\xi}=\mathbf{x}'-\mathbf{x}$, $\boldsymbol{\zeta}=\mathbf{x}''-\mathbf{x}$, and $\mathbf{H}=\nabla\mathbf{u}$ is the displacement gradient tensor. This tensor is related to the deformation gradient tensor as follows: $\mathbf{F}=\partial\mathbf{y}/\partial\mathbf{x}=\partial(\mathbf{u}+\mathbf{x})/\partial\mathbf{x}=\mathbf{H}+\mathbf{1}$, where $\mathbf{1}$ is the identity matrix. Substituting Equation 1.106 into Equation 1.105 yields

$$\begin{aligned}\boldsymbol{\nu}_0(\mathbf{x}) &= \int_{\mathcal{H}_{\mathbf{x}}(\delta_0)}\int_{\mathcal{H}_{\mathbf{x}}(\delta_0)} (\underline{\mathbb{K}}[\mathbf{x}]\langle\boldsymbol{\xi},\boldsymbol{\zeta}\rangle\,(\mathbf{H}\boldsymbol{\zeta}))\otimes\boldsymbol{\xi}\,\mathrm{d}V_{\mathbf{x}''}\,\mathrm{d}V_{\mathbf{x}'}\\ &= \int_{\mathcal{H}_{\mathbf{x}}(\delta_0)}\int_{\mathcal{H}_{\mathbf{x}}(\delta_0)} \underline{K}_{ik}[\mathbf{x}]\langle\boldsymbol{\xi},\boldsymbol{\zeta}\rangle\,H_{kl}\,\zeta_l\,\xi_j\,\mathrm{d}V_{\mathbf{x}''}\,\mathrm{d}V_{\mathbf{x}'}\,, \end{aligned} \tag{1.107}$$

where Einstein notation is used. In classical continuum mechanics, the stress tensor under the assumption of small deformations can be written as $\sigma_{ij}=C_{ijkl}\,H_{kl}$, where $C_{ijkl}$ are

the components of the fourth-order elasticity tensor $\mathbb{C}$. Therefore, the components of the fourth-order elasticity tensor are computed in peridynamics as [166]

$$C_{ijkl}(\mathbf{x}) = \int_{\mathcal{H}_{\mathbf{x}}(\delta_0)} \int_{\mathcal{H}_{\mathbf{x}}(\delta_0)} \underline{K}_{ik}[\mathbf{x}]\langle \boldsymbol{\xi}, \boldsymbol{\zeta} \rangle \, \zeta_l \, \xi_j \, \mathrm{d}V_{\mathbf{x}''} \, \mathrm{d}V_{\mathbf{x}'} \, . \tag{1.108}$$

Using Equation 1.76, this expression can be simplified as

$$\begin{aligned} C_{ijkl} &= \int_{\mathcal{H}_{\mathbf{x}}(\delta_0)} \underline{\omega}(\|\boldsymbol{\xi}\|) \int_{\mathcal{H}_{\mathbf{x}}(\delta_0)} \left( \frac{c_\theta \, k_\theta}{m^2} \, \underline{\omega}(\|\boldsymbol{\zeta}\|) + \frac{\alpha}{m} \, \frac{\boldsymbol{\Delta}(\boldsymbol{\zeta} - \boldsymbol{\xi})}{\|\boldsymbol{\xi}\| \, \|\boldsymbol{\zeta}\|} \right) \xi_i \, \xi_j \, \zeta_k \, \zeta_l \, \mathrm{d}V_{\mathbf{x}''} \, \mathrm{d}V_{\mathbf{x}'} \\ &= \frac{c_\theta \, k_\theta}{m^2} \int_{\mathcal{H}_{\mathbf{x}}(\delta_0)} \underline{\omega}(\|\boldsymbol{\xi}\|) \, \xi_i \xi_j \, \mathrm{d}V_{\mathbf{x}'} \int_{\mathcal{H}_{\mathbf{x}}(\delta_0)} \underline{\omega}(\|\boldsymbol{\zeta}\|) \, \zeta_k \zeta_l \, \mathrm{d}V_{\mathbf{x}''} + \frac{\alpha}{m} \int_{\mathcal{H}_{\mathbf{x}}(\delta_0)} \underline{\omega}(\|\boldsymbol{\xi}\|) \frac{\xi_i \xi_j \xi_k \xi_l}{\|\boldsymbol{\xi}\|^2} \, \mathrm{d}V_{\mathbf{x}'} \, . \end{aligned} \tag{1.109}$$

### 1.2.4 Numerical discretization of peridynamics

Analytical solutions to peridynamic problems are difficult to find because of the integro-differential nature of the equation of motion (integral in space to allow for discontinuities to naturally arise and differential in time). For example, analytical solutions are provided in [163, 164] by using the method of separation of variables, but this method is valid only for simple geometries of the body and when there are no discontinuities in the problem. Therefore, there is the need to discretize the peridynamic equations in order to obtain numerical solutions to any possible problem.

#### Spatial integration

Many numerical methods can be used to discretize the peridynamic equations [173]. The so-called *meshfree method* [65] is the most common one in the literature. A novel hybrid method was developed to reduce the computational cost of the meshfree method in the regions of the body away from boundaries, discontinuities, and interfaces [174, 175]. The finite element method has also been used to numerically solve the peridynamic equation [176–178], but remeshing would be required to model crack propagation. The fast convolution-based method [179, 180] takes advantage of the convolutional form of the peridynamic integral operator to improve computational efficiency by using the FFT (Fast Fourier Transform). In the following, the meshfree method is adopted.

In the meshfree method, the body is often discretized with a grid of nodes in such a way that a finite volume is associated with each node, and the union of the volumes of all nodes is the whole body. An irregular distribution of nodes is possible (see, for instance, [181–183]), but the complexity of the numerical model considerably increases. Therefore, a uniform grid of nodes, with a grid spacing equal to $h$ in all directions, is here considered [65], as shown in Figure 1.15. Under this assumption, each node is associated with a cell with a finite volume $\Delta V = h^3$ in 3D models, to $\Delta V = t \, h^2$ in 2D models (where $t$ is the thickness of the body), and $\Delta V = A \, h$ in 1D models (where $A$ is the cross-sectional area of the body).

The spatial integration of the peridynamic integral operator is carried out as follows: the integral over the neighborhood is transformed into a summation of integrals over nodal cells,

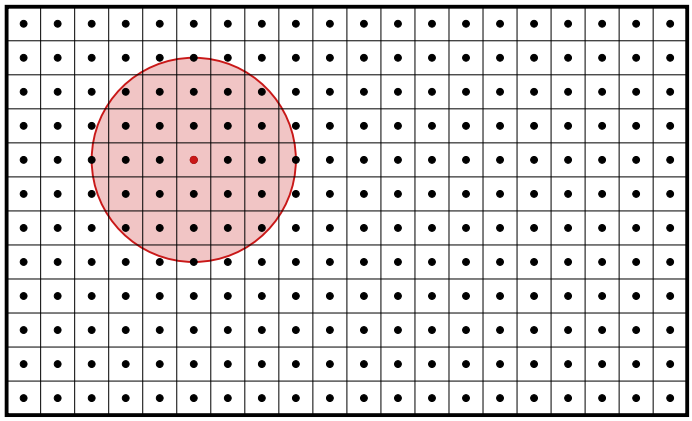

Figure 1.15: *Discretization of a body modeled with peridynamics using the meshfree method with uniform grid spacing. The neighborhood of a node is highlighted in red.*

and then the midpoint quadrature rule is applied to those integrals over the cells. Thus, the peridynamic equation of motion, discretized from Equation 1.2, at time $t \geq 0$ at a node $\mathbf{x}_i$ is given as [65]

$$\rho(\mathbf{x}_i)\,\ddot{\mathbf{u}}(\mathbf{x}_i,t) = \sum_{j\in\mathcal{H}_i} \mathbf{f}(\mathbf{x}_i,\mathbf{x}_j,t)\,\beta_{ij}\,\Delta V + \mathbf{b}(\mathbf{x}_i,t)\,, \tag{1.110}$$

where $\rho$ is the density of the material, $\ddot{\mathbf{u}}$ is the acceleration field, $\mathcal{H}_i$ is the neighborhood of node $\mathbf{x}_i$, $\mathbf{f}$ is the force state (force per unit volume squared), $\beta_{ij}$ is the quadrature coefficient associated with the bond between nodes $\mathbf{x}_i$ and $\mathbf{x}_j$, and $\mathbf{b}$ is the external force density field. Nodes $\mathbf{x}_i$ and $\mathbf{x}_j$ are often referred to as the *source node* and the *family node*, respectively. A node $\mathbf{x}_j$ belongs to the neighborhood $\mathcal{H}_i$ if at least a portion of its cell lies within $\mathcal{H}_i$, as shown in Figure 1.16. In quasi-static conditions, the peridynamic equilibrium equation in the discretized model yields

$$-\sum_{j\in\mathcal{H}_i} \mathbf{f}(\mathbf{x}_i,\mathbf{x}_j)\,\beta_{ij}\,\Delta V = \mathbf{b}(\mathbf{x}_i)\,. \tag{1.111}$$

The quadrature coefficient $\beta$ is introduced to improve the accuracy of the numerical integration of the peridynamic models. Observing Figure 1.16, one can notice that the cells of the family nodes close to the source node lie completely within the neighborhood, whereas those near the boundary of the neighborhood lie only partially within it. In the numerical integration of the peridynamic operator, the contribution of each node should be proportional to the fraction of its cell volume that actually lies within the neighborhood [158, 184]. In some sense, the quadrature coefficient represents the "weight" that each family node has in the integral over the neighborhood. Hence, $\beta_{ij} = 1$ for family nodes $\mathbf{x}_j$ that have the whole cell volume inside the neighborhood $\mathcal{H}_i$ and $0 < \beta_{ij} < 1$ for those that have only a portion of volume cell inside $\mathcal{H}_i$ (see Figure 1.16). In the latter case, the portion of cell volume (or area in 2D, or length in 1D) that lies within the neighborhood is often referred to as *partial volume* (or *partial area* in 2D, or *partial length* in 1D).

Now consider a node $\mathbf{x}_j$ with a portion of its cell lying inside the neighborhood $\mathcal{H}_i$ of

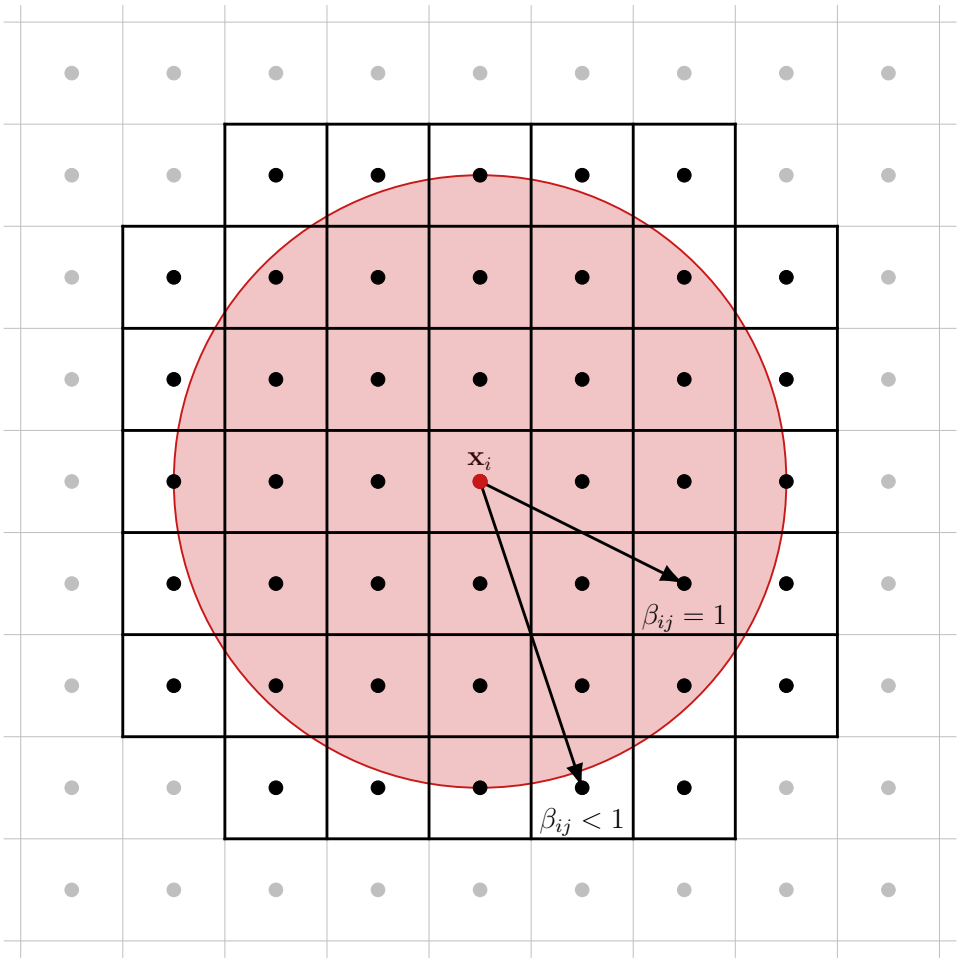


Figure 1.16: *Discretization of the neighborhood of a node* $\mathbf{x}_i$ *using the meshfree method with uniform grid spacing. The nodes colored in black belong to the neighborhood of node* $\mathbf{x}_i$*, whereas the nodes colored in gray do not.*

node $\mathbf{x}_i$. The bond connecting these nodes is described by

$$\boldsymbol{\xi}_{ij} = \mathbf{x}_j - \mathbf{x}_i \,. \tag{1.112}$$

Analogously, the relative displacement vector after the deformation of the body is defined as

$$\boldsymbol{\eta}_{ij} = \mathbf{u}(\mathbf{x}_j, t) - \mathbf{u}(\mathbf{x}_i, t) \,, \tag{1.113}$$

where $\mathbf{u}$ is the displacement field applied to a body modeled with peridynamics.

In bond-based peridynamics, the bond stretch (see Equation 1.15) in the discretized model is given as

$$s_{ij} = \frac{\|\boldsymbol{\xi}_{ij} + \boldsymbol{\eta}_{ij}\| - \|\boldsymbol{\xi}_{ij}\|}{\|\boldsymbol{\xi}_{ij}\|} \,. \tag{1.114}$$

The pairwise force of a bond in a prototype microelastic brittle material (see Equation 1.16) is discretized as

$$\mathbf{f}(\mathbf{x}_i, \mathbf{x}_j, t) = c(\boldsymbol{\xi}_{ij})\, \mu_{ij}\, s_{ij}\, \mathbf{m}_{ij} \,, \tag{1.115}$$

where $c$ is the micromodulus, $\mathbf{m}_{ij} = (\boldsymbol{\xi}_{ij} + \boldsymbol{\eta}_{ij})/\|\boldsymbol{\xi}_{ij} + \boldsymbol{\eta}_{ij}\|$ is the unit vector in the direction

of the deformed bond, and $\mu_{ij}$ is a history-dependent scalar-valued function given as

$$\mu_{ij} = \begin{cases} 1 & \text{if } s_{ij} < s_0 \text{ for any previous or current } \boldsymbol{\eta}_{ij}\,, \\ 0 & \text{otherwise,} \end{cases} \tag{1.116}$$

where $s_0$ is the critical bond stretch. The function $\mu_{ij}$ introduces the concept of (irreversibly) broken bonds in bond-based peridynamics. Under the assumption of small displacements ($\|\boldsymbol{\eta}_{ij}\| \ll \|\boldsymbol{\xi}_{ij}\|$), the pairwise force (see Equation 1.18) can be simplified as

$$\mathbf{f}(\mathbf{x}_i, \mathbf{x}_j, t) = \frac{c(\boldsymbol{\xi}_{ij})}{\|\boldsymbol{\xi}_{ij}\|}\, \mu_{ij}\, (\mathbf{m}_{ij} \otimes \mathbf{m}_{ij})\, \boldsymbol{\eta}_{ij} = \mathbf{C}(\boldsymbol{\xi}_{ij})\, \boldsymbol{\eta}_{ij}\,, \tag{1.117}$$

where "$\otimes$" stands for the dyadic product between two vectors and $\mathbf{m}_{ij} = \boldsymbol{\xi}_{ij}/\|\boldsymbol{\xi}_{ij}\|$.

In state-based peridynamics, the extension scalar state (see Equation 1.33) of bond $\boldsymbol{\xi}_{ij}$ is given as

$$\underline{e}_{ij} = \|\boldsymbol{\xi}_{ij} + \boldsymbol{\eta}_{ij}\| - \|\boldsymbol{\xi}_{ij}\|\,. \tag{1.118}$$

The deformed direction vector state in the discretized model is computed as

$$\underline{\mathbf{M}}_{ij} = \frac{\boldsymbol{\xi}_{ij} + \boldsymbol{\eta}_{ij}}{\|\boldsymbol{\xi}_{ij} + \boldsymbol{\eta}_{ij}\|}\,. \tag{1.119}$$

Under the assumption of small displacements, these variables can be simplified as $\underline{e}_{ij} = \boldsymbol{\eta}_{ij} \cdot \underline{\mathbf{M}}_{ij}$ and $\underline{\mathbf{M}}_{ij} = \boldsymbol{\xi}_{ij}/\|\boldsymbol{\xi}_{ij}\|$. The weighted volume $m_i = m(\mathbf{x}_i)$ and the dilatation $\theta_i = \theta(\mathbf{x}_i)$ (see Equations 1.42 and 1.41, respectively) are numerically evaluated with the midpoint quadrature rule applied to each cell of the family nodes:

$$m_i = \sum_{j \in \mathcal{H}_i} \underline{\omega}(\|\boldsymbol{\xi}_{ij}\|)\, \|\boldsymbol{\xi}_{ij}\|^2\, \beta_{ij}\, \Delta V\,, \tag{1.120}$$

$$\theta_i = \frac{c_\theta}{m_i} \sum_{j \in \mathcal{H}_i} \underline{\omega}(\|\boldsymbol{\xi}_{ij}\|)\, \|\boldsymbol{\xi}_{ij}\|\, \underline{e}_{ij}\, \beta_{ij}\, V\,. \tag{1.121}$$

Therefore, the force state in a bond $\boldsymbol{\xi}_{ij}$ for an ordinary state-based peridynamic material (see Equation 1.62) is given as

$$\mathbf{f}(\mathbf{x}_i, \mathbf{x}_j, t) = \underline{\omega}(\|\boldsymbol{\xi}_{ij}\|) \left[ k_\theta\, \|\boldsymbol{\xi}_{ij}\| \left( \frac{\theta_i}{m_i} + \frac{\theta_j}{m_j} \right) + \alpha \left( \frac{1}{m_i} + \frac{1}{m_j} \right) \underline{e}_{ij} \right] \underline{\mathbf{M}}_{ij}. \tag{1.122}$$

The force state can be multiplied by $\mu_{ij}$ as in bond-based peridynamics to introduce the possibility of breaking bonds in the model.

### Time integration

Peridynamics is a theory that has been developed to handle crack propagation problems with ease. As a crack or multiple cracks propagate in a body modeled with peridynamics, the bonds break accordingly, effectively resulting in a change of the stiffness properties of the material. Therefore, explicit methods for time integration are highly recommended over

implicit ones to reduce the computational cost of the simulation. Nevertheless, care should be taken because explicit methods are conditionally stable. In other words, the time-step size should be chosen below a certain limit to obtain stability for the numerical method.

In quasi-static conditions, the crack speed is assumed to be much slower than the speed of mechanical waves. Therefore, the dependence on time can be dropped, as shown in Equation 1.111. However, when a bond breaks, the internal force that that bond was carrying has to be redistributed over the nearby bonds, which can lead to the breakage of another bond. This means that the sequence with which bonds break (and, in some sense, the time at which they do) still plays a role.

For quasi-static crack propagation, the adaptive dynamic relaxation method [185] can be used. This method converts the static problem into a dynamic one by introducing fictitious inertial and damping forces. The solution of the new dynamic problem is numerically integrated via an explicit scheme, and, as the transient solution is damped out, converges to the sought static solution. Similarly, a sequentially linear analysis [73] can be used.

In dynamic problems, a variety of different time integration schemes can be used, such as the explicit central difference formula or the velocity-Verlet method. The explicit central difference formula for the acceleration [65] is presented hereinafter:

$$\ddot{\mathbf{u}}(\mathbf{x}_i, t_n) = \frac{\mathbf{u}(\mathbf{x}_i, t_{n+1}) - 2\mathbf{u}(\mathbf{x}_i, t_n) + \mathbf{u}(\mathbf{x}_i, t_{n-1})}{(\Delta t)^2}\,, \tag{1.123}$$

where $\Delta t$ is the constant time-step size and $n$ stands for the index of the current time step. The iterative procedure to obtain the displacement of node $\mathbf{x}_i$ at the time step $t_{n+1}$ is given by combining Equations 1.110 and 1.123 as

$$\mathbf{u}(\mathbf{x}_i, t_{n+1}) = 2\mathbf{u}(\mathbf{x}_i, t_n) - \mathbf{u}(\mathbf{x}_i, t_{n-1}) + \frac{(\Delta t)^2}{\rho(\mathbf{x}_i)} \left( \sum_{j \in \mathcal{H}_i} \mathbf{f}(\mathbf{x}_i, \mathbf{x}_j, t_n)\, \beta_{ij}\, \Delta V + \mathbf{b}(\mathbf{x}_i, t_n) \right). \tag{1.124}$$

However, to obtain the displacement at the first time step $\mathbf{u}(\mathbf{x}_i, t_1)$, the knowledge of $\mathbf{u}(\mathbf{x}_i, t_{-1})$ is required as well. This displacement can be computed as

$$\mathbf{u}(\mathbf{x}_i, t_{-1}) = \mathbf{u}(\mathbf{x}_i, t_0) - \Delta t\, \dot{\mathbf{u}}(\mathbf{x}_i, t_0) + \frac{(\Delta t)^2}{2}\, \ddot{\mathbf{u}}(\mathbf{x}_i, t_0)\,, \tag{1.125}$$

where the initial displacement $\mathbf{u}(\mathbf{x}_i, t_0)$ and velocity $\dot{\mathbf{u}}(\mathbf{x}_i, t_0)$ are known from the initial conditions at any node and the initial acceleration is given as

$$\ddot{\mathbf{u}}(\mathbf{x}_i, t_0) = \frac{1}{\rho(\mathbf{x}_i)} \left( \sum_{j \in \mathcal{H}_i} \mathbf{f}(\mathbf{x}_i, \mathbf{x}_j, t_0)\, \beta_{ij}\, \Delta V + \mathbf{b}(\mathbf{x}_i, t_0) \right). \tag{1.126}$$

In bond-based peridynamics under the assumption of small displacements (see Equation 1.117), the Von Neumann stability analysis yields the following maximum time-step size [65]:

$$\Delta t < \sqrt{\frac{2\rho}{\sum_{j \in \mathcal{H}_i} \mathbf{C}(\boldsymbol{\xi}_{ij})\, \beta_{ij}\, \Delta V}}\,, \tag{1.127}$$

where $\rho$ is the minimum density of any node of the body. Equation 1.127 represents the criterion for the stability of the explicit numerical method corresponding to the well-known Courant-Friedrichs-Lewy criterion in classical continuum mechanics, in which $\Delta t < \mathcal{O}(h)$. However, the maximum time-step size in peridynamics depends only weakly on the grid spacing $h$ but it is limited by the horizon size ($\Delta t < \mathcal{O}(\delta)$). Since $\delta > h$ in peridynamic models, the stability of the numerical method is achieved with a larger time-step size, with a gain in computational efficiency. It is worth noting that the criterion derived with the Von Neumann stability analysis does not consider the influence of the boundary conditions. Furthermore, no criteria for the maximum time-step size are available for state-based peridynamic models. The stability of explicit time integration schemes in peridynamics is still a largely unexplored field.

**Numerical convergence analyses**

The horizon size $\delta$ is the measure of nonlocality of the peridynamic model. It is sometimes possible to choose the value $\delta$ as a specific physical length scale of the modeled phenomenon. In this case, since the horizon size assumes a physical meaning, it can be calibrated to experimental measurements. For example, the horizon size at the nanoscale can be determined by the maximum distance of interaction between atoms. However, most of the times $\delta$ is chosen according to convenience, mainly to reduce computational time. The horizon size in discretized peridynamic models is commonly expressed as

$$\delta = \overline{m}\, h\,, \tag{1.128}$$

where $\overline{m}$ is called $\overline{m}$*-ratio* and $h$ is the uniform grid spacing. The $\overline{m}$-ratio, the value of which determines how many family nodes belong to the neighborhood of each node, is often chosen as an integer value. In practice, $\overline{m} = 3$ is a good compromise to avoid undesired grid effects for lower $\overline{m}$ values (cracks may propagate along the rows or columns of the grid), and excessive wave dispersion and computational cost for larger $\overline{m}$ values (at the same $h$ value) [65].

In peridynamics, three possible types of convergence analysis can be defined [149]:

- The $\delta$-convergence consists of decreasing the horizon size $\delta$ while keeping the $\overline{m}$-ratio fixed. As shown in Figure 1.17a, the grid spacing $h$ decreases but the number of nodes within the neighborhood remains constant. In this case, the numerical peridynamic solution converges to the solution obtained with classical continuum mechanics.

- The $\overline{m}$-convergence consists of increasing $\overline{m}$ while keeping $\delta$ fixed. As shown in Figure 1.17b, the number of nodes within the neighborhood increases as the grid spacing $h$ decreases. In this case, the numerical solution converges to the exact peridynamic solution for the given $\delta$.

- The $\delta\overline{m}$-convergence consists of decreasing $\delta$ while increasing $\overline{m}$. To obtain a uniform convergence, $\overline{m}$ needs to increase faster than $\delta$ decrases, as shown in Figure 1.17c. In this case, the numerical solution converges to both the exact peridynamic solution and the classical solution.

The last convergence analysis is less often used because the effects due to the decrease of $\delta$ and the increase of $\overline{m}$ are intertwined and difficult to distinguish from each other.

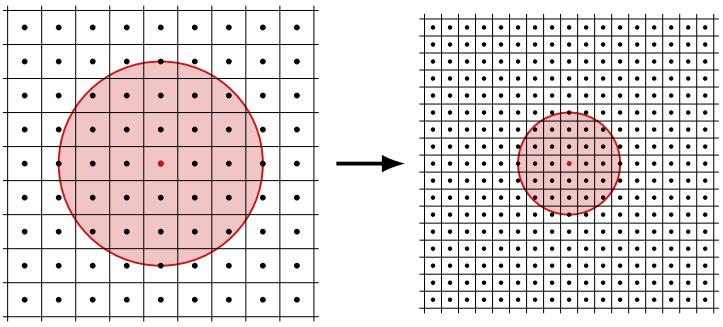

(a) *$\delta$-convergence ($\overline{m}$ fixed).*

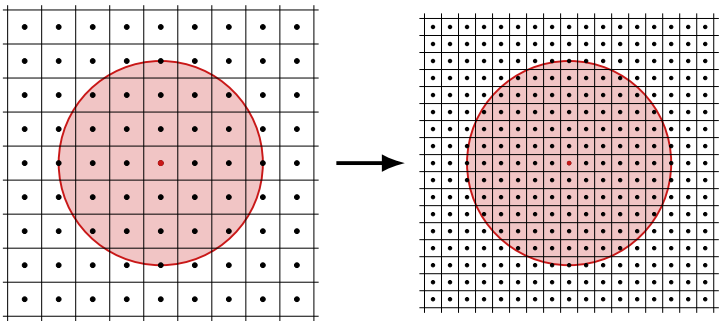

(b) *$\overline{m}$-convergence ($\delta$ fixed).*

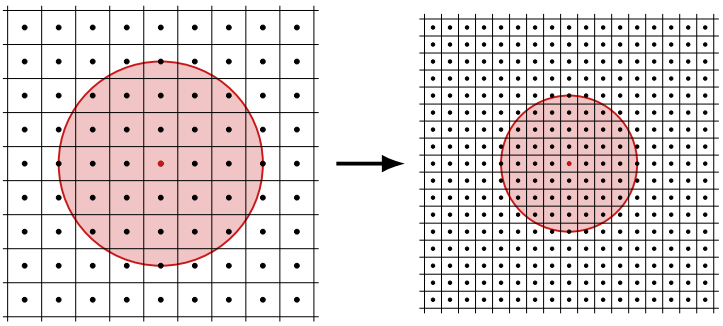

(c) *$\delta\overline{m}$-convergence ($\overline{m}$ increases more than $\delta$ decreases).*

Figure 1.17: *Possible types of convergence analysis in peridynamics.*

### 1.2.5 Main drawbacks of peridynamics

In this section, the main disadvantages related the peridynamic theory are highlighted. One of the objectives of this work is to mitigate all these issues.

#### Surface effect

The peridynamic surface effect is an undesired variation in the stiffness properties of the material in the region near the boundary of the body [186]. This effect is due to the fact that the points close to the boundary have an incomplete neighborhood, as shown in Figure 1.18, because they lack the interactions with points outside the body. Recall that

the bond properties are calibrated so that, for a body under a homogeneous deformation, the peridynamic strain energy density at a point with a complete neighborhood equalizes the strain energy density obtained with classical continuum mechanics. Therefore, if the same mechanical properties for all the bonds in the body are used, the strain energy density of points with an incomplete neighborhood near the boundary of the body is lower than that of points with a full neighborhood in the bulk of the body. This is the reason why, in bond-based peridynamics, the external layer of thickness $\delta$ of the body exhibits a softening behavior. On the other hand, in state-based peridynamics, the surface effect influences the external layer of thickness $2\delta$ since the points interact up to that distance. Nonetheless, the peridynamic surface effect has not been fully characterized in state-based peridynamics, yet.

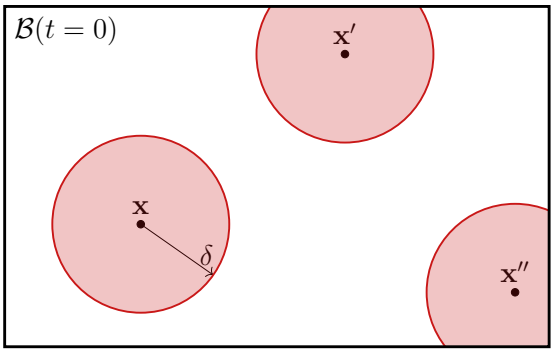


Figure 1.18: *The peridynamic surface effect is due to the fact that the points near the boundary of the body, such as points* $\mathbf{x}'$ *and* $\mathbf{x}''$*, have an incomplete neighborhood.*

In the literature, two common approaches have been used to mitigate the peridynamic surface effect:

- Instead of considering the same mechanical properties for all the bonds in the body, the properties of the bonds close to the boundary can be modified according to different methods [63, 64, 187–190]. The most general method of this type is the one that develops, in a state-based peridynamic framework, the constitutive modeling called the *position-aware linear solid* presented in [190]. In a position-aware linear solid, the mechanical properties of the bonds near the boundary of the body are tuned in such a way that the peridynamic strain energy density is equal to the classical one at any point of a body under homogeneous deformation, even close to the boundary.

- In order to keep constant the mechanical properties of bonds throughout the whole body, one can use the method of the *fictitious layer*: a layer of thickness $\delta$ in bond-based peridynamics and $2\delta$ in state-based peridynamics is introduced around the body to complete the neighborhoods of the nodes close to the boundary [148, 188, 191]. The displacements of the points within the fictitious layer are extrapolated from the displacements of the points of the body. This allows to mitigate the surface effect without changing the constitutive modeling discussed in the previous sections.

As discussed in the following section, the second approach can also be used to impose the peridynamic boundary conditions.

### Boundary conditions

Due to the nonlocal nature of peridynamics, the imposition of boundary conditions is an issue in this kind of models. In fact, the variational formulation of the integral operator in the peridynamic equations does not lead to natural boundary conditions as in the case of classical continuum mechanics [61]. Therefore, peridynamic boundary conditions are imposed on a layer of finite thickness (equal to $\delta$ in bond-based peridynamics and $2\delta$ in state-based peridynamics) under the surface of the body. However, since experiments provide only local measurements at the boundary of the domain, it is often desirable to impose local boundary conditions in a nonlocal model, i.e., boundary conditions that are applied only at the boundary of the body and not in a finite-thickness region. When using the fictitious layer method, it was suggested in [63] that this layer can be used to enforce boundary conditions. To do so, some methods based on simple geometries and specific loadings/constraints have been developed [92, 126, 150, 151, 186, 192–196]. In any case, no general method to impose local boundary conditions in peridynamic models is currently available.

### Numerical integration

The peridynamic theory is based on an integral operator. Therefore, the numerical integration plays a fundamental role in the discretization of peridynamic models. If the peridynamic integral operator is numerically evaluated in an inaccurate way, the numerical results may not converge to the analytical peridynamic solution (in the case of a $\overline{m}$-covergence analysis). As discussed in Section 1.2.4, a quadrature coefficient $\beta$ is used in the numerical integration to properly "weight" the contribution of the family nodes with the cell partially within the neighborhood of the source node (see Figure 1.16). In order to improve the accuracy of the numerical integration, $\beta$ should be computed as the fraction of cell volume that actually lies within the neighborhood, called the partial volume in 3D, the partial area in 2D, or the partial length in 1D) [158, 184].

The computation of the quadrature coefficients can be approximated with some algorithms based on the length of the bond [160, 197, 198]. These algorithms are simple and computationally efficient, but the numerical convergence behavior to the peridynamic solution is not ensured. Keeping the horizon size fixed and reducing the nodal grid spacing, the errors of the peridynamic models indeed exhibit seemingly random fluctuations. In [184], an algorithm to analytically compute partial areas in 2D peridynamic models is presented, resulting in an improved accuracy of numerical integration. Furthermore, an algorithm for the numerical computation of the partial volumes in 3D peridynamic models was developed in [158], but the associated computational cost increases significantly.

### Computational cost

On the one hand, in classical continuum mechanics, points interact only with points with which they are directly in contact (in peridynamic terms, $\delta = 0$). This translates into a great advantage in numerical models, since the computational cost is significantly reduced. For example, in the Finite Element Method (FEM), a node interacts only with nodes with

which it "shares" an element, i.e., only with the closest nodes. Hence, the bandwidth of the stiffness matrix is rather narrow, resulting in a great computational efficiency in solving the system of equations. This is arguably the benefit that makes FEM so famous and widely used in the field of computational mechanics.

On the other hand, the interaction between nodes in peridynamics occurs over a finite distance, which increases the computational cost to obtain the numerical solution, especially in 3D. In particular, the number of family nodes interacting with a source node with a complete horizon scales as $\mathcal{O}(\overline{m})$ in 1D, $\mathcal{O}(\overline{m}^2)$ in 2D, and $\mathcal{O}(\overline{m}^3)$ in 3D, as shown in Table 1.1. Figure 1.19 shows an example in 2D of the number of interactions for a node with a complete horizon as $\overline{m}$ increases. If the number of interactions for each node increases, then the bandwidth of the stiffness matrix accordingly increases, and the computational efficiency to solve the peridynamic system of equations decreases.

Table 1.1: *Number of family nodes interacting with a source node with a complete neighborhood for different values of $\overline{m}$-ratio in 1D, 2D, and 3D.*

| $\overline{m}$-ratio | Family nodes (1D) | Family nodes (2D) | Family nodes (3D) |
|---|---|---|---|
| 3 | 6 | 44 | 250 |
| 5 | 10 | 100 | 822 |
| 10 | 20 | 356 | 5232 |
| 20 | 40 | 1344 | 37464 |
| 100 | 200 | 31828 | 4283780 |

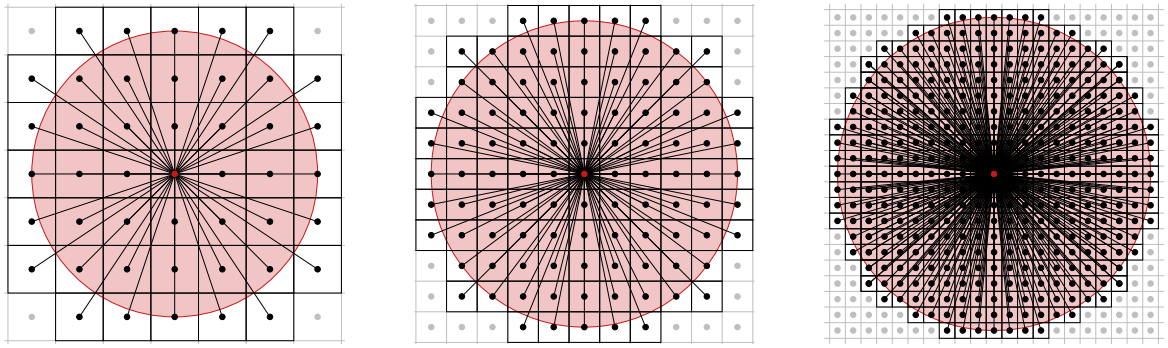

(a) $\overline{m} = 3$. (b) $\overline{m} = 5$. (c) $\overline{m} = 10$.

Figure 1.19: *Bonds in a 2D full neighborhood for different values of $\overline{m}$-ratio.*

In order to improve the computational efficiency of peridynamic models discretized with the meshfree methods, a hybrid method that modifies the numerical integration in the regions far from boundaries, interfaces, and crack surfaces was developed [174, 175]. Alternatively, the fast convolution-based method [179, 180] exploits the convolutional form of the peridynamic integral operator and the fast Fourier transform algorithm to reduce the computational cost of the peridynamic models. Although these methods speed up the computer run time for peridynamic simulations, they are still less computationally efficient than models based on classical continuum mechanics, such as FEM. This is the reason why in recent years many methods to couple peridynamics with FEM has been proposed [199–207]. Thanks to

the coupling, peridynamics is adopted only where cracks may initiate or propagate, whereas FEM is used in the rest of the structure. The coupling method proposed in [115, 171, 205, 206, 208, 209] is capable of adaptively transform FEM nodes into peridynamic ones where cracks are likely to propagate. This method has been successfully validated for quasi-static or dynamic fracture problems.

## 1.3 Innovative contributions

In this section, my personal contributions to the field of peridynamics are presented. Section 1.3.1 reviews a new method devised by myself, i.e., the surface node method, that solves the problems of the surface effect and the imposition of the boundary conditions in peridynamic models. Section 1.3.2 shows how I developed the innovative algorithm to improve the numerical integration in 3D peridynamic models by accurately computing the partial volumes. Section 1.3.3 presents my contributions to the coupling between peridynamics and the Carrera unified formulation, a computationally efficient method based on FEM. Section 1.3.4 introduces the peridynamic modeling of the complex phenomenon of zirconium carbide oxidation.

### 1.3.1 Surface Node Method

All the novelties contained in the three papers in Chapters 2, 3, and 4 were personally investigated by myself under the supervision of Prof. Galvanetto and Prof. Zaccariotto. The innovative contributions include conceptualization, software development, and validation of the Surface Node Method (SNM) that is capable of correcting the surface effect and effectively imposing local boundary conditions in peridynamic models. Furthermore, I wrote the original drafts for all three papers, which were then reviewed by Prof. Galvanetto and Prof. Zaccariotto.

One of the main novelties of the papers is the development of algorithms to numerically compute the peridynamic stress tensor or force flux. In the first paper (Chapter 2), the discretized formula to compute the force flux in a 1D body was presented (see Section 2.4.3). In the second paper (Chapter 3), an innovative algorithm to numerically compute the peridynamic stress tensor and the force flux was developed (see Sections 3.4.3 and 3.4.4). Furthermore, the peridynamic stress tensor was also analytically computed in the case of a 2D body both under homogeneous isotropic and shear deformation, and was proven to be equal to the classical stress tensor under the same conditions (see Section 3.2.2). In the third paper (Chapter 4), the algorithm was extended to numerically evaluate the force flux in 3D peridynamic models (see Section 4.3.4). The algorithm presented in the second paper to compute the numerical peridynamic stress tensor in 2D can be easily extended to 3D models.

In the first paper, the surface effect was analyzed in a 1D ordinary state-based peridynamic model by imposing a homogeneous deformation to the body and analytically computing the force flux. Thanks to this analysis, the characteristic hardening/softening behavior near the boundaries of an ordinary state-based peridynamic body was discovered for the first time (see Section 2.2.2). Furthermore, the nonlocal boundary conditions that should be

imposed over the $2\delta$-thickness layer under the surface of the body to obtain homogeneous deformation were analytically computed. The non-trivial distribution of external loads suggests that nonlocal boundary conditions are very difficult to impose without any a-posteriori knowledge (see Section 2.B). This is the reason why local boundary conditions need to be imposed in nonlocal models. In the second paper, the same analysis of the surface effect in a 2D ordinary state-based peridynamic body was carried out numerically, thanks to the new algorithm to compute the peridynamic stress tensor. A similar hardening/softening behavior was highlighted near the boundary of the body. However, a magnification of the amplitude of the stiffness variation was discovered close to the corners of the body. Moreover, some non-zero shear stresses were unexpectedly present near the corners of the body under homogeneous isotropic deformation and, viceversa, some non-zero tensile stresses were present near the corners of the body under homogeneous shear deformation (see Section 3.2.4). These undesirable characteristics due to the peridynamic surface effect underline how important it is to correct this phenomenon.

To mitigate the surface effect and impose local boundary conditions in a peridynamic model, a fictitious layer of nodes is added around the body. In order to determine the displacements of these fictitious nodes, I developed the so-called *Taylor-based extrapolation* that makes use of the nearest-node strategy (see Sections 2.4.1, 3.4.1 and 4.3.2). This method, based on multiple Taylor series expansion with a general truncation order, allows to express the displacements of the fictitious nodes as functions of the displacements of the nodes within the body near the boundary. The Taylor-based extrapolation can be effectively used for any geometry of the body, even a very complex one. Furthermore, this extrapolation is also exploited to impose Dirichlet boundary conditions.

An important innovation of my work concerns the imposition of Neumann boundary conditions through the concept of force flux. The numerical force flux computed at the boundary of the body can be interpreted as a local value of the stress, even though its computation involves all the forces of the bonds crossing the boundary. Therefore, imposing the local Neumann boundary condition as the peridynamic force flux at the boundary entails an automatic redistribution of forces through the bonds crossing the boundary. Although only a local boundary condition is imposed, this results in a nonlocal effect on the body. This imposition of Neumann boundary conditions is enforced by means of Lagrange multipliers in the first two papers (see Sections 2.4.3 and 3.4.5). However, when using the Lagrange multipliers, the system matrix is less computationally efficient to solve (it is not banded and has some zeros on the diagonal). Thus, the final version of the method presented in the third paper introduces the surface nodes that are used to discretize the surface of the body and to impose the boundary conditions without Lagrange multipliers (see Section 4.3.4).

Several numerical examples were presented in 1D, 2D, and 3D models considering quasi-static conditions to validate the surface node method. It was shown that, in general, increasing the order of truncation of the Taylor-based extrapolation improves the numerical results. In the second paper, two numerical examples involving quasi-static crack propagation were presented, demonstrating that the crack paths were affected by how peridynamic boundary conditions are imposed (see Section 3.6). In the third paper, the surface node method was also compared with other well-known correction methods (see Section 4.5). Furthermore,

the peridynamic analytical solution for a manufactured displacement field was obtained in Section 4.A and the same procedure can be applied to different displacement fields in order to attain other analytical solutions, which are rather rare in peridynamics. The validation of the surface node method applied to peridynamic problems in dynamic conditions can be found in my conference proceedings (see [210, 211]).

### 1.3.2 Accurate spatial integration in peridynamics

The main novelty of the paper in Chapter 5 is the algorithm to accurately compute the partial volumes in 3D peridynamic models. The definition of the partial volumes in an integral form, the analytical solution of those integrals, and the development and verification of the algorithm were carried out by myself under the supervision of Prof. Galvanetto and Prof. Zaccariotto. Furthermore, I wrote the original draft of the paper, which was then reviewed by Prof. Galvanetto and Prof. Zaccariotto.

The quadrature coefficients in the numerical integration of peridynamic equations play a fundamental role in the accuracy and convergence behavior of the final results. These quadrature coefficients are related to the partial areas in 2D models, i.e., the intersections between the circular neighborhood and the square nodal cells, and to the partial volumes in 3D (intersections between the spherical neighborhood and the cubic nodal cells). I was able to express the partial areas and volumes in a new integral form and solve analytically the integral formula of the partial area (see Section 5.A) and quasi-analytically that of the partial volumes (see Section 5.3.5). The word "quasi-analytical" is due to the fact that some integrals in the partial volume formula are not explicitly solvable. Therefore, the integrands of those integrals were expanded by means of a Taylor series, and the integration of the corresponding truncated polynomial was performed.

The solutions to the formulas for the partial areas and volumes are then used to develop a new algorithm for the computation of the quadrature coefficients. The computational time required by the proposed algorithm is negligible compared to that required for the numerical integration of the peridynamic equations. Several $\overline{m}$-convergence analyses were carried out to verify the algorithm (see Section 5.4). The proposed algorithm provides, on average, smaller errors and a smoother convergence behavior for the main quantities of interest, such as the volume of the neighborhood, the weighted volume, and the coefficients of the elasticity tensor.

### 1.3.3 Coupling of peridynamics with CUF

The paper in Chapter 6 was the result of my collaboration with Marco Enea, a Ph.D. student at Politecnico di Torino. My knowledge of the peridynamic theory and the coupling strategy was complemented by Marco's knowledge of the Carrera Unified Formulation (CUF). We collaborated on every aspect of the work, from the coupling realization and software development to the writing and reviewing of the draft. Therefore, we equally shared the merits of the publication of the paper.

The Carrera unified formulation is a classical theory of mechanics that combines FEM

and the theory of structure approximation. In this work, we are concerned only with 1D finite elements with variable displacements over the cross-section, which are called *high-order* 1D finite elements. CUF models based on high-order 1D finite elements enable one to reproduce 3D-like solutions with both great accuracy and computational efficiency [212]. An example of a coupling method between high-order 1D FEM based on CUF and 3D bond-based perydinamic via Lagrange multipliers, which are applied at the interface between the two domains in order to ensure displacement continuity, can be found in [213, 214]. However, spurious effects, in the form of distortions of the numerical solution, are inevitably present at the interface when using this type of coupling technique.

Inspired by the coupling technique between peridynamics (PD) and FEM in [205, 206, 209], we developed an improved CUF/PD coupling strategy to reduce the above-mentioned spurios effect at interfaces (see Section 6.4). Furthermore, the use of the ordinary state-based peridynamics, instead of the bond-based version, allows one to remove the limitation on the choice of the Poisson ratio. The coupling technique is based on the introduction of fictitious PD nodes in the CUF domain and of fictitious CUF elements in the PD domain. Since the coupling technique is based on the continuity of displacements, the displacements of the fictitious nodes are interpolated with the shape functions (along the axis of the 1D finite elements) and the expansion functions (throghout the cross-section) associated to the CUF elements. The effectiveness and computational efficiency of the improved coupling technique are shown by several examples on classical beams and thin-walled structures of aerospace interest (see Section 6.5).

### 1.3.4 Zirconium carbide oxidation

The capabilities of the peridynamic theory in modeling crack propagation can be also exploited in multi-physics problems involving fracture. One example is the complex phenomenon of the oxidation of zirconium carbide (ZrC): the volumetric expansion of ZrC during oxidation causes the formation of cracks, which, in turn, accelerate oxygen diffusion within ZrC. The two papers regarding ZrC oxidation (Chapters 7 and 8) were the result of my 6-month stay at the University of Nebraska-Lincoln under the supervision of one of the main experts in peridynamics, Prof. Florin Bobaru. The phenomenological knowledge and experimental measurements of ZrC oxidation were provided by Dr. Claudia Gasparrini. I also acknowledge the profitable discussions on numerical stability and convergence behavior with Prof. Adam Larios. The peridynamic modeling of ZrC oxidation, software development, and writing of the drafts of the papers were done by myself under the direct supervision of Prof. Bobaru. The drafts were then reviewed by Dr. Gasparrini, Prof. Zaccariotto, Prof. Galvanetto, Prof. Larios, and Prof. Bobaru.

The first paper (Chapter 7) analyzes some unexplored numerical aspects of peridynamic equations to model diffusion phenomena. Since the previous analysis on the peridynamic stability criterion for explicit time integration methods was carried out with the Von Neumann technique that does not take into account the influence of the boundary conditions, I analyzed the stability criterion with the eigenvalue technique to evaluate the effect on the stability of the boundary conditions imposed with the surface node method. This stability

analysis (see Section 7.3) showed that the criterion previously obtained with the Von Neumann technique does not guarantee the stability of the method, and a new (tighter) upper bound for the maximum time-step size was derived. Furthermore, since the ZrC sample is suddenly exposed to oxygen, the effect of a discontinuity in the concentration field at the boundary of the body had to be assessed, particularly to verify the behavior of the extrapolation over the fictitious layer. Various convergence studies proved that, when ignoring the very early times of the simulation, the convergence behavior to the analytical peridynamic solution is the same as that in a problem without discontinuities in the initial conditions (see Section 7.4). In other words, the numerical errors are higher only when a discontinuity is present at the boundary, i.e., at the beginning of the simulation, as one should expect since the discontinuity vanishes due to the oxygen diffusion as the time progresses. Therefore, the surface node method was successfully verified for a diffusion problem with both continuous and discontinuous initial conditions.

In a peridynamic diffusion model in a bi-material, it suffices to know the threshold concentration for phase change and the diffusion properties of the two phases in order to determine the motion of the interface [128]. Hence, the motion of the interface is autonomous, i.e., determined by the "constitutive model" itself. It is worth noting that the peridynamic diffusion model does not require any special conditions at the interface, such as the Stefan condition, which is instead required in classical models. To validate the autonomous motion of the interface, the numerical results of this model are compared with a manufactured analytical solution (see Section 7.5).

Thanks to these numerical analyses, it was possible to develop a reliable peridynamic model able to predict the evolution of the interface during the ZrC oxidation. We observed that two layers across the oxidation front, i.e., the intermediate layer and the transition layer, play a fundamental role in the reaction process. Since the peridynamic model is capable of reproducing the experimental measurements published in [14], it also allowed the quantification of the diffusivity of the zirconium oxide in the intermediate layer and the oxidation rate in the transition layer (see Section 8.5.1). However, the novel method provided not only the new calibration of these properties but also a deeper understanding of the mechanism of the ZrC oxidation. Nevertheless, the velocity of the oxidation front was accurately reproduced by the numerical peridynamic model. Therefore, this model can be used both to predict the growth of the oxide and to determine the shape and dimensions of the remaining unoxidized carbide (see Section 8.5.2).

# Chapter 2

# A novel and effective way to impose boundary conditions and to mitigate the surface effect in state-based Peridynamics

**Published in:** *International Journal for Numerical Methods in Engineering* (2021)

**Authors:** Francesco Scabbia, Mirco Zaccariotto, Ugo Galvanetto

## Abstract

Peridynamics is a non-local continuum theory capable of modeling effectively crack initiation and propagation in solid bodies. However, the non-local nature of this theory is the cause of two main problems near the boundary of the body: an undesired stiffness fluctuation, the so-called *surface effect*, and the difficulty of defining a rational method to properly impose the boundary conditions. The surface effect is analyzed analytically and numerically in the present paper in a state-based peridynamic model. The authors propose a modified fictitious node method based on an extrapolation with a truncated Taylor series expansion. Furthermore, a rational procedure to impose the boundary conditions is defined with the aid of the fictitious nodes. In particular, Neumann boundary conditions are implemented via the peridynamic concept of force flux. The accuracy of the proposed method is assessed by means of several numerical examples for a state-based peridynamic model: with respect to the peridynamic model adopting no corrections, the results are significantly improved even if low values of the truncation order for the Taylor expansion are chosen.

**Keywords:** Peridynamics, surface effect, boundary conditions, force flux, fictitious nodes, Taylor-based extrapolation.

## 2.1 Introduction

Peridynamics is a non-local continuum theory devised to effectively describe fracture phenomena in solid bodies [61, 62]. The first formulation of the theory [61], named bond-based Peridynamics, has been employed by many researchers for its simplicity of implementation. However, state-based Peridynamics was introduced in [62] to overcome the limited capability of prescribing the Poisson's ratio in bond-based models.

Each material point of a body modelled with Peridynamics interacts with all the neighboring points inside a sphere of radius $\delta$. The sphere and the radius are respectively named *neighborhood* and *horizon*. This non-local nature of Peridynamics is essential to embed discontinuities in the model without any ad hoc criteria, but also leads to some issues near the boundary of the body:

- In the most external layer of the body the peridynamic points have an incomplete neighborhood and "feel" the lack of the missing points beyond the boundary. This phenomenon, known as *surface effect* or *skin effect*, causes an undesired variation in stiffness near the boundary. In bond-based Peridynamics, the surface effect appears as a *softening* in the body external layer of thickness $\delta$ [187, 198], whereas in state-based Peridynamics the discrepancy due to the surface effect influences the points closer than $2\delta$ to the boundary, with a behavior which is difficult to predict a priori [186]. This behavior in a 1D state-based peridynamic model is analyzed analytically and numerically in Section 2.2.2.

- The other issue related to non-locality near the external surface of the body occurs when imposing the boundary conditions. In bond-based Peridynamics, Dirichlet boundary conditions have been commonly imposed on the peridynamic nodes closest to the boundary, named *boundary nodes*, whereas Neumann boundary conditions have been applied in several ways. For instance, in [124] a heat flux is applied over the layer of thickness $\delta$ near the boundary assuming a linear variation of temperature there. However, this approach is theoretically inexact if the horizon $\delta$ does not tend to 0 [124]. The "worst-case" scenario for the model accuracy near the boundary is given by the imposition of the external load as a force applied solely to the boundary nodes [186]. In state-based Peridynamics, a similar analysis can be applied, but the effects of the approximated boundary conditions are exhibited in the body exterior layer of thickness $2\delta$ [186].

Many strategies have been proposed to mitigate the surface effect in bond-based Peridynamics by modifying the stiffness of the bonds near the boundary: the force normalization method [187], the force density method [188], the energy method [63, 189] and the volume method [64]. The approach of computing some bond correction factors to recover the proper strain energy density of the points near the boundary under constant deformation, has been employed for state-based peridynamic models in the energy method [63] and in the position-aware linear solid constitutive model [190]. A thorough comparison of these methods has been carried out in [186], highlighting that the boundary inaccuracy is only partially miti-

gated because these model corrections do not deal with the approximated imposition of the boundary conditions.

The surface effect and the problems of the boundary conditions can be confined in a smaller region if the horizon $\delta$ approaches 0. Therefore, the variable horizon method [204, 215, 216] can be exploited to decrease the value of the horizon near the boundaries and restrict the external layer of the body affected by the surface effect [149, 193, 195, 198].

Coupling of Peridynamics with classical continuum mechanics (for instance [171, 205, 206, 209]) provides an approach to completely eliminate the surface effect and the problems of the imposition of the boundary conditions in a discretized model: the external layer is modelled with a classical continuum mechanics method, for example FEM, so that there are no peridynamic nodes with an incomplete neighborhood and the boundary conditions are implemented in a local way on FEM nodes. However, this strategy is not suitable for all the applications of interest, for instance in the case of a crack initiation at the boundary of the body. Furthermore, a crack constitutes a boundary surface of the body which is inevitably modelled with a region of peridynamic nodes.

The method of the *fictitious* or *ghost nodes* was introduced in bond-based Peridynamics to overcome the issue of the surface effect by completing the neighborhoods of the nodes near the boundaries with a layer of peridynamic material which actually does not exist [148, 188]. The strategy of the fictitious nodes has been later employed successfully also in state-based Peridynamics [191]. This approach has been exploited to impose the boundary conditions in bond-based peridynamic models: the fictitious nodes are forced to move according to some predefined functions in order to obtain the desired boundary displacement or load. In [158, 217] the displacement distribution of the fictitious nodes is chosen ad hoc for each case. In [63] the constraints are imposed by displacing the fictitious nodes with the desired constant value and the external loads are applied in the boundary layer within the body. In [92, 126, 150, 151, 186, 192–194] the Dirichlet boundary conditions are implemented by imposing an odd function over the fictitious layer. Moreover, in [92, 186, 192, 193] the displacements of the fictitious nodes to enforce the desired load are derived from the formulae of classical mechanics. In [195] the odd, polynomial and sinusoidal functions are studied to properly impose the desired constraint by means of an iterative procedure. A more theoretical approach for the fictitious layer method has been developed in [218–220].

The Taylor-based fictitious node method [194, 221], an approach similar to the polynomial extrapolation function in [195], has been proposed for bond-based Peridynamics. This approach finds, for every real node near the boundary, the corresponding fictitious node along the normal to the local tangent to the boundary and then evaluates its displacement with a linear extrapolation via the first-order truncated Taylor series. The desired boundary conditions, written as equations adapted from the form of a classical continuum mechanics model, are incorporated into the formulae of the Taylor series [194]. There are two main drawbacks using this approach [194]: the procedure of finding the corresponding fictitious node might be rather difficult in complex geometries and the displacement of each fictitious node is not unique because it depends on the real node at which the computation is carried out.

Inspired by the aforementioned works, we propose, for a state-based peridynamic model,

a generalized method of the Taylor-based extrapolation over the fictitious nodes considering the *nearest-node strategy*. This strategy allows to avoid the two described drawbacks of the Taylor-based extrapolation method, since the displacements of the fictitious nodes are determined with a Taylor series expansion centered at the closest boundary node. Therefore, the uniqueness of the displacements of the fictitious nodes is guaranteed because they depend solely on the displacement of the closest boundary node and its spatial derivatives. Moreover, the nearest-node strategy is easy to implement and suitable for any kind of geometry, even very complex. In addition to that, we show how to implement the fictitious node method in state-based Peridynamics with a fictitious layer of thickness $\delta$ (instead of $2\delta$ as in [191]) via the truncated Taylor series up to a general order $n$. The surface effect is mitigated by the presence of the fictitious nodes and Dirichlet boundary conditions are applied similarly to what is done in [194, 221]. On the other hand, we propose an innovative method to impose Neumann boundary conditions in a "peridynamic way", namely by means of the peridynamic concept of *force flux*.

The paper is organized as follows: Section 2.2 presents a review of 1D state-based Peridynamics and the analytical analysis of the surface effect in a finite body through the concept of force flux, Section 2.3 exposes the proposed method and the imposition of the boundary conditions, Section 2.4 illustrates the discrete model and its implementation, Section 2.5 shows the comparison between the 1D numerical results obtained by using the proposed method and those produced by the state-based peridynamic model without corrections, Section 2.6 introduces the extension of the Taylor-based extrapolation method to 2D problems, and finally Section 2.7 draws the conclusions of the paper and addresses new possible research developments.

## 2.2 1D state-based Peridynamics

The peridynamic theory is based on non-local interactions, the so-called *bonds*, acting between material points. Let $\Omega_\infty$ be an infinite 1D body modelled with Peridynamics, as shown in Figure 2.1. The horizon $\delta$ is defined as the minimum length at which the force interaction vanishes due to increasing distance. Therefore, a point at position $x$ is affected by the points in its neighborhood $\mathrm{H}(x) = \mathrm{H} = \{x' \in \Omega_\infty : |x' - x| \leq \delta\}$.

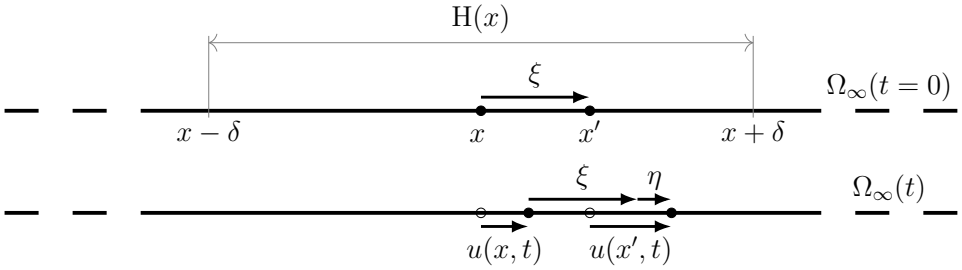


Figure 2.1: *Reference configuration at time $t = 0$ and deformed configuration at time $t$.*

A bond is the *relative position vector* in the reference configuration between the interacting points:

$$\xi = x' - x \tag{2.1}$$

In a deformed configuration, the *relative displacement vector* is defined as:

$$\eta = u(x', t) - u(x, t) \tag{2.2}$$

where $u$ is the displacement along the $x$-axis. Note that $\xi + \eta$ is the relative position of the points in the deformed configuration.

The dynamics of point $x$ in a homogeneous isotropic infinite body $\Omega_\infty$ is governed by the state-based peridynamic equation of motion [62]:

$$\rho \frac{\partial^2 u(x,t)}{\partial t^2} = \int_{\mathrm{H}} \left( \underline{\mathbf{T}}[x,t]\langle \xi \rangle - \underline{\mathbf{T}}[x',t]\langle -\xi \rangle \right) \mathrm{d}V_{x'} + b(x,t) \tag{2.3}$$

where $\rho$ is the material density, $\underline{\mathbf{T}}$ is the force density vector state, $\mathrm{d}V_{x'}$ is the infinitesimal volume associated to the point at position $x'$ and $b$ is the external force density vector. The notation $\underline{\mathbf{T}}[x,t]\langle \xi \rangle$ means that the force density scalar state $\underline{\mathbf{T}}$ depends on point $x$ and time $t$ and is applied to the bond vector $\xi$. The integrand on the right-hand side of the equation represents the peridynamic internal force due to the bond $\xi$ acting on the point $x$ (see Figure 2.2).

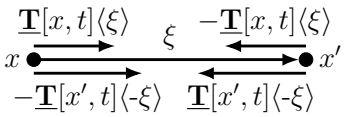


Figure 2.2: *Force density vector states* $\underline{\mathbf{T}}[x,t]\langle \xi \rangle$ *and* $\underline{\mathbf{T}}[x',t]\langle -\xi \rangle$ *of a deformed bond in a 1D state-based peridynamic solid.*

This paper is only concerned with the static solution of the peridynamic problems [72, 73, 222], hence, dropping the dependence upon time, the peridynamic equilibrium equation becomes:

$$-\int_{\mathrm{H}} \left( \underline{\mathbf{T}}\langle \xi \rangle - \underline{\mathbf{T}}'\langle -\xi \rangle \right) \mathrm{d}V' = b \tag{2.4}$$

where, for brevity, $\underline{\mathbf{T}}[x]\langle \xi \rangle = \underline{\mathbf{T}}\langle \xi \rangle$, $\underline{\mathbf{T}}[x']\langle \xi \rangle = \underline{\mathbf{T}}'\langle \xi \rangle$, $\mathrm{d}V_{x'} = \mathrm{d}V'$ and $b(x) = b$.

In the 1D model, the force density vector state can be defined as:

$$\underline{\mathbf{T}}\langle \xi \rangle = \underline{t}[x]\langle \xi \rangle \cdot \frac{\xi + \eta}{|\xi + \eta|} = \underline{t}\langle \xi \rangle \cdot \underline{\mathbf{M}}\langle \xi \rangle \tag{2.5}$$

where $\underline{t}\langle \xi \rangle$ is the force density scalar state (magnitude of $\underline{\mathbf{T}}$) and $\underline{\mathbf{M}}\langle \xi \rangle$ is the deformed direction vector state (unit vector in the direction of $\underline{\mathbf{T}}$).

For later use, the *reference position scalar state*, representing the bond length in the reference configuration, is defined as:

$$\underline{x}\langle \xi \rangle = \underline{x} = |\xi| \tag{2.6}$$

The notation $\langle \xi \rangle$ will be dropped whenever unambiguous. The elongation of the deformed

bond is described by the *extension scalar state* given as:

$$\underline{e}\langle\xi\rangle = \underline{e} = |\xi + \eta| - |\xi| \tag{2.7}$$

Based on the aforementioned notions, the *weighted volume* of a peridynamic point $x$ is given in the initial configuration as:

$$m(x) = m = \int_{\mathrm{H}} \underline{\omega x}^2 \, \mathrm{d}V' \tag{2.8}$$

where $\underline{\omega}\langle\xi\rangle = \underline{\omega}$ is a prescribed spherical influence function.

### 2.2.1 Correspondence with classical mechanics theory

In order to ensure the correspondence between classical continuum theory and state-based Peridynamics, the elastic deformation energy density computed by both approaches should coincide under the same strain conditions [62, 160]. According to classical continuum mechanics, the strain conditions for an isotropic 3D bar under axial loading in which the cross-sections remain plane and perpendicular to the longitudinal axis are given as:

$$\varepsilon_{22} = \varepsilon_{33} = -\nu\varepsilon_{11} \qquad \varepsilon_{12} = \varepsilon_{23} = \varepsilon_{13} = 0 \tag{2.9}$$

where $\varepsilon_{ij}$ with $i, j = 1, 2, 3$ are the components of the strain tensor $\boldsymbol{\varepsilon}$. The $x$-axis, denoted with 1, is considered the longitudinal axis of the bar. The classical dilatation $\theta_{cl}$ is therefore computed for small strains as:

$$\theta_{cl} = \sum_{i=1}^{3} \varepsilon_{ii} = (1 - 2\nu)\varepsilon_{11} \tag{2.10}$$

The strain energy density for a linear elastic bar in classical continuum mechanics is computed from the general 3D formula [160] by substituting in it the strains of Equation 2.9:

$$\begin{aligned} W_{cl} &= \frac{k}{2}\theta_{cl}^2 + G\sum_{i=1}^{3}\sum_{j=1}^{3}\left(\varepsilon_{ij}^d\right)^2 \\ &= \left[\frac{k}{2} + \frac{2(1+\nu)^2 G}{9(1-2\nu)^2}\right]\theta_{cl}^2 + G\left(\varepsilon_{11}^d\right)^2 \\ &= \frac{1}{2}E(\varepsilon_{11})^2 = \frac{1}{2}\sigma_{11}\varepsilon_{11} \end{aligned} \tag{2.11}$$

where $k$ is the bulk modulus, $\nu$ the Poisson's ratio, $G$ the shear modulus, $E$ the Young's modulus, $\varepsilon_{ij}^d$ with $i, j = 1, 2, 3$ are the components of the deviatoric strain tensor $\boldsymbol{\varepsilon}^d = \boldsymbol{\varepsilon} - (\theta_{cl}/3) \cdot \mathbf{1}$ where $\mathbf{1}$ is the identity matrix with a size $3 \times 3$, and $\sigma_{ij}$ with $i, j = 1, 2, 3$ are the components of the stress tensor $\boldsymbol{\sigma}$. Note that in the second line of Equation 2.11 the strain energy density is not divided into volumetric and deviatoric parts as in the first line. The second line of Equation 2.11 is useful to be compared with the peridynamic strain energy density to derive the peridynamic constants, although it could be rewritten in a more

common form (third line) after some omitted manipulations.

The peridynamic strain energy density of a linear material at point $x$ is computed as [62]:

$$W = \frac{\widehat{k}}{2}\theta^2 + \frac{\widehat{G}}{2m}\int_{\mathrm{H}} \underline{\omega}\left(\underline{e}^d\right)^2 \mathrm{d}V' \tag{2.12}$$

where $\widehat{k}$ and $\widehat{G}$ are the peridynamic constants which must be determined by the comparison with the classical strain energy density. $\theta$ and $\underline{e}^d$ are named respectively *dilatation* and *deviatoric extension scalar state* and their correspondence with the classical values are explained in the next paragraphs.

The peridynamic dilatation $\theta$ of the point $x$ is defined to match the classical dilatation under constant deformations:

$$\theta(x) = \theta = \frac{c_\theta}{m}\int_{\mathrm{H}} \underline{\omega x e}\,\mathrm{d}V' \tag{2.13}$$

where the dilatation coefficient is $c_\theta = 1 - 2\nu$. This coefficient is computed through the correspondence of the peridynamic dilatation $\theta_\infty$ of an infinite 1D body $\Omega_\infty$ with the classical dilatation $\theta_{cl}$ for an imposed small constant deformation $\varepsilon_{11} = \overline{\varepsilon}$ (the extension scalar state is $\underline{e} = \overline{\varepsilon}\underline{x}$ for every bond):

$$\theta_\infty = \frac{c_\theta}{m}\int_{\mathrm{H}} \overline{\varepsilon}\underline{\omega x}^2\,\mathrm{d}V' = c_\theta\overline{\varepsilon} = \theta_{cl} \tag{2.14}$$

The deviatoric extension scalar state is defined as:

$$\underline{e}^d[x]\langle\xi\rangle = \underline{e}^d = \underline{e} - \frac{\theta\underline{x}}{3} \tag{2.15}$$

The deviatoric extension scalar state $\underline{e}^d$ is the elongation of the bond, which can be viewed as a material element in classical continuum mechanics, due to the deviatoric strain tensor (constant in the whole body $\Omega_\infty$) [160]:

$$\underline{e}^d = \frac{1}{|\xi|}\xi\cdot\boldsymbol{\varepsilon}^d\xi = \frac{1}{|\xi|}\sum_{i=1}^{3}\sum_{j=1}^{3}\varepsilon_{ij}^d\xi_i\xi_j \tag{2.16}$$

where $\xi_1$, $\xi_2$ and $\xi_3$ are the components of the bond vector $\xi$ in $x$, $y$ and $z$ direction, respectively. In a 1D case the bonds lie on the longitudinal axis of the bar ($\xi_2 = \xi_3 = 0$), thus $\underline{e}^d = \varepsilon_{11}^d\xi_1 = \varepsilon_{11}^d\underline{x}$. The peridynamic deviatoric strain energy density $W^d$ of a point $x$ in the infinite body $\Omega_\infty$ is then given as:

$$W_\infty^d = \frac{\widehat{G}}{2m}\int_{\mathrm{H}} \underline{\omega}\left(\underline{e}^d\right)^2\mathrm{d}V' = \frac{\widehat{G}}{2m}\int_{\mathrm{H}} \underline{\omega}\left(\varepsilon_{11}^d\underline{x}\right)^2\mathrm{d}V' = \frac{\widehat{G}}{2}\left(\varepsilon_{11}^d\right)^2 \tag{2.17}$$

The peridynamic elastic constants are derived by equating the classical and peridynamic strain energy densities:

$$\widehat{k} = k + \frac{4(1+\nu)^2G}{9(1-2\nu)^2} \qquad \widehat{G} = 2G \tag{2.18}$$

The force density scalar state $\underline{t}\langle\xi\rangle$ is found by taking the Fréchet derivative of the peridynamic strain energy density [62] (see Appendix 2.A for details):

$$\underline{t} = k_\theta \frac{\underline{\omega x}}{m}\theta + k_e \frac{\underline{\omega}}{m}\underline{e} \tag{2.19}$$

where $k_\theta = (\nu E)/((1-2\nu)(1+\nu))$ and $k_e = E/(1+\nu)$. We showed here how to determine the force density scalar state $\underline{t}$ by means of the calibration against the classical strain energy density by considering the two simple loading conditions of isotropic expansion and simple shear. The reader can find in [223] an alternative approach.

**Remark 2.1.** In 1D Peridynamics there is only one independent constant since $k_\theta$ is dependent on $k_e$: $k_\theta = (\nu/(1-2\nu)) \cdot k_e$. The choice of keeping two different peridynamic constants is justified by the decision of being consistent with previous formulations [62, 160].

The properties of the bonds $\xi$ and $-\xi$ are related for symmetry reasons by the following formulae: $\underline{\mathbf{M}}\langle\xi\rangle = -\underline{\mathbf{M}}'\langle-\xi\rangle = \underline{\mathbf{M}}$, $\underline{\omega}\langle\xi\rangle = \underline{\omega}\langle-\xi\rangle = \underline{\omega}$, $\underline{x}\langle\xi\rangle = \underline{x}\langle-\xi\rangle = \underline{x}$ and $\underline{e}\langle\xi\rangle = \underline{e}\langle-\xi\rangle = \underline{e}$. The peridynamic equilibrium equation (Equation 2.4) is rewritten by exploiting Equations 2.5 and 2.19:

$$-\int_{\mathrm{H}} \left[ k_\theta \left( \frac{\theta}{m} + \frac{\theta'}{m'} \right) \underline{\omega x} + k_e \left( \frac{1}{m} + \frac{1}{m'} \right) \underline{\omega e} \right] \underline{\mathbf{M}} \, \mathrm{d}V' = b \tag{2.20}$$

where $m' = m(x')$ and $\theta' = \theta(x')$ are respectively the weighted volume and the dilatation of the peridynamic point $x'$. Equation 2.20 provides a conventional form of the equilibrium equation which equates the external force distribution, on the right-hand side, and the internal peridynamic forces, on the left-hand side. The term in the square brackets in Equation 2.20 represents the magnitude of the total force density in the bond $\xi$, namely $\underline{t}\langle\xi\rangle + \underline{t}'\langle-\xi\rangle$.

### 2.2.2 Surface effect

The formulation of the peridynamic theory for a 1D finite body $\Omega$ of length $l$ implies the existence of a boundary $\partial\Omega$, as shown in Figure 2.3. We individuate two sets of points near the boundary which will be useful to describe the surface effect: $\overline{\Omega} = \{x \in \Omega : \forall x' \in \partial\Omega,\ |x'-x| < \delta\}$ and $\widetilde{\Omega} = \{x \in (\Omega \setminus \overline{\Omega}) : \forall x' \in \partial\Omega,\ |x'-x| < 2\delta\}$. These domains are illustrated in Figure 2.3, where $\overline{\Omega} = \overline{\Omega}_0 \cup \overline{\Omega}_l$ and $\widetilde{\Omega} = \widetilde{\Omega}_0 \cup \widetilde{\Omega}_l$.

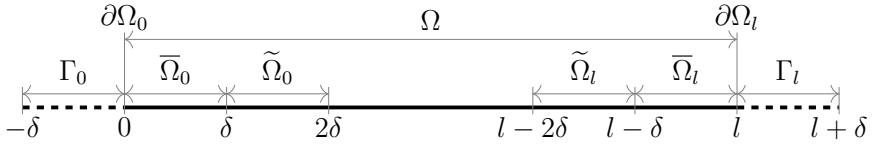


Figure 2.3: *Domains near the boundary $\partial\Omega = \partial\Omega_0 \cup \partial\Omega_l$ of a finite 1D body $\Omega$ of length $l$: $\overline{\Omega} = \overline{\Omega}_0 \cup \overline{\Omega}_l$ is the non-local boundary with a maximum distance $\delta$ from $\partial\Omega$, $\widetilde{\Omega} = \widetilde{\Omega}_0 \cup \widetilde{\Omega}_l$ is the set of points with a distance between $\delta$ and $2\delta$ from $\partial\Omega$ and $\Gamma = \Gamma_0 \cup \Gamma_l$ is the fictitious layer of thickness $\delta$.*

The derivation of the peridynamic constants $k_\theta$ and $k_e$ is strictly valid only for points with a complete neighborhood. In a bond-based peridynamic model without any correction,

the points in $\overline{\Omega}$ with an incomplete neighborhood suffer a reduction in stiffness due to the lack of bonds with points beyond the boundary [187]. In state-based Peridynamics, the domain of the body which is affected by the surface effect is extended also to $\widetilde{\Omega}$ because the peridynamic forces acting on point $x$ depend not only on the properties of the bond ($\underline{\omega}\langle\xi\rangle$, $\underline{x}\langle\xi\rangle$, $\underline{e}\langle\xi\rangle$) and of the neighborhood of the point itself ($\theta$, $m$), but also on the properties of neighborhoods of the neighboring points ($\theta'$, $m'$), as shown in Equation 2.20. Therefore, the state-based peridynamic solution of a finite body under a small constant deformation would differ from the infinite body solution in $(\overline{\Omega} \cup \widetilde{\Omega})$ [186].

Let us define $\mathrm{H}^+$ and $\mathrm{H}^-$ of a point $x$ as the halves of the neighborhood of that point respectively in the same and opposite direction of a unit vector n: $\mathrm{H}^+(x) = \mathrm{H}^+ = \{x' \in \Omega : 0 \leq (x' - x) \cdot \mathrm{n} \leq \delta\}$ and $\mathrm{H}^-(x) = \mathrm{H}^- = \{x' \in \Omega : -\delta \leq (x' - x) \cdot \mathrm{n} \leq 0\}$. The *force flux* at a point $x''$ in the direction of n (see Figure 2.4) is defined in 1D state-based Peridynamics as [61, 172]:

$$\tau(x'', \mathrm{n}) = \int_{\mathrm{H}''^-} \int_{\mathrm{H}''^+ \cap \mathrm{H}^+} \left( \underline{\mathbf{T}}\langle\xi\rangle - \underline{\mathbf{T}}'\langle -\xi\rangle \right) \mathrm{d}V' \, \mathrm{d}x \tag{2.21}$$

where $\mathrm{H}'' = \mathrm{H}(x'')$ is the neighborhood of the point $x''$. The physical meaning of this definition is that the force per unit area acting on the point $x''$ belonging to a plane with normal n is the resultant of the forces per unit area of the bonds which intersect that plane [172]. The force flux is the peridynamic concept closest to the stress in classical mechanics [61]. In order to quantify the discrepancy in stiffness due to the surface effect near the boundaries in a 1D state-based peridynamic model, the force flux $\tau$ given by a small constant deformation $\varepsilon_{11} = \overline{\varepsilon}$ of the finite body $\Omega$ is evaluated and then compared with the force flux in the infinite body $\Omega_\infty$ under the same deformation $\overline{\varepsilon}$.

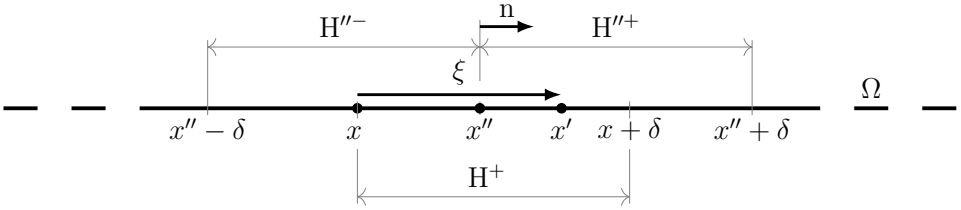


Figure 2.4: *Integration domains for the force flux definition: $x$ varies within $\mathrm{H}''^-$ and $x'$ within $\mathrm{H}''^+ \cap \mathrm{H}^+$.*

The magnitude of the force density in a bond $\xi$ of a body under a constant deformation $\overline{\varepsilon}$ ($\underline{e}\langle\xi\rangle = \overline{\varepsilon}\underline{x}\langle\xi\rangle$, $\theta(x) = c_\theta\overline{\varepsilon}$), is given from Equation 2.20 as:

$$\underline{t}\langle\xi\rangle + \underline{t}'\langle -\xi\rangle = (c_\theta k_\theta + k_e)\,\overline{\varepsilon} \left( \frac{1}{m} + \frac{1}{m'} \right) \underline{\omega x} \tag{2.22}$$

where $c_\theta k_\theta + k_e = E$. Since the influence function can be chosen arbitrarily [157], a hyperbolic influence function is adopted:

$$\underline{\omega}\langle\xi\rangle = \underline{\omega} = \frac{\delta}{|\xi|} \tag{2.23}$$

The choice of this influence function helps simplifying the analytical computation of the force

flux, which is rearranged in the case of a uniformly deformed body via Equation 2.22 as:

$$\tau(x'', +1) = E\overline{\varepsilon}A\delta \int_{x''-\delta}^{x''} \int_{x''}^{x+\delta} \left(\frac{1}{m} + \frac{1}{m'}\right) \mathrm{d}x' \, \mathrm{d}x \tag{2.24}$$

where $\mathrm{d}V' = A \, \mathrm{d}x'$ with $A$ indicating the cross-sectional area.

The computation of the weighted volume $m_\infty$ in an infinite body $\Omega_\infty$ is carried out according to Equation 2.8:

$$m_\infty(x) = \int_{x-\delta}^{x+\delta} \underline{\omega x}^2 A \, \mathrm{d}x' = A\delta \int_{-\delta}^{\delta} |\xi| \, \mathrm{d}\xi = A\delta^3 \tag{2.25}$$

The weighted volume is constant along the infinite body since all the points have a complete neighborhood. With this result, Equation 2.24 yields:

$$\begin{aligned} \tau(x'' \in \Omega_\infty, +1) = \tau''_\infty &= E\overline{\varepsilon}A\delta \int_{x''-\delta}^{x''} \int_{x''}^{x+\delta} \left(\frac{2}{m_\infty}\right) \mathrm{d}x' \, \mathrm{d}x \\ &= E\overline{\varepsilon}\frac{2}{\delta^2} \int_{x''-\delta}^{x''} (x + \delta - x'') \, \mathrm{d}x \\ &= E\overline{\varepsilon} \end{aligned} \tag{2.26}$$

Note that the force flux computed in each point of the infinite body $\Omega_\infty$ under the small uniform strain $\overline{\varepsilon}$ is equal to the stress $\sigma_{11} = E\overline{\varepsilon}$ in classical mechanics.

Dropping the assumption of infinite body, we compute the force flux in a finite bar $\Omega$ of length $l$ under a constant deformation $\overline{\varepsilon}$. The weighted volume in $(\Omega \setminus \overline{\Omega})$ is computed exactly as in Equation 2.25 because in the bulk of the bar the neighborhoods of the peridynamic points are complete. On the other hand, the weighted volume of the points in $\overline{\Omega}$ is smaller due to the lack of some points in their neighborhoods. The computation of the weighted volume in $\overline{\Omega}_0$ yields:

$$m(x \in \overline{\Omega}_0) = A\delta \int_0^{x+\delta} |x' - x| \, \mathrm{d}x' = A\delta^3 \cdot \frac{1}{2} \left( \left(\frac{x}{\delta}\right)^2 + 1 \right) \tag{2.27}$$

The computation of $m$ in $\overline{\Omega}_l$ is carried out analogously. The weighted volume distribution in a finite body normalized with respect to the value of the weighted volume in the infinite body, is reported in Table 2.1 and plotted in Figure 2.5 for different values of the horizon $\delta$. Note that the normalized weighted volume differs from 1 in a more confined domain as the horizon $\delta$ decreases.

The computation of the force flux is carried out by substituting the functions of the weighted volume, given in Table 2.1, in Equation 2.24. The force flux in $(\Omega \setminus (\overline{\Omega} \cup \widetilde{\Omega}))$ is computed in an identical way in Equation 2.26 for the case of infinite body since every bond in that domain connects solely points with a full neighborhood. On the other hand, the force

Table 2.1: *Normalized weighted volume distribution along the finite 1D body.*

| $x \in$ | $m/m_\infty$ |
|---|---|
| $\overline{\Omega}_0$ | $\frac{1}{2}\left(\frac{x}{\delta}\right)^2 + \frac{1}{2}$ |
| $(\Omega \setminus \overline{\Omega})$ | 1 |
| $\overline{\Omega}_l$ | $\frac{1}{2}\left(\frac{l-x}{\delta}\right)^2 + \frac{1}{2}$ |

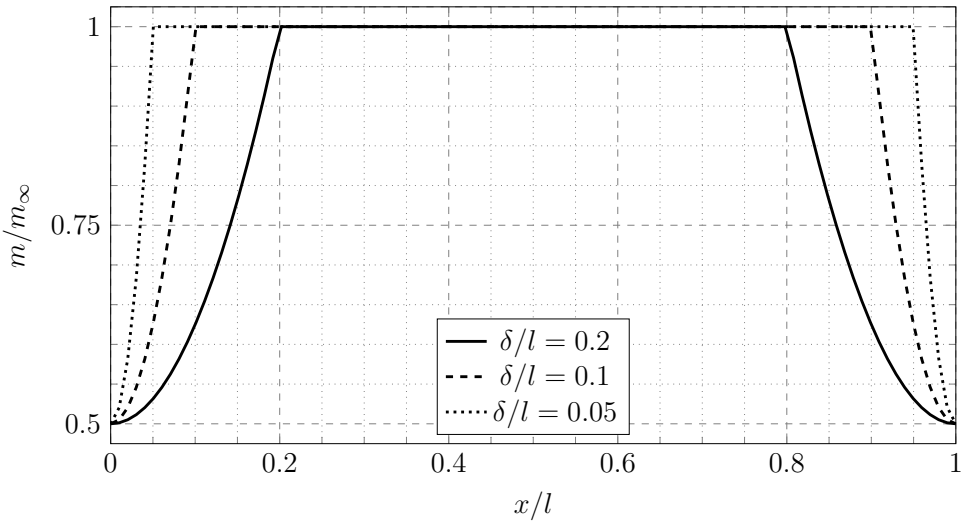


Figure 2.5: *Normalized weighted volume distribution along a finite 1D body of length $l$ for different values of the horizon $\delta$.*

flux in the domains near the boundary is computed as follows:

$$\begin{aligned}\tau(x'' \in \overline{\Omega}_0, +1) &= E\overline{\varepsilon}A\delta\Bigg\{ \int_0^{x''} \Bigg[ \int_{x''}^{\delta} \left( \frac{1}{m} + \frac{1}{A\delta^3} \frac{2}{\left(\frac{x'}{\delta}\right)^2 + 1} \right) \mathrm{d}x' \\ &\qquad + \int_{\delta}^{x+\delta} \left( \frac{1}{m} + \frac{1}{A\delta^3} \right) \mathrm{d}x' \Bigg] \mathrm{d}x \Bigg\} \\ &= E\overline{\varepsilon}\frac{1}{\delta^2}\Bigg\{ \int_0^{x''} \left[ \frac{2(\delta - x'')}{\left(\frac{x}{\delta}\right)^2 + 1} + \frac{\pi}{2}\delta - 2\delta \arctan\left(\frac{x''}{\delta}\right) + \frac{2x}{\left(\frac{x}{\delta}\right)^2 + 1} + x \right] \mathrm{d}x \Bigg\} \\ &= E\overline{\varepsilon}\Bigg\{ 2\left(1 - \frac{2x''}{\delta}\right) \arctan\left(\frac{x''}{\delta}\right) + \ln\left(\left(\frac{x''}{\delta}\right)^2 + 1\right) + \frac{1}{2}\left(\frac{x''}{\delta}\right)^2 + \frac{\pi}{2}\frac{x''}{\delta} \Bigg\}\end{aligned} \tag{2.28}$$

$$\tau(x'' \in \widetilde{\Omega}_0, +1) = E\overline{\varepsilon}A\delta\Bigg\{ \int_{x''-\delta}^{\delta} \int_{x''}^{x+\delta} \left( \frac{1}{m} + \frac{1}{A\delta^3} \right) \mathrm{d}x' \, \mathrm{d}x + \int_{\delta}^{x''} \int_{x''}^{x+\delta} \left( \frac{2}{A\delta^3} \right) \mathrm{d}x' \, \mathrm{d}x \Bigg\}$$

$$= E\overline{\varepsilon}\frac{1}{\delta^2}\left\{\int_{x''-\delta}^{\delta}\left(\frac{2}{\left(\frac{x}{\delta}\right)^2+1}+1\right)(x+\delta-x'')\,\mathrm{d}x+\int_{\delta}^{x''}2(x+\delta-x'')\,\mathrm{d}x\right\}$$
$$= E\overline{\varepsilon}\left\{2\left(\frac{x''-\delta}{\delta}\right)\arctan\left(\frac{x''-\delta}{\delta}\right)-\ln\left(\frac{1}{2}\left(\frac{x''-\delta}{\delta}\right)^2+\frac{1}{2}\right)\right.$$
$$\left.-\frac{1}{2}\left(\frac{x''-\delta}{\delta}\right)^2+\left(1-\frac{\pi}{2}\right)\frac{x''-\delta}{\delta}+\frac{1}{2}\right\} \tag{2.29}$$

The force flux $\tau(x'' \in (\overline{\Omega}_l \cup \widetilde{\Omega}_l), +1)$ is computed similarly and the result is symmetric with respect to the domain $(\overline{\Omega}_0 \cup \widetilde{\Omega}_0)$.

The force flux distribution normalized with respect to the infinite body solution, is reported in Table 2.2 and plotted for different values of the horizon $\delta$ in Figure 2.6. As expected, the material points in $(\Omega \setminus (\overline{\Omega} \cup \widetilde{\Omega}))$ behave as if the body were infinite, whereas the points in $(\overline{\Omega} \cup \widetilde{\Omega})$ "feel" the missing material points beyond the boundaries. Furthermore, it is observed that the variation of the horizon $\delta$ does not affect the values of the force flux, but only the size of the domain over which the surface effect is extended. Intuitively, as $\delta/l$ approaches to 0 (see the different curves in Figure 2.6), the domain which recovers the infinite body stiffness properties is enlarged.

Table 2.2: *Normalized force flux distribution along the finite 1D body.*

| $x \in$ | $\tau(x,1)/\tau_\infty$ |
|---|---|
| $\overline{\Omega}_0$ | $2\left(1-\frac{2x}{\delta}\right)\arctan\left(\frac{x}{\delta}\right)+\ln\left(\left(\frac{x}{\delta}\right)^2+1\right)+\frac{1}{2}\left(\frac{x}{\delta}\right)^2+\frac{\pi}{2}\frac{x}{\delta}$ |
| $\widetilde{\Omega}_0$ | $2\left(\frac{x-\delta}{\delta}\right)\arctan\left(\frac{x-\delta}{\delta}\right)-\ln\left(\frac{1}{2}\left(\frac{x-\delta}{\delta}\right)^2+\frac{1}{2}\right)-\frac{1}{2}\left(\frac{x-\delta}{\delta}\right)^2+\left(1-\frac{\pi}{2}\right)\frac{x-\delta}{\delta}+\frac{1}{2}$ |
| $(\Omega \setminus (\overline{\Omega} \cup \widetilde{\Omega}))$ | 1 |
| $\widetilde{\Omega}_l$ | $2\left(\frac{x+\delta-l}{\delta}\right)\arctan\left(\frac{x+\delta-l}{\delta}\right)-\ln\left(\frac{1}{2}\left(\frac{x+\delta-l}{\delta}\right)^2+\frac{1}{2}\right)-\frac{1}{2}\left(\frac{x+\delta-l}{\delta}\right)^2+\left(\frac{\pi}{2}-1\right)\left(\frac{x+\delta-l}{\delta}\right)+\frac{1}{2}$ |
| $\overline{\Omega}_l$ | $-2\left(2\left(\frac{x-l}{\delta}\right)+1\right)\arctan\left(\frac{x-l}{\delta}\right)+\ln\left(\left(\frac{x-l}{\delta}\right)^2+1\right)+\frac{1}{2}\left(\frac{x-l}{\delta}\right)^2-\frac{\pi}{2}\left(\frac{x-l}{\delta}\right)$ |

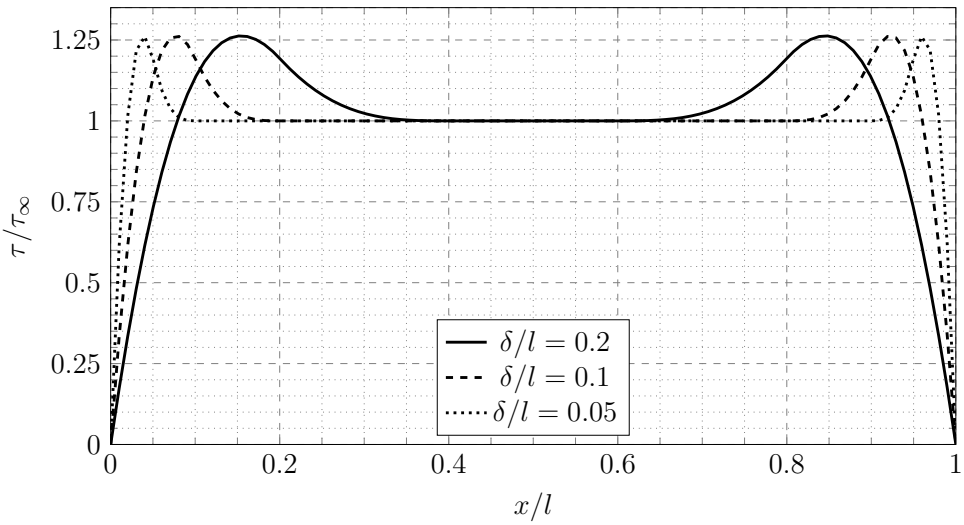


Figure 2.6: *Normalized force flux distribution along a finite 1D body of length $l$ undergoing a constant deformation $\overline{\varepsilon}$ for different values of the horizon $\delta$.*

In Figure 2.7, the normalized force flux near the boundary $\partial\Omega$ is plotted with respect to the normalized coordinate $x/\delta$. The characteristic behavior is driven by two counteracting phenomena:

- due to the lack of material points and consequent missing bonds, the force flux is reduced because less bonds intersect the section;
- since the weighted volume decreases close to the boundary, the magnitude of the nearby forces in the bonds is increased (see Equation 2.19).

In $\widetilde{\Omega}$ there are no bonds missing and the intensified magnitude of the peridynamic forces increases the stiffness of the material (*hardening*). On the other hand, both the effects are present in $\overline{\Omega}$: the intensification of the bond forces overcompensates the lack of bonds far from the boundary, but the effect of the missing bonds prevails near the boundary (*softening*).

Analyzing Figure 2.7, there is a maximum $\tau \approx 1.263\tau_\infty$ at $(x/\delta) \approx 0.772$. In addition, the force flux density matches again the classical stress at $(x/\delta) \approx 0.394$. After some numerical investigations (see Figure 2.8), one can assert that the shape of the force flux distribution changes only slightly with a different, but reasonable choice of the influence function, but the overall behavior near the boundaries is the same: the material exhibits a hardening and then a softening from the bulk towards the boundary.

The imposition of the boundary conditions in Peridynamics is correlated to the problem of the surface effect because of the non-local nature of the theory. The non-local boundary conditions are often imposed in an approximated way at the boundary points, which causes undesired displacement fluctuations near $\partial\Omega$. In fact, according to [158] the non-local constraints in state-based Peridynamics should be imposed over a region of thickness $2\delta$ outside the body, whereas the external loads should be applied in the domain $(\overline{\Omega} \cup \widetilde{\Omega})$ within the

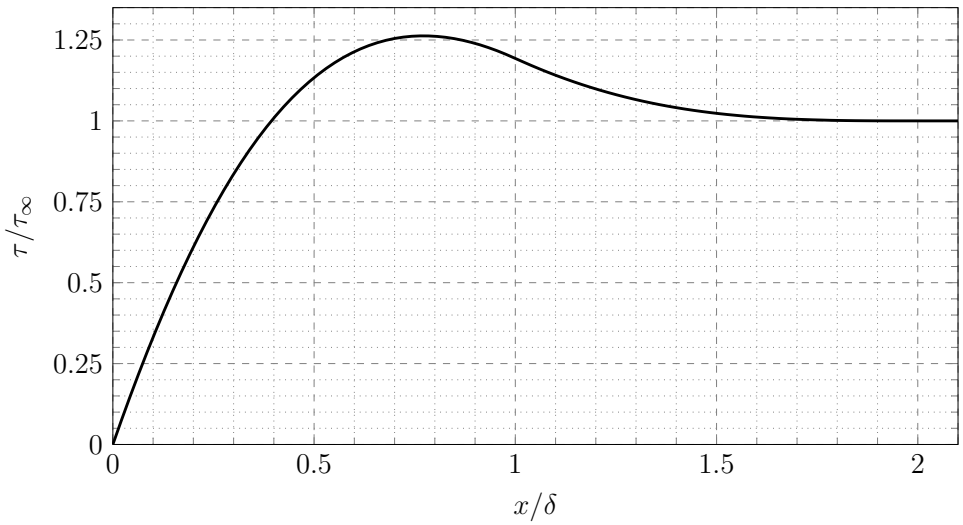


Figure 2.7: *Analytical result for the normalized force flux distribution obtained with* $\underline{\omega} = \delta/|\xi|$.

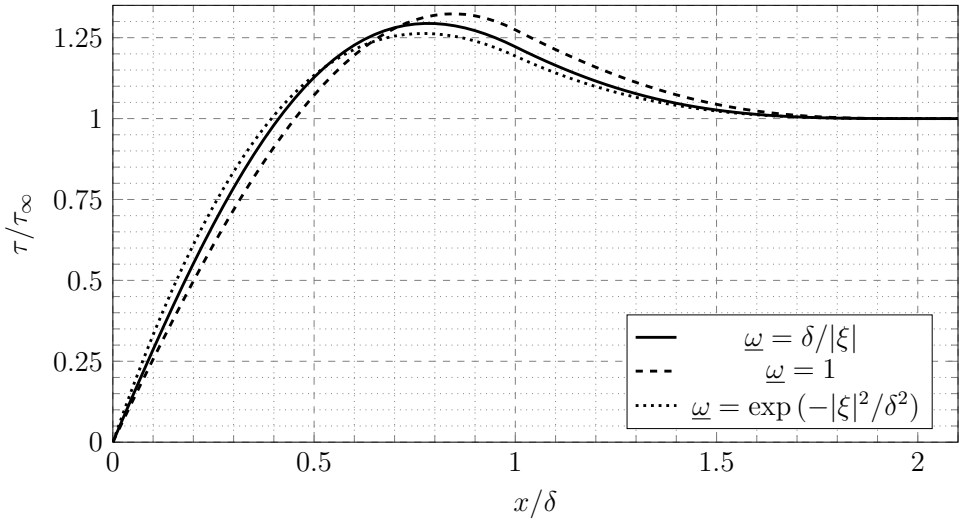


Figure 2.8: *Numerical results for the normalized force flux obtained with different influence functions.*

body, as shown in Appendix 2.B. However, the distribution of the variables which should be imposed is not known a priori.

The method proposed in the next Section compensates the surface effect and imposes in a proper way the non-local boundary conditions without any need to determine the appropriate distribution of the external displacement or force density.

## 2.3 Taylor-based extrapolation over the fictitious layer

As shown in Figure 2.3, a fictitious layer $\Gamma = \Gamma_0 \cup \Gamma_l$ of thickness $\delta$ is added at the ends of the 1D body $\Omega$. The Taylor-based extrapolation, used to determine the displacements of the fictitious points, is shown hereinafter.

According to the nearest-point strategy, the Taylor series of the displacements of the fictitious points should be centered at the closest real point, namely the boundary point.

Therefore, given a maximum order $n \geq 1$, the truncated Taylor series of the displacement in $x \in \Gamma_l$ about the boundary point $x = l$ yields:

$$u(x \in \Gamma_l) = u(l) + \sum_{k=1}^{n} \frac{(x-l)^k}{k!} \cdot \frac{\mathrm{d}^k u(l)}{\mathrm{d}x^k} \tag{2.30}$$

With this Taylor-based extrapolation, the displacements of the fictitious points are determined as functions of the unknown displacement of the boundary point and its derivatives.

In state-based Peridynamics, the properties of the points in the fictitious layer should be corrected as well. Therefore, the weighted volume $m$ of the fictitious points in $\Gamma_l$ is fixed to be $m_\infty$, namely the weighted volume of a point with a complete neighborhood, and their dilatation is extrapolated by means of the following truncated Taylor series expansion:

$$\theta(x \in \Gamma_l) = \begin{cases} \theta(l) & \text{if } n = 1 \\ \theta(l) + \displaystyle\sum_{k=1}^{n-1} \frac{(x-l)^k}{k!} \cdot \frac{\mathrm{d}^k \theta(l)}{\mathrm{d}x^k} & \text{if } n > 1 \end{cases} \tag{2.31}$$

Note that the dilatation is a measure of the strain, thus the truncation of the relevant Taylor expansion occurs with 1 order less than that of the displacement. Equations 2.30 and 2.31 are valid in $\Gamma_l$, but the same procedure is applied to the fictitious points in the domain $\Gamma_0$. An example of the extrapolation with the Taylor series expansion for $n = 1, 2, 3$ is shown in Figure 2.9.

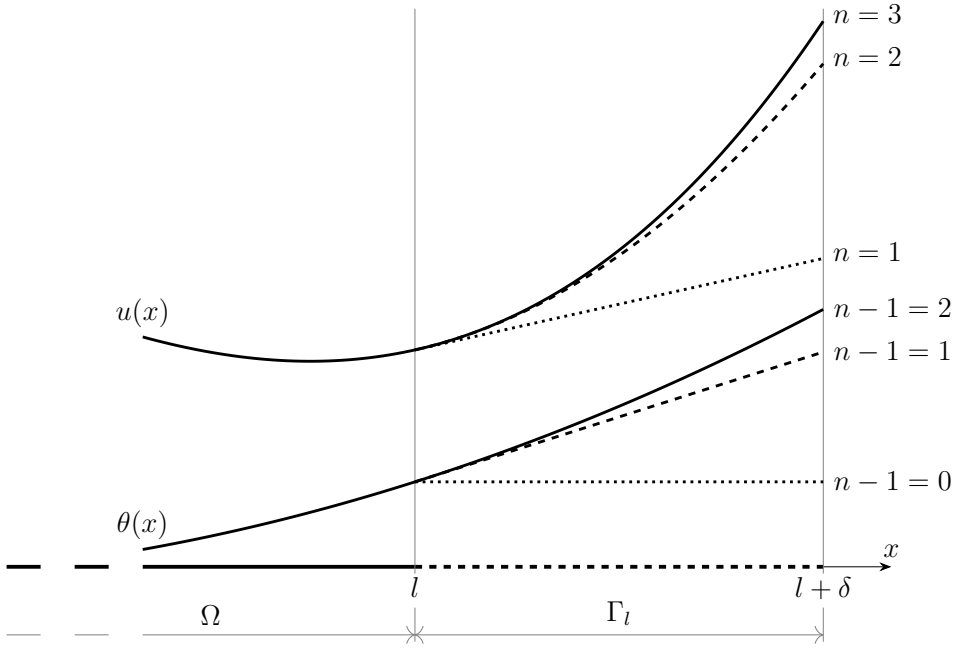


Figure 2.9: *Example of the extrapolation of the displacement $u$ (cubic function of $x$) and the dilation $\theta$ (quadratic function of $x$) over the fictitious layer $\Gamma$ with the Taylor series expansion truncated at different terms (solid line: $n = 3$, dashed line: $n = 2$, dotted line: $n = 1$, where $n$ is the order of the Taylor series expansion for the displacement extrapolation).*

In Equations 2.30 and 2.31 the unknowns are $u(l)$, $\theta(l)$, along with their derivatives. In the numerical applications presented later in Section 2.4.1, the derivatives are expressed

as functions of the displacements or dilatations of the real nodes close to the boundary. Therefore, the proposed method evaluates the displacement in the fictitious domain without the introduction of new unknowns.

### 2.3.1 Mitigation of the surface effect

This Section shows that, by implementing the method of the Taylor-based extrapolation over the fictitious points with a proper order $n$, the peridynamic solution of the force flux in a finite body $\Omega$ under a predefined smooth deformation recovers that of the infinite body.

The force flux at a point $x''$ in an infinite body $\Omega_\infty$ under a constant deformation $\overline{\varepsilon}$ is given from Equation 2.26 as $\tau''_\infty = E\overline{\varepsilon}$. Consider a finite body $\Omega$ under the same constant deformation $\overline{\varepsilon}$. Assuming, without loss of generality, $u(0) = 0$, the displacement imposed to the body is $u(x \in \Omega) = \overline{\varepsilon}x$. Thus, the proposed Taylor-based extrapolation method is applied to $\Omega$ with an order $n = 1$ (dotted line in the example of Figure 2.9). The displacement in the fictitious layer $\Gamma_l$ is determined from Equation 2.30 as:

$$u(x \in \Gamma_l) = u(l) + (x - l)\frac{\mathrm{d}u(l)}{\mathrm{d}x} = \overline{\varepsilon}l + (x - l)\overline{\varepsilon} = \overline{\varepsilon}x \tag{2.32}$$

Since this Taylor-based extrapolation induces the fictitious layer to deform in the same way as the real body, the extension scalar state of the fictitious bonds is equal to that of the real bonds $\underline{e} = \overline{\varepsilon}\underline{x}$ and the dilatation of the real points near the boundary is computed exactly as Equation 2.14, yielding $\theta(x \in \overline{\Omega}_l) = c_\theta\overline{\varepsilon} = \theta_\infty$. Therefore, thanks to the extrapolation of the displacement of the fictitious points (Equation 2.32), the force flux in $\widetilde{\Omega}_l$ is computed as the force flux of an infinite body in Equation 2.26:

$$\tau(x'' \in \widetilde{\Omega}_l, +1) = E\overline{\varepsilon} = \tau''_\infty \tag{2.33}$$

The dilatations of the fictitious points are determined by the Taylor-based extrapolation in Equation 2.31 as:

$$\theta(x \in \Gamma_l) = \theta(l) = c_\theta\overline{\varepsilon} = \theta_\infty \tag{2.34}$$

Therefore, in this case the dilatation is constant in the fictitious layer and is equal to the dilatation $\theta_\infty$ of the infinite body under the deformation $\overline{\varepsilon}$. Furthermore, the weighted volume of the fictitious points is fixed to be equal to the weighted volume of a point with a complete neighborhood: $m(x \in \Gamma_l) = m_\infty = A\delta^3$. Since the extension scalar state $\underline{e}$ of the fictitious bonds is computed with the same formula as that of the real bonds (from Equation 2.32) and the properties of the real and fictitious points are equal to those of the points in an infinite body ($m(x \in (\overline{\Omega}_l \cup \Gamma_l)) = m_\infty$ and $\theta(x \in (\overline{\Omega}_l \cup \Gamma_l)) = \theta_\infty$), the force flux near the boundary of the finite body is computed exactly as in Equation 2.26:

$$\tau(x'' \in \overline{\Omega}_l, +1) = E\overline{\varepsilon} = \tau''_\infty \tag{2.35}$$

The same results as those of Equations 2.33 and 2.35 can be obtained at the other end of the finite body through the extrapolation method applied to the fictitious layer $\Gamma_0$.

We have shown that, when the proposed Taylor-based extrapolation method is employed with the order $n = 1$ (or higher), the force flux in the whole domain (even near the boundaries) of a finite body under a constant deformation is equal to the force flux in an infinite body under the same deformation. Appendix 2.C presents the same procedure carried out for a cubic distribution of displacement imposed to a finite body, to which the proposed method is applied with $n = 3$. The force flux coincides with the one computed in the infinite body under the same condition in that case as well. Hence, we conjecture that, whenever the order $n$ of the proposed Taylor-based extrapolation method is equal to (or higher than) the order of the imposed distribution of displacement, the points near the boundary of the finite body retrieve the stiffness properties of the points in the infinite body thanks to the fictitious layer, and the surface effect is eliminated.

Since the displacement distribution is rarely known before solving the problems of interest for real application, Section 2.5 presents some numerical examples in which the displacements are initially unknown and $n$ is chosen differently from the ideal order.

### 2.3.2 Dirichlet boundary conditions

This Section analyzes how to deal with the imposition of the non-local displacement boundary conditions by means of the proposed method. The displacement constraints are implemented as in a local model: the desired displacement is imposed at the boundary point and the proposed method autonomously adjusts the displacement of the fictitious points according to the displacement of the boundary point and its derivatives.

The equation to impose a Dirichlet boundary condition, for instance, at $\partial\Omega_0$ is given as:

$$u(x = 0) = \overline{u} \tag{2.36}$$

where $\overline{u}$ is the desired value of the constraint. The extrapolation method determines the displacements and the dilatations of the fictitious points similarly to what was shown in Equations 2.30 and 2.31:

$$u(x \in \Gamma_0) = \overline{u} + \sum_{k=1}^{n} \frac{(x)^k}{k!} \cdot \frac{\mathrm{d}^k u(0)}{\mathrm{d}x^k} \tag{2.37}$$

$$\theta(x \in \Gamma_0) = \begin{cases} \theta(0) & \text{if } n = 1 \\ \theta(0) + \sum_{k=1}^{n-1} \frac{(x)^k}{k!} \cdot \frac{\mathrm{d}^k \theta(0)}{\mathrm{d}x^k} & \text{if } n > 1 \end{cases} \tag{2.38}$$

Note that in this case $u(0)$ in Equation 2.37 is constrained to be $\overline{u}$. In this way, the Dirichlet boundary condition is imposed only at the boundary $\partial\Omega$, whereas the fictitious layer $\Gamma$ mitigates the surface effect, as illustrated in Section 2.3.1.

For a detailed description of the imposition of the Dirichlet boundary condition in a discretized model, please refer to Section 2.4.3.

### 2.3.3 Neumann boundary conditions

This Section addresses the problem of applying a load to the non-local boundary of the finite 1D body. With the introduction of the fictitious layer, new interactions between real and fictitious points, named *fictitious bonds*, are generated. These fictitious bonds deform because of the displacement induced by the extrapolation on the fictitious points. Thereby, each fictitious bond exerts a force on both the interacting points (see Figure 2.2). The forces which the fictitious bonds exert on the fictitious points are "lost", in the sense that they do not contribute to the equilibrium of the real points of the body. Indeed, the fictitious points do not constitute new degrees of freedom of the model since their displacement is extrapolated via Equation 2.30. On the other hand, the forces of the fictitious bonds acting on the real points contribute to their equilibrium equation and play a role very similar to that of the external force density distribution computed in Appendix 2.B to obtain a constant deformation of the bar: the global effect of all the fictitious bonds is a force density distribution applied to the non-local boundary ($\overline{\Omega} \cup \widetilde{\Omega}$) capable of compensating the surface effect and imposing the Neumann boundary condition. Therefore, we propose to apply Neumann boundary conditions by means of the concept of force flux (Equation 2.21) at the boundary points: the resultant of the forces of the fictitious bonds which intersect the boundary is equal to the desired value of the external load (see Figure 2.13 for the discretized representation of the load boundary condition).

In order to impose an outward external force $\bar{\mathrm{f}}$, for instance, at $\partial\Omega_l$, the boundary condition is given as:

$$\tau(l,+1) = \int_{\mathrm{H}_l^-} \int_{\mathrm{H}_l^+ \cap \mathrm{H}^+} \left( \underline{\mathbf{T}}\langle \xi \rangle - \underline{\mathbf{T}}'\langle -\xi \rangle \right) \mathrm{d}V' \, \mathrm{d}x = \frac{\bar{\mathrm{f}}}{A} \tag{2.39}$$

where $H_l$ is the neighborhood of the point $x = l$. The integral in Equation 2.39 depends on the elongation (i.e., the extension scalar state) of the real bonds near the boundary and of the fictitious bonds crossing the boundary. Therefore, the Neumann boundary condition written as Equation 2.39 imposes the elongations of the bonds so that the sum of the forces per unit area in those bonds is equal to the desired value of the force flux at the boundary. The extension scalar state of the bonds involved in Equation 2.39 is determined by the displacement in ($\overline{\Omega}_l \cup \widetilde{\Omega}_l \cup \Gamma_l$), namely the domain near the boundary of the real body and the fictitious layer. However, the displacement distribution in the fictitious layer $\Gamma_l$ is defined by the Taylor-based extrapolation method. Therefore, the integral in Equation 2.39 is a function solely of the displacement distribution of the real points near the boundary. The implementation of a Neumann boundary condition in a discretized model, described in Section 2.4.3, is indeed carried out by adopting a linear combination of the displacements of the real nodes near the boundary. The discretized representation of Equation 2.39 is shown in Figure 2.13.

**Remark 2.2.** In [92], the zero-traction boundary condition is applied by removing the fictitious layer. By doing so, however, the surface effect reappears near the free boundary. In the case of zero-traction surface, we suggest to use the fictitious layer with an extrapolation method, such as the one presented in this paper, and impose the condition $\tau(x \in \partial\Omega, \mathrm{n}) = 0$.

Some numerical examples of the implementation of a zero-traction boundary condition are shown in Section 2.5.

**Remark 2.3.** The Dirichlet boundary condition described in Section 2.3.2 is imposed at the boundary point $\partial\Omega_0$ of the body. Due to the non-local nature of the peridynamic theory, the reaction to the constraint is not the force density applied to that point, but is computed as the force flux at that point multiplied by the cross-sectional area: $\mathrm{f}_{\overline{u}} = A \cdot \tau(0, -1)$, where $\mathrm{f}_{\overline{u}}$ is the reaction to the constraint imposed with Equation 2.36.

## 2.4 Numerical implementation

A mesh-free method is adopted to discretize the domain [65]. For simplicity sake, the peridynamic grid consists of a finite number of equally-spaced nodes, each of which is representative of a volume $V = A\Delta$, where $A$ is the cross-sectional area of the 1D body and $\Delta$ is the grid spacing (see Figure 2.10). Since the horizon $\delta$ is often chosen as a multiple of the grid spacing $\Delta$, the *m-ratio* $\overline{m} = \delta/\Delta$ is here considered as an integer number. The parameter $\overline{m}$ is commonly denoted as $m$ in Peridynamics, but the top bar avoids the confusion that might arise with the weighted volume symbol. The position of the nodes, shown in Figure 2.10, is given as $x_i = (i - 1/2)\Delta$ with $i = 1, \ldots, N + \overline{m}$ and $x_i = (i + 1/2)\Delta$ with $i = -\overline{m}, \ldots, -1$. The real nodes, denoted by $i = 1, \ldots, N$, are represented by the solid dots, whereas the fictitious nodes are represented by the empty dots. Note that the boundary nodes ($i = 1, N$) do not lie exactly at the boundary $\partial\Omega$ of the body.

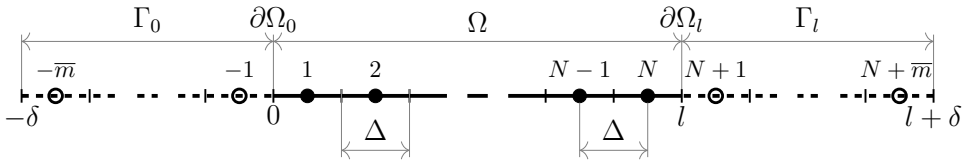


Figure 2.10: *Uniform peridynamic grid with node numeration: the solid dots represent the real nodes, whereas the empty dots represent the fictitious nodes.*

The unknowns of the problem are the displacements of the real nodes, called $u_i$ with $i = 1, \ldots, N$ and gathered in the displacement vector $\mathbf{u}$ (size: $N \times 1$). The next Section shows how to determine the displacements of the fictitious nodes as functions of the unknowns in $\mathbf{u}$.

### 2.4.1 Numerical Taylor-based extrapolation

Applying the concepts for the continuum peridynamic formulation of Section 2.3, the Taylor-based extrapolation is used in the discretized formulation to express the displacements (or dilatations) of the fictitious nodes as functions of the displacements (or dilatations) of the real nodes close to them. Initially, the procedure for the linear extrapolation ($n = 1$) of the displacements in $\Gamma$ is carried out and, thereafter, the procedure for a general extrapolation of order $n$ is presented. This procedure is similar to that exposed for the polynomial function in [195].

The displacement of a fictitious node $f$ in $\Gamma$ is evaluated by means of the Taylor series expansion about its closest real node, according to the nearest-node strategy. If the node $f$, for instance, belongs to the domain $\Gamma_0$, i.e., $f = -\overline{m}, \ldots, -1$, the linear Taylor series about node 1 yields:

$$u_f = u_1 + (x_f - x_1) \cdot \frac{\mathrm{d}u_1}{\mathrm{d}x} \tag{2.40}$$

The derivative in Equation 2.40 can be determined by another linear Taylor series about the boundary node 1 for the displacement of the real node closest to node 1:

$$\frac{\mathrm{d}u_1}{\mathrm{d}x} = \frac{u_2 - u_1}{x_2 - x_1} \tag{2.41}$$

Thus, the displacement $u_f$ can be expressed as a function of the displacements of the real nodes close to the boundary by substituting Equation 2.41 in Equation 2.40.

Now, the procedure to define the displacements of the fictitious nodes in $\Gamma_0$ with an extrapolation based on the Taylor series expansion of order $n$ is presented. The real node closest to the domain $\Gamma_0$ is node 1, thus the Taylor series expansion should be centered at that node according to the nearest-node strategy. The displacements of the fictitious nodes can be determined as functions of the displacement of node 1 and its $n$ derivatives with the following system of equations:

$$\begin{Bmatrix} u_{-\overline{m}} \\ \vdots \\ u_{-1} \end{Bmatrix} = \begin{bmatrix} 1 & (x_{-\overline{m}} - x_1) & (x_{-\overline{m}} - x_1)^2/2 & \cdots & (x_{-\overline{m}} - x_1)^n/n! \\ \vdots & \vdots & \vdots & \vdots & \vdots \\ 1 & (x_{-1} - x_1) & (x_{-1} - x_1)^2/2 & \cdots & (x_{-1} - x_1)^n/n! \end{bmatrix} \begin{Bmatrix} u_1 \\ \frac{\mathrm{d}u_1}{\mathrm{d}x} \\ \frac{\mathrm{d}^2u_1}{\mathrm{d}x^2} \\ \vdots \\ \frac{\mathrm{d}^nu_1}{\mathrm{d}x^n} \end{Bmatrix} \tag{2.42}$$

The vector of the displacements of the fictitious nodes in $\Gamma_0$ is named $\mathbf{u}_{\Gamma_0}$ (size: $\overline{m} \times 1$), the vector of the displacement of node 1 and its $n$ derivatives is named $\mathbf{d}_1$ (size: $(n+1) \times 1$) and the matrix obtained with the factors of the Taylor series expansion of the displacements of the fictitious nodes about node 1 is named $\mathbf{T}_1^{\Gamma_0}$ (size: $\overline{m} \times (n+1)$). Therefore, Equation 2.42 can be compactly written as $\mathbf{u}_{\Gamma_0} = \mathbf{T}_1^{\Gamma_0}\mathbf{d}_1$.

The derivatives in vector $\mathbf{d}_1$ can be determined as functions of the displacements of the real nodes closest to the boundary node 1, according to the nearest-node strategy. Hence, one can write the Taylor series expansions of the displacements of the $n+1$ real nodes closest to the boundary $\partial\Omega_0$ about the boundary node 1 as:

$$\begin{Bmatrix} u_1 \\ u_2 \\ \vdots \\ u_{n+1} \end{Bmatrix} = \begin{bmatrix} 1 & 0 & 0 & \cdots & 0 \\ 1 & (x_2 - x_1) & (x_2 - x_1)^2/2 & \cdots & (x_2 - x_1)^n/n! \\ \vdots & \vdots & \vdots & \vdots & \vdots \\ 1 & (x_{n+1} - x_1) & (x_{n+1} - x_1)^2/2 & \cdots & (x_{n+1} - x_1)^n/n! \end{bmatrix} \begin{Bmatrix} u_1 \\ \frac{\mathrm{d}u_1}{\mathrm{d}x} \\ \frac{\mathrm{d}^2u_1}{\mathrm{d}x^2} \\ \vdots \\ \frac{\mathrm{d}^nu_1}{\mathrm{d}x^n} \end{Bmatrix} \tag{2.43}$$

which is compactly written as $\mathbf{u}_{\Omega_0} = \mathbf{T}_1^{\Omega_0}\mathbf{d}_1$, where the displacements of the real nodes closest

to the boundary are gathered in vector $\mathbf{u}_{\Omega_0}$ (size: $(n+1)\times 1$) and the factors derived by the Taylor series expansions about node 1 are contained in $\mathbf{T}_1^{\Omega_0}$ (size: $(n+1)\times(n+1)$). The vector $\mathbf{d}_1$ is written as a function of the part $\mathbf{u}_{\Omega_0}$ of the displacement vector $\mathbf{u}$ by inverting the Taylor matrix in Equation 2.43:

$$\mathbf{d}_1 = \left[\mathbf{T}_1^{\Omega_0}\right]^{-1}\mathbf{u}_{\Omega_0} \tag{2.44}$$

Thus, the displacements of the fictitious nodes in $\Gamma_0$ can be expressed as a function of some of the unknowns of the problem:

$$\mathbf{u}_{\Gamma_0} = \mathbf{T}_1^{\Gamma_0}\left[\mathbf{T}_1^{\Omega_0}\right]^{-1}\mathbf{u}_{\Omega_0} \tag{2.45}$$

Note that the matrices in Equation 2.45 depend only on the coordinates of the fictitious and real nodes. The same procedure can be exploited for the extrapolation of the displacements in $\Gamma_l$. Moreover, the dilatations in $\Gamma$ can be analogously extrapolated with the Taylor series expansions of order $n-1$.

The numerical procedure for the Taylor-based extrapolation over the fictitious layer $\Gamma$ can be summarized as follows:

- choose the order $n$ of the truncated Taylor series;
- find the boundary nodes $i = 1, N$, which are the real nodes closest to the fictitious layer (nearest-node strategy);
- assemble the Taylor matrix $\mathbf{T}_i^{\Gamma}$ (size: $\overline{m}\times(n+1)$) with the factors of the Taylor series expansion of the displacements $\mathbf{u}_{\Gamma}$ of the fictitious nodes about node $i$ (see Equation 2.42);
- find the $n+1$ real nodes closest to the boundary $\partial\Omega$ (nearest-node strategy), whose displacements $\mathbf{u}_{\Omega}$ can be extracted from the displacement vector $\mathbf{u}$;
- assemble the Taylor matrix $\mathbf{T}_i^{\Omega}$ (size: $(n+1)\times(n+1)$) with the factors of the Taylor series expansion of the displacements $\mathbf{u}_{\Omega}$ about node $i$ (see Equation 2.43);
- compute the matrix $\mathbf{T}_i^{\Gamma}\left[\mathbf{T}_i^{\Omega}\right]^{-1}$, which expresses the displacements $\mathbf{u}_{\Gamma}$ of the fictitious nodes as functions of the displacements $\mathbf{u}_{\Omega}$ of the real nodes close to the boundary:

$$\mathbf{u}_{\Gamma} = \mathbf{T}_i^{\Gamma}\left[\mathbf{T}_i^{\Omega}\right]^{-1}\mathbf{u}_{\Omega} \tag{2.46}$$

Analogously, the Taylor-based extrapolation of the dilatations $\boldsymbol{\theta}_{\Gamma}$ (size: $\overline{m}\times 1$) of the fictitious nodes can be carried out from the dilatations $\boldsymbol{\theta}_{\Omega}$ (size: $n\times 1$) of the $n$ real nodes closest to the boundary as:

$$\boldsymbol{\theta}_{\Gamma} = \overline{\mathbf{T}_i^{\Gamma}}\left[\overline{\mathbf{T}_i^{\Omega}}\right]^{-1}\boldsymbol{\theta}_{\Omega} \tag{2.47}$$

where $\overline{\mathbf{T}_i^{\Gamma}}$ (size: $\overline{m}\times n$) and $\overline{\mathbf{T}_i^{\Omega}}$ (size: $n\times n$) are the sub-matrices obtained by eliminating the rows and the columns of $\mathbf{T}_i^{\Gamma}$ and $\mathbf{T}_i^{\Omega}$ related to the node most distant from the boundary

and the derivative with the highest order.

### 2.4.2 Discretized formulation

This Section derives the discretized form of the peridynamic equations and shows the approach to combine them with the proposed method of the Taylor-based extrapolation over the fictitious layer.

Consider a bond $ij$, either real or fictitious, connecting node $i$ to node $j$, as shown in Figure 2.11. From Equation 2.1, the relative position vector can be computed for each bond $ij$ of the peridynamic model as $\xi_{ij} = x_j - x_i$. The reference vector state $\underline{x}_{ij} = |\xi_{ij}|$ and the hyperbolic influence function $\underline{\omega}_{ij} = \delta/|\xi_{ij}|$ are computed for each bond respectively from Equations 2.6 and 2.23. Furthermore, the contribution to the neighborhood of nodes with their volume $V$ only partially within it, is corrected by the volume reduction coefficient $\beta_{ij}$, computed as the fraction of volume actually involved in the neighborhood [224]. If $V$ is completely inside the neighborhood, then $\beta_{ij} = 1$.

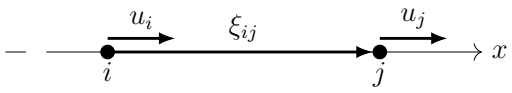


Figure 2.11: *Bond $ij$ between node $i$ and node $j$ in a 1D peridynamic model.*

Firstly, the displacements of the fictitious nodes are approximated with the extrapolation derived by the Taylor-based method previously described. Then, from Equations 2.2 and 2.7, the extension scalar state of bond $ij$ is given as:

$$\underline{e}_{ij} = \frac{\xi_{ij}}{|\xi_{ij}|}(u_j - u_i) \tag{2.48}$$

Whenever one of the nodes of the bond is fictitious, its displacement is expressed as a function of some of the unknowns in the displacement vector $\mathbf{u}$ with the Taylor-based extrapolation methods exposed in Section 2.4.1. For instance, following the example of the linear Taylor-based extrapolation for a fictitious node $f$ in Equations 2.40 and 2.41, the extension scalar state of a fictitious bond $fj$, connecting the fictitious node $f$ in $\Gamma_0$ to the real node $j$, is expressed as:

$$\begin{aligned}\underline{e}_{fj} = u_j - u_f &= u_j - \left(u_1 + (x_f - x_1)\frac{u_2 - u_1}{x_2 - x_1}\right) \\ &= u_j + \frac{x_f - x_2}{x_2 - x_1}u_1 - \frac{x_f - x_1}{x_2 - x_1}u_2\end{aligned} \tag{2.49}$$

where the node indices possibly involved in this case are $f = -\overline{m}, \ldots, -1$ and $j = 1, \ldots, \overline{m}$ (see Figure 2.10). As just shown with this example, the extension scalar state of all the bonds, both real and fictitious, can be computed as a linear combination of some of the displacements of the real nodes, i.e., the unknowns of the problem. This statement is valid also for a higher order of the truncated Taylor expansion (with $n > 1$, please refer to the Taylor-based extrapolation procedure exposed in Section 2.4.1).

The weighted volume of a node $i$ is often evaluated in Peridynamics by performing a mid-point Gauss quadrature from Equation 2.8:

$$m_i = \sum_{j \in \mathrm{H}_i} \left( \underline{\omega}_{ij} \underline{x}_{ij}^2 \beta_{ij} \right) V \tag{2.50}$$

where $\mathrm{H}_i$ is the neighborhood of node $i$. However, given the choice of the hyperbolic influence function, the weighted volume is here computed from Equation 2.25 as $m = A\delta^3$. Note that, when the proposed method is employed, the weighted volume evaluated at the real nodes near the boundary and also at the fictitious nodes is equal to the one of a node with a complete neighborhood.

The dilatation of a real node $i$ is computed by means of the mid-point Gauss quadrature from Equation 2.13 as:

$$\theta_i = \frac{c_\theta}{m_i} \sum_{j \in \mathrm{H}_i} \left( \underline{\omega}_{ij} \underline{x}_{ij} \underline{e}_{ij} \beta_{ij} \right) V \tag{2.51}$$

Similarly to the procedure for the displacements, the dilatations of the fictitious nodes are extrapolated via Equation 2.47 as a linear combination of some of the dilatations of the real nodes. Thereby, the dilatations of all the nodes, both real and fictitious, are determined as functions of previously computed parameters.

The force density scalar state is then computed from Equation 2.19 as:

$$\underline{t}_{ij} = k_\theta \frac{\theta_i}{m_i} \underline{\omega}_{ij} \underline{x}_{ij} + k_e \frac{1}{m_i} \underline{\omega}_{ij} \underline{e}_{ij} \tag{2.52}$$

In the case that the bond $ij$ was fictitious, $\theta_i$ and $\underline{e}_{ij}$ have already been determined by means of the extrapolation method.

From the integrand in Equation 2.20, the peridynamic force in bond $ij$ is given as:

$$\mathrm{f}_{ij} = \left( k_\theta \left( \frac{\theta_i}{m_i} + \frac{\theta_j}{m_j} \right) \underline{\omega}_{ij} \underline{x}_{ij} + k_e \left( \frac{1}{m_i} + \frac{1}{m_j} \right) \underline{\omega}_{ij} \underline{e}_{ij} \right) \beta_{ij} V^2 \tag{2.53}$$

where $\underline{x}_{ij} = \underline{x}_{ji}$, $\underline{\omega}_{ij} = \underline{\omega}_{ji}$, $\beta_{ij} = \beta_{ji}$ and $\underline{e}_{ij} = \underline{e}_{ji}$ for symmetry reasons. $\mathrm{f}_{ij} \underline{\mathbf{M}}_{ij}$ is the bond force acting on the node $i$ and $\mathrm{f}_{ji} \underline{\mathbf{M}}_{ji} = -\mathrm{f}_{ij} \underline{\mathbf{M}}_{ij}$ is the same force of opposite direction acting on node $j$.

Finally, the peridynamic equilibrium equation (Equation 2.4) is rewritten, in a discretized form, for every real node $i$ as:

$$-\sum_{j \in \mathrm{H}_i} \mathrm{f}_{ij} \underline{\mathbf{M}}_{ij} = b_i V \tag{2.54}$$

where $b_i$ is the external force density applied on node $i$. Thus, Equation 2.54 is repeated $N$ times, one for each real node, forming the system of equations to be solved. The right-hand side of the system equation is named body force vector $\mathbf{f}$ (size: $N \times 1$). Since the internal bond forces $\mathrm{f}_{ij}$ depend linearly on the displacements of the nodes (Equations 2.48–2.53), one can decompose the left-hand side of the system as $\mathbf{K}\mathbf{u}$, where $\mathbf{K}$ (size: $N \times N$) is the stiffness matrix and $\mathbf{u}$ (size: $N \times 1$) is the displacement vector. Therefore, the system of equations

can be written in the standard form:

$$\mathbf{K}\ \mathbf{u} = \mathbf{f} \tag{2.55}$$

Appendix 2.D shows the step-by-step assembly of $\mathbf{K}$ following the equations of this Section. The stiffness matrix $\mathbf{K}$ embeds the stiffness correction obtained with the additional internal forces due to the fictitious bonds, thus the surface effect is compensated.

### 2.4.3 Application of boundary conditions in discretized form

The concepts about the peridynamic boundary conditions presented in Sections 2.3.2 and 2.3.3 are here translated in discretized terms: the boundary conditions matrix $\mathbf{B}$ is assembled to embed the system of equations derived from the boundary conditions. The Neumann boundary condition can be transformed in a relation among nodal displacements, achieving an equation similar to that of a constraint. Therefore, the boundary conditions are written in the form $\mathbf{B}\ \mathbf{u} = \mathbf{c}$, where $\mathbf{B}$ (size: $2 \times N$) is the boundary condition matrix and $\mathbf{c}$ (size: $2 \times 1$) is the vector containing the known values of the boundary conditions. $\mathbf{B}$ and $\mathbf{c}$ have 2 rows in the 1D case because there is 1 condition for each boundary.

In order to show how to assemble $\mathbf{B}$ and $\mathbf{c}$, suppose that the following boundary conditions are imposed to a finite body of length $l$: a constraint $\overline{u}$ at $x = 0$ and a force $\overline{\mathrm{f}}$ at $x = l$. As shown in Figure 2.12, the desired constraint is not applied to any peridynamic node because each peridynamic node is centered with respect to its representative volume. However, the notions exposed in Section 2.4.1 can be exploited to extrapolate $u(0) = \overline{u}$ as a function of the nodal displacements. For instance, if a linear extrapolation was chosen (order $n = 1$), the displacement boundary condition would be written from Equations 2.40 and 2.41 as:

$$\overline{u} = u_1 - x_1 \cdot \frac{u_2 - u_1}{x_2 - x_1} \tag{2.56}$$

Equation 2.56 can be rearranged as a row of matrix $\mathbf{B}$ and vector $\mathbf{c}$ as follows:

$$\begin{bmatrix} 1 + \frac{x_1}{x_2 - x_1} & -\frac{x_1}{x_2 - x_1} & 0 & \cdots & 0 \end{bmatrix} \begin{Bmatrix} u_1 \\ u_2 \\ u_3 \\ \vdots \\ u_N \end{Bmatrix} = \left\{ \overline{u} \right\} \tag{2.57}$$

In a similar way, the constraint for a Taylor series expansion of order $n$ can be expressed as:

$$\begin{bmatrix} \mathbf{T}_1^{\partial\Omega_0} \left[ \mathbf{T}_1^{\Omega_0} \right]^{-1} & 0 & \cdots & 0 \end{bmatrix} \begin{Bmatrix} \mathbf{u}_{\Omega_0} \\ u_{n+2} \\ \vdots \\ u_N \end{Bmatrix} = \left\{ \overline{u} \right\} \tag{2.58}$$

where $\mathbf{T}_1^{\partial\Omega_0}$ (size: $1 \times (n+1)$) is the matrix containing the factors of the Taylor series expansion of the displacement of the constraint at $x = 0$ about node 1, whereas $\mathbf{T}_1^{\Omega_0}$ and $\mathbf{u}_{\Omega_0}$ were derived in Equation 2.43. A similar equation can be written for the other boundary

$(x = l)$ if a displacement constraint is present there.

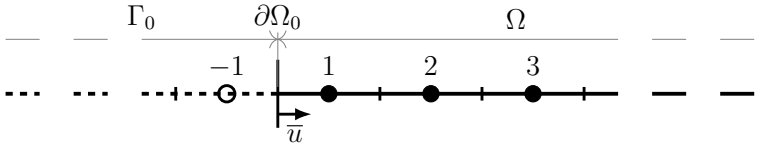


Figure 2.12: *Constraint $\overline{u}$ applied at the boundary $\partial\Omega_0$.*

The extrapolation carried out in Equation 2.58 involves only the real nodes near the boundary and the coordinate of the boundary $\partial\Omega_0$. However, the fictitious nodes play a role in the equilibrium equations of the real nodes near the boundary. The contribution of the fictitious layer $\Gamma_0$, which mitigates the surface effect, is already taken into account in the stiffness matrix $\mathbf{K}$ (see Appendix 2.D).

Consider now the imposition of an external load $\overline{\mathrm{f}}$ at the boundary $\partial\Omega_l$, as shown in Figure 2.13a. The Neumann boundary condition is imposed through the concept of force flux:

$$A \cdot \tau(l, +1) = \overline{\mathrm{f}} \tag{2.59}$$

Therefore, the resultant of the forces of the fictitious bonds crossing the boundary is enforced to match the external force $\overline{\mathrm{f}}$ (see Figure 2.13b). The vector of the forces $\mathbf{f}_b$ in the bonds, either real or fictitious, is computed in Equation 2.101 as $\mathbf{K}_b\mathbf{u}$, where $\mathbf{K}_b$ is derived from Equation 2.53 for each bond and $\mathbf{u}$ is the displacement vector. The load boundary condition can take the form of a row of matrix $\mathbf{B}$ and vector $\mathbf{c}$:

$$\begin{gathered}\begin{bmatrix}\cdots & s_{ij} & \cdots\end{bmatrix}\mathbf{K}_b\,\mathbf{u} = \mathbf{S}_l\,\mathbf{K}_b\,\mathbf{u} = \left\{\overline{\mathrm{f}}\right\} \\ \text{with } s_{ij} = \begin{cases} 1 & \text{if } (i \leq N \ \wedge \ j > N) \vee (i > N \ \wedge \ j \leq N) \\ 0 & \text{otherwise} \end{cases}\end{gathered} \tag{2.60}$$

Note that the matrix $\mathbf{S}_l$ is defined in order to sum all the force of the fictitious bonds crossing the boundary $\partial\Omega_l$. Equation 2.60 is a linear combination among the displacements of the real nodes near the boundary.

Hence, the boundary conditions for the current example are implemented as:

$$\begin{bmatrix}\mathbf{T}_1^{\partial\Omega_0}\left[\mathbf{T}_1^{\Omega_0}\right]^{-1} & \mathbf{0} \\ \mathbf{S}_l\mathbf{K}_b & \end{bmatrix}\mathbf{u} = \begin{Bmatrix}\overline{u} \\ \overline{\mathrm{f}}\end{Bmatrix} \qquad \Rightarrow \mathbf{B}\,\mathbf{u} = \mathbf{c} \tag{2.61}$$

Since Equation 2.61 expresses the boundary conditions as a relation among the displacements of the real points of the body, the technique of the Lagrange multipliers is very advantageous to include those boundary conditions in the system of equations given by the peridynamic equilibrium of the points (Equation 2.55). The Lagrangian function $\mathbf{\Pi}$ is introduced in the system as follows [225]:

$$\begin{cases}\mathbf{K}\mathbf{u} + \dfrac{\partial\mathbf{\Pi}}{\partial\mathbf{u}} = \mathbf{f} \\ \dfrac{\partial\mathbf{\Pi}}{\partial\boldsymbol{\lambda}} = \mathbf{c}\end{cases} \tag{2.62}$$

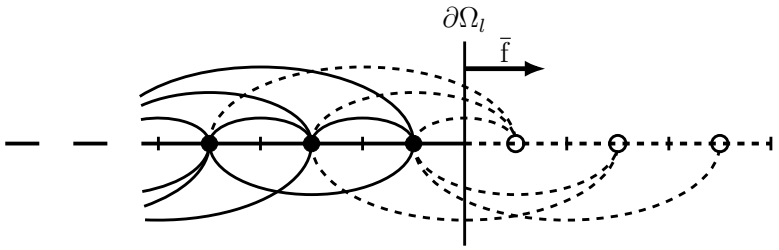


(a) *External load* $\bar{\mathrm{f}}$ *acting at the boundary:* $\bar{\mathrm{f}}$ *is applied along the line of the nodes, but for clarity reasons it is shown above it.*

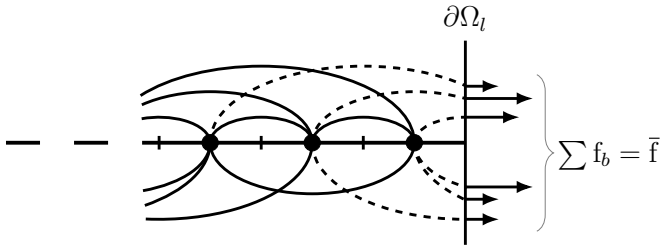


(b) *The external load is equal to the resultant of the forces of the bonds crossing the boundary.*

Figure 2.13: *Imposition of the external load* $\bar{\mathrm{f}}$ *through the concept of force flux. Empty and solid circles represent respectively fictitious and real nodes. Correspondingly, dashed and solid lines represent respectively fictitious and real bonds (*$\overline{m} = 3$ *in this example).*

where $\mathbf{\Pi} = \boldsymbol{\lambda}^\top (\mathbf{Bu})$ and $\boldsymbol{\lambda} = \{\lambda_0, \lambda_l\}^\top$ (size: $2 \times 1$) is the vector of the Lagrange multipliers. $\lambda_0$ and $\lambda_l$ are the Lagrange multipliers related to the boundary conditions at $x = 0$ and $x = l$, respectively. Equation 2.62 is simplified and rewritten in a matrix form as:

$$\begin{bmatrix} \mathbf{K} & \mathbf{B}^\top \\ \mathbf{B} & \mathbf{0} \end{bmatrix} \begin{Bmatrix} \mathbf{u} \\ \boldsymbol{\lambda} \end{Bmatrix} = \begin{Bmatrix} \mathbf{f} \\ \mathbf{c} \end{Bmatrix} \tag{2.63}$$

Equation 2.63 is a system of $N + 2$ linear equations ($N$ equations deriving from the peridynamic equilibrium equation applied at each node and 2 from the boundary conditions) with $N + 2$ unknowns ($N$ nodal displacements in $\mathbf{u}$ and 2 Lagrange multipliers in $\boldsymbol{\lambda}$). The implementation of this technique in a code is really quick and effective.

## 2.5 1D numerical examples

Some benchmark problems are presented to verify the reliability and accuracy of the proposed method of the Taylor-based extrapolation over the fictitious nodes. The numerical peridynamic results are compared with the classical continuum mechanics solution, considered as the reference solution. The discrepancy between the numerical results and the classical solution is evaluated at node $i$ by the relative percentage "error" $\epsilon$:

$$\epsilon_i = \frac{|u_i - u_{cl}(x_i)|}{|u_{cl}(x_i)|} \cdot 100 \tag{2.64}$$

where $u_{cl}$ stands for displacement solution derived with classical continuum mechanics.

As demonstrated in [165], the classical solution coincides with the peridynamic one when

the third order and higher derivatives of the displacement are equal to 0 or when the horizon $\delta$ approaches 0. Since the numerical simulations must necessarily consider a finite value of $\delta$, the classical solution can be considered the exact solution for the numerical peridynamic case solely if the highest displacement derivative is, at most, a second order derivative. When this is not respected, a part of the difference between classical solution and numerical peridynamic solution is due to the different formulations of the two theories.

The data used in the benchmark problems is reported in Table 2.3. The value of the m-ratio $\overline{m}$ is chosen to be 3, as a convenient compromise between accuracy and computational cost. Firstly, each peridynamic model is solved without the use of any correction method and, then, by means of the Taylor-based extrapolation method with different orders. In the peridynamic model adopting no corrections, a Dirichlet boundary condition is imposed by constraining the displacement of the closest node to its analytical value derived by classical continuum mechanics, whereas a Neumann boundary condition is imposed by applying the desired force to the node closest to the boundary. The imposition of the boundary conditions in the models which employ the Taylor-based extrapolation method, is described in Section 2.4.3.

Table 2.3: *Parameters for the simulation of a bar.*

| Parameter | Value |
|---|---|
| Length | $l = 1\,\mathrm{m}$ |
| Area | $A = 0.01\,\mathrm{m}^2$ |
| Young's modulus | $E = 1\,\mathrm{GPa}$ |
| Poisson's ratio | $\nu = 0.3$ |
| Grid spacing | $\Delta = 0.05\,\mathrm{m}$ |
| m-ratio | $\overline{m} = 3$ |

### 2.5.1 Clamped bar under traction

The method is tested on a clamped bar with a traction load $\bar{\mathrm{f}} = 10^4$ N imposed at the end $x = l$ of the bar, as shown in Figure 2.14. Solving the classical differential equation for an axially loaded bar with those boundary conditions yields:

$$u_{cl}(x) = \frac{\bar{\mathrm{f}}}{EA} \cdot x \tag{2.65}$$

Since $\frac{\mathrm{d}^k u_{cl}}{\mathrm{d}x^k} = 0$ with $k \geq 2$, this solution coincides with the peridynamic solution [165].

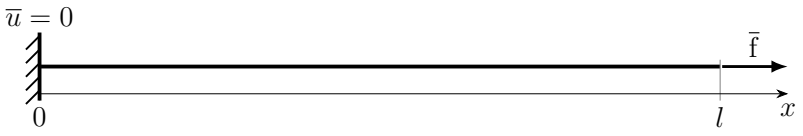


Figure 2.14: *Boundary conditions for the clamped bar under traction.*

Figure 2.15 shows the numerical peridynamic results of the clamped bar under traction loading, obtained without adopting any correction method and by implementing the pro-

posed Taylor-based extrapolation method with the order $n = 1$. The hardening/softening behavior due to the surface effect near the boundaries is evident in the peridynamic model without corrections. On the other hand, when the method of the extrapolation over the fictitious layer is adopted, the results match perfectly the reference solution and the relative "error" $\epsilon$, shown in Figure 2.16, is very close to the machine precision.

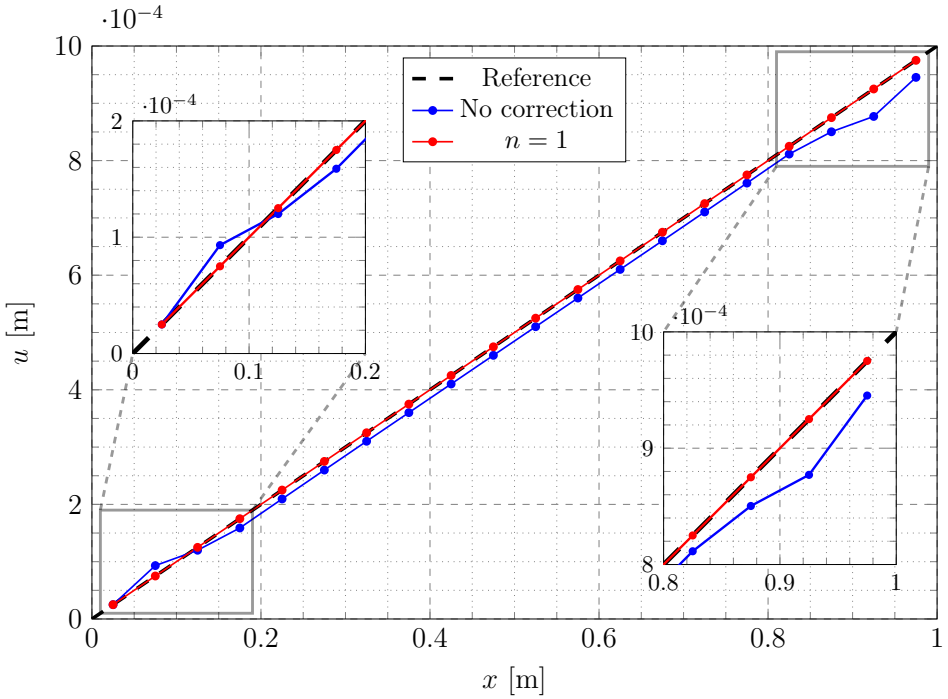


Figure 2.15: *Numerical results obtained with the peridynamic models without any correction (in blue) and with the Taylor-based extrapolation method with order $n = 1$ (in red) for the clamped bar under traction. The dashed black line represents the reference solution derived analytically by the classical continuum mechanics.*

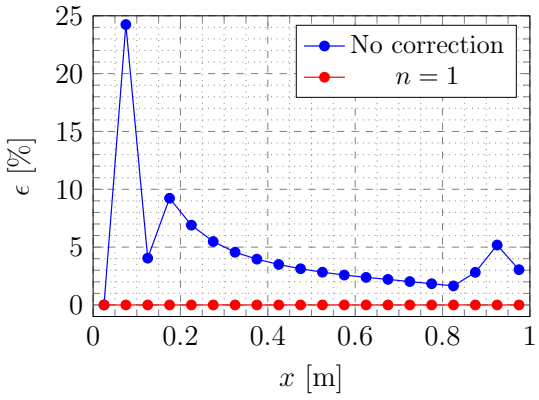


Figure 2.16: *Relative percentage "errors" for the peridynamic models without any correction (in blue) and with the Taylor-based extrapolation method with order $n = 1$ (in red) for the clamped bar under traction.*

### 2.5.2 Clamped bar under uniformly distributed load

Consider now a clamped bar, with a free end at $x = l$, subjected to a uniformly distributed load $\overline{b}_0 = 10^6$ Nm$^{-3}$, as shown in Figure 2.17. The solution derived by the classical continuum mechanics in this case is given as:

$$u_{cl}(x) = \frac{\overline{b}_0}{E}\left(lx - \frac{x^2}{2}\right) \tag{2.66}$$

Since $\frac{\mathrm{d}^k u_{cl}}{\mathrm{d}x^k} = 0$ with $k \geq 3$, the classical solution coincides with the peridynamic one [165].

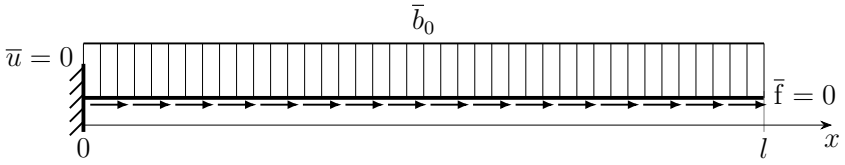


Figure 2.17: *Boundary conditions for the clamped bar under uniformly distributed load, which is acting in the direction of the bar.*

Figure 2.18 shows the numerical results for the peridynamic models with no correction and with Taylor-based extrapolation of orders $n = 1, 2$. The results of the former model exhibit a significant discrepancy with respect to the classical solution, whereas the results obtained by employing the proposed method are considerably closer to the reference solution.

Since the reference solution is a quadratic function, the order $n = 1$ for the Taylor-based extrapolation is not high enough to follow exactly that solution. However, the results are still greatly improved with respect to the model without fictitious layer (see blue and red lines in the relative "error" plot of Figure 2.19). This result is of paramount importance: in most cases the order of the truncated Taylor series to properly describe the variation of the displacement near the boundaries will be unknown, but a sufficiently high order will nonetheless provide a good approximation. On the other hand, choosing the order $n = 2$ (or higher) entails the numerical results to coincide with the analytical solution.

### 2.5.3 Clamped bar under linearly distributed load

The Taylor-based extrapolation method is tested in the case of a clamped-free bar under a linearly distributed load $\overline{b}_1 x$, where $\overline{b}_1 = 10^6$ Nm$^{-4}$, as shown in Figure 2.20. The solution of the non-homogeneous differential equation of the axially loaded bar in classical continuum mechanics is given as:

$$u_{cl}(x) = \frac{\overline{b}_1}{E}\left(\frac{l^2}{2}x - \frac{x^3}{6}\right) \tag{2.67}$$

Since $\frac{\mathrm{d}^3 u_{cl}}{\mathrm{d}x^3} \neq 0$, the peridynamic solution is different from the classical one [165]. Therefore, a part of the difference, which is computed with Equation 2.64 as relative "error" between the numerical peridynamic results and the analytical classical solution, is due to the different formulations of the theories.

Figure 2.21 shows the numerical results for the peridynamic models with and without employing the proposed method. As observed also in the plot of the relative "errors" of

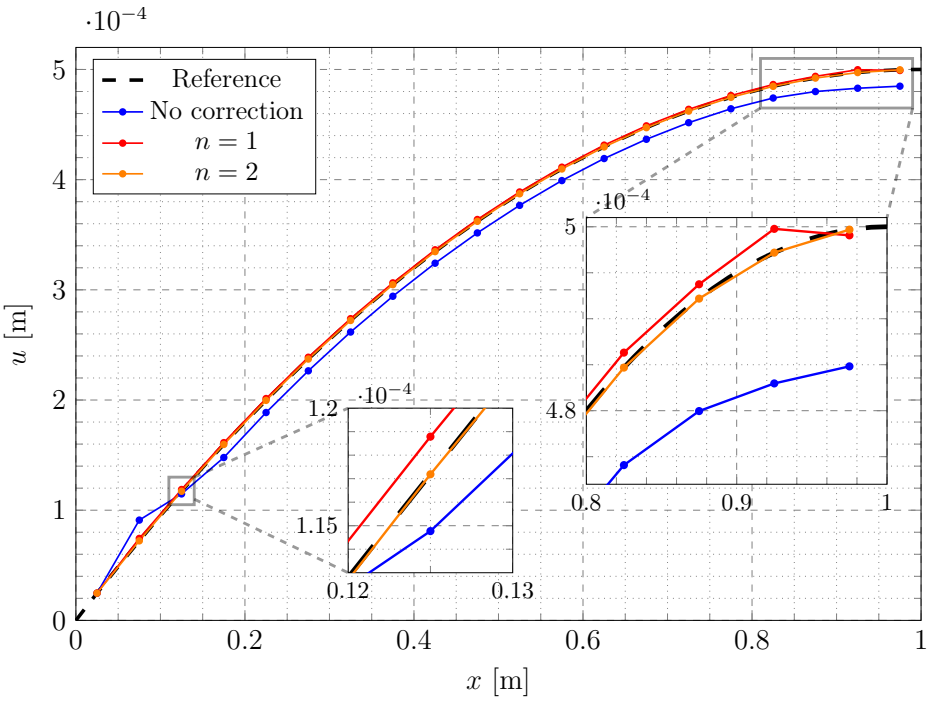


Figure 2.18: *Numerical results obtained with the peridynamic models without any correction (in blue) and with the Taylor-based extrapolation method with orders $n = 1, 2$ (respectively in red and orange) for the clamped bar under uniformly distributed load. The dashed black line represents the reference solution derived analytically by the classical continuum mechanics.*

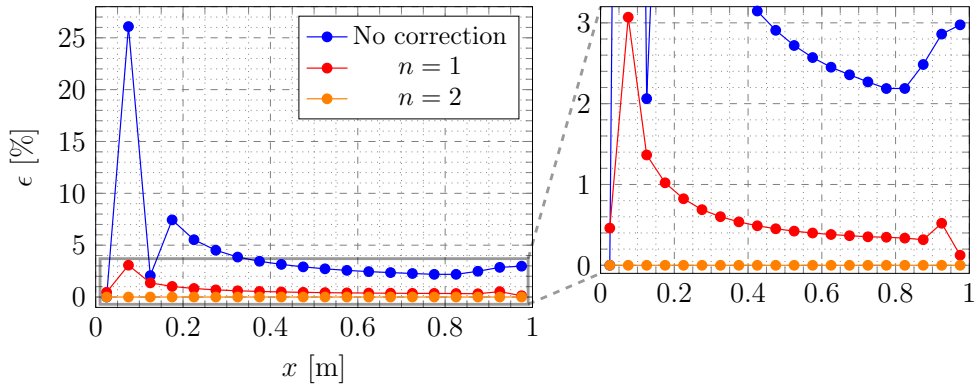


Figure 2.19: *Relative percentage "errors" for the peridynamic models without any correction (in blue) and with the Taylor-based extrapolation method with orders $n = 1, 2$ (respectively in red and orange) for the clamped bar under uniformly distributed load.*

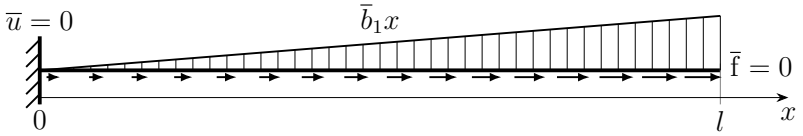


Figure 2.20: *Boundary conditions for the clamped bar under linearly distributed load, which is acting in the direction of the bar.*

Figure 2.22, there is a great improvement in the accuracy of the results when adopting the Taylor-based extrapolation method of any order $n$. However, even if the same order of the expected solution is chosen ($n = 3$), the numerical results cannot match perfectly the

classical solution because of the different formulation of the theories. Nonetheless, the choice of $n = 3$ is arguably the best one since the results do not exhibit any undesired fluctuation near the boundary due to the surface effect or the approximated imposition of the boundary conditions, whereas the results of the peridynamic models with $n \leq 2$ do (see the right-hand side of Figure 2.22).

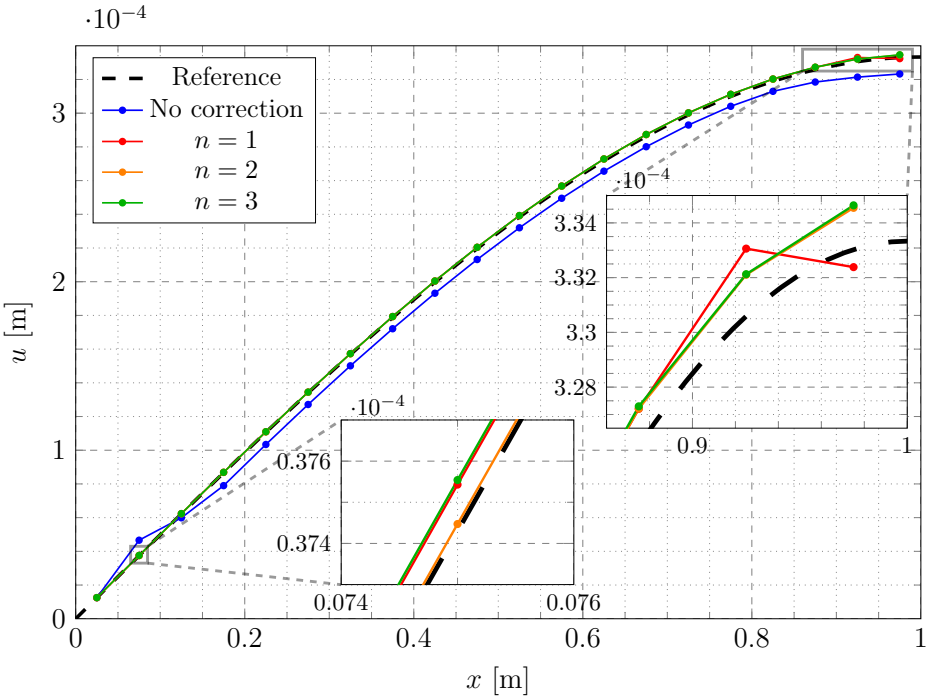


Figure 2.21: *Numerical results obtained with the peridynamic models without any correction (in blue) and with the Taylor-based extrapolation method with orders $n = 1, 2, 3$ (respectively in red, orange and green) for the clamped bar under linearly distributed load. The dashed black line represents the reference solution derived analytically by the classical continuum mechanics.*

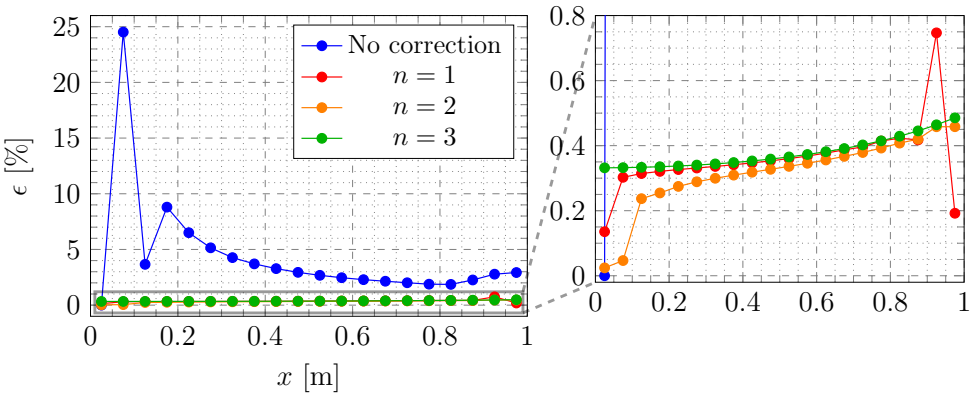


Figure 2.22: *Relative percentage "errors" for the peridynamic models without any correction (in blue) and with the Taylor-based extrapolation method with orders $n = 1, 2, 3$ (respectively in red, orange and green) for the clamped bar under linearly distributed load.*

### 2.5.4 Clamped bar under sinusoidally distributed load

The proposed method has been proven to work really well with polynomially distributed loads. In order to further investigate the performance of the method, consider a clamped-free bar under a sinusoidally distributed load $\overline{b}_s \sin\left(\frac{\pi}{l}x\right)$, where $\overline{b}_s = 10^6$ Nm$^{-3}$, as shown in Figure 2.23. The classical analytical solution in this case is given as:

$$u_{cl}(x) = \frac{\overline{b}_s}{E}\left(\frac{l}{\pi}\right)^2\left(\frac{\pi}{l}x + \sin\left(\frac{\pi}{l}x\right)\right) \tag{2.68}$$

Since $\frac{\mathrm{d}^k u_{cl}}{\mathrm{d}x^k} \neq 0$ with $k \geq 3$, the peridynamic solution does not coincide with the classical one [165]. Therefore, a part of the difference is surely due to the different formulations of the theories.

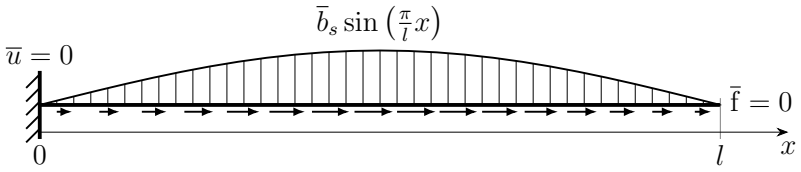


Figure 2.23: *Boundary conditions for the clamped bar under sinusoidally distributed load, which is acting in the direction of the bar.*

Figure 2.24 shows the numerical results obtained for the peridynamic model without adopting the proposed method and with the Taylor-based extrapolation of orders $n = 1, 3, 5$. Again, the proposed method greatly improves the accuracy of the solution (see the left-hand side of Figure 2.25). Furthermore, increasing the order $n$ of the Taylor-based extrapolation leads to a gradual reduction of the result fluctuations due to the boundary issues, as one can observe in the right-hand side of Figure 2.25. Therefore, the order of the Taylor-based extrapolation can be increased until the undesired fluctuations of the numerical results become negligible for the application of interest.

## 2.6 Extension to 2D problems

In this Section we show how to straightforwardly apply the 1D concepts of the Taylor-based extrapolation method to 2D peridynamic problems. In 2D the fictitious nodes surround the real body as shown in Figure 2.26. In 2D models we can have corner nodes that do not exist in 1D. The numerical results of a 2D example are also shown hereinafter. This Section is not meant to provide a complete treatment of the Taylor-based extrapolation method in 2D peridynamic models (which will be discussed in future developments), but just to show that the proposed method yields very accurate results also in 2D problems.

### 2.6.1 Taylor-based extrapolation method in 2D models

The proposed method is based on the nearest-node strategy, which entails the search for the nearest real node for each fictitious node. Clearly, all the real nodes found by this

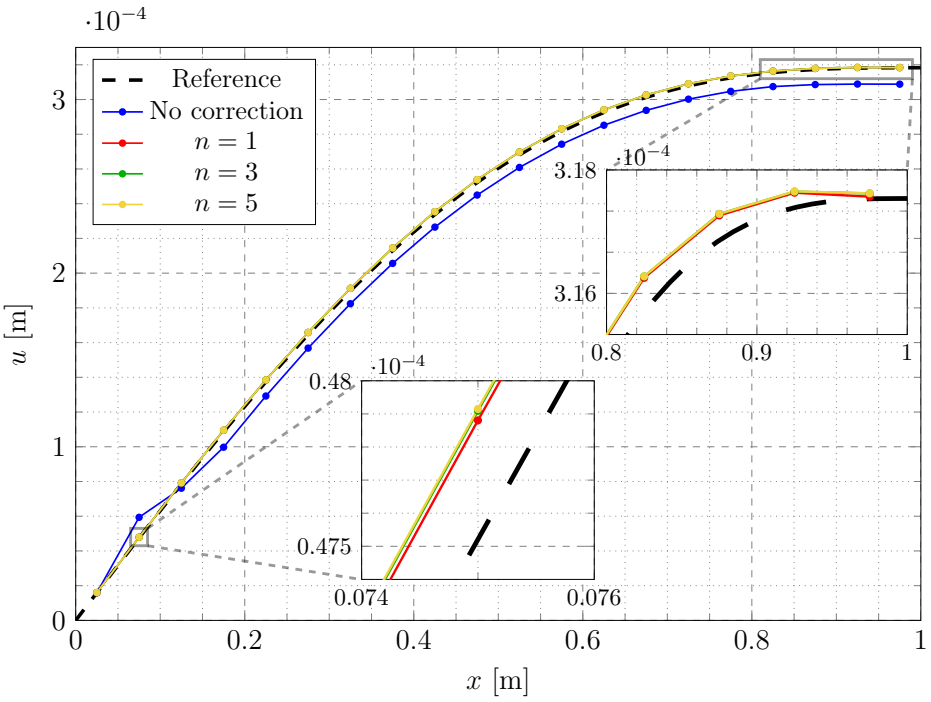


Figure 2.24: *Numerical results obtained with the peridynamic models without any correction (in blue) and with the Taylor-based extrapolation method with orders $n = 1, 3, 5$ (respectively in red, green and yellow) for the clamped bar under sinusoidally distributed load. The dashed black line represents the reference solution derived analytically by the classical continuum mechanics.*

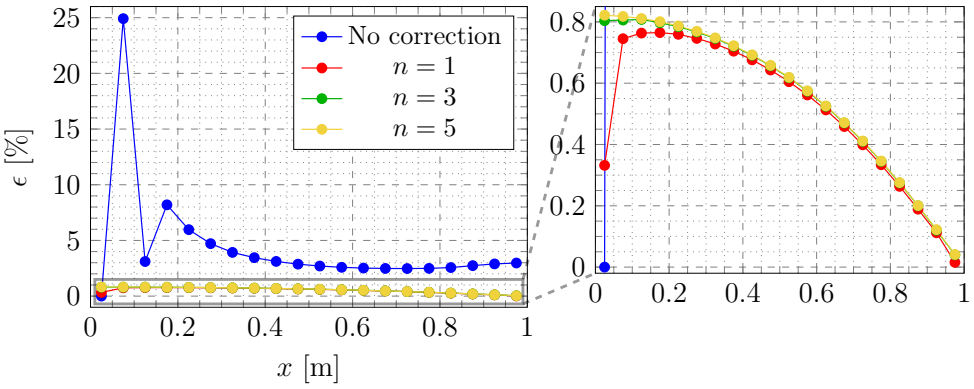


Figure 2.25: *Relative percentage "errors" for the peridynamic models without any correction (in blue) and with the Taylor-based extrapolation method with orders $n = 1, 3, 9$ (respectively in red, green and yellow) for the clamped bar under sinusoidally distributed load.*

procedure are boundary nodes (i.e., real nodes closest to the physical boundary). Moreover, most of the fictitious nodes lies on the same line as their own closest boundary nodes, as shown in Figure 2.26a. Therefore, the extrapolation for those fictitious nodes can be reduced to a 1D Taylor series expansion, which employes the same formulae already described in Section 2.4.1 (the same matrices can be used for displacements both in $x$ and $y$ direction).

However, there are still the fictitious nodes near the corner of the body that require a 2D Taylor-based extrapolation procedure. We show here, briefly, the Taylor series expansion of a fictitious node $i$ near the corner of the body (see Figure 2.26b) with a maximum order $n = 2$. This procedure can be easily generalized also for a higher order of the Taylor expansion. The

displacements in $x$ and $y$ direction, named respectively $u$ and $v$, of node $i$ can be determined by the Taylor series expansion about the corner node $j$ as:

$$\begin{cases} u_i = u_j + \ell_x \cdot \frac{\partial u_j}{\partial x} + \ell_y \cdot \frac{\partial u_j}{\partial y} + \frac{\ell_x^2}{2} \cdot \frac{\partial^2 u_j}{\partial x^2} + \ell_x \ell_y \cdot \frac{\partial^2 u_j}{\partial x \, \partial y} + \frac{\ell_y^2}{2} \cdot \frac{\partial^2 u_j}{\partial y^2} \\ v_i = v_j + \ell_x \cdot \frac{\partial v_j}{\partial x} + \ell_y \cdot \frac{\partial v_j}{\partial y} + \frac{\ell_x^2}{2} \cdot \frac{\partial^2 v_j}{\partial x^2} + \ell_x \ell_y \cdot \frac{\partial^2 v_j}{\partial x \, \partial y} + \frac{\ell_y^2}{2} \cdot \frac{\partial^2 v_j}{\partial y^2} \end{cases} \tag{2.69}$$

where $\ell_x = x_i - x_j$ and $\ell_y = y_i - y_j$. The derivatives of the displacements of the corner node $j$ can be found with a classical finite difference method in 2 dimensions (correspondent to the computation of the derivatives carried out in Section 2.4.1 for 1D models).

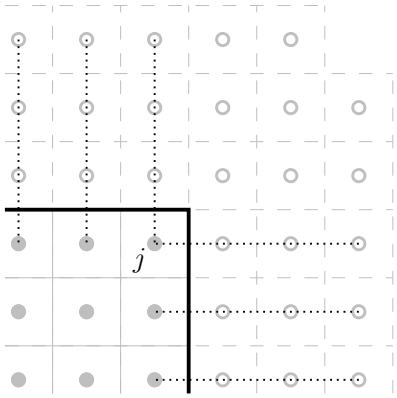


(a) *The displacements of most of the fictitious nodes can be extrapolated along lines perpendicular to the boundary (dotted lines), as in the 1D Taylor-based extrapolation method.*

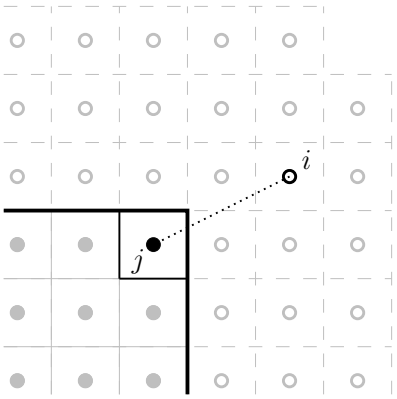


(b) *The displacements of some of the fictitious nodes (as, for instance, node i) near the corners require a 2D Taylor-based extrapolation method.*

Figure 2.26: *Generalization of the Taylor-based extrapolation method for 2D peridynamic models. Real and fictitious nodes are represented respectively with solid and empty dots.*

**Remark 2.4.** The 1D Taylor-based extrapolation procedure can be also exploited to impose Dirichlet boundary conditions by following the lines perpendicular to the boundary as shown in Figure 2.26a (please refer to Section 2.4.3 to see how to impose constraints by means of the 1D Taylor-based extrapolation). In particular, the matrices containing the factors of the Taylor series expansion (see Equation 2.58) can be used for the displacements both in $x$ and $y$ directions. Therefore, the procedure for imposing the constraints at the edges of the 2D body is the same used in 1D models, but applied twice: once to $u$ and once to $v$. However, there is an ambiguity at the corner nodes since two lines perpendicular to the boundary can be followed, as shown by node $j$ in Figure 2.26a. In order to prevent the corner node from being over-constrained, we suggest to impose the Dirichlet boundary conditions only for the displacement perpendicular to the boundary (i.e., constrain the displacement in $x$ direction for a boundary parallel to $y$-axis and the displacement in $y$ direction for a boundary parallel to $x$-axis).

### 2.6.2 Clamped plate under uniformly distributed load

The advantages of using the proposed method in 2D models to reduce the surface effect near the boundaries can be shown with the following numerical example of a clamped plate

under uniformly distributed load in $x$ direction. The boundary conditions are illustrated in Figure 2.27 and the used data is reported in Table 2.4. As in the previous Section, we solve the peridynamic problem firstly without adopting any corrections at the boundary and secondly by employing the proposed method with an increasing order $n$ of the Taylor-based extrapolation. These numerical results are compared with the reference solution (see Figure 2.28), obtained by means of the classical Finite Element Method with a uniform grid spacing $\Delta x_{FEM} = \Delta y_{FEM} = \Delta x/2$. The reference solution does not coincide with the peridynamic solution (see [162, 165]) because numerical simulations must adopt a finite value for $\delta$, but this is the closest available solution. Therefore, the percentage "errors" of the displacements are defined at each node $i$ as

$$\begin{cases} \epsilon_{u,i} = \frac{|u_i^{PD} - u_i^{FEM}|}{\max(|\mathbf{u}^{FEM}|)} \cdot 100 \\ \epsilon_{v,i} = \frac{|v_i^{PD} - v_i^{FEM}|}{\max(|\mathbf{u}^{FEM}|)} \cdot 100 \end{cases} \tag{2.70}$$

where $u_i^{PD}$ and $v_i^{PD}$ are the displacements of node $i$ in $x$ and $y$ direction computed with Peridynamics, $u_i^{FEM}$ and $v_i^{FEM}$ are the displacements of the same node obtained with the reference solution and $\mathbf{u}^{FEM}$ is the displacement vector obtained with the reference solution at all the nodes.

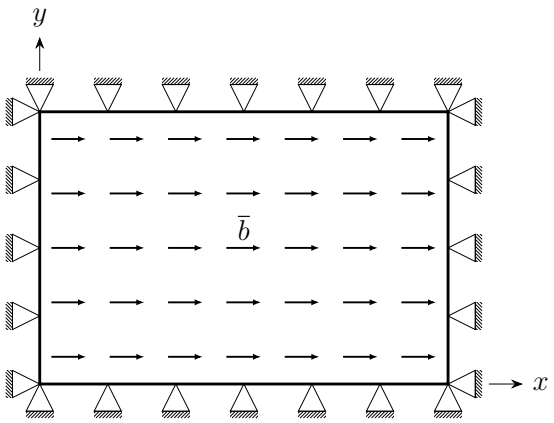


Figure 2.27: *Boundary conditions for the clamped plate under uniformly distributed load $\bar{b}$ in $x$ direction.*

Table 2.4: *Parameters for the simulation of a plate.*

| Parameter | Value |
|---|---|
| Length | $l_x = 3\,\mathrm{m}$ |
| Width | $l_y = 2\,\mathrm{m}$ |
| Thickness | $h = 0.05\,\mathrm{m}$ |
| Young's modulus | $E = 1\,\mathrm{GPa}$ |
| Poisson's ratio | $\nu = 0.2$ |
| Grid spacing | $\Delta x = \Delta y = 0.1\,\mathrm{m}$ |
| m-ratio | $\overline{m} = 3$ |

The numerical results for the percentage "errors" computed with Equation 2.70 are shown

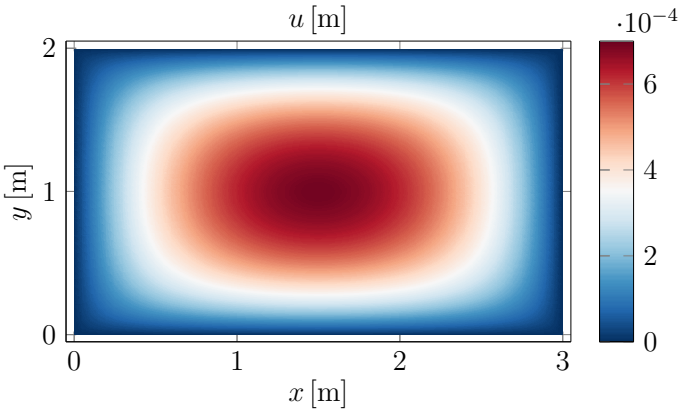


(a) *Displacement field in x direction for the clamped plate under uniformly distributed load in x direction.*

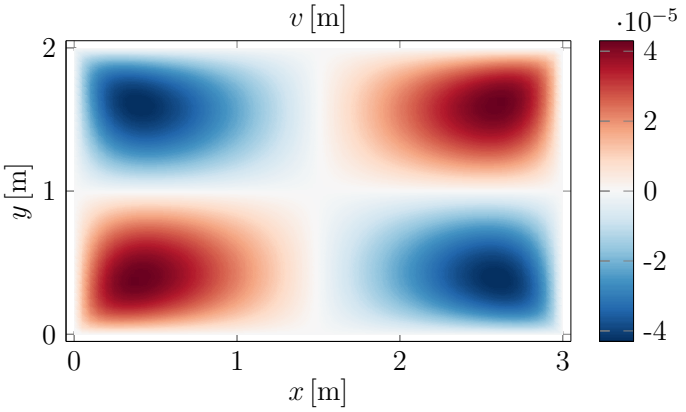


(b) *Displacement field in y direction for the clamped plate under uniformly distributed load in x direction.*

Figure 2.28: *Reference solution, obtained with the classical Finite Element Method, for the clamped plate under uniformly distributed load in x direction. Note that the colormaps refer to different values in the plots.*

in Figures 2.29 and 2.30. Note that the nodes near the corners are those with higher fluctuations. This is reasonable because the neighborhoods of the nodes near the corners are smaller than those of the nodes near the edges. Nonetheless, the numerical results are evidently improved by employing the Taylor-based extrapolation with respect to the case without corrections at the boundaries (except for $\epsilon_v$ of only one node near the corner, see Figure 2.30b). Furthermore, the increasing of the order $n$ for the Taylor-based extrapolation allows to mitigate more effectively the fluctuations near the edges and even near the corners of the body.

## 2.7 Conclusions

Two problems arising from dropping the infinite body assumption in Peridynamics have been addressed: the surface effect and the imposition of the boundary conditions.

The surface effect in the 1D state-based peridynamic theory has been analyzed both analytically and numerically: the peridynamic points distant at least $2\delta$ from the boundary

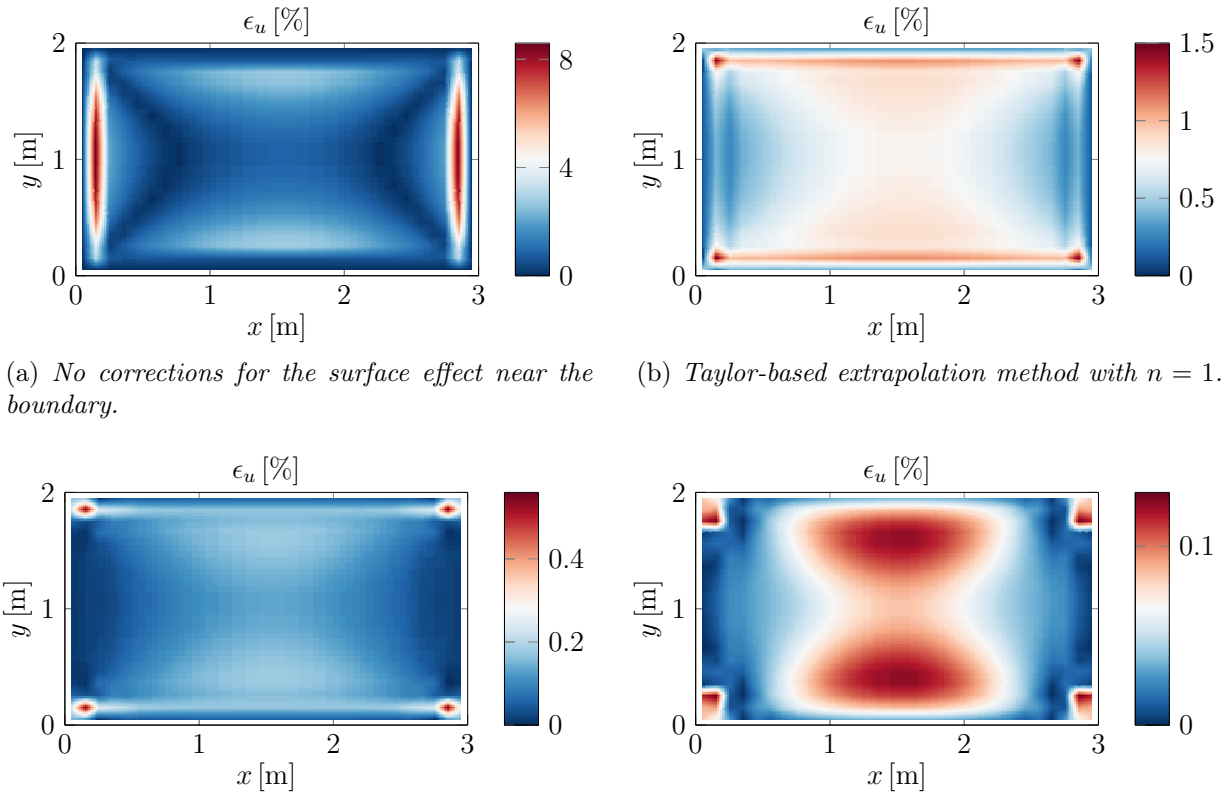


(a) *No corrections for the surface effect near the boundary.*

(b) *Taylor-based extrapolation method with $n = 1$.*

(c) *Taylor-based extrapolation method with $n = 2$.*

(d) *Taylor-based extrapolation method with $n = 3$.*

Figure 2.29: *Percentage "errors" of the displacements in $x$ direction for the clamped plate under uniformly distributed load in $x$ direction. Note that the colormaps refer to different values in the plots.*

retrieve the same mechanical properties of the points in an infinite body, whereas those near the boundary experiences a stiffness fluctuation which generates a discrepancy with respect to the infinite body solution. The characteristic hardening/softening behavior from the bulk towards the boundary due to the surface effect is driven by two counteracting phenomena: the lack of some bonds near the boundary reduces the material stiffness but the decrease of the weighted volume of the points in the most external layer of the body partially compensate the previous phenomenon.

The other issue is that there is no standard procedure to impose boundary conditions in peridynamic models and the currently adopted strategies, derived often from classical mechanics concepts, imply some kind of approximation. The authors proposed a new version of the Taylor-based extrapolation method with the introduction of a fictitious layer in order to mitigate the discrepancy due to the surface effect. The displacements of the fictitious points are expressed as a function of the displacement of the boundary point and its derivatives via the truncated Taylor series expansion. Therefore, the fictitious layer keeps deforming as the real body near the boundary and completes in a rational way the partial neighborhoods near the boundary. Furthermore, the boundary conditions are implemented in a "peridynamic way": a Dirichlet boundary condition is imposed by constraining the boundary point and the fictitious layer corrects accordingly the stiffness of the real points near the boundary, and a Neumann boundary condition is implemented via the peridynamic concept of force

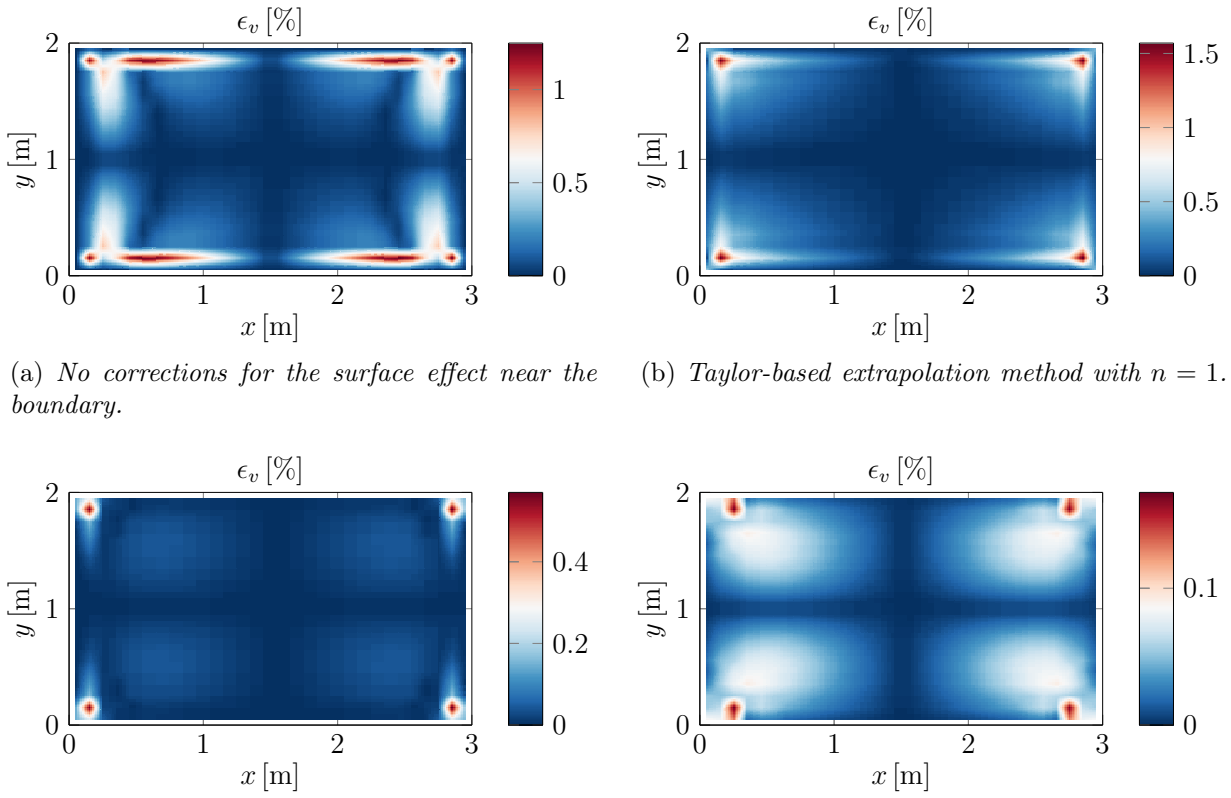


(a) *No corrections for the surface effect near the boundary.*

(b) *Taylor-based extrapolation method with* $n = 1$.

(c) *Taylor-based extrapolation method with* $n = 2$.

(d) *Taylor-based extrapolation method with* $n = 3$.

Figure 2.30: *Percentage "errors" of the displacements in y direction for the clamped plate under uniformly distributed load in x direction. Note that the colormaps refer to different values in the plots.*

flux, which involves the forces of all the fictitious bonds in the process.

The accuracy of the Taylor-based extrapolation method has been assessed by the several numerical examples, dealing with both 1D and 2D problems. The proposed method significantly improves the numerical results with respect to the peridynamic model without adopting any correction, even if low values of the Taylor expansion order $n$ are chosen. Furthermore, it has been shown that the undesired fluctuation due to the aforementioned boundary issues can be made to decrease to a negligible level by increasing the order $n$.

Since bond-based Peridynamics is a special case of the state-based one [62], the proposed method can be successfully used also in bond-based models. The authors will conduct further studies in order to complete the extension to the 2D case of the new Taylor-based extrapolation method by including the algorithm to impose Neumann boundary conditions.

# Appendices

## 2.A Force density scalar state for a linear peridynamic solid

The force density scalar state $\underline{t}\langle\xi\rangle$ is computed by taking the Fréchet derivative of the peridynamic strain energy density [62]:

$$\underline{t}\langle\xi\rangle = \nabla W(\underline{e}) \tag{2.71}$$

The definition of Fréchet derivative [62] applied to the peridynamic strain energy density $W$ as a function of the extension scalar state $\underline{e}$ yields:

$$W(\underline{e} + \Delta\underline{e}) = W(\underline{e}) + \int_{\mathrm{H}} \nabla W(\underline{e}) \cdot \Delta\underline{e}\, \mathrm{d}V' + \mathcal{O}(|\Delta\underline{e}|) \tag{2.72}$$

where $\Delta\underline{e}$ is an increment in the extension scalar state. The increment $\Delta\underline{e}$ causes the following increments in dilatation and deviatoric extension scalar state:

$$\Delta\theta = \frac{c_\theta}{m} \int_{\mathrm{H}} \underline{\omega x} \cdot \Delta\underline{e}\, \mathrm{d}V' \tag{2.73}$$

$$\Delta\underline{e}^d = \Delta\underline{e} - \frac{\Delta\theta \underline{x}}{3} \tag{2.74}$$

The strain energy density $W(\underline{e}+\Delta\underline{e})$ due to the increment $\Delta\underline{e}$ is computed via its peridynamic definition (Equation 2.12) dropping the second order terms [62]:

$$\begin{aligned}
W(\underline{e} + \Delta\underline{e}) &= \frac{\widehat{k}}{2}(\theta + \Delta\theta)^2 + \frac{\widehat{G}}{2m} \int_{\mathrm{H}} \underline{\omega} \left(\underline{e}^d + \Delta\underline{e}^d\right)^2 \mathrm{d}V' \\
&= W(\underline{e}) + \widehat{k}\theta \cdot \Delta\theta + \frac{\widehat{G}}{m} \int_{\mathrm{H}} \underline{\omega e}^d \cdot \left(\Delta\underline{e} - \frac{\Delta\theta \underline{x}}{3}\right) \mathrm{d}V' \\
&= W(\underline{e}) + \left(\widehat{k}\theta - \frac{\widehat{G}}{3m} \int_{\mathrm{H}} \underline{\omega x e}^d \, \mathrm{d}V'\right) \Delta\theta + \frac{\widehat{G}}{m} \int_{\mathrm{H}} \underline{\omega e}^d \cdot \Delta\underline{e}\, \mathrm{d}V' \\
&= W(\underline{e}) + \int_{\mathrm{H}} \left[\frac{c_\theta}{m}\left(\widehat{k}\theta - \frac{\widehat{G}}{3m} \int_{\mathrm{H}} \underline{\omega x e}^d \, \mathrm{d}V'\right) \underline{\omega x} + \frac{\widehat{G}}{m} \underline{\omega e}^d\right] \cdot \Delta\underline{e}\, \mathrm{d}V'
\end{aligned} \tag{2.75}$$

The term in square brackets is the desired force density scalar state, which can be rearranged through Equation 2.15 in a form which allows an easier computational implementation:

$$\begin{aligned}
\underline{t} &= \frac{c_\theta}{m}\left[\widehat{k}\theta - \frac{\widehat{G}}{3m} \int_{\mathrm{H}} \underline{\omega x}\left(\underline{e} - \frac{\theta \underline{x}}{3}\right) \mathrm{d}V'\right] \underline{\omega x} + \frac{\widehat{G}}{m} \underline{\omega}\left(\underline{e} - \frac{\theta \underline{x}}{3}\right) \\
&= \frac{c_\theta}{m}\left[\widehat{k}\theta - \frac{\widehat{G}\theta}{3c_\theta} + \frac{\widehat{G}\theta}{9}\right] \underline{\omega x} + \frac{\widehat{G}}{m} \underline{\omega e} - \frac{\widehat{G}}{3m} \underline{\omega x}\theta
\end{aligned}$$

$$= \left( c_\theta \widehat{k} + \frac{(c_\theta - 6)\widehat{G}}{9} \right) \frac{\underline{\underline{\omega x}}}{m} \theta + \widehat{G} \frac{\underline{\underline{\omega}}}{m} \underline{e} \; = k_\theta \frac{\underline{\underline{\omega x}}}{m} \theta + k_e \frac{\underline{\underline{\omega}}}{m} \underline{e} \tag{2.76}$$

where $k_\theta = (\nu E)/((1-2\nu)(1+\nu))$ and $k_e = E/(1+\nu)$ are the newly defined constants, which were derived from the other peridynamic constants $c_\theta$, $\widehat{k}$ and $\widehat{G}$. Note that the dilatational term vanishes for $\nu = 0$.

## 2.B Force density distribution for the non-local boundary condition

The force density distribution $b(x)$ needed to impose a constant deformation $\varepsilon_{11} = \overline{\varepsilon}$ on a finite body of length $l$ (see Figure 2.3) has been evaluated with Equations 2.4 and 2.22 solving the integrals in a way similar to that applied to the case of the force flux.

The analytical result is reported in Table 2.5 and plotted in Figure 2.31 for different values of the horizon $\delta$. This force density distribution also compensates the surface effect. As reasonably expected, the resultant of force density distribution is equal to the force which should be imposed at the boundary in classical mechanics. The obtained function changes slightly if another influence function is chosen, as one can verify with further numerical analyses.

Table 2.5: *Normalized force density distribution to obtain a constant deformation $\overline{\varepsilon}$ along the finite 1D body.*

| $x \in$ | $b/(\tau_\infty/\delta)$ |
|---|---|
| $\overline{\Omega}_0$ | $4 \arctan\left(\frac{x}{\delta}\right) + \frac{2\left(\frac{x-\delta}{\delta}\right)}{\left(\frac{x}{\delta}\right)^2 + 1} - \frac{x}{\delta} - \frac{\pi}{2}$ |
| $\widetilde{\Omega}_0$ | $-2 \arctan\left(\frac{x-\delta}{\delta}\right) + \frac{x}{\delta} - 2 + \frac{\pi}{2}$ |
| $\Omega \setminus (\overline{\Omega} \cup \widetilde{\Omega})$ | $0$ |
| $\widetilde{\Omega}_l$ | $-2 \arctan\left(\frac{x+\delta-l}{\delta}\right) + \frac{x-l}{\delta} + 2 - \frac{\pi}{2}$ |
| $\overline{\Omega}_l$ | $4 \arctan\left(\frac{x-l}{\delta}\right) + \frac{2\left(\frac{x+\delta-l}{\delta}\right)}{\left(\frac{x-l}{\delta}\right)^2 + 1} - \frac{x-l}{\delta} + \frac{\pi}{2}$ |

## 2.C Elimination of the surface effect in a finite body under cubic displacement

Here we aim to compute the force flux $\tau$, defined in Equation 2.21, in an infinite body $\Omega_\infty$ under a smooth deformation, by following a procedure similar to that illustrated for the

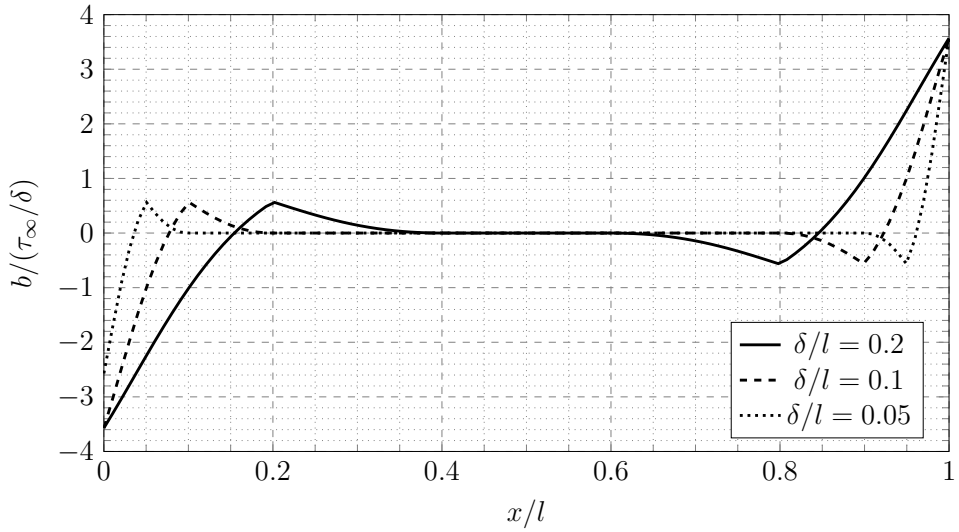


Figure 2.31: *Normalized force density distribution to obtain a constant deformation $\bar{\varepsilon}$ on a body of length $l$ for different values of the horizon $\delta$ (with surface effect compensation).*

bond-based Peridynamics in Appendix B.1 of [165]. Then, we compare the obtained solution with the solution derived with the proposed Taylor-based extrapolation method in a finite body $\Omega$ under a predefined displacement distribution.

In an infinite body $\Omega_\infty$, the weighted volume $m_\infty$ is constant in the whole domain and is equal to $A\delta^3$ when the hyperbolic influence function $\underline{\omega} = \delta/|\xi|$ is chosen (Equation 2.25). For later use, the dilatation $\theta_\infty$ of a point $x$ in an infinite body $\Omega_\infty$ is computed by means of a Taylor series expansion of $u(x') = u'$ about $x$:

$$\begin{aligned}
\theta_\infty &= \frac{c_\theta}{m_\infty} \int_{\mathrm{H}} \underline{\omega x} \cdot \underline{e}\, \mathrm{d}V' = \frac{c_\theta}{A\delta^3} \int_{x-\delta}^{x+\delta} \delta \cdot \frac{\xi}{|\xi|} \left(u' - u\right) A\, \mathrm{d}x' \\
&= \frac{c_\theta}{\delta^2} \int_{-\delta}^{\delta} \frac{\xi}{|\xi|} \left( u + \xi \frac{\mathrm{d}u}{\mathrm{d}x} + \frac{\xi^2}{2} \frac{\mathrm{d}^2u}{\mathrm{d}x^2} + \frac{\xi^3}{6} \frac{\mathrm{d}^3u}{\mathrm{d}x^3} + \ldots - u \right) \mathrm{d}\xi \\
&= c_\theta \left( \frac{\mathrm{d}u}{\mathrm{d}x} + \frac{\delta^2}{12} \frac{\mathrm{d}^3u}{\mathrm{d}x^3} + \ldots \right)
\end{aligned} \tag{2.77}$$

The dilatation converges to the classical mechanics dilatation $\theta_{cl}$ if the third order and higher derivatives of the displacement are negligible or if the horizon $\delta$ approaches 0.

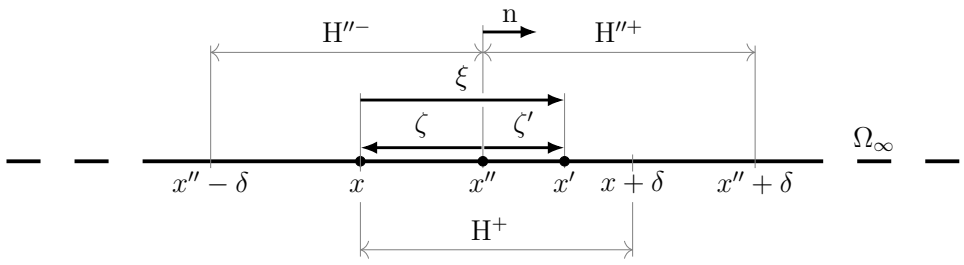


Figure 2.32: *Domains involved in the definition of the force flux at point $x''$, which is the integral of all the forces per unit area in the bonds $\xi$ crossing the section at $x''$ ($x$ varies within $\mathrm{H}''^-$ and $x'$ within $\mathrm{H}''^+ \cap \mathrm{H}^+$). The vectors $\zeta$ and $\zeta'$ are usefully defined for the Taylor expansions of the variables respectively at points $x$ and $x'$ about the point $x''$.*

Consider now the notation of Figure 2.32. The force flux $\tau(x'' \in \Omega_\infty, +1) = \tau''_\infty$ in the infinite body is therefore computed as:

$$\begin{aligned}
\tau''_\infty &= \int_{x''-\delta}^{x''} \int_{x''}^{x+\delta} \left[ k_\theta \left( \frac{\theta_\infty}{m_\infty} + \frac{\theta'_\infty}{m'_\infty} \right) \underline{\omega x} + k_e \left( \frac{1}{m_\infty} + \frac{1}{m'_\infty} \right) \underline{\omega e} \right] \underline{\mathbf{M}}\, A \, \mathrm{d}x' \, \mathrm{d}x \\
&= \frac{1}{\delta^2} \int_{x''-\delta}^{x''} \int_{x''}^{x+\delta} \left[ k_\theta \left( \theta_\infty + \theta'_\infty \right) + 2k_e \frac{\underline{e}}{|\xi|} \right] \mathrm{d}x' \, \mathrm{d}x \\
&= \frac{1}{\delta^2} \left( k_\theta \int_{-\delta}^{0} \int_{0}^{\zeta+\delta} \left( \theta_\infty + \theta'_\infty \right) \mathrm{d}\zeta' \, \mathrm{d}\zeta + 2k_e \int_{-\delta}^{0} \int_{0}^{\zeta+\delta} \frac{\underline{e}}{|\xi|} \, \mathrm{d}\zeta' \, \mathrm{d}\zeta \right)
\end{aligned} \tag{2.78}$$

where the values of the influence function and the weighted volume have been substituted. We proceed by solving the integrals separately.

The first integral in Equation 2.78 is computed with the formula obtained in Equation 2.77 by using another Taylor series expansion of the displacement derivatives about $x''$:

$$\begin{aligned}
\int_{-\delta}^{0} \int_{0}^{\zeta+\delta} \left( \theta_\infty + \theta'_\infty \right) \mathrm{d}\zeta' \, \mathrm{d}\zeta &= c_\theta \int_{-\delta}^{0} \int_{0}^{\zeta+\delta} \left( \frac{\mathrm{d}u}{\mathrm{d}x} + \frac{\delta^2}{12} \frac{\mathrm{d}^3 u}{\mathrm{d}x^3} + \frac{\mathrm{d}u'}{\mathrm{d}x} + \frac{\delta^2}{12} \frac{\mathrm{d}^3 u'}{\mathrm{d}x^3} + \dots \right) \mathrm{d}\zeta' \, \mathrm{d}\zeta \\
&= c_\theta \int_{-\delta}^{0} \int_{0}^{\zeta+\delta} \left( 2 \frac{\mathrm{d}u''}{\mathrm{d}x} + \left( \zeta' + \zeta \right) \frac{\mathrm{d}^2 u''}{\mathrm{d}x^2} \right. \\
&\qquad \left. + \left( \frac{\zeta'^2}{2} + \frac{\zeta^2}{2} + \frac{\delta^2}{6} \right) \frac{\mathrm{d}^3 u''}{\mathrm{d}x^3} + \dots \right) \mathrm{d}\zeta' \, \mathrm{d}\zeta \\
&= c_\theta \int_{-\delta}^{0} \left( 2 \left( \zeta + \delta \right) \frac{\mathrm{d}u''}{\mathrm{d}x} + \left( \frac{3}{2}\zeta^2 + 2\delta\zeta + \frac{1}{2}\delta^2 \right) \frac{\mathrm{d}^2 u''}{\mathrm{d}x^2} \right. \\
&\qquad \left. + \left( \frac{2}{3}\zeta^3 + \delta\zeta^2 + \frac{2}{3}\delta^2\zeta + \frac{1}{3}\delta^3 \right) \frac{\mathrm{d}^3 u''}{\mathrm{d}x^3} + \dots \right) \mathrm{d}\zeta \\
&= c_\theta \left( \delta^2 \frac{\mathrm{d}u''}{\mathrm{d}x} + \frac{\delta^4}{6} \frac{\mathrm{d}^3 u''}{\mathrm{d}x^3} + \dots \right)
\end{aligned} \tag{2.79}$$

where $\frac{\mathrm{d}^k u'}{\mathrm{d}x^k}$ and $\frac{\mathrm{d}^k u''}{\mathrm{d}x^k}$ are the derivatives of the displacement computed at points $x'$ and $x''$, respectively.

The second integral in Equation 2.78 is computed by means of a Taylor expansion of the displacements $u$ and $u'$ about $x''$:

$$\begin{aligned}
\int_{-\delta}^{0} \int_{0}^{\zeta+\delta} \frac{\underline{e}}{|\xi|} \, \mathrm{d}\zeta' \, \mathrm{d}\zeta &= \int_{-\delta}^{0} \int_{0}^{\zeta+\delta} \frac{1}{\zeta' - \zeta} \left( u' - u \right) \mathrm{d}\zeta' \, \mathrm{d}\zeta \\
&= \int_{-\delta}^{0} \int_{0}^{\zeta+\delta} \left( \frac{\mathrm{d}u''}{\mathrm{d}x} + \left( \frac{\zeta' + \zeta}{2} \right) \frac{\mathrm{d}^2 u''}{\mathrm{d}x^2} \right. \\
&\qquad \left. + \left( \frac{\zeta'^2 + \zeta'\zeta + \zeta^2}{6} \right) \frac{\mathrm{d}^3 u''}{\mathrm{d}x^3} + \dots \right) \mathrm{d}\zeta' \, \mathrm{d}\zeta \\
&= \int_{-\delta}^{0} \left( \left( \zeta + \delta \right) \frac{\mathrm{d}u''}{\mathrm{d}x} + \left( \frac{3}{4}\zeta^2 + \delta\zeta + \frac{1}{4}\delta^2 \right) \frac{\mathrm{d}^2 u''}{\mathrm{d}x^2} \right. \\
&\qquad \left. + \left( \frac{11}{36}\zeta^3 + \frac{1}{2}\delta\zeta^2 + \frac{1}{4}\delta^2\zeta + \frac{1}{18}\delta^3 \right) \frac{\mathrm{d}^3 u''}{\mathrm{d}x^3} + \dots \right) \mathrm{d}\zeta
\end{aligned}$$

$$= \frac{\delta^2}{2}\frac{\mathrm{d}u''}{\mathrm{d}x} + \frac{\delta^4}{48}\frac{\mathrm{d}^3u''}{\mathrm{d}x^3} + \dots \tag{2.80}$$

The force flux in an infinite body is obtained by substituting Equations 2.79 and 2.80 back in Equation 2.78:

$$\tau''_\infty = c_\theta k_\theta \left(\frac{\mathrm{d}u''}{\mathrm{d}x} + \frac{\delta^2}{6}\frac{\mathrm{d}^3u''}{\mathrm{d}x^3} + \dots\right) + k_e \left(\frac{\mathrm{d}u''}{\mathrm{d}x} + \frac{\delta^2}{24}\frac{\mathrm{d}^3u''}{\mathrm{d}x^3} + \dots\right) \tag{2.81}$$

Note that the force flux converges to the classical stress $\sigma_{11}$ if the third order and higher derivatives of the displacement are negligible or if the horizon $\delta$ approaches 0, as in [162, 165].

Now we show that, by implementing the method of the Taylor-based extrapolation over the fictitious points, the peridynamic solution of the force flux in a finite body $\Omega$ under a predefined smooth deformation matches that of the infinite body. We choose to show the case in which the fourth order or higher derivatives of the imposed displacement are equal to 0. The dilatation $\theta_\infty$ and the force flux $\tau''_\infty$ in the infinite body $\Omega_\infty$ are therefore given as:

$$\theta_\infty = c_\theta \left(\frac{\mathrm{d}u}{\mathrm{d}x} + \frac{\delta^2}{12}\frac{\mathrm{d}^3u}{\mathrm{d}x^3}\right) \tag{2.82}$$

$$\tau''_\infty = c_\theta k_\theta \left(\frac{\mathrm{d}u''}{\mathrm{d}x} + \frac{\delta^2}{6}\frac{\mathrm{d}^3u''}{\mathrm{d}x^3}\right) + k_e \left(\frac{\mathrm{d}^3u''}{\mathrm{d}x^3} + \frac{\delta^2}{24}\frac{\mathrm{d}^3u''}{\mathrm{d}x^3}\right) \tag{2.83}$$

The order of the Taylor series expansion for the proposed extrapolation method is chosen to be $n = 3$ (see the solid line in Figure 2.9), since in this case a lower order would give inexact results and higher order derivatives would be useless. When the Taylor-based extrapolation is used, the dilatation of a point $x$ in $\overline{\Omega}_l$ is computed as:

$$\begin{aligned}
\theta(x \in \overline{\Omega}_l) &= \frac{c_\theta}{m_\infty}\int_{\mathrm{H}} \underline{\omega x e}\,\mathrm{d}V' \\
&= \frac{c_\theta}{\delta^2}\int_{-\delta}^{\delta} \underline{e}\,\mathrm{d}\xi \\
&= \frac{c_\theta}{\delta^2}\left(\int_{-\delta}^{l-x} \underline{e}_r\,\mathrm{d}\xi + \int_{l-x}^{\delta} \underline{e}_f\,\mathrm{d}\xi\right)
\end{aligned} \tag{2.84}$$

Figure 2.33 shows the domains involved in the integrals of Equation 2.84. Note that the weighted volume is computed in a complete neighborhood thanks to the presence of the fictitious points in $\Gamma_l$. The integral in Equation 2.84 involves both real bonds (first integral of the last line) and fictitious bonds (second integral of the last line). The extension scalar state $\underline{e}_r$ of a real bond is computed through a Taylor series expansion of order $n = 3$ of $u'$ about $x$:

$$\underline{e}_r = \frac{\xi}{|\xi|}(u' - u) = |\xi|\left(\frac{\mathrm{d}u}{\mathrm{d}x} + \frac{\xi}{2}\frac{\mathrm{d}^2u}{\mathrm{d}x^2} + \frac{\xi^2}{6}\frac{\mathrm{d}^3u}{\mathrm{d}x^3}\right) \tag{2.85}$$

On the other hand, refer to the notation of Figure 2.33 for the computation of the extension scalar state of a fictitious bond. In particular, note that $\zeta_l = l - x$, $\zeta'_l = x' - l$ and $\xi = \zeta_l + \zeta'_l$. Furthermore, since $x$ and $x'$ belong respectively to $\overline{\Omega}_l$ and $\Gamma_l$, $\xi$ is always

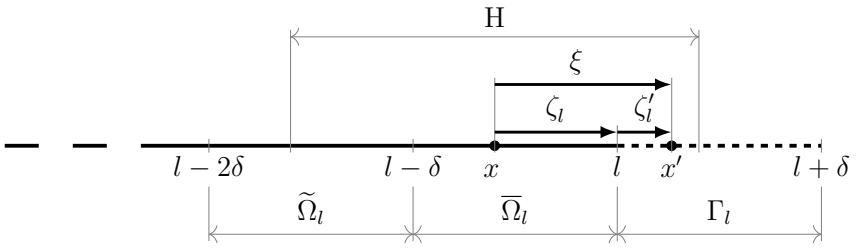


Figure 2.33: *Representation of a fictitious bond involved in the computation of the dilatation of a point $x$ in $\overline{\Omega}_l$.*

positive. The extension scalar state $\underline{e}_f$ of a fictitious bond is computed by performing two consecutive Taylor series expansions. The first one derives from the proposed extrapolation method (Equation 2.30 with $n = 3$):

$$\underline{e}_f = u' - u = u_l + \zeta_l' \frac{\mathrm{d}u_l}{\mathrm{d}x} + \frac{\zeta_l'^2}{2}\frac{\mathrm{d}^2 u_l}{\mathrm{d}x^2} + \frac{\zeta_l'^3}{6}\frac{\mathrm{d}^3 u_l}{\mathrm{d}x^3} - u \tag{2.86}$$

where $u_l$ is the displacement of the boundary point $x = l$ and $\frac{\mathrm{d}^k u_l}{\mathrm{d}x^k}$ with $k = 1, 2, 3$ are the derivatives computed at that point. The second Taylor series expansion is performed for the displacement $u_l$ and its derivatives about the point $x$:

$$\begin{aligned}
\underline{e}_f &= \left(u + \zeta_l \frac{\mathrm{d}u}{\mathrm{d}x} + \frac{\zeta_l^2}{2}\frac{\mathrm{d}^2 u}{\mathrm{d}x^2} + \frac{\zeta_l^3}{6}\frac{\mathrm{d}^3 u}{\mathrm{d}x^3}\right) + \zeta_l' \left(\frac{\mathrm{d}u}{\mathrm{d}x} + \zeta_l \frac{\mathrm{d}^2 u}{\mathrm{d}x^2} + \frac{\zeta_l^2}{2}\frac{\mathrm{d}^3 u}{\mathrm{d}x^3}\right) \\
&\qquad + \frac{\zeta_l'^2}{2}\left(\frac{\mathrm{d}^2 u}{\mathrm{d}x^2} + \zeta_l \frac{\mathrm{d}^3 u}{\mathrm{d}x^3}\right) + \frac{\zeta_l'^3}{6}\frac{\mathrm{d}^3 u}{\mathrm{d}x^3} - u \\
&= \left(\zeta_l + \zeta_l'\right)\frac{\mathrm{d}u}{\mathrm{d}x} + \frac{\left(\zeta_l + \zeta_l'\right)^2}{2}\frac{\mathrm{d}^2 u}{\mathrm{d}x^2} + \frac{\left(\zeta_l + \zeta_l'\right)^3}{6}\frac{\mathrm{d}^3 u}{\mathrm{d}x^3} \\
&= \xi\left(\frac{\mathrm{d}u}{\mathrm{d}x} + \frac{\xi}{2}\frac{\mathrm{d}^2 u}{\mathrm{d}x^2} + \frac{\xi^2}{6}\frac{\mathrm{d}^3 u}{\mathrm{d}x^3}\right)
\end{aligned} \tag{2.87}$$

Since here $\xi > 0$, the extension scalar state of the fictitious bonds can be computed with the same formula as that of the real bonds (Equation 2.85).

Substituting Equations 2.85 and 2.87 in Equation 2.84 and solving the integrals, the following result is obtained:

$$\begin{aligned}
\theta(x \in \overline{\Omega}_l) &= \frac{c_\theta}{\delta^2}\left(\int_{-\delta}^{l-x} |\xi|\left(\frac{\mathrm{d}u}{\mathrm{d}x} + \frac{\xi}{2}\frac{\mathrm{d}^2 u}{\mathrm{d}x^2} + \frac{\xi^2}{6}\frac{\mathrm{d}^3 u}{\mathrm{d}x^3}\right)\mathrm{d}\xi + \int_{l-x}^{\delta} \xi\left(\frac{\mathrm{d}u}{\mathrm{d}x} + \frac{\xi}{2}\frac{\mathrm{d}^2 u}{\mathrm{d}x^2} + \frac{\xi^2}{6}\frac{\mathrm{d}^3 u}{\mathrm{d}x^3}\right)\mathrm{d}\xi\right) \\
&= \frac{c_\theta}{\delta^2}\int_{-\delta}^{\delta} |\xi|\left(\frac{\mathrm{d}u}{\mathrm{d}x} + \frac{\xi}{2}\frac{\mathrm{d}^2 u}{\mathrm{d}x^2} + \frac{\xi^2}{6}\frac{\mathrm{d}^3 u}{\mathrm{d}x^3}\right)\mathrm{d}\xi \\
&= c_\theta\left(\frac{\mathrm{d}u}{\mathrm{d}x} + \frac{\delta^2}{12}\frac{\mathrm{d}^3 u}{\mathrm{d}x^3}\right) = \theta_\infty
\end{aligned} \tag{2.88}$$

Thus, the real points near the boundary have the same peridynamic properties as the points with a complete neighborhood, namely $\theta_\infty$ and $m_\infty$, thanks to the proposed Taylor-based extrapolation method. By executing the same operations to compute the force flux as in the infinite body (Equations 2.78–2.81), we can show that $\tau(x'' \in \widetilde{\Omega}_l, +1) = \tau''_\infty$.

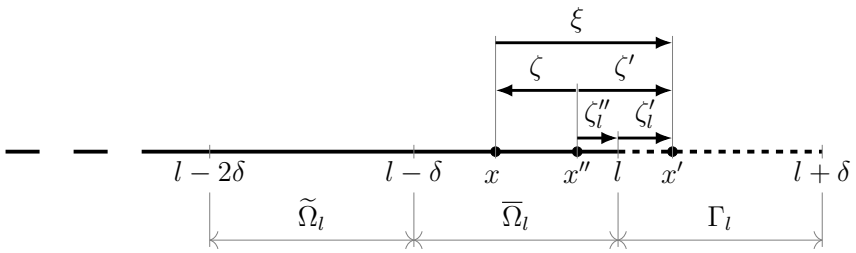


Figure 2.34: *Representation of a fictitious bond involved in the computation of the force flux of a point $x''$ in $\overline{\Omega}_l$.*

Refer now to the notation of Figure 2.34, which yields: $\zeta_l' = x' - l$, $\zeta_l'' = l - x''$, $\zeta' = \zeta_l' + \zeta_l''$, $\zeta = x - x''$ and $\xi = \zeta' - \zeta$. The force flux $\tau$ of a point $x''$ in $\overline{\Omega}_l$ is computed from Equation 2.21 as:

$$\tau(x'' \in \overline{\Omega}_l, +1) = \frac{k_\theta}{\delta^2} \int_{-\delta}^{0} \int_{0}^{\zeta+\delta} (\theta + \theta') \, \mathrm{d}\zeta' \, \mathrm{d}\zeta + \frac{2k_e}{\delta^2} \int_{-\delta}^{0} \int_{0}^{\zeta+\delta} \frac{e}{|\xi|} \, \mathrm{d}\zeta' \, \mathrm{d}\zeta \tag{2.89}$$

This Equation has considered $m = m' = m_\infty$, as prescribed from the proposed method.

Consider the first integral in Equation 2.89. Due to the limits of integration, the point $x$ can belong to $\widetilde{\Omega}_l$ or to $\overline{\Omega}_l$. In the former case, $\theta = \theta(x) = \theta_\infty$ because the point $x$ has a complete neighborhood consisting of real points. In the latter case, again $\theta = \theta_\infty$ as shown in Equation 2.88. Therefore, one can employ a Taylor series expansion of $\theta$ about $x''$:

$$\begin{aligned} \theta &= c_\theta \left( \frac{\mathrm{d}u}{\mathrm{d}x} + \frac{\delta^2}{12} \frac{\mathrm{d}^3 u}{\mathrm{d}x^3} \right) \\ &= c_\theta \left( \frac{\mathrm{d}u''}{\mathrm{d}x} + \zeta \frac{\mathrm{d}^2 u''}{\mathrm{d}x^2} + \frac{\zeta^2}{2} \frac{\mathrm{d}^3 u''}{\mathrm{d}x^3} + \frac{\delta^2}{12} \frac{\mathrm{d}^3 u''}{\mathrm{d}x^3} \right) \end{aligned} \tag{2.90}$$

By the same token, point $x'$ can lie in $\overline{\Omega}_l$ (again $\theta' = \theta(x') = \theta_\infty$ from Equation 2.88) or be a fictitious point in $\Gamma_l$. In the latter case, the Taylor-based extrapolation of order $n-1$ about the boundary point $x = l$ is performed:

$$\theta(x' \in \Gamma_l) = \theta_l + \zeta_l' \frac{\mathrm{d}\theta_l}{\mathrm{d}x} + \frac{\zeta_l'^2}{2} \frac{\mathrm{d}^2 \theta_l}{\mathrm{d}x^2} \tag{2.91}$$

where $\theta_l$ is the dilatation at $x = l$ and $\frac{\mathrm{d}^k \theta_l}{\mathrm{d}x^k}$ with $k = 1, 2$ are the derivatives computed at that point. Another Taylor series expansion is employed for $\theta_l$ and its derivatives about $x''$:

$$\begin{aligned} \theta(x' \in \Gamma_l) &= \left( \theta'' + \zeta_l'' \frac{\mathrm{d}\theta''}{\mathrm{d}x} + \frac{\zeta_l''^2}{2} \frac{\mathrm{d}^2 \theta''}{\mathrm{d}x^2} \right) + \zeta_l' \left( \frac{\mathrm{d}\theta''}{\mathrm{d}x} + \zeta_l'' \frac{\mathrm{d}^2 \theta''}{\mathrm{d}x^2} \right) + \frac{\zeta_l'^2}{2} \frac{\mathrm{d}^2 \theta''}{\mathrm{d}x^2} \\ &= \theta'' + \zeta' \frac{\mathrm{d}\theta''}{\mathrm{d}x} + \frac{\zeta'^2}{2} \frac{\mathrm{d}^2 \theta''}{\mathrm{d}x^2} \\ &= c_\theta \left( \frac{\mathrm{d}u''}{\mathrm{d}x} + \zeta' \frac{\mathrm{d}^2 u''}{\mathrm{d}x^2} + \frac{\zeta'^2}{2} \frac{\mathrm{d}^3 u''}{\mathrm{d}x^3} + \frac{\delta^2}{12} \frac{\mathrm{d}^3 u''}{\mathrm{d}x^3} \right) \end{aligned} \tag{2.92}$$

where Equation 2.82 has been substituted and the displacement derivatives of fourth and fifth orders have been cancelled because the prescribed displacement on the body is a cubic function.

Substituting Equations 2.90 and 2.92 in the first integral in Equation 2.89, one obtains:

$$\begin{aligned}\frac{k_\theta}{\delta^2}\int_{-\delta}^{0}\int_{0}^{\zeta+\delta}(\theta+\theta')\,\mathrm{d}\zeta'\,\mathrm{d}\zeta &= c_\theta\frac{k_\theta}{\delta^2}\int_{-\delta}^{0}\int_{0}^{\zeta+\delta}\left(2\frac{\mathrm{d}u''}{\mathrm{d}x}+(\zeta'+\zeta)\frac{\mathrm{d}^2u''}{\mathrm{d}x^2}\right.\\ &\qquad\left.+\left(\frac{\zeta'^2}{2}+\frac{\zeta^2}{2}+\frac{\delta^2}{6}\right)\frac{\mathrm{d}^3u''}{\mathrm{d}x^3}\right)\mathrm{d}\zeta'\,\mathrm{d}\zeta\\ &= c_\theta\frac{k_\theta}{\delta^2}\int_{-\delta}^{0}\left(2\,(\zeta+\delta)\frac{\mathrm{d}u''}{\mathrm{d}x}+\left(\frac{3}{2}\zeta^2+2\delta\zeta+\frac{1}{2}\delta^2\right)\frac{\mathrm{d}^2u''}{\mathrm{d}x^2}\right.\\ &\qquad\left.+\left(\frac{2}{3}\zeta^3+\delta\zeta^2+\frac{2}{3}\delta^2\zeta+\frac{1}{3}\delta^3\right)\frac{\mathrm{d}^3u''}{\mathrm{d}x^3}\right)\mathrm{d}\zeta\\ &= c_\theta k_\theta\left(\frac{\mathrm{d}u''}{\mathrm{d}x}+\frac{\delta^2}{6}\frac{\mathrm{d}^3u''}{\mathrm{d}x^3}\right)\end{aligned}\tag{2.93}$$

which is equal to the first term of the force flux $\tau''_\infty$ in an infinite body in Equation 2.83.

The extension scalar state in the second integral of Equation 2.89 can be related to a real or a fictitious bond (note that for the limits of integration, $\xi > 0$). In the former case, a Taylor series expansion of the displacements $u$ and $u'$ about $x''$ is performed:

$$\underline{e}_r = u' - u = (\zeta'-\zeta)\frac{\mathrm{d}u''}{\mathrm{d}x}+\left(\frac{\zeta'^2-\zeta^2}{2}\right)\frac{\mathrm{d}^2u''}{\mathrm{d}x^2}+\left(\frac{\zeta'^3-\zeta^3}{6}\right)\frac{\mathrm{d}^3u''}{\mathrm{d}x^3}\tag{2.94}$$

The extension scalar state $\underline{e}_f$ of a fictitious bond can be computed with a procedure similar to that of Equations 2.86 and 2.87 with two Taylor expansions, first about the boundary point $x = l$ and then about $x''$:

$$\begin{aligned}\underline{e}_f &= u' - u = u_l + \zeta'_l\frac{\mathrm{d}u_l}{\mathrm{d}x}+\frac{\zeta'^2_l}{2}\frac{\mathrm{d}^2u_l}{\mathrm{d}x^2}+\frac{\zeta'^3_l}{6}\frac{\mathrm{d}^3u_l}{\mathrm{d}x^3}-u\\ &= \left(u''+\zeta''_l\frac{\mathrm{d}u''}{\mathrm{d}x}+\frac{\zeta''^2_l}{2}\frac{\mathrm{d}^2u''}{\mathrm{d}x^2}+\frac{\zeta''^3_l}{6}\frac{\mathrm{d}^3u''}{\mathrm{d}x^3}\right)+\zeta'_l\left(\frac{\mathrm{d}u''}{\mathrm{d}x}+\zeta''_l\frac{\mathrm{d}^2u''}{\mathrm{d}x^2}+\frac{\zeta''^2_l}{2}\frac{\mathrm{d}^3u''}{\mathrm{d}x^3}\right)\\ &\qquad+\frac{\zeta'^2_l}{2}\left(\frac{\mathrm{d}^2u''}{\mathrm{d}x^2}+\zeta''_l\frac{\mathrm{d}^3u''}{\mathrm{d}x^3}\right)+\frac{\zeta'^3_l}{6}\frac{\mathrm{d}^3u''}{\mathrm{d}x^3}-u\\ &= \left(u''+\zeta'\frac{\mathrm{d}u''}{\mathrm{d}x}+\frac{\zeta'^2}{2}\frac{\mathrm{d}^2u''}{\mathrm{d}x^2}+\frac{\zeta'^3}{6}\frac{\mathrm{d}^3u''}{\mathrm{d}x^3}\right)-\left(u''+\zeta\frac{\mathrm{d}u''}{\mathrm{d}x}+\frac{\zeta^2}{2}\frac{\mathrm{d}^2u''}{\mathrm{d}x^2}+\frac{\zeta^3}{6}\frac{\mathrm{d}^3u''}{\mathrm{d}x^3}\right)\\ &= (\zeta'-\zeta)\frac{\mathrm{d}u''}{\mathrm{d}x}+\left(\frac{\zeta'^2-\zeta^2}{2}\right)\frac{\mathrm{d}^2u''}{\mathrm{d}x^2}+\left(\frac{\zeta'^3-\zeta^3}{6}\right)\frac{\mathrm{d}^3u''}{\mathrm{d}x^3}\end{aligned}\tag{2.95}$$

Note that $\underline{e}_r = \underline{e}_f$, so that the second integral in Equation 2.89 is computed exactly as Equation 2.80. Substituting the results back in Equation 2.89 yields $\tau(x'' \in \overline{\Omega}_l, +1) = \tau''_\infty$. The same results can be obtained at the other end of the finite body by implementing the proposed method into the fictitious layer $\Gamma_0$.

Therefore, the force flux, corrected with the proposed Taylor-based extrapolation method of order $n = 3$, in the whole domain of a finite body under a cubic distribution of displacement is equal to the force flux computed in an infinite body under the same displacement distribution.

## 2.D Assembly of the stiffness matrix

Let $N_b$ be the total number of fictitious and real bonds and $N_n = N + 2 \cdot \overline{m}$ the total number of real and fictitious nodes (see Figure 2.10). Suppose, without loss of generality, that the order $n$ of the Taylor series expansion and the number of real nodes $N$ are chosen so that: $N > 2n$. The assembling of the peridynamic stiffness matrix $\mathbf{K}$ is achieved by applying the following procedure:

- in order to obtain the vector $\mathbf{U}$ (size: $N_n \times 1$) which contains the displacements of the real and fictitious nodes, assemble the matrix $\mathbf{A}_U$ (size: $N_n \times N$) as follows:

$$\mathbf{U}_{\Gamma_0} = \left[\mathbf{T}_1^{\Gamma_0}\left[\mathbf{T}_1^{\Omega_0}\right]^{-1} \quad 0 \quad \cdots \quad 0\right] \begin{Bmatrix} \mathbf{u}_{\Omega_0} \\ u_{n+2} \\ \vdots \\ u_N \end{Bmatrix} = \mathbf{A}_{\Gamma_0}\ \mathbf{u}$$

$$\mathbf{U}_\Omega = \mathbf{1}\ \mathbf{u}$$

$$\mathbf{U}_{\Gamma_l} = \left[0 \quad \cdots \quad 0 \quad \mathbf{T}_N^{\Gamma_l}\left[\mathbf{T}_N^{\Omega_l}\right]^{-1}\right] \begin{Bmatrix} u_1 \\ \vdots \\ u_{N\text{-}n\text{-}2} \\ \mathbf{u}_{\Omega_l} \end{Bmatrix} = \mathbf{A}_{\Gamma_l}\mathbf{u}$$

$$\Rightarrow \mathbf{U} = \begin{bmatrix} \mathbf{A}_{\Gamma_0} \\ \mathbf{1} \\ \mathbf{A}_{\Gamma_l} \end{bmatrix} \mathbf{u} = \mathbf{A}_U\ \mathbf{u} \tag{2.96}$$

  where $\mathbf{U}_{\Gamma_0}$ and $\mathbf{U}_{\Gamma_l}$ are the parts of the vector $\mathbf{U}$ containing the displacements of the fictitious nodes at the two boundaries, $\mathbf{U}_\Omega$ is the part of the vector $\mathbf{U}$ containing the displacements of the real nodes, $\mathbf{u}_{\Omega_0}$ and $\mathbf{u}_{\Omega_l}$ are the parts of the displacement vector $\mathbf{u}$ containing the displacements of the $n+1$ real nodes near the two boundaries, $\mathbf{T}_i^\Gamma$ and $\mathbf{T}_i^\Omega$ are the Taylor matrices of the displacements respectively of fictitious and real nodes about the boundary nodes $i = 1, N$ (see Equation 2.46);

- in order to obtain the extension vector $\mathbf{e}$ (size: $N_b \times 1$) which contains the extension scalar states of all bonds, real and fictitious, assemble matrix $\mathbf{A}_e$ (size: $N_b \times N_n$) by carrying out the following operation for each bond (see Equation 2.48):

$$\left\{\underline{e}_{ij}\right\} = \frac{\xi_{ij}}{|\xi_{ij}|}\begin{bmatrix}-1 & 1\end{bmatrix}\begin{Bmatrix} U_i \\ U_j \end{Bmatrix} \qquad \Rightarrow \mathbf{e} = \mathbf{A}_e\ \mathbf{U} \tag{2.97}$$

- in order to obtain the dilatation vector $\boldsymbol{\theta}$ (size: $N \times 1$) which contains the dilatations of the real nodes, assemble matrix $\mathbf{A}_\theta$ (size: $N \times N_b$) by carrying out the following

operation for all bonds, real and fictitious (see Equation 2.51):

$$\begin{Bmatrix} \theta_{i,h_i} \\ \theta_{j,h_j} \end{Bmatrix} = c_\theta \underline{\omega}_{ij} \underline{x}_{ij} \beta_{ij} V \begin{bmatrix} \frac{1}{m_i} \\ \frac{1}{m_j} \end{bmatrix} \left\{ \underline{e}_{ij} \right\} \tag{2.98}$$

$$\Rightarrow \boldsymbol{\theta} = \mathbf{A}_\theta \ \mathbf{e}$$

where the subscripts $h_i$ and $h_j$ indicate the $h$-th contribution to the sum that composes the complete values of the dilatations of the real nodes $i$ and $j$, respectively;

- in order to obtain the vector $\boldsymbol{\Theta}$ (size: $N_n \times 1$) which contains the dilatations of the real and fictitious nodes, assemble the matrix $\mathbf{A}_\Theta$ (size: $N_n \times N$) as follows:

$$\boldsymbol{\Theta}_{\Gamma_0} = \left[ \overline{\mathbf{T}_1^{\Gamma_0}} \left[ \overline{\mathbf{T}_1^{\Omega_0}} \right]^{-1} \quad 0 \quad \cdots \quad 0 \right] \begin{Bmatrix} \boldsymbol{\theta}_{\Omega_0} \\ \theta_{n+1} \\ \vdots \\ \theta_N \end{Bmatrix} = \overline{\mathbf{A}}_{\Gamma_0} \ \boldsymbol{\theta}$$

$$\boldsymbol{\Theta}_\Omega = \mathbf{1} \ \boldsymbol{\theta}$$

$$\boldsymbol{\Theta}_{\Gamma_l} = \left[ 0 \quad \cdots \quad 0 \quad \overline{\mathbf{T}_N^{\Gamma_l}} \left[ \overline{\mathbf{T}_N^{\Omega_l}} \right]^{-1} \right] \begin{Bmatrix} \theta_1 \\ \vdots \\ \theta_{N\text{-}n\text{-}1} \\ \boldsymbol{\theta}_{\Omega_l} \end{Bmatrix} = \overline{\mathbf{A}}_{\Gamma_l} \ \boldsymbol{\theta}$$

$$\Rightarrow \boldsymbol{\Theta} = \begin{bmatrix} \overline{\mathbf{A}}_{\Gamma_0} \\ \mathbf{1} \\ \overline{\mathbf{A}}_{\Gamma_l} \end{bmatrix} \boldsymbol{\theta} = \mathbf{A}_\Theta \ \boldsymbol{\theta} \tag{2.99}$$

where the notation is similar to that in Equation 2.96 (see Equation 2.47 for the description of the Taylor matrices of the dilatations);

- in order to obtain the bond force vector $\mathbf{f}_b$ (size: $N_b \times 1$) which contains the forces in the bonds, assemble matrix $\mathbf{K}_e$ (size: $N_b \times N_b$) and matrix $\mathbf{K}_\theta$ (size: $N_b \times N_n$) by carrying out the following operations for each bond (see Equation 2.53):

$$\left\{ \mathrm{f}_{ij} \right\} = k_e \underline{\omega}_{ij} \beta_{ij} V^2 \left( \frac{1}{m_i} + \frac{1}{m_j} \right) \left\{ \underline{e}_{ij} \right\} + k_\theta \underline{\omega}_{ij} \underline{x}_{ij} \beta_{ij} V^2 \begin{bmatrix} \frac{1}{m_i} & \frac{1}{m_j} \end{bmatrix} \begin{Bmatrix} \Theta_i \\ \Theta_j \end{Bmatrix} \tag{2.100}$$

$$\Rightarrow \mathbf{f}_b = \mathbf{K}_e \ \mathbf{e} + \mathbf{K}_\theta \ \boldsymbol{\Theta}$$

Thus, the bond force vector $\mathbf{f}_b$ depends on the displacement vector $\mathbf{u}$ through the matrix $\mathbf{K}_b$ (size: $N_b \times N$):

$$\mathbf{f}_b = \left( \mathbf{K}_e + \mathbf{K}_\theta \ \mathbf{A}_\Theta \ \mathbf{A}_\theta \right) \mathbf{A}_e \ \mathbf{A}_U \ \mathbf{u} = \mathbf{K}_b \ \mathbf{u} \tag{2.101}$$

- in order to obtain the internal force vector $\widetilde{\mathbf{f}}$ (size: $N \times 1$) which contains the forces applied by the bonds to the real nodes, assemble matrix $\mathbf{S}$ (size: $N \times N_b$) by carrying out the following operation for each bond (see Equation 2.54):

$$\begin{Bmatrix} \widetilde{\mathrm{f}}_{i,h_i} \\ \widetilde{\mathrm{f}}_{j,h_j} \end{Bmatrix} = \begin{bmatrix} \underline{\mathbf{M}}_{ij} \\ \underline{\mathbf{M}}_{ji} \end{bmatrix} \left\{ \mathrm{f}_{ij} \right\} \qquad \Rightarrow \widetilde{\mathbf{f}} = \mathbf{S}\ \mathbf{f}_b \tag{2.102}$$

  where the subscripts $h_i$ and $h_j$ indicate the $h$-th contribution to the sum that composes the complete values of the nodal internal forces of nodes $i$ and $j$, respectively. Therefore, the stiffness matrix $\mathbf{K}$ (size: $N \times N$), assembled with the method of the Taylor-based extrapolation over the fictitious layer, is given as:

$$\mathbf{K} = -\mathbf{S}\ \mathbf{K}_b \tag{2.103}$$

# Chapter 3

# A new method based on Taylor expansion and nearest-node strategy to impose Dirichlet and Neumann boundary conditions in ordinary state-based Peridynamics

**Published in:** *Computational Mechanics* (2022)

**Authors:** Francesco Scabbia, Mirco Zaccariotto, Ugo Galvanetto

## Abstract

Peridynamics is a non-local continuum theory which is able to model discontinuities in the displacement field, such as crack initiation and propagation in solid bodies. However, the non-local nature of the theory generates an undesired stiffness fluctuation near the boundary of the bodies, phenomenon known as "surface effect". Moreover, a standard method to impose the boundary conditions in a non-local model is not currently available. We analyze the entity of the surface effect in ordinary state-based peridynamics by employing an innovative numerical algorithm to compute the peridynamic stress tensor. In order to mitigate the surface effect and impose Dirichlet and Neumann boundary conditions in a peridynamic way, we introduce a layer of fictitious nodes around the body, the displacements of which are determined by multiple Taylor series expansions based on the nearest-node strategy. Several numerical examples are presented to demonstrate the effectiveness and accuracy of the proposed method.

**Keywords:** Ordinary state-based Peridynamics, surface effect, peridynamic boundary conditions, peridynamic stress tensor, extrapolation over fictitious nodes.

## 3.1 Introduction

The propagation of cracks in solids and structures is one of the most common problems in structural engineering. In recent years, a new non-local continuum theory able to simulate crack propagation, named peridynamic theory, attracted the attention of many researchers. Each point in a body modelled with peridynamics interacts with all the neighboring points within a distance $\delta$. The non-locality of the peridynamic theory is essential to describe fracture phenomena in solid bodies without ad hoc criteria. Firstly, the so-called "bond-based peridynamics" was developed [61], which however has a limited capability of prescribing the Poisson's ratio. This shortcoming is avoided by the second formulation of the theory, named "state-based peridynamics" [62].

The non-local nature of the theory leads to two interrelated problems near the boundary of the body: the "surface effect" and the difficulty to impose the boundary conditions [74]. The surface effect, sometimes also called "skin effect", is due to the fact that peridynamic points near the boundary lack some neighboring points, leading to an undesired variation of the stiffness properties in the most external layer of the body [186, 226]. Bond-based and state-based peridynamic models exhibit respectively a softening and a hardening-softening behavior near the boundary [187, 198, 227].

Imposing boundary conditions in a peridynamic model is not a trivial task to accomplish. The application of the boundary conditions to the points on the boundary, as one would do in a local model, leads to large fluctuations of the solution near the boundary [186]. In [63] it is suggested that external loads and constraints should be imposed on a layer of finite thickness respectively inside and outside the body. This strategy is surely closer to a non-local concept, but it is not really clear the proper procedure to "distribute" the boundary conditions over the finite layers. In the following, we present some of the most commonly used methods to mitigate the surface effect and impose the boundary conditions in a peridynamic model.

A possible approach is to couple peridynamics with classical continuum mechanics: peridynamics is employed only in the interior of the body and the layer of material near the boundary is modelled, for instance, with the Finite Element Method [171, 205, 206, 208, 209, 228], with the Carrera Unified Formulation [213], with the Extended Finite Element Method [229, 230] or with the Meshless Local Exponential Basis Functions method [231]. In this way, the surface effect and the problem of the imposition of the boundary conditions in peridynamics is avoided. However, if cracks initiate or propagate near the boundary, those regions must inevitably be modelled with peridynamics and the coupling approach is not suitable to avoid the boundary issues. Furthermore, there are some spurious effects at the interface of the coupling region due to the different formulations of peridynamics and classical continuum mechanics (see the computation of out-of-balance forces in [165]).

The maximum distance of interaction, namely $\delta$, is a measure of the non-locality of the theory. Therefore, the external layer of the body which is affected by the surface effect is thinner as $\delta$ approaches 0. Similarly, the imposition of the boundary conditions in a local way (constraints and loads applied only to the points closest to the boundary) becomes a better approximation if $\delta$ tends to 0. Since the number of nodes is bound to increase as $\delta$ decreases, the computational effort may become excessive. In this case, the variable horizon

method can be employed to decrease the value of $\delta$ near the boundaries [149, 193, 195, 198, 204, 215, 216]. However, this approach of reducing the non-local nature of the peridynamic theory is solely capable of confining the solution fluctuation in a smaller region, but never of completely correcting it.

The approach of modifying the stiffness properties of the bonds near the boundary has been proposed in many methods: the force normalization method [187], the force density method [188], the energy method [63, 189], the volume method [64] and the position-aware linear solid constitutive model [190]. The comparison of these methods, carried out in [186], highlights that there are still some residual fluctuations of the solution near the boundary because they do not cope with the problem of the imposition of the boundary conditions in a non-local way. Another recently devised approach consists in modifying the peridynamic formulation in points which are affected by the surface effect in order to recover the classical mechanics solution for $\delta \to 0$ [232, 233]. Nevertheless, the treatment of the boundaries becomes much more complex.

The method of the "fictitious nodes" consists in adding around the body some nodes which provide the previously lacking interactions near the boundary, mitigating in this way the surface effect [148, 188, 191]. The fictitious nodes have been employed also to impose the boundary conditions: the displacements of the fictitious nodes are extrapolated by means of various types of functions, such as constant, linear, polynomial, sinusoidal or odd functions, in order to obtain the desired value of the constraint or load [63, 92, 126, 150, 151, 186, 192–195]. Moreover, the displacements of the fictitious nodes can be determined also by means of the formulae of classical continuum mechanics to enforce the desired load at the boundary [92, 186, 192–194]. However, these procedures to impose the boundary conditions are case-dependent and are applicable only for simple geometries and boundary conditions.

We proposed a new version of the "Taylor-based extrapolation method" adopting the nearest-node strategy [227]: the displacements of the fictitious nodes are determined as functions of the displacements of their closest real nodes by means of multiple Taylor series expansions truncated at a general order $n_{max}$. The surface effect is sensibly reduced by this effective method. Moreover, the boundary of the body is discretized by a new type of nodes, named "boundary nodes". As the fictitious nodes, the boundary nodes do not constitute new degrees of freedom in the model because their displacements are determined by means of the Taylor-based extrapolation method. Dirichlet boundary conditions are included in the Taylor series expansion of the displacements of the boundary nodes about their closest real nodes, whereas Neumann boundary conditions are imposed through the peridynamic concept of force flux.

The paper is organized as follows: Section 3.2 presents a brief review of the ordinary state-based peridynamic theory, particularly focusing on the peridynamic stress tensor, the force flux, the surface effect and the imposition of boundary conditions; Section 3.3 illustrates the Taylor-based extrapolation method and the imposition of boundary conditions in a peridynamic model; Section 3.4 shows the discretization of the peridynamic model, the numerical evaluation of the peridynamic stress tensor and of the force flux, and the numerical implementation of the proposed method; Section 3.5 compares the numerical results of several meaningful 2-dimensional examples obtained without any corrections at the boundary and

by using the proposed method; Section 3.6 shows the differences that may arise in crack propagation near the boundaries between corrected and uncorrected models; Section 3.7 draws the conclusions.

## 3.2 Review of peridynamic theory

Peridynamic points interact with each other, even within finite distance, through entities named "bonds". A bond is identified by the relative position vector in the reference configuration as

$$\boldsymbol{\xi} = \mathbf{x}' - \mathbf{x}\,, \tag{3.1}$$

where $\mathbf{x}$ and $\mathbf{x}'$ are the position vectors of two points in a body $\mathcal{B}$ modelled with peridynamics. The bond vanishes if the distance between the interacting points exceeds the value $\delta$, called "horizon". A point $\mathbf{x}$ therefore interacts with all the points $\mathbf{x}'$ inside its neighborhood, which is defined as

$$\mathcal{H}_{\mathbf{x}} = \left\{ \mathbf{x}' \in \mathcal{B}_r : \|\boldsymbol{\xi}\| \leq \delta \right\}, \tag{3.2}$$

where $\mathcal{B}_r$ is the body in the reference configuration. Point $\mathbf{x}$ is named "source point" and the points within $\mathcal{H}_{\mathbf{x}}$ are named "family points".

In the deformed body configuration $\mathcal{B}_d$ at time $t$, the relative displacement vector $\boldsymbol{\eta}$ is defined as

$$\boldsymbol{\eta} = \mathbf{u}(\mathbf{x}', t) - \mathbf{u}(\mathbf{x}, t)\,, \tag{3.3}$$

where $\mathbf{u}$ is the displacement field. Note that $\boldsymbol{\xi} + \boldsymbol{\eta}$ is the relative position of points $\mathbf{x}$ and $\mathbf{x}'$ in the deformed configuration.

The peridynamic equation of motion of a point $\mathbf{x}$ within the body $\mathcal{B}$ is given by [61, 62]:

$$\rho(\mathbf{x})\,\ddot{\mathbf{u}}(\mathbf{x}, t) = \int_{\mathcal{H}_{\mathbf{x}}} \mathbf{f}(\mathbf{x}, \mathbf{x}', t)\,\mathrm{d}V_{\mathbf{x}'} + \mathbf{b}(\mathbf{x}, t)\,, \tag{3.4}$$

where $\rho$ is the material density, $\ddot{\mathbf{u}}$ is the acceleration field, $\mathbf{f}$ is the pairwise force density, $\mathrm{d}V_{\mathbf{x}'}$ is the differential volume of a point $\mathbf{x}'$ within the neighborhood $\mathcal{H}_{\mathbf{x}}$ and $\mathbf{b}$ is the external force density field. The pairwise force density represents the force (per unit volume squared) in a bond.

The peridynamic equilibrium equation is derived from Equation 3.4 by dropping the dependence on time:

$$-\int_{\mathcal{H}_{\mathbf{x}}} \mathbf{f}(\mathbf{x}, \mathbf{x}')\,\mathrm{d}V_{\mathbf{x}'} = \mathbf{b}_{\mathbf{x}}\,. \tag{3.5}$$

where $\mathbf{b}_{\mathbf{x}} = \mathbf{b}(\mathbf{x})$. $\mathbf{f}(\mathbf{x}, \mathbf{x}')$ is the force density applied to point $\mathbf{x}$ due to the interaction with a point $\mathbf{x}'$ inside its neighborhood. Conversely, point $\mathbf{x}$ belongs to the neighborhood $\mathcal{H}_{\mathbf{x}'}$, thus a force density $\mathbf{f}(\mathbf{x}', \mathbf{x}) = -\mathbf{f}(\mathbf{x}, \mathbf{x}')$ is applied to point $\mathbf{x}'$ (see Figure 3.1). The formulae to compute the pairwise force density depending on the deformation of the body are shown in the following Section.

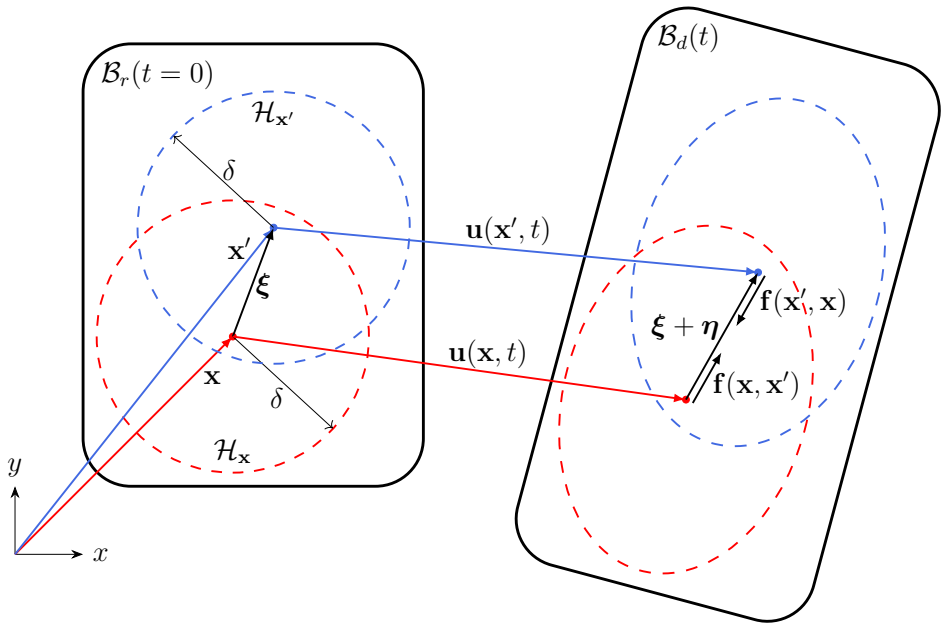


Figure 3.1: *Body modelled with ordinary state-based peridynamics in the reference configuration $\mathcal{B}_r$ and deformed configuration $\mathcal{B}_d$: a pairwise force density $\mathbf{f}$ arises in the bond $\boldsymbol{\xi}$ due to the deformation of the body.*

### 3.2.1 Ordinary state-based peridynamics

In state-based peridynamics, the pairwise force density is defined as [62]

$$\mathbf{f}(\mathbf{x},\mathbf{x}') = \underline{\mathbf{T}}[\mathbf{x}]\langle\boldsymbol{\xi}\rangle - \underline{\mathbf{T}}[\mathbf{x}']\langle-\boldsymbol{\xi}\rangle\,, \tag{3.6}$$

where $\underline{\mathbf{T}}$ is the force density vector state. $\underline{\mathbf{T}}[\mathbf{x}]\langle\boldsymbol{\xi}\rangle$ and $\underline{\mathbf{T}}[\mathbf{x}']\langle-\boldsymbol{\xi}\rangle$ depend respectively on points $\mathbf{x}$ and $\mathbf{x}'$, and they respectively operate on bonds $\boldsymbol{\xi}$ and $-\boldsymbol{\xi}$.

In an ordinary peridynamic material, the force density vector state is aligned with the corresponding bond for any deformation, as depicted in Figure 3.1, and it can be written as

$$\underline{\mathbf{T}}[\mathbf{x}]\langle\boldsymbol{\xi}\rangle = \underline{t}[\mathbf{x}]\langle\boldsymbol{\xi}\rangle\ \underline{\mathbf{M}}\langle\boldsymbol{\xi}\rangle\,, \tag{3.7}$$

where $\underline{t}$ is the force density scalar state (magnitude of $\underline{\mathbf{T}}$) and $\underline{\mathbf{M}}$ is the deformed direction vector state (unit vector in the direction of $\underline{\mathbf{T}}$), defined as

$$\underline{\mathbf{M}}\langle\boldsymbol{\xi}\rangle = \frac{\boldsymbol{\xi}+\boldsymbol{\eta}}{\|\boldsymbol{\xi}+\boldsymbol{\eta}\|}\,. \tag{3.8}$$

Note that $\underline{\mathbf{M}}\langle\boldsymbol{\xi}\rangle = -\underline{\mathbf{M}}\langle-\boldsymbol{\xi}\rangle$.

Furthermore, under the assumption of small deformation ($\boldsymbol{\eta} \ll \boldsymbol{\xi}$), the deformed direction vector state can be approximated with the bond direction unit vector in the reference configuration:

$$\mathbf{m} = \frac{\boldsymbol{\xi}}{\|\boldsymbol{\xi}\|}\,. \tag{3.9}$$

Therefore, the pairwise force density can be rewritten as

$$\mathbf{f}(\mathbf{x}, \mathbf{x}') = \left( \underline{t}[\mathbf{x}]\langle \boldsymbol{\xi} \rangle + \underline{t}[\mathbf{x}']\langle -\boldsymbol{\xi} \rangle \right) \mathbf{m} \,. \tag{3.10}$$

The reference position scalar state $\underline{x}$, representing the bond length in the reference configuration, and the extension scalar state $\underline{e}$, describing the elongation (or contraction) of the bond in the deformed body configuration, are respectively defined as

$$\underline{x} = \|\boldsymbol{\xi}\| \,, \tag{3.11}$$

$$\underline{e} = \|\boldsymbol{\xi} + \boldsymbol{\eta}\| - \|\boldsymbol{\xi}\| \,. \tag{3.12}$$

The influence of the neighborhood $\mathcal{H}_{\mathbf{x}}$ on a source point $\mathbf{x}$ is expressed by two non-local properties of that point, the weighted volume $m$ and the dilatation $\theta$, which are defined as

$$m_{\mathbf{x}} = \int_{\mathcal{H}_{\mathbf{x}}} \underline{\omega}\, \underline{x}^2 \, \mathrm{d}V_{\mathbf{x}'} \,, \tag{3.13}$$

$$\theta_{\mathbf{x}} = \frac{c_\theta}{m_{\mathbf{x}}} \int_{\mathcal{H}_{\mathbf{x}}} \underline{\omega}\, \underline{x}\, \underline{e} \, \mathrm{d}V_{\mathbf{x}'} \,, \tag{3.14}$$

where $\underline{\omega}$ is a prescribed spherical influence function and $c_\theta$ is a peridynamic constant. We adopt the Gaussian influence function

$$\underline{\omega} = e^{-\frac{\|\boldsymbol{\xi}\|^2}{\delta^2}} \,, \tag{3.15}$$

since it assures a smooth convergence of the numerical integration [184].

The weighted volume describes the "fullness" of the neighborhood: a neighborhood completely full of peridynamic points results in the maximum value of $m$, whereas the weighted volume of an incomplete neighborhood has a lower value. This lack of neighboring points is the origin of stiffness fluctuations, the so-called "surface effect" [186], near the boundary of the body. The surface effect is further analyzed in Section 3.2.4.

On the other hand, the dilatation represents the volumetric deformation of the neighborhood. Consider a point $\mathbf{x}$ subjected to a homogeneous, isotropic and small deformation $\overline{\varepsilon}$, so that $\underline{e} = \overline{\varepsilon}\, \underline{x}$ for each bond. The peridynamic dilatation $\theta$ of point $\mathbf{x}$ corresponds to the dilatation $\theta_{cl}$ in classical continuum mechanics under the same deformation if the constant $c_\theta$ is chosen as [62, 160, 227]

$$c_\theta = \begin{cases} 3 & \text{in 3D,} \\ 2 & \text{in 2D plane strain,} \\ \dfrac{2(1-2\nu)}{1-\nu} & \text{in 2D plane stress,} \\ 1-2\nu & \text{in 1D axial loading,} \end{cases} \tag{3.16}$$

where $\nu$ is the Poisson's ratio.

The force density scalar state can be computed as [227]

$$\underline{t}[\mathbf{x}]\langle\boldsymbol{\xi}\rangle = k_\theta \frac{\underline{\omega}\,\underline{x}}{m_\mathbf{x}}\,\theta_\mathbf{x} + k_e \frac{\underline{\omega}\,\underline{e}}{m_\mathbf{x}}\,. \tag{3.17}$$

where $k_\theta$ and $k_e$ are the peridynamic stiffness constants. These constants are derived by equalizing the peridynamic strain energy density in a point $\mathbf{x}$ with a complete neighborhood under homogeneous deformation, with the classical continuum mechanics strain energy density in a point subjected to the same deformation [62, 160, 227]:

$$k_\theta = \begin{cases} \dfrac{-3(1-4\nu)}{2(1+\nu)(1-2\nu)}\,E & \text{in 3D,} \\ \dfrac{-(1-4\nu)}{(1+\nu)(1-2\nu)}\,E & \text{in 2D plane strain,} \\ \dfrac{-(1-3\nu)}{(1+\nu)(1-2\nu)}\,E & \text{in 2D plane stress,} \\ \dfrac{\nu}{(1+\nu)(1-2\nu)}\,E & \text{in 1D axial loading,} \end{cases} \tag{3.18}$$

$$k_e = \begin{cases} \dfrac{15}{2(1+\nu)}\,E & \text{in 3D,} \\ \dfrac{4}{1+\nu}\,E & \text{in 2D plane strain or plane stress,} \\ \dfrac{1}{1+\nu}\,E & \text{in 1D axial loading,} \end{cases} \tag{3.19}$$

where $E$ is the Young's modulus.

By substituting Equation 3.17 in Equation 3.10, the pairwise force density is computed as

$$\mathbf{f}(\mathbf{x},\mathbf{x}') = \left[k_\theta\left(\frac{\theta_\mathbf{x}}{m_\mathbf{x}} + \frac{\theta_{\mathbf{x}'}}{m_{\mathbf{x}'}}\right)\underline{\omega}\,\underline{x} + k_e\left(\frac{1}{m_\mathbf{x}} + \frac{1}{m_{\mathbf{x}'}}\right)\underline{\omega}\,\underline{e}\right]\mathbf{m}\,. \tag{3.20}$$

Note that the magnitude of the pairwise force density in ordinary state-based peridynamics depends on the neighborhood properties ($m$ and $\theta$) of the two points $\mathbf{x}$ and $\mathbf{x}'$ connected by the bond. Hence, the resultant of all the bond forces in a point $\mathbf{x}$, obtained with the integral of the peridynamic equilibrium equation (Equation 3.5), depends on the deformation of the points within a $2\delta$-distance from $\mathbf{x}$.

### 3.2.2 Peridynamic stress tensor

The peridynamic stress tensor, introduced in [172], is defined in a point $\mathbf{x}$ with a complete neighborhood as

$$\boldsymbol{\tau}_\mathbf{x} = \frac{1}{2}\int_\Omega\int_0^\delta\int_s^\delta \mathbf{f}(\mathbf{x}-s\mathbf{m},\mathbf{x}+(r-s)\mathbf{m})\otimes\mathbf{m}\,r^2\,\mathrm{d}r\,\mathrm{d}s\,\mathrm{d}\Omega_\mathbf{m}\,, \tag{3.21}$$

where $\Omega$ is a unit sphere centered in $\mathbf{x}$ and $\mathrm{d}\Omega_\mathbf{m}$ is the differential solid angle on $\Omega$ in any bond direction $\mathbf{m}$. The points $\mathbf{x}-s\mathbf{m}$ and $\mathbf{x}+(r-s)\mathbf{m}$ are connected by a bond passing through point $\mathbf{x}$, and we respectively name them $\mathbf{x}'$ and $\mathbf{x}''$. Therefore, $s = \|\mathbf{x}'-\mathbf{x}\|$ and

$r = \|\mathbf{x}'' - \mathbf{x}'\|$, as shown in Figure 3.2. $s$ is the distance between points $\mathbf{x}$ and $\mathbf{x}'$, whereas $r$ is the length of the bond between $\mathbf{x}'$ and $\mathbf{x}''$. The definition of the integration domain allows to take into account all the bonds passing through point $\mathbf{x}$. Note that each bond passing through $\mathbf{x}$ (between $\mathbf{x}'$ and $\mathbf{x}''$) has a corresponding bond in the opposite direction (between $\mathbf{x}''$ and $\mathbf{x}'$), so that the same pairwise force density is integrated twice in Equation 3.21. This is the reason why the factor 1/2 appears at the beginning of the formula.

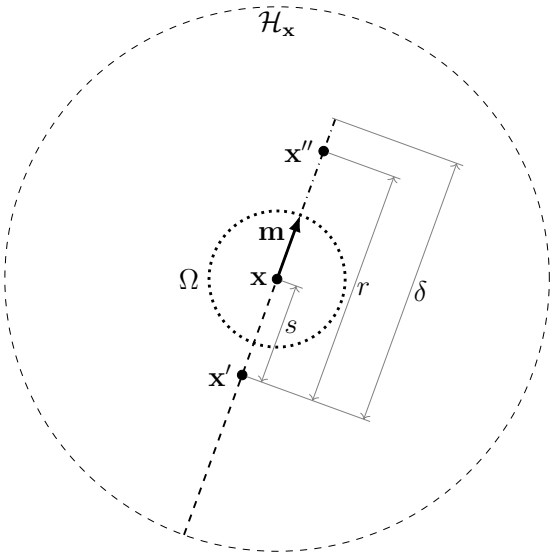


Figure 3.2: *Main variables involved in the computation of the peridynamic stress tensor in point* $\mathbf{x}$*:*
*- the bond direction* $\mathbf{m}$ *lie on the unit sphere* $\Omega$ *(dotted line);*
*- point* $\mathbf{x}'$ *lies on the opposite direction of* $\mathbf{m}$ *at a distance* $s$ *from* $\mathbf{x}$*, with* $0 < s < \delta$ *(dashed line);*
*- point* $\mathbf{x}''$ *lies on the direction* $\mathbf{m}$ *at a distance* $r$ *from* $\mathbf{x}'$*, with* $s < r < \delta$ *(dashdotted line).*

The integral over the unit sphere $\Omega$ is not affected by the variables $s$ and $r$, but it depends only on the bond direction $\mathbf{m}$. On the other hand, the integrals related to $\mathrm{d}s$ and $\mathrm{d}r$ are interdependent, as shown by the integration domain depicted in Figure 3.3. For later use, the peridynamic stress tensor in a point $\mathbf{x}$ with a complete neighborhood is rewritten by changing the order of the integrals:

$$\begin{aligned}\boldsymbol{\tau}_\mathbf{x} &= \frac{1}{2}\int_\Omega \int_0^\delta \int_0^r \mathbf{f}(\mathbf{x}', \mathbf{x}'') \otimes \mathbf{m}\, r^2 \,\mathrm{d}s\,\mathrm{d}r\,\mathrm{d}\Omega_\mathbf{m} \\ &= \frac{1}{2}\int_{\mathcal{H}_\mathbf{x}} \int_0^r \mathbf{f}(\mathbf{x}', \mathbf{x}'') \otimes \mathbf{m}\; \mathrm{d}s\,\mathrm{d}V_{\mathbf{x}''}\,, \end{aligned} \tag{3.22}$$

where $\mathrm{d}V_{\mathbf{x}''} = r^2\,\mathrm{d}r\,\mathrm{d}\Omega_\mathbf{m}$.

Under the assumption of homogeneous deformation, the bonds with the same length and direction have the same pairwise force density in any position of the body. This means that, for each bond of length $r$ and direction $\mathbf{m}$, its pairwise force density does not depend on $s$ anymore. Therefore, $\boldsymbol{\tau}_\mathbf{x}$ can be simplified from Equation 3.22 as follows:

$$\boldsymbol{\tau}_\mathbf{x} = \frac{1}{2}\int_{\mathcal{H}_\mathbf{x}} \left(\int_0^r \mathrm{d}s\right) \mathbf{f}(\mathbf{x}, \mathbf{x}'') \otimes \mathbf{m}\,\mathrm{d}V_{\mathbf{x}''}$$

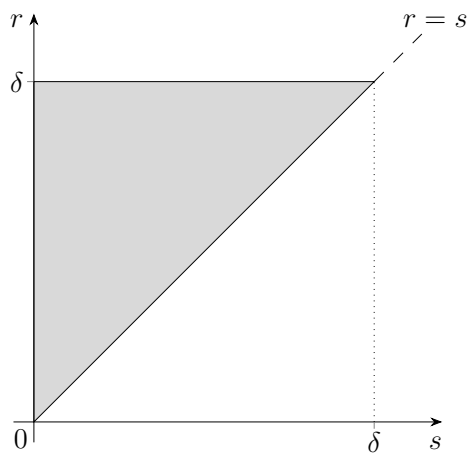


Figure 3.3: *Integration domain for the computation of the peridynamic stress tensor for a fixed bond direction:*
*- for any value of $s$ in the interval $]0,\delta[$, $r$ lies in the interval $]s,\delta[$ (see limits of integration in Equation 3.21);*
*- for any value of $r$ in the interval $]0,\delta[$, $s$ lies in the interval $]0,r[$ (see limits of integration in Equation 3.22).*

$$= \frac{1}{2}\int_{\mathcal{H}_{\mathbf{x}}} r\,\mathbf{f}(\mathbf{x},\mathbf{x}'')\otimes\mathbf{m}\,\mathrm{d}V_{\mathbf{x}''}\,. \tag{3.23}$$

Note that, since the value of $s$ does not affect $\mathbf{f}(\mathbf{x}',\mathbf{x}'')$ in a body under homogeneous deformation, we conveniently choose the pairwise force density for $s=0$, i.e., $\mathbf{f}(\mathbf{x},\mathbf{x}'')$.

We want to compare the peridynamic stress tensor with the stress tensor in classical continuum mechanics for the same deformation conditions. For simplicity sake, we choose the 2-dimensional plane stress peridynamic model for a body subjected to two different conditions of homogeneous and small deformation: isotropic deformation, indicated by the superscript *iso*, and simple shear deformation, indicated by the superscript *sh*. Under those conditions, the strain and stress tensors in a point $\mathbf{x}$ are given in classical continuum mechanics as

$$\begin{aligned} \boldsymbol{\varepsilon}_{\mathbf{x}}^{iso} &= \overline{\varepsilon}^{iso}\begin{bmatrix}1 & 0\\ 0 & 1\end{bmatrix}\\ \Rightarrow\quad \boldsymbol{\sigma}_{\mathbf{x}}^{iso} &= \frac{E}{1-\nu}\,\overline{\varepsilon}^{iso}\begin{bmatrix}1 & 0\\ 0 & 1\end{bmatrix} = \overline{\sigma}^{iso}\begin{bmatrix}1 & 0\\ 0 & 1\end{bmatrix}, \end{aligned} \tag{3.24}$$

$$\begin{aligned} \boldsymbol{\varepsilon}_{\mathbf{x}}^{sh} &= \overline{\varepsilon}^{sh}\begin{bmatrix}0 & 1\\ 1 & 0\end{bmatrix}\\ \Rightarrow\quad \boldsymbol{\sigma}_{\mathbf{x}}^{sh} &= \frac{E}{1+\nu}\,\overline{\varepsilon}^{sh}\begin{bmatrix}0 & 1\\ 1 & 0\end{bmatrix} = \overline{\sigma}^{sh}\begin{bmatrix}0 & 1\\ 1 & 0\end{bmatrix}, \end{aligned} \tag{3.25}$$

where $\overline{\varepsilon}^{iso}$ and $\overline{\varepsilon}^{sh}$ are the values of the imposed deformations and $\overline{\sigma}^{iso}$ and $\overline{\sigma}^{sh}$ are the corresponding stresses.

In the following analysis of the peridynamic stress tensor, only points with complete neighborhoods are considered. The inclination of a bond with respect to the $x$-axis is called $\phi$. Therefore, the bond direction in a 2-dimensional model can be written as $\mathbf{m} = \{\cos\phi,\, \sin\phi\}^\top$. Furthermore, the weighted volume of a point $\mathbf{x}$ with a complete neighborhood is given from Equation 3.13 by

$$\begin{aligned} m_{\mathbf{x}} &= \int_0^{2\pi} \int_0^{\delta} \|\boldsymbol{\xi}\|^3 \, e^{-\frac{\|\boldsymbol{\xi}\|^2}{\delta^2}} \, h \, \mathrm{d}\xi \, \mathrm{d}\phi \\ &= \frac{\pi(e-2)}{e} \, h\delta^4 \,, \end{aligned} \tag{3.26}$$

where $h$ is the thickness of the 2-dimensional body.

In the case of a body subjected to a small isotropic deformation, any extension scalar state is $\underline{e}^{\,iso} = \overline{\varepsilon}^{\,iso}\underline{x}$ and the corresponding dilatation in a point $\mathbf{x}$ with a complete neighborhood is $\theta_{\mathbf{x}}^{iso} = c_\theta \, \overline{\varepsilon}^{\,iso}$. The peridynamic stress tensor under this condition is given from Equation 3.23 as

$$\begin{aligned} \boldsymbol{\tau}_{\mathbf{x}}^{iso} &= \frac{1}{2} \int_0^{2\pi} \int_0^{\delta} (c_\theta k_\theta + k_e) \, \overline{\varepsilon}^{\,iso} \frac{2}{m_{\mathbf{x}}} r^2 e^{-\frac{r^2}{\delta^2}} \begin{Bmatrix} \cos\phi \\ \sin\phi \end{Bmatrix} \otimes \begin{Bmatrix} \cos\phi \\ \sin\phi \end{Bmatrix} h \, r \, \mathrm{d}r \, \mathrm{d}\phi \\ &= \frac{E}{1-\nu} \, \overline{\varepsilon}^{\,iso} \frac{2e\,h}{\pi(e-2)h\delta^4} \int_0^{\delta} r^3 e^{-\frac{r^2}{\delta^2}} \, \mathrm{d}r \int_0^{2\pi} \begin{bmatrix} \cos^2\phi & \cos\phi\sin\phi \\ \cos\phi\sin\phi & \sin^2\phi \end{bmatrix} \mathrm{d}\phi \\ &= \frac{E}{1-\nu} \, \overline{\varepsilon}^{\,iso} \frac{2e}{\pi(e-2)\delta^4} \, \frac{(e-2)\delta^4}{2e} \begin{bmatrix} \pi & 0 \\ 0 & \pi \end{bmatrix} \\ &= \frac{E}{1-\nu} \, \overline{\varepsilon}^{\,iso} \begin{bmatrix} 1 & 0 \\ 0 & 1 \end{bmatrix} . \end{aligned} \tag{3.27}$$

The obtained peridynamic stress tensor yields the same result of the stress tensor computed with classical continuum mechanics in a point under isotropic deformation. Note that only a tensile stress $\tau_{11} = \tau_{22} = \overline{\sigma}^{\,iso}$ arises from the imposed deformation $\overline{\varepsilon}^{\,iso}$ and there is no shear stress ($\tau_{12} = 0$).

In the case of a body subjected to a small shear deformation $\overline{\varepsilon}^{\,sh}$, the extension scalar state can be computed by substituting $\boldsymbol{\xi} = \{\|\boldsymbol{\xi}\|\cos\phi,\, \|\boldsymbol{\xi}\|\sin\phi\}^\top$ and $\boldsymbol{\eta} = \{\overline{\varepsilon}^{\,sh}\|\boldsymbol{\xi}\|\sin\phi,\, \overline{\varepsilon}^{\,sh}\|\boldsymbol{\xi}\|\cos\phi\}^\top$ in Equation 3.12:

$$\begin{aligned} \underline{e}^{\,sh} &= \sqrt{\left[\|\boldsymbol{\xi}\|(\cos\phi + \overline{\varepsilon}^{\,sh}\sin\phi)\right]^2 + \left[\|\boldsymbol{\xi}\|(\sin\phi + \overline{\varepsilon}^{\,sh}\cos\phi)\right]^2} - \|\boldsymbol{\xi}\| \\ &= \|\boldsymbol{\xi}\|\sqrt{1 + 4\,\overline{\varepsilon}^{\,sh}\cos\phi\sin\phi} - \|\boldsymbol{\xi}\| \\ &= 2\,\overline{\varepsilon}^{\,sh}\|\boldsymbol{\xi}\|\cos\phi\sin\phi \end{aligned} \tag{3.28}$$

where the formula is simplified under the assumption of sufficiently small deformation by dropping the second order terms and employing the Taylor series expansion for the square root. The corresponding dilatation in a point $\mathbf{x}$ with a complete neighborhood is $\theta_{\mathbf{x}}^{sh} = 0$ given the anti-symmetry of the integrand and the symmetry of the integration domain. The

peridynamic stress tensor under this condition is given from Equation 3.23 as

$$\begin{aligned}
\boldsymbol{\tau}_{\mathbf{x}}^{sh} &= \frac{1}{2}\int_0^{2\pi}\int_0^{\delta} 2\,k_e\,\overline{\varepsilon}^{\,sh}\frac{2}{m_{\mathbf{x}}} r^2 e^{-\frac{r^2}{\delta^2}}\cos\phi\,\sin\phi \begin{Bmatrix}\cos\phi\\ \sin\phi\end{Bmatrix}\otimes\begin{Bmatrix}\cos\phi\\ \sin\phi\end{Bmatrix} h\,r\,\mathrm{d}r\,\mathrm{d}\phi \\
&= \frac{4E}{1+\nu}\,\overline{\varepsilon}^{\,sh}\frac{2e\,h}{\pi(e-2)h\delta^4}\int_0^{\delta} r^3 e^{-\frac{r^2}{\delta^2}}\,\mathrm{d}r\int_0^{2\pi}\begin{bmatrix}\cos^3\phi\,\sin\phi & \cos^2\phi\,\sin^2\phi\\ \cos^2\phi\,\sin^2\phi & \cos\phi\,\sin^3\phi\end{bmatrix}\mathrm{d}\phi \\
&= \frac{4E}{1+\nu}\,\overline{\varepsilon}^{\,sh}\frac{2e}{\pi(e-2)\delta^4}\,\frac{(e-2)\delta^4}{2e}\begin{bmatrix}0 & \pi/4\\ \pi/4 & 0\end{bmatrix} \\
&= \frac{E}{1+\nu}\,\overline{\varepsilon}^{\,sh}\begin{bmatrix}0 & 1\\ 1 & 0\end{bmatrix}. \qquad (3.29)
\end{aligned}$$

The obtained peridynamic stress tensor yields the same result of the stress tensor computed with classical continuum mechanics in a point under simple shear deformation. Note that only a shear stress $\tau_{12} = \overline{\sigma}^{\,sh}$ arises from the imposed deformation $\overline{\varepsilon}^{\,sh}$ and there is no tensile stress ($\tau_{11} = \tau_{22} = 0$).

We showed that the peridynamic solution for the stress tensor corresponds to that of the classical continuum mechanics for homogeneous and small deformations, as shown also in [165] for bond-based peridynamic models. However, this statement is not valid near the boundaries of the body due to the surface effect.

### 3.2.3 Force flux

The force flux $\boldsymbol{\tau}(\mathbf{x},\mathbf{n})$ at point $\mathbf{x}$ in the direction of the unit vector $\mathbf{n}$ (see Figure 3.4) is derived from Equation 3.21 as [172]:

$$\boldsymbol{\tau}(\mathbf{x},\mathbf{n}) = \frac{1}{2}\int_{\Omega}\int_0^{\delta}\int_s^{\delta}\mathbf{f}(\mathbf{x}',\mathbf{x}'')\,(\mathbf{m}\cdot\mathbf{n})\,r^2\,\mathrm{d}r\,\mathrm{d}s\,\mathrm{d}\Omega_{\mathbf{m}}\,, \qquad (3.30)$$

where $\mathbf{x}' = \mathbf{x} - s\mathbf{m}$ and $\mathbf{x}'' = \mathbf{x} + (r-s)\mathbf{m}$. As in the definition of the peridynamic stress tensor, a factor $1/2$ is required since the integration domain takes into account the magnitude of the pairwise force density of each bond twice (for both direction $\mathbf{m}$ and $-\mathbf{m}$).

We briefly recall the mechanical interpretation of the force flux [172]. Consider a plane $\mathcal{P}$ with normal $\mathbf{n}$ passing through point $\mathbf{x}$, as shown in Figure 3.5. Points $\mathbf{x}'$ and $\mathbf{x}''$ respectively lie in the different half-spaces generated by plane $\mathcal{P}$. The differential volumes of those points are $\mathrm{d}V_{\mathbf{x}'} = r^2\,\mathrm{d}s\,\mathrm{d}\Omega_{\mathbf{m}}$ and $\mathrm{d}V_{\mathbf{x}''} = r^2\,\mathrm{d}r\,\mathrm{d}\Omega_{\mathbf{m}}$. The differential area of point $\mathbf{x}'$, which is perpendicular to the bond direction $\mathbf{m}$, is the portion of a sphere centered in $\mathbf{x}''$ with a radius $r$ which subtends the differential solid angle $\mathrm{d}\Omega_{\mathbf{m}}$, namely $\mathrm{d}A_{\mathbf{x}'} = r^2\,\mathrm{d}\Omega_{\mathbf{m}}$. By the same token, the differential area $\mathrm{d}A_{\mathbf{x}''}$ on a sphere centered in $\mathbf{x}'$ with a radius $r$ is equal to $\mathrm{d}A_{\mathbf{x}'}$. As shown in Figure 3.5, the differential area of point $\mathbf{x}$ with normal $\mathbf{n}$ is the projection in direction $\mathbf{m}$ of $\mathrm{d}A_{\mathbf{x}'} = \mathrm{d}A_{\mathbf{x}''}$ on plane $\mathcal{P}$:

$$\mathrm{d}A_{\mathbf{x}} = \frac{r^2\,\mathrm{d}\Omega_{\mathbf{m}}}{\mathbf{m}\cdot\mathbf{n}}\,. \qquad (3.31)$$

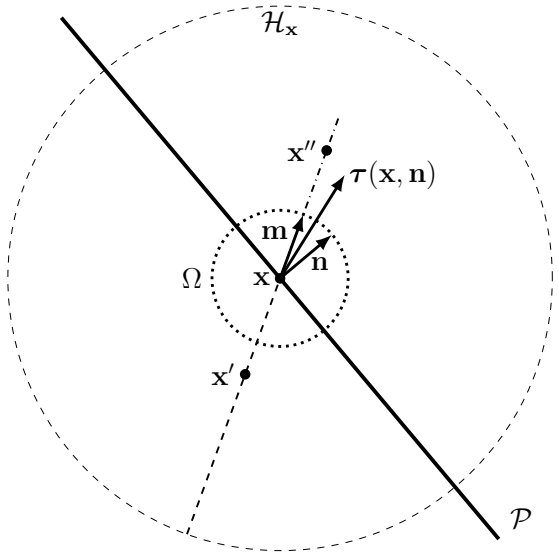


Figure 3.4: *Force flux* $\boldsymbol{\tau}(\mathbf{x}, \mathbf{n})$ *at point* $\mathbf{x}$ *in direction* $\mathbf{n}$*, computed with any bond direction* $\mathbf{m}$ *on the unit sphere* $\Omega$*, any point* $\mathbf{x}'$ *lying within* $\mathcal{H}_{\mathbf{x}}$ *on the opposite direction of* $\mathbf{m}$ *(dashed line) and any point* $\mathbf{x}''$ *lying within* $\mathcal{H}_{\mathbf{x}'}$ *on the direction* $\mathbf{m}$ *(dashdotted line). Points* $\mathbf{x}'$ *and* $\mathbf{x}''$ *lie in the different half-spaces generated by the plane* $\mathcal{P}$ *passing through point* $\mathbf{x}$ *with normal* $\mathbf{n}$*.*

The differential pairwise force acting through the bond between points $\mathbf{x}'$ and $\mathbf{x}''$ is $\mathbf{f}(\mathbf{x}', \mathbf{x}'')\, \mathrm{d}V_{\mathbf{x}'}\, \mathrm{d}V_{\mathbf{x}''}$. Therefore, the differential pairwise force per unit area on plane $\mathcal{P}$ is given by

$$\frac{\mathbf{f}(\mathbf{x}', \mathbf{x}'')\, \mathrm{d}V_{\mathbf{x}'}\, \mathrm{d}V_{\mathbf{x}''}}{\mathrm{d}A_{\mathbf{x}}} = \mathbf{f}(\mathbf{x}', \mathbf{x}'')\, (\mathbf{m} \cdot \mathbf{n})\; r^2\, \mathrm{d}r\, \mathrm{d}s\, \mathrm{d}\Omega_{\mathbf{m}}\,. \tag{3.32}$$

Note that the integrand in Equation 3.30 is the pairwise force per unit area on plane $\mathcal{P}$. This provides the mechanical interpretation of the force flux as the resultant of the pairwise forces per unit area of all the bonds intersecting $\mathcal{P}$ in $\mathbf{x}$.

### 3.2.4 Surface effect

The non-local formulation of the peridynamic theory exhibits some issues near the boundaries due to the incomplete neighborhoods of points close to free surfaces. The peridynamic constants $k_\theta$ and $k_e$ in Equations 3.18 and 3.19 are derived for points with a complete neighborhood. Therefore, the points near the boundaries, whose neighborhood is lacking some bonds, have different stiffness properties with respect to the points in the bulk. This phenomenon is called "surface effect" [186].

In ordinary state-based peridynamics, there are two non-local properties of a point which may contribute to the surface effect: the weighted volume $m$ and the dilatation $\theta$. The latter (Equation 3.14) is independent from the neighborhood "fullness" because it is normalized by the value of the weighted volume. Therefore, we focus on the value of $m$. We define the value $d_b$ as the minimum distance of a peridynamic point from any boundary of the body. The weighted volume has its maximum value when $d_b \geq \delta$, and it decreases gradually from points with $d_b = \delta$ towards points with $d_b = 0$ on the boundary. Moreover, points approaching corners, with respect to those approaching edges or surfaces, exhibit a steeper

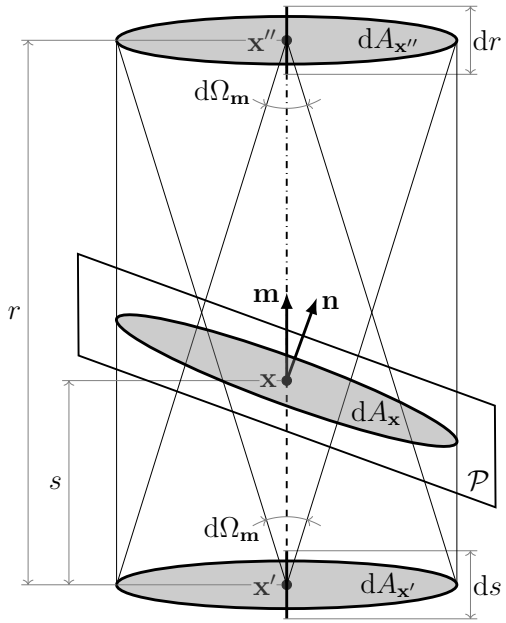


Figure 3.5: *Differential variables involved in the computation of the force flux* $\boldsymbol{\tau}(\mathbf{x}, \mathbf{n})$*: the differential volumes of points* $\mathbf{x}'$ *and* $\mathbf{x}''$ *are respectively* $\mathrm{d}V_{\mathbf{x}'} = \mathrm{d}s\,\mathrm{d}A_{\mathbf{x}'}$ *and* $\mathrm{d}V_{\mathbf{x}''} = \mathrm{d}r\,\mathrm{d}A_{\mathbf{x}''}$*, where* $\mathrm{d}A_{\mathbf{x}'} = \mathrm{d}A_{\mathbf{x}''} = r^2\,\mathrm{d}\Omega_{\mathbf{m}}$*, and the differential area* $\mathrm{d}A_{\mathbf{x}} = r^2\,\mathrm{d}\Omega_{\mathbf{m}}/(\mathbf{m}\cdot\mathbf{n})$ *is the projection of* $\mathrm{d}A_{\mathbf{x}'}$ *and* $\mathrm{d}A_{\mathbf{x}''}$ *on the plane* $\mathcal{P}$*.*

reduction in the weighted volume and a lower minimum value at the boundary.

The equilibrium of a peridynamic point $\mathbf{x}$ (Equation 3.5) is determined by the sum of the pairwise forces of all its bonds. Therefore, $\mathbf{x}$ primarily interacts with the points inside its neighborhood $\mathcal{H}_{\mathbf{x}}$. However, the magnitude of the pairwise force density (Equation 3.20) depends on the weighted volumes and dilatations of both point $\mathbf{x}$ and point $\mathbf{x}'$ within $\mathcal{H}_{\mathbf{x}}$. This means that $\mathbf{x}$ secondarily interacts with points up to a distance of $2\delta$ from itself. Thus, as shown in Figure 3.6, we can discriminate 3 types of points depending on $d_b$:

- if $d_b \geq 2\delta$, the point is of type-I;
- if $\delta \leq d_b < 2\delta$, the point is of type-II;
- if $d_b < \delta$, the point is of type-III.

Type-I points are said to be in the "bulk" of the body and they are the only ones which are not affected by the surface effect.

As the weighted volume of one or both the points of a bond decreases, the pairwise force density of that bond increases according to Equation 3.20. As shown in Figure 3.6, type-II points interact with at least one point with a partial neighborhood, so that the peridynamic forces applied to those points increase. Therefore, in the layer of the body where $\delta \leq d_b < 2\delta$ the peridynamic material is stiffer and exhibits a hardening behavior. The pairwise forces applied to type-III points increase even more. However, a type-III point is affected by less bonds than type-I or type-II points due to the lack of at least one family point. Therefore, the most external layer of the body ($d_b < \delta$) exhibits a hardening-softening behavior towards the boundary. This hardening-softening behavior can also be observed in the analytical solution of a 1-dimensional state-based body subjected to a homogeneous small deformation [227].

However, we expect that the stiffness fluctuation would be amplified near the corners of the body because the points in those regions have the smallest partial neighborhood.

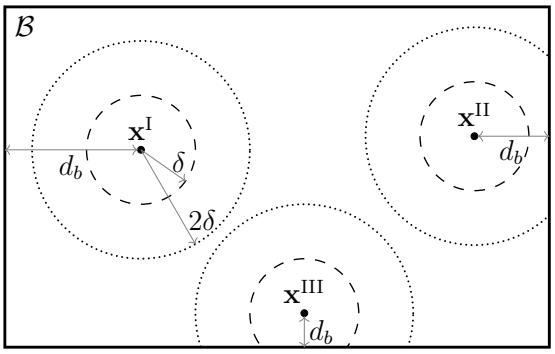


Figure 3.6: *Types of state-based peridynamic points depending on the distance $d_b$ from the closest boundary: points are of type-*I*, also named points in the "bulk", if $d_b \geq 2\delta$, type-*II *if $\delta \leq d_b < 2\delta$ and type-*III *if $d_b < \delta$. The source point $\mathbf{x}$ interacts primarily with the family points within the neighborhood $\mathcal{H}_{\mathbf{x}}$ (dashed line) and secondarily with all the points in the neighborhoods of the family points (dotted line).*

Figures 3.7 and 3.8 show the components of the peridynamic stress tensor $\boldsymbol{\tau}_{\mathbf{x}}$ in a 2-dimensional body subjected respectively to a isotropic deformation $\overline{\varepsilon}^{iso}$ and to a simple shear deformation $\overline{\varepsilon}^{sh}$. $\boldsymbol{\tau}_{\mathbf{x}}$ is computed numerically with a relatively high density of nodes within each neighborhood ($\overline{m} = 10$) and normalized with the analytical solutions derived in Section 3.2.2. Please refer to Section 3.4.3 for the numerical procedure to compute the peridynamic stress tensor. The numerical result for the points in the bulk of the body is really close to the analytical solution, whereas there are large differences for the points near the boundary, especially near the corners. Moreover, the points near the corners, due to the asymmetry of their neighborhood with respect to both $x$- and $y$-axis, have a non-zero value of the peridynamic stress even without the corresponding deformation: $\tau_{12} \neq 0$ in the case of isotropic deformation $\overline{\varepsilon}^{iso}$ and $\tau_{11} = \tau_{22} \neq 0$ in the case of simple shear deformation $\overline{\varepsilon}^{sh}$.

### 3.2.5 Imposition of the boundary conditions

Another issue in peridynamics, which is related to the surface effect, is the proper definition of the boundary conditions. The easiest method to impose the peridynamic boundary conditions would be to assign the desired value to the boundary points, as in classical continuum mechanics. However, this method does not consider the non-local nature of the theory and results in additional fluctuations of the solution near the application of the boundary conditions.

A widely used method suggests that external loads and constraints should be imposed on a layer of finite thickness respectively inside and outside the body [63]. The finite thickness is defined to be $2\delta$ in state-based peridynamics [158]. Since this method involves type-II and type-III points in the boundary conditions, it is undoubtedly more accurate than the previous one. However, it is not really clear the exact procedure of "distributing" the boundary conditions over the finite layer.

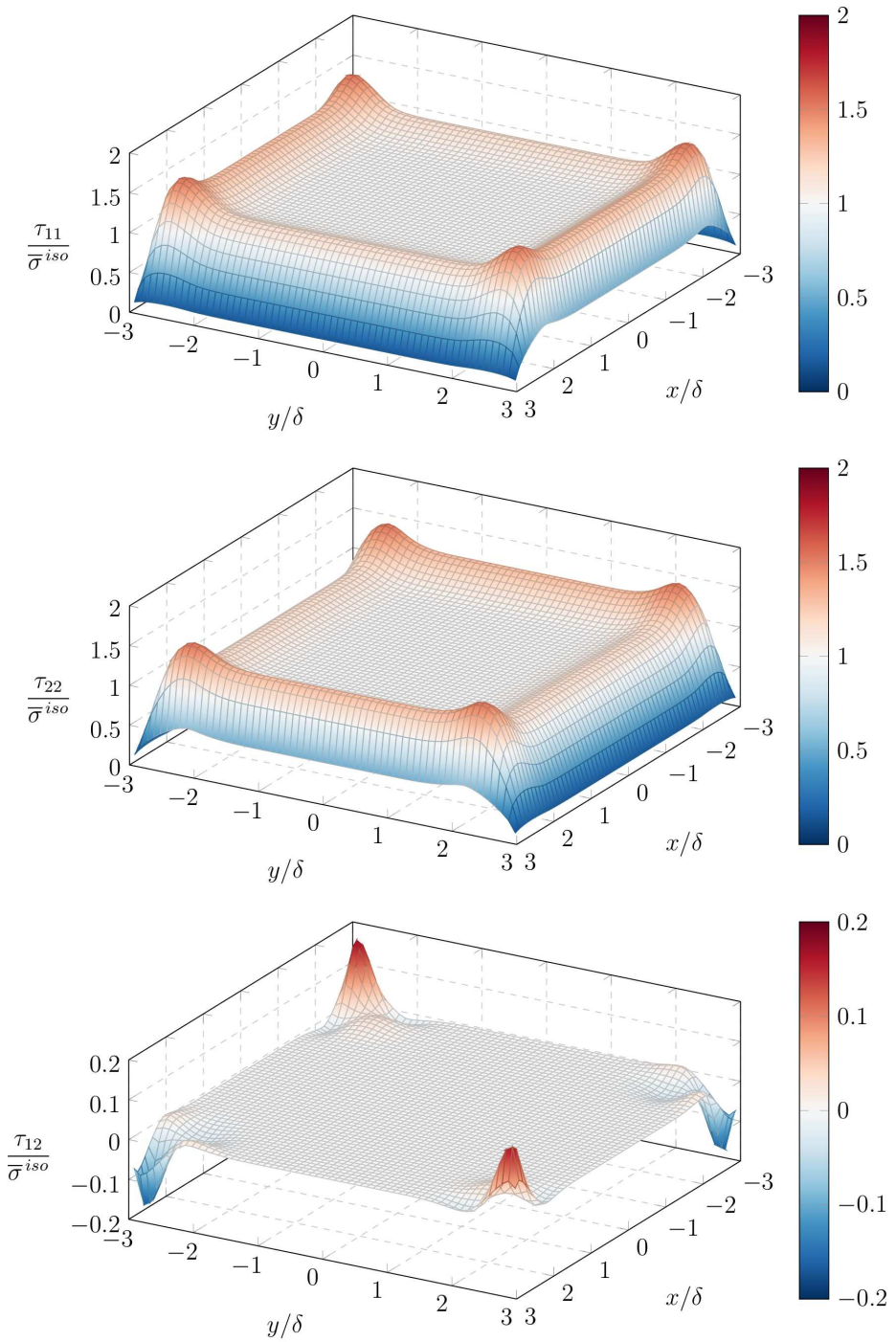


Figure 3.7: *Components of the peridynamic stress tensor $\boldsymbol{\tau}_{\mathbf{x}}$ for every point in a 2-dimensional body subjected to a isotropic deformation $\overline{\varepsilon}^{iso}$. The plots are normalized with the analytical solution of the tensile stress $\overline{\sigma}^{iso}$ for a peridynamic point with a complete neighborhood.*

We propose in the next Section a novel method capable of reducing considerably the surface effect and of imposing the boundary conditions in a "peridynamic way".

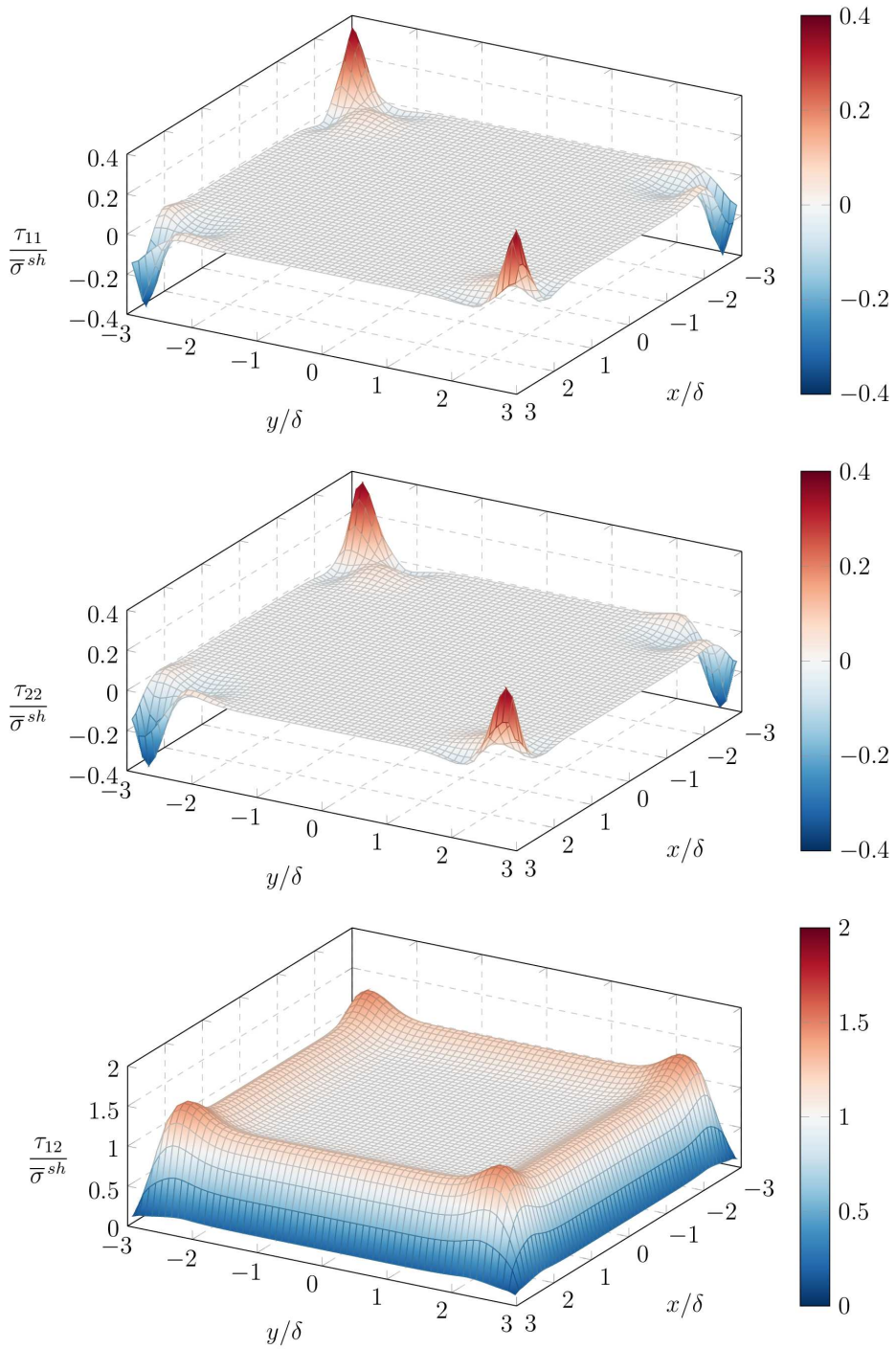


Figure 3.8: *Components of the peridynamic stress tensor $\boldsymbol{\tau}_{\mathbf{x}}$ for every point in a 2-dimensional body subjected to a simple shear deformation $\overline{\varepsilon}^{sh}$. The plots are normalized with the analytical solution of the shear stress $\overline{\sigma}^{sh}$ for a peridynamic point with a complete neighborhood.*

## 3.3 Taylor-based extrapolation method

A fictitious layer $\mathcal{F}$ of thickness $\delta$ is added around the body $\mathcal{B}$ [148], as shown in Figure 3.9. The neighborhoods of the family points of type-II points are completed thanks to the additional fictitious points, so that type-II points can be considered as points in the bulk (type-I points). Similarly, the neighborhoods of type-III points are completed by the fictitious layer, but some of the neighborhoods of their family points are not. However, we

assign to the fictitious points the value of the full weighted volume. In this way, all the points inside the body $\mathcal{B}$ behave as points in the bulk. The next Section shows a procedure to evaluate the displacement and dilatation fields over the fictitious layer.

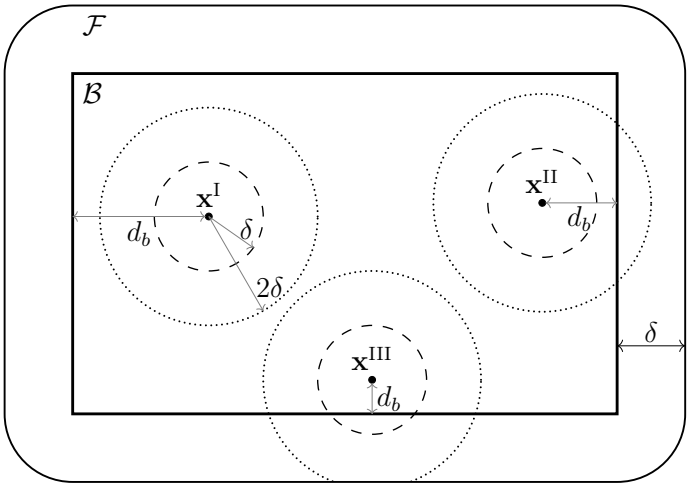


Figure 3.9: *Types of state-based peridynamic points depending on the distance from the closest boundary $d_b$ in a body with a fictitious layer of thickness $\delta$: there is no difference between type-*I *and type-*II *points anymore, whereas type-*III *points lack some secondary interactions in the neighborhoods of the family points.*

### 3.3.1 Extrapolation procedure to mitigate the surface effect

The displacements and the dilatations of the fictitious points are determined by means of the Taylor-based extrapolation method [227]. Consider the displacement $\mathbf{u}_f = \mathbf{u}(\mathbf{x}_f)$ of a fictitious point, where $\mathbf{x}_f = \{x_f, y_f, z_f\}^\top$. We name $\mathbf{u}_b = \mathbf{u}(\mathbf{x}_b)$ the displacement of the boundary point with the minimum distance from that fictitious point (nearest-point strategy). The Taylor series expansion of $\mathbf{u}_f$ about $\mathbf{x}_b = \{x_b, y_b, z_b\}^\top$ truncated at the maximum order $n_{max} \geq 1$ is given by

$$\mathbf{u}_f = \mathbf{u}_b + \sum_{n=1}^{n_{max}} \sum_{n_1=0}^{n} \sum_{n_2=0}^{n-n_1} \frac{(x_f - x_b)^{n_1}(y_f - y_b)^{n_2}(z_f - z_b)^{n_3}}{n_1!\, n_2!\, n_3!} \frac{\partial^{n_1+n_2+n_3} \mathbf{u}_b}{\partial x^{n_1}\, \partial y^{n_2}\, \partial z^{n_3}} \qquad \text{with} \quad n_3 = n - n_1 - n_2, \tag{3.33}$$

where $n$ is the global order ($n = 1$ is related to the gradient, $n = 2$ to the Hessian matrix, etc.) and $n_1$, $n_2$ and $n_3$ are the orders respectively in $x$, $y$ and $z$ directions.

Similarly, consider the dilatation $\theta_f = \theta(\mathbf{x}_f)$ of a fictitious point and the dilatation $\theta_b = \theta(\mathbf{x}_b)$ of the boundary point closest to $\mathbf{x}_f$. The Taylor series expansion of $\theta_f$ about $\mathbf{x}_b$ truncated at the maximum order $n_{max} - 1$ is given by

$$\theta_f = \begin{cases} \theta_b & \text{if } n_{max} = 1, \\ \theta_b + \displaystyle\sum_{n=1}^{n_{max}-1} \sum_{n_1=0}^{n} \sum_{n_2=0}^{n-n_1} \frac{(x_f - x_b)^{n_1}(y_f - y_b)^{n_2}(z_f - z_b)^{n_3}}{n_1! n_2! n_3!} \frac{\partial^{n_1+n_2+n_3} \theta_b}{\partial x^{n_1}\, \partial y^{n_2}\, \partial z^{n_3}} & \text{if } n_{max} > 1, \end{cases} \tag{3.34}$$

with $n_3 = n - n_1 - n_2$. Note that the dilatation is a measure of the strain, thus its truncation of the Taylor expansion occurs with 1 order less than that of the displacement.

This method allows to determine the displacement field and the dilatation field in the fictitious layer $\mathcal{F}$ as a function of the respective fields in the body $\mathcal{B}$. Since the displacement and dilatation fields in $\mathcal{F}$ are approximated by means of a Taylor series expansion, more accurate results are obtained by increasing the truncation order $n_{max}$ or by reducing the thickness of the fictitious layer.

The new bonds between real and fictitious points, called "fictitious bonds", are the interactions that are lacking in the peridynamic models without fictitious layer. The Taylor-based extrapolation method provides the displacement and dilatation values of the fictitious points, which are required to compute the pairwise forces of the fictitious bonds. In this way, the proposed method is able to mitigate the surface effect.

### 3.3.2 Peridynamic boundary conditions

We propose hereinafter a novel method to impose the boundary conditions in a peridynamic way when using the previously described fictitious layer method [227]. The desired boundary conditions are applied solely on the boundary points, exactly as in classical continuum mechanics. However, the influence of the boundary conditions on the body is non-local thanks to the Taylor-based extrapolation method. This concept is explained for Dirichlet and Neumann boundary conditions in the following.

A constraint $\overline{\mathbf{u}}$ imposed in a boundary point $\mathbf{x}_b$ is simply given as

$$\mathbf{u}(\mathbf{x}_b) = \overline{\mathbf{u}}\,. \tag{3.35}$$

This boundary condition determines the displacement field in the fictitious layer through the Taylor-based extrapolation method (by substituting Equation 3.35 in Equation 3.33). Therefore, the influence of the constraint can be seen as distributed in the whole thickness of the fictitious layer, as suggested in [63, pp. 29–30].

An external load per unit area $\overline{\mathbf{p}}$ applied to a boundary point $\mathbf{x}_b$ is expressed by means of the peridynamic concept of force flux (see Equation 3.30):

$$\boldsymbol{\tau}(\mathbf{x}_b, \mathbf{n}) = \overline{\mathbf{p}}\,, \tag{3.36}$$

where $\mathbf{n}$ is the unit vector perpendicular to the boundary in $\mathbf{x}_b$. By definition of force flux, $\boldsymbol{\tau}(\mathbf{x}_b, \mathbf{n})$ is the sum of the pairwise forces (per unit area) of all the bonds passing through $\mathbf{x}_b$. Since point $\mathbf{x}_b$ lies on the boundary, all the bonds involved in Equation 3.36 are fictitious bonds. On the one hand, the pairwise forces of those bonds applied to the fictitious points, which do not constitute new degrees of freedom, are ignored. On the other hand, the corresponding pairwise forces applied to the real points are the only ones "perceived" by the body. For how the magnitude of those forces is computed (see Equation 3.20), the boundary condition in point $\mathbf{x}_b$ affects the displacement in a sphere of radius $2\delta$ centered in $\mathbf{x}_b$. Therefore, the external load, expressed by means of the definition of the force flux, is distributed on the points in a layer of thickness $2\delta$ within the body, as suggested in [63,

pp. 30–32].

The proposed method for imposing the boundary conditions, which makes use of the Taylor-based extrapolation on the fictitious layer, defines a peridynamic way to distribute the constrains or the loads in the non-local region near the boundary.

**Remark 3.1.** The reaction force acting on a boundary point $\mathbf{x}_b$, due to a constraint imposed as in Equation 3.35, can be computed as the force flux in $\mathbf{x}_b$ in the direction of the unit vector $\mathbf{n}$ perpendicular to the boundary, i.e., $\boldsymbol{\tau}(\mathbf{x}_b, \mathbf{n})$.

**Remark 3.2.** The zero-traction boundary condition is sometimes applied by removing the fictitious layer in literature [92]. However, in order to maintain the correction of the surface effect, we suggest to keep the fictitious layer and impose the condition $\boldsymbol{\tau}(\mathbf{x}_b, \mathbf{n}) = 0$ to all the points of that boundary.

## 3.4 Numerical implementation

In order to discretize the domain, a mesh-free method is adopted [65, 184]. For simplicity sake, the peridynamic grid consists of a finite number of equally-spaced nodes, as shown in Figure 3.10. Each peridynamic node is representative of a finite volume $\Delta V = h\Delta x^2$, where $\Delta x = \Delta y$ is the grid spacing and $h$ is the thickness of the body. Please note that the most external real nodes do not lie exactly on the boundary of the body since the nodes are positioned at the center of the volume $\Delta V$. The ratio between the horizon and the grid spacing is defined as $\overline{m}$-ratio: $\overline{m} = \delta/\Delta x$. The value of this parameter determines the density of peridynamic nodes within a neighborhood. Furthermore, the fictitious layer (empty dots in Figure 3.10) is added to the real body to complete the neighborhoods of the nodes near the boundary.

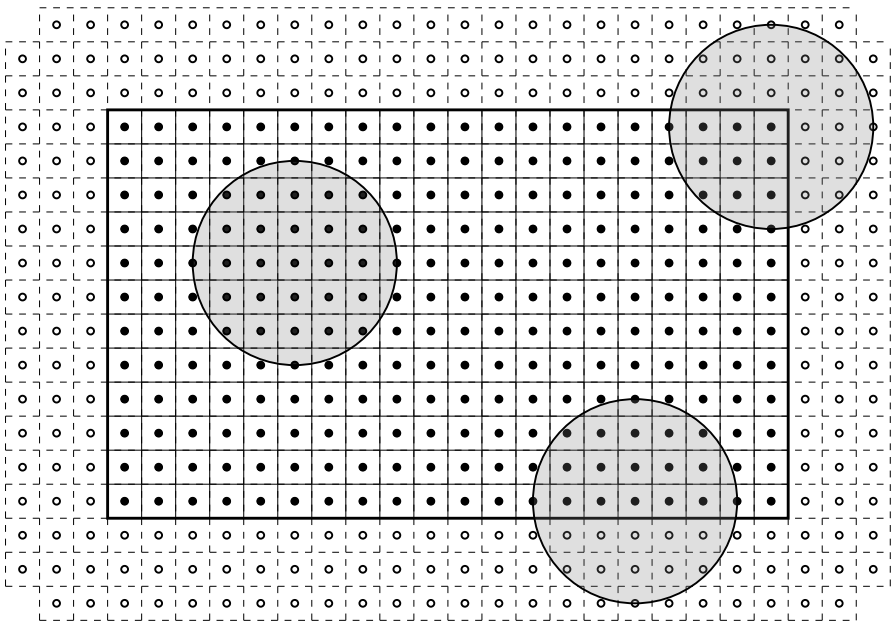

Figure 3.10: *Uniform peridynamic grid of real nodes (solid dots) and fictitious nodes (empty dots).*

### 3.4.1 Numerical Taylor-based extrapolation method

The Taylor-based extrapolation procedure in the discretized model aims to determine the values of the variables of the fictitious nodes (displacements $u$ and $v$ respectively in $x$ and $y$ directions and dilatations $\theta$ in the case of a peridynamic 2-dimensional body). The numerical procedure to determine, for instance, the displacement $u_i$ in a fictitious node $i$ with coordinates $(x_i, y_i)$ is carried out as follows:

- find the real node of index $j$ closest to node $i$;
- perform a Taylor series expansion of $u_i$ about node $j$ with coordinates $(x_j, y_j)$:

$$u_i = u_j + \sum_{n=1}^{n_{max}} \sum_{n_1=0}^{n} \frac{(x_i - x_j)^{n_1}(y_i - y_j)^{n_2}}{n_1!\, n_2!} \cdot \frac{\partial^{n_1+n_2} u_j}{\partial x^{n_1}\, \partial y^{n_2}}\,, \tag{3.37}$$

  where $u_j$ and $\frac{\partial^{n_1+n_2} u_j}{\partial x^{n_1}\, \partial y^{n_2}}$ are the displacement of node $j$ and its derivatives, $n_{max}$ is the maximum order of the truncated Taylor series, $n_1$ and $n_2$ are the orders respectively in $x$ and $y$ directions and $n$ is the global order so that $n_2 = n - n_1$.

Since the coordinates of nodes $i$ and $j$ are known, the displacement $u_i$ in Equation 3.37 is written as a function of the displacement $u_j$ and its derivatives. However, we aim to express $u_i$ as a function solely of the displacement of the real nodes. The total number of derivatives of $u_j$, considered before truncating the Taylor series, is $n_d = (n_{max}(n_{max}+1)/2) - 1$. They can be determined as functions of the displacements of the $n_d$ real nodes near node $j$ by following another Taylor-based extrapolation procedure:

- find the $n_d$ real nodes with indices $j_k$ closest to node $j$, where $k = 1, \ldots, n_d$ (see Remark below for the conditions on the node search);
- for each of those nodes with coordinates $(x_{j_k}, y_{j_k})$, perform a Taylor series expansion of their displacements $u_{j_k}$ about node $j$:

$$u_{j_k} = u_j + \sum_{n=1}^{n_{max}} \sum_{n_1=0}^{n} \frac{(x_{j_k} - x_j)^{n_1}(y_{j_k} - y_j)^{n_2}}{n_1!\, n_2!} \cdot \frac{\partial^{n_1+n_2} u_j}{\partial x^{n_1}\, \partial y^{n_2}} \qquad \text{with} \quad k = 1, \ldots, n_d; \tag{3.38}$$

- solve the system of equations in Equation 3.38 to obtain the derivatives of $u_j$ as a function of the displacements $u_j$ and $u_{j_k}$:

$$\frac{\partial^{n_1+n_2} u_j}{\partial x^{n_1}\, \partial y^{n_2}} = f(u_j, u_{j_k}) \qquad \text{with} \quad k = 1, \ldots, n_d. \tag{3.39}$$

Therefore, by combining Equations 3.37 and 3.39, the displacement of a fictitious node is a function only of the displacements of some real nodes. Note that the adopted nearest-node startegy is really simple to implement also for complex geometries. This procedure can be applied to determine the displacements $u$ and $v$ and the dilatations $\theta$ of all the fictitious nodes. In the case of the dilatations, the truncation order $n_{max}$ must be replaced by $n_{max} - 1$.

**Remark 3.3.** There might be some cases in which the system of equations (Equation 3.38) is not solvable for the nodes $j_k$ that are the closest to node $j$. For instance, if we want to determine the second derivative in $x$ direction, the nodes $j_k$ must include at least two $x_{j_k}$ coordinates different from each other and from $x_j$ (see example in Section 3.4.5). However, given the adoption a uniform grid in which nodes on the same lines share the same coordinates, this condition is not always met when searching for nodes $j_k$ via the closest-node strategy without any additional condition. Therefore, in order for the system of equations to be solvable, the nodes $j_k$ should comprise at least $n_1$ different $x_{j_k}$ coordinates and $n_2$ different $y_{j_k}$ coordinates (excluding $x_j$ and $y_j$) for each derivative of order $n_1$ in $x$ direction and $n_2$ in $y$ direction.

In the following we present an example for determining the displacement $u_i$ of a fictitious node $i$ near a corner of the body by means of the Taylor-based extrapolation method with $n_{max} = 2$. As shown in Figure 3.11, the node $j$ near the corner is the real node closest to node $i$. Thus, the displacement $u_i$ can be given via a Taylor series expansion about node $j$ (see Equation 3.37) as

$$u_i = u_j + l_x \cdot \frac{\partial u_j}{\partial x} + l_y \cdot \frac{\partial u_j}{\partial y} + \frac{l_x^2}{2} \cdot \frac{\partial^2 u_j}{\partial x^2} + l_x l_y \cdot \frac{\partial^2 u_j}{\partial x \, \partial y} + \frac{l_y^2}{2} \cdot \frac{\partial^2 u_j}{\partial y^2} \,, \tag{3.40}$$

where $l_x = x_i - x_j$ and $l_y = y_i - y_j$. Note that the number of derivatives of the displacement $u_j$ is $n_d = 5$.

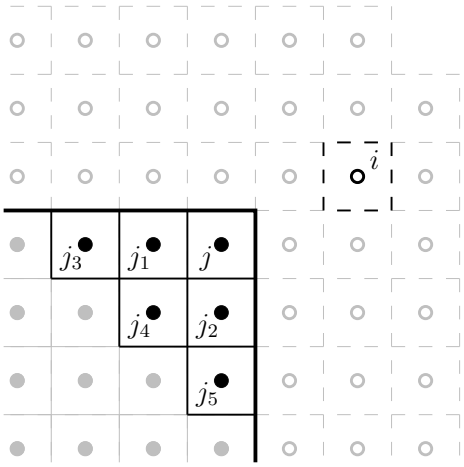


Figure 3.11: *Taylor-based extrapolation method for a fictitious node $i$ near a corner of the body: node $j$ is the real node closest to node $i$ and nodes $j_k$ with $k = 1, \ldots, 5$ are the real nodes closest to node $j$.*

As shown in Figure 3.11, $j_k$ with $k = 1, \ldots, 5$ are the 5 indices of the real nodes closest to node $j$. Note that, in order to be compliant with the condition given in Remark 3.3, the search for the closest nodes should be carried out in terms of Manhattan distance. A system of 5 equations is written by performing a Taylor series expansion of $u_{j_k}$ about node $j$ (see

Equation 3.39):

$$\begin{cases} u_{j_1} = u_j - \Delta x \cdot \dfrac{\partial u_j}{\partial x} + \dfrac{\Delta x^2}{2} \cdot \dfrac{\partial^2 u_j}{\partial x^2} \\ u_{j_2} = u_j - \Delta y \cdot \dfrac{\partial u_j}{\partial y} + \dfrac{\Delta y^2}{2} \cdot \dfrac{\partial^2 u_j}{\partial y^2} \\ u_{j_3} = u_j - 2\Delta x \cdot \dfrac{\partial u_j}{\partial x} + 2\Delta x^2 \cdot \dfrac{\partial^2 u_j}{\partial x^2} \\ u_{j_4} = u_j - \Delta x \cdot \dfrac{\partial u_j}{\partial x} - \Delta y \cdot \dfrac{\partial u_j}{\partial y} \\ \qquad + \dfrac{\Delta x^2}{2} \cdot \dfrac{\partial^2 u_j}{\partial x^2} + \Delta x \Delta y \cdot \dfrac{\partial^2 u_j}{\partial x\, \partial y} + 2\Delta y^2 \cdot \dfrac{\partial^2 u_j}{\partial y^2} \\ u_{j_5} = u_j - 2\Delta y \cdot \dfrac{\partial u_j}{\partial y} + 2\Delta y^2 \cdot \dfrac{\partial^2 u_j}{\partial y^2} \end{cases} \tag{3.41}$$

The factors of the Taylor series expansions, which are multiplied by the derivatives of $u_j$, are easily derived from Figure 3.11. After some manipulations, the system in Equation 3.41 yields:

$$\begin{cases} \dfrac{\partial u_j}{\partial x} = \dfrac{3u_j - 4u_{j_1} + u_{j_3}}{2\Delta x} \\ \dfrac{\partial u_j}{\partial y} = \dfrac{3u_j - 4u_{j_2} + u_{j_5}}{2\Delta y} \\ \dfrac{\partial^2 u_j}{\partial x^2} = \dfrac{u_j - 2u_{j_1} + u_{j_3}}{\Delta x^2} \\ \dfrac{\partial^2 u_j}{\partial x\, \partial y} = \dfrac{u_j - u_{j_1} - u_{j_2} + u_{j_4}}{\Delta x \Delta y} \\ \dfrac{\partial^2 u_j}{\partial y^2} = \dfrac{u_j - 2u_{j_2} + u_{j_5}}{\Delta y^2} \end{cases} \tag{3.42}$$

Therefore, by substituting Equation 3.42 in Equation 3.40, the displacement $u_i$ of the fictitious node is expressed as a function solely of the displacements of the real nodes. This procedure can be repeated for the required variables of all the fictitious nodes.

### 3.4.2 Numerical formulation of peridynamics

Consider a real node $i$, as shown in Figure 3.12. The neighborhood $\mathcal{H}_i$ of node $i$ embeds the complete volume of the nearest nodes and the partial volume of the nodes near the horizon limit. Therefore, all the nodes with at least a portion of their own volume within the horizon limit are considered part of the neighborhood $\mathcal{H}_i$. For each family node $j$, the volume correction coefficient $\beta_{ij} \leq 1$ is computed as the fraction of volume actually contained in the neighborhood [184]. If $\Delta V$ of node $j$ is completely inside the neighborhood, then $\beta_{ij} = 1$.

The bond $ij$, which connects node $i$ to node $j$, could be either a real bond or a fictitious bond. In both cases, its reference scalar state $\underline{x}_{ij}$, Gaussian influence function $\underline{\omega}_{ij}$ and inclination $\phi_{ij}$ with respect to the $x$-axis, can be computed from the coordinates of the two nodes. Under the assumption of small displacements, the extension scalar state of bond $ij$

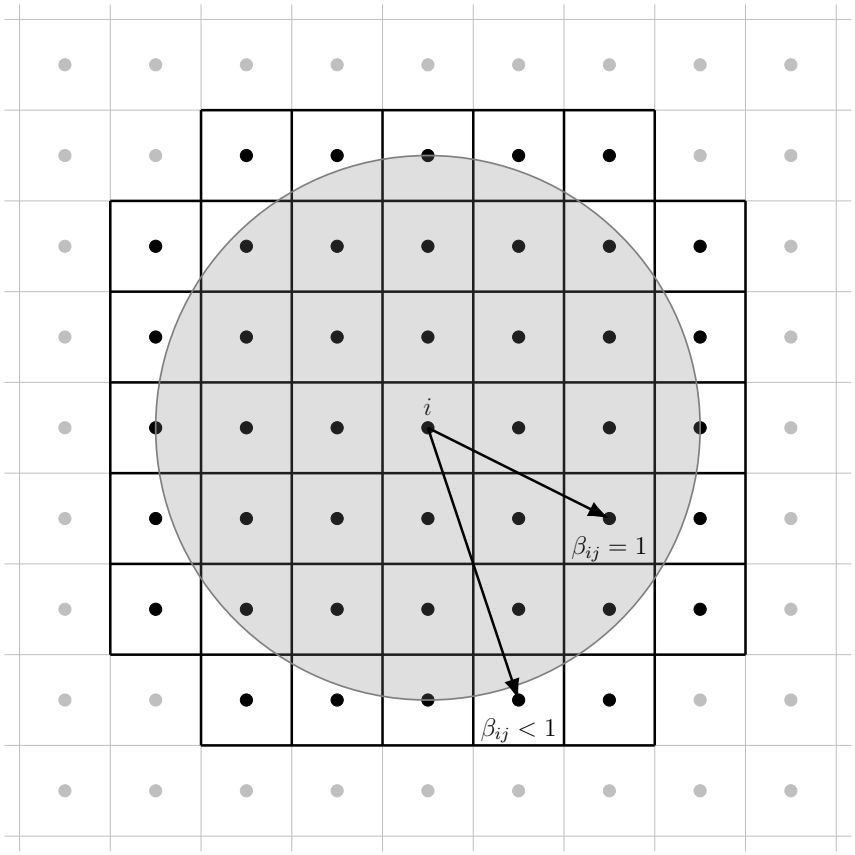


Figure 3.12: *The neighborhood $\mathcal{H}_i$ of a node $i$ is constituted by the nodes (black dots) with at least a part of their volume inside the horizon (gray line). The volume correction coefficient $\beta$ is the fraction of the volume of the family nodes $j$ within the horizon limit.*

is given as

$$\underline{e}_{ij} = (u_j - u_i)\cos\phi_{ij} + (v_j - v_i)\sin\phi_{ij}\,, \tag{3.43}$$

where $u_i$ and $u_j$ are the displacements in $x$ direction respectively of nodes $i$ and $j$ and $v_i$ and $v_j$ are the displacements in $y$ direction respectively of nodes $i$ and $j$. If the family node $j$ is fictitious, Equation 3.43 holds and $u_j$ and $v_j$ are determined as a function of the displacements of the real nodes by the Taylor-based extrapolation method exposed in Section 3.4.1.

The weighted volume of node $i$ is evaluated by performing a mid-point Gauss quadrature from Equation 3.13:

$$m_i = \sum_{j\in\mathcal{H}_i} \underline{\omega}_{ij}\,\underline{x}_{ij}^2\,\beta_{ij}\,\Delta V\,. \tag{3.44}$$

Since the neighborhoods of all the real nodes are complete thanks to the presence of the fictitious nodes, the weighted volume is constant in the whole body. Furthermore, the value of the weighted volume of the real nodes is assigned also to the fictitious nodes, as dictated by the Taylor-based extrapolation method.

Similarly, the dilatation of a real node $i$ is computed from Equation 3.14 as

$$\theta_i = \frac{c_\theta}{m_i} \sum_{j\in\mathcal{H}_i} \underline{\omega}_{ij}\,\underline{x}_{ij}\,\underline{e}_{ij}\,\beta_{ij}\,\Delta V\,. \tag{3.45}$$

On the other hand, the dilatations of the fictitious nodes are determined as a function of the dilatations of the real nodes by means of another Taylor-based extrapolation, as illustrated in Section 3.4.1.

The magnitude of the pairwise force density in bond $ij$ is given from Equation 3.20 as

$$\mathrm{f}_{ij} = \left[ k_\theta \left( \frac{\theta_i}{m_i} + \frac{\theta_j}{m_j} \right) \underline{\omega}_{ij}\, \underline{x}_{ij} + k_e \left( \frac{1}{m_i} + \frac{1}{m_j} \right) \underline{\omega}_{ij}\, \underline{e}_{ij} \right] \beta_{ij} \,. \tag{3.46}$$

Note that the constants $k_\theta$ and $k_e$ are determined by the constitutive modelling of the peridynamic theory, the parameters $m_i$, $m_j$, $\underline{\omega}_{ij}$, $\underline{x}_{ij}$ and $\beta_{ij}$ depend only on the geometric coordinates of the nodes in the reference configuration and the variables $\underline{e}_{ij}$, $\theta_i$ and $\theta_j$ can be written as functions of the displacements of the real nodes (by using the proposed Taylor-based extrapolation method for the variables of the fictitious nodes). Therefore, by combining Equations 3.43-3.46 together, one can write an equation for each bond $ij$, either real or fictitious, to relate the magnitude $\mathrm{f}_{ij}$ of its pairwise force density to the displacements of the real nodes.

Finally, under the assumption of small deformation, the peridynamic equilibrium equation (multiplied by the node volume $\Delta V$) is written for every real node $i$ as

$$-\sum_{j \in \mathcal{H}_i} \mathrm{f}_{ij}\, \mathbf{m}_{ij}\, \Delta V^2 = \mathbf{b}_i\, \Delta V \qquad \forall i \in \mathcal{B} \tag{3.47}$$

where $\mathbf{m}_{ij} = \{\cos\phi_{ij},\, \sin\phi_{ij}\}^\top$ is the bond direction in the reference configuration and $\mathbf{b}_i$ is the external force density vector applied to node $i$. The system of equations in Equation 3.47 can be rewritten in the standard form

$$\mathbf{K}\, \widetilde{\mathbf{u}} = \widetilde{\mathbf{f}} \,, \tag{3.48}$$

where $\mathbf{K}$ is the peridynamic stiffness matrix (size: $2N \times 2N$), $\widetilde{\mathbf{u}}$ is the displacement vector (size: $2N \times 1$) and $\widetilde{\mathbf{f}}$ is the force vector (size: $2N \times 1$). $N$ is the number of real nodes. The stiffness matrix $\mathbf{K}$ includes the contributions of the fictitious bonds, thus it embeds the correction of the surface effect by means of the Taylor-based extrapolation method.

### 3.4.3 Numerical evaluation of the peridynamic stress tensor

This Section deals with the numerical procedure to compute the peridynamic stress tensor. The theoretical background can be found in Section 3.2.2.

In the discretized peridynamic model, we name the nodes corresponding to the points $\mathbf{x}$, $\mathbf{x}'$ and $\mathbf{x}''$ (see Figure 3.2) respectively as $i$, $j$ and $k$. Under the assumption of point $i$ being in the bulk of a body subjected to a homogeneous deformation (see Equation 3.23), the peridynamic stress tensor can be computed as

$$\boldsymbol{\tau}_i = \frac{1}{2} \sum_{k \in \mathcal{H}_i} r_{ik}\, \mathrm{f}_{ik}\, \mathbf{m}_{ik} \otimes \mathbf{m}_{ik}\, \Delta V \,, \tag{3.49}$$

where $r_{ik}$ is the length of the bond $ik$. Equation 3.49 provides a good approximation also

in the case of non-homogeneous deformations if the horizon $\delta$ is sufficiently small, as shown in [234] for bond-based peridynamics. However, Equation 3.49 is not valid for nodes near the boundary which are affected by the surface effect (if no fictitious layer is employed).

In order to compute numerically the peridynamic stress tensor $\boldsymbol{\tau}_i$ in a general node $i$, also not in the bulk of the body, the integrand of Equation 3.22 should be evaluated for each bond $jk$ between node $j$ and node $k$. The differential volume $\mathrm{d}V_{\mathbf{x}''}$ corresponds simply to the finite volume of node $k$, i.e., $\Delta V$. On the other hand, we must distinguish two types of bonds, which are shown in Figure 3.13, to determine $\Delta s$ as the corresponding of the differential length $\mathrm{d}s$ of point $\mathbf{x}'$ in the direction of the bond $\mathbf{m}$:

$$\Delta s = \begin{cases} \dfrac{\Delta x}{|\cos\phi_{jk}|} & \text{if } \ |\cos\phi_{jk}| \geq \dfrac{\sqrt{2}}{2}\,, \\ \dfrac{\Delta y}{|\sin\phi_{jk}|} & \text{if } \ |\cos\phi_{jk}| < \dfrac{\sqrt{2}}{2}\,, \end{cases} \tag{3.50}$$

where the trigonometric functions are within the absolute value because $\Delta s > 0$. In the former case bond $jk$ is a type-A bond and, in the latter, a type-B bond, which are respectively shown in Figure 3.13a and 3.13b. A type-A bond contributes to $\boldsymbol{\tau}_i$ if it intersects the area $\Delta A_i^{\mathrm{A}} = h\Delta y$ passing through node $i$ perpendicular to $x$ direction, where $h$ is the thickness of the 2-dimensional body. Similarly, a type-B bond contributes to $\boldsymbol{\tau}_i$ if it intersects the area $\Delta A_i^{\mathrm{B}} = h\Delta x$ passing through node $i$ perpendicular to $y$ direction. Therefore, the peridynamic stress tensor in a node $i$ is given as

$$\begin{aligned} \boldsymbol{\tau}_i = \frac{1}{2} \sum_{\boldsymbol{\xi}_{jk} \cap \Delta A_i^{\mathrm{A}} \neq \emptyset} \alpha_{jk}\, \mathrm{f}_{jk}\, \mathbf{m}_{jk} \otimes \mathbf{m}_{jk}\, \frac{\Delta x}{|\cos\phi_{jk}|} \Delta V \\ + \frac{1}{2} \sum_{\boldsymbol{\xi}_{jk} \cap \Delta A_i^{\mathrm{B}} \neq \emptyset} \alpha_{jk}\, \mathrm{f}_{jk}\, \mathbf{m}_{jk} \otimes \mathbf{m}_{jk}\, \frac{\Delta y}{|\sin\phi_{jk}|} \Delta V\,, \end{aligned} \tag{3.51}$$

where $\mathrm{f}_{jk}$ is the magnitude of the pairwise force density of bond $jk$ obtained with Equation 3.46, $\mathbf{m}_{jk} = \{\cos\phi_{jk},\, \sin\phi_{jk}\}^{\top}$ is the bond direction and $\alpha_{jk}$ is a correction coefficient, given as:

$$\alpha_{jk} = \begin{cases} \dfrac{1}{2} & \text{if } \ j = i \ \text{ or } \ k = i\,, \\ \dfrac{1}{2} & \text{if } \ \boldsymbol{\xi}_{jk} \cap \partial A_i \neq \emptyset\,, \\ 1 & \text{if } \ \boldsymbol{\xi}_{jk} \cap (\Delta A_i \setminus \partial A_i) \neq \emptyset\,, \end{cases} \tag{3.52}$$

where $\partial A_i$ is the boundary of the area $\Delta A_i$, which can be referred either to type-A bonds ($\Delta A_i^{\mathrm{A}}$) or to type-B bonds ($\Delta A_i^{\mathrm{B}}$). The different cases in Equation 3.52 are illustrated in Figure 3.14:

- in the case with $j = i$ (see Figure 3.14a), since only half of the length $\Delta s$ related to node $j$ is on the opposite side of $\Delta A_i$ with respect to node $k$, then $\alpha_{jk} = 1/2$;
- similarly, in the case with $k = i$ (see Figure 3.14b), since only half of the volume $\Delta V$ of node $k$ is on the opposite side of $\Delta A_i$ with respect to node $j$, then $\alpha_{jk} = 1/2$;

- in the case that the bond intersects the boundary of $\Delta A_i$, i.e., $\boldsymbol{\xi}_{jk} \cap \partial A_i \neq \emptyset$, since $\partial A_i$ overlaps the boundary of the area of another node (node $q$ in Figure 3.14c), the magnitude of the pairwise force density of bond $jk$ is equally shared between those nodes and, therefore, $\alpha_{jk} = 1/2$;
- in the case that the bond intersects $\Delta A_i$ not on its boundary, i.e., $\boldsymbol{\xi}_{jk} \cap (\Delta A_i \setminus \partial A_i) \neq \emptyset$ (see Figure 3.14d), the magnitude of the pairwise force density of bond $jk$ contributes entirely to $\boldsymbol{\tau}_i$ and, therefore, $\alpha_{jk} = 1$;

Moreover, to improve the computational efficiency, one might remove the factors $1/2$ in Equation 3.51 and consider each bond just once (for example consider only bond $jk$ and not bond $kj$).

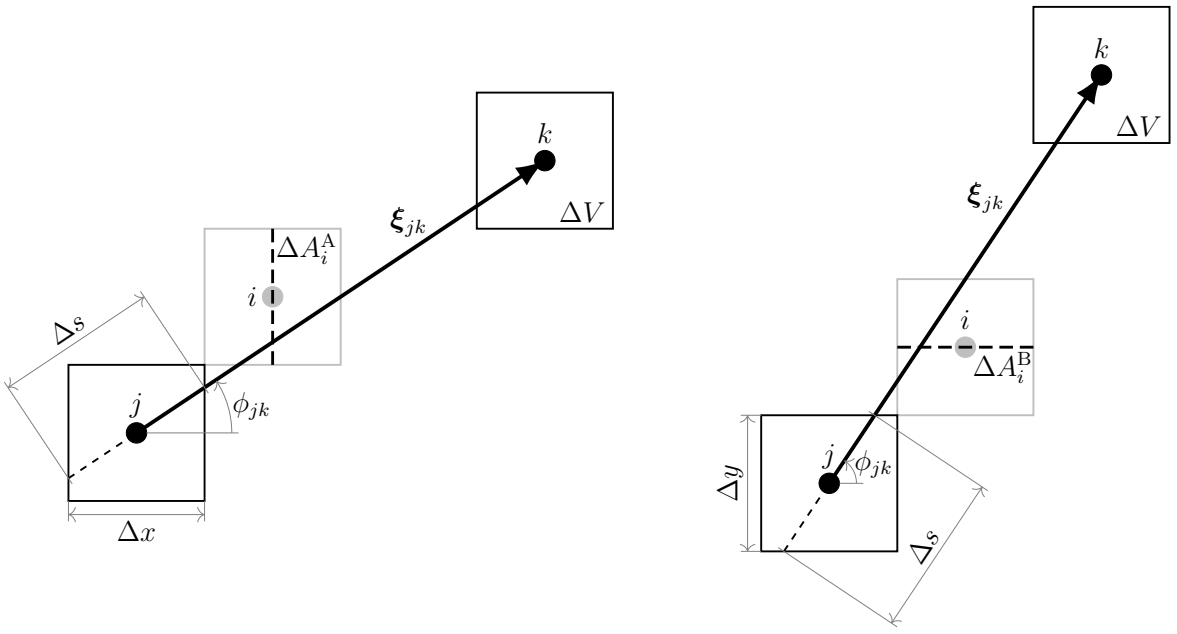


(a) *Type*-A *bond:* $|\cos\phi_{jk}| \geq \sqrt{2}/2$. (b) *Type*-B *bond:* $|\cos\phi_{jk}| < \sqrt{2}/2$.

Figure 3.13: *Examples of type*-A *and type*-B *bonds for the computation of the peridynamic stress tensor* $\boldsymbol{\tau}_i$ *in node* $i$*. The bonds contribute to* $\boldsymbol{\tau}_i$ *only if they intersect the corresponding area* $\Delta A_i$*.*

The proposed numerical procedure to compute the peridynamic stress tensor is used to highlight the surface effect in a 2-dimensional body in Section 3.2.4. Figures 3.7 and 3.8 show that the numerical computation of the peridynamic stress tensor is very close to the analytical solutions, obtained in Section 3.2.2, for nodes with a complete neighborhood.

### 3.4.4 Numerical evaluation of the force flux

Consider a finite area $\Delta A$ which constitutes one of the sides of the volume cell of a node, as shown in Figure 3.15. The numerical procedure to compute the peridynamic force flux through the finite area $\Delta A$ is exposed in this Section.

The force flux $\boldsymbol{\tau}(\mathbf{x}, \mathbf{n})$ of a point $\mathbf{x}$ in a direction $\mathbf{n}$ is interpreted in Section 3.2.3 as the sum of the pairwise forces per unit area of all the bonds intersecting the differential area $\mathrm{d}A_{\mathbf{x}}$ on the plane $\mathcal{P}$ in $\mathbf{x}$, where $\mathcal{P}$ is the plane passing through $\mathbf{x}$ perpendicular to

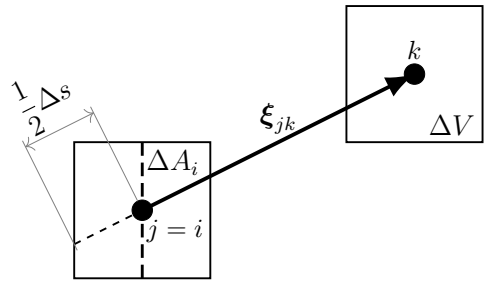


(a) *Case* $j = i$*:* $\alpha_{jk} = 1/2$.

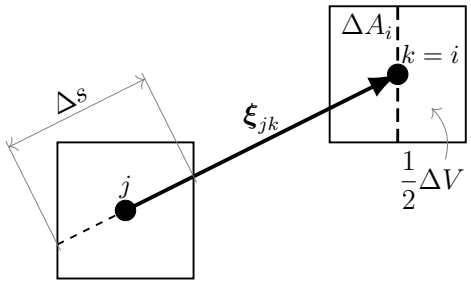


(b) *Case* $k = i$*:* $\alpha_{jk} = 1/2$.

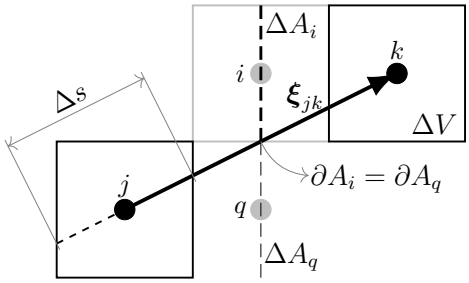


(c) *Case* $\boldsymbol{\xi}_{jk} \cap \partial A_i \neq \emptyset$*:* $\alpha_{jk} = 1/2$.

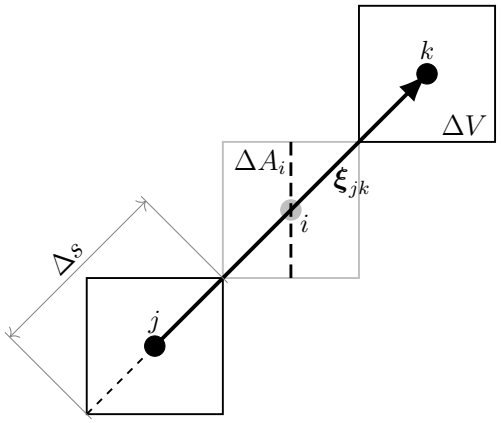


(d) *Case* $\boldsymbol{\xi}_{jk} \cap (\Delta A_i \setminus \partial A_i) \neq \emptyset$*:* $\alpha_{jk} = 1$.

Figure 3.14: *Values of the correction coefficient* $\alpha_{jk}$ *for different types of intersection between bond* $jk$ *and area* $\Delta A_i$*. These examples consider only type-A bonds, but the same concepts are valid also for type-B bonds.*

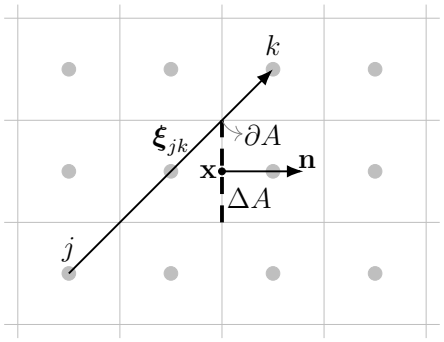


(a) *Case* $\boldsymbol{\xi}_{jk} \cap \partial A \neq \emptyset$*:* $\alpha_{jk} = 1/2$.

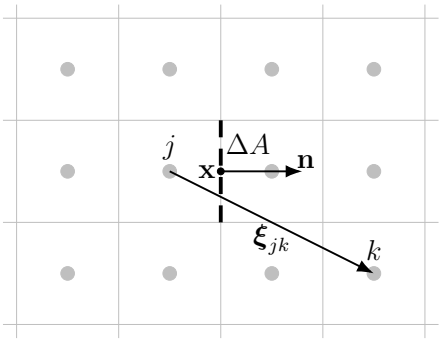


(b) *Case* $\boldsymbol{\xi}_{jk} \cap (\Delta A \setminus \partial A) \neq \emptyset$*:* $\alpha_{jk} = 1$.

Figure 3.15: *Values of the correction coefficient* $\alpha_{jk}$ *for different types of intersection between bond* $jk$ *and area* $\Delta A$*.*

$\mathbf{n}$ (see Figures 3.4 and 3.5). Therefore, the force flux through $\Delta A$ can be discretized from Equations 3.30 and 3.32 as

$$\boldsymbol{\tau}(\mathbf{x}, \mathbf{n}) = \frac{1}{\Delta A} \sum_{\substack{\boldsymbol{\xi}_{jk} \cap \Delta A \neq \emptyset \\ \mathbf{m}_{jk} \cdot \mathbf{n} > 0}} \alpha_{jk}\, \mathrm{f}_{jk}\, \mathbf{m}_{jk}\, \Delta V^2 \,, \tag{3.53}$$

where $\mathbf{x}$ and $\mathbf{n}$ are respectively the centroid and the normal of $\Delta A$, $\mathrm{f}_{jk}\, \mathbf{m}_{jk}\, \Delta V^2$ is the pairwise force of any bond $jk$ intersecting $\Delta A$ and $\alpha_{jk}$ is the correction coefficient given by

Equation 3.52 (see also in Figure 3.15a and 3.15b the possible cases in the computation of the force flux). Note that, in order to improve the computational efficiency, the factor 1/2 is removed because only bonds satisfying the condition $\mathbf{m}_{jk} \cdot \mathbf{n} > 0$ are considered. Since we are mostly interested in the force flux computed at the boundary of the body to impose Neumann boundary conditions, this concept is further analyzed in the next Section.

### 3.4.5 Numerical implementation of the peridynamic boundary conditions

The real nodes closest to the boundary are not exactly on the boundary of the body (see Figure 3.10). Therefore, by following the concepts exposed in Section 3.3.2, the boundary conditions in the discretized model should be imposed on the sides of the volume cells which overlap the boundary. We introduce a new cathegory of nodes, called "boundary nodes", at which the boundary conditions are imposed. Each boundary node is positioned at the centroid of the side of the volume cell of the nodes closest to the boundary and is representative of the finite area $\Delta A_b$ of that side, as shown in Figure 3.16. As the fictitious nodes, the boundary nodes do not constitute new degrees of freedom because their displacements are determined as a function of the displacements of the real nodes by means of the Taylor-based extrapolation method.

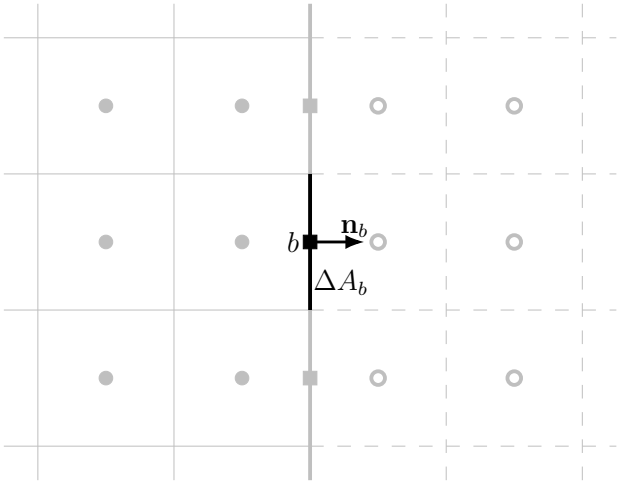


Figure 3.16: *Boundary nodes at the boundary of the body: each node b is representative of a finite area $\Delta A_b$ and is associated to the normal $\mathbf{n}_b$ external to the body.*

Suppose that the problem requires a constraint $\overline{u}$ for the displacement $u_b$ in $x$ direction of a boundary node $b$, condition given as $u_b = \overline{u}$. The Taylor-based extrapolation method is applied to the boundary node exactly as done for the fictitious nodes in Section 3.4.1. The following procedure is valid also for $\overline{u} = 0$. The displacement $u_b$ of the boundary node $b$ with coordinates $(x_b, y_b)$ is determined by a Taylor series expansion about node $j$ with coordinates $(x_j, y_j)$ as

$$u_b = u_j + \sum_{n=1}^{n_{max}} \sum_{n_1=0}^{n} \frac{(x_b - x_j)^{n_1} (y_b - y_j)^{n_2}}{n_1!\, n_2!} \frac{\partial^{n_1+n_2} u_j}{\partial x^{n_1}\, \partial y^{n_2}}\,, \tag{3.54}$$

where node $j$ is the real node closest to node $b$. The $n_d$ derivatives of $u_j$ can be expressed as functions of the displacements of the $n_d$ real nodes close to node $j$. Therefore, the Dirichlet boundary condition can be written as a function of the displacements of some real nodes:

$$\overline{u} = f(u_j, u_{j_k}) \qquad \text{with} \quad k = 1, \ldots, n_d. \tag{3.55}$$

For example, we consider the case shown in Figure 3.17 with a truncation order $n_{max} = 2$. The Taylor series expansion of the displacement $u_b$ about node $j$ is given as

$$u_b = u_j + \frac{\Delta x}{2}\frac{\partial u_j}{\partial x} + \frac{\Delta x^2}{8}\frac{\partial^2 u_j}{\partial x^2}\,. \tag{3.56}$$

In order to determine the two derivatives in $x$ direction of Equation 3.56, we find nodes $j_1$ and $j_2$, shown in Figure 3.17, as the nodes closest to node $j$ having $x$ coordinates different from each other and from $x_j$ (see Remark 3.3). We write the system of equations given by the Taylor series expansions of $u_{j_1}$ and $u_{j_2}$ about node $j$, as in Equation 3.38, and solve it to obtain the needed derivatives:

$$\begin{cases} \dfrac{\partial u_j}{\partial x} = \dfrac{3u_j - 4u_{j_1} + u_{j_2}}{2\Delta x} \\ \dfrac{\partial^2 u_j}{\partial x^2} = \dfrac{u_j - 2u_{j_1} + u_{j_2}}{\Delta x^2} \end{cases} \tag{3.57}$$

By substituting Equation 3.57 in Equation 3.56, the constraint condition $u_b = \overline{u}$ is given as a function of the displacements of some real nodes:

$$\overline{u} = \frac{15}{8}u_j - \frac{5}{4}u_{j_1} + \frac{3}{8}u_{j_2}\,. \tag{3.58}$$

More in general, the proposed method allows to write the Dirichlet boundary conditions as functions of the displacement vector $\widetilde{\mathbf{u}}$:

$$\overline{u} = f(\widetilde{\mathbf{u}})\,. \tag{3.59}$$

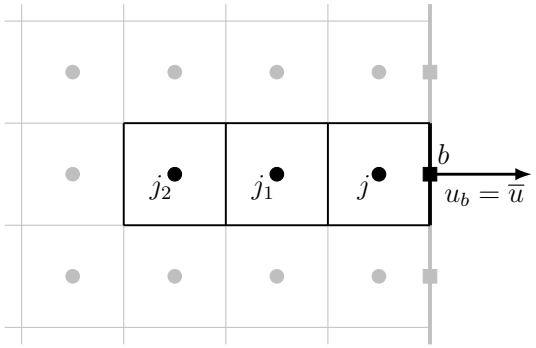


Figure 3.17: *Example of the Taylor-based extrapolation method used on a boundary node b.*

Suppose now that an external force per unit area $\overline{\mathbf{p}}$ is applied to a boundary node $b$, as shown in Figure 3.18. The Neumann boundary condition is written in terms of force flux

through the area $\Delta A_b$ associated to node $b$:

$$\boldsymbol{\tau}(\mathbf{x}_b, \mathbf{n}_b) = \frac{1}{\Delta A_b} \sum_{\substack{\boldsymbol{\xi}_{jk} \cap \Delta A_b \neq \emptyset \\ \mathbf{m}_{jk} \cdot \mathbf{n}_b > 0}} \alpha_{jk}\, \mathrm{f}_{jk}\, \mathbf{m}_{jk}\, \Delta V^2 = \overline{\mathbf{p}}\,, \tag{3.60}$$

where $\mathbf{x}_b$ is the position of node $b$ and $\mathbf{n}_b$ is the unit vector perpendicular to $\Delta A_b$ external to the body. Since the pairwise force density of any bond can be expressed as a function of the displacements of the real nodes (see Section 3.4.2), also $\boldsymbol{\tau}(\mathbf{x}_b, \mathbf{n})$ is a function of those displacements. Thus, Neumann boundary conditions can be written as functions of the displacement vector $\widetilde{\mathbf{u}}$:

$$\overline{\mathbf{p}} = f(\widetilde{\mathbf{u}})\,. \tag{3.61}$$

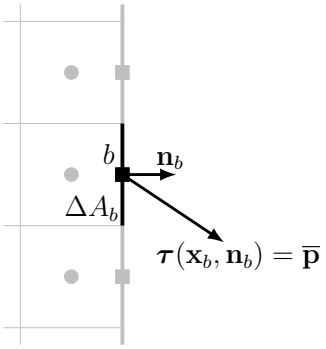


Figure 3.18: *Example of an external load $\overline{\mathbf{p}}$ applied to a boundary node $b$.*

Since both Dirichlet and Neumann boundary conditions are given by equations in which the only unknowns are the displacements of the real nodes (see Equations 3.59 and 3.61), we gather all the boundary conditions in a matrix form as

$$\mathbf{B}\,\widetilde{\mathbf{u}} = \overline{\mathbf{c}}\,, \tag{3.62}$$

where $\mathbf{B}$ is the matrix of the boundary conditions (size: $2N_b \times 2N$), $\widetilde{\mathbf{u}}$ is the displacement vector (size: $2N \times 1$) and $\overline{\mathbf{c}}$ is the vector of the known terms (size: $2N_b \times 1$). $N_b$ is the number of boundary nodes.

In order to include the boundary conditions ($\mathbf{B}\,\widetilde{\mathbf{u}} = \overline{\mathbf{c}}$) in the system of equations derived from the equilibrium of the real nodes ($\mathbf{K}\,\widetilde{\mathbf{u}} = \widetilde{\mathbf{f}}$), we conveniently use the technique of the Lagrange multipliers [225]. The vector of the Lagrange multipliers $\boldsymbol{\lambda}$ (size: $2N_b \times 1$) is introduced in the system as

$$\begin{bmatrix} \mathbf{K} & \mathbf{B}^\top \\ \mathbf{B} & \mathbf{0} \end{bmatrix} \begin{Bmatrix} \widetilde{\mathbf{u}} \\ \boldsymbol{\lambda} \end{Bmatrix} = \begin{Bmatrix} \widetilde{\mathbf{f}} \\ \overline{\mathbf{c}} \end{Bmatrix}. \tag{3.63}$$

The displacement vector $\widetilde{\mathbf{u}}$, extracted from the vector $\{\widetilde{\mathbf{u}}, \boldsymbol{\lambda}\}^\top$, is the solution to the system of equilibrium equations which satisfies the imposed boundary conditions.

## 3.5 Numerical examples

Several examples are presented to verify the reliability and accuracy of the proposed method. Whenever possible, the numerical peridynamic results are compared with the reference solutions derived from classical continuum mechanics. The reference solution coincides with the peridynamic solution only in the limit of the horizon $\delta$ approaching 0 [162, 165]. Therefore, the "difference" between these solutions includes two components: a discrepancy due to the different (local and non-local) formulations of the theories and the actual error given by the discretization and the implementation of the peridynamic model (either with or without the proposed method). The difference (in percentage) of the displacements between the peridynamic numerical results and the reference solution is computed at each node $i$ as

$$\boldsymbol{\epsilon}_i = \begin{Bmatrix} \epsilon_u \\ \epsilon_v \end{Bmatrix}_i = \begin{Bmatrix} \dfrac{|u_i - u_{ref}(\mathbf{x}_i)|}{\max(|\widetilde{\mathbf{u}}_{ref}|)} \cdot 100 \\ \dfrac{|v_i - v_{ref}(\mathbf{x}_i)|}{\max(|\widetilde{\mathbf{u}}_{ref}|)} \cdot 100 \end{Bmatrix}, \tag{3.64}$$

where $u_i$ and $v_i$ are the displacements of node $i$, $u_{ref}(\mathbf{x}_i)$ and $v_{ref}(\mathbf{x}_i)$ are the displacements obtained with the reference solution at the position $\mathbf{x}_i$ of node $i$ and $\widetilde{\mathbf{u}}_{ref}$ is the displacement vector obtained with the reference solution at all the nodes. The reference solution is defined for each example by providing either the analytical solution (if possible), or the results obtained with the Finite Element Method.

For simplicity sake, we consider a plate under plane stress conditions with different boundary conditions. The parameters adopted for the simulations of the plate are reported in Table 3.1. Firstly, we solve each example without adding the fictitious nodes. In this case, the boundary conditions are implemented by assigning the desired value of the constraints or loads to the most external nodes of the plate. In particular, Dirichlet boundary conditions are imposed by assigning to the nodes closest to the boundary the value of the displacement computed with the reference solution. Then, the same examples are solved by adopting the proposed Taylor-based extrapolation method and by implementing the boundary conditions as described in Section 3.4.5.

Table 3.1: *Parameters of the plate and of its discretization.*

| Parameter | Value |
|---|---|
| Length | $\ell_x = 0.3\,\mathrm{m}$ |
| Width | $\ell_y = 0.2\,\mathrm{m}$ |
| Thickness | $h = 0.005\,\mathrm{m}$ |
| Young's modulus | $E = 1\,\mathrm{GPa}$ |
| Poisson's ratio | $\nu = 0.2$ |
| Grid spacing | $\Delta x = \Delta y = 0.01\,\mathrm{m}$ |
| $\overline{m}$-ratio | $\overline{m} = 3$ |

### 3.5.1 Plate under traction

The boundary conditions of the first example are shown in Figure 3.19. The analytical solution is given by classical continuum mechanics as

$$\mathbf{u}(\mathbf{x}) = \begin{Bmatrix} u(x,y) \\ v(x,y) \end{Bmatrix} = \begin{Bmatrix} \dfrac{\overline{p}}{E}\left(x + \dfrac{\ell_x}{2}\right) \\ \dfrac{-\nu\,\overline{p}}{E}\left(y + \dfrac{\ell_y}{2}\right) \end{Bmatrix}, \tag{3.65}$$

where $\overline{p}$ is the traction load.

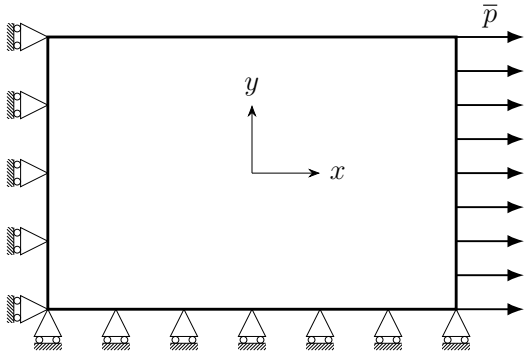


Figure 3.19: *Boundary conditions for the plate under the traction* $\overline{p} = 1\,\text{MPa}$.

The plots in Figure 3.20 show the difference of the displacement field, computed without adopting any correction to the peridynamic model, with respect to the reference solution. The surface effect and the approximated way of imposing the boundary conditions lead to large errors near the boundary of the plate, especially near the corners. On the other hand, there are no fluctuations in the displacement field when the proposed Taylor-based extrapolation method with $n_{max} = 1$ is employed. The differences of the displacement field of the corrected model (see Figure 3.21) decrease sensibly with respect to those obtained without corrections at the boundary. Similar results are obtained by choosing higher orders for the Taylor-based extrapolation.

In the case adopting the proposed method, the error can be further reduced by increasing the accuracy of the integration over the neighborhoods, i.e., by increasing $\overline{m}$ [184]. In order to show this, we compute the relative difference (in percentage) at a node $i$ as

$$\boldsymbol{\epsilon}_i^{rel} = \begin{Bmatrix} \epsilon_u^{rel} \\ \epsilon_v^{rel} \end{Bmatrix}_i = \begin{Bmatrix} \dfrac{|u_i - u_{ref}(\mathbf{x}_i)|}{|u_{ref}(\mathbf{x}_i)|} \cdot 100 \\ \dfrac{|v_i - v_{ref}(\mathbf{x}_i)|}{|v_{ref}(\mathbf{x}_i)|} \cdot 100 \end{Bmatrix}. \tag{3.66}$$

In the case employing the Taylor-based extrapolation on the fictitious nodes, the relative difference of every node inside the body is the same. Therefore, we gather in Table 3.2 the relative errors for different values of $\overline{m}$. We can observe that the relative differences decrease significantly as the value of $\overline{m}$ increase.

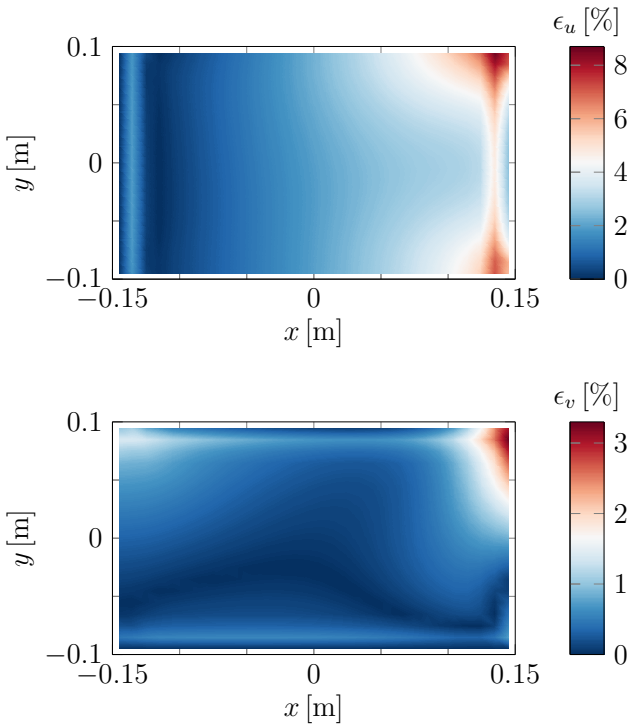


Figure 3.20: *Displacement field differences between the peridynamic numerical results for* $\overline{m} = 3$ *and the reference solution (obtained with the analytical solution in Equation 3.65) in the plate under traction obtained without corrections at the boundary. Note that the colormaps refer to different values in the two plots.*

Table 3.2: *Relative differences between the peridynamic numerical results and the reference solution in the plate under traction when improving the numerical integration by increasing* $\overline{m}$.

| $\overline{m}$ | $\epsilon_u^{rel}$ | $\epsilon_v^{rel}$ |
|---|---|---|
| 3 | 0.43 % | 2.15 % |
| 4 | 0.09 % | 0.45 % |
| 5 | 0.04 % | 0.18 % |
| 6 | 0.02 % | 0.09 % |

### 3.5.2 Plate under shear load

We present another example considering a plate under a shear load $\overline{p}$. Figure 3.22 shows the boundary conditions of this case. Classical continuum mechanics yield the following analytical solution:

$$\mathbf{u}(\mathbf{x}) = \begin{Bmatrix} u(x,y) \\ v(x,y) \end{Bmatrix} = \begin{Bmatrix} \dfrac{2\,(1+\nu)\,\overline{p}}{E}\left(y + \dfrac{\ell_y}{2}\right) \\ 0 \end{Bmatrix} . \tag{3.67}$$

The differences of the displacement field, computed without corrections at the boundary, with respect to the reference solution are shown in Figure 3.23. We observe that the differences are lower with respect to the case of the plate under traction in Section 3.5.1. However, as highlighted in Equation 3.67, one would expect the displacements $v$ in $y$ direction to be

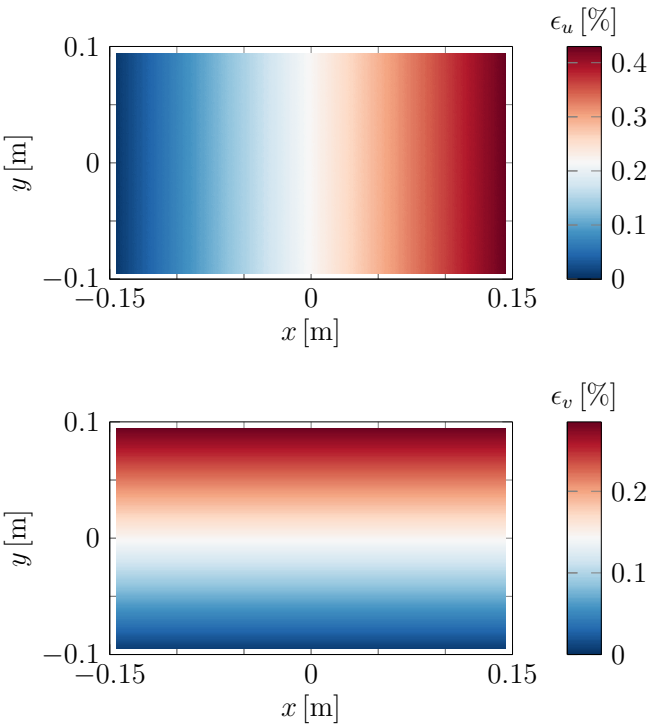


Figure 3.21: *Displacement field differences between the peridynamic numerical results for* $\overline{m} = 3$ *and the reference solution (obtained with the analytical solution in Equation 3.65) in the plate under traction obtained by means of the Taylor-based extrapolation method with* $n_{max} = 1$. *Note that the colormaps refer to different values in the two plots.*

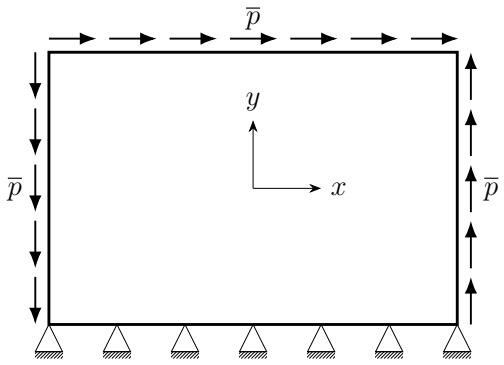


Figure 3.22: *Boundary conditions for the plate under the shear load* $\overline{p} = 1\,\text{MPa}$.

0 in the whole body. This fact is not verified in the numerical simulation because of the surface effect (see plot of the component $\tau_{22}$ of the peridynamic stress tensor in Figure 3.8). This problem is completely solved by implementing the proposed Taylor-based extrapolation method with $n_{max} = 1$, as shown in Figure 3.24. Also, the differences of the displacements $u$ in $x$ direction decreases with respect to those obtained without corrections at the boundary. Similar results are obtained by choosing higher orders for the Taylor-based extrapolation.

As in the case of the plate under traction, we compute the relative differences $\epsilon_u^{rel}$ with Equation 3.66 for different values of $\overline{m}$ when implementing the proposed method in the case of the plate under shear load. For each $\overline{m}$, the relative differences of the displacements $u$ are constant in the whole body also in this case and they are reported in Table 3.3.

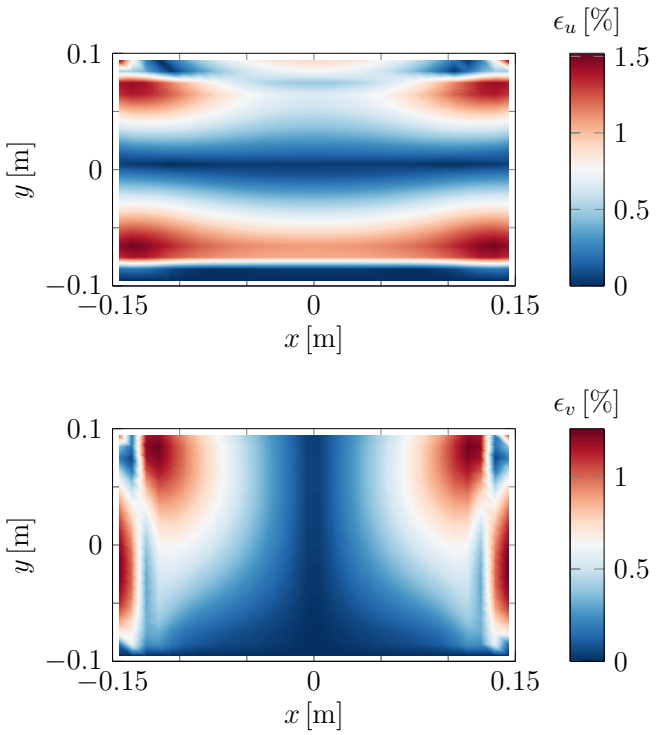


Figure 3.23: *Displacement field differences between the peridynamic numerical results for* $\overline{m} = 3$ *and the reference solution (obtained with the analytical solution in Equation 3.67) in the plate under shear load obtained without corrections at the boundary. Note that the colormaps refer to different values in the two plots.*

The numerical results show a significant reduction of the differences when the numerical integration is improved.

Table 3.3: *Relative differences between the peridynamic numerical results and the reference solution in the plate under shear load when improving the numerical integration by increasing* $\overline{m}$.

| $\overline{m}$ | $\epsilon_u^{rel}$ |
|---|---|
| 3 | 0.73 % |
| 4 | 0.15 % |
| 5 | 0.06 % |
| 6 | 0.03 % |

### 3.5.3 Plate under sinusoidal load

In the previous examples, the linear variation of the displacement field was properly captured by the Taylor-based extrapolation with the order $n_{max} = 1$ (or higher). We investigate now an example in which the order of the Taylor-based extrapolation does not match the order of variation of the displacement field. The boundary conditions of this example are shown in Figure 3.25. The force density applied thoughout the plate is given as

$$b(x, y) = \bar{b} \sin\left(\frac{\pi x}{\ell_x} - \frac{\ell_x}{2}\right) \sin\left(\frac{\pi y}{\ell_y} - \frac{\ell_y}{2}\right) , \tag{3.68}$$

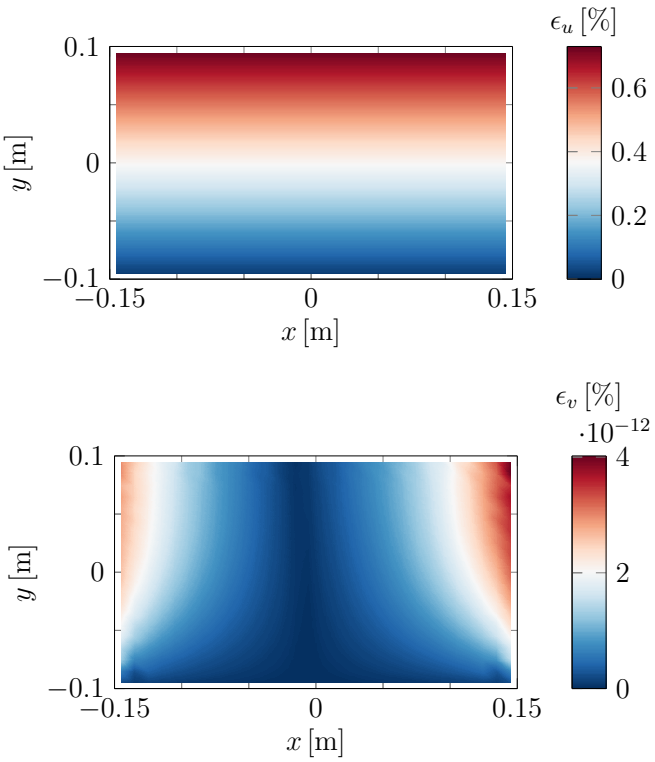


Figure 3.24: *Displacement field differences between the peridynamic numerical results for* $\overline{m} = 3$ *and the reference solution (obtained with the analytical solution in Equation 3.67) in the plate under shear load obtained by means of the Taylor-based extrapolation method with* $n_{max} = 1$*. Note that the colormaps refer to different values in the two plots.*

where $\overline{b} = 10^6\,\mathrm{N/m^3}$.

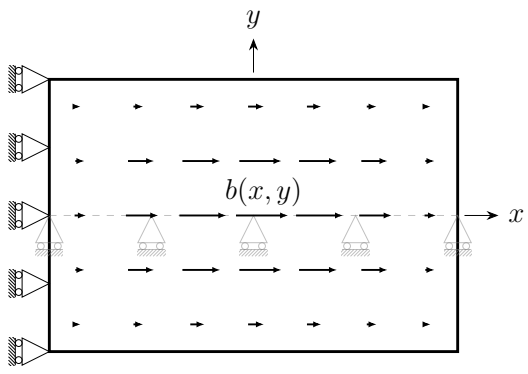


Figure 3.25: *Boundary conditions for the plate under the sinusoidal load* $b(x, y)$*, where the origin of the reference system is at the center of the plate. Given the symmetry of the boundary conditions, the displacements* $v$ *in* $y$ *direction on the* $x$*-axis are fixed to be 0.*

The reference solution, shown in Figure 3.26, is obtained with the Finite Element Method by means of a uniform grid with a spacing $\Delta x_{FEM} = \Delta x/2$. The peridynamic nodes share the coordinates with some of the FEM nodes, so that the peridynamic results can be compared with the reference solution. We expect that, by increasing $n_{max}$, the Taylor-based extrapolation would approximate better the displacements of the fictitious layer.

Figures 3.27 and 3.28 show the differences between the numerical results and the reference

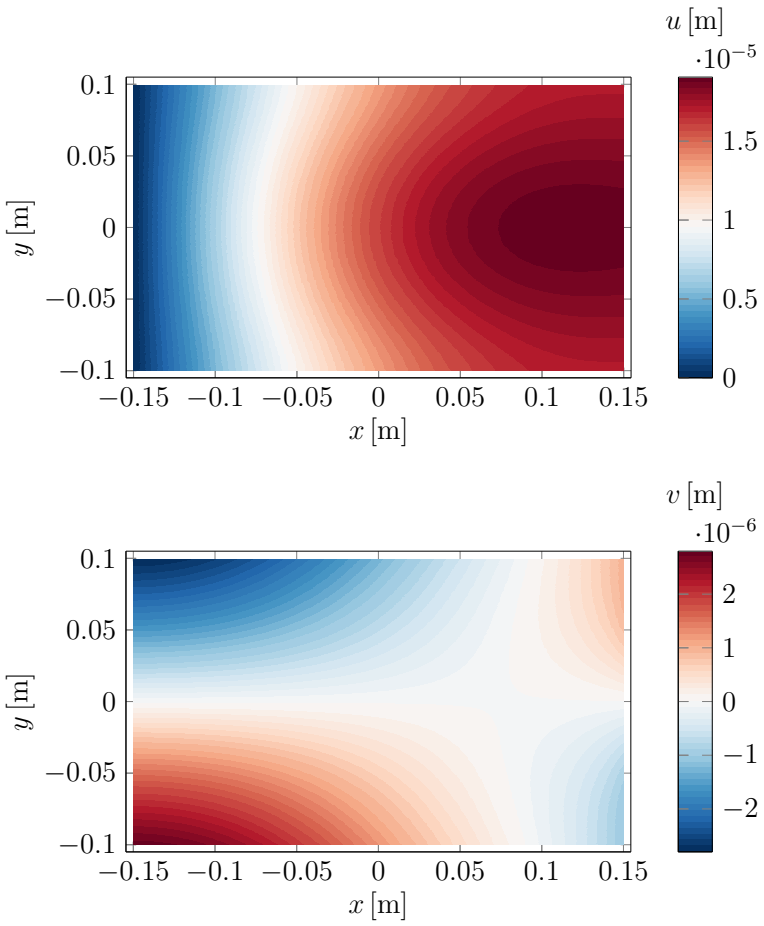


Figure 3.26: *Displacement fields of the plate under the sinusoidal load obtained with the Finite Element Method. Note that the colormaps refer to different values in the two plots.*

solution for the numerical models either without employing any correction for the surface effect or by adopting the Taylor-based extrapolation method. The differences are evidently reduced when the peridynamic model includes the Taylor-based extrapolation method. The aforementioned differences include two contributions: one due to the different (local and non-local) formulations of the theories and the other which is the actual error associated to the approximated numerical solution of the peridynamic equations. The two components of the difference cannot be separated since the analytical peridynamic solution is not available. However, the fluctuations of the differences near the boundaries due to the surface effect are evident in Figures 3.27a and 3.28a, in which no corrections at the boundary are adopted. On the other hand, by exploiting the Taylor-based extrapolation method, the magnitude of the differences decrease considerably and, also, their distribution near the boundaries becomes smoother with the increasing of the truncation order $n_{max}$, as shown in Figures 3.27b-d and 3.28b-d. This is arguably because the numerical results are getting closer to the analytical peridynamic solution by correcting the surface effect and imposing in a proper way the boundary conditions.

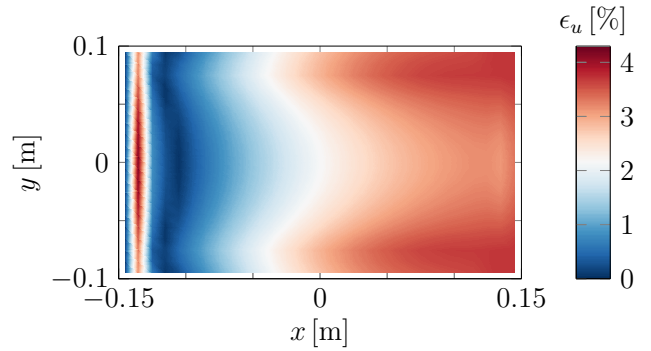


(a) *Model with no corrections at the boundaries.*

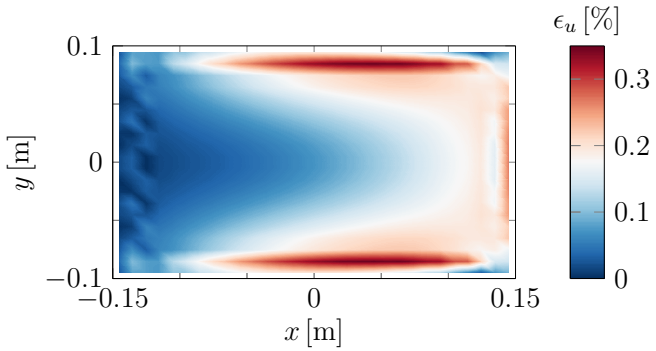


(b) *Model with corrections at the boundaries* ($n_{max} = 1$).

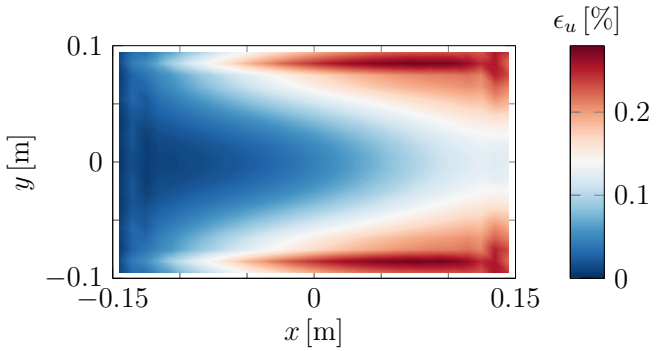


(c) *Model with corrections at the boundaries* ($n_{max} = 2$).

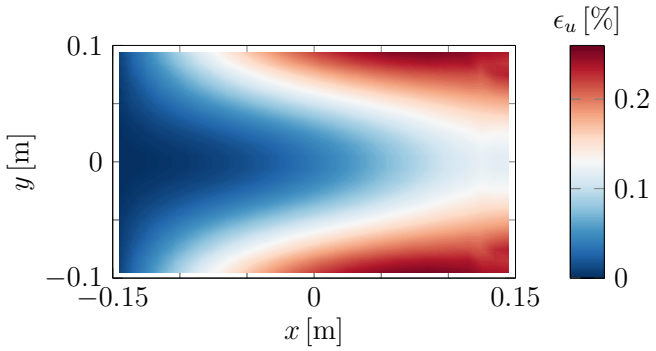


(d) *Model with corrections at the boundaries* ($n_{max} = 3$).

Figure 3.27: *Differences of the displacements in $x$ direction between the peridynamic numerical results for $\overline{m} = 3$ and the reference solution (obtained with the Finite Element Method results, as shown in Figure 3.26) in the plate under the sinusoidal load obtained either without corrections at the boundary or by adopting the Taylor-based extrapolation method with different orders $n_{max}$. Note that the colormaps refer to different values in the four plots.*

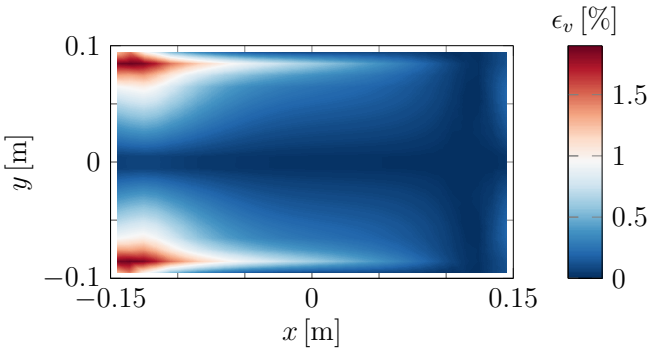


(a) *Model with no corrections at the boundaries.*

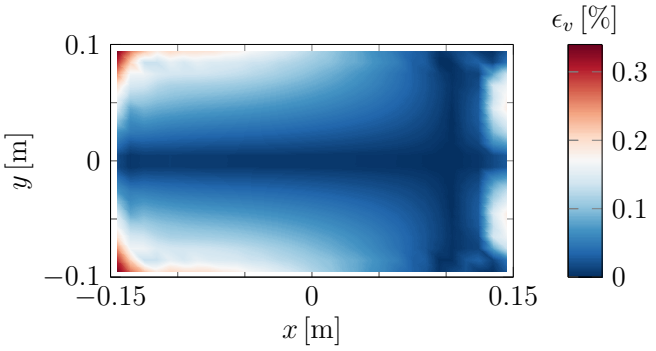


(b) *Model with corrections at the boundaries* ($n_{max} = 1$).

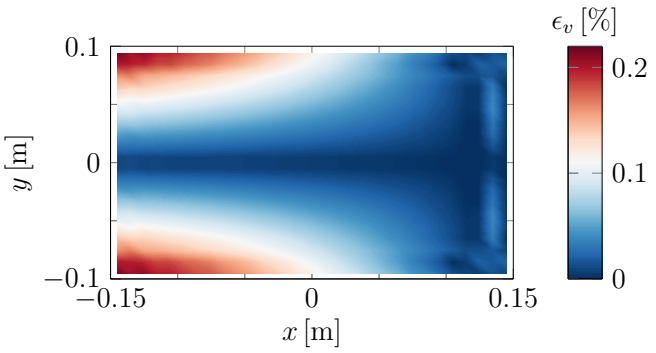


(c) *Model with corrections at the boundaries* ($n_{max} = 2$).

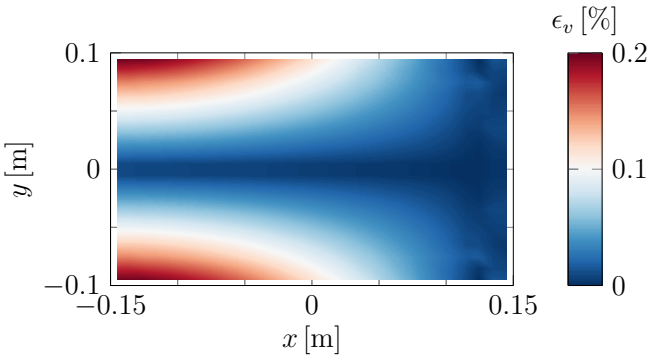


(d) *Model with corrections at the boundaries* ($n_{max} = 3$).

Figure 3.28: *Differences of the displacements in y direction between the peridynamic numerical results for* $\overline{m} = 3$ *and the reference solution (obtained with the Finite Element Method results, as shown in Figure 3.26) in the plate under the sinusoidal load obtained either without corrections at the boundary or by adopting the Taylor-based extrapolation method with different orders* $n_{max}$*. Note that the colormaps refer to different values in the four plots.*

## 3.6 Crack propagation near the boundaries

A qualitative study is hereinafter conducted to investigate the behavior of crack growth near the boundaries of the body. We compare the results provided by the proposed method with the solution obtained with peridynamics when no corrections for the surface effect are adopted and the boundary conditions are imposed in a local way, i.e., constraints and load are applied only at the nodes closest to the boundary. The surface effect near the new boundaries generated by the crack growth is not corrected in the present paper, but it will be dealt with in future works.

In order to model fracture phenomena, we introduce the scalar $\mu$ which yields the status of the bond (unbroken or broken) [65]:

$$\mu = \begin{cases} 1 & \text{if } \ s < s_c, \\ 0 & \text{otherwise,} \end{cases} \tag{3.69}$$

where $s$ is the stretch of the bond and $s_c$ is the critical stretch for plane stress conditions. These quantities are respectively computed as [171]

$$s = \frac{\|\boldsymbol{\xi} + \boldsymbol{\eta}\| - \|\boldsymbol{\xi}\|}{\|\boldsymbol{\xi}\|}\,, \tag{3.70}$$

$$s_c = \sqrt{\frac{4G_0}{9E\delta}}\,, \tag{3.71}$$

where $G_0$ is the energy release rate. The scalar $\mu$ is history-dependent since a broken bond cannot be restored. The equilibrium equation is therefore modified as

$$-\int_{\mathcal{H}_{\mathbf{x}}} \mu\, \mathbf{f}(\mathbf{x}, \mathbf{x}')\, \mathrm{d}V_{\mathbf{x}'} = \mathbf{b}_{\mathbf{x}}\,, \tag{3.72}$$

and the damage at each node can be evaluated as [65]

$$\varphi_{\mathbf{x}} = 1 - \frac{\int_{\mathcal{H}_{\mathbf{x}}} \mu\, \mathrm{d}V_{\mathbf{x}'}}{\int_{\mathcal{H}_{\mathbf{x}}} \mathrm{d}V_{\mathbf{x}'}}\,. \tag{3.73}$$

For the quasi-static crack propagation, the sequentially linear analysis used in [73] is employed:

- find the equilibrium with the given loads (if possible);
- if there are bonds with $s \geq s_c$, remove the contributions to the stiffness matrix of the 4 most stretched bonds;
- repeat the first steps until the equilibrium is not possible or there are no bonds with $s \geq s_c$.

Note that, when the Taylor-based extrapolation method is used, also the fictitious bonds can be broken along with the other bonds. If one or more fictitious bonds fail near a boundary

where a Neumann boundary condition is applied, then not only the stiffness matrix should be modified accordingly by removing the contributions of the broken bonds, but also the same external tension should be applied solely through the residual unbroken fictitious bonds.

### 3.6.1 Crack propagation due to Dirichlet boundary conditions

The geometry and the boundary conditions of a plate with a pre-existing crack are shown in Figure 3.29. The properties of the plate under plane stress conditions are: thickness $h = 0.005\,\text{m}$, Young's modulus $E = 1\,\text{GPa}$, Poisson's ratio $\nu = 0.2$ and energy release rate $G_0 = 196\,\text{J/m}^2$. The constraint is given as $\overline{u} = 0.001\,\text{m}$. A grid spacing $\Delta x = 0.0025\,\text{m}$ is used and $\overline{m} = 3$ is chosen.

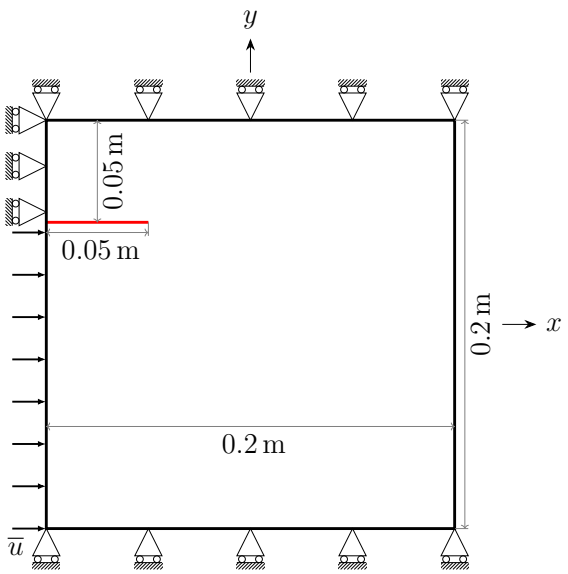


Figure 3.29: *Boundary conditions for a plate with a pre-existing crack (red line) for the case with Dirichlet boundary conditions.*

The results obtained by means of the peridynamic model with no corrections at the boundary and with the proposed method are compared in Figure 3.30, in which the difference of the displacements in a node $i$ is computed as

$$\boldsymbol{\epsilon}_i^{pd} = \begin{Bmatrix} \epsilon_u^{pd} \\ \epsilon_v^{pd} \end{Bmatrix}_i = \begin{Bmatrix} \dfrac{|u_i^{uncorr} - u_i^{corr}|}{\max(|\mathbf{u}^{corr}|)} \cdot 100 \\ \dfrac{|v_i^{uncorr} - v_i^{corr}|}{\max(|\mathbf{v}^{corr}|)} \cdot 100 \end{Bmatrix}, \tag{3.74}$$

where $\mathbf{u}^{corr}$ and $\mathbf{v}^{corr}$ are the displacement fields respectively in $x$ and $y$ directions. The superscript *uncorr* stands for "uncorrected" (peridynamic model with no corrections at the boundaries) and *corr* for "corrected" (peridynamic model with the Taylor-based extrapolation method with $n_{max} = 1$). It can be noticed that there are non-negligible differences near the crack tip that may lead to different crack paths.

As shown by the damage of the nodes in the final configuration of the model with no corrections (see Figure 3.31), the crack branches and reaches the upper edge of the plate in

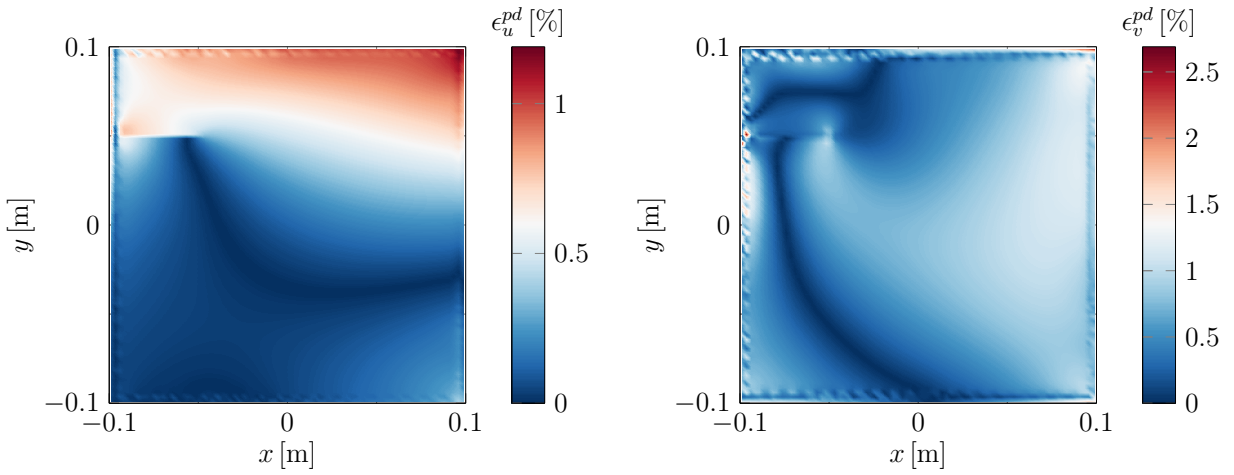


Figure 3.30: *Differences in the displacement fields (for $\overline{m} = 3$) of the pre-cracked plate computed with and without the Taylor-based extrapolation method for the case with Dirichlet boundary conditions. Note that the colormaps refer to different values in the two plots.*

two separated paths. On the other hand, when the Taylor-based extrapolation method is adopted, the crack propagates to the upper edge in a unique path and there is no branching phenomenon. Hence, the crack path may change near the boundaries if the surface effect is mitigated and the boundary conditions are imposed in a "peridynamic way".

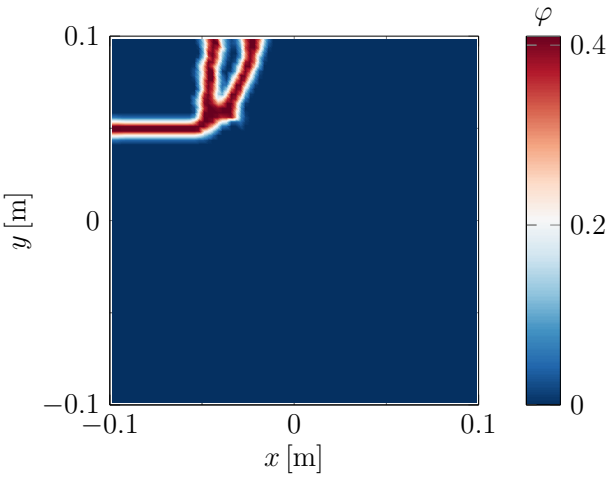


Figure 3.31: *Crack propagation in the pre-cracked plate for the case with Dirichlet boundary conditions when no correction at the boundaries are adopted.*

### 3.6.2 Crack propagation due to Neumann boundary conditions

The geometry and the boundary conditions of a plate with a pre-existing crack are shown in Figure 3.33. The properties of the plate under plane stress conditions are: thickness $h = 0.005\,\text{m}$, Young's modulus $E = 1\,\text{GPa}$, Poisson's ratio $\nu = 0.2$ and energy release rate $G_0 = 196\,\text{J/m}^2$. The plate is under a traction of $\overline{p} = 1\,\text{MPa}$. A grid spacing $\Delta x = 0.0025\,\text{m}$ is used and $\overline{m} = 3$ is chosen.

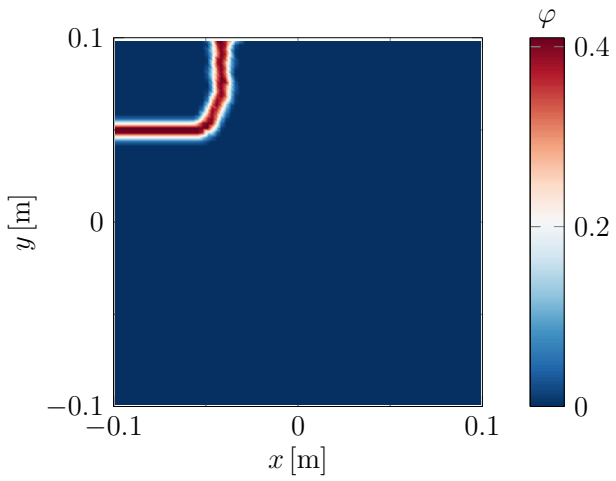


Figure 3.32: *Crack propagation in the pre-cracked plate for the case with Dirichlet boundary conditions when the Taylor-based extrapolation method is used.*

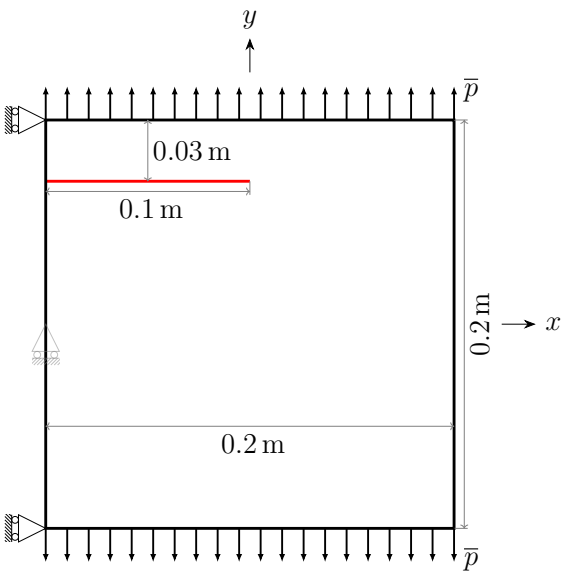


Figure 3.33: *Boundary conditions for a plate with a pre-existing crack (red line) for the case with Neumann boundary conditions.*

As in Section 3.6.1, the differences between the displacements obtained with and without the proposed method are computed as in Equation 3.74. The differences near the tip of the pre-existing crack (see Figure 3.34) are non-negligible and they may lead to different crack behaviors. The crack paths, shown in Figures 3.35 and 3.36 respectively for the case without and with boundary corrections, are indeed different between each other. Therefore, the crack behavior may be modified by the mitigation of the surface effect and the proper imposition of the Neumann boundary conditions.

## 3.7 Conclusions

Two issues arising near the boundary of a body modelled with ordinary state-based peridynamics are addressed:

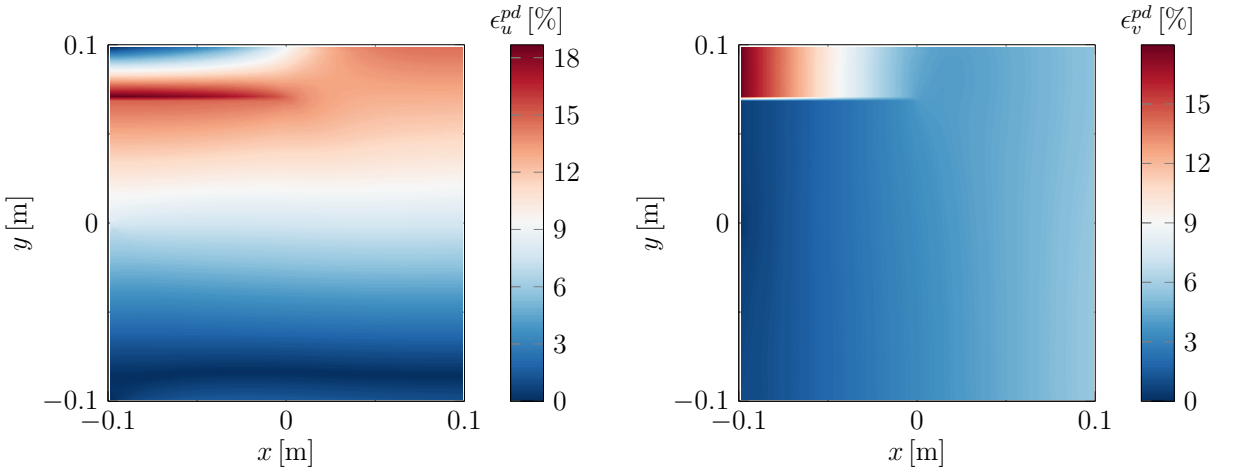


Figure 3.34: *Differences in the displacement fields (for $\overline{m} = 3$) of the pre-cracked plate computed with and without the Taylor-based extrapolation method for the case with Neumann boundary conditions. Note that the colormaps refer to different values in the two plots.*

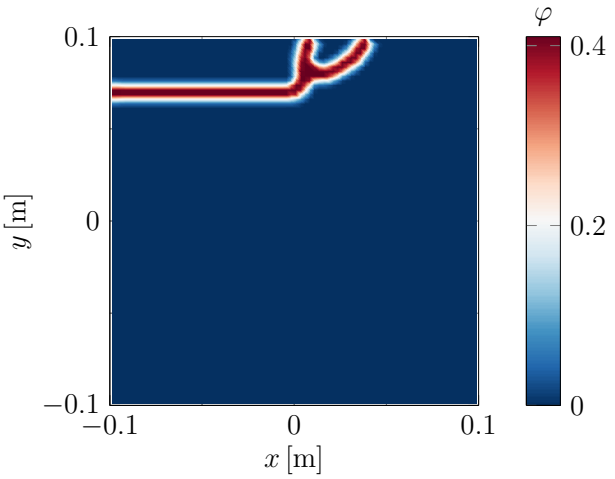


Figure 3.35: *Crack propagation in the pre-cracked plate for the case with Neumann boundary conditions when no correction at the boundaries are adopted.*

- the surface effect, i.e., the stiffness fluctuation near the boundary;
- the current lack of standard strategies to impose the boundary conditions.

The surface effect has been studied numerically by evaluating the peridynamic stress tensor with a novel discretization method (see Section 3.4.3) and the characteristic hardening/softening behavior towards the boundary has been highlighted (see Figures 3.7 and 3.8). This issue has been addressed by introducing a fictitious layer that completes the partial neighborhoods of the nodes near the boundary. We proposed a new version of the Taylor-based extrapolation method adopting the nearest-node strategy: the displacements of the fictitious nodes are expressed as functions of the displacements of the closest real nodes by means of multiple Taylor series expansions. In this way, the surface effect is mitigated.

The fictitious layer is also exploited to impose the boundary conditions in a peridynamic way. The boundary of the body is discretized by the so-called "boundary nodes". As the

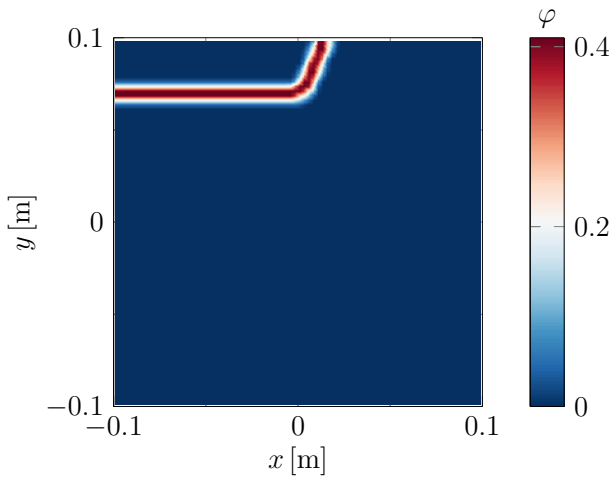


Figure 3.36: *Crack propagation in the pre-cracked plate for the case with Neumann boundary conditions when the Taylor-based extrapolation method is used.*

fictitious nodes, the boundary nodes do not constitute new degrees of freedom because their displacements are obtained with the Taylor-based extrapolation method. On the one hand, Dirichlet boundary conditions are implemented by constraining the boundary node and, accordingly, the fictitious layer mitigates the surface effect. On the other hand, Neumann boundary conditions are applied, via the numerical computation of the force flux at the boundary, to the bonds involving the fictitious nodes. Therefore, the boundary conditions are imposed in a "peridynamic way".

Several numerical examples were presented to verify the accuracy of the proposed method. The numerical results obtained with the Taylor-based extrapolation method show a great improvement with respect to the peridynamic models without corrections at the boundary. Furthermore, the order of the Taylor-based extrapolation can be increased until the undesired fluctuations of the numerical results become negligible for the application of interest. It is also shown that the numerical integration of the peridynamic equilibrium equation plays a fundamental role, so that the numerical results are improved even further by increasing the value of the $\overline{m}$-ratio.

Moreover, we carried out a qualitative study on crack propagation near the boundaries by comparing the results obtained by means of the proposed method with those of the peridynamic model without boundary corrections. We presented two numerical examples in which the crack paths are different because of the difference in the displacement fields. This highlights the importance of mitigating the surface effect and of imposing properly the peridynamic boundary conditions.

# Chapter 4

# A new surface node method to accurately model the mechanical behavior of the boundary in 3D state-based Peridynamics

**Published in:** *Journal of Peridynamics and Nonlocal Modeling* (2023)

**Authors:** Francesco Scabbia, Mirco Zaccariotto, Ugo Galvanetto

## Abstract

Peridynamics is a non-local continuum theory capable of modeling crack initiation and propagation in solid bodies. However, the layer near the boundary of the body exhibits a stiffness fluctuation due to the so-called *surface effect* and the inaccurate way of imposing the boundary conditions. Moreover, in numerical models discretized using the meshfree method with uniform grid spacing, there are no nodes on the external surface of the body where the boundary conditions should be applied. Inspired by the method of the fictitious nodes with the Taylor-based extrapolation, we propose an innovative method that introduces a new type of nodes lying on the external surface of the body, i.e., the *surface nodes*. These nodes represent the interactions between the nodes within the body and the fictitious nodes surrounding the body, and they are used to mitigate the surface effect and properly impose the boundary conditions via the concept of force flux. Moreover, a procedure to compute the analytical solution of peridynamic problems is developed: a *manufactured* displacement field is prescribed and the volume and surface forces, to obtain that displacement field, are computed. The benefits of the surface node method are shown by means of several 2D and 3D quasi-static examples by comparing the numerical results with other methods with or without boundary corrections.

**Keywords:** Surface node method, manufactured solution, 3D force flux, surface effect, boundary conditions, numerical method.

## 4.1 Introduction

Peridynamics is a non-local continuum theory of solid mechanics devised to intrinsically model discontinuities in the displacement field, such as crack initiation and propagation [61, 62]. This is possible because peridynamic equations do not contain any spatial derivatives, but only integrals. Peridynamic points interact with each other if their distance is smaller than or equal to a prescribed value $\delta$, called the *horizon size*. Therefore, the interactions of a point are contained in a sphere, named *neighborhood*, centered in that point with a radius $\delta$.

The most commonly used method to solve numerically peridynamic integrals is a uniform meshfree discretization with a mid-point quadrature rule [65, 158, 184, 235]. In the literature, there are many examples of the good agreement of peridynamic results compared to mechanical experiments involving fracture [72, 74]. Nonetheless, the non-local nature of Peridynamics leads to three main drawbacks:

- higher computational cost with respect to numerical models based on classical continuum mechanics, such as the Finite Element Method (FEM);
- undesired stiffness fluctuations near the boundary of the body, known as *surface effect* or *skin effect*;
- difficulty in imposing properly the boundary conditions.

The coupling between Peridynamics and FEM can be exploited to reduce the computational cost: Peridynamics is used only where cracks are more likely to propagate, whereas FEM-based approaches are used for the rest of the domain [115, 165, 171, 205, 206, 208, 209, 213, 214, 228–230]. The surface effect is due to the fact that the neighborhoods near the boundary of the body are incomplete, so that the most external layer of the body has different stiffness properties with respect to the bulk of the body [186, 187, 198, 226, 227, 236]. Another issue related to the boundary is that external loads and constraints should be distributed over a layer of finite thickness near the boundary [63], but the definition of a standard method for imposing non-local boundary conditions is problematic.

Both the surface effect and the problem of the imposition of the non-local boundary conditions can be reduced by decreasing the horizon size $\delta$ near the boundary with the variable horizon method [149, 193, 195, 198, 204, 215, 216]. However, this approach inevitably varies the peridynamic solution where the value of $\delta$ is modified. The mechanical properties of the interactions between nodes near the boundary can be tuned to correct the surface effect [63, 64, 187–190], but the peridynamic solution exhibits some undesired fluctuations near the boundary because of the inaccurate imposition of the boundary conditions [186]. Another approach implies the reformulation of the peridynamic equations via the peridynamic differential operator [237–241].

The method of the *fictitious nodes* is arguably the most commonly used to mitigate the boundary issues: a layer of nodes is added all around the body to complete the neighborhoods of the nodes close to the boundary, thus the surface effect vanishes [148, 188, 191]. However, the displacements of the fictitious nodes are unknown and may be extrapolated

with the displacements of the nodes within the body. Many authors suggested that this extrapolation can be used to enforce boundary conditions [63, 92, 126, 150, 151, 186, 192–196], but the formulae they used are case-dependent and applicable only to simple geometries. On the other hand, we proposed in [227, 236] that the non-local concept of force flux, i.e., the peridynamic version of stress, should be exploited to coherently impose the boundary conditions. Furthermore, we employed the extrapolation based on the Taylor series expansion, with a general truncation order $N$, which adopts the nearest-node strategy, to manage more complex body geometry. Nevertheless, the method we proposed is limited to 2-dimensional cases and makes use of the Lagrange multipliers to impose the boundary conditions. The main disadvantages in imposing the boundary conditions via Lagrange multipliers are related to the structure of the matrix to solve [225, 242]:

- the dimensions of the matrix increase because of the higher number of unknowns;
- the matrix is not, in general, positive definite;
- the matrix is not banded;
- there are zeroes on the diagonal of the matrix.

Clearly, these characteristics make the matrix more computationally expensive to invert.

Inspired by [227, 236], this paper aims at developing a novel numerical method to impose the boundary conditions in peridynamic models without the use of Lagrange multipliers. We introduce a new type of nodes, the *surface nodes*, that represent the external surface of the body. The surface nodes have their own degrees of freedom that can be used during the Taylor-based extrapolation of the displacements. The equations of motion of the surface nodes are based on the concept of force flux, thus they represent the interactions between the fictitious nodes and the nodes within the body. Thanks to this fact, the boundary conditions can be applied directly to the surface nodes, as one would do in a local model, without the use of the Lagrange multipliers. The number of unknowns is still higher than that of a model without corrections at the boundary, but the new unknowns have the physical meaning of the displacements of the external surface of the body. The stiffness matrix is still not, in general, positive definite, but its bandwidth remains the same as that of the peridynamic system without corrections to the boundary issues and there are no zeroes on its diagonal. Hence, the numerical solution to the system of equations can be found more efficiently by a computational standpoint. Furthermore, with respect to the previous method of the fictitious nodes, the surface node method allows for a simpler implementation (the boundary conditions are imposed as one would do in a local model). 3D static numerical examples are presented to show the benefits achieved by the new method. In Appendix 4.A, we also developed a procedure to obtain the peridynamic analytical solutions, which are then employed to compute the errors in the numerical models. The comparison with other methods recently developed to correct the surface effect and impose the peridynamic boundary conditions is provided as well.

The paper is organized as follows: Section 4.2 reviews briefly the main equations of ordinary state-based Peridynamics and the method of the fictitious layer to correct the boundary

issues; Section 4.3 presents the numerical implementation of the novel method of the surface nodes; Section 4.4 shows the differences between the models with and without the use of the method of the surface nodes; Section 4.5 compares the proposed method with three of the most recent methods for boundary corrections; Section 4.6 draws the conclusions. Furthermore, Appendix 4.A shows a procedure to compute the analytical solutions for peridynamic problems when prescribing an (even complex) displacement field.

## 4.2 Review of peridynamic theory

A peridynamic interaction between neighboring points $\mathbf{x}$ and $\mathbf{x}'$ is called *bond* and is identified by the relative position vector in the initial configuration as

$$\boldsymbol{\xi} = \mathbf{x}' - \mathbf{x}\,, \tag{4.1}$$

where $\|\boldsymbol{\xi}\| \leq \delta$. Therefore, point $\mathbf{x}$ interacts with all the points in the neighborhood $\mathcal{H}_{\mathbf{x}} = \left\{\mathbf{x}' \in \mathcal{B}(t_0) : \|\boldsymbol{\xi}\| \leq \delta\right\}$, where $\mathcal{B}(t_0)$ is the body in the initial configuration and $\delta$ is the horizon size, as shown in Figure 4.1. The relative displacement vector $\boldsymbol{\eta}$ is defined in the deformed configuration $\mathcal{B}(t)$ at time $t > t_0$ as

$$\boldsymbol{\eta} = \mathbf{u}(\mathbf{x}', t) - \mathbf{u}(\mathbf{x}, t)\,, \tag{4.2}$$

where $\mathbf{u}$ is the displacement field. Note that $\boldsymbol{\xi} + \boldsymbol{\eta}$ is the relative position of points $\mathbf{x}$ and $\mathbf{x}'$ in the deformed configuration.

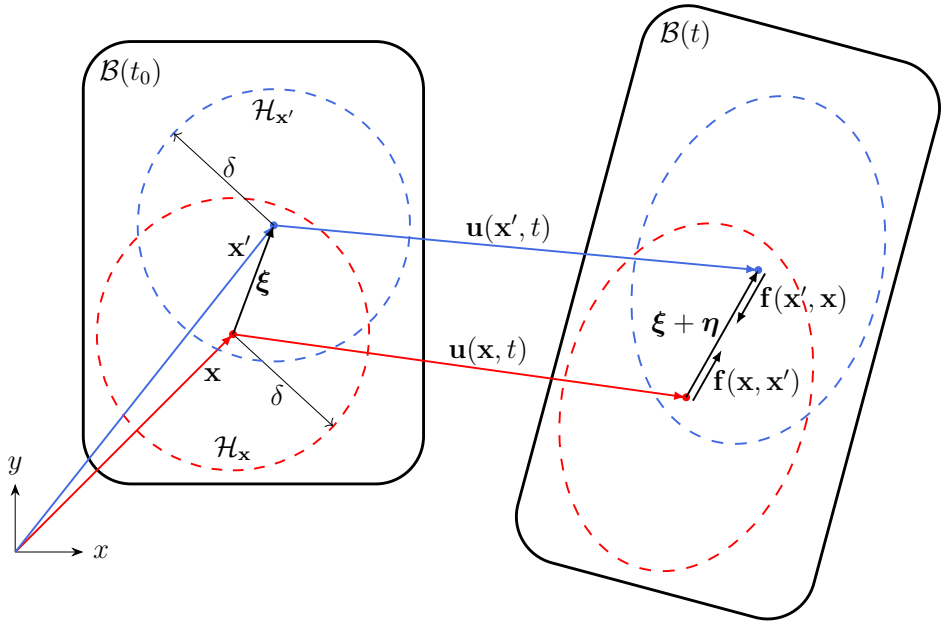


Figure 4.1: *Body modelled with Peridynamics in the initial configuration* $\mathcal{B}(t_0)$ *and deformed configuration* $\mathcal{B}(t > t_0)$*: the force state* $\mathbf{f}$ *arises due to the deformation of the body.*

The peridynamic equation of motion of a point $\mathbf{x}$ is given by [61, 62]:

$$\rho(\mathbf{x})\,\ddot{\mathbf{u}}(\mathbf{x},t) = \int_{\mathcal{H}_\mathbf{x}} \mathbf{f}(\mathbf{x},\mathbf{x}',t)\,\mathrm{d}V_{\mathbf{x}'} + \mathbf{b}(\mathbf{x},t)\,, \tag{4.3}$$

where $\rho$ is the material density, $\ddot{\mathbf{u}}$ is the acceleration field, $\mathbf{f}$ is the force state (force per unit volume squared), $\mathrm{d}V_{\mathbf{x}'}$ is the differential volume of a point $\mathbf{x}'$ within the neighborhood $\mathcal{H}_\mathbf{x}$ and $\mathbf{b}$ is the external force density field. In quasi-static conditions, Equation 4.3 becomes the equilibrium equation of point $\mathbf{x}$:

$$-\int_{\mathcal{H}_\mathbf{x}} \mathbf{f}(\mathbf{x},\mathbf{x}')\,\mathrm{d}V_{\mathbf{x}'} = \mathbf{b}(\mathbf{x})\,. \tag{4.4}$$

The value of $\mathbf{f}(\mathbf{x},\mathbf{x}')$ is determined in the following.

### 4.2.1 Ordinary state-based Peridynamics

The reference position scalar state $\underline{x}$ represents the bond length in the initial configuration:

$$\underline{x} = \|\boldsymbol{\xi}\|\,. \tag{4.5}$$

On the other hand, the extension scalar state $\underline{e}$ represents the elongation (or contraction) of the bond in the deformed configuration:

$$\underline{e} = \|\boldsymbol{\xi}+\boldsymbol{\eta}\| - \|\boldsymbol{\xi}\|\,. \tag{4.6}$$

Hereinafter, the Gaussian influence function is adopted:

$$\underline{\omega} = \exp\left(-\frac{\|\boldsymbol{\xi}\|^2}{\delta^2}\right) \tag{4.7}$$

For later use, the weighted volume $m$ and the dilatation $\theta$ of a point $\mathbf{x}$ are defined respectively as

$$m(\mathbf{x}) = \int_{\mathcal{H}_\mathbf{x}} \underline{\omega}\,\underline{x}^2\,\mathrm{d}V_{\mathbf{x}'}\,, \tag{4.8}$$

$$\theta(\mathbf{x}) = \frac{c_\theta}{m(\mathbf{x})}\int_{\mathcal{H}_\mathbf{x}} \underline{\omega}\,\underline{x}\,\underline{e}\,\mathrm{d}V_{\mathbf{x}'}\,, \tag{4.9}$$

where $c_\theta$=3 [62].

In ordinary state-based Peridynamics, the force state is aligned with the bond direction for any deformation, as depicted in Figure 4.1. The bond direction is defined as

$$\mathbf{m} = \frac{\boldsymbol{\xi}+\boldsymbol{\eta}}{\|\boldsymbol{\xi}+\boldsymbol{\eta}\|}\,. \tag{4.10}$$

Hence, the force state can be computed as [62]

$$\mathbf{f}(\mathbf{x},\mathbf{x}') = \left[k_\theta\left(\frac{\theta(\mathbf{x})}{m(\mathbf{x})}+\frac{\theta(\mathbf{x}')}{m(\mathbf{x}')}\right)\underline{\omega}\,\underline{x} + k_e\left(\frac{1}{m(\mathbf{x})}+\frac{1}{m(\mathbf{x}')}\right)\underline{\omega}\,\underline{e}\right]\mathbf{m}\,, \tag{4.11}$$

with $k_\theta = -3(1-4\nu)E/(2(1+\nu)(1-2\nu))$ and $k_e = 15E/(2(1+\nu))$, where $\nu$ is the Poisson's ratio and $E$ is the Young's modulus. The constants $k_\theta$ and $k_e$ are derived by equalizing the peridynamic strain energy density of a point with a complete neighborhood under homogeneous deformation, with the strain energy density in a point subjected to the same deformation in classical continuum mechanics [62].

### 4.2.2 Force flux

Suppose that the force flux $\boldsymbol{\tau}$, i.e., the peridynamic concept of stress, should be computed at a point $\mathbf{x}$ in the direction of the unit vector $\mathbf{n}$. As shown in Figure 4.2, the plane with normal $\mathbf{n}$ passing through point $\mathbf{x}$ is named $\mathcal{P}$. The unit sphere $\Omega$ centered in $\mathbf{x}$ represents all the directions that the bonds passing through $\mathbf{x}$ may have, and $\mathrm{d}\Omega_{\mathbf{m}}$ is the differential solid angle on $\Omega$ in direction $\mathbf{m}$ of the considered bond. In order for the bond to pass through the plane $\mathcal{P}$, the points of that bond must lie in the different half-spaces generated by $\mathcal{P}$. Therefore, we define the points of a bond in the direction $\mathbf{m}$ as $\mathbf{x}' = \mathbf{x} - s\mathbf{m}$ and $\mathbf{x}'' = \mathbf{x} + (r-s)\mathbf{m}$, where $0 \leq s \leq \delta$ and $s \leq r \leq \delta$ (see Figure 4.2).

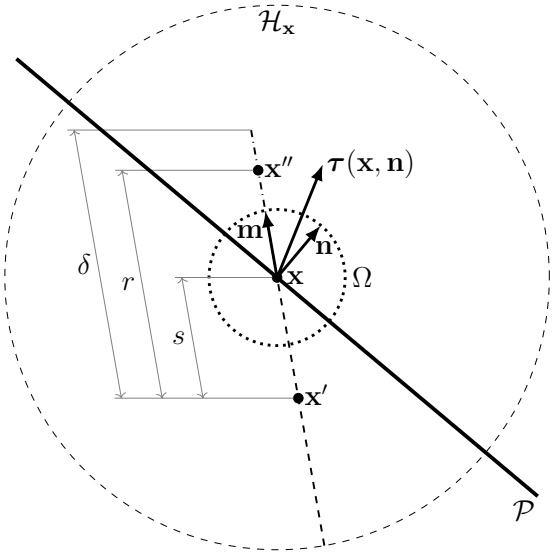


Figure 4.2: *The force flux $\boldsymbol{\tau}(\mathbf{x},\mathbf{n})$ computed at point $\mathbf{x}$ in direction $\mathbf{n}$ is the resultant of the forces per unit area of all the bonds passing through plane $\mathcal{P}$ with normal $\mathbf{n}$. The bonds may have any direction $\mathbf{m}$ within the unit sphere $\Omega$ and the two points of the bond are defined by the values $s$ and $r$ as $\mathbf{x}' = \mathbf{x} - s\mathbf{m}$ and $\mathbf{x}'' = \mathbf{x} + (r-s)\mathbf{m}$, where $0 \leq s \leq \delta$ (dashed line) and $s \leq r \leq \delta$ (dashdotted line).*

The force flux is defined as the resultant of the forces per unit area of all the bonds intersecting $\mathcal{P}$ in $\mathbf{x}$ [172]:

$$\boldsymbol{\tau}(\mathbf{x},\mathbf{n}) = \frac{1}{2}\int_\Omega \int_0^\delta \int_s^\delta \mathbf{f}(\mathbf{x}',\mathbf{x}'')\,(\mathbf{m}\cdot\mathbf{n})\; r^2\,\mathrm{d}r\,\mathrm{d}s\,\mathrm{d}\Omega_{\mathbf{m}}\,. \tag{4.12}$$

The factor $(\mathbf{m}\cdot\mathbf{n})$ in the integrand is required to project the force state along the direction $\mathbf{n}$. Note that the integration limits in Equation 4.12 allow to consider every bond passing through point $\mathbf{x}$. However, each bond is repeated twice in the integration domain (for both

directions $\mathbf{m}$ and $-\mathbf{m}$), thus the integral is divided by 2.

### 4.2.3 Problems at the boundaries

The non-local formulation of the peridynamic theory exhibits two issues near the boundary: the so-called surface effect and the difficulty of imposing properly the boundary conditions. The former is due to the incomplete neighborhoods of points close to the boundary of the body [186], as shown in Figure 4.3. The mechanical properties of peridynamic materials are indeed computed for points with a complete neighborhood, i.e., in the bulk of the body. Note that the lacking part of the neighborhood increases as the points are near the faces, the edges, or the vertices of the body, hence the stiffness fluctuations due to the surface effect are expected to increase accordingly [236].

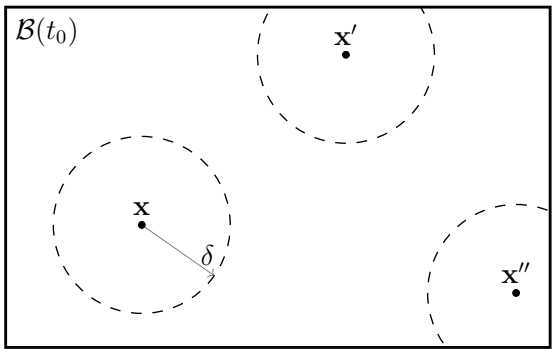


Figure 4.3: *Some points in the bulk, as* $\mathbf{x}$*, have a complete neighborhood, whereas other points near the boundary, as* $\mathbf{x}'$ *and* $\mathbf{x}''$*, have an incomplete neighborhood.*

In local models, boundary conditions are imposed on the points lying on the boundary. This is possible because, for instance, a force applied to a point has a "local" influence only on that point. On the other hand, in non-local models such as Peridynamics, a force applied to a point influences a spherical region surrounding that point (see the concept of force flux in Section 4.2.2). Therefore, peridynamic boundary conditions should be imposed in a layer of finite thickness near the boundary of the body. Nonetheless, how to "distribute" the boundary conditions over a finite layer of material is still an open issue in Peridynamics.

### 4.2.4 Method of the fictitious layer

The addition of a layer $\mathcal{F}$ of fictitious points of thickness $\delta$ around the body is a simple way to complete the neighborhoods of the points near the boundary [148], as shown in Figure 4.4. The displacements of the fictitious points are evaluated by means of an extrapolation procedure in order to ensure that the fictitious layer keeps deforming as the body.

We adopt the Taylor-based extrapolation method with the nearest-node strategy for its simplicity [227, 236]. The displacement vector of a point $\mathbf{x}_f = \{x_f, y_f, z_f\}^\top$ in the fictitious layer $\mathcal{F}$ is determined as the Taylor series expansion truncated at a general order $N \geq 1$

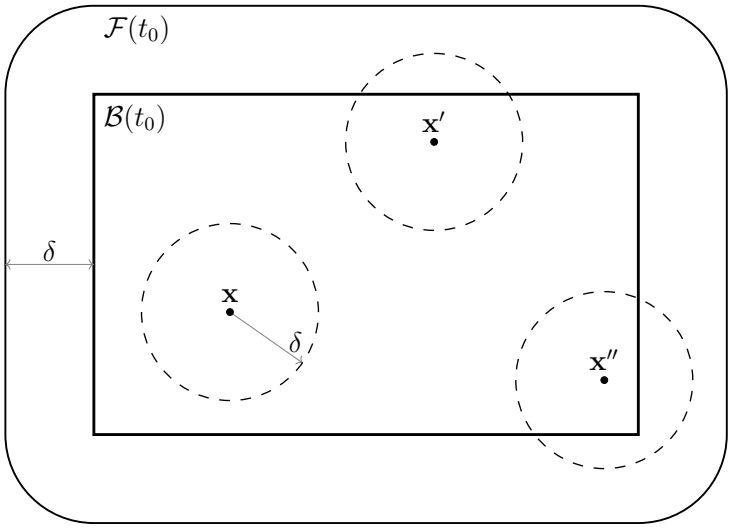


Figure 4.4: *When a fictitious layer of thickness $\delta$ is added around the body, all the points of the body have a complete neighborhood.*

about the closest point $\mathbf{x}_c = \{x_c, y_c, z_c\}^\top$ of the body:

$$\mathbf{u}(\mathbf{x}_f) = \mathbf{u}(\mathbf{x}_c) + \sum_{n=1}^{N} \sum_{n_1=0}^{n} \sum_{n_2=0}^{n-n_1} \frac{(x_f - x_c)^{n_1} (y_f - y_c)^{n_2} (z_f - z_c)^{n_3}}{n_1!\, n_2!\, n_3!} \frac{\partial^{n_1+n_2+n_3} \mathbf{u}(\mathbf{x}_c)}{\partial x^{n_1}\, \partial y^{n_2}\, \partial z^{n_3}}\,, \tag{4.13}$$

where $n_3 = n - n_1 - n_2$. Note that the points of the body closest to the fictitious points are the ones at the boundary of the body itself. To mitigate the surface effect, the weighted volume of the fictitious points is computed as if their neighborhoods were complete, thus $m(\mathbf{x}_f) = m(\mathbf{x}_c)$. Moreover, since the dilatation is a measure of strain, that of the fictitious points is evaluated by means of a Taylor series expansion as in Equation 4.13 with a truncation order $N - 1$. If the displacements are extrapolated with a truncation order $N = 1$, then the dilatation of a fictitious point is equal to the dilatation of the closest point of the body: $\theta(\mathbf{x}_f) = \theta(\mathbf{x}_c)$. Otherwise for $N \geq 2$, the dilatation of a fictitious point is determined as

$$\theta(\mathbf{x}_f) = \theta(\mathbf{x}_c) + \sum_{n=1}^{N-1} \sum_{n_1=0}^{n} \sum_{n_2=0}^{n-n_1} \frac{(x_f - x_c)^{n_1}}{n_1!} \frac{(y_f - y_c)^{n_2}}{n_2!} \frac{(z_f - z_c)^{n_3}}{n_3!} \frac{\partial^{n_1+n_2+n_3} \theta(\mathbf{x}_c)}{\partial x^{n_1}\, \partial y^{n_2}\, \partial z^{n_3}}\,, \tag{4.14}$$

where $n_3 = n - n_1 - n_2$.

The Taylor-based extrapolation method is able to correct the surface effect when the truncation order $N$ matches the order of the displacement field: for instance, if the displacements vary linearly, a Taylor series expansion with $N = 1$ exactly extrapolates the displacements in the fictitious layer. For a displacement field of general order, more accurate results are obtained by increasing the truncation order.

In order to impose the boundary conditions in a non-local way, the equation which governs the behavior of the points at the boundary of the body is based on the concept of force flux [227, 236]:

$$\boldsymbol{\tau}(\mathbf{x}_c, \mathbf{n}) = \mathbf{p}(\mathbf{x}_c)\,, \tag{4.15}$$

where $\mathbf{n}$ is the outward unit vector normal to the boundary in $\mathbf{x}_c$ and $\mathbf{p}$ is the force per unit area applied to $\mathbf{x}_c$. Because of the definition of force flux (Equation 4.12), the external load $\mathbf{p}$ is "spread", in a non-local way, within the most external layer of the body via the bonds that are passing through $\mathbf{x}_c$.

## 4.3 Method of the surface nodes

In this section, we show how to implement the method of the fictitious layer in a numerical peridynamic model via the introduction of the surface nodes. The body domain and the fictitious layer are discretized by adopting the meshfree method with a uniform grid spacing $h$ [65, 184], as shown in Figure 4.5. The nodes within the body and the fictitious layer are respectively called *interior nodes* and *fictitious nodes*. Each node of the grid is representative of a cell with cubic volume $V = h^3$. Since the boundary conditions are imposed on the external surface of the body, we add a new type of nodes, namely the *surface nodes* (marked by solid squares in Figure 4.5), near the most external interior nodes. Each surface node represents a cell face of one of the interior nodes closest to the boundary, i.e., a square area $A = h^2$ of the external surface of the body. Note that, since the surface nodes do not represent a volume cell, they do not have the properties of weighted volume and dilatation. Indeed, a surface node is not connected to any bond but is related to the bonds that intersect its area, as explained in Section 4.3.4.

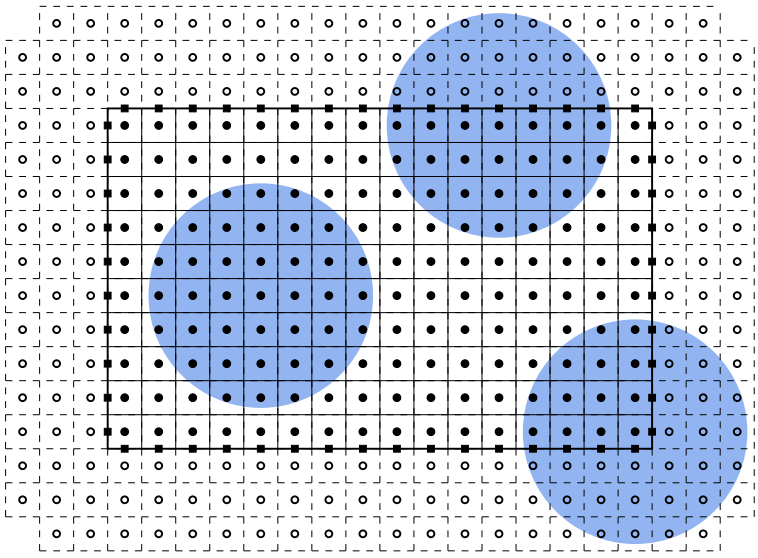

Figure 4.5: *Uniform peridynamic grid of interior nodes (solid circles) and fictitious nodes (empty circles), with the introduction of the surface nodes (solid squares) on the external surface of the body.*

### 4.3.1 Numerical force states

Consider two nodes $i$ and $j$ that are connected by the bond

$$\boldsymbol{\xi}_{ij} = \mathbf{x}_j - \mathbf{x}_i \,. \tag{4.16}$$

Surface nodes are not connected to any bond, therefore nodes $i$ and $j$ can be either interior or fictitious nodes. The relative displacement vector of this bond after the deformation of the body is computed as

$$\boldsymbol{\eta}_{ij} = \mathbf{u}_j - \mathbf{u}_i \,, \tag{4.17}$$

where $\mathbf{u}_i$ and $\mathbf{u}_j$ are the displacement vectors of nodes $i$ and $j$, respectively. If one of these nodes is in the fictitious layer, then its displacements are determined by the Taylor-based extrapolation method described in Subsection 4.3.2. The reference position scalar state and the influence function of the bond are evaluated as follows:

$$\underline{x}_{ij} = \|\boldsymbol{\xi}_{ij}\| \,, \tag{4.18}$$

$$\underline{\omega}_{ij} = \exp\left(-\frac{\|\boldsymbol{\xi}_{ij}\|^2}{\delta^2}\right) . \tag{4.19}$$

Under the assumption of small displacements, the bond direction vector is given as

$$\mathbf{m}_{ij} = \frac{\boldsymbol{\xi}_{ij} + \boldsymbol{\eta}_{ij}}{\|\boldsymbol{\xi}_{ij} + \boldsymbol{\eta}_{ij}\|} \overset{\|\boldsymbol{\eta}_{ij}\| \ll \|\boldsymbol{\xi}_{ij}\|}{\approx} \frac{\boldsymbol{\xi}_{ij}}{\|\boldsymbol{\xi}_{ij}\|} \,. \tag{4.20}$$

Similarly, the extension scalar state of the bond is computed as

$$\underline{e}_{ij} = \|\boldsymbol{\xi}_{ij} + \boldsymbol{\eta}_{ij}\| - \|\boldsymbol{\xi}_{ij}\| \overset{\|\boldsymbol{\eta}_{ij}\| \ll \|\boldsymbol{\xi}_{ij}\|}{\approx} \boldsymbol{\eta}_{ij} \cdot \frac{\boldsymbol{\xi}_{ij}}{\|\boldsymbol{\xi}_{ij}\|} \approx \boldsymbol{\eta}_{ij} \cdot \mathbf{m}_{ij} \,. \tag{4.21}$$

In the discretized model, the integrals over the neighborhood $\mathcal{H}_i$ of a node $i$ are evaluated numerically as the summation for each node $j$ with a portion of the cell within $\mathcal{H}_i$, as shown in Figure 4.6. Therefore, the weighted volume $m_i$ and the dilatation $\theta_i$ of a node $i$ are determined from Equations 4.8 and 4.9 as

$$m_i = \sum_{j \in \mathcal{H}_i} \underline{\omega}_{ij} \, \underline{x}_{ij}^2 \, \beta_{ij} V_j \,, \tag{4.22}$$

$$\theta_i = \frac{3}{m_i} \sum_{j \in \mathcal{H}_i} \underline{\omega}_{ij} \, \underline{x}_{ij} \, \underline{e}_{ij} \, \beta_{ij} V_j \,, \tag{4.23}$$

where $\beta_{ij} V_j$ represents the quadrature weight, with $V_j = V(\mathbf{x}_j)$. Note that, since surface nodes are representative of the external surface of the body, they do not have weighted volumes or dilatations which are volume properties. The quadrature coefficient $\beta_{ij}$ is computed as the volume fraction of the cell lying within the neighborhood [184, 235]. If the cell of node $j$ is completely within the neighborhood, then $\beta_{ij} = 1$, otherwise $0 < \beta_{ij} < 1$, as shown in Figure 4.6. The algorithm to compute accurately the quadrature coefficients in 3D peridynamic problems can be found in [235].

Therefore, the force state of the bond is computed from Equation 4.11 as

$$\mathbf{f}_{ij} = \left[ k_\theta \left( \frac{\theta_i}{m_i} + \frac{\theta_j}{m_j} \right) \underline{\omega}_{ij} \, \underline{x}_{ij} + k_e \left( \frac{1}{m_i} + \frac{1}{m_j} \right) \underline{\omega}_{ij} \, \underline{e}_{ij} \right] \mathbf{m}_{ij} \,. \tag{4.24}$$

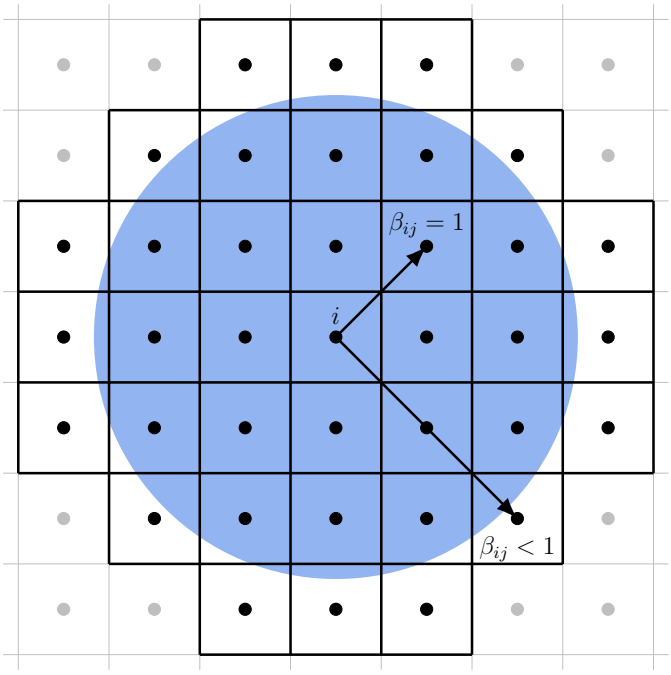


Figure 4.6: *The neighborhood $\mathcal{H}_i$ of a node $i$ is constituted by the nodes (black dots) with a portion of their cell within the neighborhood (blue area). The quadrature coefficient $\beta_{ij}$ is the volume fraction of cell of node $j$ lying inside the neighborhood.*

If either node $i$ or node $j$ is fictitious, then its weighted volume and dilatation are determined by the Taylor-based extrapolation method described in Subsection 4.3.2.

### 4.3.2 Numerical Taylor-based extrapolation method

The Taylor-based extrapolation method with the nearest-node strategy is employed to determine the values of the displacements, weighted volumes, and dilatations of the fictitious nodes as a function of the corresponding values of the interior nodes. This method has been described in [227, 236]. However, the use of the surface nodes introduces new degrees of freedom in the numerical model, in addition to the degrees of freedom of the interior nodes, and the Taylor-based extrapolation method should be adapted accordingly.

The weighted volumes and dilatations of interior nodes are numerically computed in Equations 4.22 and 4.23, respectively. The fictitious nodes are used to complete the neighborhoods of the interior nodes close to the boundary of the body, as shown in Figure 4.5. Therefore, all the interior nodes have the same value of the weighted volume. This value is assigned also to the weighted volumes of the fictitious nodes, as dictated by the Taylor-based extrapolation method.

Suppose that $N$ is the order of truncation of the Taylor series expansions to extrapolate the displacements of the fictitious nodes. If $N = 1$, then the dilatation of a fictitious node is equal to the dilatation of the closest interior node. Otherwise, the dilatations should be extrapolated with Taylor expansions truncated at the order $N-1$. The numerical procedure to determine the dilatation $\theta_f$ of a fictitious node $\mathbf{x}_f$ is carried out as follows:

1. find the interior node $\mathbf{x}_b$ which is the closest to node $\mathbf{x}_f$;

2. perform a Taylor series expansion of $\theta_f = \theta(\mathbf{x}_f)$ about node $\mathbf{x}_b$:

$$\theta_f = \theta_b + \sum_{n=1}^{N-1} \sum_{n_1=0}^{n} \sum_{n_2=0}^{n-n_1} \frac{(x_f - x_b)^{n_1}}{n_1!} \frac{(y_f - y_b)^{n_2}}{n_2!} \frac{(z_f - z_b)^{n_3}}{n_3!} \frac{\partial^{n_1+n_2+n_3} \theta_b}{\partial x^{n_1} \partial y^{n_2} \partial z^{n_3}}, \quad (4.25)$$

where $n_3 = n - n_1 - n_2$;

3. find the interior nodes $\mathbf{x}_{b_k}$ closest to $\mathbf{x}_b$ so that the set of found nodes includes at least $n_1$ different $x_{b_k}$ coordinates, $n_2$ different $y_{b_k}$ coordinates and $n_3$ different $z_{b_k}$ coordinates for each derivative in Equation 4.25, where $n_1$, $n_2$ and $n_3$ are the possible orders of the derivative in the three directions;

4. for each of the found nodes $k$, perform a Taylor series expansion of their dilatations $\theta_{b_k} = \theta(\mathbf{x}_{b_k})$ about node $\mathbf{x}_b$:

$$\theta_{b_k} = \theta_b + \sum_{n=1}^{N-1} \sum_{n_1=0}^{n} \sum_{n_2=0}^{n-n_1} \frac{(x_{b_k} - x_b)^{n_1}}{n_1!} \frac{(y_{b_k} - y_b)^{n_2}}{n_2!} \frac{(z_{b_k} - z_b)^{n_3}}{n_3!} \frac{\partial^{n_1+n_2+n_3} \theta_b}{\partial x^{n_1} \partial y^{n_2} \partial z^{n_3}}; \quad (4.26)$$

5. solve the system of equations in Equation 4.26 to obtain the derivatives of $\theta_b$ as a function of the dilatations $\theta_b$ and $\theta_{b_k}$:

$$\frac{\partial^{n_1+n_2+n_3} \theta_b}{\partial x^{n_1} \partial y^{n_2} \partial z^{n_3}} = f(\theta_b, \theta_{b_k}); \quad (4.27)$$

6. substitute Equation 4.27 in Equation 4.25 to obtain the dilatation of the fictitious node as a function of the dilatations of the interior nodes:

$$\theta_f = f(\theta_b, \theta_{b_k}). \quad (4.28)$$

On the other hand, the surface nodes can be included in the Taylor-based extrapolation method for the displacements to improve the accuracy of the procedure. Thus, the numerical procedure to determine the displacement vector $\mathbf{u}_f$ of a fictitious node $\mathbf{x}_f$ is carried out as follows:

7. find the surface node $\mathbf{x}_s$ which is the closest to node $\mathbf{x}_f$;

8. perform a Taylor series expansion of $\mathbf{u}_f = \mathbf{u}(\mathbf{x}_f)$ about node $\mathbf{x}_s$:

$$\mathbf{u}_f = \mathbf{u}_s + \sum_{n=1}^{N} \sum_{n_1=0}^{n} \sum_{n_2=0}^{n-n_1} \frac{(x_f - x_s)^{n_1}}{n_1!} \frac{(y_f - y_s)^{n_2}}{n_2!} \frac{(z_f - z_s)^{n_3}}{n_3!} \frac{\partial^{n_1+n_2+n_3} \mathbf{u}_s}{\partial x^{n_1} \partial y^{n_2} \partial z^{n_3}}, \quad (4.29)$$

where $n_3 = n - n_1 - n_2$;

9. add to the set of interior nodes $\mathbf{x}_{b_k}$ found in Step 3 the surface nodes closest to $\mathbf{x}_s$ so that the new set of found nodes $\mathbf{x}_{s_q}$ includes at least $n_1$ different $x_{s_q}$ coordinates, $n_2$ different $y_{s_q}$ coordinates and $n_3$ different $z_{s_q}$ coordinates for each derivative in Equation 4.29;

10. for each of the found nodes $q$, perform a Taylor series expansion of their displacement vectors $\mathbf{u}_{s_q} = \mathbf{u}(\mathbf{x}_{s_q})$ about node $\mathbf{x}_s$:

$$\mathbf{u}_{s_q} = \mathbf{u}_s + \sum_{n=1}^{N} \sum_{n_1=0}^{n} \sum_{n_2=0}^{n-n_1} \frac{(x_{s_q} - x_s)^{n_1}}{n_1!} \frac{(y_{s_q} - y_s)^{n_2}}{n_2!} \frac{(z_{s_q} - z_s)^{n_3}}{n_3!} \frac{\partial^{n_1+n_2+n_3} \mathbf{u}_s}{\partial x^{n_1} \partial y^{n_2} \partial z^{n_3}} ; \quad (4.30)$$

11. solve the system of equations in Equation 4.30 to obtain the derivatives of $\mathbf{u}_s$ as a function of the displacement vectors $\mathbf{u}_s$ and $\mathbf{u}_{s_q}$:

$$\frac{\partial^{n_1+n_2+n_3} \mathbf{u}_s}{\partial x^{n_1} \partial y^{n_2} \partial z^{n_3}} = f(\mathbf{u}_s, \mathbf{u}_{s_q}) ; \quad (4.31)$$

12. substitute Equation 4.31 in Equation 4.29 to obtain the displacement vector of the fictitious node as a function of the displacement vectors of the interior and surface nodes:

$$\mathbf{u}_f = f(\mathbf{u}_s, \mathbf{u}_{s_q}) . \quad (4.32)$$

Note that the procedure to determine the displacement vectors of the fictitious nodes is same as that to determine their dilatations except for Step 9, in which the number of considered nodes is increased. This is due to the fact that the Taylor series expansion for the displacement vector has a truncation order of $N$ instead of $N - 1$.

### 4.3.3 Equilibrium equation for interior nodes

An interior node is representative of the volume within its own cells. The behavior of an interior node $i$ is described by the peridynamic equilibrium equation (Equation 4.4), which can be written in the discretized form (multiplying both sides of the equation by the cell volume $V_i = V(\mathbf{x}_i)$) as

$$- \sum_{j \in \mathcal{H}_i} \mathbf{f}_{ij} \, \beta_{ij} V_j \, V_i = \mathbf{b}_i \, V_i , \quad (4.33)$$

where $\mathbf{b}_i$ is the external force density vector applied to node $i$.

If some of the nodes $j$ within the neighborhood $\mathcal{H}_i$ of node $i$ are fictitious nodes, then the force states $\mathbf{f}_{ij}$ are computed with the dilatations and the displacement vectors obtained with the Taylor-based extrapolation method (see Section 4.3.2). Since the neighborhood $\mathcal{H}_i$ is complete, the stiffness fluctuations near the boundary of the body due to the surface effect are reduced (and, in some cases, eliminated).

### 4.3.4 Equation for surface nodes

A surface node represents a portion of the external surface of the body, namely one of the cell faces lying on the external surface (see Figure 4.5). The equation of a surface node $i$ (Equation 4.15) is based on the concept of force flux:

$$\boldsymbol{\tau}(\mathbf{x}_i, \mathbf{n}_i) = \mathbf{p}_i , \quad (4.34)$$

where $\mathbf{n}_i$ is the outward unit vector normal to the face of the cell and $\mathbf{p}$ is the force per unit area applied to $\mathbf{x}_i$. Equation 4.34 equates the externally applied stress ($\mathbf{p}_i$) to the force flux, i.e., the resultant of the forces of the bonds crossing the surface node.

Suppose that $A_i = A(\mathbf{x}_i)$ is the area represented by the surface node. Since a regular grid of peridynamic nodes is used, $A_i = h^2$ where $h$ is the grid spacing. The force flux $\boldsymbol{\tau}(\mathbf{x}_i, \mathbf{n}_i)$ is computed numerically as the sum of the force states (multiplied by the volumes $V_j$ and $V_k$ of the interacting nodes $j$ and $k$ and divided by $A_i$) of all the bonds intersecting the area $A_i$ [236]:

$$\boldsymbol{\tau}(\mathbf{x}_i, \mathbf{n}_i) = \frac{1}{A_i} \sum_{\substack{\boldsymbol{\xi}_{jk} \cap A_i \neq \emptyset \\ \mathbf{m}_{jk} \cdot \mathbf{n}_i > 0}} \alpha_{jk}\, \mathbf{f}_{jk}\, \beta_{jk} V_k\, V_j \,, \tag{4.35}$$

where $\alpha_{jk}$ is a coefficient equal to 1/4 if the bond intersects $A_i$ at a vertex, 1/2 if the bond intersects $A_i$ at a point on the edges or 1 if the bond intersects $A_i$ at any other point. Figure 4.7a represents the latter case in which the contribution of the bond $\boldsymbol{\xi}_{jk}$ is completely attributed to the force flux of node $i$ ($\alpha_{jk} = 1$). If the bond $\boldsymbol{\xi}_{jk}$ intersects the area $A_i$ at a point on an edge as shown in Figure 4.7b, that edge is shared between node $i$ and an adjacent node. Therefore, only half of the force state $\mathbf{f}_{jk}$ contributes to the force flux of node $i$ ($\alpha_{jk} = 1/2$) and the other half to the force flux of the adjacent node. Similarly, if the bond $\boldsymbol{\xi}_{jk}$ intersects the area $A_i$ at a vertex as shown in Figure 4.7c, the contribution of that bond is shared equally by the 4 adjacent nodes ($\alpha_{jk} = 1/4$).

Thus, the governing equation for the surface nodes is obtained by substituting Equation 4.35 in Equation 4.34 and multiplying both sides by $A_i$:

$$\sum_{\substack{\boldsymbol{\xi}_{jk} \cap A_i \neq \emptyset \\ \mathbf{m}_{jk} \cdot \mathbf{n}_i > 0}} \alpha_{jk}\, \mathbf{f}_{jk}\, \beta_{jk} V_k\, V_j = \mathbf{p}_i A_i \,. \tag{4.36}$$

Since the bond $\boldsymbol{\xi}_{jk}$ intersects the area $A_i$ lying on the external surface of the body, at least one of the nodes in the bond is a fictitious node. Therefore Equation 4.36 involves many fictitious nodes, the displacement vectors and dilatations of which are determined by means of the Taylor-based extrapolation method illustrated in Section 4.3.2.

### 4.3.5 Peridynamic system of equations

On the one hand, Equation 4.33, which describes the equilibrium of a volume cell, can be applied to every interior node. On the other hand, Equation 4.36 can be applied to every surface node. The left-hand side of both Equation 4.33 and Equation 4.36 can be rewritten as functions of the displacements of the interior and surface nodes, as shown in Sections 4.3.1 and 3.4.1. Therefore, the peridynamic system of equation is given in the standard form as

$$\mathbf{K}\, \widetilde{\mathbf{u}} = \widetilde{\mathbf{f}} \,, \tag{4.37}$$

where $\mathbf{K}$ is the peridynamic stiffness matrix, $\widetilde{\mathbf{u}}$ is the displacement vector containing the displacements of interior and surface nodes and $\widetilde{\mathbf{f}}$ is the force vector.

Please note that the stiffness matrix $\mathbf{K}$ is different from the one described in [227, 236],

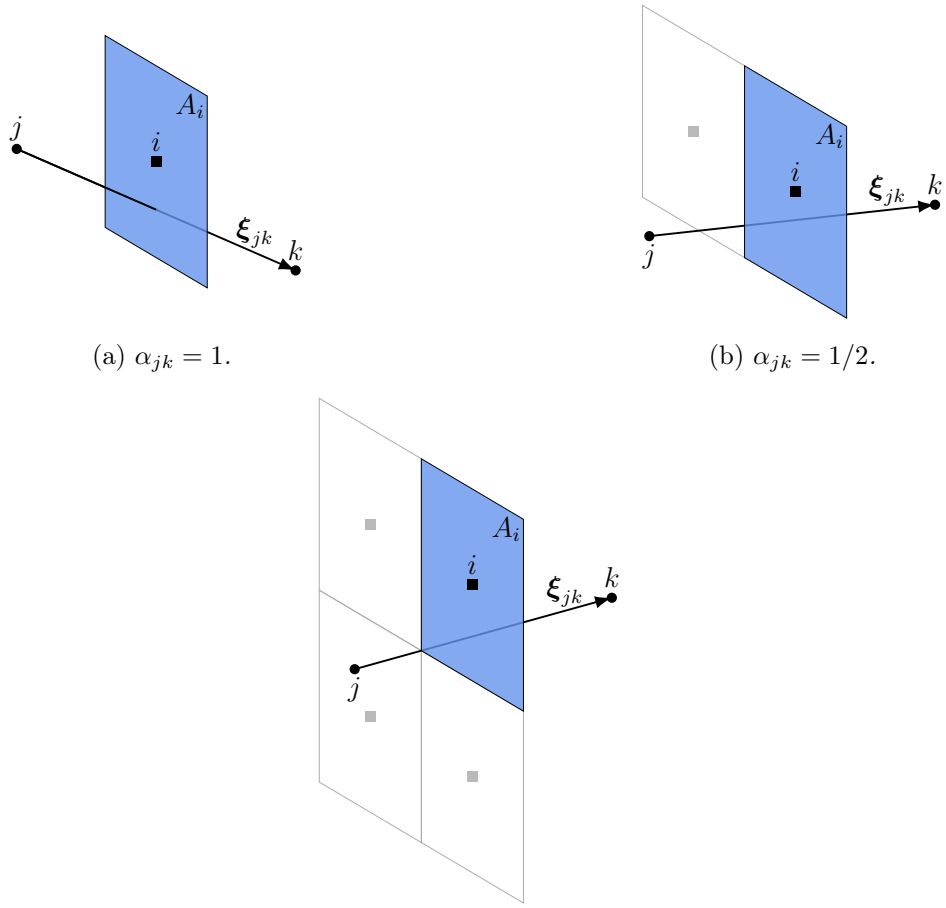


(a) $\alpha_{jk} = 1$.

(b) $\alpha_{jk} = 1/2$.

(c) $\alpha_{jk} = 1/4$.

Figure 4.7: *Values of the coefficient $\alpha_{jk}$ used in the computation of the force flux for different types of intersection between the bond $\boldsymbol{\xi}_{jk}$ and the area $A_i$ of the surface node $i$.*

in which the introduction of the Lagrange multipliers is required to solve the system of equations. In the new method, the displacements of the surface nodes are considered as degrees of freedom of the system and the stiffness matrix embeds also the equations for those nodes. This allows to solve directly the system of equations shown in Equation 4.37, without the use of the Lagrange multipliers. The advantages of this method with respect to the previous Taylor-based extrapolation method are the following:

- the new unknowns introduced in the system have the physical meaning of the displacements of the external surface of the body, so there is a better description of the mechanical behavior of the boundary of the body;
- the boundary conditions can be applied as one would do in a local model, namely by constraining the displacements in the vector $\widetilde{\mathbf{u}}$ of some nodes and by prescribing the forces in the vector $\widetilde{\mathbf{f}}$ acting on the other nodes;
- if elimination techniques are employed to impose numerically the boundary conditions, the dimensions of the stiffness matrix are reduced (this was not possible with the use of the Lagrange multipliers);
- the structure of the stiffness matrix (banded and with no zeroes on the diagonal) allows

for a more efficient inversion of the matrix itself;

- the reaction forces at constrained degrees of freedom can be simply obtained by multiplying the corresponding rows of the stiffness matrix $\mathbf{K}$ by the displacement vector $\widetilde{\mathbf{u}}$.

## 4.4 Numerical examples

Consider a body, the properties of which are reported in Table 4.1. The body is discretized with the meshfree method with a uniform grid spacing $h$. The ratio between the horizon and the grid spacing is defined as $\overline{m}$-ratio: $\overline{m} = \delta/h$. The $\overline{m}$-ratio is chosen to be equal to 3 as a compromise between the accuracy of the results and the computational cost. The quadrature coefficients for $\overline{m} = 3$ can be found in Table D1 of Appendix D in [235].

Table 4.1: *Properties of the body and its discretization parameters.*

| Property | Value |
|---|---|
| Length | $\ell_x = 0.32\,\mathrm{m}$ |
| Width | $\ell_y = 0.13\,\mathrm{m}$ |
| Depth | $\ell_z = 0.13\,\mathrm{m}$ |
| Young's modulus | $E = 10\,\mathrm{GPa}$ |
| Poisson's ratio | $\nu = 0.2$ |
| Grid spacing | $h = 0.01\,\mathrm{m}$ |
| $\overline{m}$-ratio | $\overline{m} = 3$ |

Two different sets of boundary conditions are imposed on the body in order to verify the accuracy of the results: a simple traction and a manufactured loading. In the former case, the analytical peridynamic solution is a displacement field varying linearly, the same solution which is obtained with classical continuum mechanics [165]. In the latter case, inspired by [158], we suppose that the peridynamic solution is a manufactured displacement field varying more than linearly. By prescribing this displacement field to the body, we are able to compute the force states of the bonds via Equation 4.11. Then, the volumetric loading of the interior of the body and the peridynamic stress at the boundary can be obtained by solving respectively Equations 4.4 and 4.15. Therefore, if these volumetric loading and peridynamic stress at the boundary, i.e., the manufactured loads, are imposed on the body, the analytical peridynamic solution is the displacement field prescribed at the beginning. Note that, since the manufactured displacement field varies more than linearly, the peridynamic solution is different from the analytical solution obtained with classical mechanics. The procedure shown in Appendix 4.A can be repeated with different prescribed displacement fields to obtain other analytical solutions with the peridynamic theory.

The two static examples are solved firstly without the fictitious and surface nodes. In this case, the boundary conditions are applied to the interior nodes closest to the boundary, as one would do in a local model. In particular, since the most external interior nodes are not exactly lying on the boundary (see Figure 4.5), the constraints are imposed by assigning

to those nodes the analytical value of the displacement field at their position. Subsequently, the same examples are solved by adopting the method of the surface nodes. The numerical results are compared with the analytical peridynamic solution and the magnitude of the error in a node $i$ is computed as

$$\|\boldsymbol{\epsilon}_i\| = \sqrt{\left(\frac{u_i - \overline{u}_i}{\overline{u}_{max}}\right)^2 + \left(\frac{v_i - \overline{v}_i}{\overline{v}_{max}}\right)^2 + \left(\frac{w_i - \overline{w}_i}{\overline{w}_{max}}\right)^2}, \tag{4.38}$$

where $u_i$, $v_i$ and $w_i$ are the displacements in the three directions obtained with the numerical model, $\overline{u}_i$, $\overline{v}_i$ and $\overline{w}_i$ are the displacements obtained with the analytical solution computed at $\mathbf{x}_i$ and $\overline{u}_{max}$, $\overline{v}_{max}$ and $\overline{w}_{max}$ are the maximum magnitude of the analytical displacements. The analytical solution will be computed for each example in the following sections.

### 4.4.1 Body under traction

The boundary conditions of the body subjected to simple traction are shown in Figure 4.8. The analytical solution in this case is given as

$$\mathbf{u}(\mathbf{x}) = \begin{Bmatrix} u(x,y,z) \\ v(x,y,z) \\ w(x,y,z) \end{Bmatrix} = \begin{Bmatrix} \dfrac{p}{E}\, x \\ \dfrac{-\nu\, p}{E}\left(y + \dfrac{\ell_y}{2}\right) \\ \dfrac{-\nu\, p}{E}\left(z + \dfrac{\ell_z}{2}\right) \end{Bmatrix}, \tag{4.39}$$

where $p$ is the traction load. Thus, the body is elongated along the $x$-axis and contracted in the other two directions.

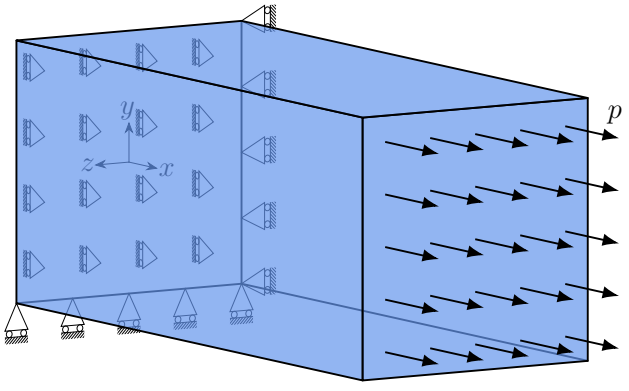


Figure 4.8: *Boundary conditions for the body under the traction* $p = 10\,\text{MPa}$. *The origin of the reference system lies at the center of the constrained face of the body. The constraints are described by the following equations:* $u(x = 0) = 0$, $v(x = 0, y = -\frac{\ell_y}{2}) = 0$ *and* $w(x = 0, z = -\frac{\ell_z}{2}) = 0$.

Figure 4.9a shows the magnitude of the displacement error computed as in Equation 4.38 for the peridynamic model without any correction at the boundaries of the body. In this case, there are evident displacement fluctuations near the external surface which are due to the surface effect and the approximated way of imposing the boundary conditions. Note

that the errors are much larger especially near the edges and the vertices of the body, as commonly observed in surface effect phenomena [236], reaching a maximum magnitude of more than 30%. On the other hand, when the method of the surface nodes is employed with an order of truncation $N = 1$ for the Taylor-based extrapolation, the fluctuations due to the surface effect are eliminated and the peridynamic boundary conditions are imposed properly (see Figure 4.9b). Nonetheless, there are still small errors, with a maximum magnitude of 0.06%, due to the discretization of the peridynamic equations.

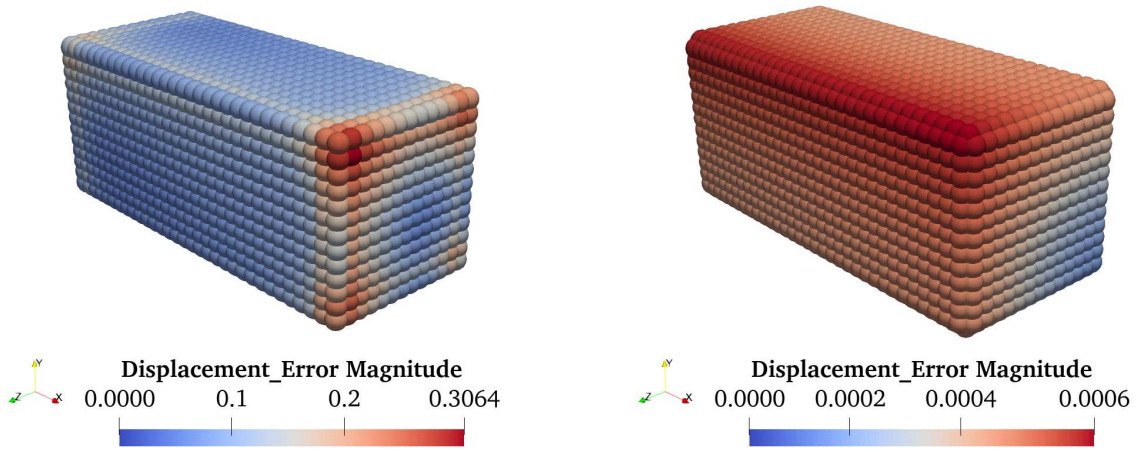


(a) *No boundary corrections.* (b) *With surface nodes ($N = 1$).*

Figure 4.9: *Magnitude of the displacement errors when no corrections at the boundaries of the body are adopted* (a) *and when the method of the surface nodes, with an order of truncation $N = 1$ for the Taylor-based extrapolation, is used* (b). *Note that the colormaps refer to different values in the two plots. The asymmetry of the errors is due to the asymmetric constraints in $y$ and $z$ directions.*

### 4.4.2 Body under manufactured loading

When considering the same mechanical problem, Peridynamics and classical continuum mechanics may provide different solutions [165]. Since Peridynamics has been developed relatively recently, it is difficult to find analytical solutions to benchmark problems. Therefore, inspired by [158], we computed in Appendix 4.A the forces that should be applied to the body to obtain a prescribed displacement field. The boundary conditions of the body subjected to the manufactured loading are shown in Figure 4.10. The manufactured volumetric loading is given as

$$\mathbf{b}(\mathbf{x}) = \begin{Bmatrix} b_1(x,y,z) \\ b_2(x,y,z) \\ b_3(x,y,z) \end{Bmatrix} = \begin{Bmatrix} -c_w \left( \dfrac{k_\theta}{3} + \dfrac{2k_e}{15} \right) \\ -c_u \left( \dfrac{k_\theta}{3} + \dfrac{2k_e}{15} \right) - c_v \dfrac{2k_e}{5} x \\ 0 \end{Bmatrix}, \tag{4.40}$$

where $c_u = 0.05\,\mathrm{m}^{-1}$, $c_v = -0.06\,\mathrm{m}^{-2}$ and $c_w = -0.02\,\mathrm{m}^{-1}$ are randomly chosen constants. The components of the manufactured peridynamic stress tensor $\boldsymbol{\tau}(\mathbf{x})$ can be computed as

$$\begin{cases} \tau_{11}(\mathbf{x}) = c_u \left(\dfrac{k_\theta}{3} + \dfrac{k_e}{5}\right) y + c_w \left(\dfrac{k_\theta}{3} + \dfrac{k_e}{15}\right) x\,, \\ \tau_{22}(\mathbf{x}) = c_u \left(\dfrac{k_\theta}{3} + \dfrac{k_e}{15}\right) y + c_w \left(\dfrac{k_\theta}{3} + \dfrac{k_e}{15}\right) x\,, \\ \tau_{33}(\mathbf{x}) = c_u \left(\dfrac{k_\theta}{3} + \dfrac{k_e}{15}\right) y + c_w \left(\dfrac{k_\theta}{3} + \dfrac{k_e}{5}\right) x\,, \\ \tau_{12}(\mathbf{x}) = c_u \dfrac{k_e}{15}\, x + c_v \left(\dfrac{k_e}{5} x^2 + \dfrac{k_e}{35}\dfrac{\Delta_2}{\Delta_1}\right)\,, \\ \tau_{13}(\mathbf{x}) = c_w \dfrac{k_e}{15}\, z\,, \\ \tau_{23}(\mathbf{x}) = 0\,, \end{cases} \tag{4.41}$$

where $\Delta_1 = \left(\frac{3}{8}\sqrt{\pi}\mathrm{erf}(1) - \frac{5}{4}\exp(-1)\right)\delta^5$ and $\Delta_2 = \left(\frac{15}{32}\sqrt{\pi}\mathrm{erf}(1) - \frac{29}{16}\exp(-1)\right)\delta^7$. "erf" and "exp" stand respectively for the Gaussian error function and the exponential function. The surface force, used to impose the surface loading at the free faces of the body, at a point $\mathbf{x}$ on the external surface of the body with an outward normal $\mathbf{n}$ can be computed as $\boldsymbol{\tau}(\mathbf{x}, \mathbf{n}) = \boldsymbol{\tau}(\mathbf{x}) \cdot \mathbf{n}$.

If the manufactured loading is applied to the body, then the analytical peridynamic solution is given as

$$\mathbf{u}(\mathbf{x}) = \begin{Bmatrix} u(x,y,z) \\ v(x,y,z) \\ w(x,y,z) \end{Bmatrix} = \begin{Bmatrix} c_u\, x\, y \\ c_v\, x^3 \\ c_w\, x\, z \end{Bmatrix}. \tag{4.42}$$

The deformation given by this displacement field is shown in Figure 4.11.

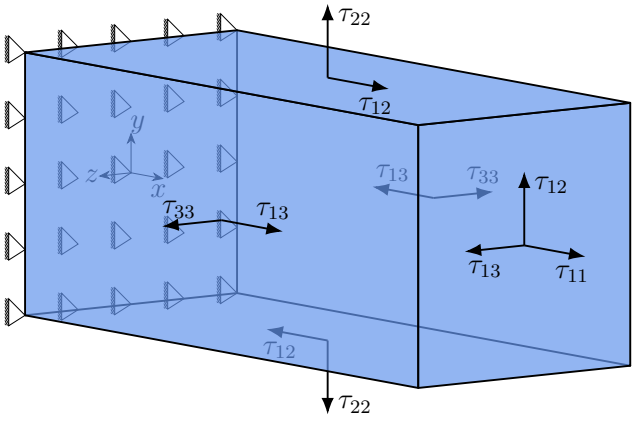


Figure 4.10: *Boundary conditions for the body under the manufactured loading. The face at $x = 0$ is constrained in all directions, whereas the loads are computed from Equations 4.40 and 4.41.*

Figure 4.12 shows the magnitude of the displacement error computed as in Equation 4.38. The errors obtained without corrections at the boundary (Figure 4.12a) are considerably higher than those obtained with the method of the surface nodes (Figures 4.12b-d). Indeed, the maximum magnitudes of the displacement errors are respectively over 130% and below

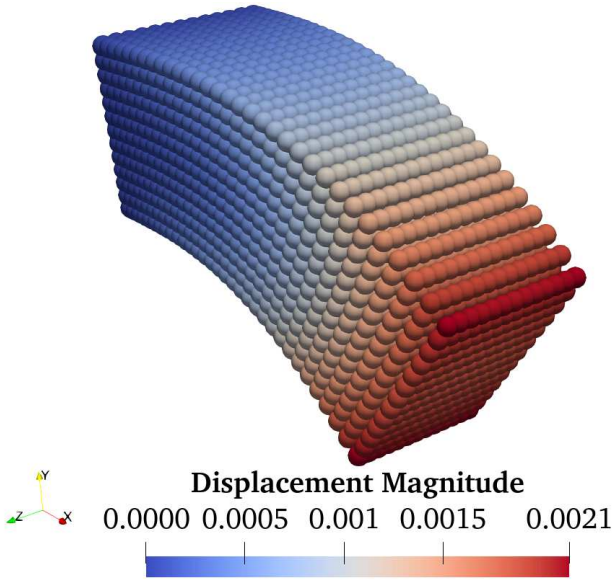


Figure 4.11: *Analytical solution of the displacement field for the body under manufactured loading. The deformation of the body is magnified by 50 times for visualization reasons.*

1%. This is due to the surface effect and, especially, to the approximated way of imposing the boundary conditions. In the model without boundary corrections, the surface loads are indeed applied to the nodes closest to the boundary of the body, which however are distant $h/2$ from the external surface (where the loads should actually be applied). On the other hand, the surface nodes lie exactly on the external surface of the body and allow to enforce the boundary conditions exactly where they are supposed to be imposed, while also mitigating the surface effect.

Since the analytical solution for the displacement field in Equation 4.42 is at most cubic, we expect to capture the proper displacements in the fictitious layer with an order of truncation $N = 3$ for the Taylor-based extrapolation. The numerical results indeed show that the magnitude of the errors decreases as the order of truncation is increased from 1 to 3 (compare Figures 4.12b-d). However, even if $N = 3$ is chosen, there are still small errors, with a maximum magnitude of 0.4%. These residual errors, due to the discretization of the peridynamic equations [235], can be further reduced by increasing the value of the $\overline{m}$-ratio, i.e., decreasing the value of the grid spacing $h$ when the horizon size $\delta$ is kept constant [236].

## 4.5 Comparison with other methods

The surface effect and the imposition of the boundary conditions are two well-known issues in Peridynamics, which were thoroughly analyzed in the literature. Many methods have been indeed devised to mitigate these problems at the boundary (see, for instance, [186]). There are mainly three types of methods for boundary corrections:

- the modification of the stiffness of the bonds near the boundary [63, 64, 187–190],
- the introduction of the fictitious nodes surrounding the body and the extrapolation of their displacements along with the implementation of the peridynamic boundary

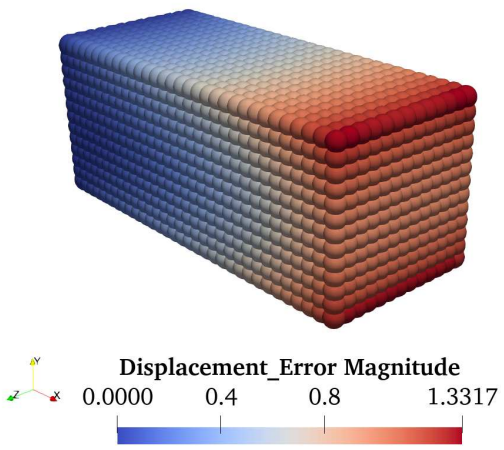


(a) *No boundary corrections.*

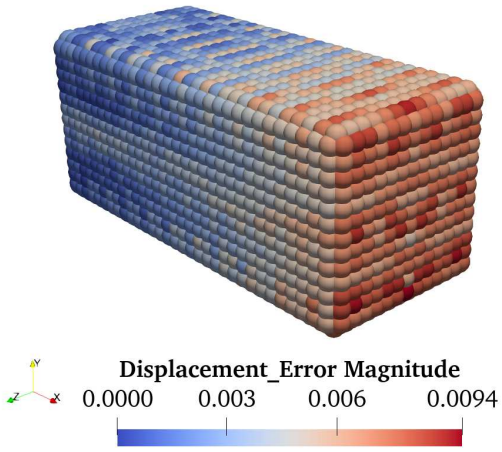


(b) *With surface nodes ($N = 1$).*

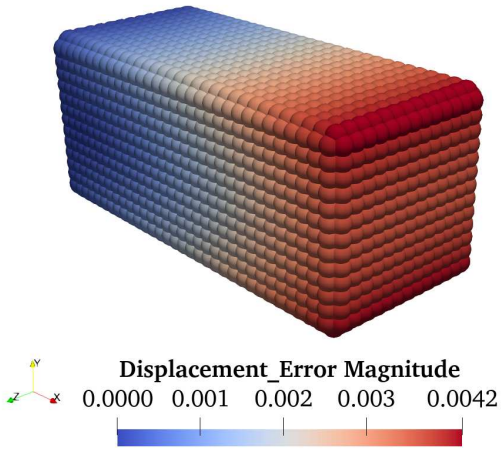


(c) *With surface nodes ($N = 2$).*

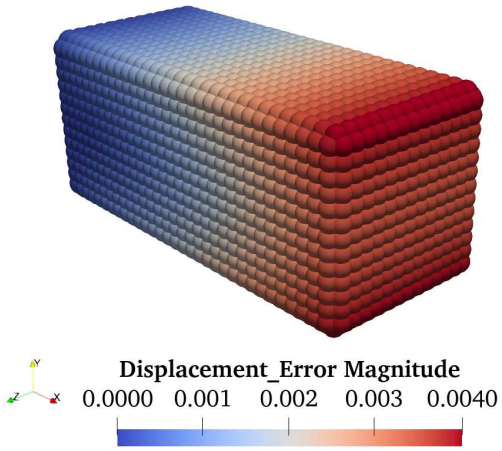


(d) *With surface nodes ($N = 3$).*

Figure 4.12: *Magnitude of the displacement errors when no corrections at the boundaries of the body are adopted* (a) *and when the method of the surface nodes, with different order of truncation for the Taylor-based extrapolation, is used* (b-d). *Note that the colormaps refer to different values in the plots. Also, note that the difference between $N = 2$ and $N = 3$ is very small because the errors due to the truncation of the Taylor series expansions in the displacement extrapolation are negligible compared to the errors due to the discretization of the peridynamic equations.*

conditions [63, 92, 126, 150, 151, 186, 192–196, 227, 236],

- the modification of the equations governing the nodes near the boundary thanks to the peridynamic differential operator [237–241].

Even though it employs the fictitious layer as in the second type of methods, the surface node method differs from all the previously proposed methods. The main difference is the introduction of new degrees of freedom at the boundary of the body, governed by new equations based on the concept of force flux. In the following, the most recent versions of the three types of methods are reviewed and compared with the surface node method.

For the comparison, we consider an example of a 2D body under plane strain conditions subjected to simple traction $p = 240\,\text{MPa}$. Note that, under these conditions, the coefficients for the computation of the dilatation (respectively Equations 4.9 and 4.11) should be modified

to $c_\theta = 2$, $k_\theta = -(1-4\nu)E/((1+\nu)(1-2\nu))$ and $k_e = 4E/(1+\nu)$. The boundary conditions and the properties of the plate, which are the same as those of a numerical example in [241], are shown respectively in Figure 4.13 and Table 4.2. The quadrature coefficients are computed with the algorithm proposed in Appendix A of [235].

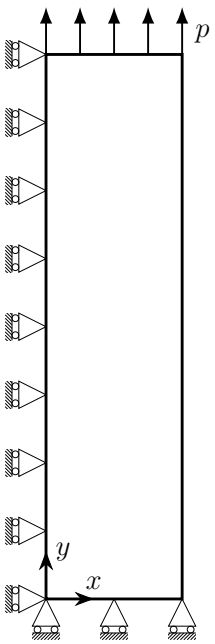


Figure 4.13: *Boundary conditions for the plate under traction p.*

Table 4.2: *Properties of the plate and its discretization parameters.*

| Property | Value |
|---|---|
| Length | $\ell_x = 5\,\text{mm}$ |
| Width | $\ell_y = 25\,\text{mm}$ |
| Young's modulus | $E = 148\,\text{GPa}$ |
| Poisson's ratio | $\nu = 0.3$ |
| Grid spacing | $h = 0.125\,\text{mm}$ |
| $\overline{m}$-ratio | $\overline{m} = 3$ |

The peridynamic analytical solution of this problem, which is the same analytical solution obtained with classical continuum mechanics [165], is given as

$$\mathbf{u}(\mathbf{x}) = \begin{Bmatrix} u(x,y) \\ v(x,y) \end{Bmatrix} = \begin{Bmatrix} \dfrac{-\nu(1+\nu)p}{E}\, x \\ \dfrac{(1-\nu^2)p}{E}\, y \end{Bmatrix}, \tag{4.43}$$

Therefore, the error in a node $i$ is computed as

$$\begin{cases} \epsilon_{u_i} = \left\| \dfrac{u_i - \overline{u}_i}{\overline{u}_{max}} \right\| , \\ \epsilon_{v_i} = \left\| \dfrac{v_i - \overline{v}_i}{\overline{v}_{max}} \right\| , \end{cases} \tag{4.44}$$

where $u_i$ and $v_i$ are the displacements in the two directions obtained with the numerical model, $\overline{u}_i$ and $\overline{v}_i$ are the displacements obtained with the analytical solution computed at $\mathbf{x}_i$, and $\overline{u}_{max}$ and $\overline{v}_{max}$ are the maximum magnitude of the analytical displacements.

### 4.5.1 Position-Aware Linear Solid (PALS)

The Position-Aware Linear Solid (PALS) constitutive model proposes a kinematic correction that modifies the influence function differently for the dilatation and the deviatoric part of the extension [186, 190]. This method introduces two sets of constraints, called *matching deformations*, which prescribe homogeneous strain conditions in the whole body. The two sets of matching deformations, representing the deformations either for uniaxial strains or for simple shear, are used to define two linear systems of equations for each node via the Lagrange multipliers. The solution of these two systems, corresponding to the matching deformations for uniaxial strains or simple shear, leads to the determination of the dilatation and deviatoric influence functions, respectively. Since only the influence functions of the nodes near the boundary are automatically modified, the method is called *position-aware*.

The modification of the bond properties through the dilatation and deviatoric influence functions allows to restore the proper values of stiffness in the whole body, also near the boundaries, under homogeneous deformations. However, the PALS approach does not deal with the problem of the imposition of the peridynamic boundary conditions and exhibits even larger errors when the deformation is non-homogeneous.

### 4.5.2 Mirror Node Method (MNM)

The Mirror Node Method (MNM), developed in [194], is based on introducing the fictitious nodes surrounding the peridynamic body. In state-based Peridynamics, the thickness of the fictitious layer for the MNM is equal to $2\delta$. Each fictitious node is associated with the node within the body closest to the point at the same (symmetric) distance from the boundary, the so-called *mirror node*. The direction for this search of the mirror node is given by the peridynamic gradient, a vector defined in such a way as to point towards the region of nodes with the more complete neighborhoods, i.e., the bulk of the body. The fictitious nodes are employed to mitigate the surface effect and to impose the boundary condition thanks to the mirror nodes. The displacements of the fictitious nodes are indeed determined depending on the values of the Dirichlet or Neumann boundary conditions at the boundary and on the displacements of the corresponding mirror nodes.

Even if he MNM is similar to the Surface Node Method (SNM) in exploiting the fictitious nodes to deal with both the surface effect and the imposition of the boundary conditions, the

two methods differ considerably in the way they do it. Indeed, the Taylor-based extrapolation used in the SNM does not need the computation of the peridynamic gradient but only the search for the nearest node of the body. Moreover, in the SNM, higher-order terms of the Taylor expansion may increase the accuracy in the case of a superlinear displacement field, and the external forces are consistently applied in the peridynamic framework.

### 4.5.3 Peridynamic Differential Operator (PDDO)

The Peridynamic Differential Operator (PDDO) was introduced in [237] and then was used to recast the formulation of the bond associated non-ordinary state-based Peridynamics [239]. In this model, the PDDO can be used to correct the surface effect and impose the boundary conditions without the fictitious layer [241]. The domain of the body is partitioned into three subdomains:

- the set of the most external layer of nodes, where the boundary conditions are enforced via the PDDO equations;
- the set of the remaining nodes with a distance from the boundary smaller than $2\delta$, where the peridynamic equations are modified to correct the surface effect;
- the set of the nodes with a distance from the boundary greater than $2\delta$, which are governed by the standard peridynamic equations.

To some extent, the PDDO method and the Surface Node Method (SNM) are similar since they use different equations than the standard ones to correct the surface effect and impose the boundary conditions. However, the differences between the two methods to implement the boundary corrections are evident: the PDDO method exploits a layer of nodes *within* the body, whereas the SNM the fictitious nodes *outside* the body. This is the reason why, in the SNM, all the nodes in the interior of the body are still governed by the standard peridynamic equations, and crack propagation is naturally included in the peridynamic formulation near the boundary of the body as well.

### 4.5.4 Comparison with Surface Node Method (SNM)

The SNM retains the unique quality of having some nodes positioned *exactly* at the boundary of the body, i.e., the surface nodes, representing the non-local mechanical behavior of the external surface of the body. Thanks to these new nodes, the boundary conditions are not imposed at a distance of $h/2$ from the boundary as in the other methods, where $h$ is the uniform grid spacing, but can be imposed *exactly* where they are supposed to. Moreover, the boundary conditions are imposed as one would do in a local model, namely by setting the values of the corresponding degrees of freedom in either the displacement vector or the force vector (in Equation 4.37). This is a very handy characteristic that is not exhibited in most of the other methods in the literature.

Figures 4.14 and 4.15 show the errors, respectively for the displacements in $x$ and $y$ directions, computed with Equation 4.44 for the example in Figure 4.13. Since the PALS

approach is expected to correct the surface effects under homogeneous deformation, the errors in Figures 4.14a and 4.15a are due to the approximated way boundary conditions were imposed. Note that this method reduces the errors of the displacements in the direction of the load ($y$ direction) but still yields significant errors in the perpendicular direction ($x$ direction). The numerical results obtained with the MNM are really close to the analytical solution for the displacements in $x$ direction, except in one of the corners (see Figure 4.14b). However, the errors for the displacements in $y$ direction (Figure 4.15b) are the highest among the four analyzed methods due to the approximated imposition of the Neumann boundary conditions via the mirror nodes.

Both PALS and MNM are implemented in the same peridynamic framework of the SNM, namely the ordinary state-based Peridynamics, but they provide, on average, larger errors than SNM. The numerical errors obtained with the method involving the PDDO are similar to those obtained with the SNM: both methods do not exhibit fluctuations of the displacements near the boundary and yield, on average, smaller errors than PALS and MNM methods. However, the PDDO method is based on the non-ordinary state-based Peridynamics framework, which is different from the model used for the SNM. Therefore, the comparison between these two methods can be only qualitative. The advantages of using the SNM over the PDDO method are mainly two:

- the complete knowledge of the mechanical behavior of the external surface of peridynamic bodies is achieved solely with the SNM thanks to the surface nodes lying exactly at the boundary,
- the PDDO method is limited to cracks that propagate far from the nodes where boundary conditions are imposed (this limitation is not present in the SNM).

## 4.6 Conclusions

Peridynamics, as typical of non-local theories, exhibits some issues near the boundaries of the body: an undesired stiffness fluctuation due to incomplete neighborhoods close to the external surface of the body, phenomenon known as surface effect, and a difficulty in imposing properly the boundary conditions. In [227, 236], we proposed an innovative method, i.e., the Taylor-based extrapolation method with the nearest-node strategy, to mitigate the surface effect by means of the introduction of the fictitious nodes and to impose properly the peridynamic boundary conditions via the concept of force flux. The main disadvantage of this method is that the system of equations is solved through the use of the Lagrange multipliers, that increases the number of unknowns and leads to an equation structure which is not computationally efficient to solve.

Therefore, we developed the method of the surface nodes which exploits the same concepts of the previous method, but also avoids the use of the Lagrange multipliers. Each surface node represents a portion of the external surface of the body. The displacements of these nodes are new degrees of freedom in the model and their corresponding equations are based on the concept of force flux. In this regard, the surface nodes may be considered as representative

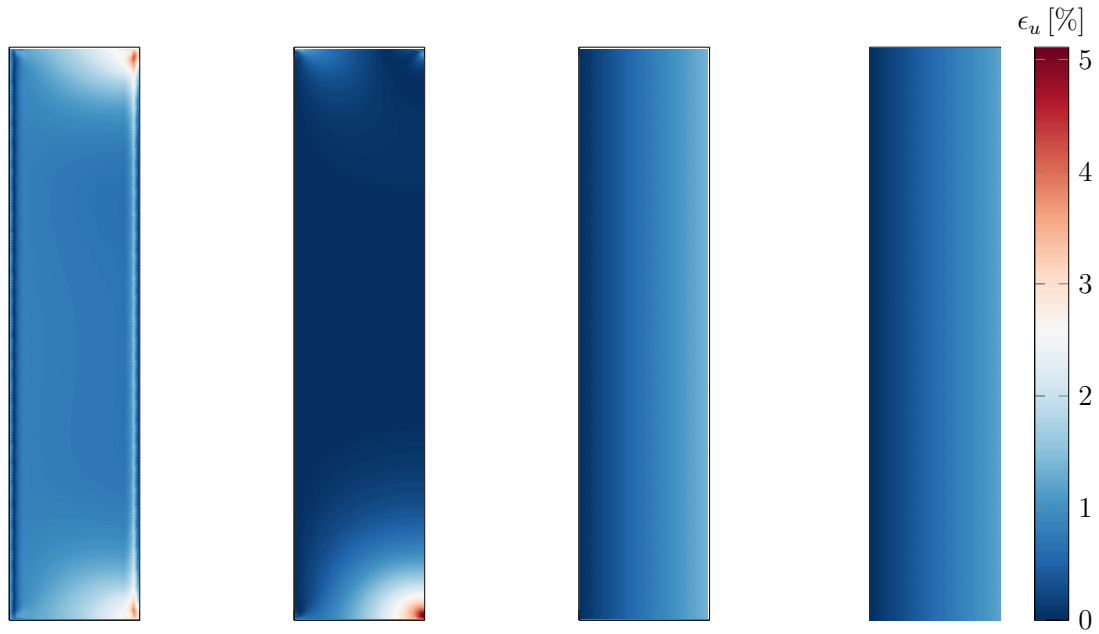


(a) *With PALS.* (b) *With MNM.* (c) *With PDDO.* (d) *With SNM.*

Figure 4.14: *Errors of the displacements in x direction for the following methods for boundary corrections:* (a) *Position-Aware Linear Solid,* (b) *Mirror Node Method,* (c) *Peridynamic Differential Operator, and* (d) *Surface Node Method.*

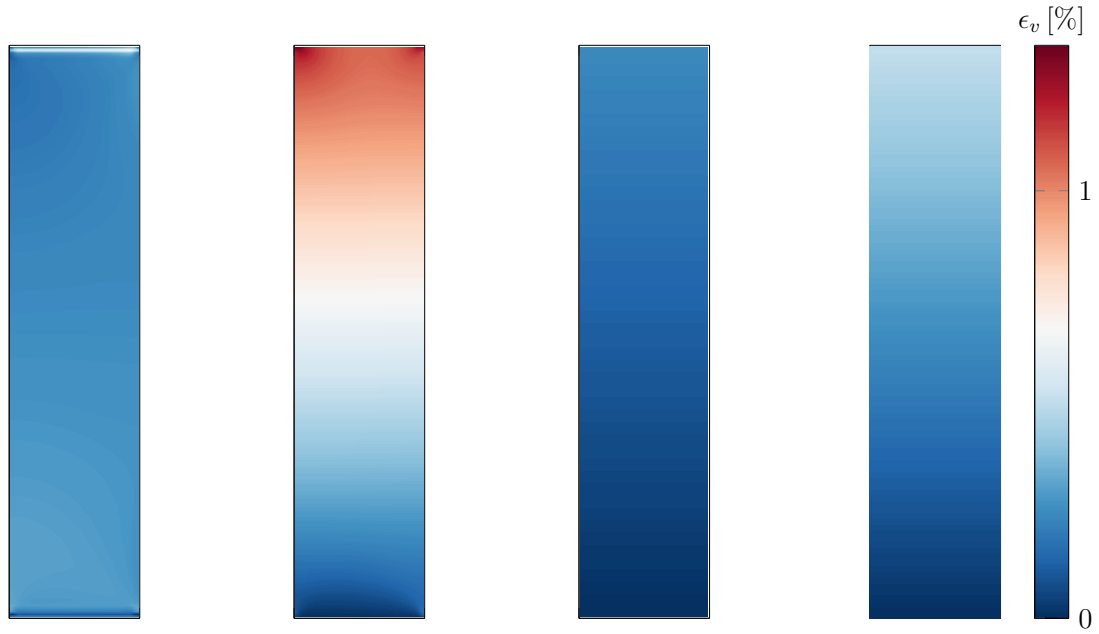


(a) *With PALS.* (b) *With MNM.* (c) *With PDDO.* (d) *With SNM.*

Figure 4.15: *Errors of the displacements in y direction for the following methods for boundary corrections:* (a) *Position-Aware Linear Solid,* (b) *Mirror Node Method,* (c) *Peridynamic Differential Operator, and* (d) *Surface Node Method.*

of the interactions between the most external layer of the body and the fictitious layer surrounding the body. The boundary conditions can be applied directly to these nodes, exactly as one would do in a local model. Moreover, the Taylor-based extrapolation is

adapted by including the contributions of the new degrees of freedom associated to the surface nodes.

For the first time, the concepts of the Taylor-based extrapolation method are applied to 3D peridynamic models: 3D static numerical examples have been carried out to verify the accuracy of the method of the surface nodes. The improvements of the proposed method are evident when compared to a peridynamic model without corrections at the boundary: the undesired stiffness fluctuations near the external surface of the body are sensibly reduced (or even eliminated) and the errors of the numerical solution decrease by 2 orders of magnitude.

Moreover, the advantages of the proposed method are the following:

- it defines in a clear way how the boundary conditions in Peridynamics are imposed and removes the arbitrariness of other methods in distributing the constraints or the external loads over the layer of the body close to the boundary;
- the introduction of the new unknowns, namely the displacements of the surface nodes, allows for a better description of the mechanical behavior of the external surface of the body;
- the implementation of the boundary conditions in peridynamic models is straightforward since it is similar to what one would do in a local model (for instance, by using elimination techniques);
- there is no need to use of the Lagrange multipliers, thus the stiffness matrix can be numerically inverted in a more efficient way.

We compared the proposed method with three of the most recently developed methods for boundary corrections. This comparison highlights that the surface node method yields the most accurate numerical results with respect to the other methods applied in the framework of ordinary state-based Peridynamics. The unique characteristics of the surface nodes, namely the knowledge of the non-local mechanical behavior of the external surface of peridynamic bodies and the imposition of the boundary conditions *exactly* at the boundary, make the proposed method one of the most attractive to use.

Moreover, we computed the peridynamic analytical solution for a relatively complex displacement field. In the literature, only few analytical solutions are available for peridynamic problems. Appendix 4.A shows a procedure to analytically obtain the volume and surface forces when a displacement field is prescribed. The same procedure can be applied to different displacement fields in order to attain other analytical solutions with the peridynamic theory.

# Appendix

## 4.A Analytical solution to the manufactured problem

A peridynamic problem is said to be *manufactured* when the forces applied to a body are computed from a given displacement field, which can be arbitrarily chosen (provided that the integrals in the peridynamic equations are explicitly solvable). Therefore, consider an infinite body which is subjected to the following displacement field:

$$\mathbf{u}(\mathbf{x}) = \begin{Bmatrix} u(x,y,z) \\ v(x,y,z) \\ w(x,y,z) \end{Bmatrix} = \begin{Bmatrix} c_u\, x\, y \\ c_v\, x^3 \\ c_w\, x\, z \end{Bmatrix} , \tag{4.45}$$

where $c_u$, $c_v$ and $c_w$ are arbitrarily chosen constants. The volume forces that should be applied to the infinite body to obtain this displacement field can be computed from Equation 4.4 as

$$\mathbf{b}(\mathbf{x}) = -\int_\Omega \int_0^\delta \mathbf{f}(\mathbf{x}, \mathbf{x}')\, l^2 \, \mathrm{d}\Omega_{\mathbf{m}} \, \mathrm{d}l \, , \tag{4.46}$$

where the differential volume $\mathrm{d}V_{\mathbf{x}'}$ has been rewritten as $l^2 \, \mathrm{d}\Omega_{\mathbf{m}} \, \mathrm{d}l$, in which $l = \|\mathbf{x}' - \mathbf{x}\|$ is the length of the bond and $\mathrm{d}\Omega_{\mathbf{m}}$ is the differential solid angle in direction $\mathbf{m}$ of the bond. The direction $\mathbf{m}$ may vary on the unit sphere $\Omega$ centered in $\mathbf{x}$ and the length $l$ of the bond is comprised between 0 and $\delta$, so that all the bonds within the neighborhood $\mathcal{H}_{\mathbf{x}}$ of the point $\mathbf{x}$ are considered within the limits of the integration domain.

However, we would like to consider a body with finite dimensions (imagine to cut out a piece of the infinite body). This means that some forces arise at the external surfaces of the finite body (where the infinite body is cut). Therefore, we need to to compute the peridynamic stress tensor as

$$\boldsymbol{\tau}(\mathbf{x}) = \frac{1}{2} \int_\Omega \int_0^\delta \int_s^\delta \mathbf{f}(\mathbf{x}', \mathbf{x}'') \otimes \mathbf{m}\, r^2 \, \mathrm{d}r \, \mathrm{d}s \, \mathrm{d}\Omega_{\mathbf{m}} \, , \tag{4.47}$$

where $r = \|\mathbf{x}'' - \mathbf{x}'\|$, $s = \|\mathbf{x}' - \mathbf{x}\|$ and "$\otimes$" stands for the dyadic product. The limits of the integration domain can be visualized in Figure 4.2. If the stress tensor is multiplied by the outward unit vector $\mathbf{n}$ normal to the external surface, one can obtain the above-mentioned forces, or force fluxes, arisen at the external surface of the finite body: $\boldsymbol{\tau}(\mathbf{x}, \mathbf{n}) = \boldsymbol{\tau}(\mathbf{x}) \cdot \mathbf{n}$.

For later use, we solve hereinafter the integrals that will appear in the computation of the forces. Since both Equations 4.46 and 4.47 contain an integral over a unit sphere $\Omega$, that integral is equal to 0 whenever the integrand involves an odd exponent for at least one of the components $\mathrm{m}_i$, with $i = 1, 2, 3$, of the vector $\mathbf{m}$ of the bond direction (antisymmetric function integrated over a symmetric domain). The analytical solutions of the integrals which involve the bond direction vector are:

$$\int_\Omega \mathrm{d}\Omega_{\mathbf{m}} = 4\pi \, , \tag{4.48}$$

$$\int_\Omega \mathrm{m}_i^2 \,\mathrm{d}\Omega_{\mathbf{m}} = \frac{4\pi}{3}\,, \tag{4.49}$$

$$\int_\Omega \mathrm{m}_i^4 \,\mathrm{d}\Omega_{\mathbf{m}} = \frac{4\pi}{5}\,, \tag{4.50}$$

$$\int_\Omega \mathrm{m}_i^2\mathrm{m}_j^2 \,\mathrm{d}\Omega_{\mathbf{m}} = \frac{4\pi}{15}\,, \tag{4.51}$$

$$\int_\Omega \mathrm{m}_i^4\mathrm{m}_j^2 \,\mathrm{d}\Omega_{\mathbf{m}} = \frac{4\pi}{35}\,, \tag{4.52}$$

where $i, j = 1, 2, 3$ with $i \neq j$. On the other hand, the integrals involving the bond length $l$ (see Equation 4.46) are solved as follows:

$$\int_0^\delta \exp\left(\frac{-l^2}{\delta^2}\right) l^4 \,\mathrm{d}l = \left(\frac{3}{8}\sqrt{\pi}\mathrm{erf}(1) - \frac{5}{4}\exp(-1)\right)\delta^5 = \Delta_1\,. \tag{4.53}$$

where "erf" is the Gaussian error function and "exp" is the exponential function. We name $\Delta_1$ the solution of Equation 4.53 to simplify and shorten the next formulae. The solutions for the integrals required to compute the peridynamic stress tensor are:

$$\int_0^\delta \int_s^\delta \exp\left(-\frac{r^2}{\delta^2}\right) r^3 \,\mathrm{d}r\,\mathrm{d}s = \Delta_1\,, \tag{4.54}$$

$$\int_0^\delta \int_s^\delta \exp\left(-\frac{r^2}{\delta^2}\right) r^3(r^2-3sr+3s^2)\,\mathrm{d}r\,\mathrm{d}s = \left(\frac{15}{32}\sqrt{\pi}\mathrm{erf}(1) - \frac{29}{16}\exp(-1)\right)\delta^7 = \Delta_2\,. \tag{4.55}$$

These analytical solutions are valid only for the Gaussian influence function in Equation 4.7, but they can be computed also if other influence functions are adopted (the values of $\Delta_1$ and $\Delta_2$ would be different).

The analytical value of the weighted volume of a point $\mathbf{x}$ with complete neighborhood (from Equation 4.8) is:

$$m(\mathbf{x}) = \int_\Omega \int_0^\delta \exp\left(-\frac{l^2}{\delta^2}\right) l^4 \,\mathrm{d}l\,\mathrm{d}\Omega_{\mathbf{m}} = 4\pi\Delta_1\,. \tag{4.56}$$

We show hereinafter how to compute the volume and surface forces applied to a peridynamic body to obtain the displacement field in Equation 4.45.

### 4.A.1 Computation of volume forces

Under the assumption of small displacements, the extension scalar state of the bond between points $\mathbf{x}$ and $\mathbf{x}'$ is computed as

$$\underline{e} = [\mathbf{u}(\mathbf{x}') - \mathbf{u}(\mathbf{x})] \cdot \mathbf{m} = \begin{Bmatrix} c_u\,(x'y' - xy) \\ c_v\,(x'^3 - x^3) \\ c_w\,(x'z' - xz) \end{Bmatrix} \cdot \begin{Bmatrix} \mathrm{m}_1 \\ \mathrm{m}_2 \\ \mathrm{m}_3 \end{Bmatrix}$$

$$
\begin{aligned}
&= \begin{Bmatrix} c_u\left(l^2\mathrm{m}_1\mathrm{m}_2 + xl\mathrm{m}_2 + yl\mathrm{m}_1\right) \\ c_v\left(l^3\mathrm{m}_1^3 + 3xl^2\mathrm{m}_1^2 + 3x^2l\mathrm{m}_1\right) \\ c_w\left(l^2\mathrm{m}_1\mathrm{m}_3 + xl\mathrm{m}_3 + zl\mathrm{m}_1\right) \end{Bmatrix} \cdot \begin{Bmatrix} \mathrm{m}_1 \\ \mathrm{m}_2 \\ \mathrm{m}_3 \end{Bmatrix} \\
&= c_u\left(l^2\mathrm{m}_1^2\mathrm{m}_2 + xl\mathrm{m}_1\mathrm{m}_2 + yl\mathrm{m}_1^2\right) + c_v\left(l^3\mathrm{m}_1^3\mathrm{m}_2 + 3xl^2\mathrm{m}_1^2\mathrm{m}_2 + 3x^2l\mathrm{m}_1\mathrm{m}_2\right) \\
&\qquad + c_w\left(l^2\mathrm{m}_1\mathrm{m}_3^2 + xl\mathrm{m}_3^2 + zl\mathrm{m}_1\mathrm{m}_3\right), \qquad (4.57)
\end{aligned}
$$

where the equations $x' = x + l\mathrm{m}_1$, $y' = y + l\mathrm{m}_2$ and $z' = z + l\mathrm{m}_3$ have been used.

By substituting Equation 4.57 in Equation 4.9 (and neglecting the terms of the extension scalar state with an odd exponent for the components of the bond direction vector), the dilatation in a point $\mathbf{x}$ is given as

$$
\begin{aligned}
\theta(\mathbf{x}) &= \frac{3}{m(\mathbf{x})}\int_\Omega\int_0^\delta \exp\left(-\frac{l^2}{\delta^2}\right) l^4\left(c_u y\mathrm{m}_1^2 + c_w x\mathrm{m}_3^2\right)\mathrm{d}l\,\mathrm{d}\Omega_{\mathbf{m}} \\
&= \frac{3}{4\pi\Delta_1}\int_0^\delta \exp\left(-\frac{l^2}{\delta^2}\right) l^4\,\mathrm{d}l\left(c_u y\int_\Omega \mathrm{m}_1^2\,\mathrm{d}\Omega_{\mathbf{m}} + c_w x\int_\Omega \mathrm{m}_3^2\,\mathrm{d}\Omega_{\mathbf{m}}\right) \\
&= \frac{3}{4\pi\Delta_1}\Delta_1\left(c_u y\frac{4\pi}{3} + c_w x\frac{4\pi}{3}\right) \\
&= c_u y + c_w x\,. \qquad (4.58)
\end{aligned}
$$

The volume force applied to a point $\mathbf{x}$ is computed by substituting Equation 4.11 in Equation 4.46 (where $m(\mathbf{x}) = m(\mathbf{x}')$):

$$
\mathbf{b}(\mathbf{x}) = -\frac{1}{m(\mathbf{x})}\int_\Omega\int_0^\delta \exp\left(-\frac{l^2}{\delta^2}\right)\left\{k_\theta l\left[\theta(\mathbf{x}) + \theta(\mathbf{x}')\right] + 2k_e\underline{e}\right\}\mathbf{m}\,l^2\,\mathrm{d}\Omega_{\mathbf{m}}\,\mathrm{d}l\,. \qquad (4.59)
$$

We rewrite the two main terms of the integrand as follows:

$$
\begin{aligned}
\left[\theta(\mathbf{x}) + \theta(\mathbf{x}')\right]\mathbf{m} &= \left[c_u\left(y + y'\right) + c_w\left(x + x'\right)\right]\begin{Bmatrix} \mathrm{m}_1 \\ \mathrm{m}_2 \\ \mathrm{m}_3 \end{Bmatrix} = \left[c_u\left(l\mathrm{m}_2 + 2y\right) + c_w\left(l\mathrm{m}_1 + 2x\right)\right]\begin{Bmatrix} \mathrm{m}_1 \\ \mathrm{m}_2 \\ \mathrm{m}_3 \end{Bmatrix} \\
&= \begin{Bmatrix} c_u l\mathrm{m}_1\mathrm{m}_2 + c_w l\mathrm{m}_1^2 + \left[c_u\left(2y + 2x\right)\right]\mathrm{m}_1 \\ c_u l\mathrm{m}_2^2 + c_w l\mathrm{m}_1\mathrm{m}_2 + \left[c_u\left(2y + 2x\right)\right]\mathrm{m}_2 \\ c_u l\mathrm{m}_2\mathrm{m}_3 + c_w l\mathrm{m}_1\mathrm{m}_3 + \left[c_u\left(2y + 2x\right)\right]\mathrm{m}_3 \end{Bmatrix}, \qquad (4.60)
\end{aligned}
$$

$$
\begin{aligned}
\underline{e}\,\mathbf{m} &= c_u l\begin{Bmatrix} l\mathrm{m}_1^3\mathrm{m}_2 + x\mathrm{m}_1^2\mathrm{m}_2 + y\mathrm{m}_1^3 \\ l\mathrm{m}_1^2\mathrm{m}_2^2 + x\mathrm{m}_1\mathrm{m}_2^2 + y\mathrm{m}_1^2\mathrm{m}_2 \\ l\mathrm{m}_1^2\mathrm{m}_2\mathrm{m}_3 + x\mathrm{m}_1\mathrm{m}_2\mathrm{m}_3 + y\mathrm{m}_1^2\mathrm{m}_3 \end{Bmatrix} \\
&\quad + c_v l\begin{Bmatrix} l^2\mathrm{m}_1^4\mathrm{m}_2 + 3xl\mathrm{m}_1^3\mathrm{m}_2 + 3x^2\mathrm{m}_1^2\mathrm{m}_2 \\ l^2\mathrm{m}_1^3\mathrm{m}_2^2 + 3xl\mathrm{m}_1^2\mathrm{m}_2^2 + 3x^2\mathrm{m}_1\mathrm{m}_2^2 \\ l^2\mathrm{m}_1^3\mathrm{m}_2\mathrm{m}_3 + 3xl\mathrm{m}_1^2\mathrm{m}_2\mathrm{m}_3 + 3x^2\mathrm{m}_1\mathrm{m}_2\mathrm{m}_3 \end{Bmatrix}
\end{aligned}
$$

$$+ c_w l \begin{Bmatrix} l\mathrm{m}_1^2\mathrm{m}_3^2 + x\mathrm{m}_1\mathrm{m}_3^2 + z\mathrm{m}_1^2\mathrm{m}_3 \\ l\mathrm{m}_1\mathrm{m}_2\mathrm{m}_3^2 + x\mathrm{m}_2\mathrm{m}_3^2 + z\mathrm{m}_1\mathrm{m}_2\mathrm{m}_3 \\ l\mathrm{m}_1\mathrm{m}_3^3 + x\mathrm{m}_3^3 + z\mathrm{m}_1\mathrm{m}_3^2 \end{Bmatrix} . \quad (4.61)$$

Therefore, keeping only the terms with all even exponents of the components of the bond direction vector, Equation 4.59 becomes

$$\begin{aligned}
\mathbf{b}(\mathbf{x}) &= -\frac{1}{m(\mathbf{x})} \int_\Omega \int_0^\delta \exp\left(-\frac{l^2}{\delta^2}\right) \left( k_\theta l^2 \begin{Bmatrix} c_w\mathrm{m}_1^2 \\ c_u\mathrm{m}_2^2 \\ 0 \end{Bmatrix} + 2k_e l^2 \begin{Bmatrix} c_w\mathrm{m}_1^2\mathrm{m}_3^2 \\ (c_u + 3c_v x)\mathrm{m}_1^2\mathrm{m}_2^2 \\ 0 \end{Bmatrix} \right) l^2 \, \mathrm{d}\Omega_{\mathbf{m}} \, \mathrm{d}l \\
&= -\frac{1}{4\pi\Delta_1} \int_0^\delta \exp\left(-\frac{l^2}{\delta^2}\right) l^4 \, \mathrm{d}l \int_\Omega \left( k_\theta \begin{Bmatrix} c_w\mathrm{m}_1^2 \\ c_u\mathrm{m}_2^2 \\ 0 \end{Bmatrix} + 2k_e \begin{Bmatrix} c_w\mathrm{m}_1^2\mathrm{m}_3^2 \\ (c_u + 3c_v x)\mathrm{m}_1^2\mathrm{m}_2^2 \\ 0 \end{Bmatrix} \right) \mathrm{d}\Omega_{\mathbf{m}} \\
&= -\frac{1}{4\pi\Delta_1}\Delta_1 \left( \frac{4\pi}{3} k_\theta \begin{Bmatrix} c_w \\ c_u \\ 0 \end{Bmatrix} + \frac{8\pi}{15} k_e \begin{Bmatrix} c_w \\ c_u + 3c_v x \\ 0 \end{Bmatrix} \right) \\
&= \begin{Bmatrix} -c_w \left( \dfrac{k_\theta}{3} + \dfrac{2k_e}{15} \right) \\ -c_u \left( \dfrac{k_\theta}{3} + \dfrac{2k_e}{15} \right) - c_v \dfrac{2k_e}{5} x \\ 0 \end{Bmatrix} .
\end{aligned} \quad (4.62)$$

This is the volume force that should be applied to the body to obtain the manufactured displacement field and the same formula is reported in Equation 4.40.

### 4.A.2 Computation of surface forces

Under the assumption of small displacements, the extension scalar state of the bond between points $\mathbf{x}' = \mathbf{x} - s\mathbf{m}$ and $\mathbf{x}'' = \mathbf{x} + (r - s)\mathbf{m}$ is computed as

$$\begin{aligned}
\underline{e} = [\mathbf{u}(\mathbf{x}'') - \mathbf{u}(\mathbf{x}')] \cdot \mathbf{m} &= \begin{Bmatrix} c_u \left(x''y'' - x'y'\right) \\ c_v \left(x''^3 - x'^3\right) \\ c_w \left(x''z'' - x'z'\right) \end{Bmatrix} \cdot \begin{Bmatrix} \mathrm{m}_1 \\ \mathrm{m}_2 \\ \mathrm{m}_3 \end{Bmatrix} \\
&= \begin{Bmatrix} c_u \left[(r^2 - 2sr)\mathrm{m}_1\mathrm{m}_2 + xr\mathrm{m}_2 + yr\mathrm{m}_1\right] \\ c_v \left[(r^3 - 3sr^2 + 3s^2 r)\mathrm{m}_1^3 + 3x(r^2 - 2sr)\mathrm{m}_1^2 + 3x^2 r\mathrm{m}_1\right] \\ c_w \left[(r^2 - 2sr)\mathrm{m}_1\mathrm{m}_3 + xr\mathrm{m}_3 + zr\mathrm{m}_1\right] \end{Bmatrix} \cdot \begin{Bmatrix} \mathrm{m}_1 \\ \mathrm{m}_2 \\ \mathrm{m}_3 \end{Bmatrix}
\end{aligned}$$

$$
\begin{aligned}
&= c_u \left[(r^2 - 2sr)\mathrm{m}_1^2\mathrm{m}_2 + xr\mathrm{m}_1\mathrm{m}_2 + yr\mathrm{m}_1^2\right] \\
&\quad + c_v \left[(r^3 - 3sr^2 + 3s^2r)\mathrm{m}_1^3\mathrm{m}_2 + 3x(r^2 - 2sr)\mathrm{m}_1^2\mathrm{m}_2 + 3x^2r\mathrm{m}_1\mathrm{m}_2\right] \\
&\quad + c_w \left[(r^2 - 2sr)\mathrm{m}_1\mathrm{m}_3^2 + xr\mathrm{m}_3^2 + zr\mathrm{m}_1\mathrm{m}_3\right], \qquad (4.63)
\end{aligned}
$$

where the equations $x' = x - s\mathrm{m}_1$, $y' = y - s\mathrm{m}_2$, $z' = z - s\mathrm{m}_3$, $x'' = x + (r-s)\mathrm{m}_1$, $y' = y + (r-s)\mathrm{m}_2$ and $z' = z + (r-s)\mathrm{m}_3$ have been used.

The peridynamic stress tensor of a point $\mathbf{x}$ is computed by substituting Equation 4.11 in Equation 4.47 (where $m(\mathbf{x}') = m(\mathbf{x}'') = m(\mathbf{x})$):

$$
\boldsymbol{\tau}(\mathbf{x}) = \frac{1}{2m(\mathbf{x})} \int_\Omega \int_0^\delta \int_s^\delta \exp\left(-\frac{r^2}{\delta^2}\right) \left\{k_\theta r \left[\theta(\mathbf{x}') + \theta(\mathbf{x}'')\right] + 2k_e \underline{e}\right\} \mathbf{m} \otimes \mathbf{m}\, r^2 \,\mathrm{d}r \,\mathrm{d}s \,\mathrm{d}\Omega_{\mathbf{m}} \qquad (4.64)
$$

We rewrite the sum of the dilatations as follows:

$$
\begin{aligned}
\theta(\mathbf{x}') + \theta(\mathbf{x}'') &= c_u \left(y' + y''\right) + c_w \left(x' + x''\right) \\
&= c_u \left[(r - 2s)\mathrm{m}_2 + 2y\right] + c_w \left[(r - 2s)\mathrm{m}_1 + 2x\right], \qquad (4.65)
\end{aligned}
$$

Then, by omitting the terms with at least one odd exponent for the components of the bond direction vector, the peridynamic stress tensor is given as

$$
\begin{aligned}
\boldsymbol{\tau}(\mathbf{x}) = \frac{1}{2m(\mathbf{x})} \int_\Omega \int_0^\delta \int_s^\delta \exp\left(-\frac{r^2}{\delta^2}\right) \Bigg( & 2k_\theta r^3 \left(c_u y + c_w x\right) \begin{bmatrix} \mathrm{m}_1^2 & 0 & 0 \\ 0 & \mathrm{m}_2^2 & 0 \\ 0 & 0 & \mathrm{m}_3^2 \end{bmatrix} \\
& + 2k_e r^3 \begin{bmatrix} c_u y\mathrm{m}_1^4 + c_w x\mathrm{m}_1^2\mathrm{m}_3^2 & (c_u x + 3c_v x^2)\mathrm{m}_1^2\mathrm{m}_2^2 & c_w z\mathrm{m}_1^2\mathrm{m}_3^2 \\ (c_u x + 3c_v x^2)\mathrm{m}_1^2\mathrm{m}_2^2 & c_u y\mathrm{m}_1^2\mathrm{m}_2^2 + c_w x\mathrm{m}_2^2\mathrm{m}_3^2 & 0 \\ c_w z\mathrm{m}_1^2\mathrm{m}_3^2 & 0 & c_u y\mathrm{m}_1^2\mathrm{m}_3^2 + c_w x\mathrm{m}_3^4 \end{bmatrix} \\
& + 2k_e r^3 (r^2 - 3sr + 3s^2) \begin{bmatrix} 0 & c_v\mathrm{m}_1^4\mathrm{m}_2^2 & 0 \\ c_v\mathrm{m}_1^4\mathrm{m}_2^2 & 0 & 0 \\ 0 & 0 & 0 \end{bmatrix} \Bigg) \mathrm{d}r \,\mathrm{d}s \,\mathrm{d}\Omega_{\mathbf{m}}
\end{aligned}
$$

$$
\begin{aligned}
= \frac{1}{8\pi\Delta_1} \Bigg( & 2k_\theta \left(c_u y + c_w x\right) \Delta_1 \frac{4\pi}{3} \begin{bmatrix} 1 & 0 & 0 \\ 0 & 1 & 0 \\ 0 & 0 & 1 \end{bmatrix} \\
& + 2k_e \Delta_1 \frac{4\pi}{15} \begin{bmatrix} 3c_u y + c_w x & c_u x + 3c_v x^2 & c_w z \\ c_u x + 3c_v x^2 & c_u y + c_w x & 0 \\ c_w z & 0 & c_u y + 3c_w x \end{bmatrix} + 2k_e c_v \Delta_2 \frac{4\pi}{35} \begin{bmatrix} 0 & 1 & 0 \\ 1 & 0 & 0 \\ 0 & 0 & 0 \end{bmatrix} \Bigg)
\end{aligned}
$$

$$= \begin{bmatrix} c_u\left(\frac{k_\theta}{3}+\frac{k_e}{5}\right)y + c_w\left(\frac{k_\theta}{3}+\frac{k_e}{15}\right)x & c_u\frac{k_e}{15}x + c_v\left(\frac{k_e}{5}x^2+\frac{k_e}{35}\frac{\Delta_2}{\Delta_1}\right) & c_w\frac{k_e}{15}z \\ c_u\frac{k_e}{15}x + c_v\left(\frac{k_e}{5}x^2+\frac{k_e}{35}\frac{\Delta_2}{\Delta_1}\right) & c_u\left(\frac{k_\theta}{3}+\frac{k_e}{15}\right)y + c_w\left(\frac{k_\theta}{3}+\frac{k_e}{15}\right)x & 0 \\ c_w\frac{k_e}{15}z & 0 & c_u\left(\frac{k_\theta}{3}+\frac{k_e}{15}\right)y + c_w\left(\frac{k_\theta}{3}+\frac{k_e}{5}\right)x \end{bmatrix}. \tag{4.66}$$

The surface force at a point $\mathbf{x}$ on the external surface of the body with a normal $\mathbf{n}$ can be computed as $\boldsymbol{\tau}(\mathbf{x},\mathbf{n}) = \boldsymbol{\tau}(\mathbf{x})\cdot\mathbf{n}$. The components of the stress tensor are reported in Equation 4.41.

# Chapter 5

# Accurate computation of partial volumes in 3D peridynamics

**Published in:** *Engineering with Computers* (2023)

**Authors:** Francesco Scabbia, Mirco Zaccariotto, Ugo Galvanetto

## Abstract

The peridynamic theory is a nonlocal formulation of continuum mechanics based on integro-differential equations, devised to deal with fracture in solid bodies. In particular, the forces acting on each material point are evaluated as the integral of the nonlocal interactions with all the neighboring points within a spherical region, called "neighborhood". Peridynamic bodies are commonly discretized by means of a meshfree method into a uniform grid of cubic cells. The numerical integration of the nonlocal interactions over the neighborhood strongly affects the accuracy and the convergence behavior of the results. However, near the boundary of the neighborhood some cells are only partially within the sphere. Therefore, the quadrature weights related to those cells are computed as the fraction of cell volume which actually lies inside the neighborhood. This leads to the complex computation of the volume of several cube-sphere intersections for different positions of the cells. We developed an innovative algorithm able to accurately compute the quadrature weights in 3D peridynamics for any value of the grid spacing (when considering fixed the radius of the neighborhood). Several examples have been presented to show the capabilities of the proposed algorithm. With respect to the most common algorithm to date, the new algorithm provides an evident improvement in the accuracy of the results and a smoother convergence behavior as the grid spacing decreases.

**Keywords:** Quadrature weights, 3D peridynamics, cube-sphere intersection, meshless method, convergence studies, improved numerical integration.

## 5.1 Introduction

The peridynamic theory provides a nonlocal reformulation of classical continuum mechanics: the internal forces are evaluated with integral equations, which are valid regardless of the presence of discontinuities in the displacement field. Hence, peridynamics can naturally model crack initiation, propagation and branching in solids. The first formulation of the peridynamic theory was the bond-based version [61], in which the Poisson's ratio is restricted to a fixed value. Subsequently, state-based peridynamics was developed [62], introducing the possibility of varying the Poisson's ratio. In the literature there are many examples of applications [74, 145], ranging from complex crack patterns, such as spontaneous branching [68], to multi-physics problems involving fracture [243, 244].

Peridynamic points interact with each other up to a finite distance $\delta$, called "horizon". The "neighborhood" of a point is the set of all the points interacting with that point. Therefore, the neighborhood has a circular shape in 2D problems and a spherical shape in 3D problems. The peridynamic equation of motion is based on the spatial integration over the neighborhood of the internal forces, which are generated by the interactions between neighboring points. In practice, the integration of the peridynamic equation of motion is carried out by means of numerical tools. The body can be discretized by a uniform or non-uniform grid (see for instance [181–183]). Various methods have been utilized to integrate numerically peridynamic equations: meshfree method with composite midpoint quadrature [65, 158, 173, 184], Gauss-Hermite quadrature [173], finite element method [173, 176, 178], collocation method [245, 246] and an adaptive integration method with error control [224]. Thanks to its simplicity of implementation and relatively low computational cost compared to other approaches, the meshfree method with a uniform grid is the most commonly used for peridynamic simulations. In this method, the body is discretized in volume cells with a square shape in 2D problems and cubic in 3D, and the nodes lie at the center of the corresponding cells. The spatial integration over the neighborhood is transformed into a summation of integrals over cells and the midpoint quadrature rule is then applied in each cell, in which the nodes are employed as quadrature points.

However, near the boundary of the neighborhood some cells are only partially within the neighborhood itself. Therefore, the quadrature weights related to those cells are computed as the fraction of cell volume which actually lies inside the neighborhood. The intersection area or volume of those cells with the neighborhood is also referred to as "partial area" in 2D and "partial volume" in 3D. The accuracy and convergence of the peridynamic results depend on the algorithm to compute the quadrature weights, i.e., the partial areas or volumes [158, 184, 247].

The first algorithm proposed in [65] considers the nodes within the neighborhood with their entire cell (even if a part of the volume is partially outside the neighborhood) and neglects the nodes outside the neighborhood (even if their cell is partially inside the neighborhood). This approach, under grid refinement, leads to an oscillatory convergence behavior in which the fluctuations seem rather random [184]. Many other algorithms to approximate the partial volumes have been proposed since then. An approximation based on the distance between neighboring nodes is proposed in [197], which improves the computation of the par-

tial volumes of nodes within the neighborhood. A similar approximation is used in [160, 198] to include the previously neglected partial volumes of nodes outside the neighborhood but with a part of the cell inside it. These algorithms reduce, but never eliminate, the seemingly random fluctuations of the convergence behavior. Subsequently, the algorithm to compute analytically the partial areas has been developed in [184]: the types of intersection between the neighborhood and the cells are rigorously categorized and then subdivided into domains of basic geometry (triangles, rectangles and circular segments), for which the analytical computation of the area is straightforward. By using this algorithm, the convergence behavior is smoothly oscillatory and the simulations yield results affected by a smaller error, on average, compared to the previously mentioned algorithms. In [184] it is also suggested to use the centroids of the partial areas as quadrature points, but this significantly increases the complexity of the computational model. The analytical computation of the partial volumes in 3D problems is much more complex and no algorithm is currently available for such purpose. The partial volumes can be computed numerically by two proposed algorithms, one based on the trapezoidal rule [224] and one based on a process of recursive subdivisions and sampling [158]. However, to reach the desired accuracy the computational cost may be very high. Other algorithms, specialized for non-uniform grids, are presented in [182, 198, 216, 248].

The aim of this paper is to simplify the implementation of the algorithm to compute analytically the partial areas presented in [184] by skipping the step of subdivision of the intersection area in basic geometries, and to develop an algorithm for the analytical computation of the partial volumes. In order to achieve this, we solve directly the integrals which describe all the possible intersection areas or volumes. Actually, some integrals involved in the computation of the partial volumes are not explicitly solvable. Hence, we perform a Taylor series expansion of those functions and integrate the polynomials. The computation of the partial volumes converges to the analytical solution if the sum of infinite terms is not truncated. This, clearly, is not possible in a numerical model, but we will show that the algorithm is able to reach values of the error very close to machine precision with little computational effort. The numerical results obtained with the new algorithm show an evident improvement in the accuracy and in the convergence behavior when compared to the results obtained by the algorithm based on the approximation proposed by [198], which is arguably the most commonly used in engineering applications. We compared the numerical results by using the ordinary state-based version of the peridynamic theory, but the algorithm can be used with the bond-based version as well.

The paper is divided as follows. Section 5.2 reviews the basics of the state-based peridynamic theory and its discretized formulation. Section 5.3 presents the innovative algorithms for the computation of the partial areas and partial volumes. Section 5.4 contains several numerical examples that show the improvements provided by the proposed algorithm for the computation of the partial volumes with respect to the most commonly used algorithm. Section 5.5 draws the conclusions of the work.

## 5.2 Peridynamic theory

The peridynamic theory is a continuum theory based on nonlocal interactions between material points [61]. The derived numerical formulation is a very useful tool for simulating crack propagation in solid bodies. In the following, we present the fundamentals of the ordinary state-based peridynamics and the discretized formulae which could be implemented in a computational code.

### 5.2.1 Continuum model

The nonlocal interaction between two points, $\mathbf{x}$ and $\mathbf{x}'$, in a peridynamic body $\mathcal{B}$ is described by a quantity named "bond":

$$\boldsymbol{\xi} := \mathbf{x}' - \mathbf{x}\,, \tag{5.1}$$

where the point $\mathbf{x}'$ is contained in the neighborhood $\mathcal{H}_{\mathbf{x}} := \left\{ \mathbf{x}' \in \mathcal{B} : \|\boldsymbol{\xi}\| \leq \delta \right\}$. The relative displacement vector $\boldsymbol{\eta}$ is defined as

$$\boldsymbol{\eta} := \mathbf{u}(\mathbf{x}', t) - \mathbf{u}(\mathbf{x}, t)\,, \tag{5.2}$$

where $\mathbf{u}$ is the displacement field. Note that $\boldsymbol{\xi} + \boldsymbol{\eta}$ is the relative position of points $\mathbf{x}$ and $\mathbf{x}'$ after the deformation occurred.

The state-based peridynamic equation of motion of a point $\mathbf{x}$ within the body $\mathcal{B}$ is given by [62]

$$\rho(\mathbf{x})\,\ddot{\mathbf{u}}(\mathbf{x}, t) = \int_{\mathcal{H}_{\mathbf{x}}} \left( \underline{\mathbf{T}}[\mathbf{x}, t]\langle \boldsymbol{\xi} \rangle - \underline{\mathbf{T}}[\mathbf{x}', t]\langle -\boldsymbol{\xi} \rangle \right) \mathrm{d}V_{\mathbf{x}'} + \mathbf{b}(\mathbf{x}, t)\,, \tag{5.3}$$

where $\rho$ is the material density, $\ddot{\mathbf{u}}$ is the acceleration field, $\underline{\mathbf{T}}$ is the force state, $\mathrm{d}V_{\mathbf{x}'}$ is the differential volume of a point $\mathbf{x}'$ within the neighborhood $\mathcal{H}_{\mathbf{x}}$ and $\mathbf{b}$ is the external force density field. The notation $\underline{\mathbf{T}}[\mathbf{x}, t]\langle \boldsymbol{\xi} \rangle$ means that the state $\underline{\mathbf{T}}$ depends on the position of the point $\mathbf{x}$ and on the time $t$, and operates on the bond $\boldsymbol{\xi}$. In an ordinary state-based peridynamic model, the force state is aligned with the corresponding bond for any deformation, as depicted in Figure 5.1. For the purposes of the paper, it suffices to limit the study to quasi-static problems [72, 73, 222]. Hence, the peridynamic equilibrium equation is derived from Equation 5.3 by dropping the dependence on time:

$$-\int_{\mathcal{H}_{\mathbf{x}}} \left( \underline{\mathbf{T}}[\mathbf{x}]\langle \boldsymbol{\xi} \rangle - \underline{\mathbf{T}}[\mathbf{x}']\langle -\boldsymbol{\xi} \rangle \right) \mathrm{d}V_{\mathbf{x}'} = \mathbf{b}(\mathbf{x})\,. \tag{5.4}$$

The reference position scalar state $\underline{x}$, representing the bond length, the extension scalar state $\underline{e}$, describing the elongation (or contraction) of the bond in the deformed body, and the deformed direction vector state $\underline{\mathbf{M}}$, the unit vector in the direction of $\underline{\mathbf{T}}$, are respectively defined as

$$\underline{x}\langle \boldsymbol{\xi} \rangle := \|\boldsymbol{\xi}\|\,, \tag{5.5}$$

$$\underline{e}\langle \boldsymbol{\xi} \rangle := \|\boldsymbol{\xi} + \boldsymbol{\eta}\| - \|\boldsymbol{\xi}\|\,, \tag{5.6}$$

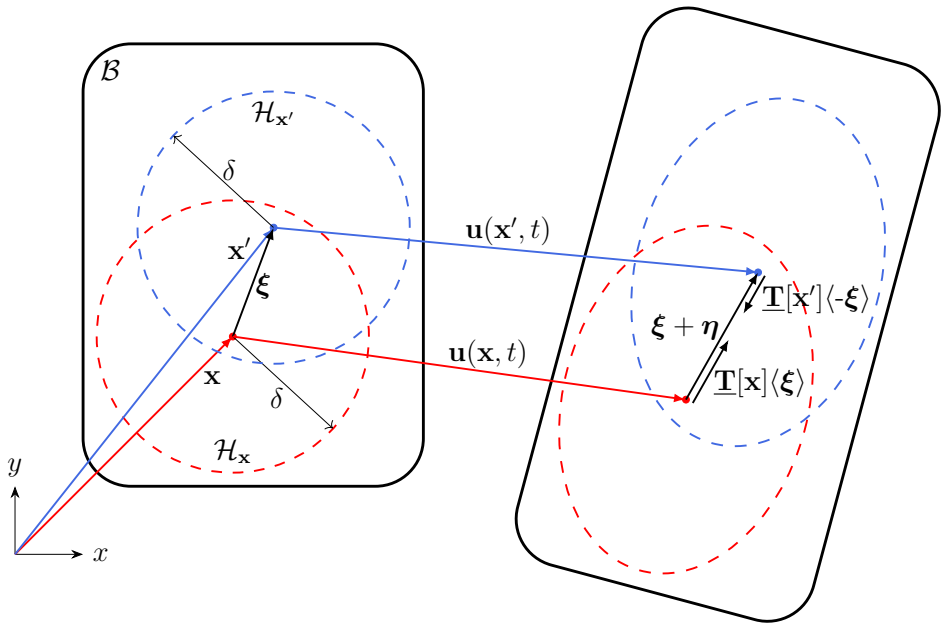


Figure 5.1: *Body $\mathcal{B}$ modelled with ordinary state-based peridynamics: the force states $\underline{\mathbf{T}}[\mathbf{x}]\langle\boldsymbol{\xi}\rangle$ and $\underline{\mathbf{T}}[\mathbf{x}']\langle-\boldsymbol{\xi}\rangle$ arise in the bond $\boldsymbol{\xi}$ due to the deformation of the body.*

$$\underline{\mathbf{M}}\langle\boldsymbol{\xi}\rangle := \frac{\boldsymbol{\xi} + \boldsymbol{\eta}}{\|\boldsymbol{\xi} + \boldsymbol{\eta}\|} \,. \tag{5.7}$$

The weighted volume $m$ and the dilatation $\theta$ of a point $\mathbf{x}$ are defined as

$$m_{\mathbf{x}} := \int_{\mathcal{H}_{\mathbf{x}}} \underline{\omega}\langle\boldsymbol{\xi}\rangle \left(\underline{x}\langle\boldsymbol{\xi}\rangle\right)^2 \mathrm{d}V_{\mathbf{x}'} \,, \tag{5.8}$$

$$\theta_{\mathbf{x}} := \frac{3}{m_{\mathbf{x}}} \int_{\mathcal{H}_{\mathbf{x}}} \underline{\omega}\langle\boldsymbol{\xi}\rangle \, \underline{x}\langle\boldsymbol{\xi}\rangle \, \underline{e}\langle\boldsymbol{\xi}\rangle \, \mathrm{d}V_{\mathbf{x}'} \,, \tag{5.9}$$

where $\underline{\omega}$ is a prescribed spherical influence function [147]. We adopt the Gaussian influence function

$$\underline{\omega}\langle\boldsymbol{\xi}\rangle := \exp\left(-\frac{\|\boldsymbol{\xi}\|^2}{\delta^2}\right) \,. \tag{5.10}$$

Adopting the linear peridynamic solid model [62], the force state is computed as

$$\underline{\mathbf{T}}[\mathbf{x}]\langle\boldsymbol{\xi}\rangle = \left[(3K - 5\mu)\, \frac{\underline{\omega}\langle\boldsymbol{\xi}\rangle \, \underline{x}\langle\boldsymbol{\xi}\rangle}{m_{\mathbf{x}}}\, \theta_{\mathbf{x}} + 15\mu\, \frac{\underline{\omega}\langle\boldsymbol{\xi}\rangle \, \underline{e}\langle\boldsymbol{\xi}\rangle}{m_{\mathbf{x}}}\right] \underline{\mathbf{M}}\langle\boldsymbol{\xi}\rangle \,, \tag{5.11}$$

where $K$ is the bulk modulus and $\mu$ is the shear modulus. Since $\underline{\mathbf{M}}\langle\boldsymbol{\xi}\rangle = -\underline{\mathbf{M}}\langle-\boldsymbol{\xi}\rangle$, the ordinary state-based peridynamic equilibrium equation becomes [62, 227, 236]

$$-\int_{\mathcal{H}_{\mathbf{x}}} \left[(3K - 5\mu)\left(\frac{\theta_{\mathbf{x}}}{m_{\mathbf{x}}} + \frac{\theta_{\mathbf{x}'}}{m_{\mathbf{x}'}}\right) \underline{\omega}\langle\boldsymbol{\xi}\rangle \, \underline{x}\langle\boldsymbol{\xi}\rangle \right. \\ \left. + 15\mu\left(\frac{1}{m_{\mathbf{x}}} + \frac{1}{m_{\mathbf{x}'}}\right) \underline{\omega}\langle\boldsymbol{\xi}\rangle \, \underline{e}\langle\boldsymbol{\xi}\rangle\right] \underline{\mathbf{M}}\langle\boldsymbol{\xi}\rangle \, \mathrm{d}V_{\mathbf{x}'} = \mathbf{b}(\mathbf{x}) \,. \tag{5.12}$$

Equation 5.12 relates the external forces to the displacement field, which might be a discon-

tinuous function with respect to the spatial coordinates.

### 5.2.2 Discretized model

We adopt a meshfree method with a uniform grid spacing $h$ to discretize the body domain (see, for instance, the discretization of a neighborhood in Figure 5.2). Therefore, the cells surrounding each node are squares in 2D and cubes in 3D respectively with an area $A = h^2$ and a volume $V = h^3$.

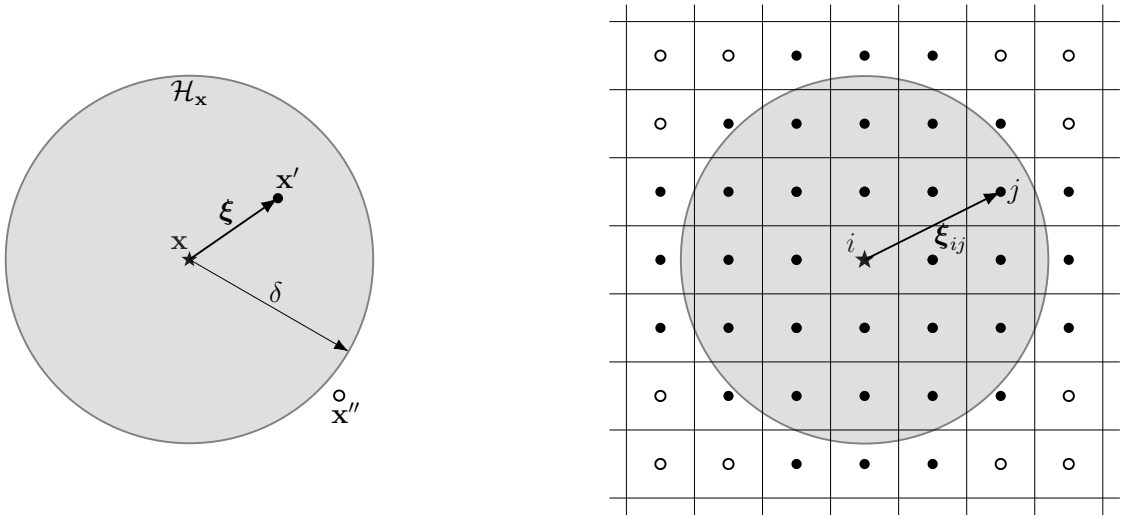


(a) *Neighborhood of point* $\mathbf{x}$ *(continuum model).* (b) *Neighborhood of node* $i$ *(discretized model).*

Figure 5.2: *In the continuum model of the neighborhood* $\mathcal{H}_{\mathbf{x}}$ *of a given point* $\mathbf{x}$*, some points (as point* $\mathbf{x}'$*) lie inside the neighborhood and some other (as point* $\mathbf{x}''$*) lie outside. Similarly, in the discretized model of the neighborhood* $\mathcal{H}_i$ *of a given node* $i$*, there are some nodes (solid circles) whose cell lies completely or partially inside the neighborhood and other nodes (empty circles) whose cell lies completely outside the neighborhood.*

Consider a node $i$ as the node at which the peridynamic equilibrium equation should be computed and a node $j$ with a portion of its cell inside the neighborhood $\mathcal{H}_i$ of node $i$. The bond connecting node $i$ to node $j$ is described by

$$\boldsymbol{\xi}_{ij} = \mathbf{x}_j - \mathbf{x}_i \,. \tag{5.13}$$

Analogously, the relative displacement vector after the deformation of the body is defined as

$$\boldsymbol{\eta}_{ij} = \mathbf{u}_j - \mathbf{u}_i \,, \tag{5.14}$$

where $\mathbf{u}_i$ and $\mathbf{u}_j$ are the displacement vectors of nodes $i$ and $j$, respectively.

Hence, the reference position scalar state and the influence function of bond $ij$ can be computed as follows:

$$\underline{x}_{ij} = \|\boldsymbol{\xi}_{ij}\| \,, \tag{5.15}$$

$$\underline{\omega}_{ij} = \exp\left(-\frac{\|\boldsymbol{\xi}_{ij}\|^2}{\delta^2}\right) . \tag{5.16}$$

Under the assumption of small displacements, the extension scalar state of bond $ij$ is given as

$$\underline{e}_{ij} = \|\boldsymbol{\xi}_{ij} + \boldsymbol{\eta}_{ij}\| - \|\boldsymbol{\xi}_{ij}\| \overset{\|\boldsymbol{\eta}_{ij}\| \ll \|\boldsymbol{\xi}_{ij}\|}{\approx} \boldsymbol{\eta}_{ij} \cdot \frac{\boldsymbol{\xi}_{ij}}{\|\boldsymbol{\xi}_{ij}\|} \,. \tag{5.17}$$

The non-local properties of node $i$, i.e., the weighted volume $m_i$ and the dilatation $\theta_i$, are determined numerically by transforming the integrals in Equations 5.8 and 5.9 into a summation of integrals over cells and applying a midpoint quadrature rule in each cell:

$$m_i = \sum_{j \in \mathcal{H}_i} \underline{\omega}_{ij} \, \underline{x}_{ij}^2 \, \beta_{ij} \, V \,, \tag{5.18}$$

$$\theta_i = \frac{c_\theta}{m_i} \sum_{j \in \mathcal{H}_i} \underline{\omega}_{ij} \, \underline{x}_{ij} \, \underline{e}_{ij} \, \beta_{ij} \, V \,, \tag{5.19}$$

where $\beta_{ij}V$ represents the quadrature weight of the contribution of node $j$ in the integral over the neighborhood of node $i$. The accurate computation of coefficients $\beta_{ij}$ is the main result of the paper, which is presented in Section 5.3. In 2D problems under plane stress conditions, the volume of the cell is given as $V = A\,t$, where $t$ is the constant thickness of the plate.

Under the assumption of small displacements ($\underline{\mathbf{M}}\langle\boldsymbol{\xi}_{ij}\rangle \approx \boldsymbol{\xi}_{ij}/\|\boldsymbol{\xi}_{ij}\|$), the peridynamic equilibrium equation in the discretized form is computed by using the quadrature scheme previously described as

$$-\sum_{j \in \mathcal{H}_i} \left[ (3K - 5\mu) \left( \frac{\theta_i}{m_i} + \frac{\theta_j}{m_j} \right) \underline{\omega}_{ij} \, \underline{x}_{ij} + 15\mu \left( \frac{1}{m_i} + \frac{1}{m_j} \right) \underline{\omega}_{ij} \, \underline{e}_{ij} \right] \frac{\boldsymbol{\xi}_{ij}}{\|\boldsymbol{\xi}_{ij}\|} \, \beta_{ij} \, V = \mathbf{b}_i \,, \tag{5.20}$$

where $m_j$ and $\theta_j$ are respectively the weighted volume and the dilatation of node $j$ computed with Equations 5.18 and 5.19, and $\mathbf{b}_i$ is the external force density vector applied to node $i$.

## 5.3 Algorithms for the computation of the quadrature weights

The quadrature coefficient $\beta_{ij}$ is the dimensionless factor defined as

$$\beta_{ij} := \begin{cases} \dfrac{\widetilde{V}}{V} & \text{in 3D,} \\[2ex] \dfrac{\widetilde{A}}{A} & \text{in 2D,} \end{cases} \tag{5.21}$$

where $\widetilde{V}$ and $\widetilde{A}$ are respectively the partial volume and partial area of the cell, which should be computed from the intersection between the neighborhood $\mathcal{H}_i$ and the cell itself. In particular, $\beta_{ij} = 1$ if the cell is completely inside $\mathcal{H}_i$, $\beta_{ij} = 0$ if the cell is completely outside $\mathcal{H}_i$ and $0 < \beta_{ij} < 1$ if the cell is partially inside $\mathcal{H}_i$. The set of nodes which constitutes $\mathcal{H}_i := \{\, j \in \mathcal{B} : \beta_{ij} > 0 \,\}$ depends on the algorithm used to compute $\beta_{ij}$.

We present one of the algorithms based on the approximation of the partial volume [198],

used as a reference to compare our results. In order to compute analitycally $\beta_{ij}$ in a convenient framework, we define a new reference system and exploit the cell-neighborhood symmetries. Then, we improve the algorithm for the analytical computation of partial areas by employing a simpler scheme and we use the same scheme to compute quasi-analytically the partial volumes. We utilize the expression "quasi-analytical" because the algorithm includes the truncation of the Taylor series expansions, but it is able to attain accurate results with a relatively small truncation order.

### 5.3.1 Approximated computation of partial areas or volumes

In the literature there are many algorithms that compute the partial areas or volumes as an approximation based on the distance between neighboring nodes [184]. The algorithm presented in [198] (see Algorithm 1) is arguably the most commonly used to date. This algorithm is based on the analytical computation of partial lengths in 1D problems, as shown in Figure 5.3. If the distance between node $i$ and the farthest side of the cell of node $j$ is smaller than the horizon size, namely $\|\boldsymbol{\xi}_{ij}\| + \frac{h}{2} < \delta$ where $h$ is the grid spacing, then $\beta_{ij} = 1$ (see Figure 5.3a). If the distance between node $i$ and the closest side of the cell of node $j$ is greater than the horizon size, namely $\|\boldsymbol{\xi}_{ij}\| - \frac{h}{2} > \delta$, then $\beta_{ij} = 0$ (see Figure 5.3c). Otherwise, $\beta_{ij}$ is computed as the difference between the horizon size and the distance of the closest side of the cell of node $j$ from node $i$, divided by the grid spacing $h$ (see Figure 5.3b).

**Algorithm 1.** Approximation of quadrature coefficients ([198]).

**Input:** $\boldsymbol{\xi}_{ij}$, $\delta$, $h$
**Output:** $\beta_{ij}$

**if** $\|\boldsymbol{\xi}_{ij}\| + \frac{h}{2} < \delta$ **then** ▷ *case-1*
    $\beta_{ij} = 1$
**else if** $\|\boldsymbol{\xi}_{ij}\| - \frac{h}{2} < \delta$ **then** ▷ *case-2*
    $\beta_{ij} = \left[\delta - \left(\|\boldsymbol{\xi}_{ij}\| - \frac{h}{2}\right)\right]/h$
**else** ▷ *case-3*
    $\beta_{ij} = 0$
**end if**
**return** $\beta_{ij}$

Algorithm 1 is applied without modifications to 2D and 3D problems. If the direction of $\boldsymbol{\xi}_{ij}$ lies along one of the axis, as for instance in Figure 5.3b, the approximation is quite accurate. However, Figure 5.4 shows other examples in which the computation of the quadrature weights with Algorithm 1 can be rather inaccurate. As a result, even if this algorithm is very simple, it leads to convergence issues [158, 184]: for small variations of the grid spacing (considering fixed the horizon size) there are considerable variations of the computed mechanical properties, as the numerical results of Sections 5.4.2 and 5.4.3 show.

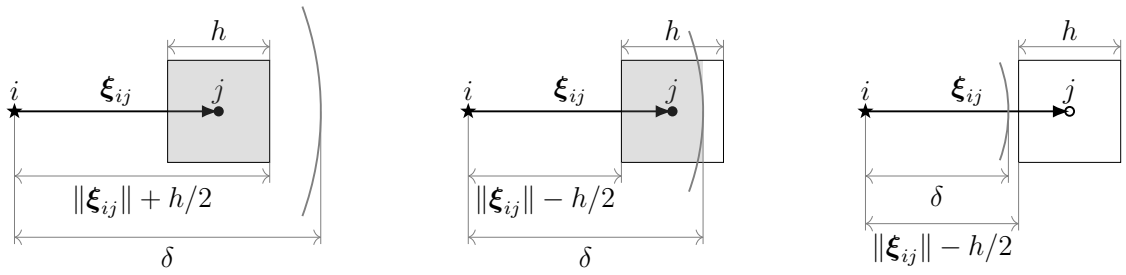


(a) *Case-1.* (b) *Case-2.* (c) *Case-3.*

Figure 5.3: *Possible cases of intersections between neighborhood and cell considered by Algorithm 1: the gray area represents the quadrature weight of the corresponding cell.*

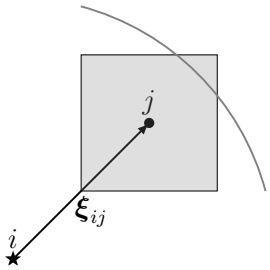


(a) *Algorithm 1:* $\beta_{ij} = 1$.
*Analytical:* $\beta_{ij} = 0.9579$.

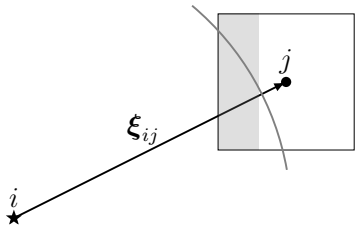


(b) *Algorithm 1:* $\beta_{ij} = 0.3$.
*Analytical:* $\beta_{ij} = 0.2489$.

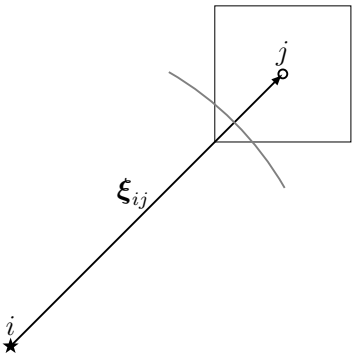


(c) *Algorithm 1:* $\beta_{ij} = 0$.
*Analytical:* $\beta_{ij} = 0.0403$.

Figure 5.4: *Some examples in which the quadrature weights computed with Algorithm 1 are rather different from their analytical values: the gray area represents the quadrature weight of the corresponding cell computed with Algorithm 1.*

### 5.3.2 Change of reference system

For simplicity sake, the concepts are hereinafter explained in the 2D case, but the generalization to a 3D case is straightforward. Since the focus is on the neighborhood of a node $i$, we adopt a new system of reference $(\overline{x}, \overline{y})$ with the origin at $(x_i, y_i)$ and the distances scaled by a factor $1/h$, as shown in Figure 5.5. Note that, since the quadrature coefficient $\beta_{ij}$ is normalized with the area or volume of the cell (see Equation 5.21), its value is not affected by the scaling of the distances. The coordinates of a node $j$ in the new reference system are

given as

$$(\overline{x}_j, \overline{y}_j) = \left( \frac{x_j - x_i}{h}, \frac{y_j - y_i}{h} \right). \tag{5.22}$$

Since the grid is uniform, $\overline{x}_j$ and $\overline{y}_j$ are integer numbers.

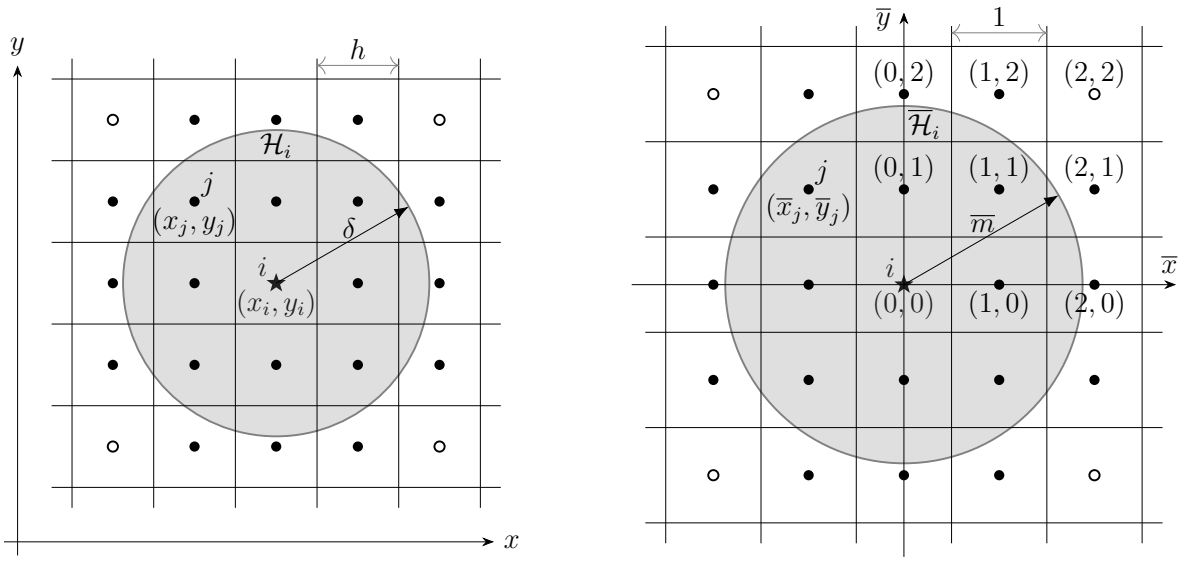


Figure 5.5: (a) $\mathcal{H}_i$ *is the neighborhood of node* $i$ *in a general reference system and* (b) $\overline{\mathcal{H}}_i$ *in the scaled reference system: the origin of the new reference system is centered at node* $i$ *and the distances are scaled by a uniform factor* $1/h$ *in all directions, where* $h$ *is the grid spacing. The coordinates of a node* $j$ *in the new reference system are given as* $\overline{x}_j = (x_j - x_i)/h$ *and* $\overline{y}_j = (y_j - y_i)/h$*, and the horizon size of the neighborhood becomes* $\overline{m} = \delta/h$*.*

As shown in Figure 5.5b, the grid spacing in the new reference system is equal to 1, so that the area or the volume of each cell are $A = 1$ and $V = 1$, respectively. Therefore, $\beta_{ij}$ is simply computed as the area or volume of the intersection between the neighborhood of node $i$ and the cell of node $j$: $\beta_{ij} = \widetilde{A}/A = \widetilde{A}$ or $\beta_{ij} = \widetilde{V}/V = \widetilde{V}$. Furthermore, the only parameter which can change the values of the quadrature coefficients is the $\overline{m}$-ratio, given as

$$\overline{m} := \frac{\delta}{h}. \tag{5.23}$$

If $\overline{m}$ is unique for the whole peridynamic body (as it is often the case), then the values of $\beta_{ij}$ can be computed only once and used for the neighborhoods of all the nodes.

### 5.3.3 Cell-neighborhood symmetries

The symmetries of the neighborhood with respect to the nodal grid, named "cell-neighborhood symmetries", can be exploited to reduce the number of cases to be considered. In [184] the symmetries with respect to the axes were used to compute the quadrature weights only in the first quadrant. On the other hand, we use four lines of symmetry for a 2D neighborhood (both the axes and the bisectors of the quadrants), as shown in Figure 5.6. Therefore, the computation of the partial area can be carried out only for the nodes satisfying the following conditions: $M \geq \overline{y}_j \geq \overline{x}_j \geq 0$, where $M := \lfloor \overline{m} + 0.5 \rfloor$ ($\lfloor \cdot \rfloor$ stands for the floor function

and finds the greatest integer smaller than or equal to the input), and $\overline{y}_j \neq 0$. The latter condition is given by the fact that the central node does not interact with itself. On the other hand, the value $M$ is used to provide an upper limit to the search for possible nodes inside the neighborhood. These nodes are enclosed by a red line in Figure 5.6. Thanks to the cell-neighborhood symmetries, $\beta_{ij}$ of the other nodes have the same values. For instance, the computation of the partial area for the node $(\overline{x}_j = 2, \overline{y}_j = 3)$ is the same for nodes $(3, 2)$, $(3, -2)$, $(2, -3)$, $(-2, -3)$, $(-3, -2)$, $(-3, 2)$ and $(-2, 3)$.

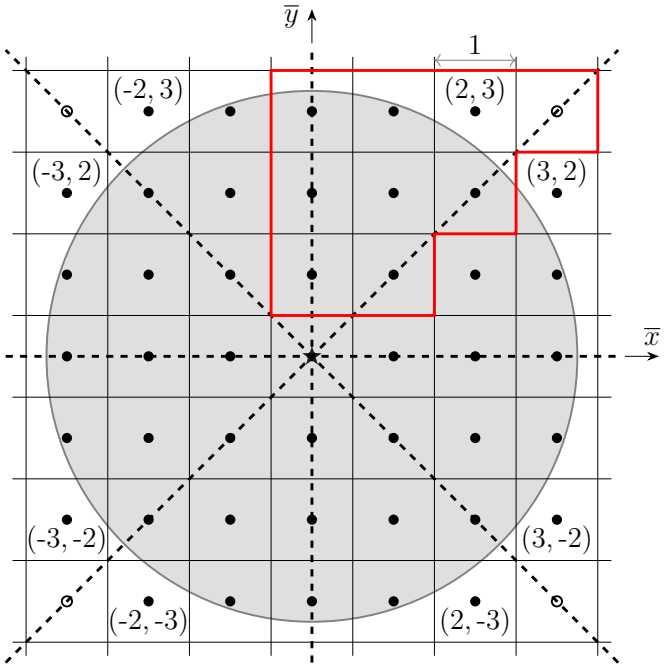


Figure 5.6: *Dashed lines represent the lines of the cell-neighborhood symmetries and the nodes enclosed by the red line are the only ones that are considered by the proposed algorithm.*

Analogously, we exploit six planes of symmetry for a neighborhood in a 3D model (planes containing two axes or one axis and one bisector of the octants). Therefore, in this case we consider only nodes that satisfy the following conditions: $M \geq \overline{z}_j \geq \overline{y}_j \geq \overline{x}_j \geq 0$ and $\overline{z}_j \neq 0$. The nodes considered in the proposed algorithm for the computation of the partial volumes for $\overline{m} = 3.2$ are represented in Figure 5.7.

Cell-neighborhood symmetries come into play also during the computation of some partial areas and volumes, as shown in Figure 5.8. In 2D problems, the intersections between the neighborhood and cells of nodes with $\overline{x}_j = 0$ (see Figure 5.8a) are symmetric with respect to the $\overline{y}$-axis. Similarly, in 3D problems, the intersections between the neighborhood and cells of nodes with $\overline{x}_j = 0$ and $\overline{y}_j \neq 0$ or $\overline{x}_j = \overline{y}_j = 0$ (see Figures 5.8b and 5.8c) are symmetric with respect to the planes perpendicular respectively to the $\overline{x}$-axis or both the $\overline{x}$- and $\overline{y}$-axis. These symmetries will be exploited in Appendix 5.A and Section 5.3.5.

### 5.3.4 Computation of partial areas

The first algorithm proposing the analytical computation of partial areas can be found in [184]: the area of intersection between the neighborhood and the cells is subdivided

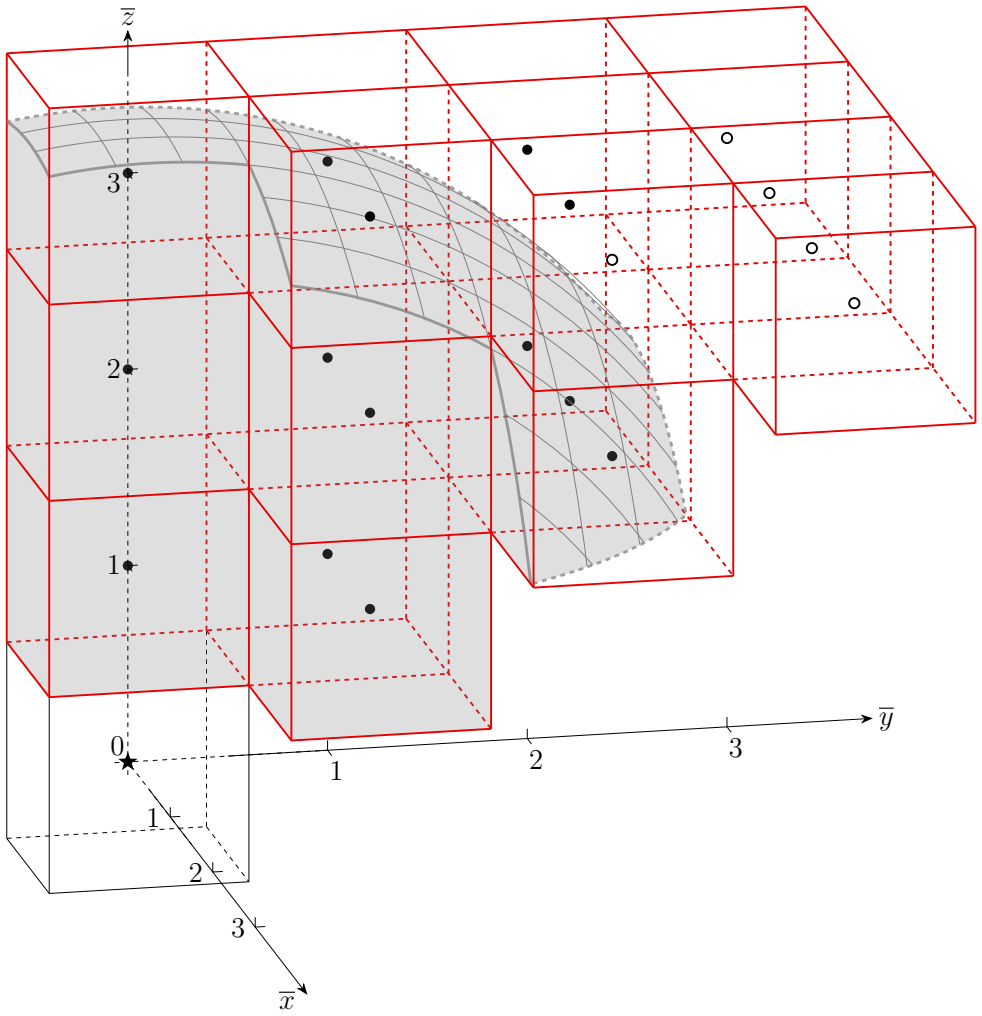


Figure 5.7: *Thanks to the cell-neighborhood symmetries, the nodes enclosed by the surfaces represented by red lines are the only ones that are considered by the proposed algorithm. The six planes of symmetry are not represented for image clarity.*

into domains of basic geometry (triangles, rectangles and circular segments), for which the analytical computation of the area is straightforward. Reference [184] proposes 8 different cases of cell-neighborhood intersection. In Appendix 5.A, we propose a novel approach to compute analytically the partial areas, which is based on the definition of the quadrature coefficient in an integral form. The integrals are then solved by distinguishing only 5 possible cases of cell-neighborhood intersections, for each of which an explicit analytical expression for the value of the quadrature coefficient is obtained.

Algorithm 2 shows how to compute analytically the quadrature coefficients in 2D with the proposed approach. Function 1 is used to solve the only non-trivial integral derived from the computation of the quadrature coefficient. Please refer to Appendix 5.A for the details of the analytical derivation, which is also very useful to better understand the extension of the formulae from 2D to 3D for the computation of the partial volumes shown in the next section.

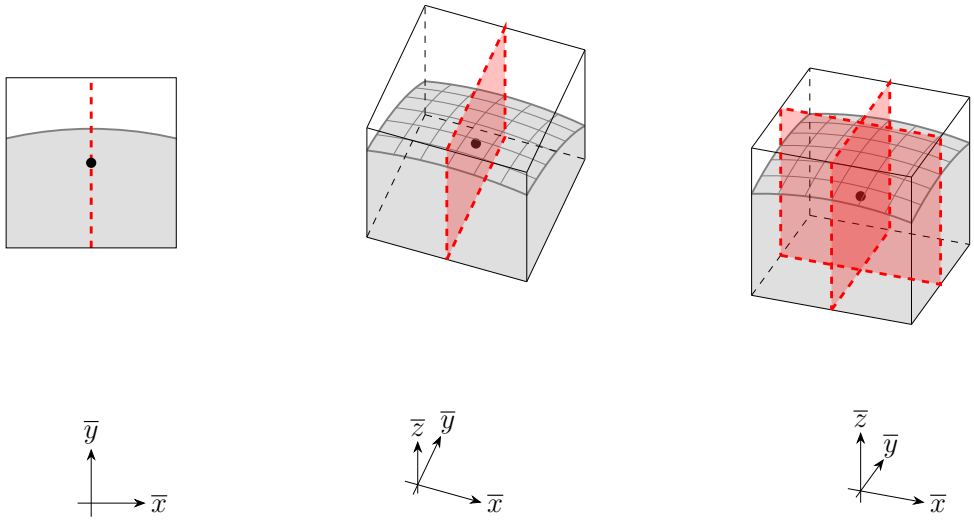


(a) $\overline{x}_j = 0$. (b) $\overline{x}_j = 0$, $\overline{y}_j \neq 0$. (c) $\overline{x}_j = \overline{y}_j = 0$.

Figure 5.8: *Examples of nodes for which the cell-neighborhood symmetry can be exploited within the cell in the computation of the partial areas or volumes.*

**Function 1.** Integral of Equation 5.51 in the interval $[a, b]$.

**function** `Int2D`($a$,$b$,$\overline{m}$)

$I = \frac{1}{2}\,\overline{m}^2 \left[\arcsin\left(\frac{b}{\overline{m}}\right) - \arcsin\left(\frac{a}{\overline{m}}\right)\right] + \frac{1}{2}\,b\,\sqrt{\overline{m}^2 - b^2} - \frac{1}{2}\,a\,\sqrt{\overline{m}^2 - a^2}$

**return** $I$

**Algorithm 2.** Analytical computation of quadrature coefficients in 2D.

**Input:** $\overline{x}_j$, $\overline{y}_j$, $\overline{m}$
**Output:** $\beta_{ij}$

$\overline{x}_j = \text{abs}(\overline{x}_j)$ ▷ *absolute value of* $\overline{x}_j$ *for symmetry* $(\overline{x}_j \geq 0)$
$\overline{y}_j = \text{abs}(\overline{y}_j)$ ▷ *absolute value of* $\overline{y}_j$ *for symmetry* $(\overline{y}_j \geq 0)$
$\overline{x}_j, \overline{y}_j = \text{sort}(\overline{x}_j, \overline{y}_j)$ ▷ *sort in ascending order for symmetry* $(\overline{x}_j \leq \overline{y}_j)$
$M = \lfloor \overline{m} + 0.5 \rfloor$
**if** $\overline{y}_j \neq 0$ and $\overline{y}_j > M$ **then**
    **return** $\beta_{ij} = 0$ ▷ *for exceeding the lower and upper limits of* $\overline{y}_j$
**end if**
$\overline{x}_1 = \overline{x}_j - 0.5$,
$\overline{x}_2 = \overline{x}_j + 0.5$
$\overline{y}_1 = \overline{y}_j - 0.5$
$\overline{y}_2 = \overline{y}_j + 0.5$
**if** $\overline{x}_j = 0$ **then**
    $s = 1$
**else**
    $s = 0$

16: **end if**
17: $a_x = \max(0, \overline{x}_1)$
18: $b_x = \min\left(\overline{x}_2, \sqrt{\overline{m}^2 - \overline{y}_1^2}\right)$
19: **if** $\overline{x}_2^2 + \overline{y}_2^2 \leq \overline{m}^2$ **then** ▷ *case-1*
20: $\quad \beta_{ij} = 1$
21: **else if** $a_x^2 + \overline{y}_2^2 \leq \overline{m}^2$ **then** ▷ *case-2*
22: $\quad \overline{x}_e = \sqrt{\overline{m}^2 - \overline{y}_2^2}$
23: $\quad \beta_{ij} = 2^s[\,\overline{y}_2\,(\overline{x}_e - a_x) + \texttt{Int2D}(\overline{x}_e, b_x, \overline{m}) - \overline{y}_1\,(b_x - a_x)\,]$
24: **else if** $a_x^2 + \overline{y}_1^2 \leq \overline{m}^2$ **then** ▷ *case-3 or case-4*
25: $\quad \beta_{ij} = 2^s[\,\texttt{Int2D}(a_x, b_x, \overline{m}) - \overline{y}_1\,(b_x - a_x)\,]$
26: **else** ▷ *case-5*
27: $\quad \beta_{ij} = 0$
28: **end if**
29: **return** $\beta_{ij}$

### 5.3.5 Computation of partial volumes

We show hereinafter how to compute quasi-analytically the quadrature weights in 3D problems. The partial volumes are computed with the same approach explained in Appendix 5.A for the partial areas. Therefore, the quadrature coefficients are computed as

$$\beta_{ij} = 2^s \int_{a_x}^{b_x} \int_{a_y}^{\min\left(\overline{y}_2, \sqrt{\overline{m}^2 - \overline{x}^2 - \overline{z}_1^2}\right)} \int_{\overline{z}_1}^{\min\left(\overline{z}_2, \sqrt{\overline{m}^2 - \overline{x}^2 - \overline{y}^2}\right)} \mathrm{d}\overline{z}\,\mathrm{d}\overline{y}\,\mathrm{d}\overline{x}\,, \tag{5.24}$$

where $\overline{x}_1 = \overline{x}_j - 0.5$, $\overline{x}_2 = \overline{x}_j + 0.5$, $\overline{y}_1 = \overline{y}_j - 0.5$, $\overline{y}_2 = \overline{y}_j + 0.5$, $\overline{z}_1 = \overline{z}_j - 0.5$ and $\overline{z}_2 = \overline{z}_j + 0.5$ are the coordinates of the faces of the cubic cell and $s$ is the number of symmetries of the cell with respect to the neighborhood ($s = 2$ if $\overline{y}_j = \overline{x}_j = 0$, $s = 1$ if $\overline{x}_j = 0$ and $\overline{y}_j \neq 0$ and $s = 0$ if $\overline{x}_j \neq 0$ and $\overline{y}_j \neq 0$, see Figures 5.8b and 5.8c). The integration limits $a_x$, $b_x$ and $a_y$ are scalar values that can be computed at the beginning of the algorithm. Similarly to what described in Appendix 5.A, the lower limits are defined to exploit the cell-neighborhood symmetry, or symmetries, shown in Figure 5.8b or Figure 5.8c:

$$a_x = \max(0, \overline{x}_1)\,, \qquad a_y = \max(0, \overline{y}_1)\,. \tag{5.25}$$

Figure 5.9 shows all the possible cases of intersection between the spherical neighborhood and a cubic cell. Note that in Figure 5.9 only cells with no symmetries are illustrated, but the portions of the symmetric cell-neighborhood intersections that are used in the computation of the quadrature weights, i.e., the portions in the first octant of Figures 5.8b and 5.8c, belong to one of those cases. The upper limit of the integral in $\overline{x}$ direction of Equation 5.24

is the greatest $\overline{x}$ coordinate of the cell-neighborhood intersection, and it can be computed as

$$b_x = \min\left(\overline{x}_2, \sqrt{\overline{m}^2 - a_y^2 - \overline{z}_1^2}\right). \tag{5.26}$$

Therefore, $b_x$ is equal to $\overline{x}_2$ from case-2 to case-8, and to $\sqrt{\overline{m}^2 - a_y^2 - \overline{z}_1^2}$ in case-9. The computation of Equation 5.26 at the beginning of the algorithm allows to compute case-8 and case-9 with the same formulae.

Similarly to Equation 5.48 in Appendix 5.A, Equation 5.24 can be solved for each case by splitting the integrals in correspondence of the intersections between the boundary of the neighborhood and the edges parallel to the $\overline{x}$-axis and the faces parallel to the $\overline{x}$-$\overline{y}$ plane (for details refer to Appendix 5.B). There are 3 types of non-trivial integrals that derive from the previous step:

$$\int \sqrt{\overline{m}^2 - \overline{x}^2 - k_1^2}\,\mathrm{d}\overline{x} = \frac{1}{2}\left(\overline{m}^2 - k_1^2\right)\arcsin\left(\frac{\overline{x}}{\sqrt{\overline{m}^2 - k_1^2}}\right) + \frac{1}{2}\,\overline{x}\,\sqrt{\overline{m}^2 - \overline{x}^2 - k_1^2} + \text{const.}\,, \tag{5.27}$$

$$\int \left(\overline{m}^2 - \overline{x}^2\right)\arcsin\left(\frac{k_2}{\sqrt{\overline{m}^2 - \overline{x}^2}}\right)\mathrm{d}\overline{x}\,, \tag{5.28}$$

$$\int \left(\overline{m}^2 - \overline{x}^2\right)\arcsin\left(\frac{\sqrt{\overline{m}^2 - \overline{x}^2 - k_3^2}}{\sqrt{\overline{m}^2 - \overline{x}^2}}\right)\mathrm{d}\overline{x}\,, \tag{5.29}$$

where $k_1$ can be equal to $a_y$, $\overline{y}_2$, $\overline{z}_1$ or $\overline{z}_2$, $k_2$ to $a_y$ or $\overline{y}_2$, and $k_3$ to $\overline{z}_1$ or $\overline{z}_2$. The parameters $k_1$, $k_2$ and $k_3$ are defined in these ways to group the same types of integrals derived from Equation 5.24. The explicit solution given in Equation 5.27 is used in Function 2 to compute the integral in a general interval $[a, b]$.

On the other hand, integrals in Equations 5.28 and 5.29 do not have an explicit solution. Therefore, we perform a Taylor series expansion centered at $\overline{x}_0$ of the following functions:

$$\arcsin\left(\frac{k_2}{\sqrt{\overline{m}^2 - \overline{x}^2}}\right) = \arcsin\left(\frac{k_2}{\sqrt{\overline{m}^2 - \overline{x}_0^2}}\right) + \sum_{n=1}^{N} \frac{\sum_{p=1}^{\lfloor 3n/2 \rfloor}\left(\sum_{q=1}^{p} c(n,p,q)\,\overline{m}^{2(p-q)}\,k_2^{2q-1}\right)\overline{x}_0^{3n-2p}}{\left(\overline{m}^2 - \overline{x}_0^2\right)^n\left(\overline{m}^2 - \overline{x}_0^2 - k_2^2\right)^{n-1/2}} \cdot \frac{\left(\overline{x} - \overline{x}_0\right)^n}{n!}\,, \tag{5.30}$$

$$\arcsin\left(\frac{\sqrt{\overline{m}^2 - \overline{x}^2 - k_3^2}}{\sqrt{\overline{m}^2 - \overline{x}^2}}\right) = \arcsin\left(\frac{\sqrt{\overline{m}^2 - \overline{x}_0^2 - k_3^2}}{\sqrt{\overline{m}^2 - \overline{x}_0^2}}\right) - \sum_{n=1}^{N} \frac{\sum_{p=1}^{\lfloor 3n/2 \rfloor}\left(\sum_{q=1}^{p} c(n,p,q)\,\overline{m}^{2(p-q)}\,k_3^{2q-1}\right)\overline{x}_0^{3n-2p}}{\left(\overline{m}^2 - \overline{x}_0^2\right)^n\left(\overline{m}^2 - \overline{x}_0^2 - k_3^2\right)^{n-1/2}} \cdot \frac{\left(\overline{x} - \overline{x}_0\right)^n}{n!}\,, \tag{5.31}$$

where $c$ is a coefficient depending on the order $n$ of the corresponding derivative and the indices $p$ and $q$. For more details about the computation of the derivatives of a general order

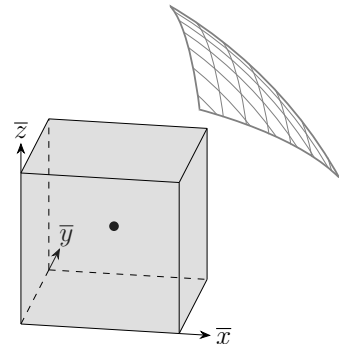


(a) *Case-1.*

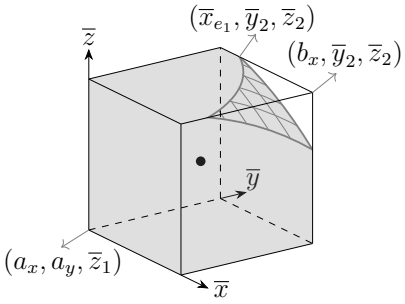


(b) *Case-2.*

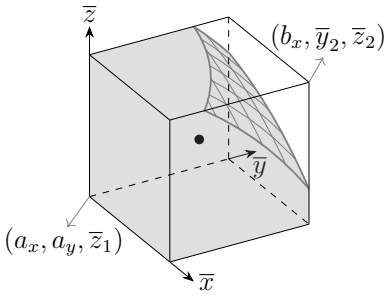


(c) *Case-3.*

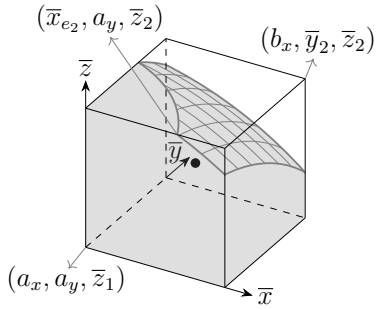


(d) *Case-4.*

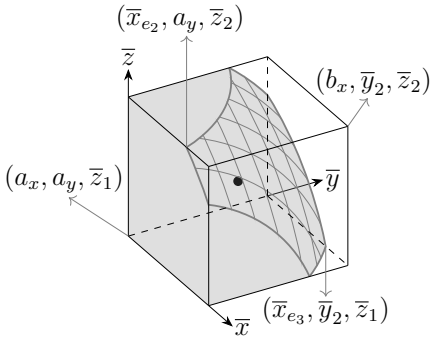


(e) *Case-5.*

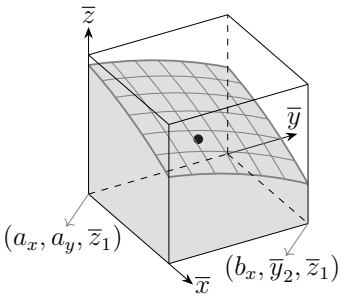


(f) *Case-6.*

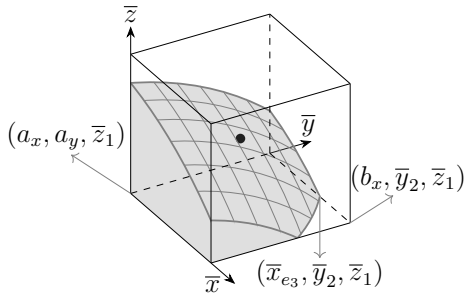


(g) *Case-7.*

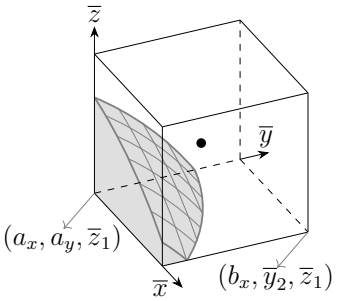


(h) *Case-8.*

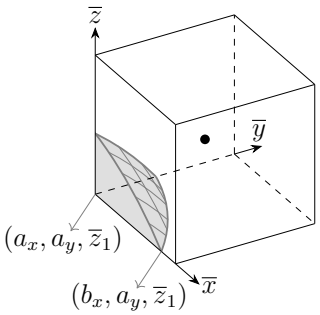


(i) *Case-9.*

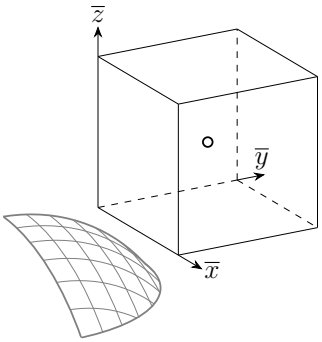


(j) *Case-10.*

Figure 5.9: *Possible cases of intersections between neighborhood and cell in 3D. Symmetric cell-neighborhood intersections are not shown here, but the unsymmetric portions of those intersections belong to one of the shown cases. Since the true origin of the reference system lies outside the images, it has been translated to one of the vertices of the cube for visualization clarity.*

$n$ (and the corresponding coefficients $c(n,p,q)$), please refer to Appendix 5.C. The matrix $\mathbf{c}$ containing all the coefficients $c$ is obtained with Algorithm 3. If the order $N$ of truncation of the Taylor series expansion tends to infinity ($N \to \infty$), then the solution of the integral is exact. Clearly, in a numerical algorithm $N$ must be a finite number, but we will show that our approach is able to attain accurate results with little computational effort (i.e., with $N$ relatively low). Hence, we substitute Equations 5.30 and 5.31 respectively in Equations 5.28 and 5.29 and solve the indefinite integrals:

$$\begin{aligned}\int \left(\overline{m}^2 - \overline{x}^2\right) f(\overline{x})\,\mathrm{d}\overline{x} &= \int \left(\overline{m}^2 - \overline{x}^2\right) \left[f(\overline{x}_0) + \sum_{n=1}^{N} \frac{f^{(n)}(\overline{x}_0)}{n!} \left(\overline{x} - \overline{x}_0\right)^n\right] \mathrm{d}\overline{x} \\ &= f(\overline{x}_0) \left(\overline{m}^2\,\overline{x} - \frac{\overline{x}^3}{3}\right) + \sum_{n=1}^{N} \frac{f^{(n)}(\overline{x}_0)}{n!} \left[\frac{\overline{m}^2 - \overline{x}_0^2}{n+1} \left(\overline{x} - \overline{x}_0\right)^{n+1}\right. \\ &\quad \left. - \frac{2\overline{x}_0}{n+2} \left(\overline{x} - \overline{x}_0\right)^{n+2} - \frac{1}{n+3} \left(\overline{x} - \overline{x}_0\right)^{n+3}\right] + \text{const.}\,,\end{aligned} \tag{5.32}$$

$$\begin{aligned}\int \left(\overline{m}^2 - \overline{x}^2\right) g(\overline{x})\,\mathrm{d}\overline{x} &= \int \left(\overline{m}^2 - \overline{x}^2\right) \left[g(\overline{x}_0) + \sum_{n=1}^{N} \frac{g^{(n)}(\overline{x}_0)}{n!} \left(\overline{x} - \overline{x}_0\right)^n\right] \mathrm{d}\overline{x} \\ &= g(\overline{x}_0) \left(\overline{m}^2\,\overline{x} - \frac{\overline{x}^3}{3}\right) + \sum_{n=1}^{N} \frac{g^{(n)}(\overline{x}_0)}{n!} \left[\frac{\overline{m}^2 - \overline{x}_0^2}{n+1} \left(\overline{x} - \overline{x}_0\right)^{n+1}\right. \\ &\quad \left. - \frac{2\overline{x}_0}{n+2} \left(\overline{x} - \overline{x}_0\right)^{n+2} - \frac{1}{n+3} \left(\overline{x} - \overline{x}_0\right)^{n+3}\right] + \text{const.}\,,\end{aligned} \tag{5.33}$$

where $f(\overline{x})$ and $g(\overline{x})$ are the arcsin functions (see Equations 5.96 and 5.101) and $f^{(n)}(\overline{x})$ and $g^{(n)}(\overline{x})$ are the corresponding $n$-th derivatives (see Equations 5.97 and 5.102). Functions 3 and 4 show the computation of the integrals in Equations 5.32 and 5.33 in a general interval $[a,b]$. In order to improve the accuracy of the algorithm, we choose $\overline{x}_0$ to be the middle point of the interval $[a,b]$.

The integrals of Equation 5.24 can be solved for each case by following the procedure described above (for details refer to Appendix 5.B). Algorithm 4 illustrates how to compute the quadrature coefficients with this procedure. At the beginning of the algorithm, the coordinates of node $j$ are considered only in their absolute value and sorted in ascending order to comply with the conditions imposed for symmetry: $0 \le \overline{x}_j \le \overline{y}_j \le \overline{z}_j$. The quadrature coefficients $\beta_{ij}$ computed for $\overline{m} = 3, 4, 6$ are reported in Appendix 5.D.

**Function 2.** Integral of Equation 5.27 in the interval $[a,b]$.

1: **function** `Int1`($a$,$b$,$k_1$,$\overline{m}$)

2: $I = \frac{1}{2}\left(\overline{m}^2 - k_1^2\right)\left[\arcsin\left(\frac{b}{\sqrt{\overline{m}^2 - k_1^2}}\right) - \arcsin\left(\frac{a}{\sqrt{\overline{m}^2 - k_1^2}}\right)\right]$
$+\frac{1}{2}\,b\,\sqrt{\overline{m}^2 - b^2 - k_1^2} - \frac{1}{2}\,a\,\sqrt{\overline{m}^2 - a^2 - k_1^2}$

3: **return** $I$

**Algorithm 3.** Computation of the matrix $\mathbf{c}$ containing the coefficients for the Taylor series expansion.

**Input:** $N$
**Output:** $\mathbf{c}$

$P = \lfloor 3(N-1)/2 \rfloor + 2$ ▷ *maximum value for indices $p$ and $q$*
$\mathbf{c} = \text{zeros}(N,P,P)$ ▷ *initialization of $\mathbf{c}$ with all zero elements*
$\mathbf{c}(1,1,1) = 1$ ▷ *from the first derivative*
**for** $n = 2 : N$ **do**
  **for** $p = 1 : \lfloor 3(n-1)/2 \rfloor + 2$ **do**
    **for** $q = 1 : p$ **do**
      **if** $1 \leq p \leq \lfloor 3(n-1)/2 \rfloor$ **then**
        $\mathbf{c}(n,p,q) = \mathbf{c}(n,p,q) + (-n-2p+2)\ \mathbf{c}(n-1,p,q)$
      **end if**
      **if** $2 \leq p \leq \lfloor 3(n-1)/2 \rfloor + 1$ and $q \leq p-1$ **then**
        $\mathbf{c}(n,p,q) = \mathbf{c}(n,p,q) + (-2n+4p-3)\ \mathbf{c}(n-1,p-1,q)$
      **end if**
      **if** $2 \leq p \leq \lfloor 3(n-1)/2 \rfloor + 1$ and $q \geq 2$ **then**
        $\mathbf{c}(n,p,q) = \mathbf{c}(n,p,q) + (n-2p+1)\ \mathbf{c}(n-1,p-1,q-1)$
      **end if**
      **if** $3 \leq p \leq \lfloor 3(n-1)/2 \rfloor + 2$ and $q \leq p-2$ **then**
        $\mathbf{c}(n,p,q) = \mathbf{c}(n,p,q) + (3n-2p+1)\ \mathbf{c}(n-1,p-2,q)$
      **end if**
      **if** $3 \leq p \leq \lfloor 3(n-1)/2 \rfloor + 2$ and $2 \leq q \leq p-1$ **then**
        $\mathbf{c}(n,p,q) = \mathbf{c}(n,p,q) + (-3n+2p-1)\ \mathbf{c}(n-1,p-2,q-1)$
      **end if**
    **end for**
  **end for**
**end for**
**return c**

**Function 3.** Integral of Equation 5.32 in the interval $[a,b]$.

**function** `Int2`$(a,b,k_2,\overline{m},N,\mathbf{c})$
$\overline{x}_0 = (a+b)/2$
$I = \arcsin\left(\frac{k_2}{\sqrt{\overline{m}^2-\overline{x}_0^2}}\right)\left[\overline{m}^2\,(b-a) - \frac{1}{3}\,(b^3-a^3)\right]$
**for** $n = 1 : N$ **do**
  $f^{(n)}(\overline{x}_0) = \dfrac{\sum\limits_{p=1}^{\lfloor 3n/2 \rfloor}\left(\sum\limits_{q=1}^{p}\mathbf{c}(n,p,q)\,\overline{m}^{2(p-q)}\,k_2^{2q-1}\right)\overline{x}_0^{3n-2p}}{\left(\overline{m}^2-\overline{x}_0^2\right)^n\left(\overline{m}^2-\overline{x}_0^2-k_2^2\right)^{n-1/2}}$
  $I_{n1} = \frac{\overline{m}^2-\overline{x}_0^2}{n+1}\left((b-\overline{x}_0)^{n+1} - (a-\overline{x}_0)^{n+1}\right)$

$I_{n2} = \frac{2\overline{x}_0}{n+2}\left((b-\overline{x}_0)^{n+2} - (a-\overline{x}_0)^{n+2}\right)$
$I_{n3} = \frac{1}{n+3}\left((b-\overline{x}_0)^{n+3} - (a-\overline{x}_0)^{n+3}\right)$
$I = I + \frac{f^{(n)}(\overline{x}_0)}{n!}\left(I_{n1} - I_{n2} - I_{n3}\right)$
**end for**
**return** $I$

**Function 4.** Integral of Equation 5.33 in the interval $[a, b]$.

**function** `Int3`($a$,$b$,$k_3$,$\overline{m}$,$N$,$\mathbf{c}$)
$\overline{x}_0 = (a+b)/2$
$I = \arcsin\left(\frac{\sqrt{\overline{m}^2-\overline{x}_0^2-k_3^2}}{\sqrt{\overline{m}^2-\overline{x}_0^2}}\right)\left[\overline{m}^2(b-a) - \frac{1}{3}(b^3-a^3)\right]$
**for** $n = 1 : N$ **do**
$g^{(n)}(\overline{x}_0) = \frac{-\sum_{p=1}^{\lfloor 3n/2\rfloor}\left(\sum_{q=1}^{p}\mathbf{c}(n,p,q)\,\overline{m}^{2(p-q)}\,k_3^{2q-1}\right)\overline{x}_0^{3n-2p}}{\left(\overline{m}^2-\overline{x}_0^2\right)^n\left(\overline{m}^2-\overline{x}_0^2-k_3^2\right)^{n-1/2}}$
$I_{n1} = \frac{\overline{m}^2-\overline{x}_0^2}{n+1}\left((b-\overline{x}_0)^{n+1} - (a-\overline{x}_0)^{n+1}\right)$
$I_{n2} = \frac{2\overline{x}_0}{n+2}\left((b-\overline{x}_0)^{n+2} - (a-\overline{x}_0)^{n+2}\right)$
$I_{n3} = \frac{1}{n+3}\left((b-\overline{x}_0)^{n+3} - (a-\overline{x}_0)^{n+3}\right)$
$I = I + \frac{g^{(n)}(\overline{x}_0)}{n!}\left(I_{n1} - I_{n2} - I_{n3}\right)$
**end for**
**return** $I$

**Algorithm 4.** Quasi-analytical computation of quadrature coefficients in 3D.

**Input:** $\overline{x}_j$, $\overline{y}_j$, $\overline{z}_j$, $\overline{m}$, $N$, $\mathbf{c}$
**Output:** $\beta_{ij}$

$\overline{x}_j = \text{abs}(\overline{x}_j)$ ▷ *absolute value of* $\overline{x}_j$ *for symmetry* $(\overline{x}_j \geq 0)$
$\overline{y}_j = \text{abs}(\overline{y}_j)$ ▷ *absolute value of* $\overline{y}_j$ *for symmetry* $(\overline{y}_j \geq 0)$
$\overline{z}_j = \text{abs}(\overline{z}_j)$ ▷ *absolute value of* $\overline{z}_j$ *for symmetry* $(\overline{z}_j \geq 0)$
$\overline{x}_j, \overline{y}_j, \overline{z}_j = \text{sort}(\overline{x}_j, \overline{y}_j, \overline{z}_j)$ ▷ *sort in ascending order for symmetry*
$M = \lfloor \overline{m} + 0.5 \rfloor$
**if** $\overline{z}_j \neq 0$ and $\overline{z}_j > M$ **then**
**return** $\beta_{ij} = 0$ ▷ *for exceeding the lower and upper limits of* $\overline{z}_j$
**end if**
$\overline{x}_1 = \overline{x}_j - 0.5$
$\overline{x}_2 = \overline{x}_j + 0.5$
$\overline{y}_1 = \overline{y}_j - 0.5$
$\overline{y}_2 = \overline{y}_j + 0.5$
$\overline{z}_1 = \overline{y}_j - 0.5$
$\overline{z}_2 = \overline{y}_j + 0.5$

**if** $\overline{x}_j = 0$ and $\overline{y}_j = 0$ **then**
  $s = 2$
**else if** $\overline{x}_j = 0$ **then**
  $s = 1$
**else**
  $s = 0$
**end if**
$a_x = \max(0, \overline{x}_1)$
$a_y = \max(0, \overline{y}_1)$
$b_x = \min\left(\overline{x}_2, \sqrt{\overline{m}^2 - a_y^2 - \overline{z}_1^2}\right)$
**if** $\overline{x}_2^2 + \overline{y}_2^2 + \overline{z}_2^2 \leq \overline{m}^2$ **then** ▷ *case-1*
  $\beta_{ij} = 1$
**else if** $a_x^2 + \overline{y}_2^2 + \overline{z}_2^2 \leq \overline{m}^2$ **then** ▷ *case-2*
  $\overline{x}_{e_1} = \sqrt{\overline{m}^2 - \overline{y}_2^2 - \overline{z}_2^2}$
  $\beta_{ij} = 2^s[\, \frac{1}{2}\overline{z}_2 \cdot \texttt{Int1}(\overline{x}_{e_1}, b_x, \overline{z}_2, \overline{m}) + \frac{1}{2}\overline{y}_2 \cdot \texttt{Int1}(\overline{x}_{e_1}, b_x, \overline{y}_2, \overline{m})$
  $+\frac{1}{2} \cdot \texttt{Int2}(\overline{x}_{e_1}, b_x, \overline{y}_2, \overline{m}, N, \mathbf{c}) - \frac{1}{2} \cdot \texttt{Int3}(\overline{x}_{e_1}, b_x, \overline{z}_2, \overline{m}, N, \mathbf{c})$
  $+\overline{z}_2\overline{y}_2\,(\overline{x}_{e_1} - a_x) - \overline{z}_2 a_y\,(b_x - a_x) - \overline{z}_1\,(\overline{y}_2 - a_y)\,(b_x - a_x)\,]$
**else if** $\overline{x}_2^2 + a_y^2 + \overline{z}_2^2 \leq \overline{m}^2$ **then** ▷ *case-3*
  $\beta_{ij} = 2^s[\, \frac{1}{2}\overline{z}_2 \cdot \texttt{Int1}(a_x, b_x, \overline{z}_2, \overline{m}) + \frac{1}{2}\overline{y}_2 \cdot \texttt{Int1}(a_x, b_x, \overline{y}_2, \overline{m})$
  $+\frac{1}{2} \cdot \texttt{Int2}(a_x, b_x, \overline{y}_2, \overline{m}, N, \mathbf{c}) - \frac{1}{2} \cdot \texttt{Int3}(a_x, b_x, \overline{z}_2, \overline{m}, N, \mathbf{c})$
  $-\overline{z}_2 a_y\,(b_x - a_x) - \overline{z}_1\,(\overline{y}_2 - a_y)\,(b_x - a_x)\,]$
**else if** $a_x^2 + a_y^2 + \overline{z}_2^2 \leq \overline{m}^2$ and $\overline{x}_2^2 + \overline{y}_2^2 + \overline{z}_1^2 \leq \overline{m}^2$ **then** ▷ *case-4*
  $\overline{x}_{e_2} = \sqrt{\overline{m}^2 - a_y^2 - \overline{z}_2^2}$
  $\beta_{ij} = 2^s[\, \frac{1}{2}\overline{z}_2 \cdot \texttt{Int1}(a_x, \overline{x}_{e_2}, \overline{z}_2, \overline{m}) + \frac{1}{2}\overline{y}_2 \cdot \texttt{Int1}(a_x, b_x, \overline{y}_2, \overline{m})$
  $-\frac{1}{2}a_y \cdot \texttt{Int1}(\overline{x}_{e_2}, b_x, a_y, \overline{m}) + \frac{1}{2} \cdot \texttt{Int2}(a_x, b_x, \overline{y}_2, \overline{m}, N, \mathbf{c})$
  $-\frac{1}{2} \cdot \texttt{Int2}(\overline{x}_{e_2}, b_x, a_y, \overline{m}, N, \mathbf{c}) - \frac{1}{2} \cdot \texttt{Int3}(a_x, \overline{x}_{e_2}, \overline{z}_2, \overline{m}, N, \mathbf{c})$
  $-\overline{z}_2 a_y\,(\overline{x}_{e_2} - a_x) - \overline{z}_1\,(\overline{y}_2 - a_y)\,(b_x - a_x)\,]$
**else if** $a_x^2 + a_y^2 + \overline{z}_2^2 \leq \overline{m}^2$ **then** ▷ *case-5*
  $\overline{x}_{e_2} = \sqrt{\overline{m}^2 - a_y^2 - \overline{z}_2^2}$
  $\overline{x}_{e_3} = \sqrt{\overline{m}^2 - \overline{y}_2^2 - \overline{z}_1^2}$
  $\beta_{ij} = 2^s[\, \frac{1}{2}\overline{z}_2 \cdot \texttt{Int1}(a_x, \overline{x}_{e_2}, \overline{z}_2, \overline{m}) + \frac{1}{2}\overline{y}_2 \cdot \texttt{Int1}(a_x, \overline{x}_{e_3}, \overline{y}_2, \overline{m})$
  $-\frac{1}{2}\overline{z}_1 \cdot \texttt{Int1}(\overline{x}_{e_3}, b_x, \overline{z}_1, \overline{m}) - \frac{1}{2}a_y \cdot \texttt{Int1}(\overline{x}_{e_2}, b_x, a_y, \overline{m})$
  $+\frac{1}{2} \cdot \texttt{Int2}(a_x, \overline{x}_{e_3}, \overline{y}_2, \overline{m}, N, \mathbf{c}) - \frac{1}{2} \cdot \texttt{Int2}(\overline{x}_{e_2}, b_x, a_y, \overline{m}, N, \mathbf{c})$
  $-\frac{1}{2} \cdot \texttt{Int3}(a_x, \overline{x}_{e_2}, \overline{z}_2, \overline{m}, N, \mathbf{c}) + \frac{1}{2} \cdot \texttt{Int3}(\overline{x}_{e_3}, b_x, \overline{z}_1, \overline{m}, N, \mathbf{c})$
  $-\overline{z}_2 a_y\,(\overline{x}_{e_2} - a_x) - \overline{z}_1\overline{y}_2\,(\overline{x}_{e_3} - a_x) + \overline{z}_1 a_y\,(b_x - a_x)\,]$
**else if** $\overline{x}_2^2 + \overline{y}_2^2 + \overline{z}_1^2 \leq \overline{m}^2$ **then** ▷ *case-6*

$\beta_{ij} = 2^s[\,\frac{1}{2}\overline{y}_2\cdot\texttt{Int1}(a_x, b_x, \overline{y}_2, \overline{m}) - \frac{1}{2}a_y\cdot\texttt{Int1}(a_x, b_x, a_y, \overline{m})$
$+\frac{1}{2}\cdot\texttt{Int2}(a_x, b_x, \overline{y}_2, \overline{m}, N, \mathbf{c}) - \frac{1}{2}\cdot\texttt{Int2}(a_x, b_x, a_y, \overline{m}, N, \mathbf{c})$
$-\overline{z}_1\,(\overline{y}_2 - a_y)\,(b_x - a_x)\,]$

**else if** $a_x^2 + \overline{y}_2^2 + \overline{z}_1^2 \leq \overline{m}^2$ **then** ▷ *case-7*

$\overline{x}_{e_3} = \sqrt{\overline{m}^2 - \overline{y}_2^2 - \overline{z}_1^2}$

$\beta_{ij} = 2^s[\,\frac{1}{2}\overline{y}_2\cdot\texttt{Int1}(a_x, \overline{x}_{e_3}, \overline{y}_2, \overline{m}) - \frac{1}{2}\overline{z}_1\cdot\texttt{Int1}(\overline{x}_{e_3}, b_x, \overline{z}_1, \overline{m})$
$-\frac{1}{2}a_y\cdot\texttt{Int1}(a_x, b_x, a_y, \overline{m}) + \frac{1}{2}\cdot\texttt{Int2}(a_x, \overline{x}_{e_3}, \overline{y}_2, \overline{m}, N, \mathbf{c})$
$-\frac{1}{2}\cdot\texttt{Int2}(a_x, b_x, a_y, \overline{m}, N, \mathbf{c}) + \frac{1}{2}\cdot\texttt{Int3}(\overline{x}_{e_3}, b_x, \overline{z}_1, \overline{m}, N, \mathbf{c})$
$-\overline{z}_1\overline{y}_2\,(\overline{x}_{e_3} - a_x) + \overline{z}_1 a_y\,(b_x - a_x)\,]$

**else if** $a_x^2 + a_y^2 + \overline{z}_1^2 \leq \overline{m}^2$ **then** ▷ *case-8 or case-9*

$\beta_{ij} = 2^s[\,-\frac{1}{2}\overline{z}_1\cdot\texttt{Int1}(a_x, b_x, \overline{z}_1, \overline{m}) - \frac{1}{2}a_y\cdot\texttt{Int1}(a_x, b_x, a_y, \overline{m})$
$-\frac{1}{2}\cdot\texttt{Int2}(a_x, b_x, a_y, \overline{m}, N, \mathbf{c}) + \frac{1}{2}\cdot\texttt{Int3}(a_x, b_x, \overline{z}_1, \overline{m}, N, \mathbf{c})$
$+\overline{z}_1 a_y\,(b_x - a_x)\,]$

**else** ▷ *case-10*

$\beta_{ij} = 0$

**end if**

**return** $\beta_{ij}$

## 5.4 Numerical results

In order to assess the accuracy of the computation of the partial volumes with respect to the order $N$ of truncation of the Taylor series expansions, we compute the relative error on the total volume of the spherical neighborhood:

$$\epsilon_V = \left\| \frac{\sum_{j\in\overline{\mathcal{H}}_i} \beta_{ij} + 1}{\frac{4}{3}\pi\,\overline{m}^3} - 1 \right\|. \tag{5.34}$$

The sum of all the quadrature coefficients $\beta_{ij}$ and the volume $V_i = 1$ of node $i$ is the numerical value of the sphere volume, whereas $(4/3)\pi\overline{m}^3$ is its analytical value. As shown in Figure 5.10, the accuracy in the computation of the partial volumes is improved by increasing the value of $N$. Furthermore, the proposed algorithm reaches values of the errors very close to machine precision with $\overline{m} \geq 3$ and $N = 20$.

We show hereinafter several numerical results that confirm the improvements in the peridynamic integration in 3D problems. In particular, we compare the numerical results of Algorithm 1, arguably the most commonly used, with those of the new algorithm (Algorithm 4). We use $N = 4$ as the order of truncation for the Taylor series in Algorithm 4 since this value assures accurate results with low computational cost.

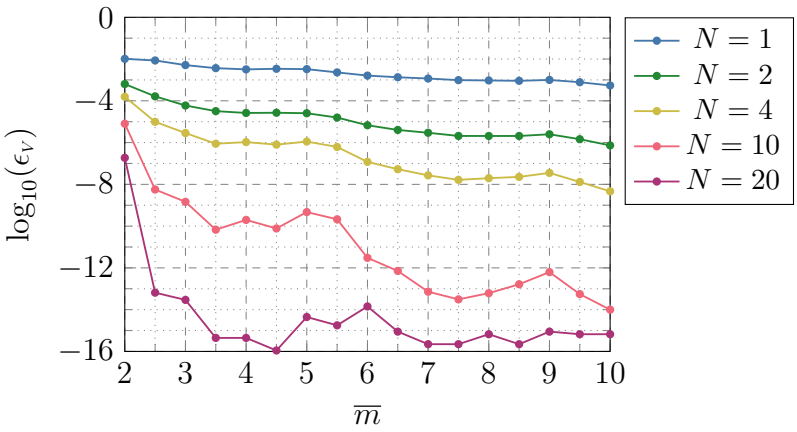


Figure 5.10: *Relative errors on the computation of the total volume of the neighborhood obtained with Algorithm 4 with different order $N$ of truncation of the Taylor series expansions. The values of $\overline{m}$ vary by $\Delta\overline{m} = 0.5$.*

### 5.4.1 Geometrical quantities

In order to assess the performance of the proposed algorithm, we compute two geometrical quantities that reflect the accuracy in the computation of the partial volumes. The first one is the neighborhood volume, computed as:

$$V_{\mathcal{H}} = 1 + \sum_{j \in \overline{\mathcal{H}}_i} \beta_{ij} \,. \tag{5.35}$$

The analytical value of the neighborhood volume is equal to the volume of a sphere: $V_{an} = (4/3)\pi\overline{m}^3$. The relative error on the neighborhood volume can be computed as in Equation 5.34. The improvements obtained by the novel algorithm are evident in Figures 5.11a and 5.11b.

The second geometrical quantity for the comparison of the algorithms is the weighted volume $m$ (Equation 5.18). The analytical computation of the weighted volume is carried out by using spherical coordinated ($\phi$ is the azimuthal angle and $\varphi$ is the polar angle):

$$\begin{aligned} m_{an} &= \int_{\mathcal{H}_{\mathbf{x}}} \exp\left(-\frac{\|\boldsymbol{\xi}\|^2}{\delta^2}\right) \|\boldsymbol{\xi}\|^2 \, \mathrm{d}V_{\mathbf{x}'} \\ &= \int_0^{\delta} \int_0^{2\pi} \int_0^{\pi} \exp\left(-\frac{r^2}{\delta^2}\right) r^2 \cdot r^2 \sin\varphi \, \mathrm{d}\varphi \, \mathrm{d}\phi \, \mathrm{d}r \\ &= \left(\frac{3}{2}\sqrt{\pi}\,\mathrm{erf}(1) - 5\exp(-1)\right) \pi\delta^5 \,, \end{aligned} \tag{5.36}$$

where $r = \|\boldsymbol{\xi}\|$ and $\mathrm{erf}(\cdot)$ is the Gaussian error function. The relative error on the weighted volume can be computed as:

$$\epsilon_m = \left\| \frac{m}{m_{an}} - 1 \right\| . \tag{5.37}$$

Figures 5.11c and 5.11d show the comparison between Algorithm 1 and Algorithm 4, with a significant improvement of the accuracy in the latter one.

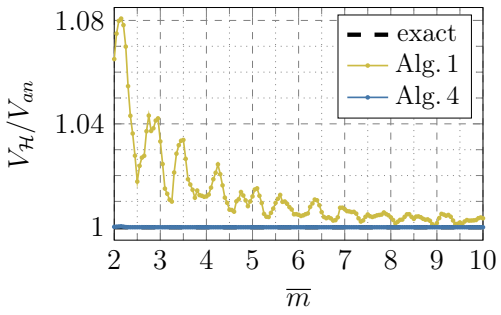


(a) *Normalized neighborhood volume.*

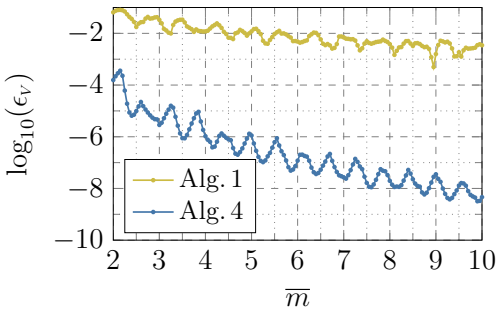


(b) *Relative error on neighborhood volume.*

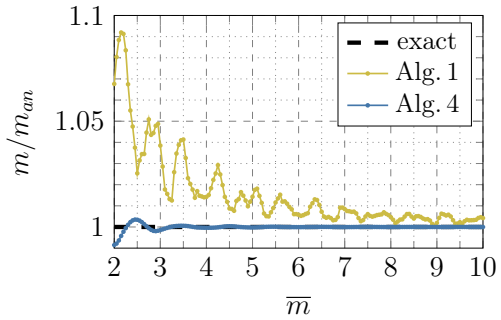


(c) *Normalized weighted volume.*

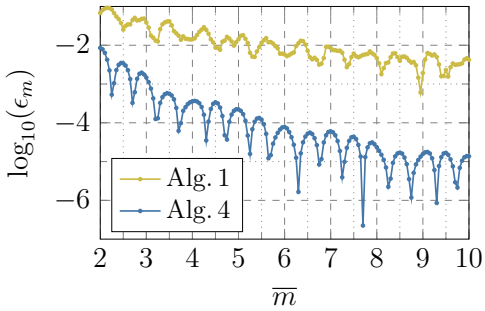


(d) *Relative error on weighted volume.*

Figure 5.11: *Geometrical quantities (neighborhood volume and weighted volume) and their relative errors computed with Algorithm 1 and Algorithm 4. The plot is realized with values of* $\overline{m}$ *varying by* $\Delta\overline{m} = 0.05$.

### 5.4.2 Coefficients of the elasticity tensor

The mechanical properties of isotropic linearly elastic materials are described by the $4^{\text{th}}$-order elasticity tensor $\mathbf{C}$. As in [184], we investigate the convergence behavior of the coefficients of the elasticity tensor. In state-based peridynamics, the elasticity tensor of a point in the bulk is given as [166]

$$C_{pqrs}(\mathbf{x}) = \int_{\mathcal{H}_\mathbf{x}} \int_{\mathcal{H}_\mathbf{x}} \underline{\mathbb{K}}_{pr}[\mathbf{x}]\langle \boldsymbol{\xi}, \boldsymbol{\zeta}\rangle \, \xi_q \, \zeta_s \, \mathrm{d}V_{\mathbf{x}''} \, \mathrm{d}V_{\mathbf{x}'} \,, \tag{5.38}$$

where $\underline{\mathbb{K}}$ is the modulus state which operates on two bonds, $\boldsymbol{\xi} = \mathbf{x}' - \mathbf{x}$ and $\boldsymbol{\zeta} = \mathbf{x}'' - \mathbf{x}$. The modulus state in a linear peridynamic solid model [62, 166] is derived as

$$\underline{\mathbb{K}}_{pr}[\mathbf{x}]\langle \boldsymbol{\xi}, \boldsymbol{\zeta}\rangle = \frac{\underline{\omega}\langle \boldsymbol{\xi}\rangle}{m_\mathbf{x}} \left( \frac{3\,(3K - 5\mu)}{m_\mathbf{x}} \, \underline{\omega}\langle \boldsymbol{\zeta}\rangle \, \underline{x}\langle \boldsymbol{\xi}\rangle \, \underline{x}\langle \boldsymbol{\zeta}\rangle + 15\mu \, \boldsymbol{\Delta}(\boldsymbol{\zeta} - \boldsymbol{\xi}) \right) \frac{\xi_p}{\|\boldsymbol{\xi}\|} \frac{\zeta_r}{\|\boldsymbol{\zeta}\|} \,, \tag{5.39}$$

where $\boldsymbol{\Delta}$ is the Dirac delta function defined as

$$\boldsymbol{\Delta}(\boldsymbol{\zeta} - \boldsymbol{\xi}) := \begin{cases} 1 & \text{if } \boldsymbol{\zeta} = \boldsymbol{\xi} \,, \\ 0 & \text{otherwise.} \end{cases} \tag{5.40}$$

A component of the tensor $\mathbf{C}$ is therefore computed as [166]

$$C_{pqrs} = \int_{\mathcal{H}_\mathbf{x}} \int_{\mathcal{H}_\mathbf{x}} \frac{\underline{\omega}\langle \boldsymbol{\xi}\rangle}{m_\mathbf{x}} \left( \frac{3\,(3K - 5\mu)}{m_\mathbf{x}} \, \underline{\omega}\langle \boldsymbol{\zeta}\rangle \, \underline{x}\langle \boldsymbol{\xi}\rangle \, \underline{x}\langle \boldsymbol{\zeta}\rangle + 15\mu \, \boldsymbol{\Delta}(\boldsymbol{\zeta} - \boldsymbol{\xi}) \right) \frac{\xi_p \xi_q}{\|\boldsymbol{\xi}\|} \frac{\zeta_r \zeta_s}{\|\boldsymbol{\zeta}\|} \, \mathrm{d}V_{\mathbf{x}''} \, \mathrm{d}V_{\mathbf{x}'}$$

$$= \int_{\mathcal{H}_\mathbf{x}} \underline{\omega}\langle\boldsymbol{\xi}\rangle \xi_p \xi_q \left( \frac{3\,(3K-5\mu)}{(m_\mathbf{x})^2} \int_{\mathcal{H}_\mathbf{x}} \underline{\omega}\langle\boldsymbol{\zeta}\rangle\, \zeta_r \zeta_s \,\mathrm{d}V_{\mathbf{x}''} + \frac{15\mu}{m_\mathbf{x}} \int_{\mathcal{H}_\mathbf{x}} \boldsymbol{\Delta}(\boldsymbol{\zeta}-\boldsymbol{\xi}) \frac{\zeta_r \zeta_s}{\|\boldsymbol{\xi}\|\|\boldsymbol{\zeta}\|} \,\mathrm{d}V_{\mathbf{x}''} \right) \mathrm{d}V_{\mathbf{x}'}$$
$$= \frac{3\,(3K-5\mu)}{(m_\mathbf{x})^2} \int_{\mathcal{H}_\mathbf{x}} \underline{\omega}\langle\boldsymbol{\xi}\rangle\, \xi_p \xi_q \,\mathrm{d}V_{\mathbf{x}'} \int_{\mathcal{H}_\mathbf{x}} \underline{\omega}\langle\boldsymbol{\zeta}\rangle\, \zeta_r \zeta_s \,\mathrm{d}V_{\mathbf{x}''} + \frac{15\mu}{m_\mathbf{x}} \int_{\mathcal{H}_\mathbf{x}} \underline{\omega}\langle\boldsymbol{\xi}\rangle \frac{\xi_p \xi_q \xi_r \xi_s}{\|\boldsymbol{\xi}\|^2} \,\mathrm{d}V_{\mathbf{x}'}\,. \tag{5.41}$$

For isotropic linearly elastic materials, there are only two coefficients of the tensor $\mathbf{C}$ which are independent from the others. The analytical value of the coefficients, for instance, $C_{1111}$ and $C_{1122}$ are

$$C^{an}_{1111} = K + \frac{4}{3}\mu\,, \qquad C^{an}_{1122} = K - \frac{2}{3}\mu\,. \tag{5.42}$$

Any component of the tensor $\mathbf{C}$ in a node $i$ can be computed numerically from Equation 5.41 as

$$C_{pqrs} = \frac{3\,(3K-5\mu)}{(m_i)^2} \left( \sum_{j\in\mathcal{H}_i} \underline{\omega}_{ij}\, \xi_p\, \xi_q\, \beta_{ij} V \right) \left( \sum_{k\in\mathcal{H}_i} \underline{\omega}_{ik}\, \zeta_r\, \zeta_s\, \beta_{ik} V \right) + \frac{15\mu}{m_i} \sum_{j\in\mathcal{H}_i} \underline{\omega}_{ij} \frac{\xi_p \xi_q \xi_r \xi_s}{\|\boldsymbol{\xi}\|^2} \beta_{ij} V, \tag{5.43}$$

where $\boldsymbol{\xi} = \mathbf{x}_j - \mathbf{x}_i$ and $\boldsymbol{\zeta} = \mathbf{x}_k - \mathbf{x}_i$. The values of the Young's modulus $E = 1$ GPa and of the Poisson's ratio $\nu = 0.2$ are chosen, which yield the following bulk and shear moduli: $K = 555.56$ MPa and $\mu = 416.67$ MPa. Figures 5.12a and 5.12c show the results of these computation respectively for the components $C_{1111}$ and $C_{1122}$. The relative errors on these coefficients are computed as

$$\epsilon_{1111} = \left\| \frac{C_{1111}}{C^{an}_{1111}} - 1 \right\|, \qquad \epsilon_{1122} = \left\| \frac{C_{1122}}{C^{an}_{1122}} - 1 \right\|, \tag{5.44}$$

and are shown in Figures 5.12b and 5.12d. It is evident that the proposed algorithm provides, on average, smaller errors. Furthermore, the oscillatory behavior as $\overline{m}$ increases is much smoother than that of Algorithm 1.

### 5.4.3 Manufactured problem

A "manufactured" problem, which consists in determining the force density distribution in a body under a prescribed displacement field, is solved analytically and numerically. Following what was shown in [158] for a 2D problem, a body is subjected to the displacements

$$\begin{cases} u = c_{u1}\, x^2 + c_{u2}\, y^2 + c_{u3}\, z^2 + c_{u4}\, xy + c_{u5}\, yz + c_{u6}\, xz\,, \\ v = c_{v1}\, x^2 + c_{v2}\, y^2 + c_{v3}\, z^2 + c_{v4}\, xy + c_{v5}\, yz + c_{v6}\, xz\,, \\ w = c_{w1}\, x^2 + c_{w2}\, y^2 + c_{w3}\, z^2 + c_{w4}\, xy + c_{w5}\, yz + c_{w6}\, xz\,, \end{cases} \tag{5.45}$$

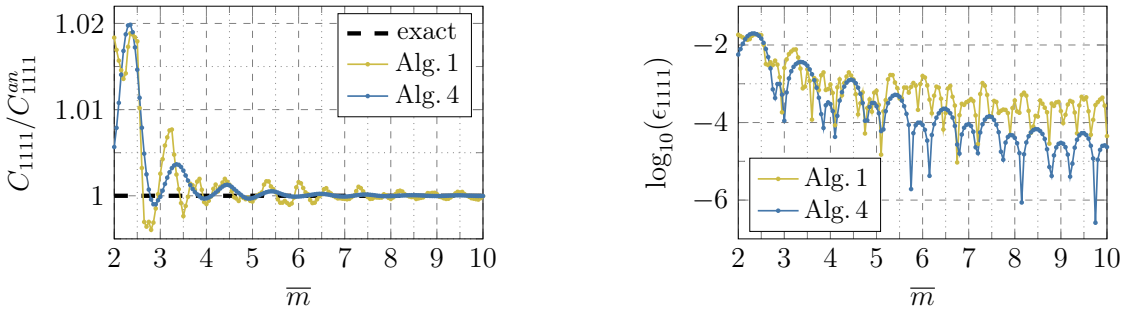


(a) *Coefficient* $C_{1111}$. (b) *Relative error on* $C_{1111}$.

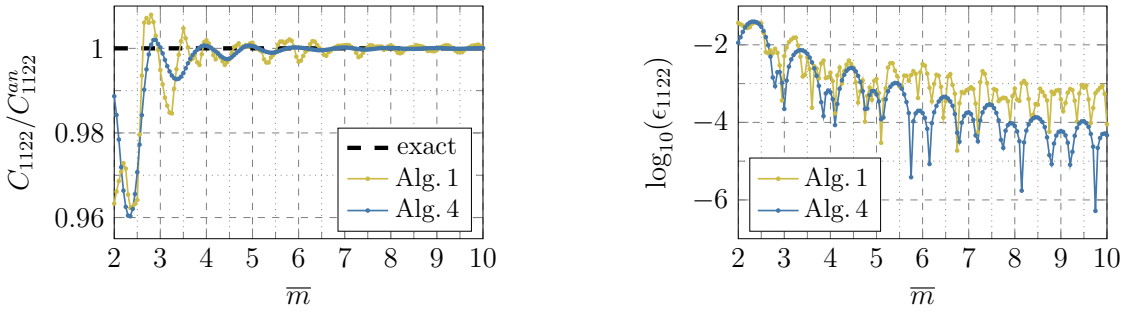


(c) *Coefficient* $C_{1122}$. (d) *Relative error on* $C_{1122}$.

Figure 5.12: *Coefficients of the* $4^{\text{th}}$*-order elasticity tensor and their relative errors computed with Algorithm 1 and Algorithm 4. The values of* $\overline{m}$ *vary by* $\Delta\overline{m} = 0.05$.

where there are 18 independent coefficients for the quadratic terms. The force density derived from this displacement field is given as [158]

$$\begin{cases} b_1^{an} = -\dfrac{3K-5\mu}{3}\left(2c_{u_1} + c_{v_4} + c_{w_6}\right) - 2\mu\left(3c_{u_1} + c_{u_2} + c_{u_3} + c_{v_4} + c_{w_6}\right), \\ b_2^{an} = -\dfrac{3K-5\mu}{3}\left(c_{u_4} + 2c_{v_2} + c_{w_5}\right) - 2\mu\left(c_{u_4} + c_{v_1} + 3c_{v_2} + c_{v_3} + c_{w_5}\right), \\ b_3^{an} = -\dfrac{3K-5\mu}{3}\left(c_{u_6} + c_{v_5} + 2c_{w_3}\right) - 2\mu\left(c_{u_6} + c_{v_5} + c_{w_1} + c_{w_2} + 3c_{w_3}\right), \end{cases} \tag{5.46}$$

where $K = 555.56$ MPa and $\mu = 416.67$ MPa. Note that the force density vector $\mathbf{b}^{an}$ is constant for all the points in the bulk of the material, i.e., in all points that have a distance from the boundary of the body greater than or equal to $2\delta$. Since $c_{u_5}$, $c_{v_6}$ and $c_{w_4}$ do not contribute to $\mathbf{b}^{an}$, these coefficients are considered to be equal to 0. The values of the other coefficients are chosen randomly as follows: $c_{u_1} = 0.6$, $c_{u_2} = 1.3$, $c_{u_3} = 0.8$, $c_{u_4} = 0.5$, $c_{u_6} = 1.8$, $c_{v_1} = 1.1$, $c_{v_2} = 1.6$, $c_{v_3} = 0.7$, $c_{v_4} = 1$, $c_{v_5} = 1.2$, $c_{w_1} = 0.3$, $c_{w_2} = 1.2$, $c_{w_3} = 0.1$, $c_{w_5} = 1.7$ and $c_{w_6} = 0.6$.

We consider only one node in the bulk of a body at which the force density vector $\mathbf{b}$ is computed with Equation 5.20. The relative errors on the components of $\mathbf{b}$ are given as

$$\epsilon_{b_p} = \left\| \frac{b_p}{b_p^{an}} - 1 \right\| \quad \text{with} \quad p = 1, 2, 3\,. \tag{5.47}$$

Figure 5.13 shows the results of the numerical computation. Algorithm 4 allows to obtain, on average, smaller relative errors and a smoother convergence behavior also in this case.

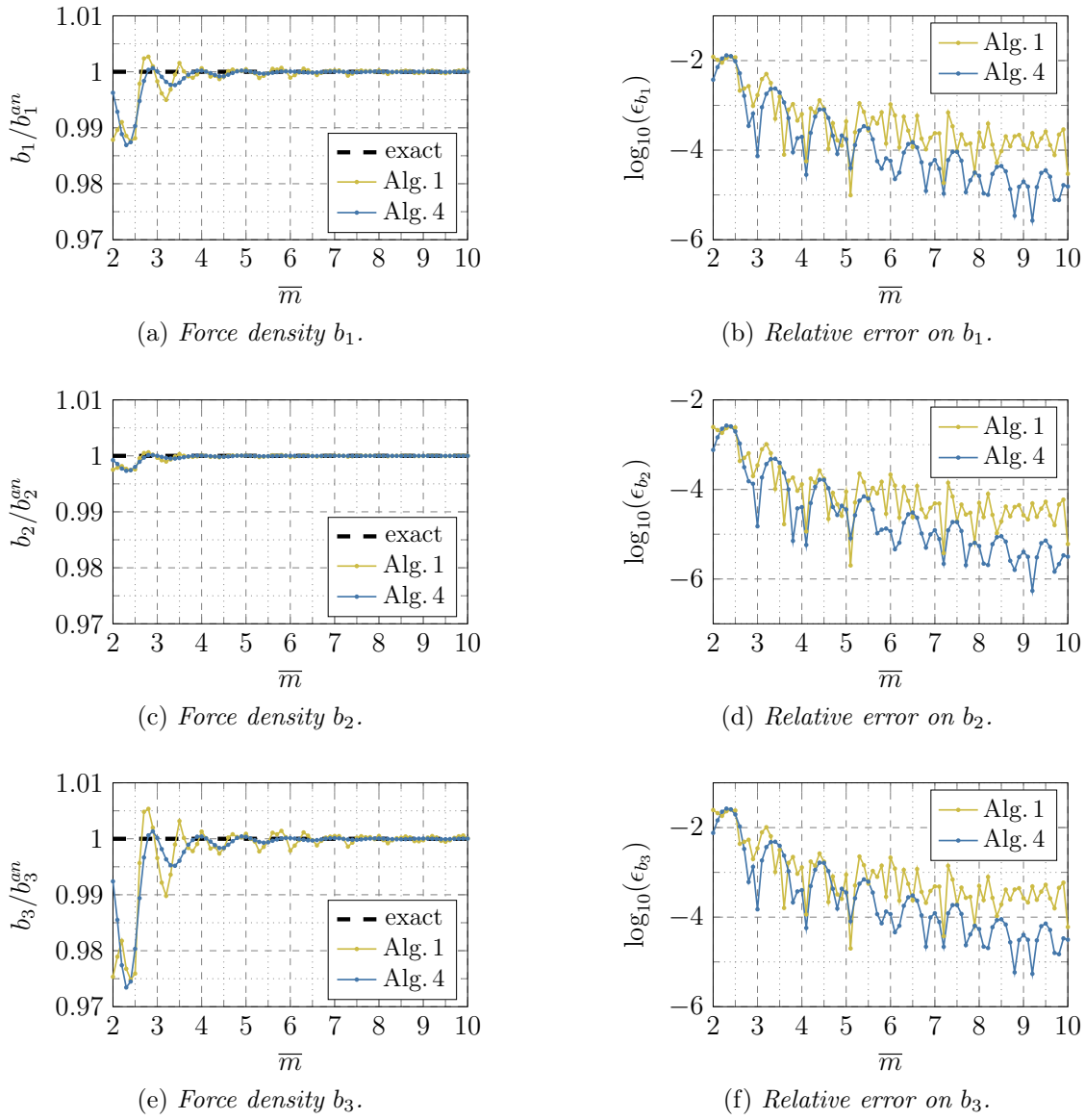


(a) *Force density* $b_1$.

(b) *Relative error on* $b_1$.

(c) *Force density* $b_2$.

(d) *Relative error on* $b_2$.

(e) *Force density* $b_3$.

(f) *Relative error on* $b_3$.

Figure 5.13: *Components of the force density vector and their relative errors computed with Algorithm 1 and Algorithm 4. The values of* $\overline{m}$ *vary by* $\Delta\overline{m} = 0.1$.

## 5.5 Conclusions

The peridynamic theory is a nonlocal reformulation of classical continuum mechanics based on integrals over the neighborhoods of nodes. Therefore, the numerical integration of peridynamic equations determines to a great extent the accuracy of the results. In particular, the quadrature weights, i.e., the partial areas in 2D (intersections between the circular neighborhood and the square cells) and the partial volumes in 3D (intersections between the spherical neighborhood and the cubic cells), should be computed accurately.

We developed an innovative algorithm able to compute quasi-analytically the partial volumes. We use the expression "quasi-analytical" because a truncated Taylor series expansion of some functions, whose integrals are not explicitly solvable, is performed to carry out the integration. However, the new algorithm computes accurately the quadrature weights with very little computational effort, i.e., with a relatively low order of truncation of the Taylor

series. The computational time required by the proposed algorithm is negligible compared to the time required to compute the bond forces and the peridynamic equilibrium equation. In particular, if $\overline{m}$ is constant in the whole domain, the same quadrature weights can be computed only once and used for every neighborhood in the body. A similar approach is also used to simplify the algorithm for the analytical computation of the partial areas, which was already developed in the literature.

Several examples have been presented to show the capabilities of the newly proposed algorithm. The numerical values of the geometrical quantities (volume of the neighborhood and weighted volume), of the coefficients of the elasticity tensor and of the manufactured problem obtained with the new algorithm are compared with those obtained with the most commonly used algorithm for the computation of the partial volumes. As the $\overline{m}$-ratio increases, the proposed algorithm provides, on average, smaller errors and a smoother convergence behavior. For the sake of convenience, the quadrature coefficients for $\overline{m} = 3, 4, 6$ are reported in Appendix 5.D.

# Appendices

## 5.A Analytical computation of partial areas

We propose a new algorithm for the computation of the quadrature coefficients in 2D (Algorithm 2) that solves the following integral:

$$\beta_{ij} = 2^s \int_{a_x}^{b_x} \int_{\overline{y}_1}^{\min\left(\overline{y}_2, \sqrt{\overline{m}^2 - \overline{x}^2}\right)} \mathrm{d}\overline{y}\, \mathrm{d}\overline{x}\,, \tag{5.48}$$

where $\overline{x}_1 = \overline{x}_j - 0.5$, $\overline{x}_2 = \overline{x}_j + 0.5$, $\overline{y}_1 = \overline{y}_j - 0.5$ and $\overline{y}_2 = \overline{y}_j + 0.5$ are the coordinates of the sides of the square cell and $s$ is the number of symmetries of the cell with respect to the neighborhood ($s = 1$ if $\overline{x}_j = 0$ and $s = 0$ if $\overline{x}_j \neq 0$, see Figure 5.8a). The upper and lower limits of the outer integral, respectively $b_x$ and $a_x$, are scalar values that can be computed at the beginning of the algorithm. The value of the lower limit $a_x$ depends on whether the cell-neighborhood intersection is symmetric, as shown in Figure 5.8a, or not. In the former case, the lower limit of the integration domain in $\overline{x}$ direction is set to $a_x = 0$ and the value of the integral is multiplied by 2 (given that $s = 1$). In the latter case, the lower limit is the smallest $\overline{x}$ coordinate of the cell, i.e., $a_x = \overline{x}_1$. These conditions can be written as

$$a_x = \max\left(0, \overline{x}_1\right)\,. \tag{5.49}$$

Since only cells with $\overline{y}_j \geq \overline{x}_j \geq 0$ are considered for symmetry reasons (see Figure 5.14), there are 5 possible cases of square-circle intersections depending on which corners of the cell lie inside the neighborhood:

- case-1 if the corner $(\overline{x}_2, \overline{y}_2)$, the farthest from node $i$, lies inside the neighborhood, i.e., $\overline{x}_2^2 + \overline{y}_2^2 \leq \overline{m}^2$, as shown in Figure 5.15a;
- case-2 if only the corner $(\overline{x}_2, \overline{y}_2)$ lies outside the neighborhood, i.e., $a_x^2 + \overline{y}_2^2 \leq \overline{m}^2 < \overline{x}_2^2 + \overline{y}_2^2$, as shown in Figure 5.15b;
- case-3 if the corners $(\overline{x}_2, \overline{y}_2)$ and $(a_x, \overline{y}_2)$ lie outside the neighborhood and the others lie inside, i.e., $\overline{x}_2^2 + \overline{y}_1^2 \leq \overline{m}^2 < a_x^2 + \overline{y}_2^2$, as shown in Figure 5.15c;
- case-4 if only the corners $(a_x, \overline{y}_1)$ lies inside the neighborhood, i.e., $a_x^2 + \overline{y}_1^2 \leq \overline{m}^2 < \overline{x}_2^2 + \overline{y}_1^2$, as shown in Figure 5.15d;
- case-5 if the corner $(a_x, \overline{y}_1)$, the closest to node $i$, lies outside the neighborhood, i.e., $a_x^2 + \overline{y}_1^2 > \overline{m}^2$, as shown in Figure 5.15e.

The comparison of these cases with the cases of the approach in [184] is summarized in Table 5.1.

Case-1 and case-5 are trivial since $\beta_{ij} = 1$ and $\beta_{ij} = 0$, respectively. Furthermore, the quadrature coefficient in case-3 and case-4 can be computed with the same formulae if the

Table 5.1: *Comparison of the cases in Figure 4 of [184] with the cases in Figure 5.15 derived from the new approach for the computation of the partial areas. The abbreviation "symm." means that the cell-neighborhood symmetry should be used for the cases of the approach in [184] to obtain the cases in the new approach.*

| Approach in [184] | New approach |
|---|---|
| Case I | Case 1 |
| Case II | Case 2 |
| Case IIIa1 | Case 3 |
| Case IIIa2 | Case 3 (symm.) |
| Case IIIb | Case 2 (symm.) |
| Case IIIc | Case 3 |
| Case IV | Case 4 |
| Case V | Case 4 (symm.) |

upper limit of the integral in $\overline{x}$ direction is defined as

$$b_x = \min\left(\overline{x}_2, \sqrt{\overline{m}^2 - \overline{y}_1^2}\right) . \tag{5.50}$$

The value of $b_x$ is indeed equal to $\overline{x}_2$ in case-3, as shown in Figure 5.15c, and to the $\overline{x}$ coordinate of the intersection between the boundary of the neighborhood and the lower side of the cell, as shown in Figure 5.15d.

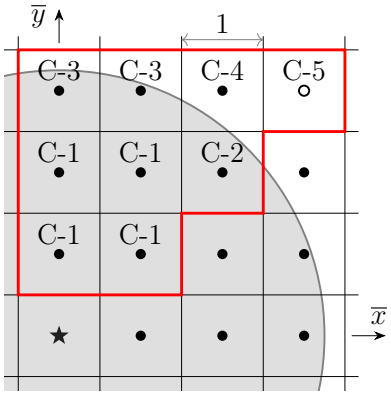


Figure 5.14: *Cases of intersection for $\overline{m} = 3.25$ in 2D depending on which corners of the cell lie inside the neighborhood. Note that the cell-neighborhood intersection of node $(0, 3)$ is symmetric with respect to the $\overline{y}$-axis, so actually only the half of it is considered, namely the half in the first quadrant.*

For later use, the following indefinite integral is analytically solved as

$$\int \sqrt{\overline{m}^2 - \overline{x}^2}\, \mathrm{d}\overline{x} = \frac{1}{2}\,\overline{m}^2 \arcsin\left(\frac{\overline{x}}{\overline{m}}\right) + \frac{1}{2}\,\overline{x}\,\sqrt{\overline{m}^2 - \overline{x}^2} + \text{const.} . \tag{5.51}$$

This solution will be used to compute the definite integrals in different intervals. Now, we show how to compute the quadrature coefficient if the considered cell belongs to case-2.

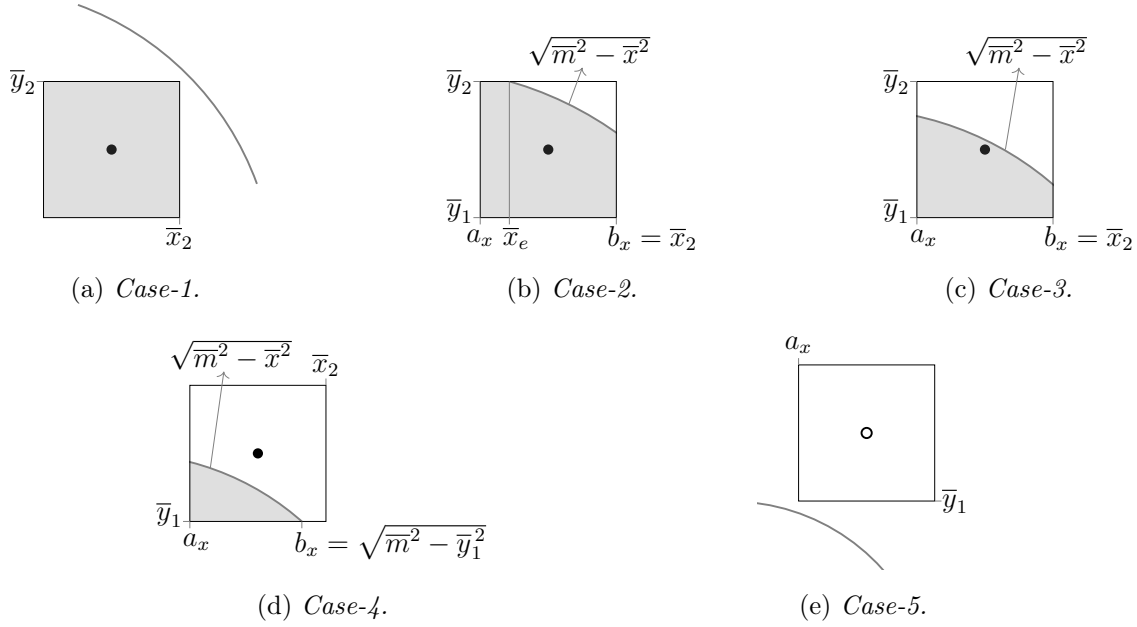


(a) *Case-1.* (b) *Case-2.* (c) *Case-3.*

(d) *Case-4.* (e) *Case-5.*

Figure 5.15: *Possible cases of intersections between neighborhood and cell in 2D. The gray line is a portion of the boundary of the neighborhood.*

Equation 5.48 can be rewritten as

$$\beta_{ij} = 2^s \int_{a_x}^{b_x} \left( \min\left( \overline{y}_2, \sqrt{\overline{m}^2 - \overline{x}^2} \right) - \overline{y}_1 \right) \mathrm{d}\overline{x} \,. \tag{5.52}$$

In case-2 (see Figure 5.15b), there is an intersection between the boundary of the neighborhood and the upper side of the cell, which has an $\overline{x}$ coordinate equal to

$$\overline{x}_e = \sqrt{\overline{m}^2 - \overline{y}_2^2} \,. \tag{5.53}$$

The integral in Equation 5.52 must be splitted because the integrand has different values in the intervals $[a_x, \overline{x}_e]$ and $[\overline{x}_e, b_x]$. Then the integral can be solved analytically by using Equation 5.51:

$$\begin{aligned} \text{Case-2} \;\Rightarrow\; \beta_{ij} &= 2^s \left[ \int_{a_x}^{\overline{x}_e} (\overline{y}_2 - \overline{y}_1) \, \mathrm{d}\overline{x} + \int_{\overline{x}_e}^{b_x} \left( \sqrt{\overline{m}^2 - \overline{x}^2} - \overline{y}_1 \right) \mathrm{d}\overline{x} \right] \\ &= 2^s \left[ \overline{y}_2 \, (\overline{x}_e - a_x) + \frac{1}{2} \, \overline{m}^2 \, \arcsin\left( \frac{b_x}{\overline{m}} \right) + \frac{1}{2} \, b_x \sqrt{\overline{m}^2 - b_x^2} \right. \\ &\quad \left. - \frac{1}{2} \, \overline{m}^2 \, \arcsin\left( \frac{\overline{x}_e}{\overline{m}} \right) - \frac{1}{2} \, \overline{x}_e \sqrt{\overline{m}^2 - \overline{x}_e^2} - \overline{y}_1 \, (b_x - a_x) \right] . \end{aligned} \tag{5.54}$$

Similarly, the quadrature coefficient for a cell belonging to case-3 or case-4 is analytically computed from Equation 5.52 as follows:

$$\text{Case-3 or case-4} \;\Rightarrow\; \beta_{ij} = 2^s \int_{a_x}^{b_x} \left( \sqrt{\overline{m}^2 - \overline{x}^2} - \overline{y}_1 \right) \mathrm{d}\overline{x}$$

$$= 2^s \left[ \frac{1}{2}\,\overline{m}^2 \,\arcsin\left(\frac{b_x}{\overline{m}}\right) + \frac{1}{2}\,b_x\,\sqrt{\overline{m}^2 - b_x^2} \right.$$
$$\left. -\frac{1}{2}\,\overline{m}^2 \,\arcsin\left(\frac{a_x}{\overline{m}}\right) - \frac{1}{2}\,a_x\,\sqrt{\overline{m}^2 - a_x^2} - \overline{y}_1\,(b_x - a_x) \right]. \quad (5.55)$$

The computation of the partial area of a cell is summarized in Algorithm 2. Function 1 is used to compute the integral of Equation 5.51 in a general interval between $a$ and $b$. The proposed algorithm yields exactly the same results of the algorithm for the computation of the partial areas presented in [184], but its implementation is simpler because it is based on a smaller number of cases.

# 5.B Quasi-analytical computation of partial volumes

We can rewrite Equation 5.24 that describes the integral to compute the quadrature coefficients as follows:

$$\beta_{ij} = 2^s \int_{a_x}^{b_x} \int_{a_y}^{\min\left(\overline{y}_2, \sqrt{\overline{m}^2 - \overline{x}^2 - \overline{z}_1^2}\right)} \left[ \min\left(\overline{z}_2, \sqrt{\overline{m}^2 - \overline{x}^2 - \overline{y}^2}\right) - \overline{z}_1 \right] \mathrm{d}\overline{y}\,\mathrm{d}\overline{x}\,, \quad (5.56)$$

where $\overline{x}_1 = \overline{x}_j - 0.5$, $\overline{x}_2 = \overline{x}_j + 0.5$, $\overline{y}_1 = \overline{y}_j - 0.5$, $\overline{y}_2 = \overline{y}_j + 0.5$, $\overline{z}_1 = \overline{z}_j - 0.5$ and $\overline{z}_2 = \overline{z}_j + 0.5$ are the coordinates of the faces of the cubic cell and $s$ is the number of symmetries of the cell with respect to the neighborhood (see Figures 5.8b and 5.8c). $a_x$, $a_y$ and $b_x$ are scalar values computed as shown in Equations 5.25 and 5.26.

Since the integrand and the upper limit of the inner integral in Equation 5.56 are discontinuous functions, the integral domain should be split into subdomains in which only continuous functions are integrated. The integral is split differently for each of the 10 cases represented in Figure 5.9. The cases are differentiated depending on the intersections between the boundary of the neighborhood and the edges of the cell parallel to the $\overline{x}$-axis and the faces parallel to the $\overline{x}$-$\overline{y}$ plane. These intersections are indeed used to split the integral of Equation 5.56, as shown in next Subsections. To begin with, we consider a cell completely within the neighborhood (case-1 in Figure 5.9a) and decrease gradually the $\overline{m}$-ratio to find other cases. We also need to check that, for the considered cells with $\overline{z}_j \geq \overline{y}_j \geq \overline{x}_j \geq 0$, other cases of intersections are not possible.

## 5.B.1 Case-1

In case-1, the cell is completely within the neighborhood, as shown in Figure 5.9a. The condition for which this case is verified is that the farthest node with coordinates $(\overline{x}_2, \overline{y}_2, \overline{z}_2)$ is inside the neighborhood:

$$\overline{x}_2^2 + \overline{y}_2^2 + \overline{z}_2^2 \leq \overline{m}^2\,. \quad (5.57)$$

In this case, the solution of Equation 5.56 is trivial:

$$\beta_{ij} = 1\,. \quad (5.58)$$

### 5.B.2 Case-2

In case-2, the boundary of the neighborhood intersects the edge of the cell between the vertices $(a_x, \overline{y}_2, \overline{z}_2)$ and $(\overline{x}_2, \overline{y}_2, \overline{z}_2)$, as shown in Figure 5.9b. Therefore, the condition in this case is

$$a_x^2 + \overline{y}_2^2 + \overline{z}_2^2 \leq \overline{m}^2 < \overline{x}_2^2 + \overline{y}_2^2 + \overline{z}_2^2 \,. \tag{5.59}$$

In order to be sure that there are no other possible intersections with edges parallel to the $\overline{x}$-axis and faces parallel to the $\overline{x}$-$\overline{y}$ plane, we need to check that the vertices $(\overline{x}_2, a_y, \overline{z}_2)$ and $(\overline{x}_2, \overline{y}_2, \overline{z}_1)$ lie within the neighborhood, so that the edge between $(a_x, a_y, \overline{z}_2)$ and $(\overline{x}_2, a_y, \overline{z}_2)$ and the face on the plane $\overline{z} = \overline{z}_1$ are respectively within the neighborhood. The condition for the vertex $(\overline{x}_2, a_y, \overline{z}_2)$ being within the neighborhood is given as

$$\overline{x}_2^2 + a_y^2 + \overline{z}_2^2 \leq \overline{m}^2 \,. \tag{5.60}$$

We rewrite the condition in Equation 5.60 as

$$a_x^2 - a_x^2 + \overline{x}_2^2 + a_y^2 + \overline{y}_2^2 - \overline{y}_2^2 + \overline{z}_2^2 \leq \overline{m}^2 \,. \tag{5.61}$$

By comparing this inequality with the condition on the left-hand side in Equation 5.59, we obtain:

$$-a_x^2 + \overline{x}_2^2 + a_y^2 - \overline{y}_2^2 \leq 0 \quad \Rightarrow \quad \overline{y}_2^2 - a_y^2 \geq \overline{x}_2^2 - a_x^2 \,. \tag{5.62}$$

If the cell has two symmetries as shown in Figure 5.8c ($s = 2$, $a_x = a_y = 0$), Equation 5.62 becomes $\overline{y}_2^2 \geq \overline{x}_2^2$ which is always verified. If the cell has one symmetry as shown in Figure 5.8b ($s = 1$, $a_x = 0$, $\overline{x}_2 = 0.5$, $\overline{y}_j \geq 1$), Equation 5.62 becomes $2\overline{y}_j \geq 0.5^2$ which is always verified. If the cell has no symmetries ($s = 0$), Equation 5.62 becomes $2\overline{y}_j \geq 2\overline{x}_j$ which is always verified. Similarly, one can show that also the vertex $(\overline{x}_2, \overline{y}_2, \overline{z}_1)$ lies within the neighborhood.

In this case (see Figure 5.9b), the outer integral of Equation 5.56 should be split at the intersection of the boundary of the neighborhood with the edge between the vertices $(a_x, \overline{y}_2, \overline{z}_2)$ and $(\overline{x}_2, \overline{y}_2, \overline{z}_2)$, namely at

$$\overline{x}_{e_1} = \sqrt{\overline{m}^2 - \overline{y}_2^2 - \overline{z}_2^2} \,. \tag{5.63}$$

Furthermore, the inner integral should be split in correspondence of the arc of circle with equation

$$\overline{y}_{f_1}(\overline{x}) = \sqrt{\overline{m}^2 - \overline{x}^2 - \overline{z}_2^2} \,, \tag{5.64}$$

which is given by the intesection of the boundary of the neighborhood with the plane $\overline{z} = \overline{z}_2$ (where the face of the cell lies). Therefore, Equation 5.56 becomes:

$$\beta_{ij} = 2^s \left[ \int_{a_x}^{\overline{x}_{e_1}} \int_{a_y}^{\overline{y}_2} \overline{z}_2 \, \mathrm{d}\overline{y} \, \mathrm{d}\overline{x} + \int_{\overline{x}_{e_1}}^{b_x} \int_{a_y}^{\overline{y}_2} \min\left(\overline{z}_2, \sqrt{\overline{m}^2 - \overline{x}^2 - \overline{y}^2}\right) \mathrm{d}\overline{y} \, \mathrm{d}\overline{x} - \int_{a_x}^{b_x} \int_{a_y}^{\overline{y}_2} \overline{z}_1 \, \mathrm{d}\overline{y} \, \mathrm{d}\overline{x} \right]$$

$$= 2^s \left[ \int_{a_x}^{\overline{x}_{e_1}} \int_{a_y}^{\overline{y}_2} \overline{z}_2 \, \mathrm{d}\overline{y} \, \mathrm{d}\overline{x} + \int_{\overline{x}_{e_1}}^{b_x} \int_{a_y}^{\sqrt{\overline{m}^2 - \overline{x}^2 - \overline{z}_2^2}} \overline{z}_2 \, \mathrm{d}\overline{y} \, \mathrm{d}\overline{x} \right.$$
$$\left. + \int_{\overline{x}_{e_1}}^{b_x} \int_{\sqrt{\overline{m}^2 - \overline{x}^2 - \overline{z}_2^2}}^{\overline{y}_2} \sqrt{\overline{m}^2 - \overline{x}^2 - \overline{y}^2} \, \mathrm{d}\overline{y} \, \mathrm{d}\overline{x} - \int_{a_x}^{b_x} \int_{a_y}^{\overline{y}_2} \overline{z}_1 \, \mathrm{d}\overline{y} \, \mathrm{d}\overline{x} \right]. \tag{5.65}$$

Note that the upper limit of the inner integral is $\overline{y}_2$ because the face of the cell on the plane $\overline{z} = \overline{z}_1$ is completely within the neighborhood. Since the solution of the inner integral of the last term in Equation 5.65 is similar to the integral solved in Equation 5.27, the quadrature coefficients in case-2 can be computed as

$$\beta_{ij} = 2^s \left[ \overline{z}_2 \left( \overline{y}_2 - a_y \right) \left( \overline{x}_{e_1} - a_x \right) + \overline{z}_2 \int_{\overline{x}_{e_1}}^{b_x} \left( \sqrt{\overline{m}^2 - \overline{x}^2 - \overline{z}_2^2} - a_y \right) \mathrm{d}\overline{x} \right.$$
$$+ \int_{\overline{x}_{e_1}}^{b_x} \frac{1}{2} \left( \left( \overline{m}^2 - \overline{x}^2 \right) \arcsin \left( \frac{\overline{y}_2}{\sqrt{\overline{m}^2 - \overline{x}^2}} \right) + \overline{y}_2 \sqrt{\overline{m}^2 - \overline{x}^2 - \overline{y}_2^2} \right.$$
$$\left. - \left( \overline{m}^2 - \overline{x}^2 \right) \arcsin \left( \frac{\sqrt{\overline{m}^2 - \overline{x}^2 - \overline{z}_2^2}}{\sqrt{\overline{m}^2 - \overline{x}^2}} \right) - \overline{z}_2 \sqrt{\overline{m}^2 - \overline{x}^2 - \overline{z}_2^2} \right) \mathrm{d}\overline{x}$$
$$\left. - \overline{z}_1 \left( \overline{y}_2 - a_y \right) \left( b_x - a_x \right) \right]. \tag{5.66}$$

The integrals in Equation 5.66 are of the types solved in Equations 5.27, 5.32 and 5.33. To shorten the formulae, we define the following functions (similar to Functions 2, 3 and 4 used in Algorithm 4):

$$I_1(a, b, k_1) := \int_a^b \sqrt{\overline{m}^2 - \overline{x}^2 - k_1^2} \, \mathrm{d}\overline{x}$$
$$= \frac{1}{2} \left( \overline{m}^2 - k_1^2 \right) \left[ \arcsin \left( \frac{b}{\sqrt{\overline{m}^2 - k_1^2}} \right) - \arcsin \left( \frac{a}{\sqrt{\overline{m}^2 - k_1^2}} \right) \right]$$
$$+ \frac{1}{2} b \sqrt{\overline{m}^2 - b^2 - k_1^2} - \frac{1}{2} a \sqrt{\overline{m}^2 - a^2 - k_1^2}, \tag{5.67}$$

$$I_2(a, b, k_2) := \int_a^b \left( \overline{m}^2 - \overline{x}^2 \right) \arcsin \left( \frac{k_2}{\sqrt{\overline{m}^2 - \overline{x}^2}} \right) \mathrm{d}\overline{x}$$
$$= \int_a^b \left( \overline{m}^2 - \overline{x}^2 \right) \left[ f(\overline{x}_0) + \sum_{n=1}^{N} \frac{f^{(n)}(\overline{x}_0)}{n!} \left( \overline{x} - \overline{x}_0 \right)^n \right] \mathrm{d}\overline{x}$$
$$= f(\overline{x}_0) \left( \overline{m}^2 \left( b - a \right) - \frac{1}{3} \left( b^3 - a^3 \right) \right)$$
$$+ \sum_{n=1}^{N} \frac{f^{(n)}(\overline{x}_0)}{n!} \left[ \frac{\overline{m}^2 - \overline{x}_0^2}{n+1} \left( (b - \overline{x}_0)^{n+1} - (a - \overline{x}_0)^{n+1} \right) \right.$$
$$- \frac{2\overline{x}_0}{n+2} \left( (b - \overline{x}_0)^{n+2} - (a - \overline{x}_0)^{n+2} \right)$$
$$\left. - \frac{1}{n+3} \left( (b - \overline{x}_0)^{n+3} - (a - \overline{x}_0)^{n+3} \right) \right], \tag{5.68}$$

$$
\begin{aligned}
I_3(a,b,k_3) &:= \int_a^b \left(\overline{m}^2-\overline{x}^2\right)\arcsin\left(\frac{\sqrt{\overline{m}^2-\overline{x}^2-k_3^2}}{\sqrt{\overline{m}^2-\overline{x}^2}}\right)\mathrm{d}\overline{x}\\
&= \int_a^b \left(\overline{m}^2-\overline{x}^2\right)\left[g(\overline{x}_0)+\sum_{n=1}^{N}\frac{g^{(n)}(\overline{x}_0)}{n!}\left(\overline{x}-\overline{x}_0\right)^n\right]\mathrm{d}\overline{x}\\
&= g(\overline{x}_0)\left(\overline{m}^2\left(b-a\right)-\frac{1}{3}\left(b^3-a^3\right)\right)\\
&\qquad+\sum_{n=1}^{N}\frac{g^{(n)}(\overline{x}_0)}{n!}\left[\frac{\overline{m}^2-\overline{x}_0^2}{n+1}\left((b-\overline{x}_0)^{n+1}-(a-\overline{x}_0)^{n+1}\right)\right.\\
&\qquad\qquad-\frac{2\overline{x}_0}{n+2}\left((b-\overline{x}_0)^{n+2}-(a-\overline{x}_0)^{n+2}\right)\\
&\qquad\qquad\left.-\frac{1}{n+3}\left((b-\overline{x}_0)^{n+3}-(a-\overline{x}_0)^{n+3}\right)\right], \qquad (5.69)
\end{aligned}
$$

where $f(\overline{x})$ and $g(\overline{x})$ are functions defined in Appendix 5.C and their corresponding $n$-th derivatives $f^{(n)}(\overline{x})$ and $g^{(n)}(\overline{x})$ are computed as in Equations 5.97 and 5.102. The parameter $k_1$ can be equal to $a_y$, $\overline{y}_2$, $\overline{z}_1$ or $\overline{z}_2$, $k_2$ to $a_y$ or $\overline{y}_2$, and $k_3$ to $\overline{z}_1$ or $\overline{z}_2$ depending on the cases.

By using the previous definitions, Equation 5.66 is solved as follows:

$$
\begin{aligned}
\beta_{ij} &= 2^s\left[\overline{z}_2\left(\overline{y}_2-a_y\right)\left(\overline{x}_{e_1}-a_x\right)+\overline{z}_2\,I_1(\overline{x}_{e_1},b_x,\overline{z}_2)-\overline{z}_2 a_y\left(b_x-\overline{x}_{e_1}\right)+\frac{1}{2}I_2(\overline{x}_{e_1},b_x,\overline{y}_2)\right.\\
&\quad\left.+\frac{1}{2}\overline{y}_2\,I_1(\overline{x}_{e_1},b_x,\overline{y}_2)-\frac{1}{2}I_3(\overline{x}_{e_1},b_x,\overline{z}_2)-\frac{1}{2}\overline{z}_2\,I_1(\overline{x}_{e_1},b_x,\overline{z}_2)-\overline{z}_1\left(\overline{y}_2-a_y\right)\left(b_x-a_x\right)\right]\\
&= 2^s\left[\frac{1}{2}\overline{z}_2\,I_1(\overline{x}_{e_1},b_x,\overline{z}_2)+\frac{1}{2}\overline{y}_2\,I_1(\overline{x}_{e_1},b_x,\overline{y}_2)+\frac{1}{2}I_2(\overline{x}_{e_1},b_x,\overline{y}_2)\right.\\
&\quad\left.-\frac{1}{2}I_3(\overline{x}_{e_1},b_x,\overline{z}_2)+\overline{z}_2\overline{y}_2\left(\overline{x}_{e_1}-a_x\right)-\overline{z}_2 a_y\left(b_x-a_x\right)-\overline{z}_1\left(\overline{y}_2-a_y\right)\left(b_x-a_x\right)\right]. \qquad (5.70)
\end{aligned}
$$

### 5.B.3 Case-3

In case-3, the boundary of the neighborhood intersects the face of the cell on the plane $\overline{z}=\overline{z}_2$, but does not intersect any edge parallel to the $\overline{x}$-axis, as shown in Figure 5.9c. Therefore, the condition in this case is

$$
\overline{x}_2^2+a_y^2+\overline{z}_2^2\le\overline{m}^2<a_x^2+\overline{y}_2^2+\overline{z}_2^2\,. \qquad (5.71)
$$

The condition on the right-hand side implies that there are no intersections of the boundary of the neighborhood with the edge of the cell between the vertices $(a_x,\overline{y}_2,\overline{z}_2)$ and $(\overline{x}_2,\overline{y}_2,\overline{z}_2)$. Similarly, the condition on the left-hand side implies that there are no intersections with the edge between the vertices $(a_x,a_y,\overline{z}_2)$ and $(\overline{x}_2,a_y,\overline{z}_2)$. With the same approach illustrated at the beginning of Subsection 5.B.2, one can also show that the vertex $(\overline{x}_2,\overline{y}_2,\overline{z}_1)$ lies within the neighborhood for the considered cells ($\overline{z}_j\ge\overline{y}_j\ge\overline{x}_j\ge 0$), so that the face of the cell on the plane $\overline{z}=\overline{z}_1$ is completely inside the neighborhood.

The quadrature coefficient in case-3 is therefore computed as

$$\begin{aligned}\beta_{ij} &= 2^s \left[ \int_{a_x}^{b_x} \int_{a_y}^{\sqrt{\overline{m}^2-\overline{x}^2-\overline{z}_2^2}} \overline{z}_2 \,\mathrm{d}\overline{y}\,\mathrm{d}\overline{x} + \int_{a_x}^{b_x} \int_{\sqrt{\overline{m}^2-\overline{x}^2-\overline{z}_2^2}}^{\overline{y}_2} \sqrt{\overline{m}^2-\overline{x}^2-\overline{y}^2}\,\mathrm{d}\overline{y}\,\mathrm{d}\overline{x} \right. \\ &\qquad \left. - \int_{a_x}^{b_x} \int_{a_y}^{\overline{y}_2} \overline{z}_1 \,\mathrm{d}\overline{y}\,\mathrm{d}\overline{x} \right] \\ &= 2^s \left[ \overline{z}_2 \int_{a_x}^{b_x} \left( \sqrt{\overline{m}^2-\overline{x}^2-\overline{z}_2^2} - a_y \right) \mathrm{d}\overline{x} \right. \\ &\qquad + \int_{a_x}^{b_x} \frac{1}{2} \left( \left(\overline{m}^2-\overline{x}^2\right) \arcsin\left( \frac{\overline{y}_2}{\sqrt{\overline{m}^2-\overline{x}^2}} \right) + \overline{y}_2 \sqrt{\overline{m}^2-\overline{x}^2-\overline{y}_2^2} \right. \\ &\qquad\qquad \left. \left. - \left(\overline{m}^2-\overline{x}^2\right) \arcsin\left( \frac{\sqrt{\overline{m}^2-\overline{x}^2-\overline{z}_2^2}}{\sqrt{\overline{m}^2-\overline{x}^2}} \right) - \overline{z}_2 \sqrt{\overline{m}^2-\overline{x}^2-\overline{z}_2^2} \right) \mathrm{d}\overline{x} \right. \\ &\qquad\qquad \left. - \overline{z}_1 \left(\overline{y}_2 - a_y\right)\left(b_x - a_x\right) \right]. \end{aligned} \tag{5.72}$$

By using Equations 5.67, 5.68 and 5.69, Equation 5.72 is solved as follows:

$$\begin{aligned}\beta_{ij} &= 2^s \left[ \overline{z}_2\, I_1(a_x, b_x, \overline{z}_2) - \overline{z}_2 a_y \left(b_x - a_x\right) + \frac{1}{2} I_2(a_x, b_x, \overline{y}_2) + \frac{1}{2}\overline{y}_2\, I_1(a_x, b_x, \overline{y}_2) \right. \\ &\qquad \left. - \frac{1}{2} I_3(a_x, b_x, \overline{z}_2) - \frac{1}{2}\overline{z}_2\, I_1(a_x, b_x, \overline{z}_2) - \overline{z}_1 \left(\overline{y}_2 - a_y\right)\left(b_x - a_x\right) \right] \\ &= 2^s \left[ \frac{1}{2}\overline{z}_2\, I_1(a_x, b_x, \overline{z}_2) + \frac{1}{2}\overline{y}_2\, I_1(a_x, b_x, \overline{y}_2) + \frac{1}{2} I_2(a_x, b_x, \overline{y}_2) \right. \\ &\qquad \left. - \frac{1}{2} I_3(a_x, b_x, \overline{z}_2) - \overline{z}_2 a_y \left(b_x - a_x\right) - \overline{z}_1 \left(\overline{y}_2 - a_y\right)\left(b_x - a_x\right) \right]. \end{aligned} \tag{5.73}$$

### 5.B.4 Case-4

In case-4, the boundary of the neighborhood intersects the edge of the cell between the vertices $(a_x, a_y, \overline{z}_2)$ and $(\overline{x}_2, a_y, \overline{z}_2)$ and the face on the plane $\overline{z} = \overline{z}_1$ lies completely within the neighborhood, as shown in Figure 5.9d. Therefore, the conditions in this case are

$$a_x^2 + a_y^2 + \overline{z}_2^2 \leq \overline{m}^2 < \overline{x}_2^2 + a_y^2 + \overline{z}_2^2 \quad \text{and} \quad \overline{x}_2^2 + \overline{y}_2^2 + \overline{z}_1^2 \leq \overline{m}^2 \,. \tag{5.74}$$

The intersection of the boundary of the neighborhood with the edge between the vertices $(a_x, \overline{y}_2, \overline{z}_2)$ and $(\overline{x}_2, \overline{y}_2, \overline{z}_2)$ is given as

$$\overline{x}_{e_2} = \sqrt{\overline{m}^2 - a_y^2 - \overline{z}_2^2} \,. \tag{5.75}$$

Given the conditions in previous case, there are no intersections of the boundary of the neighborhood with the edge of the cell between the vertices $(a_x, \overline{y}_2, \overline{z}_2)$ and $(\overline{x}_2, \overline{y}_2, \overline{z}_2)$.

The quadrature coefficient in case-4 is therefore computed as

$$\begin{aligned}
\beta_{ij} &= 2^s \left[ \int_{a_x}^{\overline{x}_{e_2}} \int_{a_y}^{\sqrt{\overline{m}^2-\overline{x}^2-\overline{z}_2^2}} \overline{z}_2 \,\mathrm{d}\overline{y}\,\mathrm{d}\overline{x} + \int_{a_x}^{\overline{x}_{e_2}} \int_{\sqrt{\overline{m}^2-\overline{x}^2-\overline{z}_2^2}}^{\overline{y}_2} \sqrt{\overline{m}^2-\overline{x}^2-\overline{y}^2}\,\mathrm{d}\overline{y}\,\mathrm{d}\overline{x} \right. \\
&\qquad \left. + \int_{\overline{x}_{e_2}}^{b_x} \int_{a_y}^{\overline{y}_2} \sqrt{\overline{m}^2-\overline{x}^2-\overline{y}^2}\,\mathrm{d}\overline{y}\,\mathrm{d}\overline{x} - \int_{a_x}^{b_x} \int_{a_y}^{\overline{y}_2} \overline{z}_1 \,\mathrm{d}\overline{y}\,\mathrm{d}\overline{x} \right] \\
&= 2^s \left[ \overline{z}_2 \int_{a_x}^{\overline{x}_{e_2}} \left( \sqrt{\overline{m}^2-\overline{x}^2-\overline{z}_2^2} - a_y \right) \mathrm{d}\overline{x} \right. \\
&\qquad + \int_{a_x}^{\overline{x}_{e_2}} \frac{1}{2} \left( \left(\overline{m}^2-\overline{x}^2\right) \arcsin\left( \frac{\overline{y}_2}{\sqrt{\overline{m}^2-\overline{x}^2}} \right) + \overline{y}_2 \sqrt{\overline{m}^2-\overline{x}^2-\overline{y}_2^2} \right. \\
&\qquad\qquad \left. - \left(\overline{m}^2-\overline{x}^2\right) \arcsin\left( \frac{\sqrt{\overline{m}^2-\overline{x}^2-\overline{z}_2^2}}{\sqrt{\overline{m}^2-\overline{x}^2}} \right) - \overline{z}_2 \sqrt{\overline{m}^2-\overline{x}^2-\overline{z}_2^2} \right) \mathrm{d}\overline{x} \\
&\qquad + \int_{\overline{x}_{e_2}}^{b_x} \frac{1}{2} \left( \left(\overline{m}^2-\overline{x}^2\right) \arcsin\left( \frac{\overline{y}_2}{\sqrt{\overline{m}^2-\overline{x}^2}} \right) + \overline{y}_2 \sqrt{\overline{m}^2-\overline{x}^2-\overline{y}_2^2} \right. \\
&\qquad\qquad \left. - \left(\overline{m}^2-\overline{x}^2\right) \arcsin\left( \frac{a_y}{\sqrt{\overline{m}^2-\overline{x}^2}} \right) - a_y \sqrt{\overline{m}^2-\overline{x}^2-a_y^2} \right) \mathrm{d}\overline{x} \\
&\qquad\qquad \left. - \overline{z}_1 \left(\overline{y}_2 - a_y\right)\left(b_x - a_x\right) \right] . \qquad (5.76)
\end{aligned}$$

By using Equations 5.67, 5.68 and 5.69, Equation 5.76 is solved as follows:

$$\begin{aligned}
\beta_{ij} &= 2^s \left[ \overline{z}_2\, I_1(a_x, \overline{x}_{e_2}, \overline{z}_2) - \overline{z}_2 a_y \left(\overline{x}_{e_2} - a_x\right) + \frac{1}{2} I_2(a_x, \overline{x}_{e_2}, \overline{y}_2) + \frac{1}{2}\overline{y}_2\, I_1(a_x, \overline{x}_{e_2}, \overline{y}_2) \right. \\
&\quad - \frac{1}{2} I_3(a_x, \overline{x}_{e_2}, \overline{z}_2) - \frac{1}{2}\overline{z}_2\, I_1(a_x, \overline{x}_{e_2}, \overline{z}_2) + \frac{1}{2} I_2(\overline{x}_{e_2}, b_x, \overline{y}_2) + \frac{1}{2}\overline{y}_2\, I_1(\overline{x}_{e_2}, b_x, \overline{y}_2) \\
&\qquad \left. - \frac{1}{2} I_2(\overline{x}_{e_2}, b_x, a_y) - \frac{1}{2} a_y\, I_1(\overline{x}_{e_2}, b_x, a_y) - \overline{z}_1 \left(\overline{y}_2 - a_y\right)\left(b_x - a_x\right) \right] \\
&= 2^s \left[ \frac{1}{2}\overline{z}_2\, I_1(a_x, \overline{x}_{e_2}, \overline{z}_2) + \frac{1}{2}\overline{y}_2\, I_1(a_x, b_x, \overline{y}_2) - \frac{1}{2} a_y\, I_1(\overline{x}_{e_2}, b_x, a_y) + \frac{1}{2} I_2(a_x, b_x, \overline{y}_2) \right. \\
&\quad \left. - \frac{1}{2} I_2(\overline{x}_{e_2}, b_x, a_y) - \frac{1}{2} I_3(a_x, \overline{x}_{e_2}, \overline{z}_2) - \overline{z}_2 a_y \left(\overline{x}_{e_2} - a_x\right) - \overline{z}_1 \left(\overline{y}_2 - a_y\right)\left(b_x - a_x\right) \right] .
\end{aligned} \qquad (5.77)$$

### 5.B.5 Case-5

In case-5, the boundary of the neighborhood intersects both the edge of the cell between the vertices $(a_x, a_y, \overline{z}_2)$ and $(\overline{x}_2, a_y, \overline{z}_2)$ and the face on the plane $\overline{z} = \overline{z}_1$, as shown in Figure 5.9e. Therefore, the conditions in this case are

$$a_x^2 + a_y^2 + \overline{z}_2^2 \le \overline{m}^2 < \overline{x}_2^2 + a_y^2 + \overline{z}_2^2 \quad \text{and} \quad \overline{m}^2 < \overline{x}_2^2 + \overline{y}_2^2 + \overline{z}_1^2 \,. \qquad (5.78)$$

With the same approach illustrated at the beginning of Subsection 5.B.2, one can also show that the vertices $(a_x, \overline{y}_2, \overline{z}_1)$ and $(\overline{x}_2, a_y, \overline{z}_1)$ lie within the neighborhood for the considered cells ($\overline{z}_j \ge \overline{y}_j \ge \overline{x}_j \ge 0$), so that there is an intersection with the edge between $(a_x, \overline{y}_2, \overline{z}_1)$

and $(\overline{x}_2, \overline{y}_2, \overline{z}_1)$ and the edge between $(a_x, a_y, \overline{z}_1)$ and $(\overline{x}_2, a_y, \overline{z}_1)$ lies completely within the neighborhood.

The intersection of the boundary of the neighborhood with the edge between the vertices $(a_x, \overline{y}_2, \overline{z}_2)$ and $(\overline{x}_2, \overline{y}_2, \overline{z}_2)$ is given in Equation 5.75, whereas the intersection with the edge between $(a_x, \overline{y}_2, \overline{z}_1)$ and $(\overline{x}_2, \overline{y}_2, \overline{z}_1)$ is given as

$$\overline{x}_{e_3} = \sqrt{\overline{m}^2 - \overline{y}_2^2 - \overline{z}_1^2}\,. \tag{5.79}$$

Note that $\overline{x}_{e_2} \leq \overline{x}_{e_3}$ since:

$$\overline{m}^2 - a_y^2 - \overline{z}_2^2 \leq \overline{m}^2 - \overline{y}_2^2 - \overline{z}_1^2 \quad \Rightarrow \quad \overline{z}_2^2 - \overline{z}_1^2 \geq \overline{y}_2^2 - a_y^2\,. \tag{5.80}$$

If the cell has two symmetries ($s = 2$, $a_y = 0$), Equation 5.80 becomes $2\overline{z}_j \geq 0.5^2$ which is always verified ($\overline{z}_j \geq 1$). If the cell has one or no symmetries, Equation 5.80 becomes $2\overline{z}_j \geq 2\overline{y}_j$ which is always verified.

In case-5, the boundary of the neighborhood intersects both faces on the planes $\overline{z} = \overline{z}_2$ and $\overline{z} = \overline{z}_1$. The equation of the former intersection is written in Equation 5.64, while the latter is given as

$$\overline{y}_{f_2}(\overline{x}) = \sqrt{\overline{m}^2 - \overline{x}^2 - \overline{z}_1^2}\,. \tag{5.81}$$

The quadrature coefficient in case-5 is computed as

$$\begin{aligned}
\beta_{ij} = 2^s \Bigg[ & \int_{a_x}^{\overline{x}_{e_2}} \int_{a_y}^{\sqrt{\overline{m}^2-\overline{x}^2-\overline{z}_2^2}} \overline{z}_2 \,\mathrm{d}\overline{y}\,\mathrm{d}\overline{x} + \int_{a_x}^{\overline{x}_{e_2}} \int_{\sqrt{\overline{m}^2-\overline{x}^2-\overline{z}_2^2}}^{\overline{y}_2} \sqrt{\overline{m}^2 - \overline{x}^2 - \overline{y}^2}\,\mathrm{d}\overline{y}\,\mathrm{d}\overline{x} \\
& + \int_{\overline{x}_{e_2}}^{\overline{x}_{e_3}} \int_{a_y}^{\overline{y}_2} \sqrt{\overline{m}^2 - \overline{x}^2 - \overline{y}^2}\,\mathrm{d}\overline{y}\,\mathrm{d}\overline{x} + \int_{\overline{x}_{e_3}}^{b_x} \int_{a_y}^{\sqrt{\overline{m}^2-\overline{x}^2-\overline{z}_1^2}} \sqrt{\overline{m}^2 - \overline{x}^2 - \overline{y}^2}\,\mathrm{d}\overline{y}\,\mathrm{d}\overline{x} \\
& - \int_{a_x}^{\overline{x}_{e_3}} \int_{a_y}^{\overline{y}_2} \overline{z}_1 \,\mathrm{d}\overline{y}\,\mathrm{d}\overline{x} - \int_{\overline{x}_{e_3}}^{b_x} \int_{a_y}^{\sqrt{\overline{m}^2-\overline{x}^2-\overline{z}_1^2}} \overline{z}_1 \,\mathrm{d}\overline{y}\,\mathrm{d}\overline{x} \Bigg] \\
= 2^s \Bigg[ & \overline{z}_2 \int_{a_x}^{\overline{x}_{e_2}} \left( \sqrt{\overline{m}^2 - \overline{x}^2 - \overline{z}_2^2} - a_y \right) \mathrm{d}\overline{x} + \int_{a_x}^{\overline{x}_{e_2}} \frac{1}{2} \left( \left(\overline{m}^2 - \overline{x}^2\right) \arcsin\left( \frac{\overline{y}_2}{\sqrt{\overline{m}^2 - \overline{x}^2}} \right) \right. \\
& \left. + \overline{y}_2 \sqrt{\overline{m}^2 - \overline{x}^2 - \overline{y}_2^2} - \left(\overline{m}^2 - \overline{x}^2\right) \arcsin\left( \frac{\sqrt{\overline{m}^2 - \overline{x}^2 - \overline{z}_2^2}}{\sqrt{\overline{m}^2 - \overline{x}^2}} \right) - \overline{z}_2 \sqrt{\overline{m}^2 - \overline{x}^2 - \overline{z}_2^2} \right) \mathrm{d}\overline{x} \\
& + \int_{\overline{x}_{e_2}}^{\overline{x}_{e_3}} \frac{1}{2} \left( \left(\overline{m}^2 - \overline{x}^2\right) \arcsin\left( \frac{\overline{y}_2}{\sqrt{\overline{m}^2 - \overline{x}^2}} \right) + \overline{y}_2 \sqrt{\overline{m}^2 - \overline{x}^2 - \overline{y}_2^2} \right. \\
& \left. - \left(\overline{m}^2 - \overline{x}^2\right) \arcsin\left( \frac{a_y}{\sqrt{\overline{m}^2 - \overline{x}^2}} \right) - a_y \sqrt{\overline{m}^2 - \overline{x}^2 - a_y^2} \right) \mathrm{d}\overline{x} \\
& + \int_{\overline{x}_{e_3}}^{b_x} \frac{1}{2} \left( \left(\overline{m}^2 - \overline{x}^2\right) \arcsin\left( \frac{\sqrt{\overline{m}^2 - \overline{x}^2 - \overline{z}_1^2}}{\sqrt{\overline{m}^2 - \overline{x}^2}} \right) + \overline{z}_1 \sqrt{\overline{m}^2 - \overline{x}^2 - \overline{z}_1^2} \right. \\
& \left. - \left(\overline{m}^2 - \overline{x}^2\right) \arcsin\left( \frac{a_y}{\sqrt{\overline{m}^2 - \overline{x}^2}} \right) - a_y \sqrt{\overline{m}^2 - \overline{x}^2 - a_y^2} \right) \mathrm{d}\overline{x} \\
& - \overline{z}_1 \left(\overline{y}_2 - a_y\right) \left(\overline{x}_{e_3} - a_x\right) - \overline{z}_1 \int_{\overline{x}_{e_3}}^{b_x} \left( \sqrt{\overline{m}^2 - \overline{x}^2 - \overline{z}_1^2} - a_y \right) \mathrm{d}\overline{x} \Bigg]\,.
\end{aligned} \tag{5.82}$$

By using Equations 5.67, 5.68 and 5.69, Equation 5.82 is solved as follows:

$$\begin{aligned}\beta_{ij} = 2^s \Bigg[ & \overline{z}_2\, I_1(a_x, \overline{x}_{e_2}, \overline{z}_2) - \overline{z}_2 a_y\, (\overline{x}_{e_2} - a_x) + \frac{1}{2} I_2(a_x, \overline{x}_{e_2}, \overline{y}_2) + \frac{1}{2}\overline{y}_2\, I_1(a_x, \overline{x}_{e_2}, \overline{y}_2) \\ & - \frac{1}{2} I_3(a_x, \overline{x}_{e_2}, \overline{z}_2) - \frac{1}{2}\overline{z}_2\, I_1(a_x, \overline{x}_{e_2}, \overline{z}_2) + \frac{1}{2} I_2(\overline{x}_{e_2}, \overline{x}_{e_3}, \overline{y}_2) + \frac{1}{2}\overline{y}_2\, I_1(\overline{x}_{e_2}, \overline{x}_{e_3}, \overline{y}_2) \\ & - \frac{1}{2} I_2(\overline{x}_{e_2}, \overline{x}_{e_3}, a_y) - \frac{1}{2} a_y\, I_1(\overline{x}_{e_2}, \overline{x}_{e_3}, a_y) + \frac{1}{2} I_3(\overline{x}_{e_3}, b_x, \overline{z}_1) + \frac{1}{2}\overline{z}_1\, I_1(\overline{x}_{e_3}, b_x, \overline{z}_1) \\ & - \frac{1}{2} I_2(\overline{x}_{e_3}, b_x, a_y) - \frac{1}{2} a_y\, I_1(\overline{x}_{e_3}, b_x, a_y) - \overline{z}_1\, (\overline{y}_2 - a_y)\, (\overline{x}_{e_3} - a_x) \\ & - \overline{z}_1\, I_1(\overline{x}_{e_3}, b_x, \overline{z}_1) + \overline{z}_1 a_y\, (b_x - \overline{x}_{e_3}) \Bigg] \\ = 2^s \Bigg[ & \frac{1}{2}\overline{z}_2\, I_1(a_x, \overline{x}_{e_2}, \overline{z}_2) + \frac{1}{2}\overline{y}_2\, I_1(a_x, \overline{x}_{e_3}, \overline{y}_2) - \frac{1}{2}\overline{z}_1\, I_1(\overline{x}_{e_3}, b_x, \overline{z}_1) \\ & - \frac{1}{2} a_y\, I_1(\overline{x}_{e_2}, b_x, a_y) + \frac{1}{2} I_2(a_x, \overline{x}_{e_3}, \overline{y}_2) - \frac{1}{2} I_2(\overline{x}_{e_2}, b_x, a_y) - \frac{1}{2} I_3(a_x, \overline{x}_{e_2}, \overline{z}_2) \\ & + \frac{1}{2} I_3(\overline{x}_{e_3}, b_x, \overline{z}_1) - \overline{z}_2 a_y\, (\overline{x}_{e_2} - a_x) - \overline{z}_1\overline{y}_2\, (\overline{x}_{e_3} - a_x) + \overline{z}_1 a_y\, (b_x - a_x) \Bigg]. \end{aligned} \tag{5.83}$$

## 5.B.6 Case-6

In case-6, the face of the cell on the plane $\overline{z} = \overline{z}_2$ is completely outside the neighborhood and the face on the plane $\overline{z} = \overline{z}_1$ is completely inside, as shown in Figure 5.9f. Therefore, the condition in this case is

$$\overline{x}_2^2 + \overline{y}_2^2 + \overline{z}_1^2 \leq \overline{m}^2 < a_x^2 + a_y^2 + \overline{z}_2^2\,. \tag{5.84}$$

The quadrature coefficient in case-6 is computed as

$$\begin{aligned}\beta_{ij} &= 2^s \left[ \int_{a_x}^{b_x} \int_{a_y}^{\overline{y}_2} \sqrt{\overline{m}^2 - \overline{x}^2 - \overline{y}^2}\, \mathrm{d}\overline{y}\, \mathrm{d}\overline{x} - \int_{a_x}^{b_x} \int_{a_y}^{\overline{y}_2} \overline{z}_1\, \mathrm{d}\overline{y}\, \mathrm{d}\overline{x} \right] \\ &= 2^s \Bigg[ \int_{a_x}^{b_x} \frac{1}{2} \Bigg( \left(\overline{m}^2 - \overline{x}^2\right) \arcsin\left( \frac{\overline{y}_2}{\sqrt{\overline{m}^2 - \overline{x}^2}} \right) + \overline{y}_2 \sqrt{\overline{m}^2 - \overline{x}^2 - \overline{y}_2^2} \\ &\quad - \left(\overline{m}^2 - \overline{x}^2\right) \arcsin\left( \frac{a_y}{\sqrt{\overline{m}^2 - \overline{x}^2}} \right) - a_y \sqrt{\overline{m}^2 - \overline{x}^2 - a_y^2} \Bigg) \mathrm{d}\overline{x} - \overline{z}_1\, (\overline{y}_2 - a_y)\, (b_x - a_x) \Bigg]. \end{aligned} \tag{5.85}$$

By using Equations 5.67, 5.68 and 5.69, Equation 5.85 is solved as follows:

$$\begin{aligned}\beta_{ij} = 2^s \Bigg[ & \frac{1}{2} I_2(a_x, b_x, \overline{y}_2) + \frac{1}{2}\overline{y}_2\, I_1(a_x, b_x, \overline{y}_2) - \frac{1}{2} I_2(a_x, b_x, a_y) - \frac{1}{2} a_y\, I_1(a_x, b_x, a_y) \\ & - \overline{z}_1\, (\overline{y}_2 - a_y)\, (b_x - a_x) \Bigg] \\ = 2^s \Bigg[ & \frac{1}{2}\overline{y}_2\, I_1(a_x, b_x, \overline{y}_2) - \frac{1}{2} a_y\, I_1(a_x, b_x, a_y) + \frac{1}{2} I_2(a_x, b_x, \overline{y}_2) - \frac{1}{2} I_2(a_x, b_x, a_y) \\ & - \overline{z}_1\, (\overline{y}_2 - a_y)\, (b_x - a_x) \Bigg]. \end{aligned} \tag{5.86}$$

### 5.B.7 Case-7

In case-7, the boundary of the neighborhood intersects the edge of the cell between the vertices $(a_x, \overline{y}_2, \overline{z}_1)$ and $(\overline{x}_2, \overline{y}_2, \overline{z}_1)$, as shown in Figure 5.9g. Therefore, the condition in this case is

$$a_x^2 + \overline{y}_2^2 + \overline{z}_1^2 \leq \overline{m}^2 < \overline{x}_2^2 + \overline{y}_2^2 + \overline{z}_1^2 \,. \tag{5.87}$$

With the same approach illustrated at the beginning of Subsection 5.B.2, one can also show that the vertex $(\overline{x}_2, a_y, \overline{z}_1)$ lies within the neighborhood for the considered cells ($\overline{z}_j \geq \overline{y}_j \geq \overline{x}_j \geq 0$), so that the edge between $(a_x, a_y, \overline{z}_1)$ and $(\overline{x}_2, a_y, \overline{z}_1)$ lies completely within the neighborhood. The intersection of the boundary of the neighborhood with the edge between the vertices $(a_x, \overline{y}_2, \overline{z}_1)$ and $(\overline{x}_2, \overline{y}_2, \overline{z}_1)$ is given by $\overline{x}_{e_3}$ in Equation 5.79.

Therefore, the quadrature coefficient in case-7 is computed as

$$\begin{aligned}
\beta_{ij} = 2^s \Bigg[ & \int_{a_x}^{\overline{x}_{e_3}} \int_{a_y}^{\overline{y}_2} \sqrt{\overline{m}^2 - \overline{x}^2 - \overline{y}^2}\, \mathrm{d}\overline{y}\, \mathrm{d}\overline{x} + \int_{\overline{x}_{e_3}}^{b_x} \int_{a_y}^{\sqrt{\overline{m}^2 - \overline{x}^2 - \overline{z}_1^2}} \sqrt{\overline{m}^2 - \overline{x}^2 - \overline{y}^2}\, \mathrm{d}\overline{y}\, \mathrm{d}\overline{x} \\
& - \int_{a_x}^{\overline{x}_{e_3}} \int_{a_y}^{\overline{y}_2} \overline{z}_1\, \mathrm{d}\overline{y}\, \mathrm{d}\overline{x} - \int_{\overline{x}_{e_3}}^{b_x} \int_{a_y}^{\sqrt{\overline{m}^2 - \overline{x}^2 - \overline{z}_1^2}} \overline{z}_1\, \mathrm{d}\overline{y}\, \mathrm{d}\overline{x} \Bigg] \\
= 2^s \Bigg[ & \int_{a_x}^{\overline{x}_{e_3}} \frac{1}{2} \Bigg( \left(\overline{m}^2 - \overline{x}^2\right) \arcsin\left( \frac{\overline{y}_2}{\sqrt{\overline{m}^2 - \overline{x}^2}} \right) + \overline{y}_2 \sqrt{\overline{m}^2 - \overline{x}^2 - \overline{y}_2^2} \\
& - \left(\overline{m}^2 - \overline{x}^2\right) \arcsin\left( \frac{a_y}{\sqrt{\overline{m}^2 - \overline{x}^2}} \right) - a_y \sqrt{\overline{m}^2 - \overline{x}^2 - a_y^2} \Bigg) \mathrm{d}\overline{x} \\
& + \int_{\overline{x}_{e_3}}^{b_x} \frac{1}{2} \Bigg( \left(\overline{m}^2 - \overline{x}^2\right) \arcsin\left( \frac{\sqrt{\overline{m}^2 - \overline{x}^2 - \overline{z}_1^2}}{\sqrt{\overline{m}^2 - \overline{x}^2}} \right) + \overline{z}_1 \sqrt{\overline{m}^2 - \overline{x}^2 - \overline{z}_1^2} \\
& - \left(\overline{m}^2 - \overline{x}^2\right) \arcsin\left( \frac{a_y}{\sqrt{\overline{m}^2 - \overline{x}^2}} \right) - a_y \sqrt{\overline{m}^2 - \overline{x}^2 - a_y^2} \Bigg) \mathrm{d}\overline{x} \\
& - \overline{z}_1 \left(\overline{y}_2 - a_y\right) \left(\overline{x}_{e_3} - a_x\right) - \overline{z}_1 \int_{\overline{x}_{e_3}}^{b_x} \left( \sqrt{\overline{m}^2 - \overline{x}^2 - \overline{z}_1^2} - a_y \right) \mathrm{d}\overline{x} \Bigg] .
\end{aligned} \tag{5.88}$$

By using Equations 5.67, 5.68 and 5.69, Equation 5.88 is solved as follows:

$$\begin{aligned}
\beta_{ij} = 2^s \Bigg[ & \frac{1}{2} I_2(a_x, \overline{x}_{e_3}, \overline{y}_2) + \frac{1}{2} \overline{y}_2\, I_1(a_x, \overline{x}_{e_3}, \overline{y}_2) - \frac{1}{2} I_2(a_x, \overline{x}_{e_3}, a_y) - \frac{1}{2} a_y\, I_1(a_x, \overline{x}_{e_3}, a_y) \\
& + \frac{1}{2} I_3(\overline{x}_{e_3}, b_x, \overline{z}_1) + \frac{1}{2} \overline{z}_1\, I_1(\overline{x}_{e_3}, b_x, \overline{z}_1) - \frac{1}{2} I_2(\overline{x}_{e_3}, b_x, a_y) - \frac{1}{2} a_y\, I_1(\overline{x}_{e_3}, b_x, a_y) \\
& - \overline{z}_1 \left(\overline{y}_2 - a_y\right) \left(\overline{x}_{e_3} - a_x\right) - \overline{z}_1\, I_1(\overline{x}_{e_3}, b_x, \overline{z}_1) + \overline{z}_1 a_y \left(b_x - \overline{x}_{e_3}\right) \Bigg] \\
= 2^s \Bigg[ & \frac{1}{2} \overline{y}_2\, I_1(a_x, \overline{x}_{e_3}, \overline{y}_2) - \frac{1}{2} \overline{z}_1\, I_1(\overline{x}_{e_3}, b_x, \overline{z}_1) - \frac{1}{2} a_y\, I_1(a_x, b_x, a_y) + \frac{1}{2} I_2(a_x, \overline{x}_{e_3}, \overline{y}_2) \\
& - \frac{1}{2} I_2(a_x, b_x, a_y) + \frac{1}{2} I_3(\overline{x}_{e_3}, b_x, \overline{z}_1) - \overline{z}_1 \overline{y}_2 \left(\overline{x}_{e_3} - a_x\right) + \overline{z}_1 a_y \left(b_x - a_x\right) \Bigg] .
\end{aligned} \tag{5.89}$$

### 5.B.8 Case-8 or case-9

In case-8 or case-9, the edge of the cell between the vertices $(a_x, a_y, \overline{z}_1)$ and $(\overline{x}_2, a_y, \overline{z}_1)$ may be intersected by the boundary of the neighborhood or may be completely within the neighborhood, but all the other edges parallel to the $\overline{x}$-axis are completely outside the neighborhood, as shown in Figures 5.9h andFigures 5.9i. Therefore, the condition in this case is

$$a_x^2 + a_y^2 + \overline{z}_1^2 \leq \overline{m}^2 < a_x^2 + \overline{y}_2^2 + \overline{z}_1^2 \,. \tag{5.90}$$

The intersection of the boundary of the neighborhood with the edge between the vertices $(a_x, a_y, \overline{z}_1)$ and $(\overline{x}_2, a_y, \overline{z}_1)$ is given as

$$\overline{x}_{e_4} = \sqrt{\overline{m}^2 - a_y^2 - \overline{z}_1^2} \,. \tag{5.91}$$

Case-8 and case-9 can be treated as a single case because of the definition of the upper limit of the outer integral as $b_x = \min\left(\overline{x}_2, \overline{x}_{e_4}\right)$ (see Equation 5.26).

Therefore, the quadrature coefficient in case-8 and case-9 is computed as

$$\begin{aligned}
\beta_{ij} &= 2^s \left[ \int_{a_x}^{b_x} \int_{a_y}^{\sqrt{\overline{m}^2 - \overline{x}^2 - \overline{z}_1^2}} \sqrt{\overline{m}^2 - \overline{x}^2 - \overline{y}^2} \, \mathrm{d}\overline{y} \, \mathrm{d}\overline{x} - \int_{a_x}^{b_x} \int_{a_y}^{\sqrt{\overline{m}^2 - \overline{x}^2 - \overline{z}_1^2}} \overline{z}_1 \, \mathrm{d}\overline{y} \, \mathrm{d}\overline{x} \right] \\
&= 2^s \left[ \int_{a_x}^{b_x} \frac{1}{2} \left( \left(\overline{m}^2 - \overline{x}^2\right) \arcsin\left( \frac{\sqrt{\overline{m}^2 - \overline{x}^2 - \overline{z}_1^2}}{\sqrt{\overline{m}^2 - \overline{x}^2}} \right) + \overline{z}_1 \sqrt{\overline{m}^2 - \overline{x}^2 - \overline{z}_1^2} \right. \right. \\
&\qquad \left. - \left(\overline{m}^2 - \overline{x}^2\right) \arcsin\left( \frac{a_y}{\sqrt{\overline{m}^2 - \overline{x}^2}} \right) - a_y \sqrt{\overline{m}^2 - \overline{x}^2 - a_y^2} \right) \mathrm{d}\overline{x} \\
&\qquad \left. - \overline{z}_1 \int_{a_x}^{b_x} \left( \sqrt{\overline{m}^2 - \overline{x}^2 - \overline{z}_1^2} - a_y \right) \mathrm{d}\overline{x} \right] .
\end{aligned} \tag{5.92}$$

By using Equations 5.67, 5.68 and 5.69, Equation 5.92 is solved as follows:

$$\begin{aligned}
\beta_{ij} &= 2^s \left[ \frac{1}{2} I_3(a_x, b_x, \overline{z}_1) + \frac{1}{2} \overline{z}_1 \, I_1(a_x, b_x, \overline{z}_1) - \frac{1}{2} I_2(a_x, b_x, a_y) - \frac{1}{2} a_y \, I_1(a_x, b_x, a_y) \right. \\
&\qquad \left. - \overline{z}_1 \, I_1(a_x, b_x, \overline{z}_1) + \overline{z}_1 a_y \left(b_x - a_x\right) \right] \\
&= 2^s \left[ -\frac{1}{2} \overline{z}_1 \, I_1(a_x, b_x, \overline{z}_1) - \frac{1}{2} a_y \, I_1(a_x, b_x, a_y) - \frac{1}{2} I_2(a_x, b_x, a_y) + \frac{1}{2} I_3(a_x, b_x, \overline{z}_1) \right. \\
&\qquad \left. + \overline{z}_1 a_y \left(b_x - a_x\right) \right] .
\end{aligned} \tag{5.93}$$

### 5.B.9 Case-10

In case-10, the cell is completely outside the neighborhood, as shown in Figure 5.9j. The condition for which this case is verified is that the closest node with coordinates $(a_x, a_y, \overline{z}_1)$ lies outside the neighborhood:

$$\overline{m}^2 < a_x^2 + a_y^2 + \overline{z}_1^2 \,. \tag{5.94}$$

In this case, the solution of Equation 5.56 is trivial:

$$\beta_{ij} = 0\,. \tag{5.95}$$

## 5.C Derivatives for the Taylor series expansion

We need to perform the Taylor series expansion of the function:

$$f(\overline{x}) := \arcsin\left(\frac{k_2}{\sqrt{\overline{m}^2 - \overline{x}^2}}\right). \tag{5.96}$$

Therefore, we have to compute the derivatives of $f(\overline{x})$, which will be denoted as $f^{(n)}(\overline{x})$ where $n > 1$ is the order of the derivative. After taking the first derivatives, one can recognize the following recursive pattern:

$$f^{(n)}(\overline{x}) = \frac{\sum_{p=1}^{\lfloor 3n/2 \rfloor} \left( \sum_{q=1}^{p} c(n,p,q)\, \overline{m}^{2(p-q)}\, k_2^{2q-1} \right) \overline{x}^{3n-2p}}{\left(\overline{m}^2 - \overline{x}^2\right)^n \left(\overline{m}^2 - \overline{x}^2 - k_2^2\right)^{n-1/2}}\,, \tag{5.97}$$

where $c(n,p,q)$ are some coefficients depending on the order $n$ of the corresponding derivative and on the indices $p$ and $q$. In order to compute these coefficients $c$, we take the derivative of $f^{(n-1)}(\overline{x})$ and the final solution should be equal to $f^{(n)}(\overline{x})$:

$$\begin{aligned}
\frac{\mathrm{d}}{\mathrm{d}\overline{x}} f^{(n-1)}(\overline{x}) &= \frac{\mathrm{d}}{\mathrm{d}\overline{x}} \left[ \frac{\sum_{p=1}^{\lfloor 3(n-1)/2 \rfloor} \left( \sum_{q=1}^{p} c(n-1,p,q)\, \overline{m}^{2(p-q)}\, k_2^{2q-1} \right) \overline{x}^{3(n-1)-2p}}{\left(\overline{m}^2 - \overline{x}^2\right)^{n-1} \left(\overline{m}^2 - \overline{x}^2 - k_2^2\right)^{n-3/2}} \right] \\
&= \Bigg\{ \left[ \sum_{p=1}^{\lfloor 3(n-1)/2 \rfloor} \left( \sum_{q=1}^{p} c(n-1,p,q)\, \overline{m}^{2(p-q)}\, k_2^{2q-1} \right) (3n-2p-3)\, \overline{x}^{3n-2p-4} \right] \\
&\qquad \cdot \left(\overline{m}^2 - \overline{x}^2\right)^{n-1} \left(\overline{m}^2 - \overline{x}^2 - k_2^2\right)^{n-3/2} \\
&\quad - \left[ \sum_{p=1}^{\lfloor 3(n-1)/2 \rfloor} \left( \sum_{q=1}^{p} c(n-1,p,q)\, \overline{m}^{2(p-q)}\, k_2^{2q-1} \right) \overline{x}^{3n-2p-3} \right] \\
&\quad \cdot \Bigg[ (n-1) \left(\overline{m}^2 - \overline{x}^2\right)^{n-2} (-2\overline{x}) \left(\overline{m}^2 - \overline{x}^2 - k_2^2\right)^{n-3/2} \\
&\qquad + \left(\overline{m}^2 - \overline{x}^2\right)^{n-1} \left(n - \frac{3}{2}\right) \left(\overline{m}^2 - \overline{x}^2 - k_2^2\right)^{n-5/2} (-2\overline{x}) \Bigg] \Bigg\} \\
&\quad \cdot \frac{1}{\left(\overline{m}^2 - \overline{x}^2\right)^{2(n-1)} \left(\overline{m}^2 - \overline{x}^2 - k_2^2\right)^{2n-3}}\,.
\end{aligned} \tag{5.98}$$

We multiply the numerator and denominator by $\left(\overline{m}^2-\overline{x}^2\right)^{-n+2}\left(\overline{m}^2-\overline{x}^2-k_2^2\right)^{-n+5/2}$, so that the denominator is equal to the denominator of $f^{(n)}(\overline{x})$. Therefore, the numerator becomes:

$$
\begin{aligned}
&\left\{\left[\sum_{p=1}^{\lfloor 3(n-1)/2\rfloor}\left(\sum_{q=1}^{p}c(n-1,p,q)\,\overline{m}^{2(p-q)}\,k_2^{2q-1}\right)(3n-2p-3)\,\overline{x}^{3n-2p-4}\right]\right.\\
&\qquad\cdot\left(\overline{m}^2-\overline{x}^2\right)\left(\overline{m}^2-\overline{x}^2-k_2^2\right)\\
&\quad-\left[\sum_{p=1}^{\lfloor 3(n-1)/2\rfloor}\left(\sum_{q=1}^{p}c(n-1,p,q)\,\overline{m}^{2(p-q)}\,k_2^{2q-1}\right)\overline{x}^{3n-2p-3}\right]\\
&\qquad\left.\cdot\left[-2\overline{x}\,(n-1)\left(\overline{m}^2-\overline{x}^2-k_2^2\right)-2\overline{x}\left(n-\frac{3}{2}\right)\left(\overline{m}^2-\overline{x}^2\right)\right]\right\}\\
&=\left\{\left[\sum_{p=1}^{\lfloor 3(n-1)/2\rfloor}\left(\sum_{q=1}^{p}c(n-1,p,q)\,\overline{m}^{2(p-q)}\,k_2^{2q-1}\right)(3n-2p-3)\,\overline{x}^{3n-2p-4}\right]\right.\\
&\qquad\cdot\left(\overline{m}^4-2\overline{m}^2\overline{x}^2-\overline{m}^2k_2^2+\overline{x}^4+k_2^2\overline{x}^2\right)\\
&\quad-\left[\sum_{p=1}^{\lfloor 3(n-1)/2\rfloor}\left(\sum_{q=1}^{p}c(n-1,p,q)\,\overline{m}^{2(p-q)}\,k_2^{2q-1}\right)\overline{x}^{3n-2p-3}\right]\\
&\qquad\left.\cdot\left[(-4n+5)\,\overline{m}^2\overline{x}+(4n-5)\,\overline{x}^3+2\,(n-1)\,k_2^2\overline{x}\right]\right\}\\
&=\left\{\sum_{p=1}^{\lfloor 3(n-1)/2\rfloor}(3n-2p-3)\left(\sum_{q=1}^{p}c(n-1,p,q)\,\overline{m}^{2(p-q+2)}\,k_2^{2q-1}\right)\overline{x}^{3n-2p-4}\right.\\
&\quad+\sum_{p=1}^{\lfloor 3(n-1)/2\rfloor}(-2n+4p+1)\left(\sum_{q=1}^{p}c(n-1,p,q)\,\overline{m}^{2(p-q+1)}\,k_2^{2q-1}\right)\overline{x}^{3n-2p-2}\\
&\quad+\sum_{p=1}^{\lfloor 3(n-1)/2\rfloor}(-3n+2p+3)\left(\sum_{q=1}^{p}c(n-1,p,q)\,\overline{m}^{2(p-q+1)}\,k_2^{2q+1}\right)\overline{x}^{3n-2p-4}\\
&\quad+\sum_{p=1}^{\lfloor 3(n-1)/2\rfloor}(-n-2p+2)\left(\sum_{q=1}^{p}c(n-1,p,q)\,\overline{m}^{2(p-q)}\,k_2^{2q-1}\right)\overline{x}^{3n-2p}\\
&\quad\left.+\sum_{p=1}^{\lfloor 3(n-1)/2\rfloor}(n-2p-1)\left(\sum_{q=1}^{p}c(n-1,p,q)\,\overline{m}^{2(p-q)}\,k_2^{2q+1}\right)\overline{x}^{3n-2p-2}\right\}. \qquad (5.99)
\end{aligned}
$$

We can now change the lower and upper limits of the summations to equalize the exponents of the numerator of $f^{(n)}(\overline{x})$ as follows:

$$\left\{ \sum_{p=3}^{\lfloor 3(n-1)/2 \rfloor+2} (3n-2p+1) \left( \sum_{q=1}^{p-2} c(n-1,p-2,q)\, \overline{m}^{2(p-q)}\, k_2^{2q-1} \right) \overline{x}^{3n-2p} \right.$$
$$+ \sum_{p=2}^{\lfloor 3(n-1)/2 \rfloor+1} (-2n+4p-3) \left( \sum_{q=1}^{p-1} c(n-1,p-1,q)\, \overline{m}^{2(p-q)}\, k_2^{2q-1} \right) \overline{x}^{3n-2p}$$
$$+ \sum_{p=3}^{\lfloor 3(n-1)/2 \rfloor+2} (-3n+2p-1) \left( \sum_{q=2}^{p-1} c(n-1,p-2,q-1)\, \overline{m}^{2(p-q)}\, k_2^{2q-1} \right) \overline{x}^{3n-2p}$$
$$+ \sum_{p=1}^{\lfloor 3(n-1)/2 \rfloor} (-n-2p+2) \left( \sum_{q=1}^{p} c(n-1,p,q)\, \overline{m}^{2(p-q)}\, k_2^{2q-1} \right) \overline{x}^{3n-2p}$$
$$\left. + \sum_{p=2}^{\lfloor 3(n-1)/2 \rfloor+1} (n-2p+1) \left( \sum_{q=2}^{p} c(n-1,p-1,q-1)\, \overline{m}^{2(p-q)}\, k_2^{2q-1} \right) \overline{x}^{3n-2p} \right\}. \quad (5.100)$$

Therefore, $c(n,p,q)$ can be computed from Equation 5.100 (see Algorithm 3).

Also, we need the Taylor series expansion of a similar function:

$$g(\overline{x}) := \arcsin\left( \frac{\sqrt{\overline{m}^2 - \overline{x}^2 - k_3^2}}{\sqrt{\overline{m}^2 - \overline{x}^2}} \right). \quad (5.101)$$

By repeating the previous procedure for $g(\overline{x})$, we obtain the same coefficients with a negative sign:

$$g^{(n)}(\overline{x}) = \frac{-\sum_{p=1}^{\lfloor 3n/2 \rfloor} \left( \sum_{q=1}^{p} c(n,p,q)\, \overline{m}^{2(p-q)}\, k_3^{2q-1} \right) \overline{x}^{\,3n-2p}}{\left(\overline{m}^2 - \overline{x}^{\,2}\right)^n \left(\overline{m}^2 - \overline{x}^{\,2} - k_3^2\right)^{n-1/2}}. \quad (5.102)$$

## 5.D Quadrature coefficients for $\overline{m} = 3, 4, 6$

We report in Tables 5.2, 5.3 and 5.4 the values of the quadrature coefficients derived from Algorithm 4 for $\overline{m} = 3, 4, 6$ respectively. The Taylor series expansion is truncated at an order $N = 20$ to maintain the errors of the computations close to machine precision (see Figure 5.10). The bonds are identified by the coordinates $(\overline{x}_j, \overline{y}_j, \overline{z}_j)$ of node $j$ in the system of reference specified in Section 5.3.2, as shown in Figure 5.16. The quadrature coefficients which are not listed in the tables are equal to 0.

Table 5.2: *Quadrature coefficients for* $\overline{m} = 3$.

| Coordinates $(\overline{x}_j, \overline{y}_j, \overline{z}_j)$ of node $j$ | $\beta_{ij}$ |
|---|---|
| $(0,0,1)$, $(0,0,2)$, $(0,1,1)$, $(0,1,2)$, $(1,1,1)$ | 1 |
| $(1,1,2)$ | 0.973726549278437 |
| $(0,2,2)$ | 0.676019006545153 |
| $(0,0,3)$ | 0.472039364938528 |
| $(1,2,2)$ | 0.452222876981391 |
| $(0,1,3)$ | 0.296813994273711 |
| $(1,1,3)$ | 0.135469082591897 |
| $(2,2,2)$ | 0.051318527160244 |
| $(0,2,3)$ | 0.005723631798072 |
| $(1,2,3)$ | 0.000153662617015 |

Table 5.3: *Quadrature coefficients for* $\overline{m} = 4$.

| Coordinates $(\overline{x}_j, \overline{y}_j, \overline{z}_j)$ of node $j$ | $\beta_{ij}$ |
|---|---|
| $(0,0,1)$, $(0,0,2)$, $(0,0,3)$, $(0,1,1)$, $(0,1,2)$, $(0,1,3)$, $(0,2,2)$, $(1,1,1)$, $(1,1,2)$, $(1,2,2)$ | 1 |
| $(1,1,3)$ | 0.998768863060338 |
| $(2,2,2)$ | 0.966687702325083 |
| $(0,2,3)$ | 0.892821241940852 |
| $(1,2,3)$ | 0.775199178007998 |
| $(0,0,4)$ | 0.479090049888385 |
| $(0,1,4)$ | 0.350647333158876 |
| $(2,2,3)$ | 0.316083719616023 |
| $(1,1,4)$ | 0.218887022520336 |
| $(0,3,3)$ | 0.198987147856524 |
| $(1,3,3)$ | 0.108751981636951 |
| $(0,2,4)$ | 0.042953209732511 |
| $(1,2,4)$ | 0.010206581019384 |
| $(2,3,3)$ | 0.003887002534346 |

Table 5.4: *Quadrature coefficients for* $\overline{m} = 6$.

| Coordinates $(\overline{x}_j, \overline{y}_j, \overline{z}_j)$ of node $j$ | $\beta_{ij}$ |
|---|---|
| $(0,0,1)$, $(0,0,2)$, $(0,0,3)$, $(0,0,4)$, $(0,0,5)$, $(0,1,1)$, $(0,1,2)$, $(0,1,3)$, $(0,1,4)$, $(0,1,5)$, $(0,2,2)$, $(0,2,3)$, $(0,2,4)$, $(0,3,3)$, $(0,3,4)$, $(1,1,1)$, $(1,1,2)$, $(1,1,3)$, $(1,1,4)$, $(1,1,5)$, $(1,2,2)$, $(1,2,3)$, $(1,2,4)$, $(1,3,3)$, $(1,3,4)$, $(2,2,2)$, $(2,2,3)$, $(2,2,4)$, $(2,3,3)$ | 1 |
| $(3,3,3)$ | 0.999790182328854 |
| $(0,2,5)$ | 0.996792906342336 |
| $(2,3,4)$ | 0.987734967536850 |
| $(1,2,5)$ | 0.972240389996081 |
| $(0,4,4)$ | 0.859401538943377 |
| $(1,4,4)$ | 0.784526552214560 |
| $(2,2,5)$ | 0.770548513294528 |
| $(3,3,4)$ | 0.690805241353979 |
| $(0,3,5)$ | 0.677365640339469 |
| $(1,3,5)$ | 0.579443674979575 |
| $(0,0,6)$ | 0.486088519387858 |
| $(2,4,4)$ | 0.476199633943112 |
| $(0,1,6)$ | 0.401767018323396 |
| $(1,1,6)$ | 0.316210827911515 |
| $(2,3,5)$ | 0.285658718830588 |
| $(0,2,6)$ | 0.144371394514214 |
| $(0,4,5)$ | 0.086400028994142 |
| $(3,4,4)$ | 0.081510711534106 |
| $(1,2,6)$ | 0.079306290046733 |
| $(1,4,5)$ | 0.046394967777568 |
| $(3,3,5)$ | 0.022174412588457 |
| $(2,2,6)$ | 0.002888370932027 |
| $(2,4,5)$ | 0.001586472847643 |

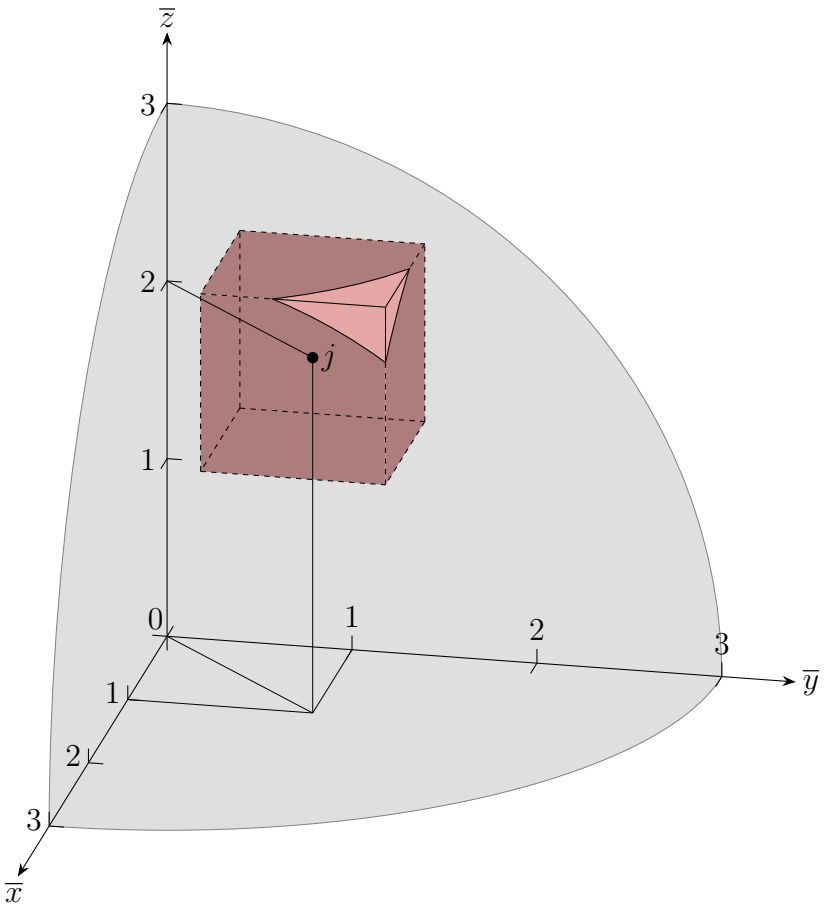


Figure 5.16: *The quadrature coefficient $\beta_{ij}$ (for $\overline{m} = 3$) of the cell identified, for instance, by the coordinates $(1, 1, 2)$ of node $j$, is reported in the third row of Table 5.2.*

# Chapter 6

# An improved coupling of 3D state-based Peridynamics with high-order 1D finite elements to reduce spurious effects at interfaces

**Published in:** *International Journal for Numerical Methods in Engineering* (2023)

**Authors:** Francesco Scabbia, Marco Enea

## Abstract

Peridynamics (PD) is a nonlocal continuum theory capable of handling fracture mechanisms with ease. However, its use involves high computational costs. On the other hand, Carrera Unified Formulation (CUF) allows one to use one-dimensional high-order finite elements, resulting in excellent accuracy while improving computational efficiency. To address the high computational cost of solving fracture problems, a coupling technique between these two theories is necessary. Various approaches have been proposed to couple peridynamic grids with finite element meshes in the literature. However, most of these approaches are affected by arbitrary choices of blending functions and tuning parameters or exhibit spurious effects at the interfaces. To overcome these issues, we propose a simple coupling technique based on overlapping PD/CUF regions and continuity of the displacement field at the interfaces. This approach is verified through static analysis of classical beams and thin-walled structures with applications in the aerospace industry.

**Keywords:** Peridynamics, finite element method, higher-order elements, coupling.

## 6.1 Introduction

Peridynamic (PD) theory has been introduced for the first time by Silling in [61]. This first formulation of the theory was named Bond-Based Peridynamics (BB-PD) and has the limitation that the Poisson's ratio value is fixed (for instance, $\nu = 0.25$ in 3D models). A more general formulation of the theory that overcomes this restriction, namely the State-Based Peridynamics (SB-PD), has been proposed in [62]. The main idea of the peridynamic theory relies on the fact that two PD points in a solid body interact with each other when their distance is lower than the horizon radius, called $\delta$. Thus, PD is a non-local theory, and it is based on integro-differential equations. For this reason, PD has been widely used for dealing with discontinuous displacement fields, such as those in fracture mechanic problems [67, 207], due to the possibility of avoiding the shortcomings of classical continuum mechanics.

However, it should be highlighted that the non-local nature of PD theory leads to higher computational analysis costs if compared with those from classical computational methods, i.e., finite element method (FEM). Indeed, PD leads to solving systems with sparse, large, and not banded matrices, making the solution of fully 3D problems of practical engineering interest impossible. Furthermore, the handling of the non-local boundaries requires specific methods, such as, for example, [186, 227, 236, 249], to reduce the PD surface effect, i.e. an undesired stiffness fluctuation near the external surface of the body, and to impose the boundary conditions. If FEM is used at the external boundary of the body, these problems are avoided altogether.

On these bases, researches are now focused on providing coupling strategies between FEM models and PD domains in order to exploit the advantages of both numerical methods and adopt PD in relatively small regions of interest. Kilic and Madenci [199] propose a coupled method where an overlap region is identified. In this region, both peridynamic and finite element equations are used at the same time. In [200, 201], a progressive morphing between local and non-local interactions is adopted. A transition affecting only the constitutive parameters is employed to perform the coupling strategy. Seleson and co-workers [202, 203] propose a strong coupling between local and non-local approaches for integrated fracture modelling. In [204], the coupling is achieved by the introduction of the partial stress concept for the connection of nonlocal models with differen horizon radius. Sun and Fish [207] introduced a superposition-based coupling model between bond-based PD and FEM. A partial superposition of nonlocal (PD) and local (FEM) solution is considered. The continuity of the solution is achieved by imposing appropriate homogeneous boundary conditions. Galvanetto and his co-workers [205, 206] propose a coupling strategy based on the adaptive transformation of FEM nodes into PD particles, which has shown to be effective for static, dynamic, and fracture problems and from one-dimensional to three-dimensional models [115, 171, 205, 206, 208, 209].

It should be underlined that most of the aforementioned methods are able to couple FEM and PD domains of consistent dimensions. However, some particular situations may need the adoption of 3D peridynamics domains in local zones of the structure. In this case, the coupling of 3D FEM with 3D PD models may be unfeasible, due to the consequent huge computational cost. An example of a coupling method between refined 1D models and a

3D bond-based perydinamic grid is provided in [213]. The 1D models are based on the Carrera Unified Formulation (CUF), whose governing equations are formulated in terms of fundamental nuclei, which are invariant with the theory approximation order. The coupling is realized through the adoption of Lagrange multipliers [225, 250, 251], which are applied at the interface between the two domains in order to assure continuity. This technique demonstrates to be general and consistent, due to the fact that Lagrange multipliers have a clear physical meaning. Results show that this method allows to obtain 3D-like accuracy solutions by adopting a one-dimensional refined model and 3D Peridynamic, thus reducing the computational cost. Moreover, the use of Lagrange multipliers allows the possibility of introducing 3D PD regions only in zones of interest, which can also be embedded into the FE domain. Nevertheless, some numerical distortions are detected at the FE-PD interface, requiring some artificial expedient (i.e., overlapping region) to eliminate these errors.

In this work, the authors propose a different coupling method, which can fully exploit the CUF formulation's potentiality in combination with the 3D peridynamics domain and greatly reduce numerical error at the interface between two different domains [165]. This method is based on the continuity of the displacement field at the interface [205, 209]. The forces acting at the interface are provided by introducing fictitious nodes beyond the interface itself: a fictitious FEM node is added in the PD region, and some fictitious PD nodes are added in the FEM region. The coupling is then achieved by considering that peridynamic forces are exerted only on PD nodes, while finite elements apply forces only on FE nodes. The effectiveness of this strategy has already been proven when applied to couple classical FE elements with PD domains [205, 206, 209]. Thanks to this improved coupling approach, the spurious effects that were present at the interfaces in [213] can be considerably reduced. Moreover, for the first time State-Based Peridynamics has been coupled with CUF formulation, which allows the model to have no restrictions on the value of the Poisson's ratio. The paper is organized as follows: Section 6.2 explains the basis of the state-based peridynamics formulation; high-order one-dimensional CUF-based elements are discussed in Section 6.3; then, the proposed coupling approach is described in Section 6.4; some numerical results, such as thin-walled beams and a reinforced aeronautical panel, are discussed in Section 6.5; finally, the main conclusions are drawn in Section 6.6.

## 6.2 State-based Peridynamics

The first formulation of the peridynamic theory, named bond-based Peridynamics [61], has been extensively exploited for its simplicity of implementation. However, due to the assumptions of this formulation, the Poisson's ratio is constrained to $\nu = 0.25$ in 3D bodies. To overcome this limitation, the state-based formulation of the theory was introduced in [62]. The state-based Peridynamics is used in this work.

### 6.2.1 Continuum formulation

Two peridynamic points, for instance $\mathbf{x}$ and $\mathbf{x}'$ shown in Fig. 6.1, interact through a *bond* that is identified by their relative position vector

$$\boldsymbol{\xi} = \mathbf{x}' - \mathbf{x}\,. \tag{6.1}$$

This interaction vanishes if the distance between the interacting points exceeds the value $\delta$, which is called *horizon size*. Therefore, a peridynamic point interacts with all the points within a sphere centered in that point and with a radius equal to $\delta$. The set of the points within this sphere is named *neighborhood* and denoted by $\mathcal{H}$. In the deformed configuration, the relative displacement vector $\boldsymbol{\eta}$ is defined as

$$\boldsymbol{\eta} = \mathbf{u}(\mathbf{x}', t) - \mathbf{u}(\mathbf{x}, t)\,, \tag{6.2}$$

where $\mathbf{u}$ is the displacement field. Note that the relative position vector at instant $t$ between points $\mathbf{x}$ and $\mathbf{x}'$ is given by $\boldsymbol{\xi} + \boldsymbol{\eta}$.

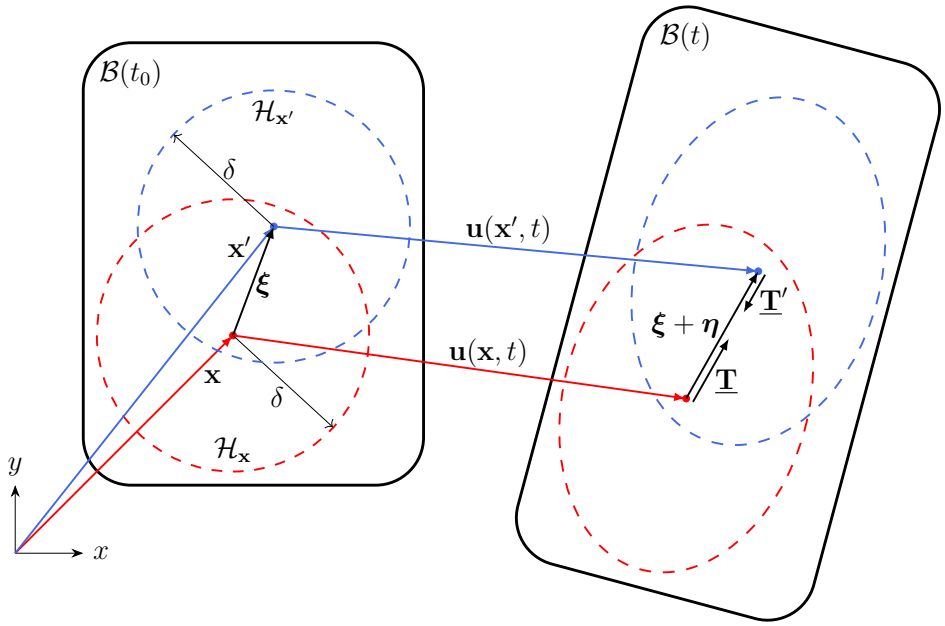


Figure 6.1: *Reference configuration of the body $\mathcal{B}$ at instant $t_0$ (on the left) and deformed configuration at instant $t$ (on the right). When the bond $\boldsymbol{\xi}$ between points $\mathbf{x}$ and $\mathbf{x}'$ is deformed, the force density vector states $\underline{\mathbf{T}} = \underline{\mathbf{T}}[\mathbf{x}, t]\langle\boldsymbol{\xi}\rangle$ and $\underline{\mathbf{T}}' = \underline{\mathbf{T}}[\mathbf{x}', t]\langle-\boldsymbol{\xi}\rangle$ arise within the bond.*

The peridynamic equation of motion of point $\mathbf{x}$ is given by [62]

$$\rho(\mathbf{x})\,\ddot{\mathbf{u}}(\mathbf{x}, t) = \int_{\mathcal{H}_{\mathbf{x}}} \left(\underline{\mathbf{T}}[\mathbf{x}, t]\langle\boldsymbol{\xi}\rangle - \underline{\mathbf{T}}[\mathbf{x}', t]\langle-\boldsymbol{\xi}\rangle\right) \mathrm{d}V_{\mathbf{x}'} + \mathbf{b}(\mathbf{x}, t)\,, \tag{6.3}$$

where $\rho$ is the material density, $\ddot{\mathbf{u}}$ is the acceleration field, $\underline{\mathbf{T}}$ is the force density vector state (force per unit volume squared), $\mathrm{d}V_{\mathbf{x}'}$ is the differential volume of a point $\mathbf{x}'$ within the neighborhood $\mathcal{H}_{\mathbf{x}}$ and $\mathbf{b}$ is the external body force density field. The notation $\underline{\mathbf{T}}[\mathbf{x}, t]\langle\boldsymbol{\xi}\rangle$ means that the force density scalar state $\underline{\mathbf{T}}$ depends on point $\mathbf{x}$ and instant $t$ and is applied

to the bond vector $\boldsymbol{\xi}$. In quasi-static conditions, the equilibrium equation of point $\mathbf{x}$ is given as

$$-\int_{\mathcal{H}_\mathbf{x}} \left(\underline{\mathbf{T}}[\mathbf{x}]\langle\boldsymbol{\xi}\rangle - \underline{\mathbf{T}}[\mathbf{x}']\langle-\boldsymbol{\xi}\rangle\right) \mathrm{d}V_{\mathbf{x}'} = \mathbf{b}(\mathbf{x})\,. \tag{6.4}$$

Note that $\underline{\mathbf{T}}[\mathbf{x}]\langle\boldsymbol{\xi}\rangle$ and $\underline{\mathbf{T}}[\mathbf{x}']\langle-\boldsymbol{\xi}\rangle$ must have the same magnitude in bond-based Peridynamics, whereas may have different magnitudes in state-based Peridynamics (see Fig. 6.1).

In the following, we define some quantities that will be useful to compute the force density vector state $\underline{\mathbf{T}}[\mathbf{x}]\langle\boldsymbol{\xi}\rangle$. The reference position scalar state $\underline{x}$, which represents the bond length in the initial configuration, and the extension scalar state $\underline{e}$, which represents the elongation (or contraction) of the bond in the deformed configuration, are defined respectively as

$$\underline{x}\langle\boldsymbol{\xi}\rangle = \|\boldsymbol{\xi}\|\,. \tag{6.5}$$

$$\underline{e}\langle\boldsymbol{\xi}\rangle = \|\boldsymbol{\xi}+\boldsymbol{\eta}\| - \|\boldsymbol{\xi}\|\,. \tag{6.6}$$

On the other hand, the weighted volume $m$ and the dilatation $\theta$ of a point $\mathbf{x}$ are defined respectively as

$$m(\mathbf{x}) = \int_{\mathcal{H}_\mathbf{x}} \underline{\omega}\,\underline{x}^2\,\mathrm{d}V_{\mathbf{x}'}\,, \tag{6.7}$$

$$\theta(\mathbf{x}) = \frac{3}{m(\mathbf{x})}\int_{\mathcal{H}_\mathbf{x}} \underline{\omega}\,\underline{x}\,\underline{e}\,\mathrm{d}V_{\mathbf{x}'}\,, \tag{6.8}$$

where $\underline{\omega}$ is a prescribed spherical influence function. We adopt in this work the Gaussian influence function:

$$\underline{\omega} = \exp\left(-\frac{\|\boldsymbol{\xi}\|^2}{\delta^2}\right)\,. \tag{6.9}$$

In ordinary state-based Peridynamics, the force density vector state is aligned with the deformed direction vector state (unit vector in the direction of the corresponding bond):

$$\underline{\mathbf{M}}\langle\boldsymbol{\xi}\rangle = \frac{\boldsymbol{\xi}+\boldsymbol{\eta}}{\|\boldsymbol{\xi}+\boldsymbol{\eta}\|}\,. \tag{6.10}$$

Therefore, adopting the linear peridynamic solid model [62], the force density vector state is computed as

$$\underline{\mathbf{T}}[\mathbf{x}]\langle\boldsymbol{\xi}\rangle = \frac{\underline{\omega}\langle\boldsymbol{\xi}\rangle}{m(\mathbf{x})}\big[\,(3K-5\mu)\,\theta(\mathbf{x})\,\underline{x}\langle\boldsymbol{\xi}\rangle + 15\mu\,\underline{e}\langle\boldsymbol{\xi}\rangle\big]\underline{\mathbf{M}}\langle\boldsymbol{\xi}\rangle\,, \tag{6.11}$$

where $K$ is the bulk modulus and $\mu$ is the shear modulus.

### 6.2.2 Discretization

The peridynamic body is discretized by the meshfree method with a uniform grid spacing $h$, which is arguably the most commonly used method [65, 184, 235]. Each node represents a cell with a volume $V = h^3$. Consider a node $i$ and its neighborhood $\mathcal{H}_i$, as shown in Fig. 6.2. We define as $\beta$, called *quadrature coefficient*, the fraction of volume cell that lies within $\mathcal{H}_i$. The value of the quadrature coefficient $\beta$ is comprised between the extreme values 0

(if the cell is completely outside $\mathcal{H}_i$) and 1 (if the cell is completely outside $\mathcal{H}_i$). Clearly, a node is considered part of the neighborhood only if the quadrature coefficient of its cell is $\beta > 0$. The computation of the quadrature coefficients in 3D Peridynamics can be carried out in several ways (see, for instance, [158, 198, 235]). For simplicity, we adopt the method illustrated in [252] for this work.

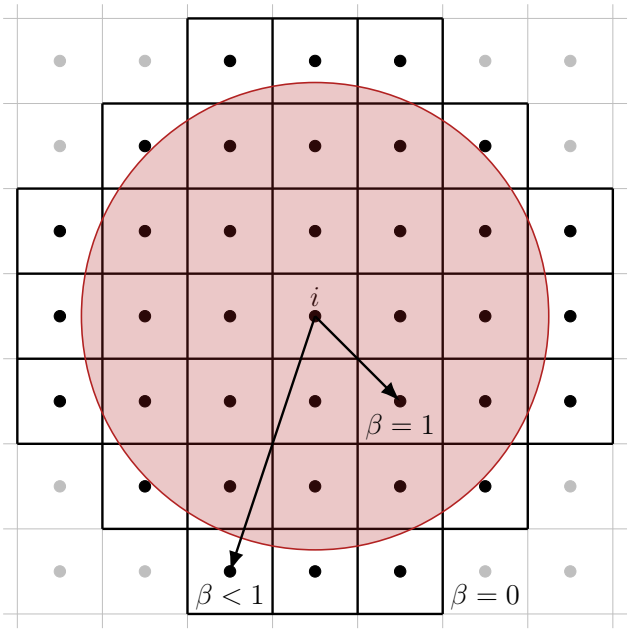


Figure 6.2: *The neighborhood $\mathcal{H}_i$ of a node $i$ consists of the nodes with $\beta > 0$, where $\beta$ is the quadrature coefficient computed as the fraction of the cell volume lying within the neighborhood.*

The relative position vector of the bond $ij$ that connects nodes $i$ and $j$ can be computed as

$$\boldsymbol{\xi}_{ij} = \mathbf{x}_j - \mathbf{x}_i \,, \tag{6.12}$$

where $\mathbf{x}_i$ and $\mathbf{x}_j$ are the position vectors of the two nodes. Similarly, the relative displacement vector of the bond is evaluated as

$$\boldsymbol{\eta}_{ij} = \mathbf{u}_j^{PD} - \mathbf{u}_i^{PD} \,, \tag{6.13}$$

where $\mathbf{u}_i^{PD}$ and $\mathbf{u}_j^{PD}$ are the displacement vectors of the peridynamic nodes. The reference position scalar state and the influence function of the bond are computed as

$$\underline{x}_{ij} = \|\boldsymbol{\xi}_{ij}\| \,, \tag{6.14}$$

$$\underline{\omega}_{ij} = \exp\left(-\frac{\|\boldsymbol{\xi}_{ij}\|^2}{\delta^2}\right) . \tag{6.15}$$

Under the assumption of small displacements ($\|\boldsymbol{\eta}_{ij}\| \ll \|\boldsymbol{\xi}_{ij}\|$), the deformed direction vector state and the extension scalar state are respectively given as

$$\underline{\mathbf{M}}_{ij} = \frac{\boldsymbol{\xi}_{ij} + \boldsymbol{\eta}_{ij}}{\|\boldsymbol{\xi}_{ij} + \boldsymbol{\eta}_{ij}\|} \approx \frac{\boldsymbol{\xi}_{ij}}{\|\boldsymbol{\xi}_{ij}\|} \,. \tag{6.16}$$

$$\underline{e}_{ij} = \|\boldsymbol{\xi}_{ij} + \boldsymbol{\eta}_{ij}\| - \|\boldsymbol{\xi}_{ij}\| \approx \boldsymbol{\eta}_{ij} \cdot \underline{\mathbf{M}}_{ij} \,. \tag{6.17}$$

In the discretized model, the integrals over a neighborhood are numerically computed as the summation of the integrand evaluated for each node contained in that neighborhood. Therefore, the weighted volume $m$ and the dilatation $\theta$ of a node $i$ are given as

$$m_i = \sum_{j \in \mathcal{H}_i} \underline{\omega}_{ij}\, \underline{x}_{ij}^2\, \beta_{ij} V \,, \tag{6.18}$$

$$\theta_i = \frac{3}{m_i} \sum_{j \in \mathcal{H}_i} \underline{\omega}_{ij}\, \underline{x}_{ij}\, \underline{e}_{ij}\, \beta_{ij} V \,, \tag{6.19}$$

where $\beta_{ij}$ is the quadrature coefficient of the bond $ij$ and $V$ is the volume of the cell of node $j$. Therefore, the force density vector state is computed as

$$\underline{\mathbf{T}}_{ij} = \frac{\underline{\omega}_{ij}}{m_i} \big[ (3K - 5\mu)\, \theta_i\, \underline{x}_{ij} + 15\mu\, \underline{e}_{ij} \big] \underline{\mathbf{M}}_{ij} \,. \tag{6.20}$$

Now, we can write the equilibrium equation of a node $i$ in the discretized form (multiplying both sides of the equation by the cell volume $V_i = V$) as follows:

$$-\sum_{j \in \mathcal{H}_i} \big( \underline{\mathbf{T}}_{ij} - \underline{\mathbf{T}}_{ji} \big)\, \beta_{ij} V^2 = \mathbf{b}_i\, V \,, \tag{6.21}$$

where $\mathbf{b}_i$ is the external force density vector applied to node $i$. Equation 6.21 can be rewritten in the standard form

$$\mathbf{K}^{PD} \mathbf{U}^{PD} = \mathbf{F}^{PD} \,, \tag{6.22}$$

where $\mathbf{K}^{PD}$ is the peridynamic stiffness matrix, $\mathbf{U}^{PD}$ is the peridynamic displacement vector and $\mathbf{F}^{PD}$ is the peridynamic force vector.

## 6.3 High order 1D finite elements

The major shortcoming of the perdynamic theory is that the resulting stiffness matrix is sparse and generally not banded. Furthermore, the non-local nature of this methos makes the computational costs arise exponentially. Therefore, researchers are working on coupling peridynamics with finite elements. In this work, 3D PD domains are coupled with 1D FEs, based on the Carrera Unified Formulation (CUF). This formulation is known in the literature as capable of generating high-order theories with great accuracy and considerably reducing the overall computational weight [212].

### 6.3.1 The Carrera unified formulation

Let's consider a generic beam structure aligned along the y-axis and measuring $l$ in length and $\Omega$ in cross-section. In this formulation, the cross-sectional shape of the beam has no influence on its validity. In the CUF's framework, the 3D displacement field of this beam

can be formulated as follows:

$$\mathbf{u}(x,y,z) = F_\tau(x,z)\mathbf{u}_\tau(y), \qquad \tau = 1,2,....,M \tag{6.23}$$

where $\mathbf{u}(x,y,z)$ is the displacement vector; $F_\tau$ are the cross-section expansion functions; $\mathbf{u}_\tau$ is the generalized displacement vector; $M$ is the number of terms in the expansion. The subscript $\tau$ indicates summation. In addition, $F_\tau$ and $M$ may be freely chosen. Based on the selected expansion functions, the class of the 1D CUF model is determined. A first example is denoted by the Taylor expansion (TE) models, which have been widely employed in CUF's framework, as in [253, 254]. In the case of TE models, Mclaurin polynomials of truncated order $N$ are employed to expand the generalized displacements $\mathbf{u}_\tau$ around the beam axis. TE models could be very efficient for different problems. However, some errors can be detected if complex structures are investigated. In order to solve these kinds of problems, Lagrange expansion (LE) models are employed. In this case, Lagrange-like polynomials are used to expand the generalized displacements around the beam axis. The most important feature of LE models is that they make use of local expansions of pure displacement variables. The main advantage is that LE models allow a more refined discretization in specific regions of interest, leading to a higher solution accuracy. Furthermore, LE models enables to reproduce 3D-like solutions at a global-local scale.

### 6.3.2 Finite element approximation

Using 1D finite elements, the generalized displacement $\mathbf{u}_\tau$ is approximated along the beam axis:

$$\mathbf{u}_\tau(y) = N_i(y)\ \mathbf{u}_{\tau i}, \qquad i = 1,2,...,p+1 \tag{6.24}$$

where $p$ is the number of nodes for each element. In Eq. (6.24), the index $i$ means summation. The generalized displacements are expressed as a function of the unknown nodal vector, $\mathbf{u}_{\tau i}$, and the 1D shape functions, $N_i$. Note that Eq. (6.24) does not depend on the adopted refined 1D theory.
The governing equations are written using the principle of virtual work. For linear static problems, it is formulated in the following way:

$$\delta L_{\text{int}} = \delta L_{\text{ext}} \tag{6.25}$$

where $\delta$ is the virtual variation, $L_{\text{int}}$ the work of the internal strain energy, and $L_{\text{ext}}$ the work of the external forces. The internal work expression reads as:

$$\delta L_{\text{int}} = \int_l \int_\Omega \delta\boldsymbol{\epsilon}^T \boldsymbol{\sigma}\, \mathrm{d}\Omega\, \mathrm{d}y \tag{6.26}$$

where $\boldsymbol{\sigma}$ and $\boldsymbol{\epsilon}$ are the vectors of 3D stresses and strains. By replacing the constitutive and geometric equations along with Eqs (6.23) and (6.24), the internal work formula can be reformulated as follows:

$$\delta L_{\text{int}} = \delta \mathbf{u}_{sj}^T \mathbf{K}^{\tau sij} \mathbf{u}_{\tau i} \tag{6.27}$$

where $\mathbf{K}^{\tau sij}$ is the $3 \times 3$ fundamental nucleus of the element stiffness matrix of the refined 1D beam theory. Using the four indexes $/tau$, $s$, $i$, and $j$, the fundamental nucleus can be expanded to form any refined beam model. Then, after expansion of the stiffness matrix and after assembly over the whole domain, Eq. (6.25) is written as follows:

$$\mathbf{K}^{FE}\mathbf{U}^{FE} = \mathbf{F}^{FE} \tag{6.28}$$

where $\mathbf{K}^{FE}$ is the stiffness matrix, $\mathbf{U}^{FE}$ is the vector of the FE nodal unknowns and $\mathbf{F}^{FE}$ is the vector of external forces.

## 6.4 Improved coupling

Given its high computational cost, Peridynamics is preferably used only in regions where cracks are likely to propagate, whereas the rest of the body can be modelled by methods derived from classical continuum mechanics, such as the Carrera Unified Formulation (CUF). The coupling of high-order 1D FEs with a peridynamic grid of nodes has already been achieved via the use of Lagrange multipliers [213, 214]. However, the numerical solution obtained with this method exhibits undesired fluctuations of the solution near the interfaces.

An improved method to couple Finite Element Method (FEM) and Peridynamics (PD) has been developed in [171, 205, 206, 208, 209]. This method, based on the continuity of the displacement field at the interfaces, is reviewed in the following subsection. Inspired by that, we develop a method to couple high-order 1D FEs and PD nodes.

### 6.4.1 1D coupling of FEs and PD nodes

Consider a 1D body, in which a region is discretized with 1D FEs and another region with equispaced PD nodes, as shown in Fig. 6.3. Each PD node represents a portion of the 1D body of length $\Delta x$ and is positioned at the center of this portion. Therefore, the PD node closest to the interface is distant $\Delta x/2$ from the interface itself, as shown in Fig. 6.3a. On the other hand, the closest FEM node lies exactly at the interface. For simplicity, the length $\Delta\ell$ of the FEs is considered to be constant. The length $\Delta\ell$ of the FEs and the PD spacing $\Delta x$ are not necessarily equal to each other.

The improved coupling method is based on the continuity of the displacement field at the interface [205, 209]. The forces acting at the interface are provided by the introduction of fictitious nodes beyond the interface itself: a fictitious FEM node is added in the PD region and some fictitious PD nodes are added in the FEM region.

On the one hand, the new fictitious FEM node is positioned, for simplicity, at a distance $\Delta\ell$ from the interface, as shown in Fig. 6.3b. Its displacement is determined by interpolation of the displacements of the real PD nodes surrounding it. Since the fictitious FEM node lies in the PD region and cannot "feel" FEM forces, it is not subjected to the force of the fictitious FE. However, that force is applied to the real FEM node at the interface. Note that, due to the displacement interpolation, the force of the fictitious FE depends on the displacements of the real PD nodes.

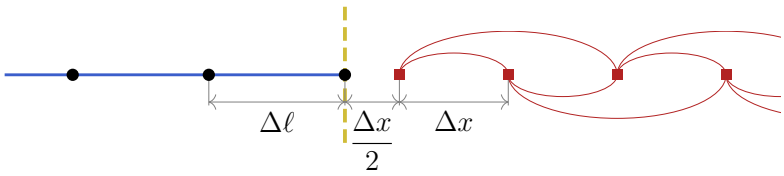


(a) *Initial geometry with real FEs (blue lines) of length $\Delta\ell$ and real PD nodes (red squares) with a uniform spacing $\Delta x$ The bonds are represented by the red line ($\delta = 2\Delta x$) and the interface between FEM and PD regions is represented by a yellow dashed line.*

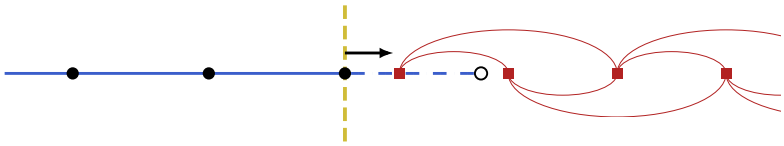

(b) *Introduction of a fictitious FE in the PD region to provide the force acting on the real FEM node at the interface. The displacement of the fictitious FEM node (empty circle) is determined by interpolation of the displacements of the real PD nodes.*

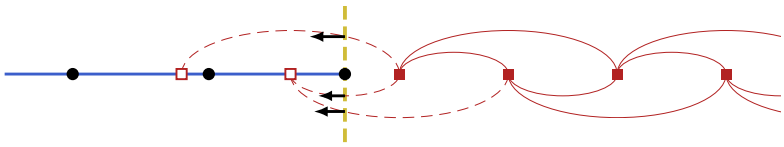

(c) *Introduction of some fictitious PD nodes in the FEM region to provide through the fictitious bonds (red dashed lines) the forces acting on the real PD nodes near the interface. The displacements of the fictitious PD nodes (empty squares) are determined by interpolation of the displacements of the real FEM nodes.*

Figure 6.3: *Coupling between 1D FEs and peridynamic nodes: the described interpolations ensure the continuity of the displacement field at the interface.*

On the other hand, some fictitious PD nodes are introduced in the FEM region to complete the neighborhoods of the real PD nodes near the interface, as shown in Fig. 6.3c. The displacements of the fictitious PD nodes can be determined by means of an interpolation of the real FEM nodes. The forces of the fictitious bonds, i.e., the bonds crossing the interface, are applied only to the real PD nodes because the fictitious PD nodes lie in the FEM region. Note that, due to the displacement interpolation, the forces of the fictitious bonds depends on the displacements of the real FEM nodes.

In the case of a linear displacement field, the force applied to the FEM node at the interface through the fictitious FE (see Fig. 6.3b) is equal to the sum of the forces applied to the real PD nodes through the fictitious bonds (see Fig. 6.3c) [165]. The concepts of this improved coupling method are hereinafter extended to couple a 3D peridynamic grid with high-order 1D elements (or CUF elements), as shown, for instance, in Fig. 6.4.

### 6.4.2 Interpolation of PD nodal displacements with FEM

In state-based Peridynamics, each node interact with all the nodes within a distance of $2\delta$ [166]. Therefore, the fictitious PD nodes are added within the FEs up to a distance of $2\delta$ from the interfaces [171], as shown in Fig. 6.5. The displacements of these nodes can be

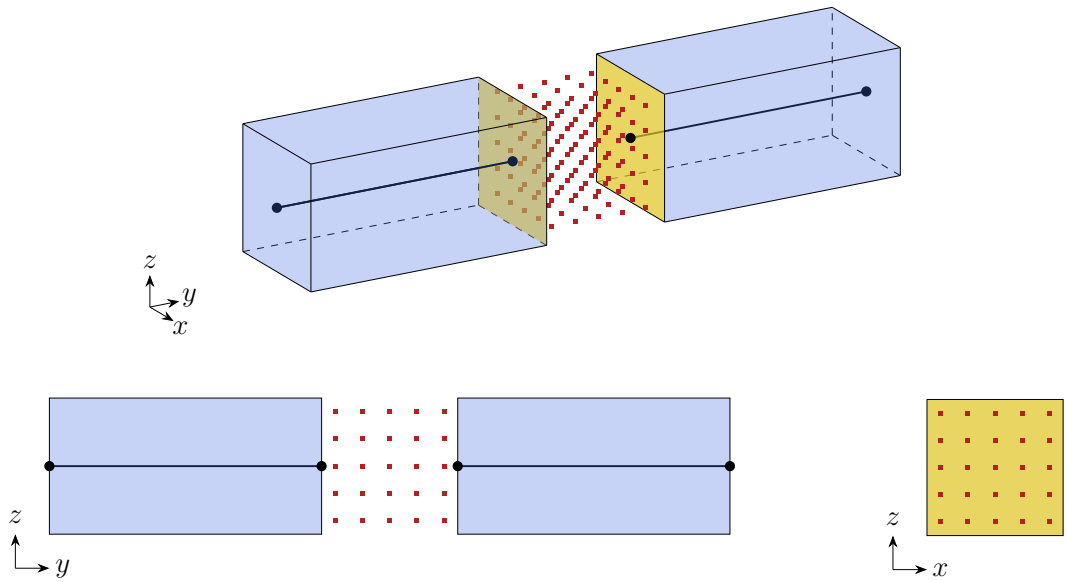


Figure 6.4: *Coupling of high-order 1D FEs (blue region) with 3D peridynamic nodes (red squares). The yellow surfaces are the interfaces between FEM and peridynamic regions.*

evaluated by interpolating the displacements of the FE nodes.

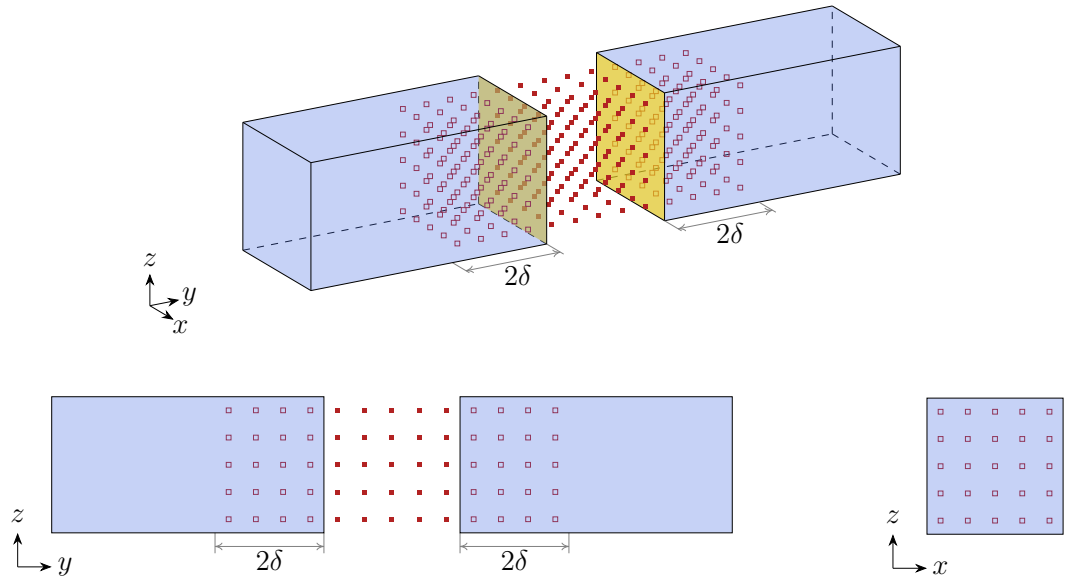


Figure 6.5: *Coupling of FEs (blue region) with 3D peridynamic nodes (red solid squares): the fictitious PD nodes (red empty squares) are added within the FEs up to a distance of $2\delta$ from the interfaces (yellow surfaces).*

Let us consider, for instance, a fictitious PD node $p$ with a position vector $\mathbf{x}_p = \{x_p, y_p, z_p\}^\top$. Since its position is known, it is straightforward to determine within which FE node $p$ lies. Hence, the FE shape functions $N_i$ and the expansion functions $F_\tau$ of that element are used to compute the displacement of node $p$:

$$\mathbf{u}^{f\text{-}PD}(x_p, y_p, z_p) = \sum_i \sum_\tau N_i(y_p) F_\tau(x_p, z_p) \mathbf{u}_{\tau i}^{FE}\,, \tag{6.29}$$

where $f\text{-}PD$ stands for "fictitious peridynamic" nodes. By repeating Equation 6.29 for each fictitious PD node, we obtain the following system of equations:

$$\mathbf{U}^{f\text{-}PD} = \mathbf{I}^{f\text{-}PD}\mathbf{U}^{FE}\,, \tag{6.30}$$

where $\mathbf{U}_f^{PD}$ is the peridynamic displacement vector of the fictitious peridynamic nodes, $\mathbf{I}^{f\text{-}PD}$ is the fictitious PD interpolation matrix and $\mathbf{U}^{FE}$ is the vector of the FE nodal unknowns. Note that the dimensions of $\mathbf{I}^{f\text{-}PD}$ are $3N^{f\text{-}PD} \times 3N^{FE}$, where $N^{f\text{-}PD}$ is the number of fictitious PD nodes and $3N^{FE}$ is the number of the FE nodal unknowns.

### 6.4.3 Interpolation of FE nodal displacements with PD

To begin with, let us consider a simple case in which the FE sections are perpendicular to the FEs. As shown in Fig. 6.6, the fictitious FE nodes are introduced so that the sections associated to those nodes lie over the plane of the real nodes closest to the interface. We can write the following equation for each real PD node $q$ that lies on the section of a fictitious FE node:

$$\mathbf{u}^{PD}(x_q, y_q, z_q) = \sum_i \sum_\tau N_i(y_q) F_\tau(x_q, z_q) \mathbf{u}_{\tau i}^{f\text{-}FE}\,, \tag{6.31}$$

where $\mathbf{u}_{\tau i}^{f\text{-}FE}$ contains the generalized degrees of freedom associated to the fictitious FE node. Equation 6.31 can be written in a matrix form as:

$$\mathbf{U}^{PD} = \mathbf{I}^{fs\text{-}PD}\mathbf{U}^{fs\text{-}FE}\,, \tag{6.32}$$

where $\mathbf{U}^{PD}$ is the peridynamic displacement vector, $\mathbf{I}^{fs\text{-}PD}$ is the interpolation matrix and $\mathbf{U}^{fs\text{-}FE}$ is the vector of the degrees of freedom of the section associated to a fictitious FE node.

However, we would like to express the latter degrees of freedom ($\mathbf{U}^{fs\text{-}FE}$) as functions of the displacements of the real PD nodes ($\mathbf{U}^{PD}$) by inverting the matrix $\mathbf{I}^{fs\text{-}PD}$. Note that, in general, $\mathbf{I}^{fs\text{-}PD}$ is not a square matrix and, hence, is not invertible. Therefore, we exploit the relation of each degree of freedom of the fictitious FE node with the shape function $N_i$ and expansion function $F_\tau$. These functions can be used as weights to compute, for each FE degree of freedom, the weighted average of the displacements of all the real PD nodes lying on the section of the fictitious FE node:

$$\mathbf{u}_{\tau i}^{AV} = \frac{\sum_q |N_i(y_q) F_\tau(x_q, z_q)| \mathbf{u}^{PD}(x_q, y_q, z_q)}{\sum_q |N_i(y_q) F_\tau(x_q, z_q)|}\,, \tag{6.33}$$

or

$$\mathbf{U}^{AV} = \mathbf{A}\,\mathbf{U}^{PD}\,, \tag{6.34}$$

where $\mathbf{u}_{\tau i}^{AV}$ is the generic averaged displacement of the fictitious section and $\mathbf{U}^{AV}$ is the vector containing them. Note that $\mathbf{U}^{AV}$ has the same dimension of $\mathbf{U}^{fs\text{-}FE}$, so that $\left[\mathbf{A}\,\mathbf{I}^{fs\text{-}PD}\right]$ is a square matrix. This allow us to express the degrees of freedom of the fictitious FE node as

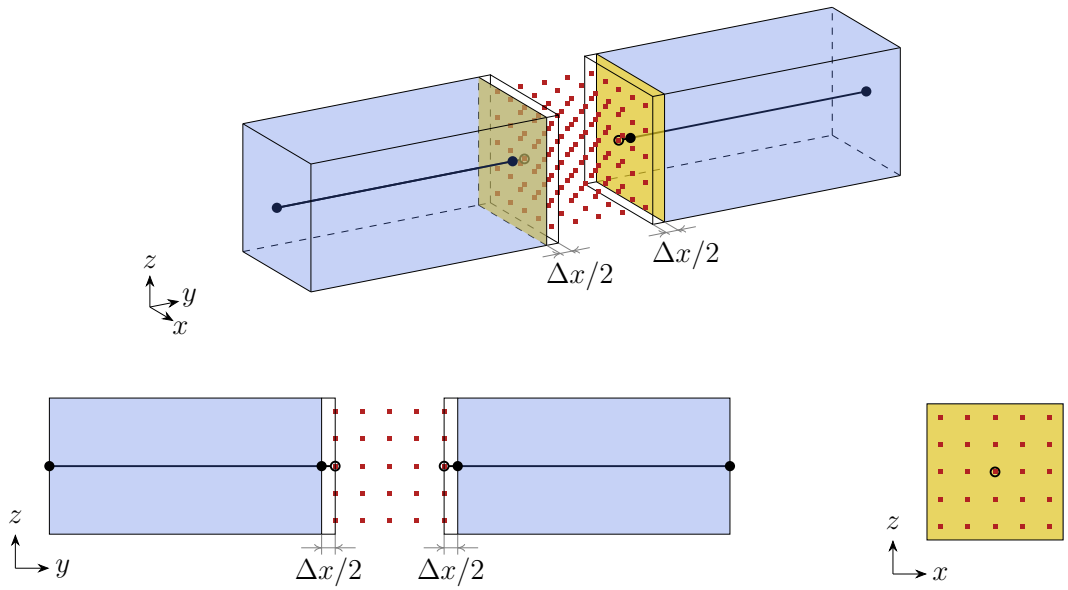


Figure 6.6: *Coupling of FEs (blue region) with 3D peridynamic nodes (red squares): the fictitious FEs are added so that the sections of the fictitious FE nodes (empty circles) lie over the plane of the real PD nodes closest to the interfaces (yellow surfaces).*

functions of the displacements of the real PD nodes:

$$\begin{aligned}\mathbf{U}^{fs\text{-}FE} &= \left[\mathbf{A}\,\mathbf{I}^{fs\text{-}PD}\right]^{-1}\mathbf{U}^{AV} \\ &= \left[\mathbf{A}\,\mathbf{I}^{fs\text{-}PD}\right]^{-1}\mathbf{A}\,\mathbf{U}^{PD}\,.\end{aligned} \tag{6.35}$$

If this procedure is repeated for all the fictitious FE nodes, then the following matrix can be assembled:

$$\mathbf{U}^{f\text{-}FE} = \mathbf{I}^{f\text{-}FE}\mathbf{U}^{PD}\,, \tag{6.36}$$

where $\mathbf{U}^{f\text{-}FE}$ is the vector of the degrees of freedom of the fictitious FE nodes and $\mathbf{I}^{f\text{-}FE}$ is the fictitious FE interpolation matrix. Note that the dimensions of $\mathbf{I}^{f\text{-}FE}$ are $3N^{f\text{-}FE} \times 3N^{PD}$, where $3N^{f\text{-}FE}$ is the number of the FE nodal unknowns and $N^{PD}$ is the number of real PD nodes.

**Remark 6.1.** There might be the case in which a fictitious CUF node is associated to more-than-one section, as for instance shown in Fig. 6.7. Let us call $n$ the number of sections to which the CUF node belongs. In this case, the procedure explained above should be repeated $n$ times, and the row of $\mathbf{I}^{f\text{-}FE}$ should be divided by $n$. In this way, the interpolation of the FE node is the average of the contributions of the $n$ sections.

**Remark 6.2.** There might be the case in which some real PD nodes lie in more-than-one fictitious FE section, as for instance shown in Fig. 6.7. In this case, the PD nodes are involved in the interpolation of each CUF section they lie on.

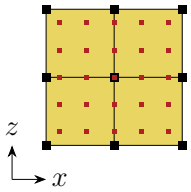


Figure 6.7: *Example of a FE node with multiple FE sections in which some fictitious FE nodes belong to more-than-one section and some real PD nodes lie on more-than-one section.*

### 6.4.4 Interfaces parallel to FEs

Let us consider another example in which there is an interface that is parallel to $y$ axis, i.e., the axis of the bar, as in Fig. 6.8. It is straightforward to generalize this example to more complex cases in which there are interfaces perpendicular to both $x$ and $z$ axes. Similarly to what exposed in Section 6.4.2, the fictitious PD nodes are introduced within the FEs in such a way to surround the interfaces with a PD layer with thickness $2\delta$, as shown in Fig. 6.9. Equation 6.29 is still valid and can be used to assemble the fictitious PD interpolation matrix $\mathbf{I}^{f\text{-}PD}$.

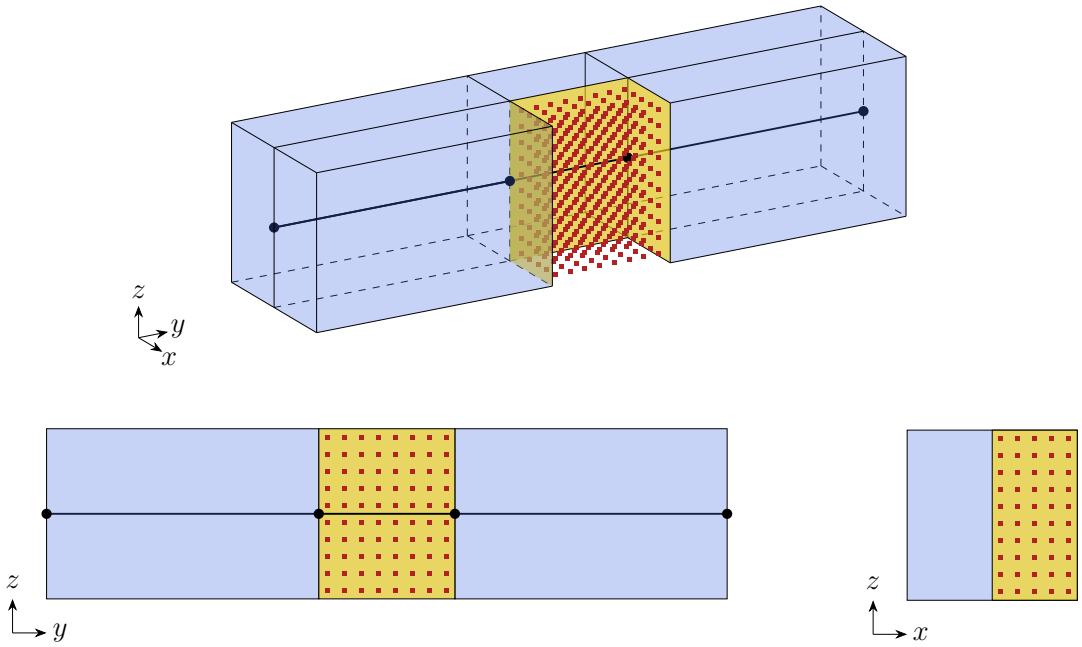


Figure 6.8: *Coupling of high-order 1D FEs (blue region) with 3D peridynamic nodes (red squares) when one of the interfaces (yellow surfaces) is parallel to the axis of the bar.*

On the other hand, the fictitious FE sections are added in the PD region so that they lie on the closest plane of real PD nodes, as shown in Fig. 6.10. Note that a new kind of fictitious FEs is generated by this geometry: close to the edge between the interfaces there are some fictitious FEs with just one edge lying on a row of real PD nodes. The other edges of that kind of elements lie on the external surface of real FEs. This means that, for these new elements, there are no sections as the ones used in Section 6.4.3 to interpolate the displacements of the fictitious FE nodes.

In this case, the displacements of the fictitious FE nodes lying on the row of PD nodes

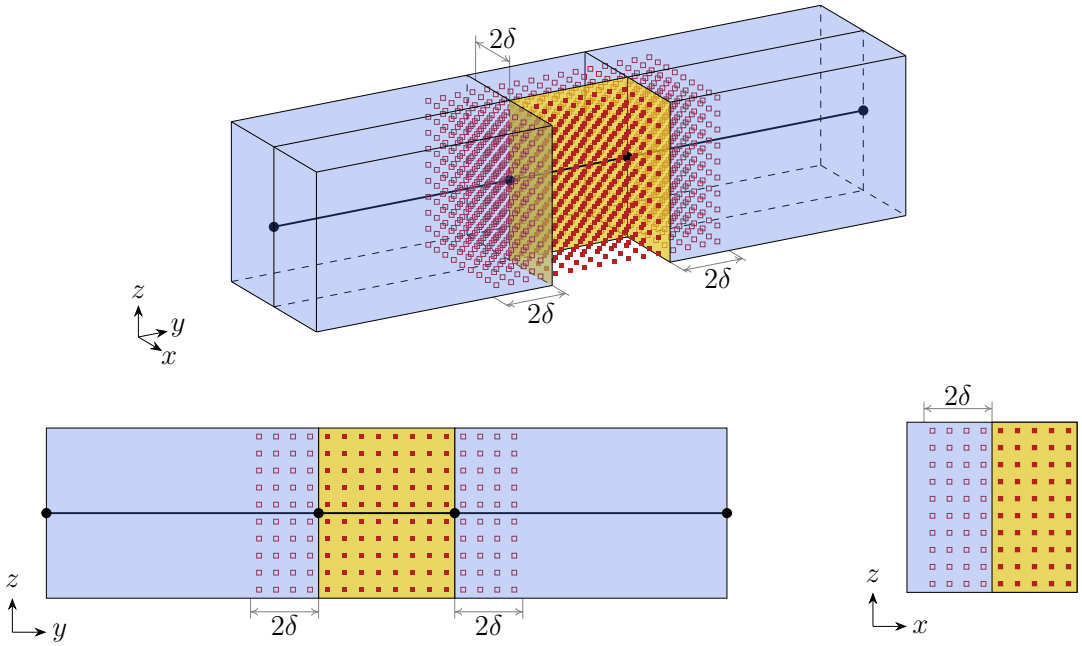


Figure 6.9: *Coupling of FEs (blue region) with 3D peridynamic nodes (red solid squares): the fictitious PD nodes (red empty squares) are added within the FEs up to a distance of* $2\delta$ *from all the interfaces (yellow surfaces), even the interfaces parallel to the axis of the bar.*

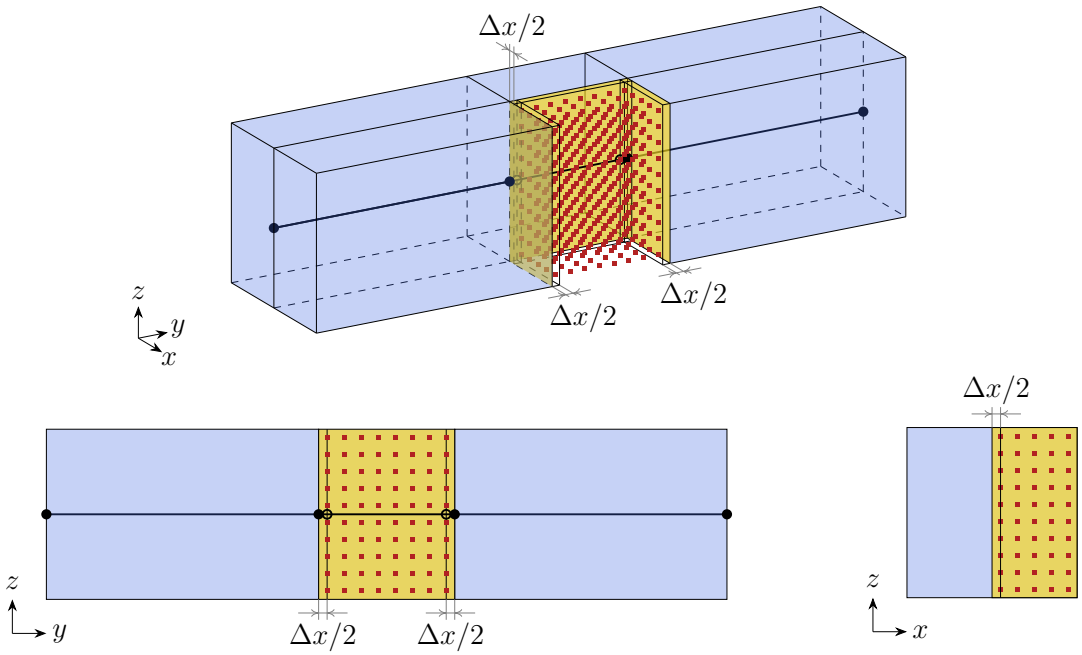


Figure 6.10: *Coupling of FEs (blue region) with 3D peridynamic nodes (red squares): the fictitious FEs are added so that the fictitious sections lie over the plane of the real PD nodes closest to the interfaces (yellow surfaces). Note that a new type of elements appears near the edges between the interfaces.*

are interpolated thanks to the two fictitious FE sections as explained in Section 6.4.3. Note that that the row of PD nodes is involved in both the interpolations of the two fictitious FE sections (see Remark 6.2). Analogously, since the fictitious FE nodes lying on that edge are "shared" between the two fictitious FE sections, the displacements of these nodes are the

averages of the interpolations of the two sections (see Remark 6.1). The fictitious FE nodes of the remaining edges, lying on the external surfaces of real FEs, are simply interpolated via the FE shape functions $N_i$ and the expansion functions $F_\tau$ of those elements:

$$\mathbf{u}^{fe\text{-}FE}(x_p, y_p, z_p) = \sum_i \sum_\tau N_i(y_p) F_\tau(x_p, z_p) \mathbf{u}_{\tau i}^{FE}\,, \tag{6.37}$$

where $\mathbf{u}^{fe\text{-}FE}$ is the vector of the degrees of freedom of the fictitious FE nodes on one of these edges. Equation 6.37 is employed during the assembling of the fictitious FE interpolation matrix $\mathbf{I}^{f\text{-}FE}$.

### 6.4.5 3D coupling of FEs and PD nodes

In this section, we aim at assembling the stiffness matrix of the complete system of (both FE and PD) equations. We assemble the global FE stiffness matrix $\mathbf{K}^{gl-FE}$ as explained in Section 6.3 by considering both real and fictitious elements. The real FE stiffness matrix $\mathbf{K}^{FE}$ is retrieved by eliminating all the rows and columns of $\mathbf{K}^{gl-FE}$ corresponding to fictitious FE degrees of freedom. On the other hand, the fictitious FE stiffness matrix $\mathbf{K}^{f-FE}$ is obtained by eliminating the rows corresponding to fictitious FE degrees of freedom and the columns corresponding to real FE degrees of freedom. Note that the rows of the fictitious degrees of freedom are not utilized because they correspond to the fictitious FE forces. The fictitious FE nodes indeed lie in the peridynamic region and do not "feel" any FE force, as explained in Section 6.4.1.

Similarly, as explained in Section 6.2, we assemble the global PD stiffness matrix $\mathbf{K}^{gl-PD}$ by considering both real and fictitious PD nodes. Since the fictitious PD nodes lie within FEs, there are no fictitious PD forces applied to those nodes. Therefore, the rows of $\mathbf{K}^{gl-PD}$ are eliminated. We obtain the real PD stiffness matrix $\mathbf{K}^{PD}$ and the fictitious PD stiffness matrix $\mathbf{K}^{f-PD}$ by eliminating the columns corresponding to the fictitious and real degrees of freedom, respectively.

Thus, the system of equations can be written in the following matrix form:

$$\begin{bmatrix} \mathbf{K}^{FE} & \mathbf{K}^{f-FE}\,\mathbf{I}^{f-FE} \\ \mathbf{K}^{f-PD}\,\mathbf{I}^{f-PD} & \mathbf{K}^{PD} \end{bmatrix} \begin{bmatrix} \mathbf{U}^{FE} \\ \mathbf{U}^{PD} \end{bmatrix} = \begin{bmatrix} \mathbf{F}^{FE} \\ \mathbf{F}^{PD} \end{bmatrix}\,, \tag{6.38}$$

or

$$\mathbf{K}\mathbf{U} = \mathbf{F}\,, \tag{6.39}$$

where $\mathbf{K}$ is the stiffness matrix of the entire system, $\mathbf{U}$ is the displacement vector and $\mathbf{F}$ is the force vector.

## 6.5 Numerical examples

In the following Section, we will analyze various numerical examples to verify the accuracy of the proposed coupling method. We will compare these results with full FEM solutions, even if the different formulations of Peridynamics and classical continuum mechanics lead

to a discrepancy in the results between the two theories [165]. Moreover, no corrections to the surface effect has been applied for the external surfaces of the PD regions (the surfaces that do not correspond to interfaces with FEM regions) [186, 227, 236, 249]. As one will see hereinafter, these sources of error affect only slightly the accuracy of the numerical results.

### 6.5.1 Isotropic bar

The first case study is a 3D isotropic bar subjected to uniaxial traction. Geometry, boundary conditions, and mesh information are highlighted in Fig. 6.11. The bar has a squared cross-section, and each side is 10 mm long, whereas the longitudinal length of the beam is equal to 100 mm. The material is isotropic and homogeneous, with an elastic modulus $E = 10$ GPa and Poisson's ratio $\nu = 0.2$. The central portion of the isotropic bar is modelled with a 3D peridynamics grid. A grid spacing of $\Delta x = 1$ mm and an m-ratio equal to 3 is adopted, resulting in a horizon radius $\delta = 3$ mm. The remaining portions of the bar are described by linear two-nodes finite elements (B2), one for each region. Hence, by using CUF, the kinematics associated with the finite elements goes from classical beam models to high-order LE. More specifically, Taylor expansion of different orders N (TEN) are adopted. Thus, for instance, the notation TE1 refers to the use of first-order polynomials as expansion function. Nine-node quadratic Lagrange elements (LE9) are also used in the present case. Three-dimensional peridynamics has already been coupled with CUF before [213]. The same bar has been here investigated. However, a bond-based formulation has been adopted in that case, leading to a constrained value of Poisson ratio $\nu = 0.25$. The extension to a state-based formulation eliminates this constraint. Moreover, in [213] the coupling method is based on the application of Lagrange multipliers at the FEM-PD interface. The results from this coupling approach showed to be in good accordance with the full FEM solution. Nevertheless, some discrepancies at the interface have been detected. The present work's objective is to reduce these numerical errors at FEM - PD domain interfaces.

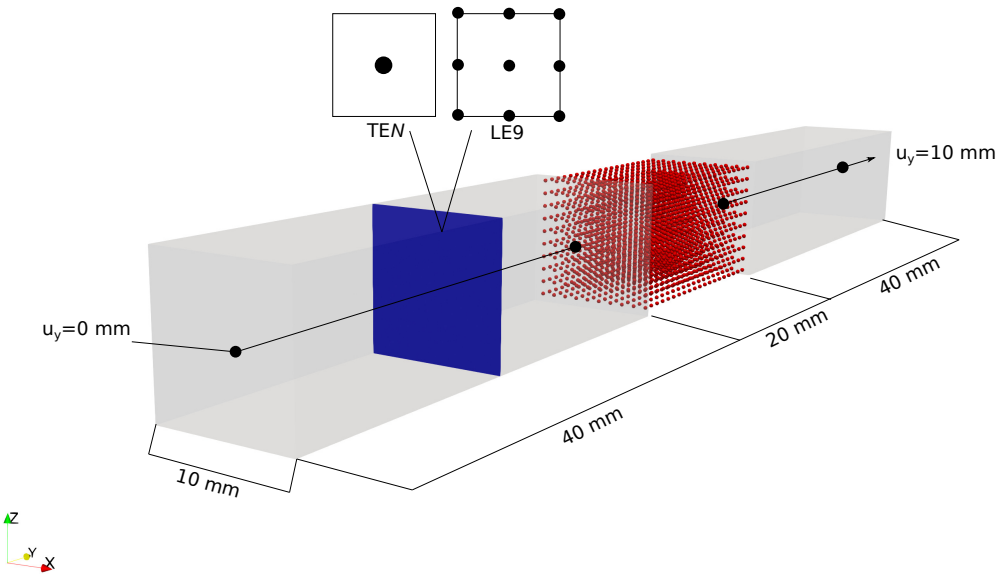


Figure 6.11: *Geometrical and modelling features of the investigated beam.*

A first result is shown in Fig. 6.12. The deformed shape of the bar under uniaxial displacement is represented. In this particular case, a single LE9 element has been adopted for the cross-section discretization. Figure 6.13 shows the consistency of the solutions when 3D PD is coupled with different FE models. Indeed, the longitudinal displacement evaluated in the central point of the section along the bar length is not affected by the cross-section discretization. A comparison between the aforementioned method and the present one is displayed in Fig. 6.14. This figure shows the presence of some distortions for displacements at interface regions when the Lagrange multipliers method is adopted (see Fig. 6.14b). Figure 6.14c shows that these discrepancies are nearly eliminated when the proposed model is adopted, especially at the interfaces. In fact, a relative error with respect to the full FEM solution greater than 5% is computed at the FEM - PD interfaces, when the Lagrange multipliers method is adopted. On the other hand, the error is significantly reduced with the present coupling technique, leading to a maximum relative error of 0.69%.

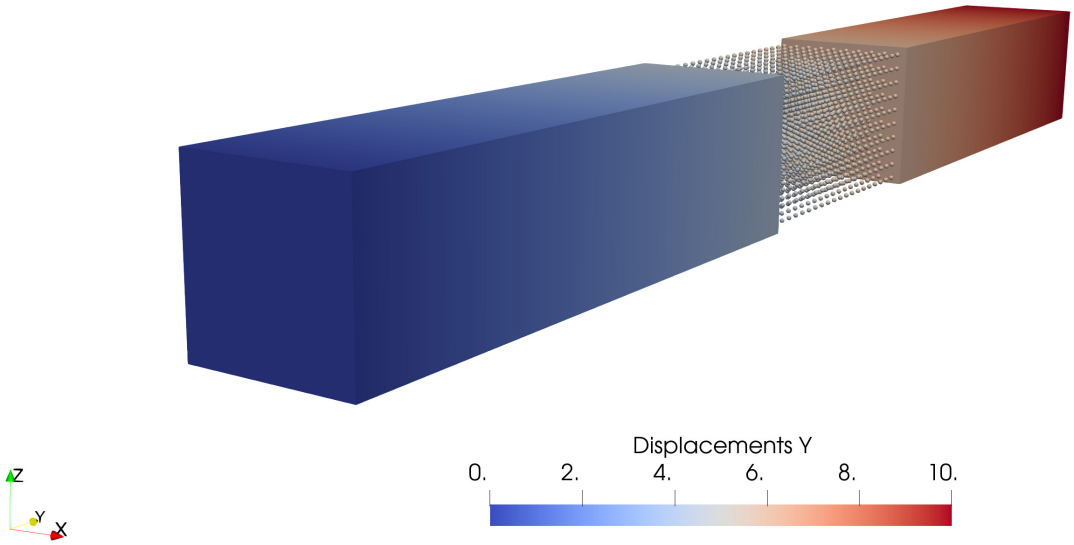


Figure 6.12: *Deformed configuration under uniaxial traction. In this numerical case, the 1D finite elements adopt a quadratic (L9) kinematics.*

### 6.5.2 C-shaped section beam under bending and torsion

The second analysis case is a C-section beam subjected to bending and torsion. The information about dimensions, boundary conditions, and modelling features are detailed in Fig. 6.15. The entire beam is made of the same isotropic material, with elastic modulus $E = 200$ GPa and Poisson ratio $\nu = 0.2$. The main objective of this case study is to highlight the 3D nature of the proposed coupling model. In fact, high-order LE elements are required to accurately describe the beam behaviour under both bending and torsion. It has been widely demonstrated that classical low-order beam theories have significant difficulties in reproducing these 3D phenomena.

In this case study, the axial FEM discretization consists of 10 four-node cubic elements (B4). The 3D PD region is not adopted for modelling the whole cross-section, as in the

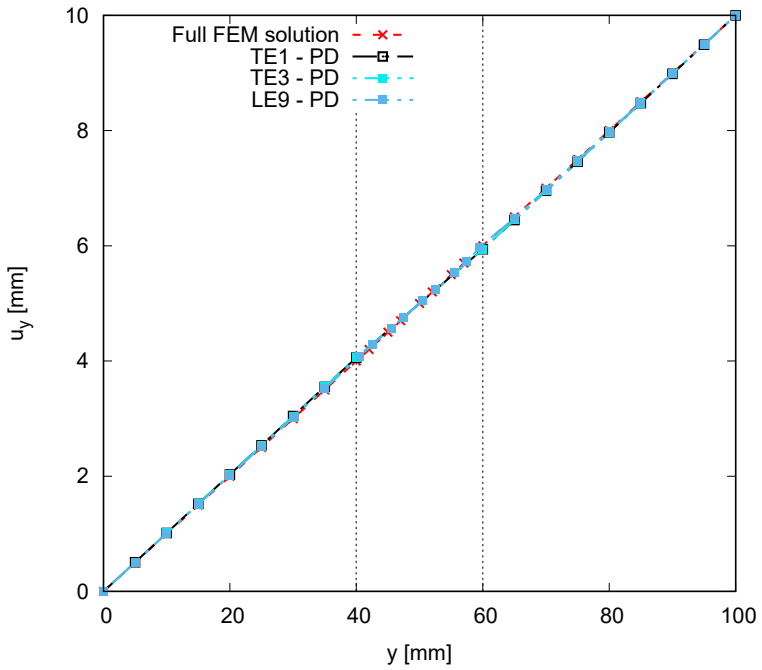


Figure 6.13: *Effect of different 1D-CUF models for FEM regions on the axial displacement of the beam.*

previous case. Instead, the PD region is here embedded into the finite element domain itself. This solution is obtained by varying the cross-section of the 1D FEs along the axial direction; it is represented by a disconnected region wherever PD is employed, i.e. $490 \leq y \leq 510$ mm (see Fig. 6.15). A grid spacing of $\Delta x = 1$ mm and horizon radius $\delta = 3$ mm is chosen. In Fig. 6.16, the deformed shape of the C-section beam for both full FEM (Fig. 6.16 (a)) and coupled PD-FEM model (Fig. 6.16 (b)) are shown. Furthermore, a close detail of the deformed state is displayed in Fig. 6.17. One can notice that the three-dimensional PD domain is perfectly consistent with the FEM regions.

Table 6.1: *Transverse displacements in middle point of the free-end section (Point A) and at the loading point (Point B).*

| Model | FE dof's | PD dof's | $-u_z$ [mm] Point A | $-u_z$ [mm] Point B |
|---|---|---|---|---|
| TE1 | 333 | - | 0.1713 | 0.1732 |
| TE4 | 1665 | - | 0.1959 | 0.2658 |
| TE8 | 4995 | - | 0.2646 | 0.5252 |
| L9 | 9657 | - | 0.2403 | 0.5436 |
| L9-PD | 9432 | 20040 | 0.2344 | 0.5337 |

These considerations support the choice of using high-order Lagrange elements capable of reproducing 3D-like phenomena. Table 6.1 compares the vertical displacements at points A and B (see Fig. 6.15) from the improved coupled FE-PD model with those from reference solutions, obtained by using CUF-based TE and LE refined models. Displacements in two different points are evaluated in order to highlight further the capability of the refined CUF models to capture both bending and torsional behaviour of the investigated beam. A first remark can be identified in the difficulty of low-order theories in computing the correct

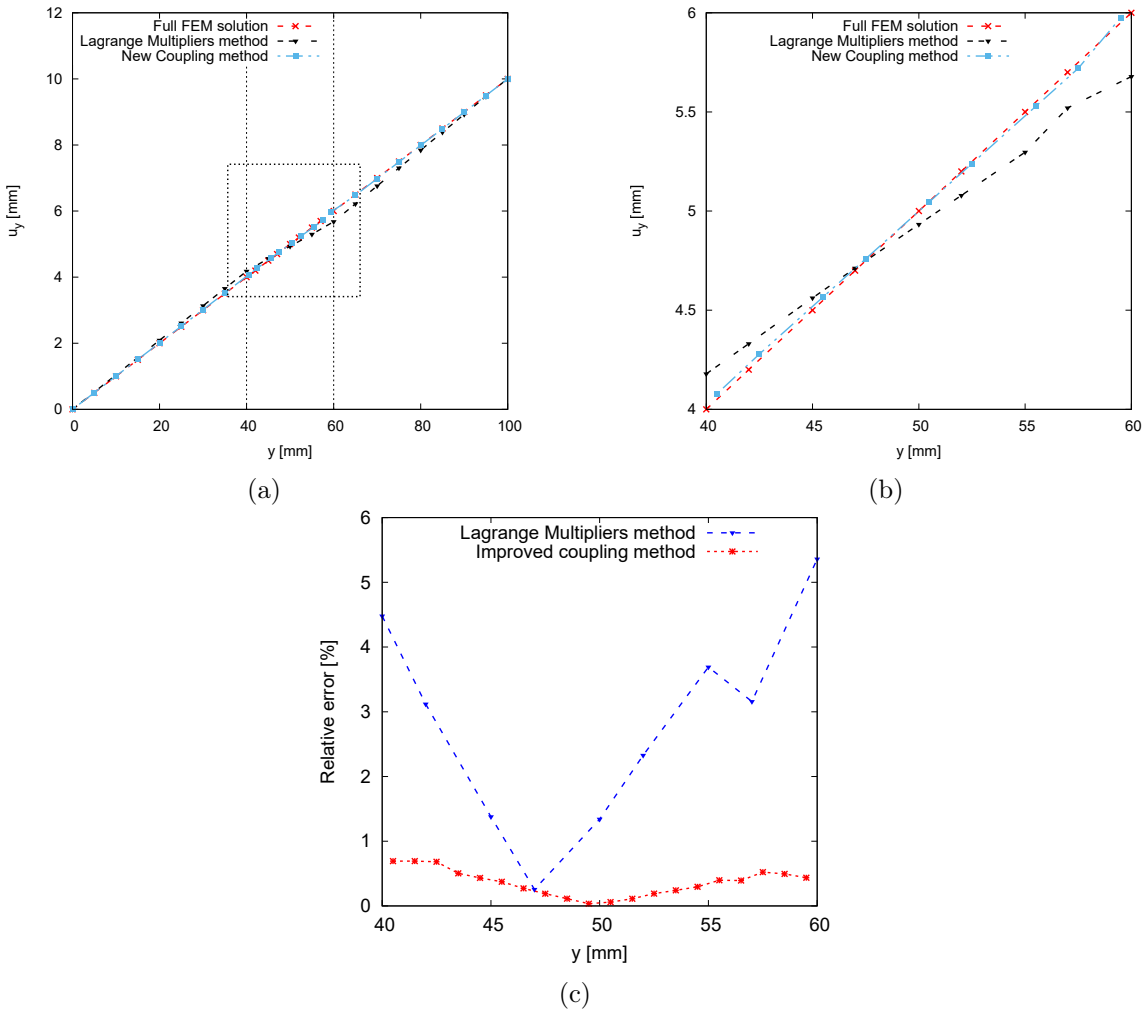


Figure 6.14: *Axial displacement of the bar subjected to traction along a) the entire lenght and b) the perydinamic region. FE-PD interfaces are subjected to distortions when the Lagrange multipliers coupling approach is adopted. These distortions are eliminated when the improved coupling method is applied. A comparison of the errors retrieved with both methods with respect to the full FEM solution is presented in (c).*

displacements in both investigated points. The model adopting LE9 elements for cross-section discretization reaches an optimal solution, as shown in recent works (i.e. [250]). Moreover, the present improved coupling model leads to transverse displacements comparable to those obtained with fully refined models, with an error of 1 % and 2 % detected in points A and B, respectively.

Finally, the vertical displacement along the beam span is given in Fig. 6.18. The green line in Fig. 6.15 indicates the followed path. Results from the present coupling model are compared with a full FEM solution. The displacement evolution along the beam span is correctly reproduced by the FEM-PD model. Furthermore, it should be underlined the capability of the improving coupling solution in avoiding any distortions at domain interfaces. In fact, a smooth transition between FEM (red dots) and PD (green dots) displacements is retrieved. The residual errors that are still noticeable in Fig. 6.18 are due to the different (local and nonlocal) solutions of Peridynamics and CUF when the displacement field is a superlinear function [165]. Moreover, the lack of corrections for the peridynamic surface

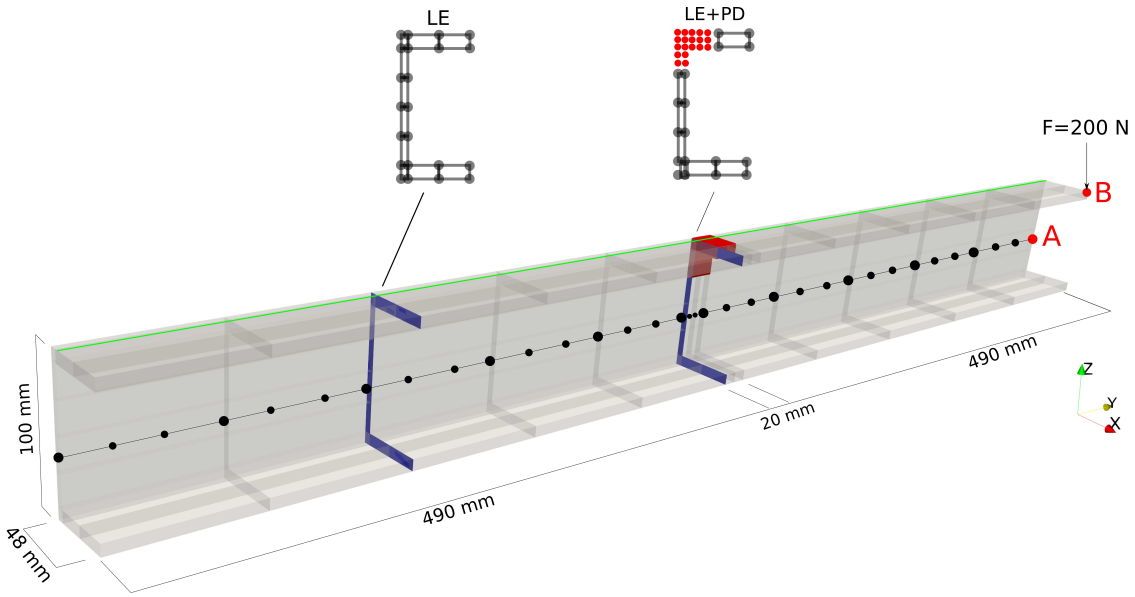


Figure 6.15: *Geometrical and modelling features of C-shaped section beam subjected to bending and torsion.*

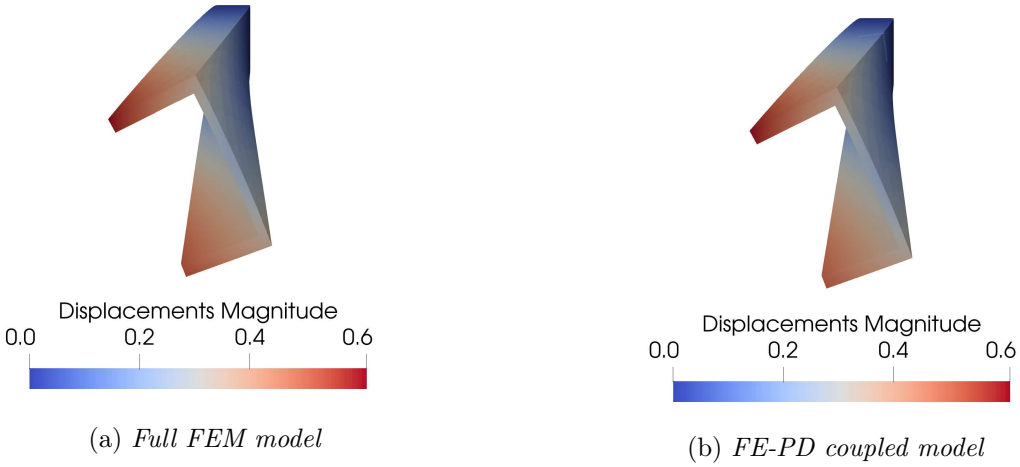


(a) *Full FEM model*

(b) *FE-PD coupled model*

Figure 6.16: *Deformed configuration of the C-section beam for FEM and FE-PD coupled model.*

effect may further increase the differences between the results obtained with the full FEM approach and the CUF-PD coupling. The simplest way to reduce these residual errors is decreasing the horizon size.

### 6.5.3 Stiffened panel

A stiffened panel is investigated as final example to underline the ability of the proposed method to introduce PD domains in complex structures. Figure 6.19 summarizes geometric and modeling features. The material properties are the same adopted in the first numerical case. The structure is composed of two stringers and one panel, which are independently modelled with high-order four-node beam elements in a component-wise manner [255].

The main novelty introduced with this numerical case is the possibility of investigating a structure with two distinct peridynamics domains. In fact, two different square regions, one

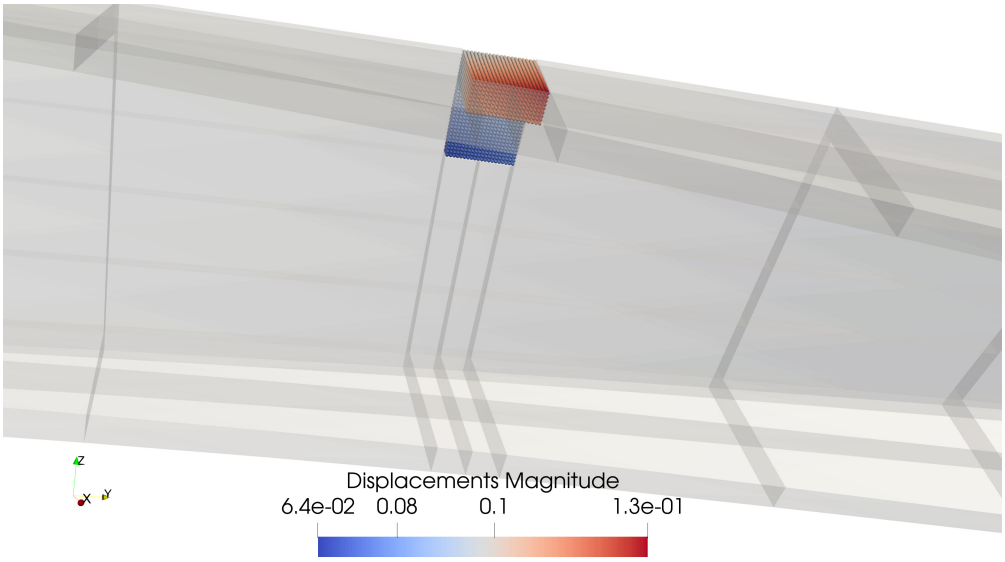


Figure 6.17: *Close view of the deformed PD zone for the investigated beam. A clear consistency between the two formulation is shown.*

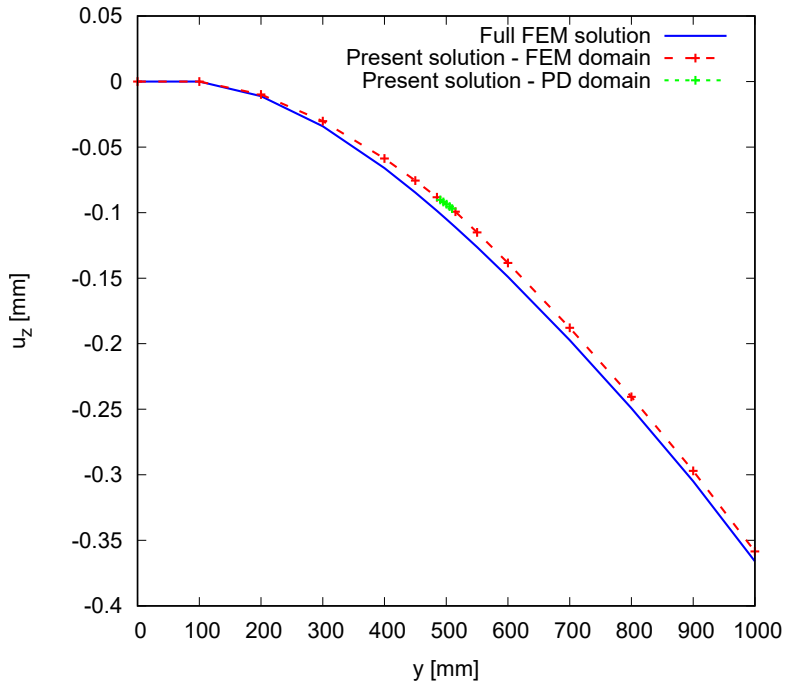


Figure 6.18: *Vertical displacement of the C-section beam along the beam span (green line in Fig. 6.15). A full FEM solution (solid blue line) is used as reference, while red and green dots represent the displacement in FEM and PD domains, respectively.*

for each stringer, are modelled through 3D peridynamics. The PD domain is discretized in a meshless manner with a grid spacing of $\Delta x = 1$ mm and horizon radius $\delta = 3$ mm.

Table 6.2 displays the vertical displacement and the value of longitudinal stress $\sigma_{yy}$ in some characteristic points (see Fig. 6.19) for the present coupled model and for reference solutions obtained through full FEM analysis. These results underline once again the capability of the proposed coupling model in accurately reproducing three-dimensional phenomena.

Furthermore, the accurate prediction of the axial stress in point C of the structure should be highlighted. Figure 6.20 also shows the complete axial stress state in the structure for a

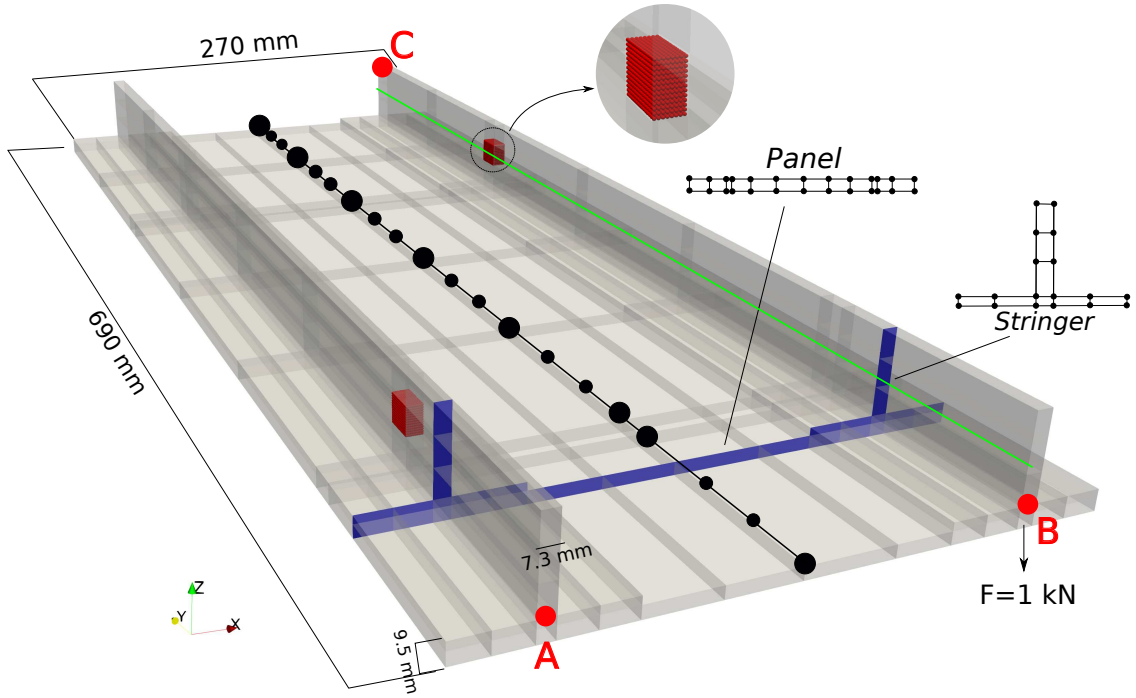


Figure 6.19: *Geometrical and modelling features of the investigated reinforced panel. Two distinct peridynamic regions are introduced, one for each stringer.*

Table 6.2: *Vertical displacements and axial stress $\sigma_{yy}$ are evaluated in some characteristic points of the structure for reference solutions and present FE-PD coupled model.*

| Model | FE dof's | PD dof's | $-u_z$ [mm] @Point A | $-u_z$ [mm] @Point B | $\sigma_{yy}$ [MPa] @ Point C |
|---|---|---|---|---|---|
| TE1 | 225 | - | 29.532 | 29.368 | 71.274 |
| TE4 | 1125 | - | 31.471 | 27.513 | 89.505 |
| TE8 | 3378 | - | 40.765 | 18.396 | 114.42 |
| L9 | 10659 | - | 44.942 | 14.153 | 126.916 |
| L9-PD | 10641 | 15480 | 45.346 | 14.719 | 126.847 |

FEM solution (Fig. 6.20a) and the coupled model (Fig. 6.20b). It is important to remark here that the PD domain embedded into the structure does not affect the stress state, opening the possibility of using FEM-PD coupled models for fracture mechanics problems (see [214]).

Vertical displacement along the green line in Fig. 6.19 is displayed in Fig. 6.21. The solution from a full FEM analysis is depicted with a solid blue line, while red and green dots represent displacements in FEM and PD domains, respectively. The coupled model completely matches the FEM solution along the beam span and across the perydinamic region without any sign of distortion in both FE-PD interfaces. Similarly to the previous case presented in Section 5.2, the residual errors are due to the different formulations of Peridynamics and CUF theories.

## 6.6 Conclusions

In this research, a method for the coupling of three-dimensional (3D) peridynamics grids and one-dimensional (1D) refined finite elements (FEs) based on Carrera Unified Formula-

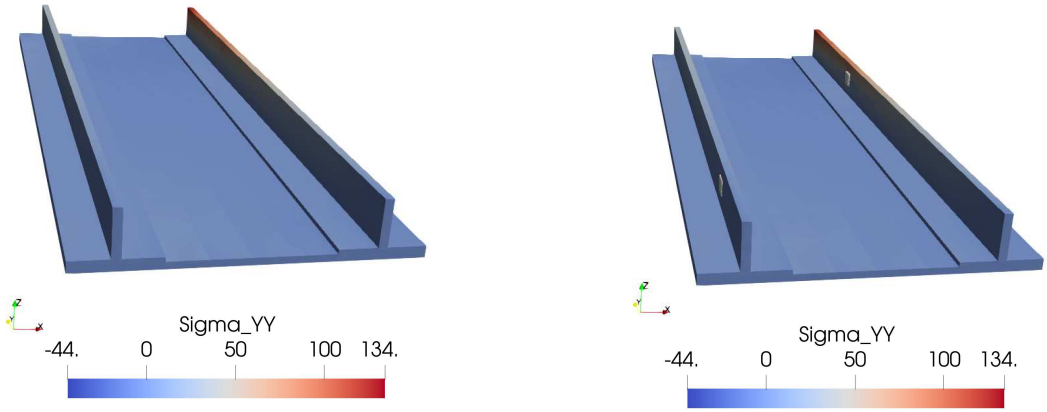


(a) *Full FEM model* (b) *Coupled FE-PD model*

Figure 6.20: *Distribution of longitudinal stress $\sigma_{yy}$ in the reinforced panel for a full FEM analysis and for a coupled FE-PD model.*

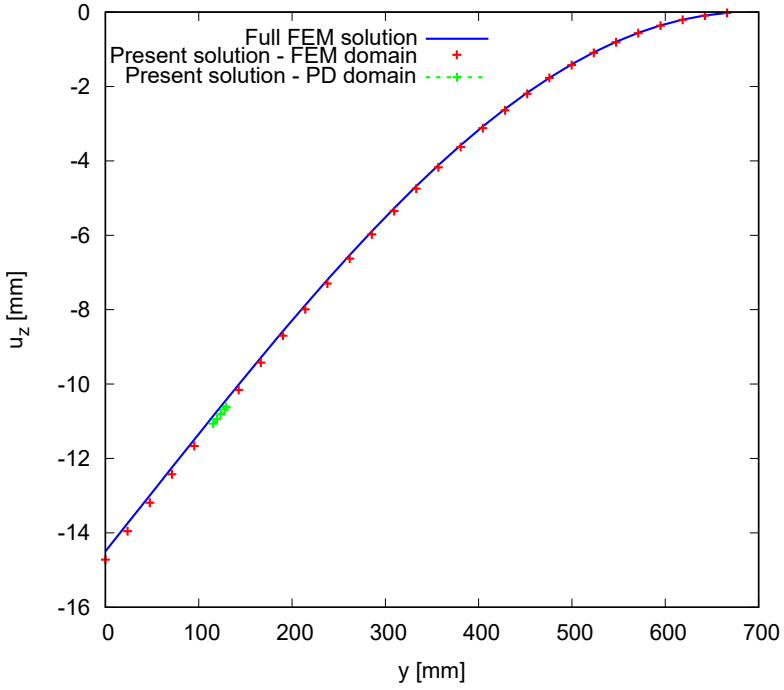


Figure 6.21: *Vertical displacements along the structure span, following the green line in Fig. 6.19. A full FEM solution (solid blue line) is used as reference, while red and green dots represent the displacement in FEM and PD domains, respectively.*

tion (CUF) is proposed. The advantages of CUF are exploited to obtain 3D solutions with a significant reduction in computational demand. In fact, CUF allows coupling 3D peridynamics domains with 1D finite elements of any order. By adopting high-order 1D models, full 3D solutions are retrieved, even when peridynamics is introduced in multiple regions of the investigated structure. The proposed technique has proven to be general and capable of greatly reducing any numerical inaccuracies at the interfaces between the two domains. Furthermore, the use of the State-Based Peridynamics (instead of the Bond-Based Peridynamics) allows to remove the limitation of modeling only materials with a Poisson's ratio equal to 0.25. The present coupling method is based on the continuity of the displacement

field in a non-local region near the interfaces. The employed coupled models show a very low computational cost when compared with full 3D approaches while maintaining a great degree of accuracy. The effectiveness and efficiency of the present coupling strategy are proven on classical beams and thin-walled structures of aerospace interest.

# Chapter 7

# Moving interfaces in peridynamic diffusion models and the influence of discontinuous initial conditions: Numerical stability and convergence

**Accepted to:** *Computers and Mathematics with Applications* (2023)

**Authors:** Francesco Scabbia, Claudia Gasparrini, Mirco Zaccariotto, Ugo Galvanetto, Adam Larios, Florin Bobaru

## Abstract

We derive numerical stability conditions and analyze convergence to analytical nonlocal solutions of 1D peridynamic models for transient diffusion with and without a moving interface. In heat transfer or oxidation, for example, one often encounters initial conditions that are discontinuous, as in thermal shock or sudden exposure to oxygen. We study the numerical error in these models with continuous and discontinuous initial conditions and determine that the initial discontinuities lead to lower convergence rates, but this issue is present at early times only. Except for the early times, the convergence rates of models with continuous and discontinuous initial conditions are the same. In problems with moving interfaces, we show that the numerical solution captures the exact interface location well, in time. These results can be used in simulating a variety of reaction-diffusion type problems, such as the oxidation-induced damage in zirconium carbide at high temperatures.

**Keywords:** Peridynamics, diffusion-reaction problem, numerical stability, discontinuous initial conditions, phase change, moving interface.

## 7.1 Introduction

Discontinuities are difficult to handle in classical models involving partial differential equations (PDEs). Nonetheless, discontinuities take place in many physical phenomena in nature, such as fracture, thermal shock in heat transfer, or oxidation-induced damage. For problems with moving interfaces, classical theories do require special treatment to govern the motion of the interface, such as the Stefan condition [128, 256–258]. The peridynamic theory has been proven to effectively solve these types of problems without any *ad-hoc* conditions at the interface: the motion of the interface is implicitly determined by the diffusion and phase properties of the involved materials, as shown in, for example, [128, 129]. Other important problems in which moving interfaces are involved in conjunction with fracture is the problem of oxidation-induced fracture in high temperature zirconium-carbide [13, 14]. To study these types of problems, one needs numerical approximations of transient diffusion with moving interfaces. In this work we analyze the stability of the so-called "meshfree method" for discretizing peridynamic models, the influence of discontinuous initial conditions (due to, for example, sudden exposure of the body to a non-zero temperature/concentration), and the accuracy of the numerical solution for transient diffusion problems with a moving interface.

Peridynamics (PD) is a non-local continuum theory able to model discontinuities in a mathematically consistent way [61, 62]. In the peridynamic formulation, the spatial derivatives of the PDEs are replaced by integrals over a sphere of radius $\delta > 0$. The so-called *horizon size* $\delta$ is the measure of nonlocality of the theory, i.e., the maximum distance at which two points interact with each other. This PD interaction is named *bond*.

It is well-known that in peridynamic models the behavior in that region is different from the behavior in the bulk since points close to the boundary of the domain have an incomplete horizon region. This phenomenon is known as the *PD surface effect* [186, 187, 198, 226, 227, 236]. The properties of the interactions of the points near the boundary can be modified to mitigate the PD surface effect with several methods [63, 64, 186–190]. However, the results obtained with these methods may still exhibit some residual fluctuations, depending on how the PD boundary conditions are applied.

Boundary conditions in local models are applied at the domain boundary, whereas nonlocal boundary conditions need to be specified over a boundary layer of finite thickness. This is the reason why the nonlocal boundary conditions are sometimes called *volume constraints* [259]. However, since experiments provide only local measurements at the boundary of the domain, it is often desirable to impose local boundary conditions in a nonlocal model. To do so, several methods have been developed. For instance, the interior of the body could be modeled with PD and the layer near the external surface of the body with a classical model, but only if discontinuities do not arise in this layer of material. To do so, a coupling method is required (see, e.g., [115, 171, 205, 206, 208, 209, 213, 214, 228]), which may lead to spurious effects at the interface of the coupling region due to the different (local and nonlocal) formulations [165]. Another approach is reducing the nonlocal radius $\delta$ with the variable horizon method (see, e.g., [149, 193, 195, 198, 204, 215, 216]), so that $\delta \to 0$ at the boundary. However, in this case, for transient problems, for example, material length-scales may not be matched (e.g., wave dispersion will be different near the surface compared to

in the bulk in elasto-dynamic problems). The *fictitious node method* is the most commonly used to impose local boundary conditions in a nonlocal model (see, e.g., [63, 92, 126, 148, 150, 151, 186, 188, 191–196, 227, 236, 249]): a fictitious layer is added all around the body, to complete the horizon region for nodes in the PD boundary layer, and is used to impose the PD boundary conditions. Among all these methods, here we employ the "surface node" method (SNM) [227, 236, 249] because it provides a problem-independent, accurate way to impose local boundary conditions in a PD model for any loading conditions and (even complex) geometry.

The peridynamic theory has been already successfully applied to simple diffusion problems [124, 125] and more complex phenomena (for instance, diffusion coupled with corrosion mechanisms [128, 129]). However, some numerical aspects have not been studied yet:

- a stability criterion for time-integration of PD diffusion equations accounting for the boundary conditions applied; existing stability results were limited to von Neumann analysis which assumes infinite domain;
- the influence of discontinuities in initial conditions on the accuracy of the numerical solution;
- the accuracy of numerical solutions for diffusion-type problems with moving interfaces.

To investigate these issues in a simple framework, we analyze several 1D examples, but the obtained conclusions may be generalized to higher-dimension problems. Moreover, for the first time, we apply the SNM to a time-dependent problem, and for discontinuous initial conditions. The stability of numerical methods has been observed to be considerably affected by the behavior of the system near the boundaries due to the high gradients imposed by the boundary conditions (such as in the case of no-slip boundary conditions in Navier-Stokes equations [260, 261], for example). Therefore, including the effect of the surface node method near the boundaries of the body is critically important for deriving an accurate stability criterion.

The paper is structured as follows. Section 7.2 gives a brief review of the peridynamic theory applied to diffusion problems with or without moving interfaces, and their discretized equations. In Section 7.3, we derive the stability criterion for peridynamic diffusion problems by including the influence of boundary conditions. Section 7.4 presents the numerical results of a 1D diffusion problem for a homogeneous material with no phase changes and, for the first time, the surface node method for enforcing nonlocal boundary conditions is applied to a transient problem. We then analyze the numerical convergence to an exact nonlocal solution of a PD model for initial conditions with and without discontinuities. Section 7.5 shows an example of a diffusion-type model with a moving interface problem in which the motion of the interface is controlled by local concentration values, similar to diffusion in a bi-material enhanced with a phase-change model in [128], as some PD models of corrosion have employed. The results are compared with an analytical solution (obtained via the manufactured solution method) for a moving interface problem. Section 7.6 discusses extensions of the obtained results in 1D problems to the 2D and 3D cases. Section 7.7 draws some conclusions and discusses future work.

## 7.2 Brief review of PD model of diffusion

In peridynamics, points in a body $\Omega$ interact with each other up to a finite distance $\delta$, called the *horizon size* [61, 62]. The interaction between two points is called *bond*. This means that a point $x$ interacts with the set of points $\mathcal{H}_x = \{x' \in \Omega : |x' - x| < \delta\}$, which is called the *neighborhood* of point $x$. Therefore, the neighborhood is the set $[x - \delta, x + \delta]$, as shown in Figure 7.1. The peridynamic equation governing diffusion phenomena is given as in [128, 129]:

$$\begin{aligned} \frac{\partial C(x,t)}{\partial t} &= \int_{\mathcal{H}_x} d(x,x')\,\mu(|x'-x|)\big[C(x',t) - C(x,t)\big]\,\mathrm{d}x' \\ &= \int_{\mathcal{H}_x} \mathrm{j}(x,x',t)\,\mathrm{d}x'\,, \end{aligned} \tag{7.1}$$

where $C$ is the concentration of the species, $\mu$ is the kernel function, and $d$ is the micro-diffusivity (that can be calibrated to the classical diffusivity). The integrand in equation (7.1) is called the *micro-flux* $\mathrm{j}(x,x',t)$. We choose the kernel function $\mu(|x'-x|) = |x'-x|^{-2}$, which ensures that the convergence to the classical theory does not depend on the refinement of the nodal grid [150].

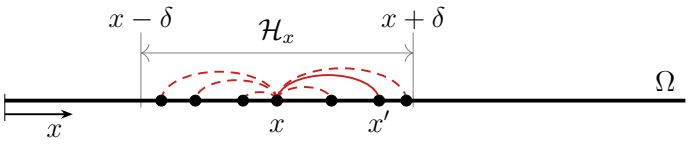


Figure 7.1: *Neighborhood $\mathcal{H}_x$ of a point in a peridynamic body $\Omega$ in 1D: red lines represent the PD interactions (bonds) between points.*

Each bond can be thought as a pipe into which the monitored species is allowed to flow. The peridynamic flux at a point is defined as the sum of the micro-fluxes of the bonds crossing the surface passing through that point [172]. Therefore, in 1D the PD flux at a point $x$ is computed as [227]:

$$J(x,t) = -\int_{x-\delta}^{x}\int_{x}^{x'+\delta} \mathrm{j}(x',x'',t)\,\mathrm{d}x''\,\mathrm{d}x'\,. \tag{7.2}$$

Figure 7.2 shows the limits of integration accounting for each bond intersecting the surface passing through point $x$.

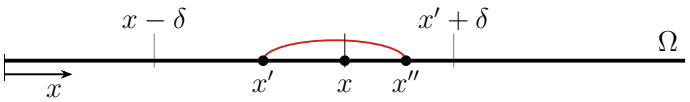


Figure 7.2: *Example of a bond involved in the computation of the peridynamic flux in a point $x$: for the limits of integration in equation (7.2), $x'$ and $x''$ are points respectively in the intervals $[x-\delta, x]$ and $[x, x'+\delta]$, therefore each bond between $x'$ and $x''$ intersects the surface passing through point $x$.*

The micro-diffusivity function $d$ is calibrated to the classical diffusivity $D$. To do so, for example, one equates the classical flux with the peridynamic flux for a linear distribution

of concentration $C$ [124, 125, 128]. The peridynamic flux at a point $x$ with a complete neighborhood (away from the boundaries of the domain) for a homogeneous concentration gradient is computed as [124, 236]:

$$J(x,t) = -\int_{x}^{x+\delta} (x'-x)\,\mathrm{j}(x,x',t)\,\mathrm{d}x' \,. \tag{7.3}$$

Therefore, by choosing a constant micro-diffusivity function over the neighborhood [124, 125, 128], the micro-diffusivity of a PD bond is given as:

$$d(x,x') = \frac{D}{\delta} \,. \tag{7.4}$$

Since equation (7.4) is computed for points with a complete neighborhood, the properties of the points near the boundary of the body (with an incomplete neighborhood) turn out to be different from those of the points in the bulk (see Figure 7.3a). This phenomenon is called PD *surface effect* [186, 227, 236]. In order to mitigate this surface effect, a fictitious layer, of thickness $\delta$, surrounding the body is introduced as first suggested in [148] (see Figure 7.3b). Furthermore, nonlocal models require the imposition of nonlocal boundary conditions, also known as *volume constraints*. However, experiments provide only measurements at the boundary of the domain, so the imposition of local boundary conditions is desirable. In order to enforce a set of local boundary conditions into a nonlocal model, several methods have been developed (see, e.g., [63, 64, 194, 195]). However, all these methods do not guarantee the accuracy of the results near the boundaries for any loading condition or complex geometry. On the other hand, the surface node method (see, e.g., [227, 236, 249]) provides an accurate way to impose local boundary conditions in a nonlocal model for any loading condition and geometry (for any domain with sufficiently smooth boundary). According to this method, concentrations of the fictitious nodes are determined by a Taylor series expansion about the closest point on the external surface of the body. Then, the flux at points on the external surface of the body is imposed via the equation of the peridynamic flux:

$$J(x,\mathrm{n},t) = J(x,t)\cdot \mathrm{n}\,, \tag{7.5}$$

where $\mathrm{n} = \pm 1$ is the unit vector normal to the external surface. Thanks to this equation, the points on the boundary represent the nonlocal behavior of the entire fictitious layer; this aspect will be explained in detail in the discretized model in Section 7.2.2.

### 7.2.1 Modeling of diffusion with moving interface/phase-change

Diffusion-controlled or reaction-controlled problems are involved in many physical phenomena. Oxidation of zirconium carbide at high temperatures is one such example [13, 14]. The diffusion of oxygen within the high-temperature zirconium carbide triggers oxidation, the final products of which are carbon dioxide and zirconium oxide. The carbon dioxide is dispersed in the external environment (through cracks or porosities). The interface between zirconium oxide and carbide moves according to the diffusivities of the two phases.

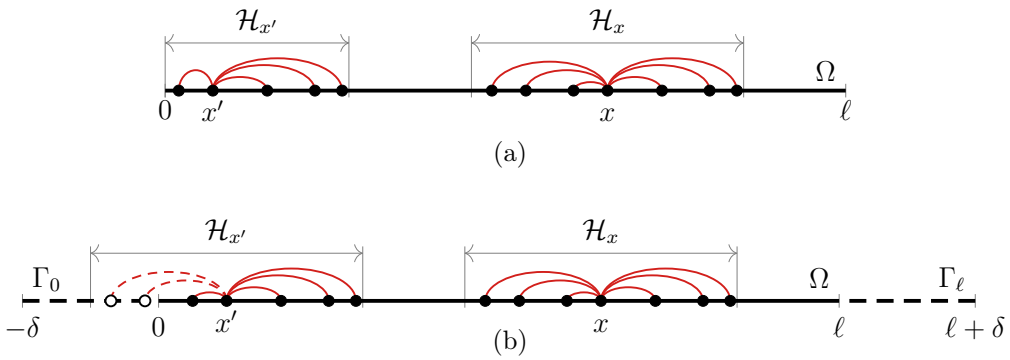


Figure 7.3: *In order to complete the neighborhoods of the points near the boundary* (a)*, a fictitious layer* $\Gamma = \Gamma_0 + \Gamma_\ell$ *surrounding the body* $\Omega$ *is introduced* (b)*.*

This phenomenon can be described as a diffusion problem in a bi-material enhanced with a phase-change model, which was analyzed in [128].

The phase of each peridynamic point depends on its current concentration. Let us denote the concentration of phase change by $C_i$, where $i$ stands for "interface". The micro-diffusivity of a bond is determined as [128]:

$$d(x,x',t) = \begin{cases} d_1 & \text{if } C(x,t) < C_i \text{ and } C(x',t) < C_i\,, \\ d_2 & \text{if } C(x,t) > C_i \text{ and } C(x',t) > C_i\,, \\ d_3 & \text{if } C(x,t) \le C_i \le C(x',t) \text{ or } C(x',t) \le C_i \le C(x,t)\,. \end{cases} \tag{7.6}$$

Figure 7.4 shows the three possible types of bonds that may have different micro-diffusivities properties. Therefore, in a peridynamic diffusion model, it suffices to know the threshold concentration for phase change and the micro-diffusivities in equation (7.6) in order to determine the motion of the interface. With this, the motion of the interface is autonomous, and determined by the "constitutive model" itself. Note that this model does not require any special conditions at the interface, such as Stefan condition (that is instead required in classical models [256–258]). Moreover, a damage mechanism can be easily introduced in this PD model (see for instance [128–130, 137, 262–265]). This will be investigated in a future work [266].

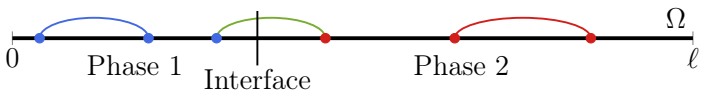


Figure 7.4: *Three possible types of bonds for diffusion in a two-phase material separated by a material interface: each type of bond may have different micro-diffusivity properties.*

### 7.2.2 The "meshfree method" discretization of the PD diffusion equations

Many different methods can be used to discretize peridynamic diffusion equations, such as the "meshfree method" [65, 184, 235], the Finite Element Method (FEM) [177, 178], and

the Fast Convolution-Based Method (FCBM) [179, 180]. When using the FEM, remeshing would be required to model the moving interface. The FCBM allows to considerably reduce the computational cost of finding PD solutions by utilizing the convolutional structure of PD integral operators and the Fast Fourier Transform (FFT). However, since in this work we consider stability and convergence of numerical algorithms in the 1D setting for which the cost is less of an issue, for the sake of simplicity we here adopt the meshfree method of discretization of the PD equations, and we use uniform grids. Therefore, the body is discretized in cells (segments), at the center of each of which there is a node representing that cell. To mitigate the PD surface effect, we add the fictitious nodes around the body up to a distance $\delta$ from the boundary (see Figure 7.5). The concentrations of the fictitious nodes can be determined via the Taylor-based extrapolation [227, 236, 249] or some other type of extrapolation (see, e.g., [194, 195]). In this work, we use the Taylor-based method with linear extrapolation for its simplicity.

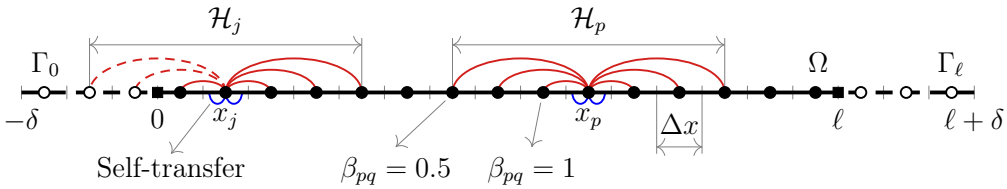


Figure 7.5: *Discretization of a 1D body by means of the meshfree method: the neighborhood $\mathcal{H}_p$ of a node $p$ (or $\mathcal{H}_j$ of a node $j$) is constituted by the nodes with a portion of their cell within the neighborhood. The quadrature coefficient $\beta_{pq}$ is the volume fraction of the cell of node $q$ lying inside the neighborhood of node $p$ [235]. The fictitious nodes (empty dots) are added near the boundary of the body to complete the neighborhoods of all the nodes within the body (solid dots). Moreover, the boundary of the body is represented by the surface nodes (solid squares).*

The integrals in the peridynamic equations (equations (7.1) and (7.2)) can be numerically approximated by splitting them into a summation of integrals over cells and applying a midpoint quadrature rule in each cell [65, 184, 235]. Therefore, the micro-flux in a bond between the nodes $p$ and $q$ can be computed as:

$$\mathrm{j}(x_p, x_q, t) = d(x_p, x_q)\, \mu(|x_q - x_p|)\big[C(x_q, t) - C(x_p, t)\big]\,, \tag{7.7}$$

where $x_p$ and $x_q$ are the coordinates respectively of nodes $p$ and $q$, and $\mu(|x_q - x_p|) = |x_q - x_p|^{-2}$.

As shown in Figure 7.5, the cells of some nodes are contained only partially within the neighborhood. In order to properly "weight" their contribution, the quadrature coefficients $\beta$ are computed as the fraction of the nodal cell lying inside the neighborhood using the algorithms presented in [198]. Hence, a node $p$ within the body is governed by the following discretized equation [124, 125, 128]:

$$\frac{\partial C(x_p, t)}{\partial t} = \sum_{q \in \mathcal{H}_p} \mathrm{j}(x_p, x_q, t)\, \beta_{pq} \Delta x + \mathrm{j}_{st}(x_p, t) \Delta x\,, \tag{7.8}$$

where $\Delta x$ is the grid spacing, the index $q$ stands for any node within the neighborhood $\mathcal{H}_p$

of node $p$, and $\mathrm{j}_{st}$ is the so-called *self-transfer* micro-flux. This self-transfer term appears in equation (7.8) due to the discretization of the body. In fact, the "discretized" neighborhood $\mathcal{H}_p$ lacks the central portion because the node $x_p$ does not interact with the two halves of its own cell. As shown in Figure 7.5, the self-transfer is added to take into account these lacking contributions. The self-transfer micro-flux of node $p$ can be approximated as the average of the micro-fluxes of the two adjacent nodes [150]:

$$\begin{aligned}\mathrm{j}_{st}(x_p,t) = \frac{1}{2}\Big[&d(x_p,x_{p+1})\,\mu(|x_{p+1}-x_p|)\big(C(x_{p+1},t)-C(x_p,t)\big)\\ &+ d(x_p,x_{p-1})\,\mu(|x_{p-1}-x_p|)\big(C(x_{p-1},t)-C(x_p,t)\big)\Big]\,,\end{aligned} \tag{7.9}$$

where the sequential numbering of the nodes is assumed, so that nodes $p-1$ and $p+1$ are the two nodes adjacent to node $p$.

Let us call *interior nodes* the nodes within the body (solid dots in Figure 7.5). To apply the surface node method (with the linear Taylor-based extrapolation) for imposing the boundary conditions, we introduce new nodes at the boundary of the body, called *surface nodes* (solid squares in Figure 7.5). The surface nodes do *not* have cells as the interior nodes, but they are used to discretize the external surface of the body. In 1D the surface nodes are the points at the ends of the body, as shown in Figure 7.5, and lie at a distance of $\Delta x/2$ from the closest interior node.

In order to complete the neighborhoods of the interior nodes near the boundaries, a $\delta$-thick layer of fictitious nodes is introduced, as shown in Figure 7.6. The concentration of these nodes is determined by extrapolating the concentrations of the real nodes. Different extrapolation methods may be employed, but the Taylor-based extrapolation method is straightforward and applicable to any (even complex) geometry [227, 236, 249]. Therefore, here we show how to extrapolate the concentrations of the fictitious nodes with a linear Taylor series expansion. Consider a fictitious node $f$ and its closest surface node $s$ and interior node $b$ and respectively denote their coordinates by $x_f$, $x_s$ and $x_b$, as shown in Figure 7.6. The concentration of the fictitious node $f$ is computed as:

$$\begin{aligned}C(x_f,t) &\approx C(x_s,t) + (x_f-x_s)\,\frac{\partial C(x_s,t)}{\partial x}\\ &\approx C(x_s,t) + (x_f-x_s)\,\frac{C(x_s,t)-C(x_b,t)}{x_s-x_b}\\ &\approx \frac{x_f-x_b}{x_s-x_b}C(x_s,t) - \frac{x_f-x_s}{x_s-x_b}\,C(x_b,t)\,,\end{aligned} \tag{7.10}$$

where the derivative $\frac{\partial C(x_s,t)}{\partial x}$ is approximated by the finite difference method. Note that the concentrations of the fictitious nodes are determined as functions of the concentrations of the real (both interior and surface) nodes of the body, which are often the unknowns of the problem. Figure 7.6 shows an example of the linear Taylor-based extrapolation.

The surface nodes do *not* interact directly with other nodes. In other words, no PD bonds are connected to surface nodes. The degrees of freedom of the surface nodes are governed by new equations based on the concept of peridynamic flux. Therefore, the equation of a

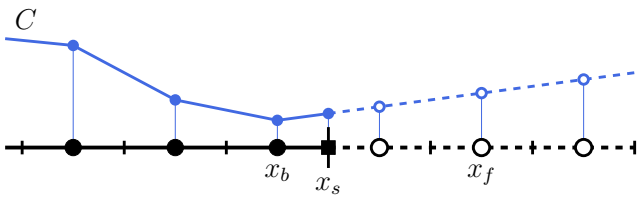


Figure 7.6: *Example of the linear Taylor-based extrapolation applied to an arbitrary concentration field.*

surface node $x_s$ with normal $\mathrm{n}_s$ is given as [249]:

$$J(x_s, \mathrm{n}_s, t) = -\sum_{\mathcal{B}_s} \mathrm{j}(x_p, x_q, t) \cdot \mathrm{n}_s \, \beta_{pq} \Delta x^2 \,, \tag{7.11}$$

where $\mathcal{B}_s$ is the set of all the bonds such that $x_p < x_s < x_q$, i.e., all the bonds crossing the boundary. These bonds are depicted in Figure 7.7. Thus, the boundary conditions can be imposed directly on the surface nodes as one would do in a local model [249]: a constrained concentration $\overline{C}(t)$ at a surface node $s$ is imposed as $C(x_s, t) = \overline{C}(t)$ and a flux $\overline{J}(t)$ through the cell of a surface node $s$ is imposed as $J(x_s, \mathrm{n}_s, t) = \overline{J}(t)$.

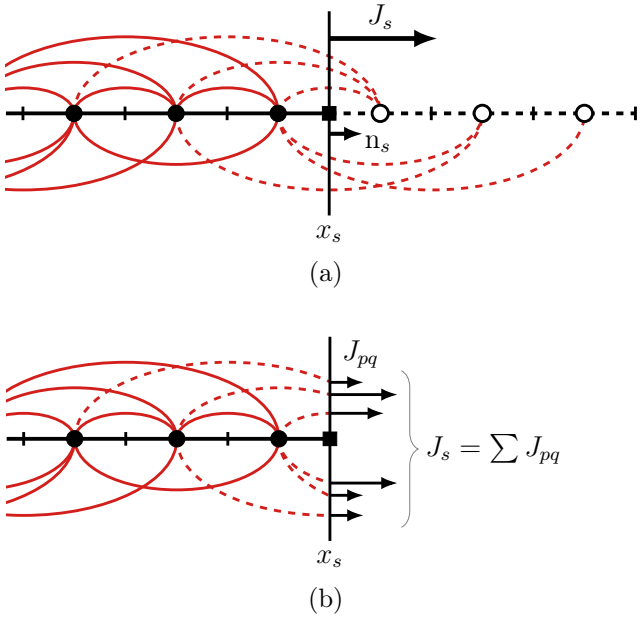


Figure 7.7: *Representation of the equation of a surface node s:* (a) *the flux* $J_s = J(x_s, \mathrm{n}_s, t)$ *is computed as* (b) *the sum of the fluxes* $J_{pq} = -\mathrm{j}(x_p, x_q, t) \cdot \mathrm{n}_s \, \beta_{pq} \, \Delta x^2$ *of the bonds intersecting node s.*

Thanks to equation (7.11), the surface nodes are affected by all the bonds connected to fictitious nodes (see Figure 7.7). In fact, the bond fluxes that should be applied to the fictitious nodes, are instead applied to the surface node. Therefore, the surface nodes represent the nonlocal behavior of the whole fictitious layer. This is why the local boundary conditions imposed at the surface nodes can be seen as similar to volume constraints (nonlocal boundary conditions).

For the time integration, the forward Euler (first-order explicit) method is employed:

$$C_p^{n+1} = C_p^n + \Delta t \, \frac{\partial C_p^n}{\partial t} \,, \tag{7.12}$$

where the subscript and superscript stand respectively for the corresponding position of the node and time-step so that, for instance, $C_p^n = C(x_p, t_n)$. Therefore, the time integration is carried out by combining equations (7.7), (7.8) and (7.12) as:

$$C_p^{n+1} = C_p^n + d\Delta t \sum_{q \in \mathcal{H}_p} \mu_{pq} \big(C_q^n - C_p^n\big) \beta_{pq} \Delta x + \frac{1}{2} \, d \, \mu(\Delta x) \left(C_{p+1}^n - 2C_p^n + C_{p-1}^n\right) \Delta x \tag{7.13}$$

where $d$ is computed with equation (7.4) and $\mu_{pq} = \mu(|x_q - x_p|)$. This system of equations can also be written in the matrix form as:

$$\mathbf{C}^{n+1} = \mathbf{A} \, \mathbf{C}^n \,, \tag{7.14}$$

where $\mathbf{C}^n$ and $\mathbf{C}^{n+1}$ are the concentration vectors at time-steps $n$ and $n+1$, respectively.

## 7.3 Stability analysis

The stability analysis in peridynamic models has been carried out via the Von Neumann stability analysis for hyperbolic equations discretized with the meshfree method in [65, 267] and for parabolic equations considering the fast convolution-based method in [179, 180]. Note that this type of analysis considers only pure initial value problems and completely neglects the influence of the boundary conditions [268]. In [269, 270] the stability condition of the forward Euler scheme applied to parabolic equations discretized in space with the finite element method is discussed. Here we follow the general analysis (that also includes the treatment of boundary conditions), known as the *eigenvalue technique* for stability analysis, to find the restriction on the time-step $\Delta t$ for peridynamic parabolic equations discretized with the meshfree method.

A numerical method is semi-stable if the numerical errors do not grow as the solution progresses in time. According to the eigenvalue technique for stability analysis, the numerical method in equation (7.14) is semi-stable if the largest eigenvalue $\lambda_{max}$ of the matrix $\mathbf{A}$ is such that $|\lambda_{max}| \leq 1$. In this work we consider a body under Dirichlet boundary conditions at both ends, i.e., at the surface nodes. Therefore, since the values of the concentrations at those nodes are known, the surface nodes do not contribute to the numerical errors. In order to bound the eigenvalues of matrix $\mathbf{A}$ with entries $a_{ij}$, we use the Gershgorin Theorem which states that each eigenvalue of $\mathbf{A}$ lies within at least one of the circles centered in $a_{ii}$ with a radius $\sum_{j \neq i} |a_{ij}|$ (the so-called Gershgorin discs in the complex plane):

$$|\lambda - a_{ii}| \leq \sum_{j \neq i} |a_{ij}| \,, \tag{7.15}$$

where $a_{ii}$ and $a_{ij}$ are the diagonal and off-diagonal entries of matrix $\mathbf{A}$.

The stability criterion without considering the influence of the boundary conditions and the self-transfer term is given as:

$$\Delta t \leq \frac{1}{d \sum\limits_{q \in \mathcal{H}_p} \mu_{pq} \, \Delta x} \, . \tag{7.16}$$

This inequality is obtained by applying the Gershgorin Theorem to the rows of matrix $\mathbf{A}$ corresponding to a generic node $p$ lying in the bulk of the body, i.e. a node without fictitious nodes in its neighborhood (see the following proof). Note that, for simplicity's sake, the quadrature coefficient $\beta$ is neglected in the determination of the upper bound for the time-step size. However, the entries of the rows of $\mathbf{A}$ corresponding to the nodes near the boundary of the body are different from those considered to obtain equation (7.16), due to the presence of the fictitious nodes inside the neighborhood of those nodes. In fact, some of the entries of $\mathbf{A}$ are modified according to the linear Taylor-based extrapolation (equation (7.10)). The tighter upper bound for the time-step size is found by applying the Gershgorin Theorem to the row of $\mathbf{A}$ corresponding to the interior node closest to the boundary, as shown in the following.

**Theorem.** *For the peridynamic equation of transient diffusion discretized in space with the meshfree method and in time with the forward Euler scheme, in which the boundary conditions are imposed via the surface node method with a linear Taylor-based extrapolation, the stability condition is given as*

$$\Delta t \leq \frac{1}{d \left( \sum\limits_{q \in \mathcal{H}_b} \mu_{bq} + \frac{1}{2} \sum\limits_{f \in \mathcal{H}_b} \mu_{bf} \left( \frac{x_f - x_s}{x_s - x_b} - 1 \right) \right) \Delta x} \tag{7.17}$$

*when the self-transfer term is not considered, and*

$$\Delta t \leq \frac{1}{d \left( \sum\limits_{q \in \mathcal{H}_b} \mu_{bq} + \frac{1}{2} \sum\limits_{f \in \mathcal{H}_b} \mu_{bf} \left( \frac{x_f - x_s}{x_s - x_b} - 1 \right) + \frac{1}{2} \mu(\Delta x) \right) \Delta x} \tag{7.18}$$

*when the self-transfer term is considered.*

*Proof.* For simplicity and conciseness, we prove the stability condition in equation (7.17) without considering the self-transfer term. The upper bound for the time-step size, when the self-transfer term is considered, can be found following the same steps. For simplicity's sake, we also neglect the quadrature coefficients $\beta$ in all the following formulas. If $\beta$ was included in the analysis, the upper bound for the time-step size would slightly increase.

The concentration at a node $p$ in the bulk of the body, i.e., a node without fictitious nodes within its neighborhood, at the time-step $n+1$, is given as (see equation (7.13)):

$$C_p^{n+1} = \left[ 1 - d \Delta t \sum_{q \in \mathcal{H}_p} \mu_{pq} \Delta x \right] C_p^n + d \Delta t \sum_{q \in \mathcal{H}_p} \mu_{pq} C_q^n \Delta x \, . \tag{7.19}$$

where $\mu_{pq} = \mu(|x_q - x_p|)$. The Gershgorin Theorem applied to the rows of $\mathbf{A}$ corresponding to node $p$ yields:

$$\left| \lambda - 1 + d\Delta t \sum_{q \in \mathcal{H}_p} \mu_{pq} \Delta x \right| \leq \sum_{q \in \mathcal{H}_p} \left| d\Delta t \mu_{pq} \Delta x \right| . \tag{7.20}$$

Note that the terms within the summation on the right-hand side of this equation are always positive. Therefore, equation (7.20) becomes:

$$-d\Delta t \sum_{q \in \mathcal{H}_p} \mu_{pq} \Delta x \leq \lambda - 1 + d\Delta t \sum_{q \in \mathcal{H}_p} \mu_{pq} \Delta x \leq d\Delta t \sum_{q \in \mathcal{H}_p} \mu_{pq} \Delta x \, . \tag{7.21}$$

According to the eigenvalue technique, the stability of the numerical method is achieved when $-1 \leq \lambda \leq 1$. The right inequality yields $\lambda \leq 1$, whereas the left inequality is:

$$\lambda \geq 1 - 2d\Delta t \sum_{q \in \mathcal{H}_p} \mu_{pq} \Delta x \, . \tag{7.22}$$

Thus, one obtains $\lambda \geq -1$ if the following condition holds:

$$\Delta t \leq \frac{1}{d \sum\limits_{q \in \mathcal{H}_p} \mu_{pq} \Delta x} \, . \tag{7.23}$$

This is the stability criterion for the choice of a stable time-step when no correction methods for the PD surface effect or the imposition of the nonlocal boundary conditions are used.

We consider now a node $p$ having one or more fictitious nodes within its neighborhood. In equation (7.19), we subdivide the last summation over the nodes within the neighborhood of node $p$ as the sum of the summations of the real (denoted with $r$) and fictitious (denoted with $f$) nodes within the neighborhood of node $p$:

$$C_p^{n+1} = \left[ 1 - d\Delta t \sum_{q \in \mathcal{H}_p} \mu_{pq} \Delta x \right] C_p^n + d\Delta t \sum_{r \in \mathcal{H}_p} \mu_{pr} C_r^n \Delta x + d\Delta t \sum_{f \in \mathcal{H}_p} \mu_{pf} C_f^n \Delta x \, . \tag{7.24}$$

As shown in Figure 7.8, consider a surface node, named $s$, and the real node closest to it, named $b$. As dictated by the surface node method with a linear Taylor-based extrapolation [227, 236, 249], the concentration $C_f^n$ of the fictitious nodes is computed with a linear Taylor series expansion as in equation (7.10). However, since there are no numerical errors at the surface nodes (where Dirichlet boundary conditions are imposed), we neglect the contributions to matrix $\mathbf{A}$ of the concentrations $C_s^n$ of the surface nodes. Hence, we obtain:

$$C_p^{n+1} = \left[ 1 - d\Delta t \sum_{q \in \mathcal{H}_p} \mu_{pq} \Delta x \right] C_p^n + d\Delta t \sum_{r \in \mathcal{H}_p} \mu_{pr} e_r^n \Delta x - d\Delta t \sum_{f \in \mathcal{H}_p} \mu_{pf} c_f C_b^n \, \Delta x \, , \tag{7.25}$$

where $c_f = \frac{x_f - x_s}{x_s - x_b}$ is a positive scalar value derived from equation (7.10).

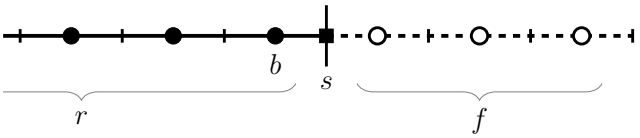


Figure 7.8: *Notation used for the indices of the nodes for the stability analysis: $r$ are the real nodes, $f$ are the fictitious nodes, $s$ is the surface node, and $b$ is the real node closest to node $s$.*

When $p \neq b$ (i.e., node $p$ is not the interior node closest to the boundary):

$$C_p^{n+1} = \left[1 - d\Delta t \sum_{q \in \mathcal{H}_p} \mu_{pq} \Delta x\right] C_p^n + d\Delta t \sum_{r \in \mathcal{H}_p - \{b\}} \mu_{pr} C_r^n \Delta x + d\Delta t \left[\mu_{pb} \Delta x - \sum_{f \in \mathcal{H}_p} \mu_{pf} c_f \Delta x\right] C_b^n \,. \tag{7.26}$$

The Gershgorin Theorem applied to this case yields:

$$\left|\lambda - 1 + d\Delta t \sum_{q \in \mathcal{H}_p} \mu_{pq} \Delta x\right| \leq d\Delta t \left(\sum_{r \in \mathcal{H}_p - \{b\}} \mu_{pr} + \left|\mu_{pb} - \sum_{f \in \mathcal{H}_p} \mu_{pf} c_f\right|\right) \Delta x \,. \tag{7.27}$$

Following the same steps as before, the first inequality deriving from equation (7.27) is given as:

$$\lambda \leq 1 + d\Delta t \left(-\sum_{q \in \mathcal{H}_p} \mu_{pq} + \sum_{r \in \mathcal{H}_p - \{b\}} \mu_{pr} + \left|\mu_{pb} - \sum_{f \in \mathcal{H}_p} \mu_{pf} c_f\right|\right) \Delta x \,. \tag{7.28}$$

Since the set of nodes in the neighborhood $\mathcal{H}_p$ is the sum of the disjointed sets of real and fictitious nodes, the inequality is rewritten as:

$$\lambda \leq 1 + d\Delta t \left(-\sum_{f \in \mathcal{H}_p} \mu_{pf} - \mu_{pb} + \left|\mu_{pb} - \sum_{f \in \mathcal{H}_p} \mu_{pf} c_f\right|\right) \Delta x \,. \tag{7.29}$$

We have that $\lambda \leq 1$ if the following condition holds:

$$-\sum_{f \in \mathcal{H}_p} \mu_{pf} - \mu_{pb} + \left|\mu_{pb} - \sum_{f \in \mathcal{H}_p} \mu_{pf} c_f\right| \leq 0 \,, \tag{7.30}$$

which leads to:

$$-\sum_{f \in \mathcal{H}_p} \mu_{pf} - \mu_{pb} \leq \mu_{pb} - \sum_{f \in \mathcal{H}_p} \mu_{pf} c_f \leq \sum_{f \in \mathcal{H}_p} \mu_{pf} + \mu_{pb} \,. \tag{7.31}$$

The right inequality is always true, whereas the left inequality becomes:

$$\mu_{pb} \geq \frac{1}{2} \sum_{f \in \mathcal{H}_p} \mu_{pf} \left(c_f - 1\right) \,. \tag{7.32}$$

Note that here no term depends on the time-step size $\Delta t$, but this inequality depends on the kernel $\mu$ and on how many fictitious nodes are present in the neighborhood of node $p$. Therefore, to satisfy the condition in equation (7.32), an appropriate kernel can be chosen or one can make use of a preconditioner to modify accordingly the entries of matrix $\mathbf{A}$. If neither of the above options is adopted, the stability criterion still provides a good first guess for the time-step size.

The second inequality deriving from equation (7.27) is given as:

$$\lambda \geq 1 - d\Delta t \left( \sum_{q \in \mathcal{H}_p} \mu_{pq} + \sum_{r \in \mathcal{H}_p - \{b\}} \mu_{pr} + \left| \mu_{pb} - \sum_{f \in \mathcal{H}_p} \mu_{pf} c_f \right| \right) \Delta x \,. \tag{7.33}$$

Since $\lambda \geq -1$, the following condition holds:

$$d\Delta t \left( \sum_{q \in \mathcal{H}_p} \mu_{pq} + \sum_{r \in \mathcal{H}_p - \{b\}} \mu_{pr} + \left| \mu_{pb} - \sum_{f \in \mathcal{H}_p} \mu_{pf} c_f \right| \right) \Delta x \leq 2 \,. \tag{7.34}$$

This inequality becomes:

$$\frac{-2}{d\Delta t \Delta x} + \sum_{q \in \mathcal{H}_p} \mu_{pq} + \sum_{r \in \mathcal{H}_p} \mu_{pr} - \mu_{pb} \leq \mu_{pb} - \sum_{f \in \mathcal{H}_p} \mu_{pf} c_f \leq \frac{2}{d\Delta t \Delta x} - \sum_{q \in \mathcal{H}_p} \mu_{pq} - \sum_{r \in \mathcal{H}_p} \mu_{pr} + \mu_{pb} \,. \tag{7.35}$$

The right inequality yields:

$$d\Delta t \left( 2 \sum_{q \in \mathcal{H}_p} \mu_{pq} - \sum_{f \in \mathcal{H}_p} \mu_{pr} \left( c_f + 1 \right) \right) \Delta x \leq 2 \,, \tag{7.36}$$

or, more simply:

$$\Delta t \leq \frac{1}{d \left( \sum_{q \in \mathcal{H}_p} \mu_{pq} - \frac{1}{2} \sum_{f \in \mathcal{H}_p} \mu_{pr} \left( c_f + 1 \right) \right) \Delta x} \,. \tag{7.37}$$

This restriction on the time-step size is always verified if equation (7.23) holds. On the other hand, the left inequality yields:

$$d\Delta t \left( 2 \sum_{q \in \mathcal{H}_p} \mu_{pq} + \sum_{f \in \mathcal{H}_p} \mu_{pf} \left( c_f - 1 \right) - 2\mu_{pb} \right) \Delta x \leq 2 \,, \tag{7.38}$$

which leads to:

$$\Delta t \leq \frac{1}{d \left( \sum_{q \in \mathcal{H}_p} \mu_{pq} + \frac{1}{2} \sum_{f \in \mathcal{H}_p} \mu_{pf} \left( c_f - 1 \right) - \mu_{pb} \right) \Delta x} \,. \tag{7.39}$$

If the inequality in equation (7.32) holds, then the restriction on the time-step size given in equation (7.23) is tighter than the one in equation (7.39).

The last case to analyze is the row of matrix $\mathbf{A}$ corresponding to the interior node closest to the boundary ($p = b$ in equation (7.25)):

$$C_b^{n+1} = \left[1 - d\Delta t \left(\sum_{q\in\mathcal{H}_b} \mu_{bq}\Delta x + \sum_{f\in\mathcal{H}_b} \mu_{bf} c_f \Delta x\right)\right] C_b^n + d\Delta t \sum_{r\in\mathcal{H}_b} \mu_{br} C_r^n \Delta x\,. \tag{7.40}$$

In this case the Gershgorin Theorem yields:

$$\left|\lambda - 1 + d\Delta t \left(\sum_{q\in\mathcal{H}_b} \mu_{bq} + \sum_{f\in\mathcal{H}_b} \mu_{bf} c_f\right) \Delta x\right| \leq d\Delta t \sum_{r\in\mathcal{H}_b} \mu_{br}\Delta x\,, \tag{7.41}$$

which leads to:

$$-\,d\Delta t \sum_{r\in\mathcal{H}_b} \mu_{br}\Delta x \leq \lambda - 1 + d\Delta t \left(\sum_{q\in\mathcal{H}_b} \mu_{bq} + \sum_{f\in\mathcal{H}_b} \mu_{bf} c_f\right) \Delta x \leq d\Delta t \sum_{r\in\mathcal{H}_b} \mu_{br}\Delta x\,. \tag{7.42}$$

On the one hand, to ensure that $\lambda \leq 1$, the right inequality becomes:

$$-\sum_{f\in\mathcal{H}_b} \mu_{bf}\,(c_f + 1) \leq 0\,, \tag{7.43}$$

which is always true. On the other hand, to have $\lambda \geq -1$, we obtain from the left inequality:

$$d\Delta t \left(2\sum_{q\in\mathcal{H}_b} \mu_{bq} + \sum_{f\in\mathcal{H}_b} \mu_{bf}\,(c_f - 1)\right) \Delta x \leq 2\,, \tag{7.44}$$

Note that this inequality is more restrictive than the one in equation (7.23). From here, equation (7.17) is straightforwardly derived. □

It is worth noting that the stability condition in equation (7.17) is more restrictive than the one in equation (7.16). Hence, neglecting the boundary conditions (as in the Von Neumann analysis) may lead to a poor guess of the time-step size to obtain the stability of the method. Furthermore, when the self-transfer term is considered, the upper bound for time-step size is even tighter than the one provided in equation (7.17).

To simplify the formula of the stability criterion for quicker implementation, the symmetry of the neighborhood is employed. We denote the bond length by $m\Delta x$ with $m = 1, 2, \ldots, \overline{m}$, where $\overline{m} = \delta/\Delta x$ is assumed to be a positive integer for simplicity. If this is not the case, $\overline{m}$ can be replaced with the integer number $M$ such as $M\Delta x$ is the maximum distance from node $p$ of a node with a portion of its cell within the neighborhood of node $p$ itself. In peridynamic models, the value of $\overline{m}$ is often referred to as $\overline{m}$-ratio. Hence, the stability criterion when the influence of the boundary conditions and the self-transfer term are not considered is given as:

$$\Delta t \leq \frac{1}{d\displaystyle\sum_{m=1}^{\overline{m}} \mu(m\Delta x)\Delta x}\,. \tag{7.45}$$

A tighter upper bound for the time-step size is found by considering the influence of the boundary conditions (see equation (7.17)):

$$\Delta t \leq \frac{1}{d\left(2\sum_{m=1}^{\overline{m}}\mu(m\Delta x)+\frac{1}{2}\sum_{m=1}^{\overline{m}}\mu(m\Delta x)\,(2m-2)\right)\Delta x}\,, \tag{7.46}$$

where, given the symmetry of the neighborhood, here we considered only one half of it and multiply the summations by 2. This stability criterion can be further simplified as:

$$\Delta t \leq \frac{1}{d\sum_{m=1}^{\overline{m}}\mu(m\Delta x)\,(m+1)\,\Delta x}\,. \tag{7.47}$$

The time-step size is bounded even more tightly when the self-transfer term is considered:

$$\Delta t \leq \frac{1}{d\left(\sum_{m=1}^{\overline{m}}\mu(m\Delta x)\,(m+1)+\frac{1}{2}\mu(\Delta x)\right)\Delta x}\,. \tag{7.48}$$

The derived stability condition is analogous to the Courant-Friedrichs-Lewy (CFL) condition in classical convection equations, but it is intrinsically different: a stable $\Delta t$ is not limited by $\mathcal{O}(\Delta x^2)$ (as in models based on classical diffusion equations) but depends only weakly on $\Delta x$ for a fixed value of $\delta$. By analyzing the right-hand side of equation (7.47), one can see that the upper bound for a stable time-step is given by $\mathcal{O}(\delta^2)$ instead. For instance, choosing the kernel $\mu(|\xi|) = |\xi|^{-2}$ (for which $d = D/\delta$) yields:

$$\Delta t \leq \frac{\delta}{D\sum_{m=1}^{\overline{m}}\frac{(m+1)}{m^2\Delta x}+\frac{1}{2\Delta x}} = \frac{\delta}{\mathcal{O}(1/\delta)} = \mathcal{O}(\delta^2)\,. \tag{7.49}$$

**Remark 7.1.** For the case of bi-material diffusion (as used in, for example, PD modeling of corrosion damage [128–130, 137, 262–265], and ZrC oxidation [266]), the stability criterion derived above can still be used to determine the time-step size by employing the highest diffusivity/dissolvability between the two phases.

## 7.4 Convergence studies for diffusion problems with continuous and discontinuous initial conditions

To begin with, we consider the diffusion problem in a homogeneous bar without any phase change. In this section, we will focus on the role of discontinuities in initial conditions in peridynamic problems. Some phenomena require to be modeled with discontinuous initial conditions, such as the oxidation of a zirconium carbide sample which is suddenly exposed to an oxidizing environment [13, 14]. To simulate these experimental conditions, we assume

that the two ends of the bar are maintained at the maximum concentration of oxygen $\overline{C}$ and that the initial oxygen concentration is equal to 0 in the whole bar (except the two ends), as depicted in Figure 7.9b. However, the surface node method has never been used in a problem evolving in time, let alone with discontinuous initial conditions at the boundary. Therefore, we also analyze the same problem with continuous (quadratic) initial conditions, as shown in Figure 7.9a. The analytical solutions to the problem with the initial conditions with and without discontinuities are determined via the method of separation of variables [163]. Thus, we analyze the convergence behaviors in space (with $\delta$ fixed) and time to the exact nonlocal solution of the problem with continuous and discontinuous initial conditions.

In what follows, we will use specific units because of the direct applicability of these derivations and results to oxidation-induced damage in the ZrC problem [13, 14, 210]. The results, however, are independent of these units and the conclusions remain valid for non-dimensionalized form of the problem.

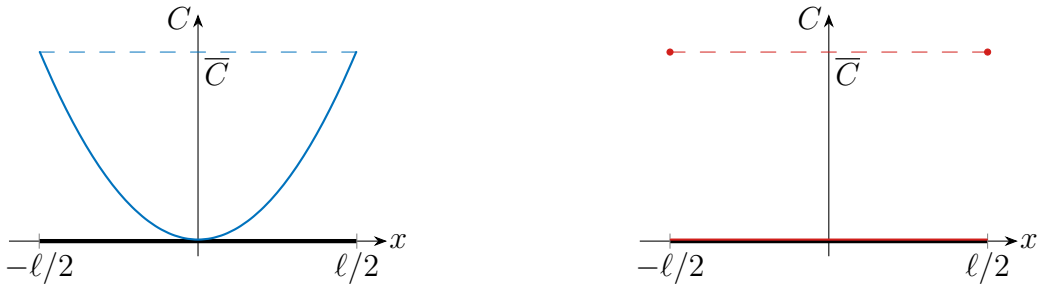


(a) *Continuous initial conditions.* (b) *Discontinuous initial conditions.*

Figure 7.9: *Different initial conditions for the 1D diffusion problem without phase change.*

### 7.4.1 Analytical solutions

The 1D problem with continuous initial conditions, i.e., a quadratic function (Figure 7.9a), is given as:

$$\begin{cases} \dfrac{\partial C(x,t)}{\partial t} = \displaystyle\int_{\mathcal{H}_x} \mathrm{j}(x,x',t)\,\mathrm{d}x' & \text{for } -\ell/2 < x < \ell/2\,,\ 0 < t < \infty\,, \\ C(-\ell/2,t) = C(\ell/2,t) = \overline{C} & \text{for } 0 < t < \infty\,, \\ C(x,0) = \dfrac{4\overline{C}}{\ell^2}\,x^2 & \text{for } -\ell/2 < x < \ell/2\,, \end{cases} \tag{7.50}$$

where $\ell$ is the length of the rod. The peridynamic solution of this problem is obtained via the method of separation of variables [163]:

$$\frac{\widehat{C}(x,t)}{\overline{C}} = 1 - \sum_{m=1}^{\infty} \frac{32\sin(k_m\ell/2)}{k_m^3\ell^3}\cos(k_m x)\exp(-D\psi t)\,, \tag{7.51}$$

where $k_m = (2m-1)\pi/\ell$ and $\psi = \psi(\delta)$ is the nonlocal factor computed as:

$$\begin{aligned}\psi(\delta) &= \int_{-\delta}^{\delta} \frac{\cos\left(k_m \xi\right) - 1}{\delta \xi^2} \, \mathrm{d}\xi \\ &= \frac{2}{\delta}\left[k_m \mathrm{Si}(k_m \delta) + \frac{\cos(k_m \delta) - 1}{\delta}\right],\end{aligned} \tag{7.52}$$

where $\xi = x' - x$ and $\mathrm{Si}(y) = \int_0^y \frac{\sin z}{z} \, \mathrm{d}z$ is the sine integral function. Note that in the computation of the nonlocal factor the assumption of an infinite body is made, i.e., the integral is computed assuming a complete horizon region. Therefore, the analytical solution in equation (7.51) is valid outside of the body as well. This is equivalent to choosing an extrapolation of the unknowns over the fictitious layer that is antisymmetric with respect to the boundary, as shown in Figure 7.10a.

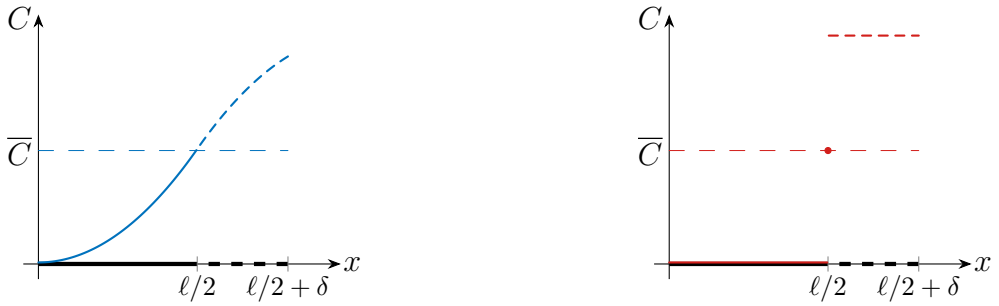


(a) *Continuous initial conditions.* (b) *Discontinuous initial conditions.*

Figure 7.10: *Antisymmetric extrapolation over the fictitious layer assumed to derive the nonlocal analytical solution for different initial conditions.*

Similarly, the 1D problem with discontinuous initial conditions, i.e., the constant zero-valued function (Figure 7.9b), is given as:

$$\begin{cases} \dfrac{\partial C(x,t)}{\partial t} = \displaystyle\int_{\mathcal{H}_x} \mathrm{j}(x,x',t) \, \mathrm{d}x' & \text{for } -\ell/2 < x < \ell/2\,,\ 0 < t < \infty\,, \\ C(-\ell/2,t) = C(\ell/2,t) = \overline{C} & \text{for } 0 < t < \infty\,, \\ C(x,0) = 0 & \text{for } -\ell/2 < x < \ell/2\,. \end{cases} \tag{7.53}$$

The peridynamic solution of this problem can be computed as [163]:

$$\frac{\widehat{C}(x,t)}{\overline{C}} = 1 - \sum_{m=1}^{\infty} \frac{4\sin(k_m \ell/2)}{k_m \ell} \cos(k_m x) \exp(-D\psi t)\,, \tag{7.54}$$

where $k_m = (2m-1)\pi/\ell$ and $\psi = \psi(\delta)$ is the same nonlocal factor of equation (7.52). As shown in Figure 7.10b, the antisymmetric extrapolation over the fictitious layer is assumed to compute the nonlocal factor $\psi(\delta)$.

### 7.4.2 Numerical results

The values for the model parameters are shown in Table 7.1. The same parameters are used for both the continuous and discontinuous initial conditions. These parameters are not realistic, but are used to verify the numerical model. Since the problem is symmetric, we consider only half of the domain and enforce a zero-flux at $x = 0$ by imposing symmetric boundary conditions as described in [271].

Table 7.1: *Properties of the rod.*

| Property | Value |
|---|---|
| Length of the rod | $\ell = 1\,\text{cm}$ |
| Horizon size | $\delta = 0.05\,\text{cm}$ |
| Classical diffusivity | $D = 1\,\text{cm}^2/\text{s}$ |
| Maximum concentration | $\overline{C} = 1\,\text{mol/cm}^3$ |

The numerical results, compared to the analytical solution, for the continuous and discontinuous initial conditions are shown in Figures 7.11 and 7.12, respectively. These plots are obtained for a value of the $\overline{m}$-ratio equal to 4 ($\Delta x = 125\,\mu\text{m}$) and the time-step size equal to 0.1 ms. This value of the time-step meets the requirement of equation (7.48) for numerical stability. Moreover, no qualitative differences are visible in the plots if smaller time-steps are chosen. The numerical results are in excellent agreement with their corresponding analytical solutions. This is also observed in the case of discontinuous initial conditions.

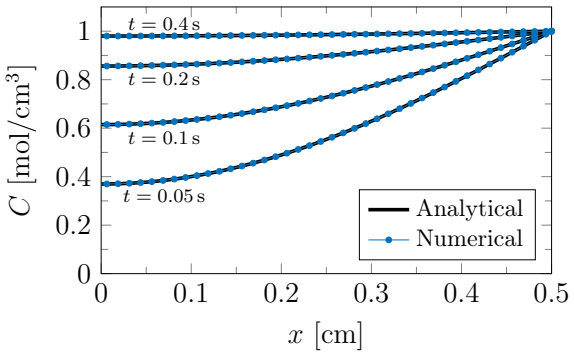


Figure 7.11: *Numerical results (for $\Delta x = 125\,\mu\text{m}$ and $\Delta t = 0.1\,\text{ms}$) and corresponding analytical solution at different times t for the problem with continuous initial conditions.*

Nonetheless, analyzing in more detail the early times of the simulation, we observed that the errors for the discontinuous initial conditions are localized near the boundary and are non-negligible only at the early times of the simulation, as shown for instance in Figure 7.13. Furthermore, since the analytical solution is given in the form of an infinite summation of Fourier terms, some inaccuracies arise due to the truncation of higher-order terms, especially when there is a discontinuity in the solution. Therefore, in the following convergence analysis, we study the influence of ignoring the initial time interval of the simulation in the computation of the error for the case with discontinuous initial conditions.

The errors can be computed by averaging the concentration errors in space and taking

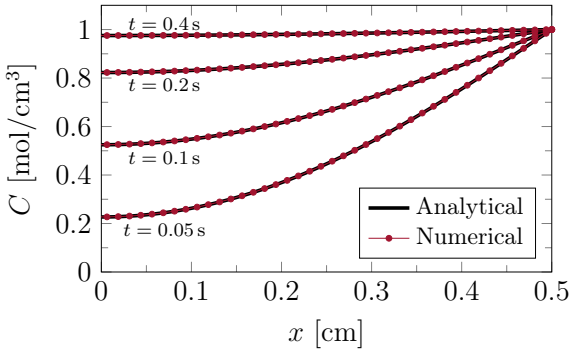


Figure 7.12: *Numerical results (for a grid spacing $\Delta x = 125\,\mu\mathrm{m}$ and a time-step size $\Delta t = 0.1\,\mathrm{ms}$) and corresponding analytical solution at different times t for the problem with discontinuous initial conditions.*

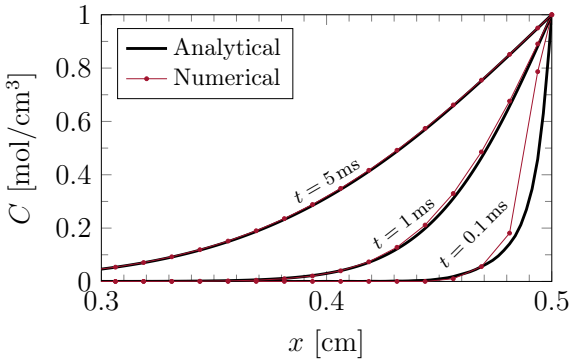


Figure 7.13: *Example of the behavior of the analytical and numerical solutions near the boundary of the body in the initial time-steps of a simulation with $\Delta x = 125\,\mu\mathrm{m}$ and $\Delta t = 0.1\,\mathrm{ms}$.*

the maximum error in time:

$$e = \max_{t_0 \le t \le t_f} \left( \sqrt{\frac{\sum_{p=1}^{N} \left[ C(x_p, t) - \widehat{C}(x_p, t) \right]^2}{N\,\overline{C}^2}} \right), \tag{7.55}$$

where $t_0$ and $t_f$ are respectively the initial and final considered instants of time, $C$ is the numerical result for the degree of freedom of node $p$, $\widehat{C}$ is the analytical solution evaluated at $x_p$, and $N$ is the number of degrees of freedom of the model. The error is computed in this way to obtain a single value for each simulation and compare them when the grid spacing or the time-step size are changed. The analytical solution (equation (7.51) for the continuous initial conditions or equation (7.54) for the discontinuous ones) is truncated after 200 terms. For what was discussed before, we choose $t_0 = 0\,\mathrm{s}$ for the problem with continuous initial condition and $t_0 = 1\,\mathrm{ms}$ for the one with discontinuous initial condition. On the other hand, $t_f = 0.5\,\mathrm{s}$ for both cases.

The first convergence analysis was performed with the peridynamic model with the linear extrapolation over the fictitious layer, but the results were not good. For instance, the $\overline{m}$-convergence behavior of the model with continuous initial conditions shows a low convergence rate, whereas the numerical solution of the problem with discontinuous initial

conditions slightly diverges from the nonlocal analytical solution. These poor results are due to the different assumptions that the analytical solution and the numerical model use to extrapolate the concentrations over the fictitious layer: the former one employs an antisymmetric extrapolation, while the latter one a linear extrapolation. Therefore, to obtain reasonable convergence behaviors for the peridynamic diffusion models, we need to use the same type of extrapolation in both analytical and numerical solutions.

Thus, only in the following convergence analyses are the concentrations of the fictitious nodes in the discretized model imposed to be antisymmetric with respect to the concentration of the surface node:

$$C(x_f, t) = 2C(x_s, t) + C(x_m, t)\,, \tag{7.56}$$

where $x_f$, $x_s$, and $x_m$ are the coordinates of the fictitious node, the surface node, and the node symmetric to node $f$ with respect to the boundary, respectively. Note that the stability criterion derived in Section 7.3 is not valid in this case due to the different extrapolations that are assumed. However, following the same steps as shown for the linear extrapolation, one could easily derive the stability criterion also in the case of antisymmetric extrapolation.

We perform a $\overline{m}$-convergence analysis (grid refinement keeping the value of the horizon $\delta$ fixed) for a time-step size $\Delta t = 5 \times 10^{-8}\,\mathrm{s}$. We chose a very small time-step size to reduce the errors related to the time-integration compared to those related to the space discretization. The values of the $\overline{m}$-ratio are varied as $\overline{m} = 2^k$, with $k = 1, 2, \ldots, 6$. Figure 7.14 shows the results of the $\overline{m}$-convergence studies, which highlight larger errors in the case discontinuous initial conditions compared to the case with continuous initial conditions. Nevertheless, the errors are considerably small also when a discontinuity is present in the initial conditions. Furthermore, the rate of convergence is not affected by the presence of a discontinuity (when the early times of the simulation are ignored).

Figure 7.15 shows the convergence behaviors for different time intervals skipped at the beginning of the simulation. When early times are considered, the maximum errors in time are found in the first time-steps. This is due to the fact that the representation of the discontinuity in the initial conditions is only approximated in the numerical model. On the other hand, when a sufficiently long time interval is ignored, the convergence rate is approximately the same as for the numerical model with continuous initial conditions.

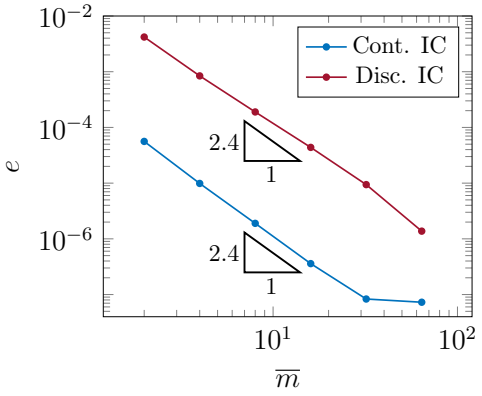


Figure 7.14: *$\overline{m}$-convergence (for $\Delta t = 5 \times 10^{-8}\,\mathrm{s}$) for continuous and discontinuous initial conditions (discontinuous case skips over the first 1 ms).*

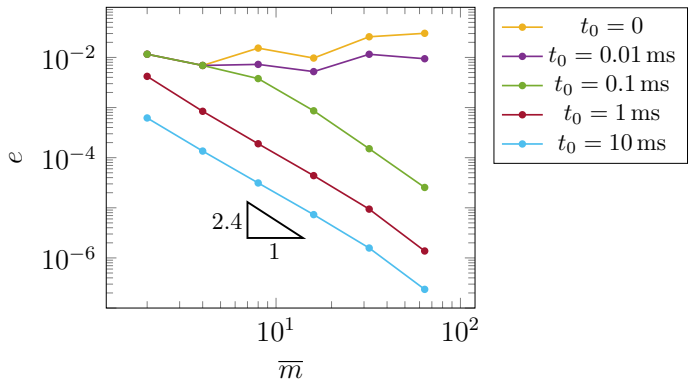


Figure 7.15: *Influence of initial skipped time interval on the $\overline{m}$-convergence properties to the analytical solution to the nonlocal problem (all results are for $\Delta t = 5 \times 10^{-8}\,\text{s}$).*

Similarly, we analyze the convergence behavior due to the refinement of the time-step size $\Delta t$ for a fixed value of grid spacing $\Delta x = 50\,\mu\text{m}$, shown in Figure 7.16. As in the case of $\overline{m}$-convergence, the numerical results for the problem with discontinuous initial conditions exhibit the same rate of convergence as those for the problem with continuous initial conditions. However, the numerical errors are higher when a discontinuity is present in the initial conditions. As shown in Figure 7.17, the discontinuity in the initial conditions influences only the early times of the simulation.

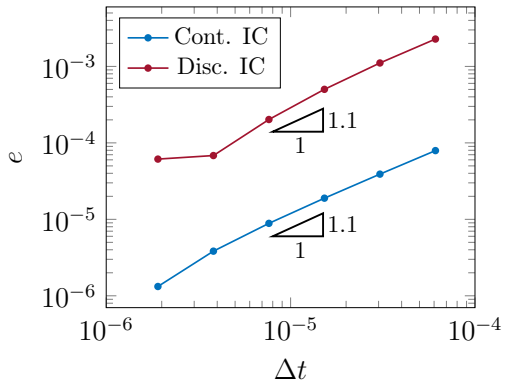


Figure 7.16: *Time-convergence (for $\Delta x = 50\,\mu\text{m}$) for continuous and discontinuous initial conditions (discontinuous case skips over the first 1 ms).*

Several parameters may affect the size of the initial time interval that has to be skipped in the computation of the error to obtain the same convergence rate as the model with continuous initial conditions. Among those parameters, the value of the diffusivity is arguably the most influential. Increasing the diffusivity leads to a reduction of the time interval mentioned above. More precisely, the size of the initial time interval ignored to obtain the "expected" convergence behavior is inversely proportional to the diffusivity value.

## 7.5 Diffusion problem with moving interface

In this section, the peridynamic model for a bi-material body with a moving interface is analyzed. As pointed out before, the motion of the interface is not related to a condition

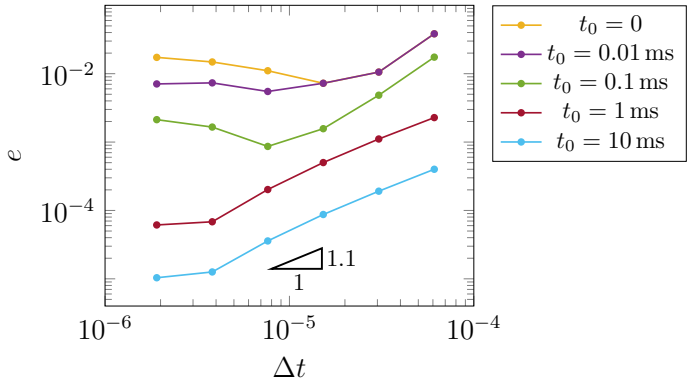


Figure 7.17: *Influence of initial skipped time interval on the time-convergence properties to the analytical solution to the nonlocal problem (all results are for* $\Delta x = 50\,\mu\text{m}$*).*

imposed at the interface itself, but it is part of the peridynamic solution of the problem. Therefore, we are interested in monitoring the accuracy of the numerical results for the position of the interface at each instant of time. Since the analytical solution to this type of nonlocal problem is difficult (if not impossible) to obtain, we use the solution of a manufactured problem instead.

### 7.5.1 Manufactured solution

We assume that the manufactured solution is given as:

$$\frac{\widehat{C}(x,t)}{\overline{C}} = 1 + \left(\frac{4}{\ell^2}\,x^2 - 1\right)\left(1 - \frac{t}{t_f}\right), \tag{7.57}$$

where $t_f$ is the final instant of time in which the solution is equal to $C(x,t) = \overline{C}$. The manufactured solution is plotted in Figure 7.18 at different instants of time. Note that equation (7.57) does not describe the "natural" evolution of the concentration, but the verification of a manufactured problem does not require physically realistic solutions [272]. The manufactured solution is chosen to be symmetric with respect to the origin of the axis, thus we consider only the positive part of the coordinate axis.

The motion of the interface can be described by equalizing equation (7.57) with the concentration of phase change $C_i$:

$$\frac{C_i}{\overline{C}} = 1 + \left(\frac{4}{\ell^2}\,x_i^2 - 1\right)\left(1 - \frac{t}{t_f}\right), \tag{7.58}$$

where $x_i$ is the interface position. By solving the previous equation for $x_i$, the position of the interface in time is given as:

$$x_i = \pm\frac{\ell}{2}\sqrt{1 + \left(\frac{C_i}{\overline{C}} - 1\right)\left(\frac{t_f}{t_f - t}\right)}, \tag{7.59}$$

in which we consider only the positive solution for symmetry reasons.

Since the manufactured solution is not the "natural" evolution of the concentration, an

external flux has to be "pushed into" the body. This flux can be computed as the remainder of equation (7.1) as:

$$\begin{aligned}\overline{J}(x,t) &= \frac{\partial C(x,t)}{\partial t} - \int_{\mathcal{H}_x} \mathrm{j}(x,x',t)\,\mathrm{d}x' \\ &= -\frac{\overline{C}}{t_f}\left(\frac{4}{\ell^2}\,x^2 - 1\right) - \int_{\mathcal{H}_x} d(x,x',t)\,\frac{\widehat{C}(x',t) - \widehat{C}(x,t)}{(x'-x)^2}\,\mathrm{d}x'\,.\end{aligned} \tag{7.60}$$

The integral on the right-hand side of the equation depends on the value of the micro-diffusivities obtained with equation (7.6). Note that the concentration distribution (and, therefore, the phase of each point) is known in each instant of time from the manufactured solution. Hence, the integral can accordingly be split into a sum of integrals with a constant micro-diffusivity $d(x,x',t) = d_k$, where $k = 1,2,3$ (see equation (7.6)). Here we solve the indefinite integral that can be used to compute the external flux in equation (7.60):

$$\begin{aligned}\int d_k\,\frac{\widehat{C}(x',t) - \widehat{C}(x,t)}{(x'-x)^2}\,\mathrm{d}x' &= d_k \int \frac{\overline{C}\left[\left(\frac{4}{\ell^2}\,x'^2 - 1\right) - \left(\frac{4}{\ell^2}\,x^2 - 1\right)\right]\left(1 - \frac{t}{t_f}\right)}{(x'-x)^2}\,\mathrm{d}x' \\ &= \frac{4\,d_k\,\overline{C}}{\ell^2}\left(1 - \frac{t}{t_f}\right)\int \frac{x'^2 - x^2}{(x'-x)^2}\,\mathrm{d}x' \\ &= \frac{4\,d_k\,\overline{C}}{\ell^2}\left(1 - \frac{t}{t_f}\right)\int \frac{\xi\,(\xi + 2x)}{\xi^2}\,\mathrm{d}\xi \\ &= \frac{4\,d_k\,\overline{C}}{\ell^2}\left(1 - \frac{t}{t_f}\right)\left[\xi + 2x\frac{\xi}{|\xi|}\log(|\xi|) + \text{const.}\right]\,,\end{aligned} \tag{7.61}$$

where $\xi = x' - x$.

### 7.5.2 Numerical results

The data used is the same as in Table 7.1, except for the diffusivity that is chosen to be different in each phase. The following data is thought to be applied in the case of the zirconium carbide oxidation, but the model of the diffusion-reaction phenomenon in a bi-material enhanced with a phase-change mechanism is also applicable to other phenomena with similar characteristics. Since no diffusion occurs in the carbide region (in fact, no concentration of oxygen is present in the carbide), the diffusivity of the carbide phase is $D_c = 0\,\mathrm{cm}^2/\mathrm{s}$. On the other hand, the diffusivities of the oxide phase and at the interface are arbitrarily chosen to be $D_o = 1\,\mathrm{cm}^2/\mathrm{s}$ and $D_i = 0.8\,\mathrm{cm}^2/\mathrm{s}$, respectively. Therefore, the three micro-diffusivities of equation (7.6) are respectively $d_1 = 0$, $d_2 = D_i/\delta$, and $d_3 = D_o/\delta$. The concentration of phase change is arbitrarily chosen to be $C_i = 0.9\overline{C}$. The grid spacing and the time-step size are respectively $\Delta x = 0.003\,125\,\mathrm{cm}$ ($\overline{m} = 16$) and $\Delta t = 1 \times 10^{-5}\,\mathrm{s}$. The value for the time-step size is chosen on the basis of the stability criterion in equation (7.48) by using the diffusivity of the oxide phase in the formula (see Remark 7.1).

The analytical solution of the manufactured problem is computed by using the interface position determined in equation (7.59) to change the diffusivity of the points. In the discretized model, however, there is no clear way to know precisely the position of the interface

when it lies between two adjacent nodes. Therefore, the position of the interface is chosen to be in the middle point between the two adjacent carbide and oxide nodes. The obtained interface position is used to compute the external flux at each node with equations (7.60) and (7.61). The fluxes at the nodes can be gathered in the flux vector $\overline{\mathbf{J}}$ and the system of equations to solve becomes:

$$\mathbf{C}^{n+1} = \mathbf{A}\,\mathbf{C}^{n} + \overline{\mathbf{J}}\,. \tag{7.62}$$

The numerical results are shown at different instants of time in Figure 7.18, and they are compared with the analytical (manufactured) solution. The numerical and analytical solutions are in good agreement throughout the whole timespan. It is also interesting to analyze the motion of the interface in the numerical model with respect to the analytical solution in equation (7.59). Figure 7.19 shows that the position of the interface in the numerical model and the manufactured solution are very close to one another at any instant of time. Therefore, the peridynamic model has been shown to be effective in capturing the motion of the interface as a result of the diffusivities of the different phases.

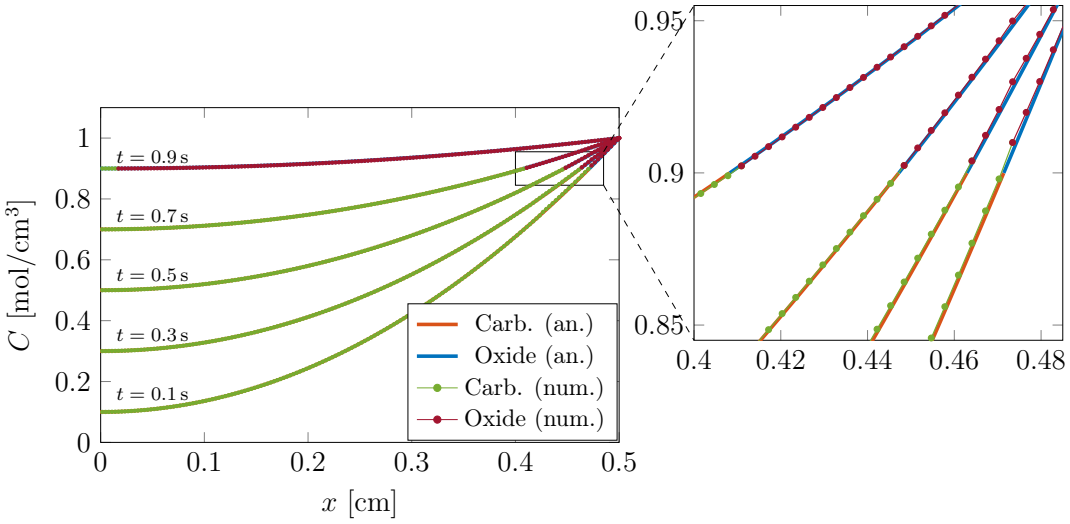


Figure 7.18: *Numerical results (for a grid spacing* $\Delta x = 0.003\,125\,\text{cm}$ *and a time-step size* $\Delta t = 1 \times 10^{-5}\,\text{s}$*) and corresponding analytical solution at different times* $t$ *for the manufactured problem with phase change.*

An interesting extension of the work shown here is to consider the moving interface problem with discontinuities. Such an example is considered in [266], in which a peridynamic model of zirconium carbide oxidation is used to simulate the effect of cracks induced by the expansion of the oxide in the outer layer. Comparison of PD results with experimental observations show an excellent agreement between the two.

## 7.6 Discussion on the extension to 2D and 3D problems

In this work, we considered only 1D transient diffusion problems for simplicity's sake. However, we believe that all the obtained results are also valid for 2D and 3D peridynamic diffusion problems. The equations for a 2D or 3D peridynamic transient diffusion problem

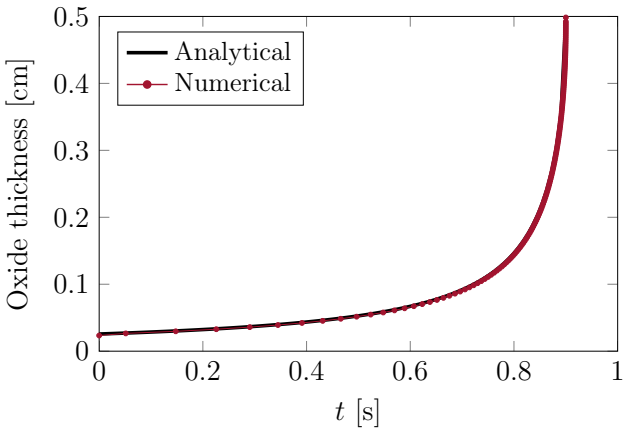


Figure 7.19: *Numerical results and corresponding analytical solution of the position of the interface for the manufactured problem with phase change.*

are presented in Section 3 of [266], and are very similar to the equation governing diffusion in a 1D peridynamic body. In fact, the only difference is that the position of the points/nodes is determined by a vector instead of a scalar value.

It is common practice to derive the stability criterion for numerical methods in 1D problems and then extend it to higher-dimension problems (see, for instance, [65, 273]). We therefore use equation (7.17) in Section 7.3 for the generalization. The linear Taylor-based extrapolation method for the 3D case used to determine the concentration at a fictitious node $\mathbf{x}_f$ at time $t$ yields [227, 236, 249]:

$$\begin{aligned} C(\mathbf{x}_f,t) &\approx C(\mathbf{x}_s,t) + (x_f - x_s)\,\frac{\partial C(\mathbf{x}_s,t)}{\partial x} + (y_f - y_s)\,\frac{\partial C(\mathbf{x}_s,t)}{\partial y} + (z_f - z_s)\,\frac{\partial C(\mathbf{x}_s,t)}{\partial z} \\ &\approx \left(1 + \frac{x_f - x_b}{x_s - x_b} + \frac{y_f - y_b}{y_s - y_b} + \frac{z_f - z_b}{z_s - z_b}\right) C(\mathbf{x}_s,t) - \left(\frac{x_f - x_s}{x_s - x_b} + \frac{y_f - y_s}{y_s - y_b} + \frac{z_f - z_s}{z_s - z_b}\right) C(\mathbf{x}_b,t) \\ &\approx (1 + c_f)\, C(\mathbf{x}_s,t) - c_f\, C(\mathbf{x}_b,t)\,, \end{aligned} \tag{7.63}$$

where node $\mathbf{x}_s$ is the surface node closest to node $\mathbf{x}_f$, node $\mathbf{x}_b$ is the real node closest to node $\mathbf{x}_s$, and the derivatives are approximated by the finite difference method as shown in equation (7.10). Note that equation (7.63) is also valid in 1D with $c_f = \frac{x_f - x_s}{x_s - x_b}$ and in 2D with $c_f = \frac{x_f - x_s}{x_s - x_b} + \frac{y_f - y_s}{y_s - y_b}$. Therefore, since the governing equations in 2D or 3D diffusion problems have the same "structure" as those in 1D problems, we deduce that the stability criterion generalized for a higher-dimension transient diffusion problem is as follows:

$$\Delta t \leq \frac{1}{d\left(\sum_{q \in \mathcal{H}_b} \mu_{bq} + \frac{1}{2}\sum_{f \in \mathcal{H}_b} \mu_{bf}\,(c_f - 1)\right)\Delta x}\,, \tag{7.64}$$

where $c_f = \frac{x_f - x_s}{x_s - x_b}$ in 1D, $c_f = \frac{x_f - x_s}{x_s - x_b} + \frac{y_f - y_s}{y_s - y_b}$ in 2D, and $c_f = \frac{x_f - x_s}{x_s - x_b} + \frac{y_f - y_s}{y_s - y_b} + \frac{z_f - z_b}{z_s - z_b}$ in 3D. The nodes near the corners of the body, i.e., the nodes with the highest number of fictitious nodes

inside their neighborhood, are likely to provide the smallest upper bound for the time-step size.

As shown in Section 7.4 for a 1D peridynamic transient diffusion problem, a discontinuity at the boundary in the initial conditions affects the numerical convergence rate only at the very early stages of the simulation. This is due to the fact that the discontinuity is quickly "smoothed out" by the diffusion phenomenon that tends to reduce the high gradients of concentration, as shown for example in the analytical solution depicted in Figure 7.13. This effect of diffusion is obviously independent of the considered number of dimensions of the model. Therefore, it is expected that the same conclusions that were obtained in the 1D case are also valid in the 2D and 3D cases.

In this work, we quantitatively evaluated the accuracy of the position of the autonomously moving interface in a 1D peridynamic diffusion problem when compared to a manufactured solution. Except for the (possibly) slightly higher errors due to the numerical integration of the peridynamic operator in 2D and 3D problems, we expect that the accuracy of the position of the moving interface should be similar to that obtained in the proposed 1D numerical example. Furthermore, the 2D and 3D peridynamic diffusion models for a bi-material have already been used to successfully reproduce complex phenomena, such as corrosion [128–130, 137, 262–265] and zirconium carbide oxidation [266]. These works show that the peridynamic modeling in 1D, 2D, and 3D cases is capable of accurately predicting the motion of interfaces in excellent agreement with experimental observations.

## 7.7 Conclusions

In this work, we analyzed several numerical aspects in the peridynamic model for a diffusion problem with and without moving interface. To this end, we considered the example of the zirconium carbide oxidation for the choice of initial/boundary conditions and material properties, but the results may be easily generalized to other physical phenomena with similar characteristics. Moreover, the boundary conditions are imposed, for the first time, by means of the surface node method in a problem evolving over time.

It is well-known that explicit numerical methods for time integration of the diffusion equation incurs in instability unless the time-step size is sufficiently small. The Von Neumann method can provide a first guess for the time-step size allowed to obtain the stability of the numerical method, but this method does not consider the influence of the boundary conditions. Thanks to the eigenvalue technique for stability analysis and the Gershgorin Theorem, we have determined a more general stability criterion for peridynamic diffusion models that takes into account the numerical method as a whole, including the effect of the boundary conditions. In fact, considering the boundary conditions provides a tighter upper bound for the time-step size to obtain the stability of the numerical method.

Then, we showed the numerical results and the convergence to the exact peridynamic solution of a diffusion problem with continuous and discontinuous initial conditions in a homogeneous body without phase change. The presence of a discontinuity in the initial conditions affects the numerical approximation only in the early stages of the simulation. When a sufficiently long initial time interval is ignored, the convergence rate of the model

with discontinuous initial conditions is the same as that of the model with continuous initial conditions. This fact has been verified for both $\overline{m}$-convergence (grid refinement while keeping the horizon size $\delta$ constant) and time-convergence analysis.

Furthermore, we solved a diffusion problem in a bi-material enhanced with a phase-change model. This model makes use of the diffusion equation to determine both the concentration of the considered species within the body and the position of the interface between different phases. In fact, the phase-change is driven by the concentration of the species itself. The numerical results, in terms of concentration profile and position of the interface, are in good agreement with the analytical (manufactured) solution. These analyses pave the way for the modeling of more complex phenomena, including reaction-induced damage mechanisms that can be easily introduced within the peridynamic framework.

# Chapter 8

# A peridynamic model for oxidation and damage in zirconium carbide ceramics

**Submitted to:** *Journal of Nuclear Materials* (2023)

**Authors:** Francesco Scabbia, Claudia Gasparrini, Mirco Zaccariotto, Ugo Galvanetto, Florin Bobaru

## Abstract

Zirconium carbide (ZrC) has potential to be applied in next-generation nuclear reactors for space missions and industrial applications. The mechanisms controlling ZrC oxidation dependence on temperature, material composition, pressure, porosity are not fully understood. In this work, we use a peridynamic modeling of diffusion/reaction across several regions observed in previous experiments using $^{18}O$ as a tracer to explain the oxygen diffusion mechanism and reaction kinetics. We emphasize the importance in the oxidation and damage process of a transition layer of partially-oxidized ZrC. The PD model has an autonomously moving oxidation interface, and the delamination/detachment of oxide (induced by large volumetric expansion) is simulated here with an oxygen concentration-driven damage model. The 1D numerical results show that the proposed model is capable of reliably reproducing the experimental oxygen concentration profiles across the oxidation front and the oxide layer thickness, in time, observed in the experiments. An extension to 2D finds the shape of remaining unoxidized ZrC conforming to experimental observations.

**Keywords:** Peridynamics, zirconium carbide, oxidation, diffusion, delamination.

## 8.1 Introduction

Nowadays nuclear power plays a fundamental role in reducing the environmental impact of energy and electricity production, thanks to its low $CO_2$ emissions. Future applications beyond electricity production are also regaining interest. Nuclear thermal propulsion (NTP) reactor, for space applications, is being reconsidered because of the high energy density and superior engine efficiency compared to conventional space propulsion systems. The use of an NTP system enables to halve the duration of space missions, reducing the exposure of astronauts to harmful radiations and other hazards found in space. At the same time, the deployment of Very-High-Temperature Reactors (VHTR) [274] or High-Temperature Gas Reactors (HTGR) [275] will offer increased outlet temperature fluids that can serve industrial processes like high-temperature electrolysis and thermolysis. One of the major challenges for these innovative and advanced nuclear applications rely on the development of materials that can withstand the harsh conditions present during operation in these reactors.

To improve the knowledge about the performance of these advanced materials, the use of both experimental and modelling efforts is essential. In this regard, this work focuses the attention on the understanding and modelling of the oxidation behavior of zirconium carbide (ZrC). ZrC has attractive properties such as high melting point ($\sim$3500 K), high thermal conductivity at very high temperatures and low neutron absorption cross section, and is a candidate material for the development of NTP systems for space and a substitute material for SiC in the tri-isotropic coated nuclear fuel (TRISO) particles thanks to its promising fission products retention [276]. One of the drawbacks of ZrC is its affinity to oxygen, since ZrC is often considered an oxygen getter, and poor oxidation resistance.

The oxidation of ZrC proceeds readily and with a considerable associated volume increase which changes materials dimensions [14]. The oxidation mechanism is affected by several parameters such as temperature, partial pressure of oxygen and materials chemical composition. The oxide layer can assume different crystal lattice structures depending on the environmental temperature, oxygen partial pressure and oxygen content. Thermomechanical properties and oxidation resistance properties for ZrC are heavily debated in the literature due to its high degree of non-stoichiometric range [277, 278]. Moreover, the transition between unoxidized and oxidized material involves a volumetric expansion that induces stresses in the oxide layer. Crack initiation and propagation within the oxide layer accelerate the oxygen penetration because they generate preferential paths towards the bulk of the body causing significant volume expansion and stresses which need to be better understood and predicted, especially when ZrC is found in a sandwich structure in coatings.

Several experiments have been carried out on the oxidation of carbides or nitrides of this class of materials often named Ultra-High Temperature Ceramics (UHTCs) [14, 279–281]. Furthermore, some numerical models have been developed based on classical continuum mechanics and making use of the Finite Element Method (FEM): in [282] the stress distribution arising from the tetragonal-to-monoclinic phase transformation of a single grain of zirconium oxide is computed and in [283] an oxidation model is proposed based on the assumption of the a priori knowledge of the interface motion. Neither of these models was designed to or is capable of predicting the autonomous motion of the carbide-oxide interface, like it has been

developed in this work.

Peridynamics is a nonlocal continuum theory which allows for discontinuities in the displacement field to initiate and evolve spontaneously [61, 62]. This theory has already been extended to diffusion phenomena [124, 125] and multi-physics problems involving diffusion with a moving interface [128, 129, 266]. Oxidation phenomena have been dealt with by means of peridynamic modeling in [284, 285]. The peridynamic modeling of fracture in a single grain of zirconia undergoing a transformation (involving volume expansion) from tetragonal to monoclinic phase, can be found in [286]. In [287], a peridynamic thermo-mechanical model to simulate crack propagation in a TRISO particle is presented. However, to the best of our knowledge, no numerical model able to capture the motion of the oxidation interface without a priori assumptions has been developed yet.

The aim of this work is to develop a numerical tool, based on the peridynamic framework, able to predict the evolution, in time, of the carbide-oxide interface. To do so, we use the experimental data described in [14] as reference to compare the numerical results of the proposed model. This experiment consists in exposing a cubic sample of hot-pressed zirconium carbide, maintained at a constant temperature (1073 K), to an oxidative environment. The transition of the cubic sample to a Maltese-cross shape and the formation of cracks leading to the repeated delamination/detachment of the oxide from the carbide bulk can be observed in Figure 8.1 (experimental results published in [14]). These experiments in [14] enabled to assess the oxygen concentration profile across different layers formed during oxidation of ZrC. The different layers are comprised by the ZrC bulk, an intermediate dense layer made primarily of carbon and tetragonal or cubic zirconium oxide (t/c-$ZrO_2$) and an outer cracked layer made of monoclinic zirconia (m-$ZrO_2$). To the best of the author's knowledge, this was the first measurement of oxygen in ZrC. Moreover, the growth in volume of the oxide was measured in [14]. These experimental results, obtained in [14], are used to calibrate the parameters of the proposed peridynamic model.

A similar approach to the one introduced here may be used in modeling damage in lithium-ion batteries, due to the similarities between the type of oxidation phenomenon discussed here and lithiation. Electrodes in solid-state batteries may experience fracture (with a subsequent reduction of life cycles) due to lithium diffusion and intercalation that causes volumetric expansion of the storage material [15, 16]. Many experiments and numerical models on this phenomenon have been developed in the literature [288–297]. A peridynamic model of lithiation based on the same principles used in this paper may enhance the understanding of the phenomenon and, possibly, increase the life time of lithium-ion batteries.

The paper is structured as follows. Section 8.2 summarizes the experimental setup, methodology and results described in [14] for the oxidation of the zirconium carbide. Section 8.3 gives a brief review of the peridynamic theory applied to diffusion problems and its discretized equations. Section 8.4 presents the numerical approach to model the zirconium carbide oxidation. Section 8.5 shows the calibration process of the diffusivity values based on the experimental observations and the qualitative validation of the model in a 2D scenario. Section 8.6 presents conclusions and suggests potential areas for future investigation.

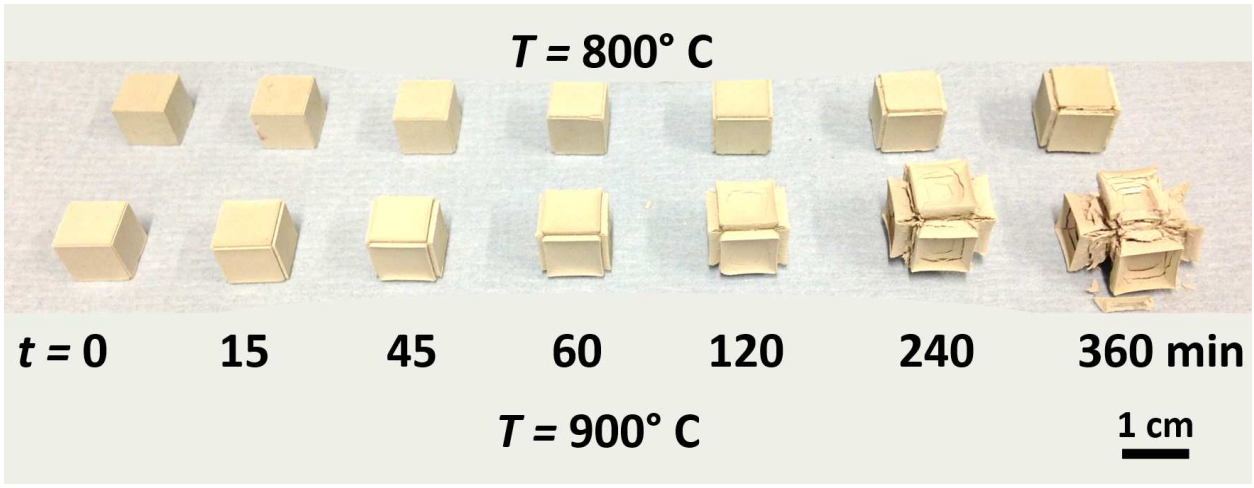


Figure 8.1: *Photograph of a cubic ZrC sample during the oxidation phenomenon with different environmental temperatures* [14]. *The mechanical properties of the zirconium carbide are clearly compromised.*

## 8.2 Brief review of experimental results

In [14], a hot pressed sintered ZrC sample was oxidized inside a furnace and exposed to $^{16}O$ oxygen atmosphere for 4 minutes and to $^{18}O$ oxygen atmosphere for 4 more minutes, approximately at a temperature of 1073K. A Secondary Ion Mass Spectroscopy (SIMS) analysis has been carried out to obtain the oxygen concentration across the oxidation front. The total oxygen concentration across the sample cross-section is monitored in the numerical simulations, so the sum of the measured concentrations of the two isotopes is considered here. Details of the experiments can be found in [14]. The oxygen concentration has been normalized by dividing it by the highest concentration value of the experimental data and replotted in Figure 8.2. Three different regions can be clearly distinguished across the cross-section:

- the outer layer of zirconium oxide where the normalized oxygen concentration is close to 1 (red region);
- the *intermediate layer*, which is a layer of thermodynamically unstable oxide, where the concentration is close to 0.5 (light blue region);
- the zirconium carbide where the concentration is close to 0 (blue region at the bottom of the image).

The other regions with a very low concentration within the oxide and the intermediate layer are due to the presence of pores, since this experimental analysis is able to detect the oxygen content only in the solid matter.

The zirconium oxide is known to exhibit polymorphs that are stable in different temperature ranges. From the chemical analyses carried out in [14], the cracked zirconium oxide is the monoclinic phase, which is stable at 1073 K. We will denote this phase by m-$ZrO_2$. On the other hand, the zirconium oxide in the intermediate layer exhibits the presence of carbon and both the cubic and tetragonal phases, which are thermodynamically unstable at 1073

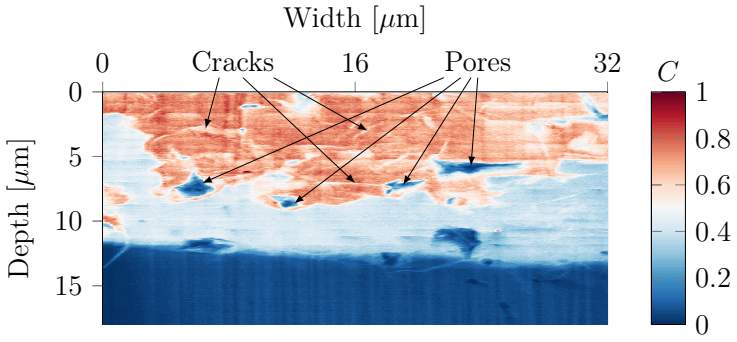


Figure 8.2: *Normalized oxygen concentration obtained with the Secondary Ion Mass Spectroscopy (SIMS) analysis obtained in* [14]. *The vertical axis represents the depth inside the material, where the external surface lies at* 0 $\mu m$. *For the original experimental data and details on the SIMS analysis, please see* [14].

K. These polymorphs will be denoted t/c-$ZrO_2$. Furthermore, we will denote the zirconium carbide by ZrC.

In [14], the oxygen diffusion coefficient was measured thanks to the use of a $^{18}O$ tracer by observing the diffusion profile across the intermediate layer. The value for the oxygen diffusion coefficient ($D = 0.09\,\mu m^2/s$) was determined by fitting the experimental results with the analytical solution derived from Fick's second law for a semi-infinite medium with a constant source of oxygen. However, it is important to note that this approach relied on certain preliminary assumptions that impact the calibration of the diffusivity (see Remark 8.1 below). In order to address these limitations, we present in Section 8.4 a peridynamic model in which the parameters are calibrated directly from the experimental data.

Oxide growth is of paramount importance in many applications. The oxide thickness of a cubic ZrC sample exposed to an oxidizing environment has been measured at different stages of the oxidation [14]. Since the oxidized samples present a peculiar shape of a Maltese cross, the oxide layer measurements were made through sample cross-section made at the center of the faces to avoid the corners where the oxide thickness grows faster. These experiments showed that the oxide grows linearly in time, as shown in Figure 8.3 (see Remark 8.2).

The linear growth is in agreement with the observations made on the oxide cross section showing a porous, cracked, non-protective oxide layer: the stable phase of the oxide cracks and tends to delaminate/detach allowing oxygen to access easier pathways of ingression. This mechanism generates an intermediate layer with a constant thickness moving at a constant rate. Furthermore, the growth rate of the oxide thickness depends on temperature. At the temperature of 1073K, the rate constant, obtained by the slope of the linear fitting shown in Figure 8.3, is equal to $6.5 \times 10^{-6}\,cm/s$ [14].

**Remark 8.1.** The approach used in [14] for diffusivity calibration considered solely the concentration profile of the intermediate layer. As we shall see, a transition layer is also present at the interface between the intermediate layer and the ZrC bulk. Furthermore, the approach in [14] assumes that the boundary, i.e., the interface between the stable (m-$ZrO_2$) and unstable (t/c-$ZrO_2$) phases of the oxide, remains stationary. However, it is important to acknowledge that the reaction occurs during oxidation with the $^{18}O$ isotope, leading to

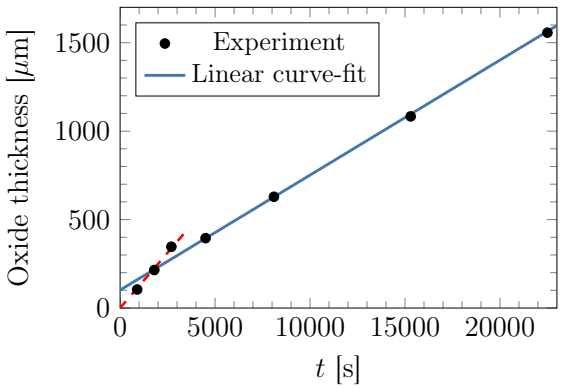


Figure 8.3: *Oxide growth in time at* 1073 K *and its linear curve-fit* [14]. *The red dashed line represents the linear curve-fit of the first three experimental measurements (in the initial transient).*

movement of that interface within the considered time frame.

**Remark 8.2.** Note that, according to the linear curve-fit in Figure 8.3, the oxide thickness is $\sim 100$ $\mu$m at the beginning of the experiment at $t = 0\,\text{s}$, whereas it is expected to be equal to 0 $\mu$m. As pointed out in [14], this is due to the fact that there is a transient in the initial stage of the oxidation (see the red dashed linear curve-fit in Figure 8.3). In the peridynamic model presented in Section 8.4, we focus on the steady-state condition of the reaction, neglecting the initial transient. However, when a visual comparison is required between the numerical results and the experimental data, one of the two plots needs to be translated due to this initial offset of the experimental results.

## 8.3 Peridynamic modeling of diffusion

Points within a body $\mathcal{B}$ modeled with peridynamics interact with each other through *bonds* [61, 62]. The maximum length of a bond between any two points is limited to a finite value denoted as $\delta$ and referred to as the *horizon size*, as shown in Figure 8.4. In the peridynamic model of ZrC oxidation, the horizon size represents the thickness of the transition layer between pure zirconium carbide and the unstable phase of the oxide. The calibration of the horizon size to this physical parameter is presented in Section 8.4.4. Bond properties are calibrated against classical (measured) properties and are named after them by adding the prefix "micro-".

We use an effective diffusion-controlled model to simulate the evolution of oxidation because of the similarities of the phenomenon with the corrosion damage models [128, 129, 131, 137, 262–265, 298]. In those models, the micro-dissolvability of bonds with one end in the metal and the other in the electrolyte are calibrated to the corrosion rate, whereas the micro-diffusivity of bonds with both ends in the electrolyte are calibrated to the diffusivity of dissolved metal ions in the electrolyte. Similarly, in the ZrC oxidation model, the micro-oxidability of bonds with one end in the carbide phase and the other in the oxide phase are calibrated to the oxidation rate, whereas the micro-diffusivity of bonds with both ends in the oxide phase are calibrated to the diffusivity of oxygen in the oxide phase.

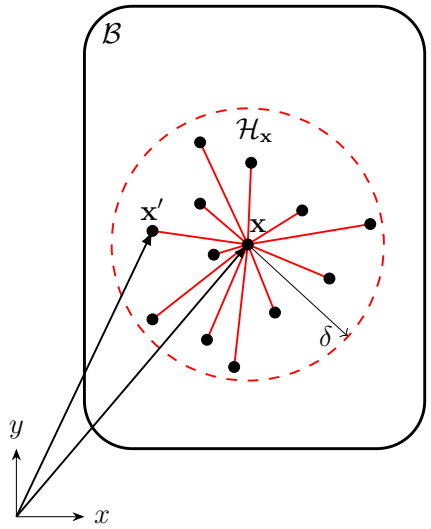


Figure 8.4: *Neighborhood $\mathcal{H}_{\mathbf{x}}$ of a point in a peridynamic body $\mathcal{B}$: red lines represent the interactions (bonds) between points.*

In a peridynamic body, a point $\mathbf{x}$ interacts with a set of points defined as $\mathcal{H}_{\mathbf{x}} = \{\mathbf{x}' \in \mathcal{B} : |\mathbf{x}' - \mathbf{x}| \leq \delta\}$, which is known as the *neighborhood* of point $\mathbf{x}$. The neighborhood is respectively a segment, a disk or a sphere in 1D, 2D or 3D bodies. The horizon size can be thought of as a material length-scale, or as a surrogate for a combination of multiple length-scales, if they are present. When comparing against classical models, which usually lack length-scales, one, however, takes the horizon size to go to zero. This is called $\delta$-convergence, see [149].

The peridynamic equation governing diffusion phenomena is given as [128, 129]

$$\begin{aligned} \frac{\partial C(\mathbf{x},t)}{\partial t} &= \int_{\mathcal{H}_{\mathbf{x}}} k(\mathbf{x},\mathbf{x}',t)\,\frac{C(\mathbf{x}',t)-C(\mathbf{x},t)}{\|\mathbf{x}'-\mathbf{x}\|^2}\,\mathrm{d}V_{\mathbf{x}'} \\ &= \int_{\mathcal{H}_{\mathbf{x}}} \mathrm{j}(\mathbf{x},\mathbf{x}',t)\,\mathrm{d}V_{\mathbf{x}'}\,, \end{aligned} \tag{8.1}$$

where $C$ is the concentration of oxygen, $k$ is the micro-diffusivity or micro-oxidability (see Remark 8.3), $V_{\mathbf{x}'}$ is the volume of point $\mathbf{x}'$, $d$ is the micro-diffusivity, and $\mathrm{j}(\mathbf{x},\mathbf{x}',t)$ is the micro-flux. In this work we adopted the kernel function constructed in [150] with the bond length in the denominator appearing with the $n = 2$ exponent. The 2D and 1D governing equations can be obtained by considering respectively a unit thickness $h$, such that $\mathrm{d}V_{\mathbf{x}'} = h\,\mathrm{d}A_{\mathbf{x}'} = \mathrm{d}A_{\mathbf{x}'}$, and a unit area $A$, such that $\mathrm{d}V_{x'} = A\,\mathrm{d}x' = \mathrm{d}x'$. The micro-diffusivity (or micro-oxidability) $k$ is calibrated to the measured diffusivity (or oxidation rate) $K$ as follows [124, 125, 128]:

$$k(\mathbf{x},\mathbf{x}',t) = \begin{cases} \dfrac{K}{\delta} & \text{in 1D,} \\ \dfrac{4K}{\pi\delta^2} & \text{in 2D,} \\ \dfrac{9K}{2\pi\delta^3} & \text{in 3D.} \end{cases} \tag{8.2}$$

Therefore, the micro-diffusivity (or micro-oxidability) has different units for different number

of dimensions of the model: [m/s] in 1D, [1/s] in 2D, and [1/(m s)] in 3D. As highlighted in Remark 8.3, $k$ assumes different physical meanings (of micro-diffusivity $d$ or micro-oxidability $r$) depending on the phases of the points connected by the bond. Analogously, $K$ can assume the physical meaning of either diffusivity $D$ or oxidation rate $R$. Moreover, $k$ may also vary in time due to the possible change of phase of the points.

**Remark 8.3.** Similarly to the peridynamic corrosion model [131], the bond property $k$ can represent different physical mechanisms depending on the phase of the points that the bond itself connects. In the ZrC oxidation, if a bond connects two points in the oxide phase, $k$ is called "micro-diffusivity" $d$ and represents the diffusion of oxygen. If a bond connects a point in the oxide phase and a point in the carbide phase, $k$ is called "micro-oxidability" $r$ and represents the oxidation of the carbide modeled as a diffusion-controlled reaction. These aspects are discussed in detail in Section 8.4.2.

### 8.3.1 Discretization of the peridynamic equations

The discretization of the peridynamic diffusion equation can be carried out by means of several different methods, such as the meshfree method [65, 184, 235], the Finite Element Method [177, 178] or the Fast Convolution-Based Method [179, 180]. In this work, we adopt the meshfree method with a uniform grid, in which nodes are spaced by a constant distance $\Delta x$. Each node represents a portion of the body, called *cell*.

The micro-flux in a bond between the nodes $p$ and $q$ can be computed as

$$\mathrm{j}(\mathbf{x}_p, \mathbf{x}_q, t) = k(\mathbf{x}_p, \mathbf{x}_q, t)\, \frac{C(\mathbf{x}_q, t) - C(\mathbf{x}_p, t)}{\|\mathbf{x}_q - \mathbf{x}_p\|^2}\,, \tag{8.3}$$

where $\mathbf{x}_p$ and $\mathbf{x}_q$ is the position vector of nodes $p$ and $q$, respectively. The bond property $k$ is either the micro-diffusivity $d$ or the micro-oxidability $r$ (see Remark 8.3). Therefore, the peridynamic diffusion equation (Eq. (8.1)) is computed by means of the midpoint quadrature rule in each cell [65, 124, 125, 128, 184]:

$$\frac{\partial C(\mathbf{x}_p, t)}{\partial t} = \sum_{q \in \mathcal{H}_p} \mathrm{j}(\mathbf{x}_p, \mathbf{x}_q, t)\, \beta_{pq}\, \Delta x^N\,, \tag{8.4}$$

where $N$ is the number of dimensions of the model, so that $\Delta x^N$ is the length, area or volume of the cell in 1D, 2D or 3D, respectively. As shown in Figure 8.5, the index $q$ stands for any node within the neighborhood $\mathcal{H}_p$ of node $p$ and the quadrature coefficient $\beta_{pq}$ is the fraction of cell of node $q$ lying within $\mathcal{H}_p$.

Due to the nonlocal nature of the theory, when using the same bond properties determined for points in the bulk for points near the surface, the effective material response is different from the one in the bulk because of incomplete families of points at locations within a horizon size distance away from a material surface. This phenomenon is known as the "peridynamic surface effect" [186]. Examples in which the peridynamics surface effect is desired/useful are when modeling at the atomic scale, or in modeling discrete dislocation dynamics [196, 299]. Moreover, peridynamic boundary conditions should be imposed over a finite-thickness layer

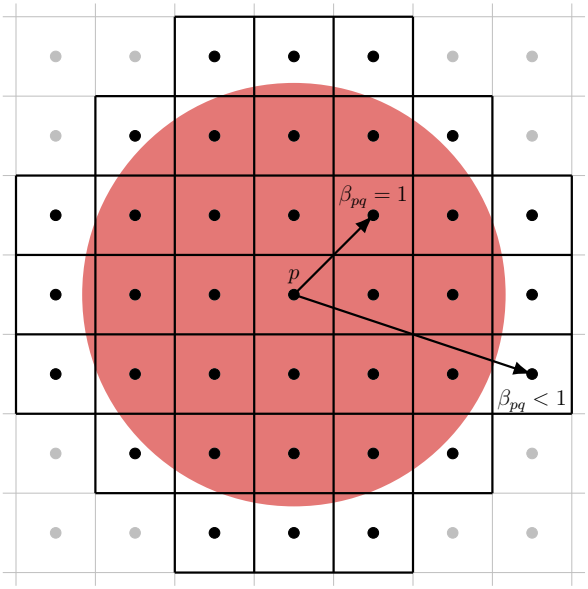


Figure 8.5: *The neighborhood $\mathcal{H}_p$ (red area) of a node $p$ is constituted by the nodes (black dots) with a portion of their cell within the neighborhood. The quadrature coefficient $\beta_{pq}$ is the volume fraction of cell of node $q$ lying inside the neighborhood [235].*

inside or outside the body [63, 64]. However, these issues have been addressed in elastic problems, for example, by means of the surface node method [227, 236, 249].

By using this method, we add fictitious nodes around the body, up to a distance $\delta$ from the boundary (see Figure 8.6). The oxygen concentrations of the fictitious nodes can be determined via the Taylor-based extrapolation truncated at the linear term [227, 236, 249]. Moreover, new nodes, namely the *surface nodes*, are introduced at the boundary of the body, as depicted in Figure 8.6, and are used to impose the boundary conditions as explained in Appendix 8.A.

### 8.3.2 Time integration

For the time integration, the forward Euler method is employed:

$$C(\mathbf{x}_p, t_{n+1}) = C(\mathbf{x}_p, t_n) + \Delta t \, \frac{\partial C(\mathbf{x}_p, t_n)}{\partial t} \,, \tag{8.5}$$

where $\Delta t$ is the time step size and $n$ is the number of the time step. Therefore, by substituting Eq. (8.4) into Eq. (8.5), we obtain:

$$C(\mathbf{x}_p, t_{n+1}) = C(\mathbf{x}_p, t_n) + \Delta t \sum_{q \in \mathcal{H}_p} \mathrm{j}(\mathbf{x}_p, \mathbf{x}_q, t_n) \, \beta_{pq} \, \Delta x^N \,. \tag{8.6}$$

For more details about the stability analisys and the convergence studies about the forward Euler method applied to the meshfree method in Peridynamics, see [266].

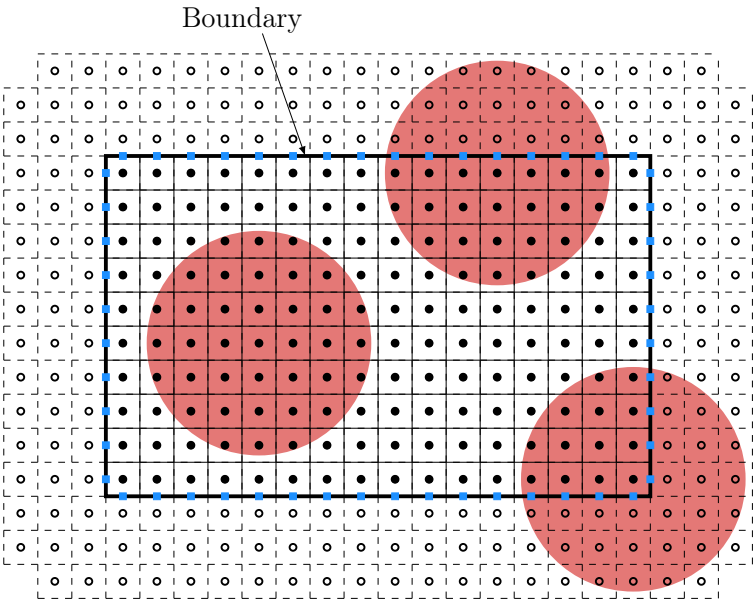


Figure 8.6: *Discretization of a 2D body by means of the meshfree method. The fictitious nodes (empty dots) are added around the body to complete the neighborhoods (red circles) of all the nodes within the body (solid dots). The external surface of the body is discretized using surface nodes (blue solid squares).*

## 8.4 Modeling approach

In this section, we present the methodology employed for modeling the oxidation of ZrC using the PD model framework presented in the previous sections and the underlying rationale. Our approach relies on a thorough examination of the experimental data pertaining to the distribution of oxygen concentration within the layer of material in which the reaction occurs. Subsequently, the peridynamic model for ZrC oxidation is constructed with the aim of faithfully reproducing the observed phenomenon, while employing fewer limiting assumptions in contrast to previous analyses.

The peridynamic model offers several advantages over classical models, including the following:

- Unlike classical models, the peridynamic model does not require the imposition of conditions at the interface, such as the Stefan condition (see, for instance, [128, 256–258]). Instead, the motion of the interface is implicitly determined through the "constitutive model" of the material under investigation [128, 129, 266].

- Because of the absence of spatial derivatives from the peridynamic formulation, damage is naturally represented, and crack formation can be spontaneous and does not lead to mathematical inconsistencies like they do in PDE-based models. This allows for a more accurate representation of fracture phenomena [68, 72, 78, 79, 90, 300, 301].

These advantages collectively contribute to the enhanced capabilities and versatility of the peridynamic model, distinguishing it from classical approaches in the field.

### 8.4.1 Analysis of the experimental measurements from [14]

We extract a concentration profile along the depth of the sample using the experimental results obtained in [14] and replotted considering the normalized total oxygen concentration depicted in Figure 8.2 (also reproduced in the upper portion of Figure 8.7). We chose to consider the region enclosed within the black rectangle in Figure 8.2, characterized by the absence of major pores and nearly parallel borders of the intermediate layer. We therefore calculate the average concentrations in the width direction within that region by summing up the oxygen concentrations of all sampled points in the black rectangle in Figure 8.7 at the same depth and dividing by the number of those points.

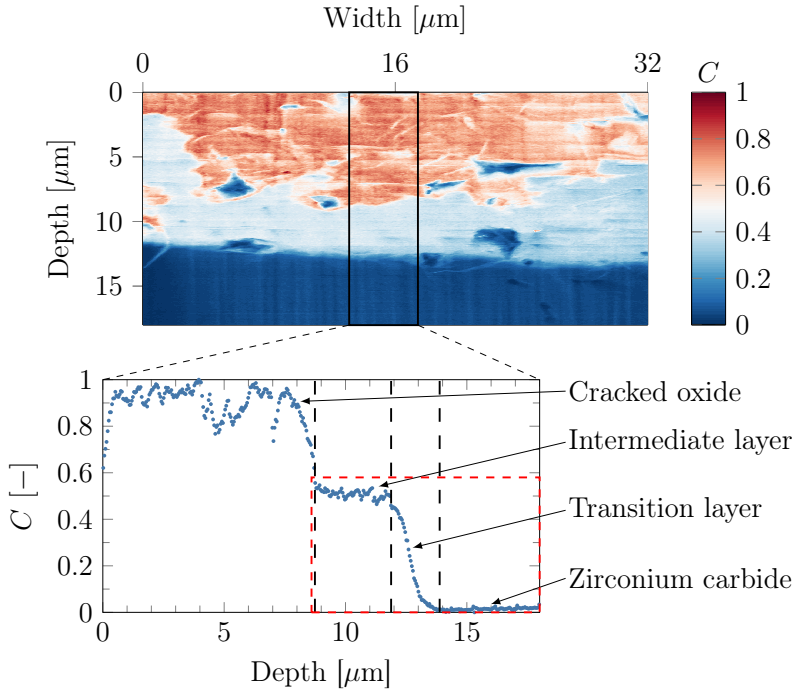


Figure 8.7: *Normalized oxygen concentration profile (bottom plot) obtained with the average of the experimental data from* [14] *(SIMS analysis already shown in Figure 8.2) along the width of the sample. For the peridynamic model we only consider the portion of the concentration profile contained inside the red dashed rectangle.*

The normalized profile of oxygen concentration is depicted in the lower portion of Figure 8.7, revealing the presence of four distinct regions. These regions consist of m-$ZrO_2$ (cracked, stable oxide) spanning from 0 to $\sim 9$ $\mu$m, t/c-$ZrO_2$ (unstable oxide) representing the intermediate layer extending from $\sim 9$ to $\sim 12$ $\mu$m, partially-oxidized ZrC between $\sim 12$ and $\sim 14$ $\mu$m, and ZrC commencing from $\sim 14$ $\mu$m. The m-$ZrO_2$ region exhibits random oscillations in oxygen concentration, attributable to the presence of cracks. In contrast, the concentration profile within the intermediate layer shows a quasi-linear descent. Meanwhile, the ZrC region is characterized by the complete absence of oxygen.

At the interface between m-$ZrO_2$ and t/c-$ZrO_2$, a sharp jump in concentration, due to oxygen flow within cracks, is observed. However, the interface between t/c-$ZrO_2$ and ZrC exhibits a gradual transition over a region of thickness $\sim 2$ $\mu$m. Thus, we call this region (where the partially-oxidized phase lies) as "transition layer", as shown in Figure 8.7. The

transition layer was characterized by Transmission Electron Microscope (TEM) in [13] and is made of amorphous carbon with nanoparticles of ZrC and t/c-$ZrO_2$ embedded within it (see Figure 8.8). It is worth noting that this transition layer, which acts as the main diffusion barrier, assumes a fundamental role in the overall phenomenon, as will be further discussed subsequently. The layer of cracked oxide is not relevant in the applications we currently consider. Hence, our modeling approach concentrates on capturing solely the effects oxidation has on the region marked by the red rectangle in Figure 8.7.

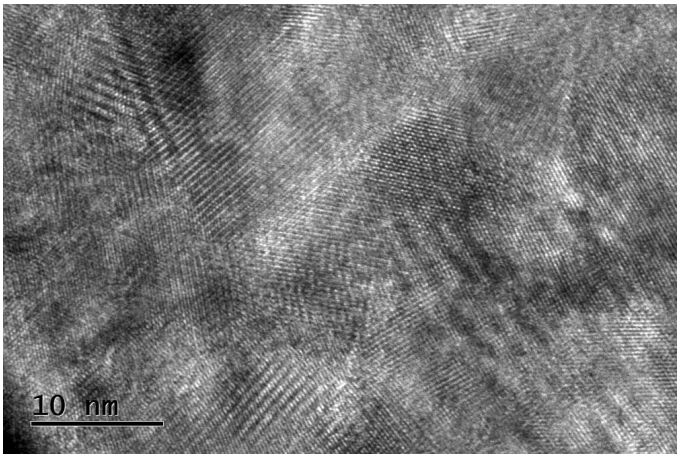


Figure 8.8: *Amorphous carbon with nanoparticles of ZrC and t/c-$ZrO_2$ within the transition layer obtained with Bright-Field Transmission Electron Microscopy (BFTEM) in* [302].

### 8.4.2 Modeling of the phase changes

As previously discussed, the region of interest where oxygen diffusion and the oxidation reaction front evolve in time is within the red dashed rectangle in Figure 8.7. Therefore, in this section, we describe the modeling approach employed to simulate the diffusion process occurring in the intermediate and transition layers within a peridynamic framework. We disregard, for now, the behavior of the cracked oxide, which can be modeled by the damage mechanism explained in Section 8.4.3. The ZrC oxidation involves three distinct phases: the oxygen-free zirconium carbide (ZrC), the partially-oxidized phase observed within the transition layer, and the unstable phase of zirconium oxide (t/c-$ZrO_2$) present within the intermediate layer. Hence, we name any peridynamic point lying in the carbide phase as "carbide point", in the partially-oxidized phase as "partially-oxidized point", and in the oxide phase as "oxide point".

Since the chemical reaction that transforms the ZrC into $ZrO_2$ is much faster than diffusion, we assume that the phase change between the two is instantaneous in the model. This diffusion-controlled reaction can be simulated as in the corrosion damage modeling by formulating the nonlocal (peridynamic) version of a simplified Nernst-Planck equation [128],

in which the micro-diffusivity (see Eqs. (8.1) and (8.2), and Remark 8.3) becomes:

$$k(\mathbf{x}, \mathbf{x}', t) = \begin{cases} d & \text{if } (\mathbf{x}, \mathbf{x}') \text{ is an oxide bond,} \\ r & \text{if } (\mathbf{x}, \mathbf{x}') \text{ is an interface bond,} \\ 0 & \text{if } (\mathbf{x}, \mathbf{x}') \text{ is any other bond,} \end{cases} \tag{8.7}$$

where:

- "Oxide bonds" are bonds connecting two (stable or unstable) oxide points. The micro-diffusivity $d$ models the diffusion within t/c-$ZrO_2$ phase and is calibrated to the classical diffusivity $D$.
- "Interface bonds" are bonds connecting a partially-oxidized point to an oxide point. The micro-oxidability $r$ models the diffusion-controlled reaction between ZrC and t/c-$ZrO_2$ taking place within the transition layer and is calibrated to the oxidation rate $R$.
- All the other bonds connecting partially-oxidized or carbide points have zero micro-diffusivity because oxygen diffusion does not occur in those phases.

Figure 8.9 illustrates the different types of bonds that are used in the peridynamic model.

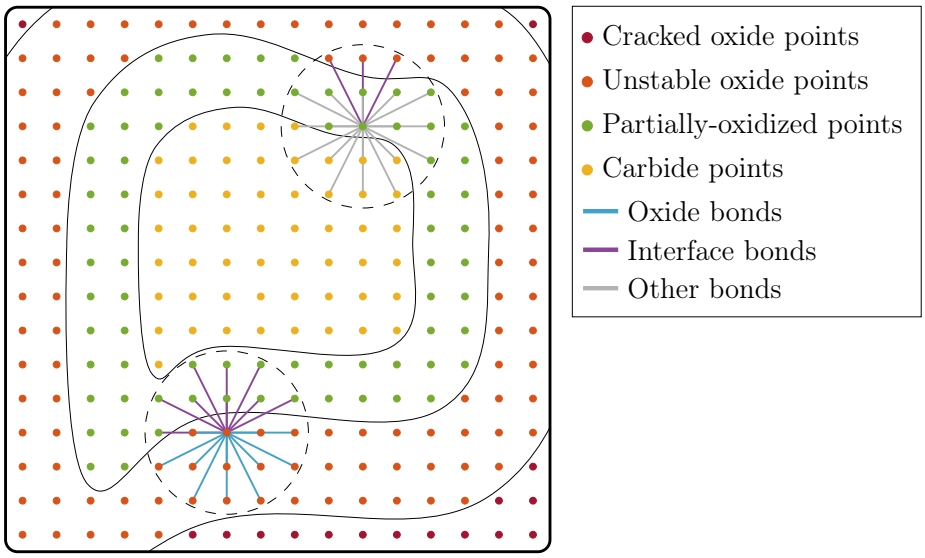


Figure 8.9: *Example of possible types of points and bonds.*

To distinguish between oxide and partially-oxidized points, a concentration threshold $\widehat{C}_p$ between the two phases is set. A partially-oxidized point transitions into an oxide node when its oxygen concentration is higher than this threshold. The value of the concentration $\widehat{C}_p$ can be derived from the experimental data as shown in Section 8.4.4. This straightforward mechanism enables the modeling of the phase change from ZrC to t/c-$ZrO_2$ and, simultaneously, governs the motion of the unstable oxide/ZrC interface.

As the oxygen content of the points within the transition layer starts to rise, a fraction of the zirconium carbide undergoes a transition to the oxidized phase. Since the zirconium

oxide expands in volume compared to the carbide, additional space becomes available for the oxygen to diffuse towards the carbide phase. With more oxygen available, the oxygen diffusion and, subsequently, the reaction rate would increase. This leads us to consider micro-oxidability not a constant, but a function of the oxygen concentration. Here, for simplicity, we consider a linear dependence between these two quantities in regions of partially-oxidized point:

$$r(\mathbf{x}, \mathbf{x}', t) = \left(\overline{r} - \frac{\widetilde{r}}{2}\right) + \frac{\widetilde{r}}{\widehat{C}_p} C(\mathbf{x}_{p\text{-}o}, t)\,, \tag{8.8}$$

where $C(\mathbf{x}_{p\text{-}o}, t)$ is the oxygen concentration of the partially-oxidized point, $\overline{r}$ is the average of the micro-oxidability of the interface bond, and $\widetilde{r}$ is the total variation of the micro-oxidability of the interface bond. The micro-oxidability as a linear function of the concentration of the partially-oxidized node of the interface bond is shown in Figure 8.10.

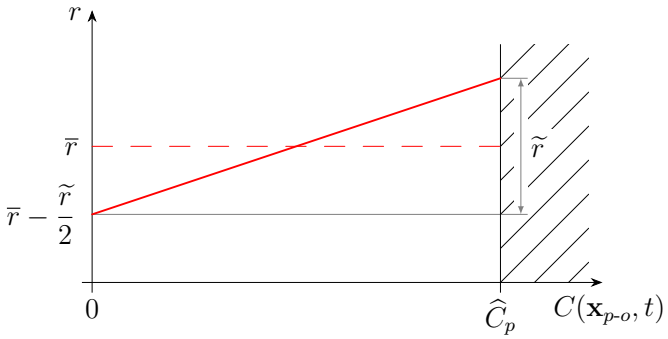


Figure 8.10: *Micro-oxidability $r$ of an interface bond as a linear function of the concentration $C(\mathbf{x}_{p\text{-}o}, t)$ of the partially-oxidized point. $\overline{r}$ is the average micro-oxidability and $\widetilde{r}$ is the total variation of the micro-oxidability for $C(\mathbf{x}_{p\text{-}o}, t)$ varying between 0 and the concentration $\widehat{C}_p$ at which phase change from partially-oxidized to oxide points happens.*

The values of micro-diffusivity $d$ and micro-oxidability $r$ (i.e., both $\overline{r}$ and $\widetilde{r}$) are calibrated via the discretized model presented in Sections 8.3.1 and 8.3.2 by comparison with the experimental observations (see Section 8.5.1). The effects these values have on the oxygen concentration profile are shown in the parametric studies in Appendix 8.B. Note that a constant value of micro-oxidability, i.e., $r = \overline{r} = \text{const.}$ with $\widetilde{r} = 0$, does not allow the peridynamic model to accurately reproduce the experimental concentration profile within the transition layer.

### 8.4.3 Concentration-driven model for damage evolution

In this work our focus lies on simulating only the effects of the cracked oxide on the intermediate layer. Voids are formed as a result of crack propagation and volumetric expansion within the stable phase of the oxide (m-$ZrO_2$), generating paths for the oxygen to unobstructedly flow towards the external boundary of the intermediate layer. This phenomenon can be effectively represented by a model in which the interface between the stable and unstable phases serves as a constant source of oxygen (at constant concentration).

Thus, to determine the extent of damaged oxide, we introduce an additional threshold for oxygen concentration, denoted as $\widehat{C}_d$. When the concentration at a given node overcomes

this threshold, the node is defined as damaged. Note that this simplified definition of damage does not include the simulation of crack propagation within the oxide, but, instead, models the effects cracks have on the evolution of the oxidation front. Once a node is classified as damaged, its concentration is set equal to the concentration $\widehat{C}_m$, namely the concentration that the oxide of the intermediate layer "feels" from the cracked oxide. The values of the concentrations $\widehat{C}_d$ and $\widehat{C}_m$ can be obtained from the experimental data as shown in the next section.

### 8.4.4 Data extracted from experiments

As shown in Figure 8.11, one can determine the appropriate concentration $\widehat{C}_m$ of the damaged oxide, the concentration $\widehat{C}_d$ between the damaged oxide and the intermediate layer, and the oxidation threshold $\widehat{C}_p$. The concentration $\widehat{C}_m$ of the cracked oxide can be established as the maximum concentration shown in Figure 8.11. To identify the damaged nodes, the concentration threshold $\widehat{C}_d$ corresponds to the highest concentration within the intermediate layer, i.e., the second-highest concentration in Figure 8.11. Regarding the concentration threshold $\widehat{C}_p$ for phase change, it can be selected as an intermediate value between the concentrations at the interface separating t/c-$ZrO_2$ and ZrC. The values of these concentration thresholds are reported in Figure 8.11 and in Table 8.1. It is worth noting that the threshold values are not univocally determined due to measurement uncertainties. However, we carried out several sensitivity studies showing that small deviations from the chosen values change only slightly the results.

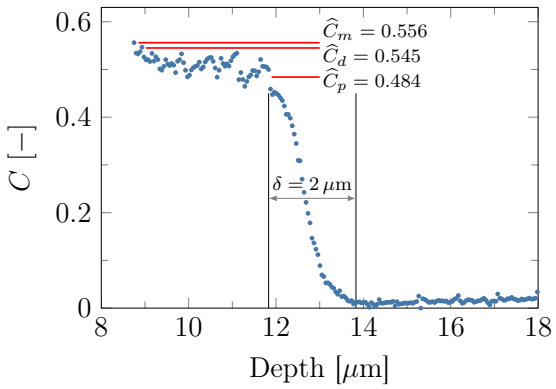


Figure 8.11: *Concentration thresholds derived by the normalized experimental data. The* $\sim 2$-$\mu m$ *thick transition layer is shown.*

Carbide points become partially-oxidized points when their oxygen concentration rises above 0. Since all the bonds connecting carbide or partially oxidized points have zero diffusivity, oxygen can diffuse into a carbide point only through the interface bonds. The maximum length of the interface bonds, as for every bond in the PD model, is equal to the horizon size $\delta$. Therefore, since interface bonds have one end in the oxide phase, the farthest point from the unstable oxide that can change phase from carbide to partially-oxidized is at a distance equal to $\delta$. This means that, in the PD model, the thickness of the transition layer has to be equal to the horizon size $\delta$. Hence, we select $\delta = 2$ $\mu$m, that is the thickness of

the transition layer in the experimental observations (see Figure 8.11), in the ZrC oxidation problem.

## 8.5 Numerical results for the evolution of the oxidation front in ZrC

In this section, we present the outcomes of the calibration process of the diffusivities, that allows to have good agreement between the experimental data and the 1D peridynamic model. For the first time, the micro-diffusivity of the intermediate layer and the micro-oxidability within the transition layer are accurately calibrated. Additionally, we present results from the 2D model of the same problem and qualitatively compare them with experimental data. For comparable 3D simulations, the present meshfree discretization becomes expensive and either a parallel implementation is required, or the use of the Fast Convolution-Based Method [179, 180].

### 8.5.1 Calibration of micro-diffusivity and micro-oxidability

The calibration of bond properties is carried out by using the discretization discussed in Sections 8.3.1 and 8.3.2 and comparing the 1D numerical results with the experimental observations. In the 1D peridynamic model, a time step size of $\Delta t = 0.01\,\mathrm{s}$ and a grid spacing of $\Delta x = 0.2\,\mu\mathrm{m}$ are used. As these values are reduced, the accuracy in time and space integration of the peridynamic equations is higher and this may lead to slightly different values of micro-diffusivity and micro-oxidability than those calibrated in this work.

Thanks to the discretized peridynamic model, we are able to calibrate the micro-diffusivity and micro-oxidability based on experimental data. Parametric studies on these values are shown in Appendix 8.B. In order to achieve a global concentration distribution similar to the experimental observations, the micro-diffusivity of the oxide is set at $d = 0.5\,\mu\mathrm{m/s}$, whereas the average micro-oxidability is $\overline{r} = 0.1\,\mu\mathrm{m/s}$ (the units of measurements are related to a 1D model, see Eq. (8.2)). To accurately reproduce the oxygen concentration profile within the transition layer, the variation of the micro-oxidability is chosen as $\widetilde{r} = 0.1\,\mu\mathrm{m}^2/\mathrm{s}$. This means that the micro-oxidability $r$ varies linearly between $0.05\,\mu\mathrm{m/s}$ and $0.15\,\mu\mathrm{m/s}$ depending on the concentration of the partially-oxidized node.

Table 8.1 reports the values of micro-diffusivity and micro-oxidability, along with the corresponding values of classical diffusivity ($D$) and oxidation rate ($\overline{R}$ and $\widetilde{R}$). The classical properties are obtained by multiplying the bond properties by $\delta$ (see Eq. (8.2)). In [14], the oxygen diffusivity was computed as $D = 0.09\,\mu\mathrm{m}^2/\mathrm{s}$ following some limiting assumptions (see Remark 8.1). Dropping those assumptions and using the proposed peridynamic model, the diffusivity is calibrated to be $D = 1\,\mu\mathrm{m}^2/\mathrm{s}$. Furthermore, the oxidation rate of the zirconium carbide has been determined for the first time: $R = 0.1 + 0.41\,C(\mathbf{x}_{p\text{-}o}, t)\ \mu\mathrm{m}^2/\mathrm{s}$, where $C(\mathbf{x}_{p\text{-}o}, t)$ is the oxygen concentration of the partially-oxidized point. Note that the classical oxidation rate varies linearly as the micro-oxidability, where the average oxidation rate is $\overline{R} = 0.2\,\mu\mathrm{m}^2/\mathrm{s}$ and the total variation of the oxidation rate is $\widetilde{R} = 0.2\,\mu\mathrm{m}^2/\mathrm{s}$ (see

Eq. (8.8)).

Table 8.1: *Calibration of the concentration thresholds and diffusivities for the ZrC oxidation.*

| Property | Value |
|---|---|
| Maximum concentration | $\widehat{C}_m = 0.556$ |
| Damage concentration | $\widehat{C}_d = 0.545$ |
| Phase change concentration | $\widehat{C}_p = 0.484$ |
| Oxide micro-diffusivity | $d = 0.5\,\mu\text{m/s}$ |
| Average micro-oxidability | $\overline{r} = 0.1\,\mu\text{m/s}$ |
| Variation of micro-oxidability | $\widetilde{r} = 0.1\,\mu\text{m/s}$ |
| Oxide diffusivity | $D = 1\,\mu\text{m}^2/\text{s}$ |
| Average oxidation rate | $\overline{R} = 0.2\,\mu\text{m}^2/\text{s}$ |
| Variation of oxidation rate | $\widetilde{R} = 0.2\,\mu\text{m}^2/\text{s}$ |
| Horizon size | $\delta = 2\,\mu\text{m}$ |

Figure 8.12 depicts the concentration distribution across the interface, for both the results of the numerical model and the experimental data. The numerical results exhibit a remarkable agreement with the experimental observations. Hence, we can conclude that the chosen values of micro-diffusivity and micro-oxidability employed in the peridynamic model are accurately calibrated.

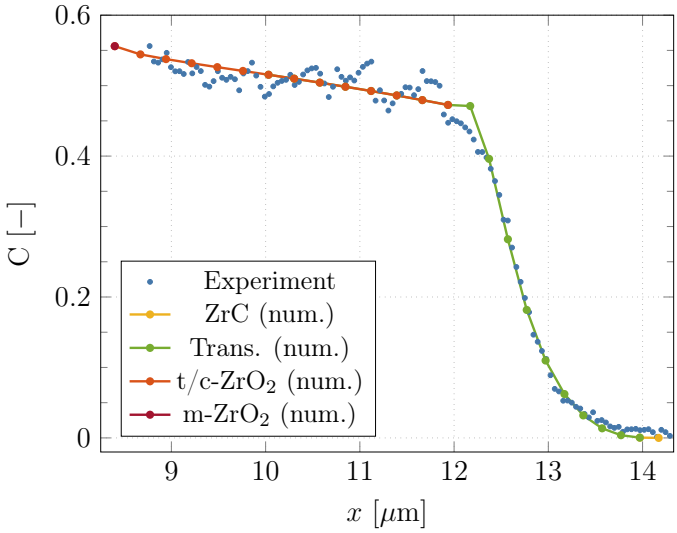


Figure 8.12: *Experimental data and numerical results of the concentration profile at $t = 480$ s. The numerical results are translated along the $x$-axis for visual reasons (see Remark 8.2).*

Figure 8.13 shows the progressive evolution of the concentration profile at different stages. The initial conditions are shown in Figure 8.13a, in which the node at the boundary has a concentration set to the value of $\widehat{C}_m$ and all the other nodes have no oxygen content. A transient occurs at the beginning of the simulation (see Figure 8.13b), after which the concentration pattern, in a steady-state condition, gradually advances within the material (see Figures 8.13c and 8.13d).

Since the oxide phase is subjected to volume expansion during the phase change, we need to post-process the results in order to estimate the growth of the oxide thickness. Note that the peridynamic approach presented in this paper does not model the volumetric expansion of the oxide phase. This volumetric expansion and the subsequent induced stresses that result in the fragmentation of the oxide will be modeled in future work. By considering a perfect crystal structure, it has been determined that m-$ZrO_2$ exhibits a volume increase of 36% compared to the carbide. Based on this calculations, we estimate in the post-processing stage the thickness of the oxide in the numerical model by increasing the volume of the region occupied by oxide nodes by 36%. Hence, Figure 8.14 illustrates that the oxidation interface penetrates the material at a constant velocity, in agreement with the experimental results. It is worth noting that the peridynamic model not only successfully reproduces the linear growth of the oxide but also accurately matches the interface velocity observed in the experiments.

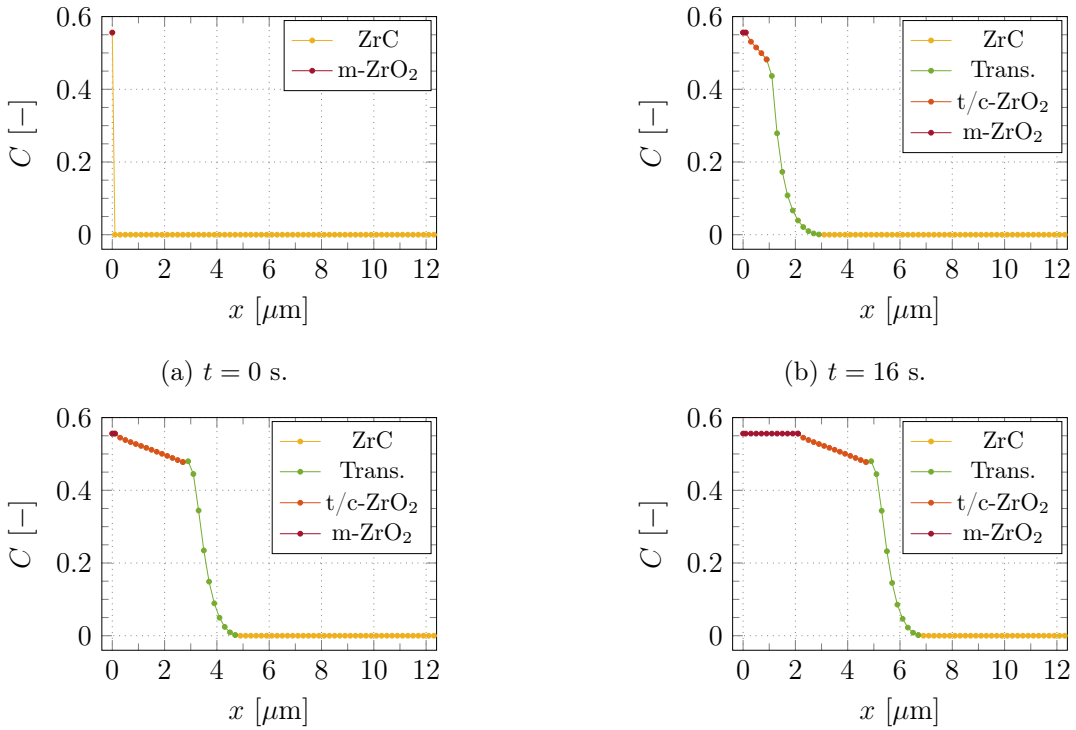


(a) $t = 0$ s. (b) $t = 16$ s.

(c) $t = 40$ s. (d) $t = 80$ s.

Figure 8.13: *Normalized oxygen concentration profile at different time instants.*

### 8.5.2 Results from a 2D model

After successfully calibrating the bond properties in the 1D model, we now extend its application to a 2D scenario. The discretization presented in Sections 8.3.1 and 8.3.2 is valid also in 2D. The quadrature coefficients are computed with the algorithm presented in [235]. The PD model of ZrC oxidation can be used both for predicting the growth of the oxide (as in the previous section) and for determining the shape and dimensions of the remaining unoxidized carbide. This section specifically focuses on the latter aspect.

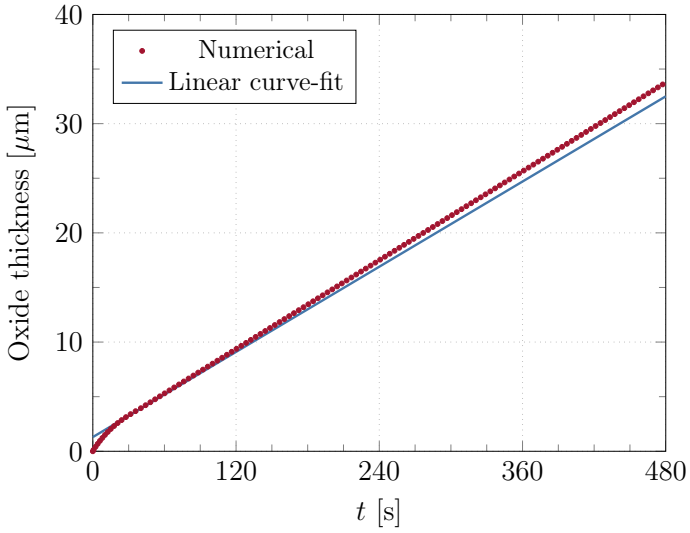


Figure 8.14: *Oxide growth obtained with the proposed model compared to the experimental results. The linear curve-fit of the experimental data has been translated along y-axis for visual reasons (see Remark 8.2).*

As illustrated in Figure 8.15 taken from [302], the cubic zirconium carbide sample undergoes a transformation under an oxidizing environment, transitioning from its initial square shape with sharp corners to a more rounded and eventually spherical shape. This change in morphology occurs due to the accelerated oxidation process at the corners, leading to a faster degradation of material in those regions. Therefore, we expect to obtain the transition from a square to a circular shape of the ZrC in the numerical results of the 2D peridynamic model, in a similar way in which the cube leads to a sphere in the actual experiments (see [302] and Figure 8.15).

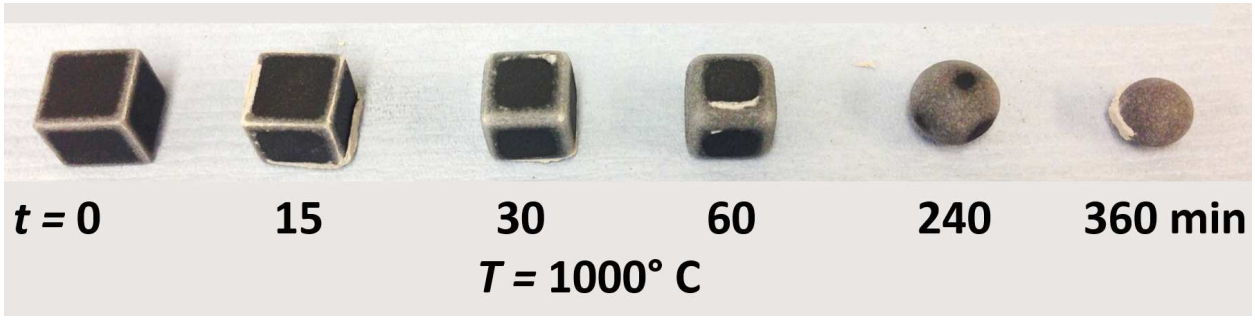


Figure 8.15: *Shape of the carbide (black material in the bottom portion of the figure) as the oxidation of the sample progresses* [302].

Peridynamics, due to its nonlocal nature, is known for its high computational cost. Thus, we chose to simulate the oxidation of ZrC in a smaller sample size. As a result, the transition from a square to a circular shape occurs at a faster rate than in the experiment shown in Figure 8.15. However, this also implies that a quantitative comparison between the numerical and experimental results is not possible, and only a qualitative comparison can be made.

The 2D model utilized the same classical material parameters (refer to Table 8.1) obtained through the calibration process in the 1D scenario. Therefore, using Eq. (8.2) in the 2D case, the micro-diffusivity is $d \approx 0.32\ \mathrm{s}^{-1}$, the average micro-oxidability is $\overline{r} \approx 0.06\ \mathrm{s}^{-1}$ and the

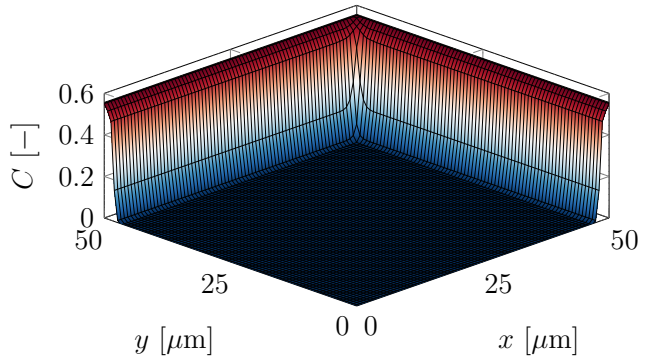


(a) $t = 20$ s.

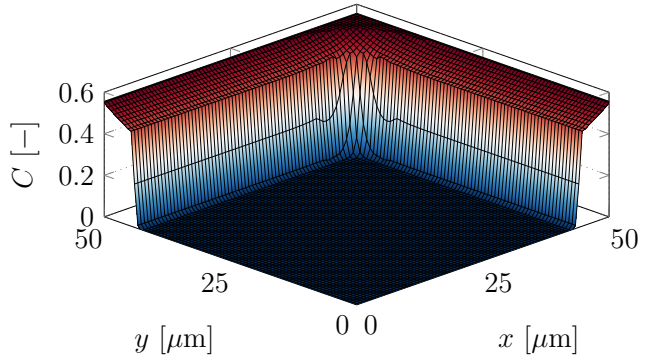


(b) $t = 100$ s.

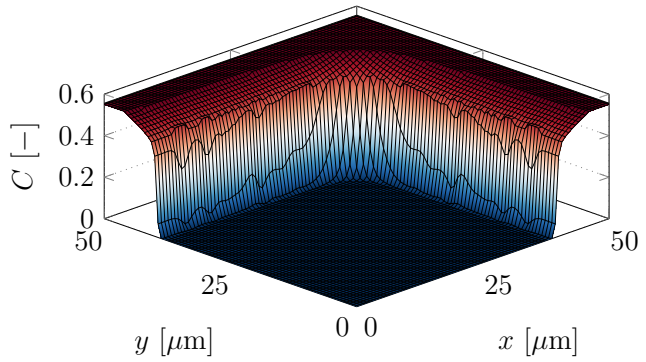


(c) $t = 240$ s.

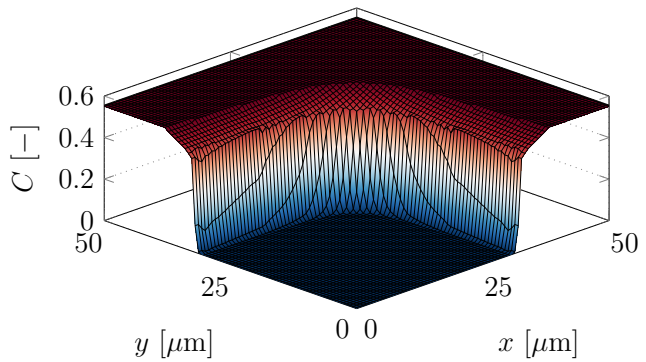


(d) $t = 480$ s.

Figure 8.16: *Normalized oxygen concentration field at different time instants (displayed for one fourth of the square sample thanks to the symmetries of the problem).*

variation of micro-oxidability is $\widetilde{r} \approx 0.06\ \mathrm{s}^{-1}$ (the units of measurements are related to

a 2D PD model). The computational domain chosen for the 2D simulation is a square with dimensions of $100 \times 100\ \mu\text{m}^2$. A time step size of $\Delta t = 0.01\,\text{s}$ and a grid spacing of $\Delta x = 0.667\,\mu\text{m}$ are used. Similarly to the 1D case, the initial conditions prescribe that the concentrations of the nodes at the boundary are set equal to $\widehat{C}_m$, whereas all other nodes have no oxygen content.

Figure 8.16 shows the evolution of the concentration field at various time steps during the simulation. The dark blue region represents zirconium carbide with no oxygen concentration. Initially (see Figure 8.16a), the carbide shape is square with sharp corners. As the oxidation front progresses within the material, the square corners gradually become rounder, as evidenced in Figures 8.16b and 8.16c. In the final stage of the simulation (see Figure 8.16d), the carbide shape approximates a quasi-circular form, which is consistent with the observations from the experimental results in [302].

## 8.6 Conclusions

Zirconium carbide has recently gained major interest due to its promising properties in nuclear applications for both energy production or space missions. However, its low resistance to oxidation leads to volume expansion and associated stresses that crack/damage the oxide layer. In this work, we shed light on the evolution of oxidation process by analyzing the oxygen concentration profile obtained from experimental data using $^{18}\text{O}$ as a tracer and modeling oxygen diffusion and oxidation processes using a peridynamic (PD) model that accounts for the volume expansion of the oxide and the effects of the cracked stable-oxide layer on the ZrC oxidation process.

We have quantified, for the first time, the oxidation rate across the transition layer between the zirconium carbide and the intermediate layer of thermodynamically unstable oxide. Peridynamics has been used to model the diffusion-controlled oxidation with an autonomously moving interface and simulate the bulk phase transformazion of sintered pellets of ZrC. The phase changes are determined by oxygen concentration thresholds, which are derived from experimental observations. The horizon size, i.e., the size of nonlocality in the peridynamic model, is selected so that it matches the thickness of the transition layer measured in experiments. Additionally, a simple yet effective damage mechanism has been introduced to model the expected influence of crack growth on the oxygen diffusion in the outer layer of oxide.

The peridynamic model allowed us to calibrate the properties of oxygen diffusion in the intermediate layer and oxidation rate in the transition layer. Through this calibration process, the concentration profile across the reaction layer and the velocity of the interface were reproduced in excellent agreement with the experimental results. Furthermore, we successfully carried out a qualitative simulation of the model in 2D.

The developed peridynamic model is not limited to the simulation of the oxidation of zirconium carbide. Indeed, it can be used for any phenomenon with similar characteristics, such as oxidation of transition metal carbides of group IV and lithiation in solid-state batteries, by recalibrating to the diffusion properties of the specific material system. The proposed model allows to estimate the growth of the oxide and determine the shape and di-

mensions of the remaining carbide phase. The model will be further improved in future work by introducing the coupling with the mechanical field to simulate the actual crack/damage initiation and propagation within the oxide. This advancement is expected to enable the model to reproduce the Maltese-cross shape of zirconia and provide a more general framework for simulating the chemo-mechanical behavior of zirconium carbide and other carbides of interest for energy applications, including nuclear ones.

# Appendices

## 8.A Imposition of peridynamic boundary conditions via the surface node method

To impose the peridynamic boundary conditions, we adopt the surface node method [249]. A new type of nodes, i.e., the *surface nodes*, are introduced to discretize the boundary of the body, as depicted in Figure 8.6: in 1D, 2D and 3D each surface node represents respectively a boundary point, a segment of length $\Delta x$ and a square with area $\Delta x^2$. A surface node $\mathbf{x}_s$ with normal $\mathbf{n}_s$ is governed by the following equation based on the concept of peridynamic flux [249]:

$$J(\mathbf{x}_s, \mathbf{n}_s, t) = -\sum_{pq \in \mathcal{I}} \alpha_{pq}\, \mathrm{j}(\mathbf{x}_p, \mathbf{x}_q, t)\, (\mathbf{m}_{pq} \cdot \mathbf{n}_s)\, \beta_{pq}\, \Delta x^{N+1}\,, \tag{8.9}$$

where $J$ is the external flux, $\mathcal{I}$ is the set of all the bonds, $\mathbf{m}_{pq}$ is the bond direction unit vector, and $N$ is the number of dimensions of the model. $\alpha_{pq}$ is a coefficient given as follows (see [236, 249] for more details and figures):

- In 1D, 2D or 3D, $\alpha_{pq} = 0$ if the bond does not intersect the boundary region associated to the surface node $s$.
- In 3D, $\alpha_{pq} = 1/4$ if the bond intersects the corner of the square associated to the surface node $s$ (the bond is "shared" among four surface nodes) or $\alpha_{pq} = 1/2$ if the bond intersects the edge of the square (the bond is "shared" between two surface nodes).
- In 2D, $\alpha_{pq} = 1/2$ if the bond intersects the end of the segment associated to the surface node $s$ (the bond is "shared" between two surface nodes).
- $\alpha_{pq} = 1$ otherwise.

The boundary conditions can be imposed directly on the surface nodes as one would do in a local model [249]: a concentration $\overline{C}(t)$ at a surface node $s$ is imposed as $C(\mathbf{x}_s, t) = \overline{C}(t)$ and a flux $\overline{J}(t)$ through the surface node $s$ is imposed as $J(\mathbf{x}_s, \mathbf{n}_s, t) = \overline{J}(t)$.

## 8.B Parametric studies

The modeling approach using the peridynamic framework described in Section 8.4 is based on the calibration of the values of micro-diffusivity $d$ of the oxide phase and the micro-oxidability $r$. The micro-oxidability is modeled as a linear function of the oxygen concentration of the partially-oxidized node, and is univocally determined by the values of the average micro-oxidability $\overline{r}$ and the micro-oxidability variation $\widetilde{r}$ (see Eq. (8.8)). In this section, we perform two parametric studies to show how the "shape" of the concentration profile across the oxidation interface changes depending on the ratios $d/\overline{r}$ and $\widetilde{r}/\overline{r}$.

The numerical results of the normalized oxygen concentration for different values of the ratio $d/\overline{r}$ are shown in Figure 8.17. It is evident that, by increasing $d/\overline{r}$, the velocity of the

oxidation front is higher and the thickness of the intermediate layer is reduced. Differences in oxygen concentration profiles within the transition layer are negligible. These results are used in Section 8.5.1 for the calibration of the ratio $d/\overline{r}$ in order to obtain in the numerical model a thickness of the intermediate layer similar to the one observed in the experiments. In the model of ZrC oxidation, the chosen value of $d/\overline{r}$ is 5.

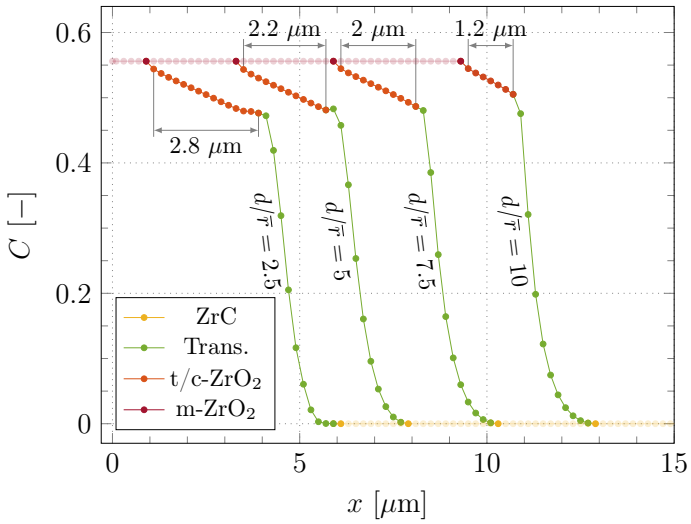


Figure 8.17: *Normalized oxygen concentration across the oxidation interface at* $t = 100\,\mathrm{s}$ *for different ratios between the micro-diffusivity* $d$ *of the oxide phase and the average micro-oxidability* $\overline{r}$*. The plots are obtained by using a value of average micro-oxidability equal to* $\overline{r} = 0.1\,\mu\mathrm{m/s}$*.*

The value of the ratio $\widetilde{r}/\overline{r}$ affects the normalized oxygen concentration profile only within the transition layer, as shown in Figure 8.18. For higher values of the ratio $\widetilde{r}/\overline{r}$, the steepness of the concentration distribution in the transition layer increases accordingly. Therefore, the appropriate value of $\widetilde{r}/\overline{r}$ is chosen in Section 8.5.1 to reproduce the experimental observations. In the model of ZrC oxidation, the chosen value of $\widetilde{r}/\overline{r}$ is 1.

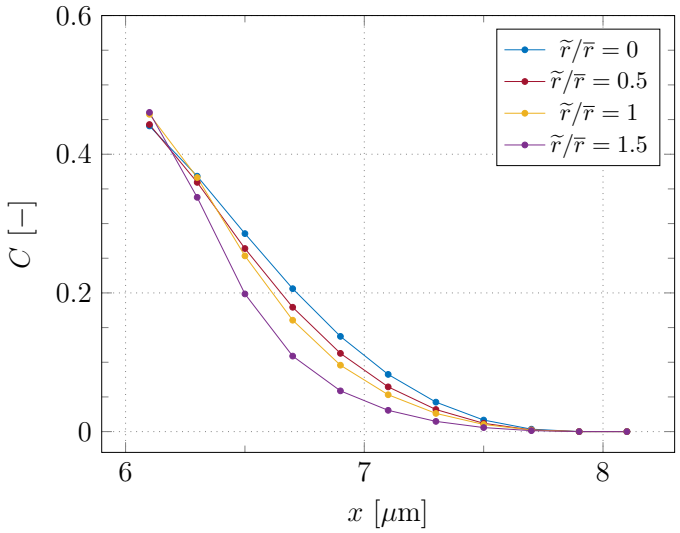


Figure 8.18: *Normalized oxygen concentration within the transition layer at* $t = 100\,\mathrm{s}$ *for different ratios between the micro-oxidability variation* $\widetilde{r}$ *and the average micro-oxidability* $\overline{r}$*. The plots are obtained by using a value of average micro-oxidability equal to* $\overline{r} = 0.1\,\mu\mathrm{m/s}$*.*

# Chapter 9

# Conclusions and future developments

## 9.1 Final remarks

The main objective of this work was to improve the numerical applications of the peridynamic theory by:

- correcting the surface effect,
- imposing local boundary conditions, and
- developing an algorithm for the accurate computation of the quadrature weights.

The improved numerical methods can then be applied in a small portion (where cracks are more likely to propagate) of a possibly very large structure thanks to the coupling with numerical methods based on classical continuum mechanics, such as the finite element method or the Carrera unified formulation. Furthermore, a complex multi-physics phenomenon, i.e., the oxidation of zirconium carbide, was addressed with the above-mentioned numerical tools based on peridynamics.

The main results of this work are presented in the papers in the list of page 15, and are as follows:

- The development of algorithms to numerically compute the peridynamic stress tensor and the force flux in 1D, 2D, and 3D models (Papers 1, 2 and 3).
- The analytical and numerical analysis of the peridynamic surface effect and of its characteristic hardening/softening behavior near the boundaries of a body in ordinary state-based peridynamics (Papers 1 and 2).
- The definition of the Taylor-based extrapolation method with the nearest-node strategy to determine the displacements of the fictitious nodes for any (possibly complex) geometry of the body (Papers 1, 2 and 3).
- The development of algorithms to numerically impose of local boundary conditions in peridynamic models through the surface node method. That is achieved by discretizing the boundary of the body with the surface nodes and by using the equation of the force flux to govern their motion (Paper 3).

- The development of an efficient algorithm to accurately compute the quadrature weights in 2D and 3D peridynamic models. That produces a smoother convergence behavior of the numerical peridynamic solution (Paper 4).
- The definition of a coupling technique between peridynamics and Carrera unified formulation that reduces spurious effects at interfaces (Paper 5).
- The derivation of a stability criterion for an explicit time integration method applied to the peridynamic diffusion equation. The new stability criterion takes into account the effect of the boundary conditions imposed with the surface node method (Paper 6).
- The numerical analysis of the convergence behavior of a peridynamic diffusion problem with discontinuity at the boundary in the initial conditions (Paper 6).
- The development of a peridynamic model able to predict the growth of the oxide and determine the shape and dimensions of the remaining unoxidized carbide (Paper7).

All algorithms and numerical methods mentioned above were validated by multiple practical examples by comparing the numerical results with either analytical solutions or experimental observations.

## 9.2 Future research activities

The peridynamic model of zirconium carbide oxidation will be improved by introducing the coupling with the mechanical field to simulate the actual crack initiation and propagation within the oxide. This advancement is expected to enable the model to reproduce the Maltese-cross shape of zirconia and to have an even better agreement with the experimental observations. Furthermore, phenomena similar to zirconium carbide oxidation, such as oxidation of transition metal carbides of group IV and lithiation in solid-state batteries, can be simulated with the same model if a recalibration of the diffusion properties of the specific material system is performed. Therefore, my future research goal is to develop a more general framework for simulating the chemo-mechanical behavior of oxidation and lithiation phenomena. The peridynamic theory is particularly suitable for modeling these phenomena because the motion of interfaces and the propagation of cracks can be directly embedded in a general constitutive model of the material. This is not possible in numerical methods based on classical continuum mechanics, such as interface elements with cohesive zone modeling, extended finite element method or phase field method, which require special criteria at interfaces and crack surfaces.

# Bibliography


[1] O. Amman, T. Von Kármán, and G. Woodruff, "The failure of the Tacoma Narrows Bridge," 1941, URL: authors.library.caltech.edu/45680/.

[2] A. Lichtenstein, "The silver bridge collapse recounted," *Journal of Performance of Constructed Facilities*, vol. 7, no. 4, pp. 249–261, 1993, DOI: 10.1061/(ASCE)0887-3828(1993)7:4(249).

[3] G. Calvi, M. Moratti, G. O'Reilly, N. Scattarreggia, R. Monteiro, D. Malomo, P. Calvi, and R. Pinho, "Once upon a time in Italy: The tale of the Morandi Bridge," *Structural Engineering International*, vol. 29, no. 2, pp. 198–217, 2019, DOI: 10.1080/10168664.2018.1558033.

[4] W. Hendricks, "The Aloha Airlines accident—a new era for aging aircraft," in *Structural integrity of aging airplanes*, URL: 10.1007/978-3-642-84364-8_11, Springer, 1991, pp. 153–165.

[5] B. Murphy, J. O'Callaghan, M. Fox, L. Ilcewicz, and J. Starnes, "Overview of the structures investigation for the American Airlines Flight 587 investigation," in *46th AIAA/ASME/ASCE/AHS/ASC Structures, Structural Dynamics and Materials Conference*, DOI: 10.2514/6.2005-2251, 2005, p. 2251.

[6] A. Kemp, J. Dalal, U. Tassawar, and C. Lu, "Safety analysis of uncontained engine failure-Southwest Airlines Flight 1380," *International Journal of Crisis Management*, vol. 11, no. 1, pp. 13–23, 2021, DOI: 10.6929/IJCM.202101_11(1).0002.

[7] A. Osiptsov, "Fluid mechanics of hydraulic fracturing: A review," *Journal of Petroleum Science and Engineering*, vol. 156, pp. 513–535, 2017, DOI: 10.1016/j.petrol.2017.05.019.

[8] B. Chen, B. Barboza, Y. Sun, J. Bai, H. Thomas, M. Dutko, M. Cottrell, and C. Li, "A review of hydraulic fracturing simulation," *Archives of Computational Methods in Engineering*, pp. 1–58, 2021, DOI: 10.1007/s11831-021-09653-z.

[9] E. Reis, J. Mozer, A. Bianchini, and C. Kesler, "Causes and control of cracking in concrete reinforced with high-strength steel bars: A review of research," *University of Illinois. Engineering Experiment Station. Bulletin; no. 479*, 1965, URL: ideals.illinois.edu/items/119862.

[10] O. Selezneva, M. Darter, D. Zollinger, and S. Shoukry, "Characterization of transverse cracking spatial variability: Use of long-term pavement performance data for continuously reinforced concrete pavement design," *Transportation Research Record*, vol. 1849, no. 1, pp. 147–155, 2003, DOI:10.3141/1849-16.

[11] G. McKenzie, B. Samali, and C. Zhang, "Design criteria for a controlled demolition (implosion)," *GEOMATE Journal*, vol. 16, no. 53, pp. 101–112, 2019, DOI: 10.21660/2019.53.90374.

[12] J. Williams, Y. Patel, and B. Blackman, "A fracture mechanics analysis of cutting and machining," *Engineering Fracture Mechanics*, vol. 77, no. 2, pp. 293–308, 2010, DOI: 10.1016/j.engfracmech.2009.06.011.

[13] C. Gasparrini, R. Podor, D. Horlait, R. Chater, and W. Lee, "Zirconium carbide oxidation: Maltese cross formation and interface characterization," *Oxidation of Metals*, vol. 88, pp. 509–519, 2017, DOI: 10.1007/s11085-016-9672-6.

[14] C. Gasparrini, R. Chater, D. Horlait, L. Vandeperre, and W. Lee, "Zirconium carbide oxidation: Kinetics and oxygen diffusion through the intermediate layer," *Journal of the American Ceramic Society*, vol. 101, no. 6, pp. 2638–2652, 2018, DOI: 10.1111/jace.15479.

[15] M. McDowell, S. Lee, W. Nix, and Y. Cui, "25th anniversary article: Understanding the lithiation of silicon and other alloying anodes for lithium-ion batteries," *Advanced Materials*, vol. 25, no. 36, pp. 4966–4985, 2013, DOI: 10.1002/adma.201301795.

[16] V. Deshpande and R. McMeeking, "Models for the interplay of mechanics, electrochemistry, thermodynamics, and kinetics in lithium-ion batteries," *Applied Mechanics Reviews*, vol. 75, no. 1, p. 010 801, 2023, DOI: 10.1115/1.4056289.

[17] O. Zienkiewicz, R. Taylor, and J. Zhu, *The finite element method: Its basis and fundamentals*. Elsevier, 2005, DOI:10.1016/C2009-0-24909-9.

[18] O. Zienkiewicz and R. Taylor, *The finite element method for solid and structural mechanics*. Elsevier, 2005, DOI:10.1016/C2009-0-26332-X.

[19] G. Johnson and R. Stryk, "Eroding interface and improved tetrahedral element algorithms for high-velocity impact computations in three dimensions," *International Journal of Impact Engineering*, vol. 5, no. 1-4, pp. 411–421, 1987, DOI: 10.1016/0734-743X(87)90057-1.

[20] T. Belytschko and J. Lin, "A three-dimensional impact-penetration algorithm with erosion," *International Journal of Impact Engineering*, vol. 5, no. 1-4, pp. 111–127, 1987, DOI: 10.1016/0734-743X(87)90033-9.

[21] H. Lee, J. Choi, K. Jung, and Y. Im, "Application of element deletion method for numerical analyses of cracking," *Journal of Achievements in Materials and Manufacturing Engineering*, vol. 35, no. 2, pp. 154–161, 2009, URL: jamme.acmsse.h2.pl/papers_vol35_2/3526.pdf.

[22] J. Song, H. Wang, and T. Belytschko, "A comparative study on finite element methods for dynamic fracture," *Computational Mechanics*, vol. 42, no. 2, pp. 239–250, 2008, DOI: 10.1007/s00466-007-0210-x.

[23] M. Elices, G. Guinea, J. Gomez, and J. Planas, "The cohesive zone model: Advantages, limitations and challenges," *Engineering Fracture Mechanics*, vol. 69, no. 2, pp. 137–163, 2002, DOI: 10.1016/S0013-7944(01)00083-2.

[24] M. Gift, P. Selvakumar, and S. Alexis, "A review on the cohesive zone models for crack propagation analysis," *The Journal of Mechanical*, pp. 12 760–12 763, 2013, URL: elixirpublishers.com/articles/1679462023_201405045.

[25] W. Wciślik and T. Pała, "Selected aspects of cohesive zone modeling in fracture mechanics," *Metals*, vol. 11, no. 2, p. 302, 2021, DOI: 10.3390/met11020302.

[26] G. Camacho and M. Ortiz, "Computational modelling of impact damage in brittle materials," *International Journal of Solids and Structures*, vol. 33, no. 20-22, pp. 2899–2938, 1996, DOI: 10.1016/0020-7683(95)00255-3.

[27] J. Rimoli, J. Rojas, and F. Khemani, "On the mesh dependency of cohesive zone models for crack propagation analysis," in *53rd AIAA/ASME/ASCE/AHS/ASC Structures, Structural Dynamics and Materials Conference 20th AIAA/ASME/AHS Adaptive Structures Conference 14th AIAA*, DOI: 10.2514/6.2012-1536, 2012, p. 1536.

[28] N. Moës, J. Dolbow, and T. Belytschko, "A finite element method for crack growth without remeshing," *International Journal for Numerical Methods in Engineering*, vol. 46, no. 1, pp. 131–150, 1999, DOI: 10.1002/(SICI)1097-0207(19990910)46:1<131::AID-NME726>3.0.CO;2-J.

[29] B. Karihaloo and Q. Xiao, "Modelling of stationary and growing cracks in FE framework without remeshing: A state-of-the-art review," *Computers & Structures*, vol. 81, no. 3, pp. 119–129, 2003, DOI:10.1016/S0045-7949(02)00431-5.

[30] Y. Abdelaziz and A. Hamouine, "A survey of the extended finite element," *Computers & structures*, vol. 86, no. 11-12, pp. 1141–1151, 2008, DOI: 10.1016/j.compstruc.2007.11.001.

[31] T. Fries and T. Belytschko, "The extended/generalized finite element method: An overview of the method and its applications," *International Journal for Numerical Methods in Engineering*, vol. 84, no. 3, pp. 253–304, 2010, DOI: 10.1002/nme.2914.

[32] A. Menk and S. Bordas, "A robust preconditioning technique for the extended finite element method," *International Journal for Numerical Methods in Engineering*, vol. 85, no. 13, pp. 1609–1632, 2011, DOI: 10.1002/nme.3032.

[33] I. Babuška and U. Banerjee, "Stable generalized finite element method (SGFEM)," *Computer Methods in Applied Mechanics and Engineering*, vol. 201, pp. 91–111, 2012, DOI: 10.1016/j.cma.2011.09.012.

[34] Q. Zhang, I. Babuška, and U. Banerjee, "Robustness in stable generalized finite element methods (SGFEM) applied to Poisson problems with crack singularities," *Computer Methods in Applied Mechanics and Engineering*, vol. 311, pp. 476–502, 2016, DOI: 10.1016/j.cma.2016.08.019.

[35] C. Cui, Q. Zhang, U. Banerjee, and I. Babuška, "Stable generalized finite element method (SGFEM) for three-dimensional crack problems," *Numerische Mathematik*, vol. 152, no. 2, pp. 475–509, 2022, DOI: 10.1007/s00211-022-01312-0.

[36] J. Chessa, H. Wang, and T. Belytschko, "On the construction of blending elements for local partition of unity enriched finite elements," *International Journal for Numerical Methods in Engineering*, vol. 57, no. 7, pp. 1015–1038, 2003, DOI:10.1002/nme.777.

[37] T. Fries, "A corrected XFEM approximation without problems in blending elements," *International Journal for Numerical Methods in Engineering*, vol. 75, no. 5, pp. 503–532, 2008, DOI: 10.1002/nme.2259.

[38] J. Tarancón, A. Vercher, E. Giner, and F. Fuenmayor, "Enhanced blending elements for XFEM applied to linear elastic fracture mechanics," *International Journal for Numerical Methods in Engineering*, vol. 77, no. 1, pp. 126–148, 2009, DOI: 10.1002/nme.2402.

[39] J. Bellec and J. Dolbow, "A note on enrichment functions for modelling crack nucleation," *Communications in Numerical Methods in Engineering*, vol. 19, no. 12, pp. 921–932, 2003, DOI:10.1002/cnm.641.

[40] C. Daux, N. Moës, J. Dolbow, N. Sukumar, and T. Belytschko, "Arbitrary branched and intersecting cracks with the extended finite element method," *International Journal for Numerical Methods in Engineering*, vol. 48, no. 12, pp. 1741–1760, 2000, DOI: 10.1002/1097-0207(20000830)48:12<1741::AID-NME956>3.0.CO;2-L.

[41] T. Belytschko, N. Moës, S. Usui, and C. Parimi, "Arbitrary discontinuities in finite elements," *International Journal for Numerical Methods in Engineering*, vol. 50, no. 4, pp. 993–1013, 2001, DOI: 10.1002/1097-0207(20010210)50:4<993::AID-NME164>3.0.CO;2-M.

[42] G. Zi, J. Song, E. Budyn, S. Lee, and T. Belytschko, "A method for growing multiple cracks without remeshing and its application to fatigue crack growth," *Modelling and Simulation in Materials Science and Engineering*, vol. 12, no. 5, p. 901, 2004, DOI:10.1088/0965-0393/12/5/009.

[43] E. Budyn, G. Zi, N. Moës, and T. Belytschko, "A method for multiple crack growth in brittle materials without remeshing," *International Journal for Numerical Methods in Engineering*, vol. 61, no. 10, pp. 1741–1770, 2004, DOI:10.1002/nme.1130.

[44] J. Song and T. Belytschko, "Cracking node method for dynamic fracture with finite elements," *International Journal for Numerical Methods in Engineering*, vol. 77, no. 3, pp. 360–385, 2009, DOI: 10.1002/nme.2415.

[45] D. Xu, Z. Liu, X. Liu, Q. Zeng, and Z. Zhuang, "Modeling of dynamic crack branching by enhanced extended finite element method," *Computational Mechanics*, vol. 54, pp. 489–502, 2014, DOI: 10.1007/s00466-014-1001-9.

[46] G. Francfort and J. Marigo, "Revisiting brittle fracture as an energy minimization problem," *Journal of the Mechanics and Physics of Solids*, vol. 46, no. 8, pp. 1319–1342, 1998, DOI: 10.1016/S0022-5096(98)00034-9.

[47] B. Bourdin, G. Francfort, and J. Marigo, "Numerical experiments in revisited brittle fracture," *Journal of the Mechanics and Physics of Solids*, vol. 48, no. 4, pp. 797–826, 2000, DOI: 10.1016/S0022-5096(99)00028-9.

[48] B. Bourdin, G. Francfort, and J. Marigo, "The variational approach to fracture," *Journal of elasticity*, vol. 91, pp. 5–148, 2008, DOI: 10.1007/s10659-007-9107-3.

[49] H. Amor, J. Marigo, and C. Maurini, "Regularized formulation of the variational brittle fracture with unilateral contact: Numerical experiments," *Journal of the Mechanics and Physics of Solids*, vol. 57, no. 8, pp. 1209–1229, 2009, DOI: 10.1016/j.jmps.2009.04.011.

[50] V. Hakim and A. Karma, "Laws of crack motion and phase-field models of fracture," *Journal of the Mechanics and Physics of Solids*, vol. 57, no. 2, pp. 342–368, 2009, DOI: 10.1016/j.jmps.2008.10.012.

[51] B. Bourdin, C. Larsen, and C. Richardson, "A time-discrete model for dynamic fracture based on crack regularization," *International journal of fracture*, vol. 168, pp. 133–143, 2011, DOI: 10.1007/s10704-010-9562-x.

[52] J. Wu, V. Nguyen, C. Nguyen, D. Sutula, S. Sinaie, and S. Bordas, "Phase-field modeling of fracture," *Advances in Applied Mechanics*, vol. 53, pp. 1–183, 2020, DOI: 10.1016/bs.aams.2019.08.001.

[53] C. Miehe, M. Hofacker, and F. Welschinger, "A phase field model for rate-independent crack propagation: Robust algorithmic implementation based on operator splits," *Computer Methods in Applied Mechanics and Engineering*, vol. 199, no. 45-48, pp. 2765–2778, 2010, DOI: 10.1016/j.cma.2010.04.011.

[54] C. Miehe, F. Welschinger, and M. Hofacker, "Thermodynamically consistent phase-field models of fracture: Variational principles and multi-field FE implementations," *International Journal for Numerical Methods in Engineering*, vol. 83, no. 10, pp. 1273–1311, 2010, DOI: 10.1002/nme.2861.

[55] M. Hofacker and C. Miehe, "A phase field model of dynamic fracture: Robust field updates for the analysis of complex crack patterns," *International Journal for Numerical Methods in Engineering*, vol. 93, no. 3, pp. 276–301, 2013, DOI: 10.1002/nme.4387.

[56] M. Borden, C. Verhoosel, M. Scott, T. Hughes, and C. Landis, "A phase-field description of dynamic brittle fracture," *Computer Methods in Applied Mechanics and Engineering*, vol. 217, pp. 77–95, 2012, DOI: 10.1016/j.cma.2012.01.008.

[57] J. Mehrmashhadi, M. Bahadori, and F. Bobaru, "On validating peridynamic models and a phase-field model for dynamic brittle fracture in glass," *Engineering Fracture Mechanics*, vol. 240, p. 107 355, 2020, DOI: 10.1016/j.engfracmech.2020.107355.

[58] N. Grilli, C. Duarte, and M. Koslowski, "Dynamic fracture and hot-spot modeling in energetic composites," *Journal of Applied Physics*, vol. 123, no. 6, p. 065 101, 2018, DOI: 10.1063/1.5009297.

[59] C. Duarte, N. Grilli, and M. Koslowski, "Effect of initial damage variability on hot-spot nucleation in energetic materials," *Journal of Applied Physics*, vol. 124, no. 2, p. 025 104, 2018, DOI: 10.1063/1.5030656.

[60] T. Rabczuk, "Computational methods for fracture in brittle and quasi-brittle solids: State-of-the-art review and future perspectives," *International Scholarly Research Notices*, vol. 2013, 2013, DOI: 10.1155/2013/849231.

[61] S. Silling, "Reformulation of elasticity theory for discontinuities and long-range forces," *Journal of the Mechanics and Physics of Solids*, vol. 48, no. 1, pp. 175–209, 2000, DOI: 10.1016/S0022-5096(99)00029-0.

[62] S. Silling, M. Epton, O. Weckner, J. Xu, and E. Askari, "Peridynamic states and constitutive modeling," *Journal of Elasticity*, vol. 88, no. 2, pp. 151–184, 2007, DOI: 10.1007/s10659-007-9125-1.

[63] E. Madenci and E. Oterkus, *Peridynamic theory and its applications*. Springer, 2014, vol. 17, DOI: 10.1007/978-1-4614-8465-3.

[64] F. Bobaru, J. Foster, P. Geubelle, and S. Silling, *Handbook of peridynamic modeling*. CRC press, 2016, DOI: books.google.it/books?id=cBgNDgAAQBAJ.

[65] S. Silling and E. Askari, "A meshfree method based on the peridynamic model of solid mechanics," *Computers & structures*, vol. 83, no. 17-18, pp. 1526–1535, 2005, DOI: 10.1016/j.compstruc.2004.11.026.

[66] Y. Ha and F. Bobaru, "Studies of dynamic crack propagation and crack branching with peridynamics," *International Journal of Fracture*, vol. 162, pp. 229–244, 2010, DOI: 10.1007/s10704-010-9442-4.

[67] Y. Ha and F. Bobaru, "Characteristics of dynamic brittle fracture captured with peridynamics," *Engineering Fracture Mechanics*, vol. 78, no. 6, pp. 1156–1168, 2011, DOI: 10.1016/j.engfracmech.2010.11.020.

[68] F. Bobaru and G. Zhang, "Why do cracks branch? A peridynamic investigation of dynamic brittle fracture," *International Journal of Fracture*, vol. 196, no. 1-2, pp. 59–98, 2015, DOI: 10.1007/s10704-015-0056-8.

[69] S. Silling, "Dynamic fracture modeling with a meshfree peridynamic code," in *Computational Fluid and Solid Mechanics 2003*, DOI:10.1016/B978-008044046-0.50157-3, Elsevier, 2003, pp. 641–644.

[70] A. Agwai, I. Guven, and E. Madenci, "Predicting crack propagation with peridynamics: A comparative study," *International Journal of Fracture*, vol. 171, pp. 65–78, 2011, DOI: 10.1007/s10704-011-9628-4.

[71] T. Warren, S. Silling, A. Askari, O. Weckner, M. Epton, and J. Xu, "A non-ordinary state-based peridynamic method to model solid material deformation and fracture," *International Journal of Solids and Structures*, vol. 46, no. 5, pp. 1186–1195, 2009, DOI: 10.1016/j.ijsolstr.2008.10.029.

[72] M. Zaccariotto, F. Luongo, U. Galvanetto, and G. Sarego, "Examples of applications of the peridynamic theory to the solution of static equilibrium problems," *The Aeronautical Journal*, vol. 119, no. 1216, pp. 677–700, 2015, DOI: 10.1017/S0001924000010770.

[73] T. Ni, M. Zaccariotto, Q. Zhu, and U. Galvanetto, "Static solution of crack propagation problems in peridynamics," *Computer Methods in Applied Mechanics and Engineering*, vol. 346, pp. 126–151, 2019, DOI: 10.1016/j.cma.2018.11.028.

[74] P. Diehl, S. Prudhomme, and M. Lévesque, "A review of benchmark experiments for the validation of peridynamics models," *Journal of Peridynamics and Nonlocal Modeling*, vol. 1, pp. 14–35, 2019, DOI: 10.1007/s42102-018-0004-x.

[75] S. Silling and E. Askari, "Peridynamic modeling of impact damage," in *ASME Pressure Vessels and Piping Conference*, DOI:10.1115/PVP2004-3049, vol. 46849, 2004, pp. 197–205.

[76] P. Demmie and S. Silling, "An approach to modeling extreme loading of structures using peridynamics," *Journal of Mechanics of Materials and Structures*, vol. 2, no. 10, pp. 1921–1945, 2007, DOI: 10.2140/jomms.2007.2.1921.

[77] E. Oterkus, I. Guven, and E. Madenci, "Impact damage assessment by using peridynamic theory," *Central European Journal of Engineering*, vol. 2, pp. 523–531, 2012, DOI: 10.2478/s13531-012-0025-1.

[78] F. Bobaru, Y. Ha, and W. Hu, "Damage progression from impact in layered glass modeled with peridynamics," *Central European Journal of Engineering*, vol. 2, pp. 551–561, 2012, DOI: 10.2478/s13531-012-0020-6.

[79] W. Hu, Y. Wang, J. Yu, C. Yen, and F. Bobaru, "Impact damage on a thin glass plate with a thin polycarbonate backing," *International Journal of Impact Engineering*, vol. 62, pp. 152–165, 2013, DOI: 10.1016/j.ijimpeng.2013.07.001.

[80] C. Sun and Z. Huang, "Peridynamic simulation to impacting damage in composite laminate," *Composite Structures*, vol. 138, pp. 335–341, 2016, DOI: 10.1016/j.compstruct.2015.12.001.

[81] J. Rivera, J. Berjikian, R. Ravinder, H. Kodamana, S. Das, N. Bhatnagar, M. Bauchy, and N. Krishnan, "Glass fracture upon ballistic impact: New insights from peridynamics simulations," *Frontiers in Materials*, vol. 6, p. 239, 2019, DOI: 10.3389/fmats.2019.00239.

[82] M. Isiet, I. Mišković, and S. Mišković, "Review of peridynamic modelling of material failure and damage due to impact," *International Journal of Impact Engineering*, vol. 147, p. 103 740, 2021, DOI: 10.1016/j.ijimpeng.2020.103740.

[83] Y. Jafaraghaei, T. Yu, and T. Bui, "Peridynamics simulation of impact failure in glass plates," *Theoretical and Applied Fracture Mechanics*, vol. 121, p. 103 424, 2022, DOI: 10.1016/j.tafmec.2022.103424.

[84] S. Silling and A. Askari, "Peridynamic model for fatigue cracking," Sandia National Laboratories, Tech. Rep., 2014, DOI: 10.2172/1160289.

[85] G. Zhang, Q. Le, A. Loghin, A. Subramaniyan, and F. Bobaru, "Validation of a peridynamic model for fatigue cracking," *Engineering Fracture Mechanics*, vol. 162, pp. 76–94, 2016, DOI: 10.1016/j.engfracmech.2016.05.008.

[86] Y. Hu and E. Madenci, "Peridynamics for fatigue life and residual strength prediction of composite laminates," *Composite Structures*, vol. 160, pp. 169–184, 2017, DOI: 10.1016/j.compstruct.2016.10.010.

[87] R. Lipton, "Dynamic brittle fracture as a small horizon limit of peridynamics," *Journal of Elasticity*, vol. 117, pp. 21–50, 2014, DOI: 10.1007/s10659-013-9463-0.

[88] D. Huang, G. Lu, and P. Qiao, "An improved peridynamic approach for quasi-static elastic deformation and brittle fracture analysis," *International Journal of Mechanical Sciences*, vol. 94, pp. 111–122, 2015, DOI: 10.1016/j.ijmecsci.2015.02.018.

[89] J. Lee and J. Hong, "Dynamic crack branching and curving in brittle polymers," *International Journal of Solids and Structures*, vol. 100, pp. 332–340, 2016, DOI: 10.1016/j.ijsolstr.2016.09.002.

[90] Z. Xu, G. Zhang, Z. Chen, and F. Bobaru, "Elastic vortices and thermally-driven cracks in brittle materials with peridynamics," *International Journal of Fracture*, vol. 209, pp. 203–222, 2018, DOI: 10.1007/s10704-017-0256-5.

[91] J. Amani, E. Oterkus, P. Areias, G. Zi, T. Nguyen-Thoi, and T. Rabczuk, "A non-ordinary state-based peridynamics formulation for thermoplastic fracture," *International Journal of Impact Engineering*, vol. 87, pp. 83–94, 2016, DOI: 10.1016/j.ijimpeng.2015.06.019.

[92] E. Madenci and S. Oterkus, "Ordinary state-based peridynamics for plastic deformation according to von Mises yield criteria with isotropic hardening," *Journal of the Mechanics and Physics of Solids*, vol. 86, pp. 192–219, 2016, DOI: 10.1016/j.jmps.2015.09.016.

[93] M. M. Rahaman, P. Roy, D. Roy, and J. Reddy, "A peridynamic model for plasticity: Micro-inertia based flow rule, entropy equivalence and localization residuals," *Computer Methods in Applied Mechanics and Engineering*, vol. 327, pp. 369–391, 2017, DOI: 10.1016/j.cma.2017.07.034.

[94] F. Mousavi, S. Jafarzadeh, and F. Bobaru, "An ordinary state-based peridynamic elastoplastic 2D model consistent with J2 plasticity," *International Journal of Solids and Structures*, vol. 229, p. 111 146, 2021, DOI: 10.1016/j.ijsolstr.2021.111146.

[95] M. Ghajari, L. Iannucci, and P. Curtis, "A peridynamic material model for the analysis of dynamic crack propagation in orthotropic media," *Computer Methods in Applied Mechanics and Engineering*, vol. 276, pp. 431–452, 2014, DOI: 10.1016/j.cma.2014.04.002.

[96] V. Diana and S. Casolo, "A bond-based micropolar peridynamic model with shear deformability: Elasticity, failure properties and initial yield domains," *International Journal of Solids and Structures*, vol. 160, pp. 201–231, 2019, DOI: 10.1016/j.ijsolstr.2018.10.026.

[97] V. Diana and S. Casolo, "A full orthotropic micropolar peridynamic formulation for linearly elastic solids," *International Journal of Mechanical Sciences*, vol. 160, pp. 140–155, 2019, DOI: 10.1016/j.ijmecsci.2019.06.036.

[98] V. Diana and R. Ballarini, "Crack kinking in isotropic and orthotropic micropolar peridynamic solids," *International Journal of Solids and Structures*, vol. 196, pp. 76–98, 2020, DOI: 10.1016/j.ijsolstr.2020.03.025.

[99] V. Diana, A. Bacigalupo, M. Lepidi, and L. Gambarotta, "Anisotropic peridynamics for homogenized microstructured materials," *Computer Methods in Applied Mechanics and Engineering*, vol. 392, p. 114 704, 2022, DOI: 10.1016/j.cma.2022.114704.

[100] Z. Chen, S. Niazi, and F. Bobaru, "A peridynamic model for brittle damage and fracture in porous materials," *International Journal of Rock Mechanics and Mining Sciences*, vol. 122, p. 104 059, 2019, DOI: 10.1016/j.ijrmms.2019.104059.

[101] J. Mehrmashhadi, Z. Chen, J. Zhao, and F. Bobaru, "A stochastically homogenized peridynamic model for intraply fracture in fiber-reinforced composites," *Composites Science and Technology*, vol. 182, p. 107 770, 2019, DOI: 10.1016/j.compscitech.2019.107770.

[102] P. Wu, J. Zhao, Z. Chen, and F. Bobaru, "Validation of a stochastically homogenized peridynamic model for quasi-static fracture in concrete," *Engineering Fracture Mechanics*, vol. 237, p. 107 293, 2020, DOI: 10.1016/j.engfracmech.2020.107293.

[103] P. Wu, F. Yang, Z. Chen, and F. Bobaru, "Stochastically homogenized peridynamic model for dynamic fracture analysis of concrete," *Engineering Fracture Mechanics*, vol. 253, p. 107 863, 2021, DOI: 10.1016/j.engfracmech.2021.107863.

[104] W. Gerstle, N. Sau, and S. Silling, "Peridynamic modeling of concrete structures," *Nuclear Engineering and Design*, vol. 237, no. 12-13, pp. 1250–1258, 2007, DOI: 10.1016/j.nucengdes.2006.10.002.

[105] D. Huang, G. Lu, and Y. Liu, "Nonlocal peridynamic modeling and simulation on crack propagation in concrete structures," *Mathematical Problems in Engineering*, vol. 2015, p. 858 723, 2015, DOI: 10.1155/2015/858723.

[106] J. Zhao, Z. Chen, J. Mehrmashhadi, and F. Bobaru, "A stochastic multiscale peridynamic model for corrosion-induced fracture in reinforced concrete," *Engineering Fracture Mechanics*, vol. 229, p. 106 969, 2020, DOI: 10.1016/j.engfracmech.2020.106969.

[107] L. Wu, D. Huang, Y. Xu, and L. Wang, "A rate-dependent dynamic damage model in peridynamics for concrete under impact loading," *International Journal of Damage Mechanics*, vol. 29, no. 7, pp. 1035–1058, 2020, DOI: 10.1177/1056789519901162.

[108] Y. Liu, F. Yang, W. Zhou, Z. Chen, and F. Bobaru, "Peridynamic modeling of early-age cracking behaviour in continuously reinforced concrete pavement," *International Journal of Pavement Engineering*, pp. 1–19, 2022, DOI: 10.1080/10298436.2022.2111422.

[109] J. Xu, A. Askari, O. Weckner, and S. Silling, "Peridynamic analysis of impact damage in composite laminates," *Journal of Aerospace Engineering*, vol. 21, no. 3, pp. 187–194, 2008, DOI: 10.1061/(ASCE)0893-1321(2008)21:3(187).

[110] W. Hu, Y. Ha, and F. Bobaru, "Modeling dynamic fracture and damage in a fiber-reinforced composite lamina with peridynamics," *International Journal for Multiscale Computational Engineering*, vol. 9, no. 6, 2011, DOI: 10.1615/IntJMultCompEng.2011002651.

[111] W. Hu, Y. Ha, and F. Bobaru, "Peridynamic model for dynamic fracture in unidirectional fiber-reinforced composites," *Computer Methods in Applied Mechanics and Engineering*, vol. 217, pp. 247–261, 2012, DOI: 10.1016/j.cma.2012.01.016.

[112] E. Oterkus and E. Madenci, "Peridynamic analysis of fiber-reinforced composite materials," *Journal of Mechanics of Materials and Structures*, vol. 7, no. 1, pp. 45–84, 2012, DOI: 10.2140/jomms.2012.7.45.

[113] A. Askari, Y. Azdoud, F. Han, G. Lubineau, and S. Silling, "Peridynamics for analysis of failure in advanced composite materials," in *Numerical modelling of failure in advanced composite materials*, DOI: 10.1016/B978-0-08-100332-9.00012-8, Elsevier, 2015, pp. 331–350.

[114] A. Jenabidehkordi, R. Abadi, and T. Rabczuk, "Computational modeling of meso-scale fracture in polymer matrix composites employing peridynamics," *Composite Structures*, vol. 253, p. 112 740, 2020, DOI: 10.1016/j.compstruct.2020.112740.

[115] G. Ongaro, R. Bertani, U. Galvanetto, A. Pontefisso, and M. Zaccariotto, "A multi-scale peridynamic framework for modelling mechanical properties of polymer-based nanocomposites," *Engineering Fracture Mechanics*, vol. 274, p. 108 751, 2022, DOI: 10.1016/j.engfracmech.2022.108751.

[116] X. Zhou, X. Gu, and Y. Wang, "Numerical simulations of propagation, bifurcation and coalescence of cracks in rocks," *international journal of Rock Mechanics and Mining Sciences*, vol. 80, pp. 241–254, 2015, DOI: 10.1016/j.ijrmms.2015.09.006.

[117] Y. Wang, X. Zhou, and X. Xu, "Numerical simulation of propagation and coalescence of flaws in rock materials under compressive loads using the extended non-ordinary state-based peridynamics," *Engineering Fracture Mechanics*, vol. 163, pp. 248–273, 2016, DOI: 10.1016/j.engfracmech.2016.06.013.

[118] X. Zhou and Y. Shou, "Numerical simulation of failure of rock-like material subjected to compressive loads using improved peridynamic method," *International Journal of Geomechanics*, vol. 17, no. 3, p. 04 016 086, 2017, DOI: 10.1061/(ASCE)GM.1943-5622.0000778.

[119] V. Diana, J. Labuz, and L. Biolzi, "Simulating fracture in rock using a micropolar peridynamic formulation," *Engineering Fracture Mechanics*, vol. 230, p. 106 985, 2020, DOI: 10.1016/j.engfracmech.2020.106985.

[120] Q. Deng, Y. Chen, and J. Lee, "An investigation of the microscopic mechanism of fracture and healing processes in cortical bone," *International Journal of Damage Mechanics*, vol. 18, no. 5, pp. 491–502, 2009, DOI: 10.1177/1056789508096563.

[121] M. Taylor, I. Gözen, S. Patel, A. Jesorka, and K. Bertoldi, "Peridynamic modeling of ruptures in biomembranes," *PloS one*, vol. 11, no. 11, e0165947, 2016, DOI: 10.1371/journal.pone.0165947.

[122] P. Perré, G. Almeida, M. Ayouz, and X. Frank, "New modelling approaches to predict wood properties from its cellular structure: Image-based representation and meshless methods," *Annals of Forest Science*, vol. 73, pp. 147–162, 2016, DOI: 10.1007/s13595-015-0519-0.

[123] E. Lejeune and C. Linder, "Modeling tumor growth with peridynamics," *Biomechanics and modeling in mechanobiology*, vol. 16, no. 4, pp. 1141–1157, 2017, DOI: 10.1007/s10237-017-0876-8.

[124] F. Bobaru and M. Duangpanya, "The peridynamic formulation for transient heat conduction," *International Journal of Heat and Mass Transfer*, vol. 53, no. 19-20, pp. 4047–4059, 2010, DOI: 10.1016/j.ijheatmasstransfer.2010.05.024.

[125] F. Bobaru and M. Duangpanya, "A peridynamic formulation for transient heat conduction in bodies with evolving discontinuities," *Journal of Computational Physics*, vol. 231, no. 7, pp. 2764–2785, 2012, DOI: 10.1016/j.jcp.2011.12.017.

[126] S. Oterkus, E. Madenci, and A. Agwai, "Peridynamic thermal diffusion," *Journal of Computational Physics*, vol. 265, pp. 71–96, 2014, DOI: 10.1016/j.jcp.2014.01.027.

[127] J. Zhao, A. Larios, and F. Bobaru, "Construction of a peridynamic model for viscous flow," *Journal of Computational Physics*, vol. 468, p. 111 509, 2022, DOI: 10.1016/j.jcp.2022.111509.

[128] Z. Chen and F. Bobaru, "Peridynamic modeling of pitting corrosion damage," *Journal of the Mechanics and Physics of Solids*, vol. 78, pp. 352–381, 2015, DOI: 10.1016/j.jmps.2015.02.015.

[129] S. Jafarzadeh, Z. Chen, and F. Bobaru, "Peridynamic modeling of repassivation in pitting corrosion of stainless steel," *Corrosion*, vol. 74, no. 4, pp. 393–414, 2018, DOI: 10.5006/2615.

[130] S. Jafarzadeh, Z. Chen, and F. Bobaru, "Peridynamic modeling of intergranular corrosion damage," *Journal of The Electrochemical Society*, vol. 165, no. 7, p. C362, 2018, DOI: 10.1149/2.0821807jes.

[131] S. Jafarzadeh, Z. Chen, J. Zhao, and F. Bobaru, "Pitting, lacy covers, and pit merger in stainless steel: 3D peridynamic models," *Corrosion Science*, vol. 150, pp. 17–31, 2019, DOI: 10.1016/j.corsci.2019.01.006.

[132] A. Katiyar, J. Foster, H. Ouchi, and M. Sharma, "A peridynamic formulation of pressure driven convective fluid transport in porous media," *Journal of Computational Physics*, vol. 261, pp. 209–229, 2014, DOI: 10.1016/j.jcp.2013.12.039.

[133] R. Jabakhanji and R. Mohtar, "A peridynamic model of flow in porous media," *Advances in Water Resources*, vol. 78, pp. 22–35, 2015, DOI: 10.1016/j.advwatres.2015.01.014.

[134] S. Oterkus, E. Madenci, and A. Agwai, "Fully coupled peridynamic thermomechanics," *Journal of the Mechanics and Physics of Solids*, vol. 64, pp. 1–23, 2014, DOI: 10.1016/j.jmps.2013.10.011.

[135] Y. Wang, X. Zhou, and M. Kou, "A coupled thermo-mechanical bond-based peridynamics for simulating thermal cracking in rocks," *International Journal of Fracture*, vol. 211, no. 1-2, pp. 13–42, 2018, DOI: 10.1007/s10704-018-0273-z.

[136] D. De Meo, C. Diyaroglu, N. Zhu, E. Oterkus, and M. Siddiq, "Modelling of stress-corrosion cracking by using peridynamics," *International Journal of Hydrogen Energy*, vol. 41, no. 15, pp. 6593–6609, 2016, DOI: 10.1016/j.ijhydene.2016.02.154.

[137] S. Jafarzadeh, Z. Chen, S. Li, and F. Bobaru, "A peridynamic mechano-chemical damage model for stress-assisted corrosion," *Electrochimica Acta*, vol. 323, p. 134 795, 2019, DOI: 10.1016/j.electacta.2019.134795.

[138] W. Li and L. Guo, "A mechanical-diffusive peridynamics coupling model for meso-scale simulation of chloride penetration in concrete under loadings," *Construction and Building Materials*, vol. 241, p. 118 021, 2020, DOI: 10.1016/j.conbuildmat.2020.118021.

[139] R. Wildman and G. Gazonas, "A dynamic electro-thermo-mechanical model of dielectric breakdown in solids using peridynamics," *Journal of Mechanics of Materials and Structures*, vol. 10, no. 5, pp. 613–630, 2015, DOI: 10.2140/jomms.2015.10.613.

[140] R. Wildman and G. Gazonas, "A multiphysics time-dependent model of dielectric breakdown in solids," in *2018 International Applied Computational Electromagnetics Society Symposium (ACES)*, DOI: 10.23919/ROPACES.2018.8364191, IEEE, 2018, pp. 1–2.

[141] V. Diana and V. Carvelli, "An electromechanical micropolar peridynamic model," *Computer Methods in Applied Mechanics and Engineering*, vol. 365, p. 112 998, 2020, DOI: 10.1016/j.cma.2020.112998.

[142] F. Vieira and A. Araújo, "Implicit non-ordinary state-based peridynamics model for linear piezoelectricity," *Mechanics of Advanced Materials and Structures*, vol. 29, no. 28, pp. 7329–7350, 2022, DOI: 10.1080/15376494.2021.1995798.

[143] F. Vieira and A. Araújo, "A peridynamic model for electromechanical fracture and crack propagation in piezoelectric solids," *Computer Methods in Applied Mechanics and Engineering*, vol. 412, p. 116 081, 2023, DOI: 10.1016/j.cma.2023.116081.

[144] S. Oterkus, E. Madenci, and E. Oterkus, "Fully coupled poroelastic peridynamic formulation for fluid-filled fractures," *Engineering geology*, vol. 225, pp. 19–28, 2017, DOI: 10.1016/j.enggeo.2017.02.001.

[145] A. Javili, R. Morasata, E. Oterkus, and S. Oterkus, "Peridynamics review," *Mathematics and Mechanics of Solids*, vol. 24, no. 11, pp. 3714–3739, 2019, DOI: 10.1177/1081286518803411.

[146] J. Traseger and P. Seleson, "Bond-based peridynamics: A tale of two Poisson's ratios," *Journal of Peridynamics and Nonlocal Modeling*, vol. 2, no. 3, pp. 278–288, 2020, DOI: 10.1007/s42102-019-00021-x.

[147] P. Seleson and M. Parks, "On the role of the influence function in the peridynamic theory," *International Journal for Multiscale Computational Engineering*, vol. 9, no. 6, 2011, DOI: 10.1615/IntJMultCompEng.2011002527.

[148] W. Gerstle, N. Sau, and S. Silling, "Peridynamic modeling of plain and reinforced concrete structures," *18th International Conference on Structural Mechanics in Reactor Technology*, 2005, URL: repository.lib.ncsu.edu/handle/1840.20/31420.

[149] F. Bobaru, M. Yang, L. Alves, S. Silling, E. Askari, and J. Xu, "Convergence, adaptive refinement, and scaling in 1d peridynamics," *International Journal for Numerical Methods in Engineering*, vol. 77, no. 6, pp. 852–877, 2009, DOI: 10.1002/nme.2439.

[150] Z. Chen and F. Bobaru, "Selecting the kernel in a peridynamic formulation: A study for transient heat diffusion," *Computer Physics Communications*, vol. 197, pp. 51–60, 2015, DOI: 10.1016/j.cpc.2015.08.006.

[151] Z. Chen, D. Bakenhus, and F. Bobaru, "A constructive peridynamic kernel for elasticity," *Computer Methods in Applied Mechanics and Engineering*, vol. 311, pp. 356–373, 2016, DOI: 10.1016/j.cma.2016.08.012.

[152] S. Silling and F. Bobaru, "Peridynamic modeling of membranes and fibers," *International Journal of Non-Linear Mechanics*, vol. 40, no. 2-3, pp. 395–409, 2005, DOI: 10.1016/j.ijnonlinmec.2004.08.004.

[153] H. Chen, "Bond-associated deformation gradients for peridynamic correspondence model," *Mechanics Research Communications*, vol. 90, pp. 34–41, 2018, DOI: 10.1016/j.mechrescom.2018.04.004.

[154] H. Chen and B. Spencer, "Peridynamic bond-associated correspondence model: Stability and convergence properties," *International Journal for Numerical Methods in Engineering*, vol. 117, no. 6, pp. 713–727, 2019, DOI: 10.1002/nme.5973.

[155] F. Vieira and A. Araújo, "On the role of bond-associated stabilization and discretization on deformation and fracture in non-ordinary state-based peridynamics," *Engineering Fracture Mechanics*, vol. 270, p. 108 557, 2022, DOI: 10.1016/j.engfracmech.2022.108557.

[156] S. Silling and R. Lehoucq, "Peridynamic theory of solid mechanics," *Advances in Applied Mechanics*, vol. 44, pp. 73–168, 2010, DOI: 10.1016/S0065-2156(10)44002-8.

[157] X. Gu, E. Madenci, and Q. Zhang, "Revisit of non-ordinary state-based peridynamics," *Engineering fracture mechanics*, vol. 190, pp. 31–52, 2018, DOI: 10.1016/j.engfracmech.2017.11.039.

[158] P. Seleson and D. Littlewood, "Convergence studies in meshfree peridynamic simulations," *Computers & Mathematics with Applications*, vol. 71, no. 11, pp. 2432–2448, 2016, DOI: 10.1016/j.camwa.2015.12.021.

[159] D. Littlewood, "Roadmap for peridynamic software implementation," Sandia National Laboratories, Tech. Rep., 2015, DOI: 10.2172/1226115.

[160] Q. Le, W. Chan, and J. Schwartz, "A two-dimensional ordinary, state-based peridynamic model for linearly elastic solids," *International Journal for Numerical Methods in Engineering*, vol. 98, no. 8, pp. 547–561, 2014, DOI: 10.1002/nme.4642.

[161] S. Lenci, *Lezioni di meccanica strutturale*. Società Editrice Esculapio, 2023.

[162] S. Silling and R. Lehoucq, "Convergence of peridynamics to classical elasticity theory," *Journal of Elasticity*, vol. 93, no. 1, pp. 13–37, 2008, DOI: 10.1007/s10659-008-9163-3.

[163] Z. Chen, X. Peng, S. Jafarzadeh, and F. Bobaru, "Analytical solutions of peridynamic equations. Part I: Transient heat diffusion," *Journal of Peridynamics and Nonlocal Modeling*, vol. 4, no. 3, pp. 303–335, 2022, DOI: 10.1007/s42102-022-00080-7.

[164] Z. Chen, X. Peng, S. Jafarzadeh, and F. Bobaru, "Analytical solutions of peridynamic equations. Part II: Elastic wave propagation," *International Journal of Engineering Science*, vol. 188, p. 103 866, 2023, DOI: 10.1016/j.ijengsci.2023.103866.

[165] G. Ongaro, P. Seleson, U. Galvanetto, T. Ni, and M. Zaccariotto, "Overall equilibrium in the coupling of peridynamics and classical continuum mechanics," *Computer Methods in Applied Mechanics and Engineering*, vol. 381, p. 113 515, 2021, DOI: 10.1016/j.cma.2020.113515.

[166] S. Silling, "Linearized theory of peridynamic states," *Journal of Elasticity*, vol. 99, no. 1, pp. 85–111, 2010, DOI: 10.1007/s10659-009-9234-0.

[167] D. Dipasquale, G. Sarego, M. Zaccariotto, and U. Galvanetto, "A discussion on failure criteria for ordinary state-based peridynamics," *Engineering Fracture Mechanics*, vol. 186, pp. 378–398, 2017, DOI: 10.1016/j.engfracmech.2017.10.011.

[168] O. Karpenko, S. Oterkus, and E. Oterkus, "An in-depth investigation of critical stretch based failure criterion in ordinary state-based peridynamics," *International Journal of Fracture*, vol. 226, pp. 97–119, 2020, DOI: 10.1007/s10704-020-00481-z.

[169] J. Foster, S. Silling, and W. Chen, "An energy based failure criterion for use with peridynamic states," *International Journal for Multiscale Computational Engineering*, vol. 9, no. 6, 2011, DOI: 10.1615/IntJMultCompEng.2011002407.

[170] D. Dipasquale, G. Sarego, P. Prapamonthon, S. Yooyen, and A. Shojaei, "A stress tensor-based failure criterion for ordinary state-based peridynamic models," *Journal of Applied and Computational Mechanics*, vol. 8, no. 2, 2022, DOI: 10.22055/jcam.2021.38664.3264.

[171] T. Ni, M. Zaccariotto, Q. Zhu, and U. Galvanetto, "Coupling of FEM and ordinary state-based peridynamics for brittle failure analysis in 3D," *Mechanics of Advanced Materials and Structures*, vol. 28, no. 9, pp. 875–890, 2021, DOI: 10.1080/15376494.2019.1602237.

[172] R. Lehoucq and S. Silling, "Force flux and the peridynamic stress tensor," *Journal of the Mechanics and Physics of Solids*, vol. 56, no. 4, pp. 1566–1577, 2008, DOI: 10.1016/j.jmps.2007.08.004.

[173] E. Emmrich and O. Weckner, "The peridynamic equation and its spatial discretisation," *Mathematical Modelling and Analysis*, vol. 12, no. 1, pp. 17–27, 2007, DOI: 10.3846/1392-6292.2007.12.17-27.

[174] A. Shojaei, A. Hermann, C. Cyron, P. Seleson, and S. Silling, "A hybrid meshfree discretization to improve the numerical performance of peridynamic models," *Computer Methods in Applied Mechanics and Engineering*, vol. 391, p. 114 544, 2022, DOI: 10.1016/j.cma.2021.114544.

[175] G. Ongaro, A. Shojaei, F. Mossaiby, A. Hermann, C. Cyron, and P. Trovalusci, "Multi-adaptive spatial discretization of bond-based peridynamics," *International Journal of Fracture*, pp. 1–24, 2023, DOI: 10.1007/s10704-023-00709-8.

[176] X. Chen and M. Gunzburger, "Continuous and discontinuous finite element methods for a peridynamics model of mechanics," *Computer Methods in Applied Mechanics and Engineering*, vol. 200, no. 9-12, pp. 1237–1250, 2011, DOI: 10.1016/j.cma.2010.10.014.

[177] Q. Du, L. Tian, and X. Zhao, "A convergent adaptive finite element algorithm for nonlocal diffusion and peridynamic models," *SIAM Journal on Numerical Analysis*, vol. 51, no. 2, pp. 1211–1234, 2013, DOI: 10.1137/120871638.

[178] Q. Du, L. Ju, L. Tian, and K. Zhou, "A posteriori error analysis of finite element method for linear nonlocal diffusion and peridynamic models," *Mathematics of Computation*, vol. 82, no. 284, pp. 1889–1922, 2013, DOI: 10.1090/S0025-5718-2013-02708-1.

[179] S. Jafarzadeh, A. Larios, and F. Bobaru, "Efficient solutions for nonlocal diffusion problems via boundary-adapted spectral methods," *Journal of Peridynamics and Nonlocal Modeling*, vol. 2, no. 1, pp. 85–110, 2020, DOI: 10.1007/s42102-019-00026-6.

[180] S. Jafarzadeh, L. Wang, A. Larios, and F. Bobaru, "A fast convolution-based method for peridynamic transient diffusion in arbitrary domains," *Computer Methods in Applied Mechanics and Engineering*, vol. 375, p. 113 633, 2021, DOI: 10.1016/j.cma.2020.113633.

[181] S. Henke and S. Shanbhag, "Mesh sensitivity in peridynamic simulations," *Computer Physics Communications*, vol. 185, no. 1, pp. 181–193, 2014, DOI: 10.1016/j.cpc.2013.09.010.

[182] T. Ni, Q. Zhu, L. Zhao, and P. Li, "Peridynamic simulation of fracture in quasi brittle solids using irregular finite element mesh," *Engineering Fracture Mechanics*, vol. 188, pp. 320–343, 2018, DOI: 10.1016/j.engfracmech.2017.08.028.

[183] H. Chen, "A comparison study on peridynamic models using irregular non-uniform spatial discretization," *Computer Methods in Applied Mechanics and Engineering*, vol. 345, pp. 539–554, 2019, DOI: 10.1016/j.cma.2018.11.001.

[184] P. Seleson, "Improved one-point quadrature algorithms for two-dimensional peridynamic models based on analytical calculations," *Computer Methods in Applied Mechanics and Engineering*, vol. 282, pp. 184–217, 2014, DOI: 10.1016/j.cma.2014.06.016.

[185] B. Kilic and E. Madenci, "An adaptive dynamic relaxation method for quasi-static simulations using the peridynamic theory," *Theoretical and Applied Fracture Mechanics*, vol. 53, no. 3, pp. 194–204, 2010, DOI: 10.1016/j.tafmec.2010.08.001.

[186] Q. Le and F. Bobaru, "Surface corrections for peridynamic models in elasticity and fracture," *Computational Mechanics*, vol. 61, no. 4, pp. 499–518, 2018, DOI: 10.1007/s00466-017-1469-1.

[187] R. Macek and S. Silling, "Peridynamics via finite element analysis," *Finite Elements in Analysis and Design*, vol. 43, no. 15, pp. 1169–1178, 2007, DOI: 10.1016/j.finel.2007.08.012.

[188] B. Kilic, "Peridynamic theory for progressive failure prediction in homogeneous and heterogeneous materials," *Ph.D. thesis*, 2008, URL: repository.arizona.edu/handle/10150/193658.

[189] E. Oterkus, "Peridynamic theory for modeling three-dimensional damage growth in metallic and composite structures," *Ph.D. thesis*, 2010, URL: repository.arizona.edu/handle/10150/145366.

[190] J. Mitchell, S. Silling, and D. Littlewood, "A position-aware linear solid constitutive model for peridynamics," *Journal of Mechanics of Materials and Structures*, vol. 10, no. 5, pp. 539–557, 2015, DOI: 10.2140/jomms.2015.10.539.

[191] G. Sarego, Q. Le, F. Bobaru, M. Zaccariotto, and U. Galvanetto, "Linearized state-based peridynamics for 2-D problems," *International Journal for Numerical Methods in Engineering*, vol. 108, no. 10, pp. 1174–1197, 2016, DOI: 10.1002/nme.5250.

[192] S. Oterkus, "Peridynamics for the solution of multiphysics problems," *Ph.D. thesis*, 2015, URL: repository.arizona.edu/handle/10150/555945.

[193] S. Prudhomme and P. Diehl, "On the treatment of boundary conditions for bond-based peridynamic models," *Computer Methods in Applied Mechanics and Engineering*, vol. 372, p. 113 391, 2020, DOI: 10.1016/j.cma.2020.113391.

[194] J. Zhao, S. Jafarzadeh, Z. Chen, and F. Bobaru, "An algorithm for imposing local boundary conditions in peridynamic models on arbitrary domains," 2020, DOI: 10.31224/osf.io/7z8qr.

[195] J. Chen, P. Qingdao, Y. Jiao, W. Jiang, and Y. Zhang, "Peridynamics boundary condition treatments via the pseudo-layer enrichment method and variable horizon approach," *Mathematics and Mechanics of Solids*, vol. 26, no. 5, pp. 631–666, 2021, DOI: 10.1177/1081286520961144.

[196] W. Dong, H. Liu, J. Du, X. Zhang, M. Huang, Z. Li, Z. Chen, and F. Bobaru, "A peridynamic approach to solving general discrete dislocation dynamics problems in plasticity and fracture: Part I. Model description and verification," *International Journal of Plasticity*, vol. 157, p. 103 401, 2022, DOI: 10.1016/j.ijplas.2022.103401.

[197] M. Parks, R. Lehoucq, S. Plimpton, and S. Silling, "Implementing peridynamics within a molecular dynamics code," *Computer Physics Communications*, vol. 179, no. 11, pp. 777–783, 2008, DOI: 10.1016/j.cpc.2008.06.011.

[198] F. Bobaru and Y. Ha, "Adaptive refinement and multiscale modeling in 2D peridynamics," *Journal for Multiscale Computational Engineering*, vol. 9, no. 6, pp. 635–659, 2011, DOI: 10.1615/IntJMultCompEng.2011002793.

[199] B. Kilic and E. Madenci, "Coupling of peridynamic theory and the finite element method," *Journal of Mechanics of Materials and Structures*, vol. 5, no. 5, pp. 707–733, 2010, DOI: 10.2140/jomms.2010.5.707.

[200] G. Lubineau, Y. Azdoud, F. Han, C. Rey, and A. Askari, "A morphing strategy to couple non-local to local continuum mechanics," *Journal of the Mechanics and Physics of Solids*, vol. 60, no. 6, pp. 1088–1102, 2012, DOI: 10.1016/j.jmps.2012.02.009.

[201] F. Han and G. Lubineau, "Coupling of nonlocal and local continuum models by the Arlequin approach," *International Journal for Numerical Methods in Engineering*, vol. 89, no. 6, pp. 671–685, 2012, DOI: 10.1002/nme.3255.

[202] P. Seleson, S. Beneddine, and S. Prudhomme, "A force-based coupling scheme for peridynamics and classical elasticity," *Computational Materials Science*, vol. 66, pp. 34–49, 2013, DOI: 10.1016/j.commatsci.2012.05.016.

[203] P. Seleson, Y. Ha, and S. Beneddine, "Concurrent coupling of bond-based peridynamics and the Navier equation of classical elasticity by blending," *International Journal for Multiscale Computational Engineering*, vol. 13, no. 2, 2015, DOI: 10.1615/IntJMultCompEng.2014011338.

[204] S. Silling, D. Littlewood, and P. Seleson, "Variable horizon in a peridynamic medium," *Journal of Mechanics of Materials and Structures*, vol. 10, no. 5, pp. 591–612, 2015, DOI: 10.2140/jomms.2015.10.591.

[205] U. Galvanetto, T. Mudric, A. Shojaei, and M. Zaccariotto, "An effective way to couple fem meshes and peridynamics grids for the solution of static equilibrium problems," *Mechanics Research Communications*, vol. 76, pp. 41–47, 2016, DOI: 10.1016/j.mechrescom.2016.06.006.

[206] M. Zaccariotto, T. Mudric, D. Tomasi, A. Shojaei, and U. Galvanetto, "Coupling of FEM meshes with Peridynamic grids," *Computer Methods in Applied Mechanics and Engineering*, vol. 330, pp. 471–497, 2018, DOI: 10.1016/j.cma.2017.11.011.

[207] W. Sun, J. Fish, and G. Zhang, "Superposition of non-ordinary state-based peridynamics and finite element method for material failure simulations," *Meccanica*, vol. 55, pp. 681–699, 2020, DOI: 10.1007/s11012-019-01098-w.

[208] A. Shojaei, T. Mudric, M. Zaccariotto, and U. Galvanetto, "A coupled meshless finite point/Peridynamic method for 2D dynamic fracture analysis," *International Journal of Mechanical Sciences*, vol. 119, pp. 419–431, 2016, DOI: 10.1016/j.ijmecsci.2016.11.003.

[209] M. Zaccariotto, D. Tomasi, and U. Galvanetto, "An enhanced coupling of PD grids to FE meshes," *Mechanics Research Communications*, vol. 84, pp. 125–135, 2017, DOI: 10.1016/j.mechrescom.2017.06.014.

[210] F. Scabbia, M. Zaccariotto, U. Galvanetto, and F. Bobaru, "Peridynamic simulation of elastic wave propagation by applying the boundary conditions with the surface node method," in *III Aerospace PhD-Days*, AIDAA, 2023.

[211] F. Scabbia, M. Zaccariotto, and U. Galvanetto, "Surface node method for the peridynamic simulation of elastodynamic problems with neumann boundary conditions," in *AIDAA XXVII International Congress*, AIDAA, 2023.

[212] E. Carrera, M. Cinefra, M. Petrolo, and E. Zappino, *Finite element analysis of structures through unified formulation*. John Wiley & Sons, 2014, DOI: 10.1002/9781118536643.

[213] A. Pagani and E. Carrera, "Coupling three-dimensional peridynamics and high-order one-dimensional finite elements based on local elasticity for the linear static analysis of solid beams and thin-walled reinforced structures," *International Journal for Numerical Methods in Engineering*, vol. 121, no. 22, pp. 5066–5081, 2020, DOI: 10.1002/nme.6510.

[214] A. Pagani, M. Enea, and E. Carrera, "Quasi-static fracture analysis by coupled three-dimensional peridynamics and high order one-dimensional finite elements based on local elasticity," *International Journal for Numerical Methods in Engineering*, vol. 123, no. 4, pp. 1098–1113, 2022, DOI: 10.1002/nme.6890.

[215] H. Ren, X. Zhuang, Y. Cai, and T. Rabczuk, "Dual-horizon peridynamics," *International Journal for Numerical Methods in Engineering*, vol. 108, no. 12, pp. 1451–1476, 2016, DOI: 10.1002/nme.5257.

[216] H. Ren, X. Zhuang, and T. Rabczuk, "Dual-horizon peridynamics: A stable solution to varying horizons," *Computer Methods in Applied Mechanics and Engineering*, vol. 318, pp. 762–782, 2017, DOI: 10.1016/j.cma.2016.12.031.

[217] P. Seleson, M. Gunzburger, and M. Parks, "Interface problems in nonlocal diffusion and sharp transitions between local and nonlocal domains," *Computer Methods in Applied Mechanics and Engineering*, vol. 266, pp. 185–204, 2013, DOI: 10.1016/j.cma.2013.05.018.

[218] B. Aksoylu and F. Celiker, "Nonlocal problems with local Dirichlet and Neumann boundary conditions," *Journal of Mechanics of Materials and Structures*, vol. 12, no. 4, pp. 425–437, 2017, DOI: 10.2140/jomms.2017.12.425.

[219] B. Aksoylu, H. Beyer, and F. Celiker, "Theoretical foundations of incorporating local boundary conditions into nonlocal problems," *Reports on Mathematical Physics*, vol. 80, no. 1, pp. 39–71, 2017, DOI: 10.1016/S0034-4877(17)30061-7.

[220] B. Aksoylu, H. Beyer, and F. Celiker, "Application and implementation of incorporating local boundary conditions into nonlocal problems," *Numerical Functional Analysis and Optimization*, vol. 38, no. 9, pp. 1077–1114, 2017, DOI: 10.1080/01630563.2017.1320674.

[221] J. Wang, W. Hu, X. Zhang, and W. Pan, "Modeling heat transfer subject to inhomogeneous Neumann boundary conditions by smoothed particle hydrodynamics and peridynamics," *International Journal of Heat and Mass Transfer*, vol. 139, pp. 948–962, 2019, DOI: 10.1016/j.ijheatmasstransfer.2019.05.054.

[222] M. Breitenfeld, P. Geubelle, O. Weckner, and S. Silling, "Non-ordinary state-based peridynamic analysis of stationary crack problems," *Computer Methods in Applied Mechanics and Engineering*, vol. 272, pp. 233–250, 2014, DOI: 10.1016/j.cma.2014.01.002.

[223] E. Madenci, "Peridynamic integrals for strain invariants of homogeneous deformation," *ZAMM-Journal of Applied Mathematics and Mechanics*, vol. 97, no. 10, pp. 1236–1251, 2017, DOI: 10.1002/zamm.201600242.

[224] K. Yu, X. Xin, and K. Lease, "A new adaptive integration method for the peridynamic theory," *Modelling and Simulation in Materials Science and Engineering*, vol. 19, no. 4, p. 045 003, 2011, DOI: 10.1088/0965-0393/19/4/045003.

[225] E. Carrera, A. Pagani, and M. Petrolo, "Use of Lagrange multipliers to combine 1D variable kinematic finite elements," *Computers & Structures*, vol. 129, pp. 194–206, 2013, DOI: 10.1016/j.compstruc.2013.07.005.

[226] W. Liu and J. Hong, "Discretized peridynamics for linear elastic solids," *Computational Mechanics*, vol. 50, no. 5, pp. 579–590, 2012, DOI: 10.1007/s00466-012-0690-1.

[227] F. Scabbia, M. Zaccariotto, and U. Galvanetto, "A novel and effective way to impose boundary conditions and to mitigate the surface effect in state-based Peridynamics," *International Journal for Numerical Methods in Engineering*, vol. 122, no. 20, pp. 5773–5811, 2021, DOI: 10.1002/nme.6773.

[228] W. Sun and J. Fish, "Superposition-based coupling of peridynamics and finite element method," *Computational Mechanics*, vol. 64, no. 1, pp. 231–248, 2019, DOI: 10.1007/s00466-019-01668-5.

[229] I. Giannakeas, T. Papathanasiou, A. Fallah, and H. Bahai, "Coupling XFEM and peridynamics for brittle fracture simulation—part I: Feasibility and effectiveness," *Computational Mechanics*, vol. 66, no. 1, pp. 103–122, 2020, DOI: 10.1007/s00466-020-01843-z.

[230] I. Giannakeas, T. Papathanasiou, A. Fallah, and H. Bahai, "Coupling XFEM and Peridynamics for brittle fracture simulation: Part II—adaptive relocation strategy," *Computational Mechanics*, vol. 66, no. 3, pp. 683–705, 2020, DOI: 10.1007/s00466-020-01872-8.

[231] A. Shojaei, M. Zaccariotto, and U. Galvanetto, "Coupling of 2D discretized Peridynamics with a meshless method based on classical elasticity using switching of nodal behaviour," *Engineering Computations*, 2017, DOI: 10.1108/EC-03-2016-0078.

[232] Y. Yu, H. You, and N. Trask, "An asymptotically compatible treatment of traction loading in linearly elastic peridynamic fracture," *Computer Methods in Applied Mechanics and Engineering*, vol. 377, p. 113 691, 2021, DOI: 10.1016/j.cma.2021.113691.

[233] S. Butt and G. Meschke, "Peridynamic analysis of dynamic fracture: Influence of peridynamic horizon, dimensionality and specimen size," *Computational Mechanics*, vol. 67, pp. 1719–1745, 2021, DOI: 10.1007/s00466-021-02017-1.

[234] A. Fallah, I. Giannakeas, R. Mella, M. Wenman, Y. Safa, and H. Bahai, "On the computational derivation of bond-based peridynamic stress tensor," *Journal of Peridynamics and Nonlocal Modeling*, vol. 2, no. 4, pp. 352–378, 2020, DOI: 10.1007/s42102-020-00036-9.

[235] F. Scabbia, M. Zaccariotto, and U. Galvanetto, "Accurate computation of partial volumes in 3D peridynamics," *Engineering with Computers*, vol. 39, no. 1, pp. 959–991, 2023, DOI: 10.1007/s00366-022-01725-3.

[236] F. Scabbia, M. Zaccariotto, and U. Galvanetto, "A new method based on Taylor expansion and nearest-node strategy to impose Dirichlet and Neumann boundary conditions in ordinary state-based Peridynamics," *Computational Mechanics*, vol. 70, no. 1, pp. 1–27, 2022, DOI: 10.1007/s00466-022-02153-2.

[237] E. Madenci, A. Barut, and M. Futch, "Peridynamic differential operator and its applications," *Computer Methods in Applied Mechanics and Engineering*, vol. 304, pp. 408–451, 2016, DOI: 10.1016/j.cma.2016.02.028.

[238] E. Madenci, M. Dorduncu, A. Barut, and M. Futch, "Numerical solution of linear and nonlinear partial differential equations using the peridynamic differential operator," *Numerical Methods for Partial Differential Equations*, vol. 33, no. 5, pp. 1726–1753, 2017, DOI: 10.1002/num.22167.

[239] E. Madenci, M. Dorduncu, N. Phan, and X. Gu, "Weak form of bond-associated non-ordinary state-based peridynamics free of zero energy modes with uniform or non-uniform discretization," *Engineering Fracture Mechanics*, vol. 218, p. 106 613, 2019, DOI: 10.1016/j.engfracmech.2019.106613.

[240] E. Madenci, A. Barut, and M. Dorduncu, *Peridynamic differential operator for numerical analysis*. Springer, 2019, vol. 10, DOI: 10.1007/978-3-030-02647-9.

[241] D. Behera, P. Roy, S. Anicode, E. Madenci, and B. Spencer, "Imposition of local boundary conditions in peridynamics without a fictitious layer and unphysical stress concentrations," *Computer Methods in Applied Mechanics and Engineering*, vol. 393, p. 114 734, 2022, DOI: 10.1016/j.cma.2022.114734.

[242] Y. Lu, T. Belytschko, and L. Gu, "A new implementation of the element free Galerkin method," *Computer Methods in Applied Mechanics and Engineering*, vol. 113, no. 3-4, pp. 397–414, 1994, DOI: 10.1016/0045-7825(94)90056-6.

[243] T. Ni, F. Pesavento, M. Zaccariotto, U. Galvanetto, Q. Zhu, and B. Schrefler, "Hybrid FEM and peridynamic simulation of hydraulic fracture propagation in saturated porous media," *Computer Methods in Applied Mechanics and Engineering*, vol. 366, p. 113 101, 2020, DOI: 10.1016/j.cma.2020.113101.

[244] H. Ren, X. Zhuang, E. Oterkus, H. Zhu, and T. Rabczuk, "Nonlocal strong forms of thin plate, gradient elasticity, magneto-electro-elasticity and phase field fracture by nonlocal operator method," *Engineering with Computers*, pp. 1–22, 2021, DOI: 10.1007/s00366-021-01502-8.

[245] B. Kilic and E. Madenci, "Structural stability and failure analysis using peridynamic theory," *International Journal of Non-Linear Mechanics*, vol. 44, no. 8, pp. 845–854, 2009, DOI: 10.1016/j.ijnonlinmec.2009.05.007.

[246] B. Aksoylu, F. Celiker, and G. Gazonas, "Higher order collocation methods for nonlocal problems and their asymptotic compatibility," *Communications on Applied Mathematics and Computation*, vol. 2, no. 2, pp. 261–303, 2020, DOI: 10.1007/s42967-019-00051-8.

[247] P. Seleson and D. Littlewood, "Numerical tools for improved convergence of meshfree peridynamic discretizations," *Handbook of nonlocal continuum mechanics for materials and structures*, 2018, DOI: 10.1007/978-3-319-22977-5_39-1.

[248] G. Zheng, J. Wang, G. Shen, Y. Xia, and W. Li, "A new quadrature algorithm consisting of volume and integral domain corrections for two-dimensional peridynamic models," *International Journal of Fracture*, vol. 229, no. 1, pp. 39–54, 2021, DOI: 10.1007/s10704-021-00540-z.

[249] F. Scabbia, M. Zaccariotto, and U. Galvanetto, "A new surface node method to accurately model the mechanical behavior of the boundary in 3D state-based Peridynamics," *Journal of Peridynamics and Nonlocal Modeling*, pp. 1–35, 2023, DOI: 10.1007/s42102-022-00094-1.

[250] E. Carrera and A. Pagani, "Analysis of reinforced and thin-walled structures by multi-line refined 1D/beam models," *International Journal of Mechanical Sciences*, vol. 75, pp. 278–287, 2013, DOI: 10.1016/j.ijmecsci.2013.07.010.

[251] E. Carrera and A. Pagani, "Multi-line enhanced beam model for the analysis of laminated composite structures," *Composites Part B: Engineering*, vol. 57, pp. 112–119, 2014, DOI: 10.1016/j.compositesb.2013.09.046.

[252] M. Parks, S. Plimpton, R. Lehoucq, and S. Silling, "Peridynamics with LAMMPS: A user guide.," Sandia National Laboratories, Tech. Rep., 2008, DOI: 10.2172/1031301.

[253] A. Pagani and M. Enea, "Displacement and strain data-driven damage detection in multi-component and heterogeneous composite structures," *Mechanics of Advanced Materials and Structures*, pp. 1–16, 2022, DOI: 10.1080/15376494.2022.2149907.

[254] M. Refat, E. Zappino, A. Racionero Sánchez-Majano, and A. Pagani, "Dynamic characterization of 3D printed lightweight structures," *Advances in Aircraft and Spacecraft Science*, vol. 9, no. 4, pp. 301–318, 2022, DOI: 10.12989/aas.2022.9.4.301.

[255] E. Carrera, A. Pagani, and M. Petrolo, "Classical, refined, and component-wise analysis of reinforced-shell wing structures," *AIAA Journal*, vol. 51, no. 5, pp. 1255–1268, 2013, DOI: 10.2514/1.J052331.

[256] A. Visintin, "Introduction to Stefan-type problems," *Handbook of differential equations: evolutionary equations*, vol. 4, pp. 377–484, 2008, DOI: 10.1016/S1874-5717(08)00008-X.

[257] S. Mitchell and M. Vynnycky, "On the numerical solution of two-phase Stefan problems with heat-flux boundary conditions," *Journal of Computational and Applied Mathematics*, vol. 264, pp. 49–64, 2014, DOI: 10.1016/j.cam.2014.01.003.

[258] M. Khalid, M. Zubair, and M. Ali, "An analytical method for the solution of two phase Stefan problem in cylindrical geometry," *Applied Mathematics and Computation*, vol. 342, pp. 295–308, 2019, DOI: 10.1016/j.amc.2017.09.013.

[259] L. Lopez and S. Pellegrino, "A space-time discretization of a nonlinear peridynamic model on a 2D lamina," *Computers & Mathematics with Applications*, vol. 116, pp. 161–175, 2022, DOI: 10.1016/j.camwa.2021.07.004.

[260] J. Guermond, P. Minev, and J. Shen, "An overview of projection methods for incompressible flows," *Computer Methods in Applied Mechanics and Engineering*, vol. 195, no. 44-47, pp. 6011–6045, 2006, DOI: 10.1016/j.cma.2005.10.010.

[261] D. Shirokoff and R. Rosales, "An efficient method for the incompressible Navier–Stokes equations on irregular domains with no-slip boundary conditions, high order up to the boundary," *Journal of Computational Physics*, vol. 230, no. 23, pp. 8619–8646, 2011, DOI: 10.1016/j.jcp.2011.08.011.

[262] Z. Chen, G. Zhang, and F. Bobaru, "The influence of passive film damage on pitting corrosion," *Journal of The Electrochemical Society*, vol. 163, no. 2, p. C19, 2015, DOI: 10.1149/2.0521602jes.

[263] S. Jafarzadeh, Z. Chen, and F. Bobaru, "Computational modeling of pitting corrosion," *Corrosion Reviews*, vol. 37, no. 5, pp. 419–439, 2019, DOI: 10.1515/corrrev-2019-0049.

[264] J. Zhao, S. Jafarzadeh, M. Rahmani, Z. Chen, Y. Kim, and F. Bobaru, "A peridynamic model for galvanic corrosion and fracture," *Electrochimica Acta*, vol. 391, p. 138 968, 2021, DOI: 10.1016/j.electacta.2021.138968.

[265] S. Jafarzadeh, J. Zhao, M. Shakouri, and F. Bobaru, "A peridynamic model for crevice corrosion damage," *Electrochimica Acta*, vol. 401, p. 139 512, 2022, DOI: 10.1016/j.electacta.2021.139512.

[266] F. Scabbia, C. Gasparrini, M. Zaccariotto, U. Galvanetto, A. Larios, and F. Bobaru, "Moving interfaces in peridynamic diffusion models and influence of discontinuous initial conditions: Numerical stability and convergence," *Computers and Mathematics with Applications*, 2023, accepted.

[267] P. Seleson, M. Parks, M. Gunzburger, and R. Lehoucq, "Peridynamics as an upscaling of molecular dynamics," *Multiscale Modeling & Simulation*, vol. 8, no. 1, pp. 204–227, 2009, DOI: 10.1137/09074807X.

[268] L. Lapidus and G. Pinder, *Numerical solution of partial differential equations in science and engineering*. John Wiley & Sons, 2011, DOI: 10.1002/9781118032961.

[269] Q. Guan and M. Gunzburger, "Stability and convergence of time-stepping methods for a nonlocal model for diffusion," *Discrete & Continuous Dynamical Systems-Series B*, vol. 20, no. 5, 2015, DOI: 10.3934/dcdsb.2015.20.1315.

[270] Q. Guan and M. Gunzburger, "Stability and accuracy of time-stepping schemes and dispersion relations for a nonlocal wave equation," *Numerical Methods for Partial Differential Equations*, vol. 31, no. 2, pp. 500–516, 2015, DOI: 10.1002/num.21931.

[271] A. Yaghoobi and M. Chorzepa, "Formulation of symmetry boundary modeling in non-ordinary state-based peridynamics and coupling with finite element analysis," *Mathematics and Mechanics of Solids*, vol. 23, no. 8, pp. 1156–1176, 2018, DOI: 10.1177/1081286517711495.

[272] P. Roache, "The method of manufactured solutions for code verification," in *Computer Simulation Validation*, DOI: 10.1007/978-3-319-70766-2_12, Springer, 2019, pp. 295–318.

[273] S. Larsson and V. Thomée, *Partial differential equations with numerical methods*. Springer, 2003, vol. 45, DOI:10.1007/978-3-540-88706-5.

[274] S. Maloy, K. Natesan, D. Holcomb, C. Fazio, and P. Yvon, "Overview of reactor systems and operational environments for structural materials in Gen-IV fission reactors," in *Structural Alloys for Nuclear Energy Applications*, DOI: 10.1016/B978-0-12-397046-6.00002-2, Elsevier, 2019, pp. 23–49.

[275] K. Verfondern, H. Nabielek, and J. Kendall, "Coated particle fuel for high temperature gas cooled reactors," *Nuclear Engineering and Technology*, vol. 39, no. 5, p. 603, 2007, DOI: 10.5516/NET.2007.39.5.603.

[276] Y. Katoh, G. Vasudevamurthy, T. Nozawa, and L. Snead, "Properties of zirconium carbide for nuclear fuel applications," *Journal of Nuclear Materials*, vol. 441, no. 1-3, pp. 718–742, 2013, DOI: 10.1016/j.jnucmat.2013.05.037.

[277] C. Gasparrini, D. Rana, N. Le Brun, D. Horlait, C. Markides, I. Farnan, and W. Lee, "On the stoichiometry of zirconium carbide," *Scientific Reports*, vol. 10, no. 1, p. 6347, 2020, DOI: 10.1038/s41598-020-63037-0.

[278] T. Davey and Y. Chen, "The effect of oxygen impurities on the stability and structural properties of vacancy-ordered and -disordered ZrCx," *RSC Advances*, vol. 12, no. 6, pp. 3198–3215, 2022, DOI: 10.1039/D1RA07768F.

[279] C. Gasparrini, R. Podor, D. Horlait, M. Rushton, O. Fiquet, and W. Lee, "Oxidation of UC: An in situ high temperature environmental scanning electron microscopy study," *Journal of Nuclear Materials*, vol. 494, pp. 127–137, 2017, DOI: 10.1016/j.jnucmat.2017.07.016.

[280] C. Gasparrini, R. Podor, O. Fiquet, D. Horlait, S. May, M. Wenman, and W. Lee, "Uranium carbide oxidation from 873 K to 1173 K," *Corrosion Science*, vol. 151, pp. 44–56, 2019, DOI: 10.1016/j.corsci.2019.01.044.

[281] A. Paul, J. Binner, and B. Vaidhyanathan, "UHTC composites for hypersonic applications," *Ultra-High Temperature Ceramics: Materials for Extreme Environment Applications*, pp. 144–166, 2014, DOI: 10.1002/9781118700853.ch7.

[282] P. Platt, P. Frankel, M. Gass, R. Howells, and M. Preuss, "Finite element analysis of the tetragonal to monoclinic phase transformation during oxidation of zirconium alloys," *Journal of Nuclear Materials*, vol. 454, no. 1-3, pp. 290–297, 2014, DOI: 10.1016/j.jnucmat.2014.08.020.

[283] M. Pettinà, R. Harrison, L. Vandeperre, F. Biglari, P. Brown, W. Lee, and K. Nikbin, "Diffusion-based and creep continuum damage modelling of crack formation during high temperature oxidation of ZrN ceramics," *Journal of the European Ceramic Society*, vol. 36, no. 9, pp. 2341–2349, 2016, DOI: 10.1016/j.jeurceramsoc.2015.11.023.

[284] A. Vasenkov, "Multi-physics peridynamic modeling of damage processes in protective coatings," *Journal of Peridynamics and Nonlocal Modeling*, vol. 3, no. 2, pp. 167–183, 2021, DOI: 10.1007/s42102-020-00046-7.

[285] D. Behera, P. Roy, E. Madenci, and S. Oterkus, "Prediction of thermal oxidation damage in polymers by using peridynamics," in *2021 IEEE 71st Electronic Components and Technology Conference (ECTC)*, DOI: 10.1109/ECTC32696.2021.00232, IEEE, 2021, pp. 1457–1463.

[286] P. Platt, R. Mella, W. DeMaio, M. Preuss, and M. Wenman, "Peridynamic simulations of the tetragonal to monoclinic phase transformation in zirconium dioxide," *Computational Materials Science*, vol. 140, pp. 322–333, 2017, DOI: 10.1016/j.commatsci.2017.09.001.

[287] T. Haynes, A. Battistini, A. Leide, D. Liu, L. Jones, D. Shepherd, and M. Wenman, "Peridynamic modelling of cracking in TRISO particles for high temperature reactors," *Journal of Nuclear Materials*, p. 154 283, 2023, DOI: 10.1016/j.jnucmat.2023.154283.

[288] M. Pharr, K. Zhao, X. Wang, Z. Suo, and J. Vlassak, "Kinetics of initial lithiation of crystalline silicon electrodes of lithium-ion batteries," *Nano Letters*, vol. 12, no. 9, pp. 5039–5047, 2012, DOI: 10.1021/nl302841y.

[289] M. Pharr, Z. Suo, and J. Vlassak, "Measurements of the fracture energy of lithiated silicon electrodes of Li-ion batteries," *Nano Letters*, vol. 13, no. 11, pp. 5570–5577, 2013, DOI: 10.1021/nl403197m.

[290] S. Huang, F. Fan, J. Li, S. Zhang, and T. Zhu, "Stress generation during lithiation of high-capacity electrode particles in lithium ion batteries," *Acta Materialia*, vol. 61, no. 12, pp. 4354–4364, 2013, DOI: 10.1016/j.actamat.2013.04.007.

[291] Z. Ma, T. Li, Y. Huang, J. Liu, Y. Zhou, and D. Xue, "Critical silicon-anode size for averting lithiation-induced mechanical failure of lithium-ion batteries," *RSC Advances*, vol. 3, no. 20, pp. 7398–7402, 2013, DOI: 10.1039/C3RA41052H.

[292] C. Becker, K. Strawhecker, Q. McAllister, and C. Lundgren, "In situ atomic force microscopy of lithiation and delithiation of silicon nanostructures for lithium ion batteries," *ACS Nano*, vol. 7, no. 10, pp. 9173–9182, 2013, DOI: 10.1021/nn4037909.

[293] H. Cho, M. Glazer, Q. Xu, H. Han, and D. Dunand, "Numerical and experimental investigation of (de)lithiation-induced strains in bicontinuous silicon-coated nickel inverse opal anodes," *Acta Materialia*, vol. 107, pp. 289–297, 2016, DOI: 10.1016/j.actamat.2016.01.064.

[294] F. Shi, Z. Song, P. Ross, G. Somorjai, R. Ritchie, and K. Komvopoulos, "Failure mechanisms of single-crystal silicon electrodes in lithium-ion batteries," *Nature Communications*, vol. 7, no. 1, p. 11 886, 2016, DOI: 10.1038/ncomms11886.

[295] S. Zhang, "Chemomechanical modeling of lithiation-induced failure in high-volume-change electrode materials for lithium ion batteries," *NPJ Computational Materials*, vol. 3, no. 1, p. 7, 2017, DOI: 10.1038/s41524-017-0009-z.

[296] S. Basu, N. Koratkar, and Y. Shi, "Structural transformation and embrittlement during lithiation and delithiation cycles in an amorphous silicon electrode," *Acta Materialia*, vol. 175, pp. 11–20, 2019, DOI: 10.1016/j.actamat.2019.05.055.

[297] Z. Zhang, N. Liao, H. Zhou, and W. Xue, "Insight into silicon-carbon multilayer films as anode materials for lithium-ion batteries: A combined experimental and first principles study," *Acta Materialia*, vol. 178, pp. 173–178, 2019, DOI: 10.1016/j.actamat.2019.08.009.

[298] Z. Chen, S. Jafarzadeh, J. Zhao, and F. Bobaru, "A coupled mechano-chemical peridynamic model for pit-to-crack transition in stress-corrosion cracking," *Journal of the Mechanics and Physics of Solids*, vol. 146, p. 104 203, 2021, DOI: 10.1016/j.jmps.2020.104203.

[299] W. Dong, H. Liu, J. Du, X. Zhang, M. Huang, Z. Li, Z. Chen, and F. Bobaru, "A peridynamic approach to solving general discrete dislocation dynamics problems in plasticity and fracture: Part II. Applications," *International Journal of Plasticity*, vol. 159, p. 103 462, 2022, DOI: 10.1016/j.ijplas.2022.103462.

[300] P. Qiao, M. Yang, and F. Bobaru, "Impact mechanics and high-energy absorbing materials," *Journal of Aerospace Engineering*, vol. 21, no. 4, pp. 235–248, 2008, DOI: 10.1061/(ASCE)0893-1321(2008)21:4(235).

[301] G. Zhang, G. Gazonas, and F. Bobaru, "Supershear damage propagation and sub-Rayleigh crack growth from edge-on impact: A peridynamic analysis," *International Journal of Impact Engineering*, vol. 113, pp. 73–87, 2018, DOI: 10.1016/j.ijimpeng.2017.11.010.

[302] C. Gasparrini, "Oxidation of zirconium and uranium carbides," *Ph.D. thesis*, 2018, DOI: 10.25560/59006.